

Making sustainable aluminum by recycling scrap: The science of “dirty” alloys



Dierk Raabe^{a,*}, Dirk Ponge^a, Peter J. Uggowitzer^b, Moritz Roscher^a, Mario Paolantonio^a, Chuanlai Liu^a, Helmut Antrekowitsch^b, Ernst Kozeschnik^c, David Seidmann^d, Baptiste Gault^{a,e}, Frédéric De Geuser^f, Alexis Deschamps^f, Christopher Hutchinson^g, Chunhui Liu^h, Zhiming Liⁱ, Philip Prangnell^j, Joseph Robson^j, Pratheek Shanthraj^j, Samad Vakili^a, Chad Sinclair^k, Laure Bourgeois^l, Stefan Pogatscher^{m,*}

^a Max-Planck-Institut für Eisenforschung, Max-Planck-Str. 1, 40237 Düsseldorf, Germany

^b Chair of Nonferrous Metallurgy, Montanuniversität Leoben, Franz-Josef-Str. 18, 8700 Leoben, Austria

^c Institute of Materials Science and Technology, Technische Universität Wien, Getreidemarkt 9, 1060 Wien, Austria

^d Northwestern University, Cook Hall, 2220 Campus Drive, Evanston, IL 60208, USA

^e Department of Materials, Imperial College, South Kensington, London SW7 2AZ, UK

^f Univ. Grenoble Alpes, CNRS, Grenoble INP, SIMAP, F-38000 Grenoble, France

^g Department of Materials Science and Engineering, Monash University, Room 249, Building 82, Clayton Campus, Clayton, VIC 3800, Australia

^h Light Alloy Research Institute, State Key Laboratory of High-Performance Complex Manufacturing, Central South University, Changsha 410083, China

ⁱ School of Materials Science and Engineering, Central South University, Changsha 410083, China

^j Henry Royce Institute, University of Manchester, Royce Hub Building, Manchester M13 9PL, UK

^k Department of Materials Engineering, The University of British Columbia, 309-6350 Stores Rd., Vancouver V6T 1Z4, Canada

^l Monash Centre for Electron Microscopy, and Department of Materials Science and Engineering, Monash University, Victoria 3800, Australia

^m Christian Doppler Laboratory for Advanced Aluminum Alloys, Chair of Nonferrous Metallurgy, Montanuniversität Leoben, Franz-Josef-Str. 18, 8700 Leoben, Austria

ARTICLE INFO

Keywords:

Aluminum
Alloy design
Precipitation
Sustainability
Recycling
Properties
Processing
Corrosion
Thermodynamics

ABSTRACT

There are several facets of aluminum when it comes to sustainability. While it helps to save fuel due to its low density, producing it from ores is very energy-intensive. Recycling it shifts the balance towards higher sustainability, because the energy needed to melt aluminum from scrap is only about 5% of that consumed in ore reduction. The amount of aluminum available for recycling is estimated to double by 2050. This offers an opportunity to bring the metallurgical sector closer to a circular economy. A challenge is that large amounts of scrap are post-consumer scrap, containing high levels of elemental contamination. This has to be taken into account in more sustainable alloy design strategies. A “green aluminum” trend has already triggered a new trading platform for low-carbon aluminum at the London Metal Exchange (2020). The trend may lead to limits on the use of less-sustainable materials in future products. The shift from primary synthesis (ore reduction) to secondary synthesis (scrap melting) requires to gain better understanding of how multiple scrap-related contaminant elements act on aluminum alloys and how future alloys can be designed upfront to become scrap-compatible and composition-tolerant. The paper

* Corresponding authors.

E-mail addresses: d.raabe@mpie.de (D. Raabe), stefan.pogatscher@unileoben.ac.at (S. Pogatscher).

therefore discusses the influence of scrap-related impurities on the thermodynamics and kinetics of precipitation reactions and their mechanical and electrochemical effects; impurity effects on precipitation-free zones around grain boundaries; their effects on casting microstructures; and the possibilities presented by adjusting processing parameters and the associated mechanical, functional and chemical properties. The objective is to foster the design and production of aluminum alloys with the highest possible scrap fractions, using even low-quality scrap and scrap types which match only a few target alloys when recycled.

1. Introduction and motivation for scrap-based aluminum alloys

About 100 Mt (million metric tons) of aluminum are currently produced per year, ~35% of which comes from scrap while ~40% has already been scrapped in the manufacturing chain [1,2]. Aluminum is a material with two facets when it comes to sustainability [3,4]. On the one hand, it reduces energy consumption in products and processes, e.g. in lightweight transport, packaging and construction, due to its low mass density (2.7 kg dm^{-3}). It is also used for low-resistive, low-weight electrical conduction, as with $37 \times 10^6 \text{ A (Vm)}^{-1}$ it reaches 64% of the conductivity of pure Cu with about 3 times less mass. On the other hand, aluminum is also one of the greatest greenhouse gas (GHG) producers and energy-intensive industrial metals produced from ores [5,6]. Its GHG emissions include carbon dioxide, methane, nitrous oxides, hydrofluorocarbons, perfluorocarbons and sulphur hexafluoride. Globally, aluminum production contributes ~3% of all GHG emissions (~15% of all emissions in the industrial sector), with a ca. 1.1 Gt carbon dioxide equivalent per year [1,7,8]. This means that aluminum from primary production generates about 12–16.5 t of GHG per t of metal produced [1,3,9–12]. About 65% of these emissions occur because ~67% of the electricity used for electrolysis is produced from fossil fuels [1,9,13,14]. Aluminum production requires ~13 Exa J energy per year, which is ~1% of total global energy consumption [14]. The synthesis of aluminum also creates multiple harmful by-products during mining and electrolysis [3]. This impact is accelerating due to growing population (and the growth of the middle class, now about half of the total population) and per-capita consumption of aluminum, which is driven by several current trends in transportation, urbanization, electrification and manufacturing. For the first time in history the production of aluminum is now facing sustainability limits (see Fig. 1).

Aluminum is an infinitely recyclable material [21–24]: today, about 75% of all the aluminum produced in history – nearly a billion metric tons – is still in use [25,26]. Recycling involves re-melting the metal, which requires only 5% of the energy used to make new aluminum from bauxite ore [6]: the primary synthesis of Al from ores expends 45 kWh/kg because of the large enthalpy of its oxide, and about 12 kg CO₂/kg, while re-melting Al scrap (secondary synthesis) expends only 2.8 kWh/kg because of its low melting point (660 °C), and about 0.6 kg CO₂/kg [27]. This means that recycling has the potential to shift aluminum's energy and carbon balance substantially towards much greater sustainability [2].

On average, a third of the aluminum used today is produced from recycled scrap [21], although this fraction is predicted to rise to 50% by 2050, according to data (2019) from the International Aluminum Institute (see Fig. 2) [1,9,13]. The huge differences between primary and secondary synthesis in terms of GHG and energy consumption make aluminum alloys, as an important pillar of a circular economy, important subjects for sustainable metallurgy research [4,28,29].

In scrap recycling a differentiation must be made between pre-consumer scrap, produced during manufacturing and often featuring well-defined alloy classification, and mixed, low-quality post-consumer scrap, which must be sorted before remelting (see Fig. 3) [1,2].

A good example of circularity is aluminum beverage cans. In some regions, the recycling rates for such alloy grades reach 95% [30]. However, even though used beverage cans (UBC) are easily collected, have a short lifetime and can theoretically be made of a single

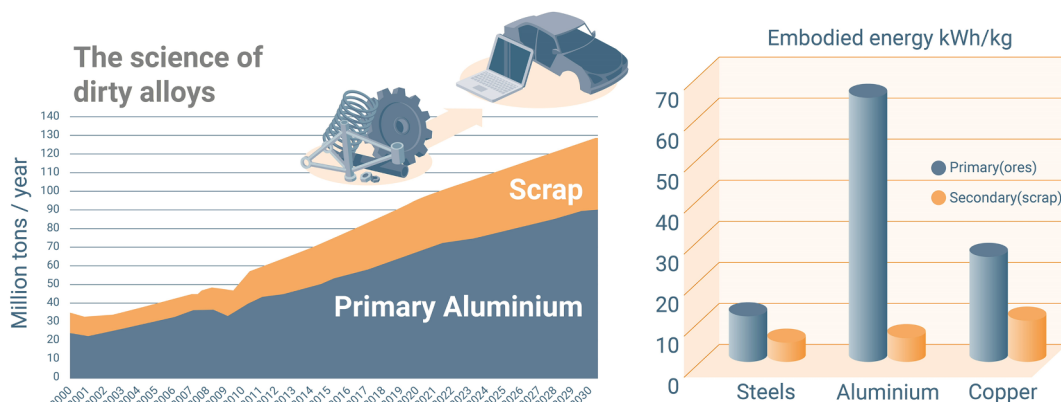


Fig. 1. Aluminum alloys made entirely from scrap can reduce energy consumption and GHG emissions by > 90% compared to alloys made by primary synthesis [1]. Advanced alloy design aims at improving and developing alloys via built-in recyclability, for maximum scrap compatibility and use [15]. On average the values for the embodied energy for primary aluminum production range between 53 and 65 kWh/kg (190–235 MJ / kg), depending on slightly different approximations and year [6,16–20].

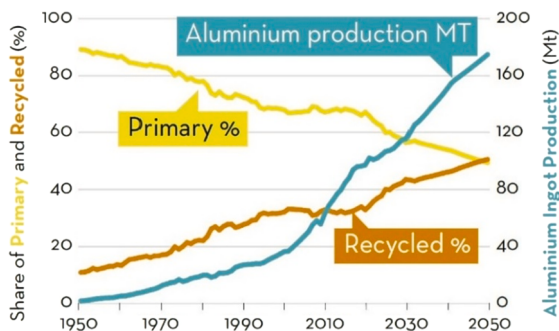


Fig. 2. Development of primary and recycled aluminum through 2050, based on numbers in 2019 for end-of-life product collection rates (data sourced in 2021 from the International Aluminum Institute (IAI)). MT: million metric tons.

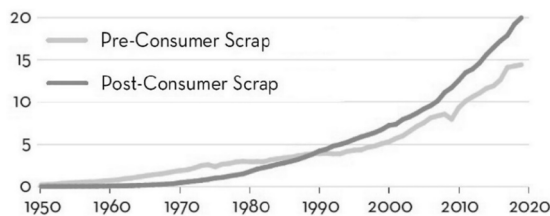


Fig. 3. Development of global aluminum scrap intake in metric tons. Since 1990, post-consumer scrap availability from end-of-life (EOL) products has exceeded pre-consumer scrap (data sourced in 2021 from the International Aluminum Institute (IAI)).

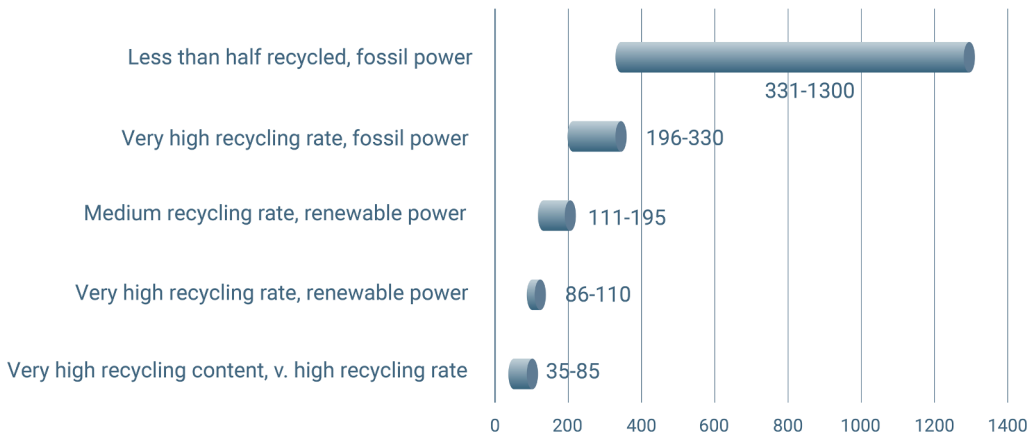


Fig. 4. Carbon footprint of an aluminum can, analysed by Eric Onstad of Reuters, using data from the Carbon Trust. The minimum and maximum values give the grams of CO₂ embedded in a 300 ml standard package unit.

alloy (today two are typically used) [31], the can-to-can cycle is still not a closed loop [30]. An analysis by Reuters, using data from the Carbon Trust, shows that the overall sustainability of aluminum can packaging depends greatly on the recycled fraction and on the origin of the energy used for melting and for generating the additional primary material (see Fig. 4).

The challenge presented by such issues increases exponentially in multi-material products such as vehicles [32-36]. This issue needs to be addressed, because the use of aluminum in cars is increasing. Figures from 2019 indeed show that most post-consumer scrap, in terms of tonnage, now stems from packaging and vehicles (see Fig. 5).

Fig. 6 shows an example where using recycled Al (instead of material from primary synthesis) in a vehicle generates not only a 28% reduction in mass (and therefore fuel) but also a 35% reduction in energy consumption and GHG emissions during manufacture.

Today aluminum recycling is conducted primarily within established alloy classes, and only small scrap tonnages are exchanged among compositionally dissimilar alloy groups [37-40]. The recycling rates for aluminum are generally rather high, but they differ substantially by product, alloy and region, ranging from as low as 20% to as high as 80% for some packaging products [25,26].

The quality, abundance and flow of scrap in this field vary greatly, as do the target alloys and their composition requirements [1]. They range from contaminated and mixed low-price scraps (also referred to as old scrap or post-consumer scrap) and lower-purity-

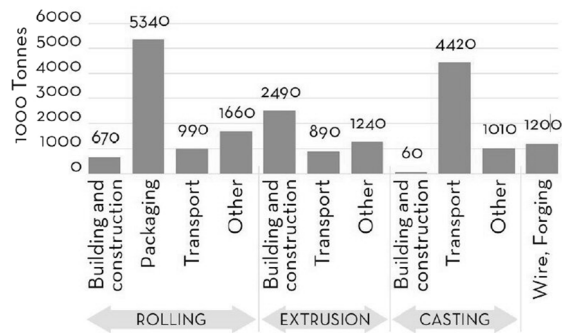


Fig. 5. Numbers from 2019 showing the distribution of the global aluminum post-consumer scrap intake as a function of manufacturing methods and sector (data represent the year 2019; source: the International Aluminum Institute (IAI)).



Fig. 6. Example revealing the dual effect of aluminum alloys made from scrap: weight reduction and the associated fuel savings (left) plus reduction in energy consumption and GHG output from synthesis when using alloys made from scrap (right). Step 1 (data from Al Association) shows how much mass is saved when increasing Al from 9 to 37 wt%. Step 2 shows that this generates a 28% reduction in mass plus a 35% reduction in energy consumption and GHG emission when using scrap-based Al.

sensitive commodity alloys to well-defined high-quality secondary material (retrieved from closed-loop industry processes where little further improvement can be achieved) and very impurity-sensitive high-performance alloys with little tolerance for tramp elements [34,41–43]. It is this variety in the scrap landscape and the great diversity in the types of aluminum alloys used, which set the stage for our investigation of the role of scrap-usage in aluminum alloys and their potential recycling-friendly design. Here several questions are of interest with respect to the metallurgy of these alloys [44]. One set of questions concerns the number and quantities of scrap-related tramp elements that can be tolerated in existing high-performance aluminum alloys, and what can be done to make them more impurity-tolerant while retaining comparable properties [45–47]. The extensive use of scrap for the synthesis of aluminum alloys turns the underlying phase diagrams into multi-component equilibria scenarios: while conventional phase diagrams for alloys reside in low-dimensional composition corners with two or three prevalent alloying elements, the phase diagrams required to design scrap-tolerant alloys may have to juggle up to 15 composition axes. This is particularly important for aluminum alloys, due to their low solubility for most scrap-related tramp elements.

Another set of challenges lies in whether new alloy design strategies might target a compromise between higher scrap usage on the one hand, and modestly reduced properties that satisfy the requirements of a broader range of commodity products on the other. This trade-off could be quantified by balancing the reduction in energy use and GHG production through higher scrap use with performance loss and the associated sustainability reduction when the material is in service. Other questions concern the design of so-called crossover or uni-alloys [48], with chemical overlap between separate alloy classes [34]. If sufficient performance is achieved, such materials would be more recycling-friendly from the outset. Another avenue would be to develop compositionally lean alloys, which realize properties less through fine-tuning of composition than through processing and microstructure tuning. This allows the decoupling of properties from compositions and permits compositionally simple alloys to be more readily recycled and mixed.

The following article addresses the current status of established and novel aluminum alloys and their development, processing and optimization for high performance if we use recycling as the production route. We provide guidelines for creating materials with more built-in recyclability, launching a new field, which we call “sustainability alloy design”. It targets a shift from primary synthesis (reducing ores) to secondary synthesis (melting scrap). In this context it must be emphasized that the amount of energy needed to melt aluminum from scrap is much lower than that needed to reduce ores. It should also be noted that scrap availability, quality and supply

chains obviously impose limits, although markets are currently nowhere near reaching even these [1,49–52]. In Europe, the amount of aluminum available for recycling is estimated to more than double by 2050 [49,53]. However, in this scenario supply chains and increasing costs due to demand growth will also play important roles. This means that a large-scale business such as secondary aluminum production will only prosper if the supply chains for recycled material are logically robust, quality-controlled (in both their pre- and post-consumer scrap fractions and their sorting technology), sufficient in magnitude and economically competitive.

Identifying pathways towards sustainability alloy design requires us to understand how multiple scrap-related contaminant elements act on aluminum alloys, and to utilize the knowledge. Here we have coined a further term: the “science of dirty alloys” (SoDA). This term addresses the fundamental question of how alloys can be designed upfront to be scrap-compatible and composition-tolerant, in order to maximize the use of scrap. Most of the aluminum scrap today is post-consumer scrap [1,2,40,54]. This scrap usually has a high contaminant content, meaning the intrusion of mostly unwanted tramp elements. In other words, most scrap in the next few decades will be “dirty”. This article explores how what initially sounds inauspicious can become the basis for a new and fruitful science.

The article presents and discusses the scientific and engineering tasks required to achieve the goal of a circular aluminum economy. These have been broken down into specific metallurgy research topics such as the influence of scrap-related contaminant elements on the thermodynamics and kinetics of precipitation reactions [55] and their mechanical and electrochemical effects; precipitation free zones around grain boundaries; casting microstructures; the adjustments required in processing parameters; and the resulting mechanical, functional and chemical properties. We also review advanced experimental methods to identify the partitioning of tramp elements among lattice defects, precipitates and the matrix and the associated effects on precipitation kinetics, thermodynamics and mechanical response. We follow two main research directions. One involves an asymptotic approach, where we evaluate how to improve existing alloys and make them more scrap-tolerant. The other, where we discuss ideas for developing new generations of compositionally robust and lean alloys that are more scrap-tolerant from the outset, is more disruptive. Ultimately we wish to steer the design and production of aluminum alloys towards using the highest possible scrap fractions, low-quality post-consumer scrap, and scrap types which serve only a few matching target alloys when recycled.

The “green aluminum” trend (encompassing both primary synthesis on the basis of hydropower and scrap in conjunction with recycling) resonates with international markets. The London Metal Exchange announced in June 2020 a new trading platform for sustainable aluminum. The future may see a scenario where alloys that fail to achieve a certain level of sustainability face limitations on use in products. Investor, consumer and legislative pressure is intensifying on industries which pollute, and manufacturers are increasingly being forced to source materials responsibly. These trends are starting to create premium markets in cleaner-footprint metal, and sustainable metallurgy is attracting market awareness in turn.

Exploring SoDA – the science behind sustainable metallurgy and green alloys – in this way can guide the development of a generation of more sustainable metallic materials. This will contribute not only to the metallurgical science, but also to a more sustainable society and a circular economy where sustainable materials can be translated into successful, safe, high-performance products that meet the highest quality standards.

2. What defines a sustainable aluminum alloy?

2.1. Sustainability and circular economy measures for aluminum alloys

To frame the leverage effects of individual sustainability measures, we first need to describe what defines a sustainable aluminum alloy. Several academic studies, legislative measures and industry-driven initiatives have made suggestions for defining sustainable metallic alloys, processes and elements of a corresponding circular metallurgical economy [3,15,56,57]. This section applies the essence of these suggestions to aluminum alloys.

The sustainability of materials must be broadly defined [10,18,22,58]. It needs to consider the environmentally relevant aspects associated with mining, processing, chemistry, waste and by-product treatment. It has to include energetic, recycling and metallurgical aspects, the amount of material scrapped during manufacturing, and the responsible and lean use of alloying elements [37,40,59,60]. It must also incorporate social, ethical and work standards. These dimensions must be applied to the entire product and to supply chain pathways, and must include implementation of sustainability risk analysis and risk mitigation strategies. These must be transparent, well-documented and quantifiable by internationally acknowledged standardization methods, since the market for aluminum and aluminum products is global. This requires transparent life cycle assessments (LCA) based on data and boundaries that are agreed upon by research and economic associations, customers, legislators and standardization boards [58,61–63]. The tracking of sustainability measures must be extended over the entire value chain. For the specific case of aluminum this involves all stages of mining, production and processing, including bauxite mining and transport; alumina refining; primary and secondary aluminum production including energy sources; red mud treatment and waste management; semi-finished processing such as casting, hot rolling, cold rolling, heat treatment, extrusion and forging; and the minimization, collection, alloy-specific sorting, refining and re-melting of scrap [15,41,52,64].

The colossal production, GHG, scrap and energy figures outlined above speak for themselves and illustrate the urgency of this approach. It is also important to identify the measures that have the biggest effects on the sustainability of aluminum alloys. For different alloy groups, Fig. 7 shows the technology readiness level (TRL) versus scaled potential for the impact of different sustainability measures throughout value chains [3]. In the specific case of aluminum alloys, using electrical energy from renewable resources such as hydropower leverages the highest impact at high TRL, making it one of the most efficient measures. Particularly in the area of primary synthesis, aluminum production can only get as sustainable as the power source used to operate electrolysis [65–67] (see Fig. 4). This reflects the trend in the market, which shows that primary aluminum synthesis from renewable energy sources,

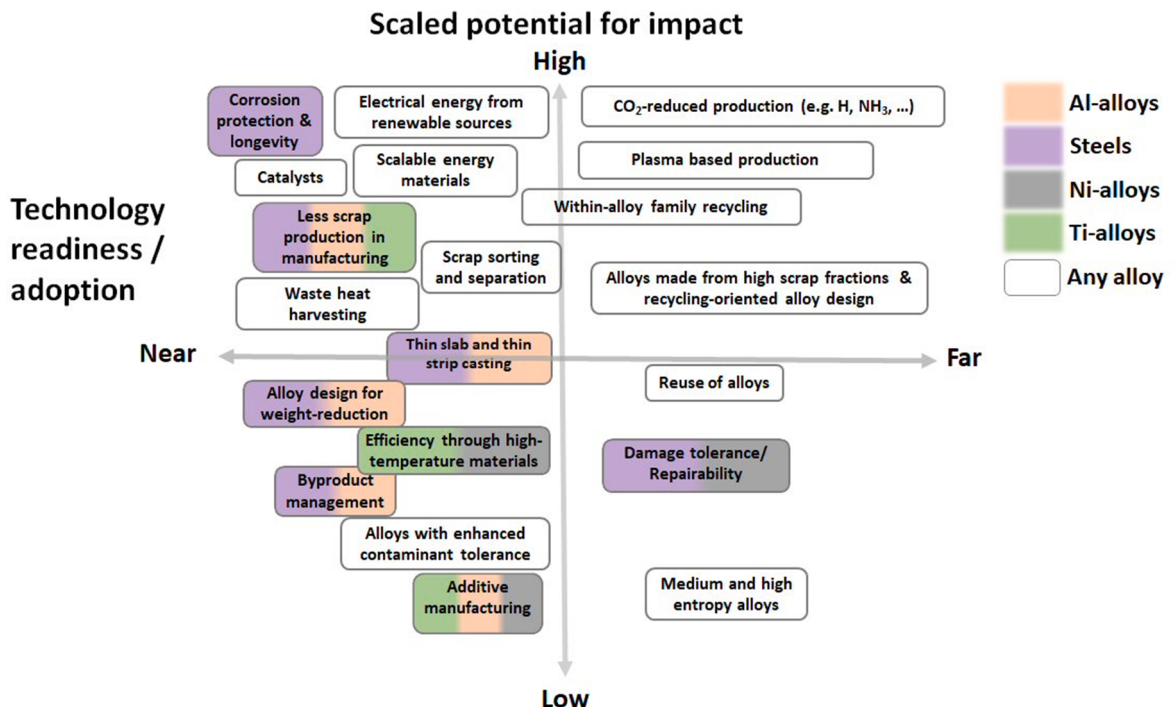


Fig. 7. Technology readiness and scaled potential for impact of different sustainability measures throughout the value chains of different alloy groups. Modified version reproduced with permission from [3].

particularly from hydropower, has in some regions advanced market share (see Fig. 8) [13].

High leverage for improved sustainability also comes from electrification (from renewable sources) and avoidance of CO₂ related energy and heating sources for the entire downstream manufacturing chain that follows primary smelting. One trend, for instance, is to use hydrogen-based energy carriers instead of fossil fuels to heat furnaces.

Further sustainability measures with high leverage but different degrees of technology readiness are shown in Fig. 7. They are related to the main topic of this paper, i.e. secondary synthesis [68,69]. They include measures associated with the role of scrap-related tramp elements and scrap-compatible alloy design [4,28,70]. The impact analysis suggests that strong leverage is expected from advanced and machine-learning-assisted scrap sorting and separation techniques; the general increase in scrap fractions used in alloys (where scrap collected during or after production, and post-consumer scrap, must be separated from each other); upfront recycling-oriented alloy design; reduced chipping and scrapping during manufacturing; and within-alloy-family recycling.

If we consider the origin and sustainability of energy sources (for both primary and secondary synthesis), the quantity and quality

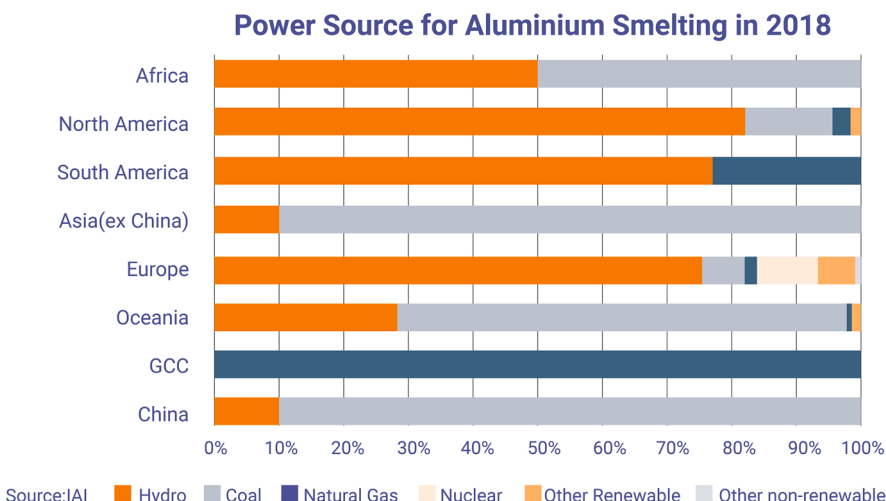


Fig. 8. Power sources for primary aluminum synthesis by electrolysis, plotted after data from the International Aluminum Institute (IAI) [13].

of the scrap and the impact of mining and labour conditions (evaluated on the basis of transparent and quantitative LCA validation methods), it becomes apparent that a sustainable alloy does not necessarily have to be based on secondary synthesis. However, in most cases secondary synthesis provides considerable benefits, as LCAs show [41,52,61]. It is therefore conceivable that one and the same alloy can be produced with very different levels of sustainability. This underlines the fact that commonly accepted standards must be introduced to document the origin and sustainability of the material before it is used in products or processes.

[Fig. 7](#) also suggests that for both primary and secondary synthesis, downstream production benefits from deploying manufacturing processes with low energy consumption. These can involve avoidance of re-heating of melts and slabs; lower thickness reduction in sheet manufacturing; temperature and time optimized heat treatments; and near-net-shape casting processes. Such methods are also advantageous in that the coarse intermetallic precipitates that can form in materials with high scrap-related impurity intrusion remain smaller than in conventional thick slab casting.

Kümmerer et al. [57] have translated these aspects into rules for the integration of chemical and materials products and processes into a circular economy. Although formulated for all material classes, many of these rules also apply to aluminum. One rule suggests keeping the chemical complexity and number of components used in materials to the minimum required for achieving a certain performance. This should include recycling and all end-of-life considerations. Increasing chemical complexity requires more complex synthesis pathways and makes recycling more challenging. Another rule suggests building recycling considerations upfront into material design, manufacturing processes and scrap collection streams, including auxiliaries, unused substrates and – for aluminum – particular by-products such as red mud. Further rules suggest reducing alloy, material and product diversity, dynamics and flows, and making alloys with the lowest possible resource intensity. This can in fact be realized in the case of aluminum alloys made from scrap, which are also suitable to serve as scrap in new alloys. In this article reduction in product diversity is addressed in the section on uni- or crossover alloys [48]. This is a new alloy design concept which aims to unify in one material the properties of several alloy types with originally different compositions.

Reaching higher circularity for aluminum also requires bringing the innovation speed for new alloys and products into better synchrony with the speed of recycling. In particular, the use of rare and expensive alloy ingredients should be reduced; if they are required, they must be suitable for efficient recovery and recycling to prevent their gradual loss and dissipation as landfill. The authors called such scenarios “entropic losses” [46,71,72].

Something else that should be avoided are so-called “rebound effects” [57]. These can arise when sustainable technologies are applied that on the one hand help to reduce GHG emissions, but on the other generate higher demand for the metals needed for the technology. Examples are wind parks, photovoltaics and the electrification of transport and industry: manufacturing all of the involved parts and the associated infrastructures to put these technologies into service over the next few decades will require substantial additional amounts of metal and production processes which can be very carbon-intense. LCAs must take into account such unintended leverage effects. The rule that circular metrics should be developed and adopted by the producer and customer community, encompassing responsibility for toxic waste or the use of by-products, can engender similar effects. Using fewer high-strength aluminum alloys, for example, could in some applications lead to greater use of stainless steels, carbon-fiber-reinforced composites or titanium alloys – i.e. materials which can generate even higher energy costs and GHG emissions.

Producers should also take full responsibility for their alloys and products throughout their respective life cycles. This includes recycling protocols. Digital measures might be involved, such as digital passports which carry traceable, transparent and forgery-proof information on alloy composition and production and manufacturing processes. Finally, processing could be simplified. For aluminum this means that processing has to be streamlined for efficiency, e.g. avoiding homogenization treatments where appropriate, and favoring temperature- and time-optimized annealing treatments. Of considerable importance are also near-net-shape and thin-strip casting, i.e. avoidance of energy losses due to unnecessary cooling and re-heating through just-in-time workflows. Other efficiency measures include the flexible operation of electrolysis cells. This approach uses electrical power when smart grids provide inexpensive surplus energy and/or when ample sustainable energy is available, such as on windy or sunny days. Similar advantages are provided by just-in-time delivery of pre-alloyed liquid material (rather than pre-alloyed slabs) to customers. This turns liquid aluminum alloys into batteries, as their high heat capacity stores huge amounts of energy efficiently, thereby qualifying the technique as an efficient means of buffering power.

The essence of the rules suggested by Kümmerer et al. is summarized in [Table 1](#). In the case of aluminum this means that certain community-agreed limits on GHG emissions, energy consumption, waste and by-products must be adhered to if a material is to qualify as a sustainable alloy. This leverages the use of the most efficient processing methods.

On the metallurgical side, the essence of the rules is that alloys must be designed from the outset to be impurity-tolerant, making them suitable for high levels of recycled content. This would mean that they can be collected and used again as scrap in the most compatible way possible for the secondary synthesis of new alloys, i.e. without poisoning the latter [28]. Thus the title of the current paper, “the science of dirty alloys”. In other words, sustainable alloys should be “scrap-compatible”, and designed not for single use but rather for repeated use and recycling. This means that scrap-compatible alloys must be created which accept maximum scrap content when synthesized, i.e. they must be tolerant of tramp elements and minor composition variations, including rare impurities stemming e.g. from mixed post-consumer, automotive and electronic scrap.

Impurity tolerance is particularly important in the design of aluminum alloys. This is because aluminum, unlike many steels, has small solubility for many elements (except Mg and Zn) (see [Fig. 9](#)) [73–75]. This means that intermetallic phases form more readily than in many transition metal alloys when contamination by tramp elements occurs. In conventional alloys, modest changes in the solid solution state are usually associated with relatively modest property changes, while altering the material’s precipitation state can be more disruptive and cause brittleness, corrosion or hydrogen embrittlement.

The low solubility of aluminum for tramp elements suggests that from a sustainability perspective compositionally lean alloys are

Table 1

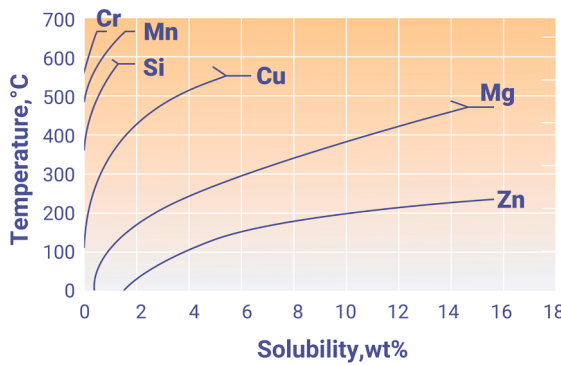
Elements of a circular economy applied to aluminum alloys.

Circular economy measures related to aluminum alloys		
General	Specific	Metallurgical and engineering measures
Use of renewable energy sources and responsible use of resources	Use of renewable energy sources	Transition to use of hydro-, solar and wind power for electrolysis and manufacturing
	Use of sources with reduced GHG emissions	Avoidance of carbon carriers as fuels for re-heating, aging heat treatments and related processes
	Energy efficient processes	Use of high scrap fractions in alloys; near-net-shape manufacturing; thin-slab casting; thin-strip casting; reduction of required thickness; in-line processing, i.e. avoidance of reheating of melts and slabs through just-in-time inter-process logistics; low-temperature heat treatments
	Waste and by-product management	Responsible deposition or recycling of mining and metallurgical waste by-products and of toxic substances; reduced use of products, additives and by-products that cannot be separated and recycled
	Adherence to social and ethical standards	Absence of child and slave-like labour; appropriate salary and commitment to labour and union rights; fair working conditions and payment; adherence to inclusion and diversity standards; professional development and career training; adequate equal opportunity and diversity measures
	Process simplification and product portfolio streamlining	Develop process workflows with minimum number of process steps, auxiliaries and energy requirements; develop low-temperature warm rolling protocols, omit/optimize homogenization, low temperature annealing treatments; reduce product diversity
	Quantification of measures by life cycle assessment	Develop and apply suitable metrics that capture and quantify sustainability measures; make results of such calculations open
	Responsible use of alloying elements	Use alloying elements with low energy and GHG footprint; reduce use of critical alloying elements; ensure efficient recovery and recycling of critical alloying elements; reduce alloy complexity in terms of required processing and chemical composition
	Circular economy business models	Develop closed-loop business models with customers
	Advanced scrap sorting	Automated chipping, spectroscopy and artificial-intelligence-assisted alloy detection, classification and sorting
Scrap management	Avoidance of scrap during manufacturing	Product and process design for less scrap
	In-production scrap collection	Alloy-specific scrap collection during synthesis and manufacturing; develop processes to collect and sort scrap during production
	Post-consumer scrap use	Develop low-grade and composition-tolerant alloys and identify products that can accommodate higher scrap-related contaminant content in alloys
	Green branding for alloys containing high levels of scrap	Develop marketing methods to brand high-scrap-content alloys
	Digital twin of products and processes	
Digitalization	Improvement of databases	Thermodynamic, kinetic, process and mechanical simulations for knowledge-based sustainable design of alloys, processes and products; identify thermodynamic, kinetic and mechanical limits of tramp-related effects; establish lifetime and corrosion simulations for higher product longevity; higher digitalization degree of manufacturing enables better tracking and management of material, scrap and by-product flows; sustainability considerations and quantitative life-cycle-relevant measures should become an integral part of digitalization, sensoring and tracking strategy
	Digital material and product passports	Maintenance and improvement of thermodynamic and kinetic databases to include scrap-related tramp elements, specifically taking into account metastable and intermetallic phases and contaminant effects on vacancies
		Alloys and products should be fully traceable, e.g. by using product- and alloy-specific digital passports and history trackers that include the composition of products, components, and processes; this also implies claiming responsibility and an awareness of the history of products throughout their life cycles, including recycling; establish digital tracking and digital workflows with customers; using digital material passports for chemical composition of products, components, and processes can become part of product marketing to demonstrate and “brand” sustainable products and processes
Alloy design	Novel approaches to sustainable alloy design	Most compositions in use today were developed many decades ago. With today's understanding of physical metallurgy, thermodynamics and kinetics, new opportunities in sustainable alloy design are emerging
	Lean alloys	Design of alloys with minimal use of processing steps and chemical ingredients; achieve properties more by microstructure and less by composition adjustment
	Less use of harmful and critical alloying elements	Selection of alloying elements according to lowest energy consumption and GHG production; avoidance of rare and less-responsible elements as ingredients
	Fewer alloys	Design of uni-alloys and crossover alloys that combine usually separated or even contradictory features of different alloys or different alloy classes
	Scrap-tolerant alloys	Design of alloys for high-scrap-related tramp element content
	High-strength alloys	Alloys that enable reduced vehicle weights and enhanced fuel efficiency

(continued on next page)

Table 1 (continued)

Circular economy measures related to aluminum alloys		
General	Specific	Metallurgical and engineering measures
Product use	Recycling as part of alloy design	Ensure that alloys and by-products can be collected and recycled; recyclability should be an integral part of alloy and process design and that of scrap collection loops in-house and with customers; processes and alloys should be designed for optimal material recovery of auxiliaries, scrap and unintended by-products
	Longevity	Alloys with high resistance to corrosion, hydrogen embrittlement and abrasion
	Damage tolerance and self-repair Use optimization	Alloys with high damage tolerance and self-healing properties Re-manufacturing, repair, reuse and sharing of products

**Fig. 9.** Solubility limits of tramp and alloying elements in aluminum [73].

generally preferable to over-alloyed materials as acceptors and donators of scrap. It is a general feature and an advantage of structural alloys that they obtain many of their mechanical properties primarily through microstructure. This means that what matters is not only global composition, but the way it helps to realize specific microstructures. Of course, certain effects such as precipitate formation do not occur without alloying, but the fine-tuning of properties (which today often takes place through composition adjustment) can in part be replaced by the tweaking of microstructure, for two main reasons. First, composition is a conserved quantity, while microstructure does not depend on conservation laws. This means that any alteration of an alloy through composition adjustment will reappear in the form of a modified mass balance somewhere in a circular economy, as every single atom is conserved. This does not apply to microstructure, which can be modified over multiple orders of magnitude in terms of dislocation density, grain size, precipitate dispersion, clusters or crystallographic textures without hindrance from any conservation law except mass balance. Second, tweaking microstructure is very efficient for improving mechanical properties. Among the various microstructure-based hardening and ductilization methods, controlling and increasing precipitate dispersion (at given total volume of precipitates) are effective because, due to the high mobility of the dislocations in Al-alloys, they reduce the mean free path of the gliding dislocations (which translates inversely into strength increase) to much lower values than do grain size control, dislocation cell size control or strain hardening alone. Formability, strength and surface appearance can also be substantially influenced by the crystallographic texture.

The effectiveness of microstructure control is seen in Fig. 10, where the yield strength is plotted for a variety of commercial wrought aluminum alloys as a function of both chemical composition and microstructure variation [74]. The compilation shows that a variation in strength of up to 50% is achieved for the same composition. Alloys of the 1xxx group, on the left-hand side, are relatively pure packaging grades. The 3xxx series alloys, blended primarily with manganese, serve in cans and buildings. Next are the medium-strength alloys, the 5xxx and 6xxx series. Alloys of the 5xxx series are essentially blended with magnesium, while those of the 6xxx series use magnesium and silicon. These two alloy classes are deployed in large quantities in vehicles, mobile phones and computers [76–80]. 2xxx alloys use copper as their primary alloying element. They serve mostly in highly mechanically loaded parts in the aerospace sector. Even higher strength levels can be achieved if aluminum is doped with copper, zinc, and magnesium, producing the 7xxx alloys. These are used in electrical vehicles and aerospace applications. This means that from left to right, most increases in strength are obtained by adjusting chemical compositions, together with the corresponding heat treatment required to achieve the desired nano-precipitation state. In essence Fig. 10 thus shows that in many of the high-strength aluminum alloys a broad range of tensile strengths can be obtained by adequate adjustment of microstructures rather than alterations in chemistry.

Opportunities for improved microstructure control lie in the development of more complex thermal treatments in particular. Fifty years ago, when most alloys in use today were originally developed, the thermal profiles deployed for precipitation heat treatments were quite simple as far as ramps, isothermal holding and cooling are concerned [55,81]. An important consideration in the development of well-tailored future thermal treatments is the large scope for designing composition-specific and non-isothermal thermal profiles to control precipitation and increase efficiency in advanced microstructure and property design [82–85]. Such heat treatments have to be robustly tolerant of scrap-related impurities and their effect on solutionising and precipitation.

Crossover alloys [48], also referred to as uni-alloys, occupy a special niche, as they aim to merge existing alloy concepts to make

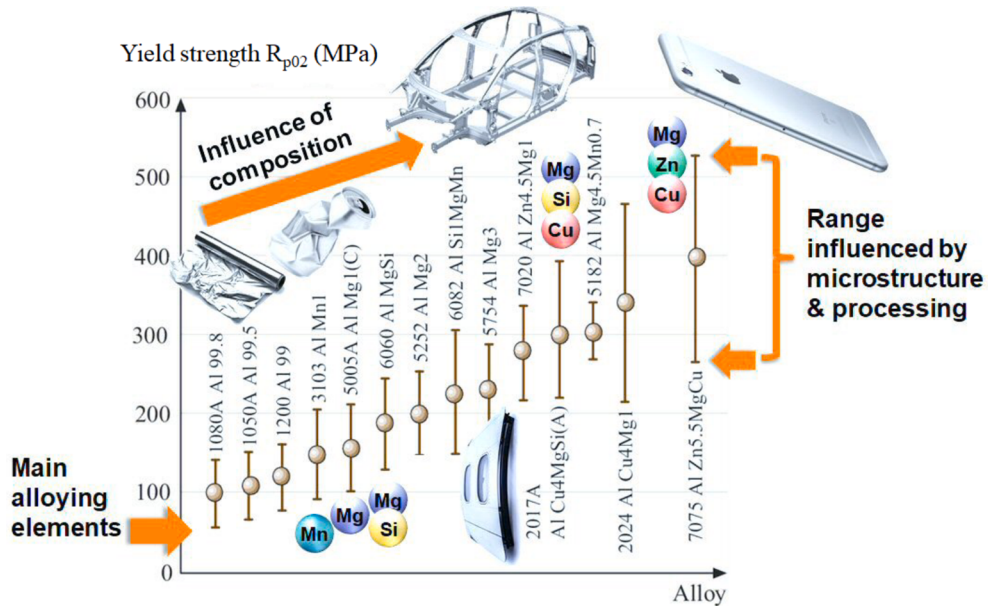


Fig. 10. Overview of the flow stress values for wrought aluminum alloys. The trend shows the strength spectrum accessible through composition variation, while the vertical variation bars reveal how much the strength can be influenced – for the same chemical composition – by microstructure alone. The trend may be of special interest for the future design of thermal treatments with composition-specific and non-isothermal profiles for advanced properties that can possibly even tolerate minor variations in tramp elements [82–85]. The figure is reproduced with permission, from the original version published in [74].

new materials which combine averaged composition concepts from different alloy groups. This could lead to less chemical sensitivity and to a smaller number of alloys in use and in scrap. The advantage of crossover alloys is also shown in their capability of strength adjustment by microstructure manipulation. Alloy 5182, shown in Fig. 10, with a relatively narrow range, spans a tensile strength of 300 to 550 MPa in the crossover variant, i.e. after modification with Zn, Cu and Ag [69].

The influence of different alloying elements on an alloy's overall sustainability was discussed by Jarfors et al. [88]. They suggested imposing energy- and GHG-related measures for more responsible use of alloying elements. More specifically, they show that certain elements, such as Mn, offer a much higher gain in strength (and also in Young's modulus) than other alloying elements for a given sustainability footprint. The aim of their calculations was to show how to achieve a maximum increase in strength at the lowest possible embodied energy and GHG footprint associated with the specific choice of alloying element.

Although the rules for sustainable alloy design outlined above provide a framework for moving forward, fundamental challenges remain. The compositional tolerance values discussed are alloy-, customer-, and application-specific. This means that not all aluminum products can be provided easily by secondary synthesis alone, as several classes of high-end products, such as those needed for safety-relevant parts in transportation or conductive devices, require alloys which are carefully engineered with respect to toughness, corrosion, hydrogen, fatigue, conductivity or surface finish – which usually tolerate only small variations or uncertainties introduced from scrap. However, it is important to emphasize that even small variations in the tolerance limits, sometimes also coupled with adequate alloying or processing counter-measures, can generate considerable changes in the level of acceptable scrap content. Also, apart from these sensitive parts, there are many products in architecture, design, construction, machines, consumer electronics and packaging where over-engineered alloys are not actually needed. This means that designing scrap-tolerant alloys must proceed in concert with the market, i.e. green-branded alloys would first target market niches where sustainability plays a particularly important role and customers are inclined to pay more for green branded products, or niches where minor property variations can be tolerated.

In areas which are entirely cost-driven, the scrap content must be high enough to beat the price of aluminum products that come from primary synthesis. In such fields, new scrap-tolerant / highly sustainable alloys and novel crossover alloys must both also meet the highest quality standards in their properties in order to compete with existing primary synthesis alloys that are potentially less sustainable [48]. In many cases this might mean that alloys with high scrap fractions will cost more (we do not give price ranges here because trading and prices vary too much from month to month). This could be balanced by green branding strategies. In addition, metallic materials are sometimes not very visible to customers in the products that contain them, and they frequently comprise a small price fraction relative to the added value of the entire product. This means that the higher costs accrued by using a more sustainable alloy often change the price of the entire product only modestly.

The next question is: what concrete, specific metallurgical research challenges do the elements which define a sustainable alloy present? In this context, the main topics addressed in the following sections are:

- (i) What effects do contaminants have, individually and collectively, on alloy properties? How (for instance) do they influence interface decohesion, phase formation, precipitation free zones, precipitation kinetics, surface finish, mechanical properties and corrosion?
- (ii) Are thermodynamic and kinetic databases sufficiently detailed and reliable as foundations for the development of “dirty alloys”, in particular in the areas of spinodal, metastable and intermetallic phases and contaminant effects on vacancies?
- (iii) Can scrap-related contaminants get trapped at lattice defects and inside precipitates? Could such trapping be used to render them harmless? Which types of thermal treatment should be applied to this end? Are all contaminant-related phases that form harmful, or are there beneficial features associated with any of the tramp elements?
- (iv) How impurity-tolerant can we make green near-commercial Al-alloys, and which contaminants are most relevant? What upper limits apply to contaminants in near-engineering Al-alloys?
- (v) Which crossover alloys are the most promising for combining beneficial mechanisms across established alloy families? Such broad-band, multi-purpose alloys must be designed as universal and not as niche alloys. They should be broad in their composition tolerance and application range.
- (vi) What combinatorial high-throughput methods are suitable for revealing scrap-related composition-microstructure-kinetics-property trends and ranges? How can we probe damage-tolerance in the associated experiments?
- (vii) For which phases is it necessary to use atomistic simulation methods to understand phase (meta-) stability, impurity trapping, sublattice occupancy and phase stoichiometry ranges? In general, are there sufficiently suitable modeling techniques available by which we can analyse the effects of tramp elements on aluminum alloys?
- (viii) How does deploying meso- and near atomic-scale characterization methods address these challenges? How can the main effects associated with tramp elements be observed and identified?
- (ix) Can supervised, knowledge-informed machine learning identify suitable nanostructure-composition-processing-property relations for the field of sustainability alloy design?
- (x) How must solidification, solutionizing and heat treatment processes be adjusted to deal with the effects of contaminant elements and the associated intermetallic phases?
- (xi) What measures and approaches promise to be the most effective in improving the sustainability of secondary synthesis?

2.2. Balance between sustainable primary metal and scrap use in green aluminum

Primary aluminum will continue to play an important role in alloy production because of the need for both dilution and alloy composition adjustment even in closed-loop scrap streams. Moreover, it is projected that demand for aluminum products will continue to outstrip scrap supply, requiring significant primary aluminum production well into the future (see Fig. 2). It is clear, though, that solutions are needed which allow increased scrap uptake without downcycling in secondary aluminum production. Here we are also required to consider how improvements in the production of primary aluminum might reduce its environmental impact. As seen in Table 2 [15], it is primary aluminum production, particularly electrolysis, that generates most of the energy consumption and CO₂ emissions during the manufacture of a product from aluminum. For example, if we compare the energy required during aluminum beverage can production stages, nearly the same amount of energy is required to produce the proportion of the liquid metal arising from scrap as is needed to produce the much smaller amount of primary aluminum used as a sweetener [8]. Anything – increased scrap usage, improved processing, or both – that reduces these negative energy and emissions effects would be a great boon.

One specific component in the electrolysis process is the electrode material, which is a particularly strong source of CO₂ emissions, even where renewable electrical energy feeds the overall process. The standard primary aluminum production method deploys the Hall-Héroult electrolysis process, which involves consumable carbon electrodes [89,90]. In this process, alumina is dissolved in a sodium-aluminum-fluoride (cryolite and aluminum fluoride) salt at 960 °C, where the species containing aluminum is reduced to metallic aluminum at the cathode and the species containing oxide is oxidized to carbon dioxide at the (carbon) anode following the reaction.

Table 2

Estimated energy consumption (on an annual basis) and emissions (per metric ton of product) for aluminum manufacturing processes, adapted from [15]. The data reveal that the main steps required for primary synthesis, i.e. bauxite extraction, alumina production and electrolysis, generate a much greater environmental burden than secondary production through scrap preparation, sorting and refining.

Process	Energy Consumption (EJ/year)	Emissions (t CO ₂ /t)
Bauxite extraction + Alumina production	1.1	1.02
Electrolysis	5	5.5
Scrap preparation + re-melting	0.04	0.6
Scrap refining	0.15	0.6
Ingot casting	0.05	0.2
Hot + cold rolling	0.23	0.2
Extrusion	0.09	0.3
Wire drawing	0.09	0.3
Shape casting	0.17	0.5



In addition to CO₂, CO (via the Boudouard reaction) and perfluorocarbons (tetrafluoromethane, CF₄, and hexafluoroethane, C₂F₆) are generated, the latter resulting from insufficient oxide content of the electrolyte. All of these products contribute significantly to GHG and global warming. On top of this, the significant energy consumption required to drive the above reaction causes indirect emissions via electricity generation from non-renewable sources. A worrying trend is emerging from the circumstance that the fraction of renewable energy being used in the production of primary aluminum is in decline. While in 2000, 50% of primary aluminum was produced using low emission, renewable or nuclear power, by 2018 this figure had dropped to only 29% [89].

Recognizing the CO₂ emissions accruing from traditional consumable carbon anodes as a serious issue, research and development over the past 40 years has focused on the development of inert anodes that can achieve the reduction with only oxygen as a product:



This reaction completely eliminates the formation of CO₂, CO and perfluorocarbons. It also (potentially) eliminates the need for an anode plant and rodding shop and reduces the frequency of anode changes. Technologically, however, the development of inert anode technologies has been limited by the availability of suitable materials. Anode materials must demonstrate (among other properties) a combination of high electrical conductivity, fluoridation resistance, stability with respect to oxide formation, low cost, easy fabrication, high thermal shock resistance and mechanical strength [91,92]. Candidate materials have been proposed which range from ceramics to cermets to metals [91,92] and metal anodes are the current preferred choice [92,93]. Some significant hurdles have apparently been overcome in this context, as Rusal [92] and a joint Alcoa / Rio Tinto Aluminum venture (Elysis) [94] will launch commercial products in 2021 and 2024, respectively.

Superficially, the environmental benefits of inert anodes appear clear in that they eliminate CO₂ as a product of electrolysis. This, however, comes at the cost of the increased energy required to perform the reduction via reaction (2) compared to (1). Considering only the energy required to heat the reactants and to supply the heat of reaction, Solheim [93] has estimated the minimum energy costs involved in reduction via carbon and inert anodes, respectively. His calculations predict that carbon anodes require a minimum of ~6.2 kWh/kg Al, while inert anodes require a minimum of ~9.2 kWh/kg Al. It is notable that the current average energy consumed globally in conventional Hall-Héroult processes is ~12.0 kWh/kg Al [93]. This is not very far from the *minimum* energy required by the inert anode process.

If renewable hydroelectric energy or, alternatively, nuclear energy are used to provide electricity for electrolysis then the benefits in terms of reduced CO₂ emissions from inert anodes are clear. However, as shown above, <1/3 of current aluminum is produced in this fashion. Thus this analysis must be expanded to include the CO₂ emissions arising from non-renewable electricity generation. If we consider the use of inert anodes in connection with energy produced from either coal or natural gas-based electricity, the advantages of using inert anodes evaporate. This is because most CO₂ emissions come from electricity production, not electrolysis. For example, in the conventional Hall-Héroult process ~12.9 t CO₂ /t Al are generated if coal-fired electricity is used, this accounting for ~87% of all the CO₂ generated in the process [93]. In the case of inert anodes ~15.9 t CO₂ /t Al would be generated, far surpassing the amount saved due to the reduction in CO₂ emissions from the reduction reaction itself [93].

In conclusion, because the capacity for renewable energy to drive primary aluminum production is limited, the prospects for inert anode production as a generator of “clean” primary aluminum are also limited. Indeed, the value of diverting renewable electricity to aluminum production rather than using it for other purposes is questionable [15]. Solheim [93] argued that carbon capture may be a more promising avenue for reducing environmental impact, but this comes at the cost of increased energy demand. Ultimately, all of this provides a further incentive to reduce the use of primary aluminum and increase the use of scrap for synthesis.

3. Scrap-related production steps and their sensitivity to tramp elements

3.1. Recycling rates: Definitions, industry branches and regional aspects

The estimates of different aluminum associations suggest that 1–1.5 billion metric tons of aluminum have been produced since the Hall-Héroult and Bayer processes were introduced in 1886–1892. Roughly three quarters of this enormous quantity are still in use. Of this about one third each are found in buildings / infrastructure, electrical devices, and transport. Aluminum material used in packaging can return to the recycling stream within a few weeks. Approximately 30% of today’s annual global aluminum production comes from scrap. However, substantial regional deviations apply: for example, the rate in the US is about 30%, versus about 50% in the EU. On average the total worldwide recycling rates for aluminum are estimated to be ~40% (see Fig. 2 and Fig. 3). At about 98% the yield in scrap-based aluminum production is very high, as the metal lost from recycling processes once collected is usually below 2%. Today the collection figures for recycled aluminum produced from old scrap are circa 33% from the transportation sector, 26% from packaging, 13% from cables and electrical devices and 16% from building applications (see Fig. 5).

The growth of the aluminum scrap market parallels that of the entire aluminum market. In 2009, 18 million metric tons of aluminum scrap were available globally. In 2019 this increased to 33 million metric tons, translating to an average annual growth rate of 6% (see Fig. 2 and Fig. 3). The amount of aluminum produced from old scrap increased from one million metric tons in 1980 to as many as 20 million metric tons in 2019. Obtaining an overview of the recycled aluminum amount can be challenging, however, because academia, governmental agencies and industry use different indicators. This applies particularly to recycling performance

indicators: the recycling input rate, the total (or overall) recycling rate and the end-of-life recycling rate [40,54].

The recycling input rate describes the amount of aluminum that is produced from new scrap and old scrap (see definitions in section 3.1) as a fraction of the total amount of aluminum, including that obtained from primary and secondary (recycled) sources, that is shipped to manufacturing markets. The overall recycling efficiency rate describes the total fraction of recycled aluminum that is produced from both new scrap and old scrap as a percentage of the aluminum that is available from new and old scrap sources. This means that the recycling efficiency rate describes how much of the available scrap is actually turned into recycled aluminum. The end-of-life recycling efficiency rate measures the amount of recycled aluminum that is made from old scrap as a fraction of the aluminum available from old scrap sources. This means that the end-of-life recycling rate quantifies how much of the post-consumer aluminum scrap is really recycled into new material. The same applies to the end-of-life collection rate, which describes the fraction of aluminum collected from old scrap as a percentage of the aluminum that is in principle available when collecting from all old scrap sources. Along the same lines, the end-of-life processing rate is the aluminum produced from old scrap as a percentage of the material collected from old scrap sources [26].

Industrial operators of re-melting plants often take their total scrap input (counting both new and old scrap) divided by the total amount of aluminum they produce to measure their recycling. Depending on region, company and specialization their values can range between 60% and 95%. It is also important to differentiate between end-of-life recycling performance as a key indicator and the total recycled amount of aluminum. Although it is usually best from a metallurgical perspective to recycle an alloy-specific product which has reached the end of its lifetime directly into its new counterpart, this is not always economically worthwhile. Re-melting an old product into an equivalent new one obviously provides the best composition match, but the sheer longevity of many large-volume aluminum products, for instance in transportation, buildings and construction, often renders it less attractive from an economic and sustainability perspective.

The fact that overall global aluminum demand exceeds the available scrap by about two thirds (with substantial regional variations) makes aluminum scrap a product of limited availability. This means that aluminum should be reused as soon as possible after it returns to the market as scrap, and not just when the exact same alloy is needed. Short-lived products such as cans or related packing products, however, are recycled directly into new equivalent products [31,52,95,96].

The global aluminum recycling fractions for scraped parts from the transportation and building sectors, with their characteristically long lifetimes, range between 80% and 95% depending on region (differences are mainly due to market access and logistics). From the time systematic scrap collection began, the transportation sector has been the most important source of aluminum from end-of-life products. Scrap aluminum from buildings (which have greater longevity) only became available in the 2000 s, and originally only in the modest quantities used when the buildings were erected 30–40 years previously. Scrap from aluminum beverage cans, which have an average lifetime of only a few weeks, is collected and recycled at rates of 30%–100%, with very high differences among regions.

Due to its large market share it is of interest to take a closer look at the aluminum which comes from the transportation sector [97–102]. Here alloys that return as scrap include mainly body sheet, frame, bumper and structure parts from the 2xxx alloys class (Al-Cu), the 5xxx alloy class (Al-Mg), the 6xxx alloy class (Al-Mg-Si), and the 7xxx alloys class (Al-Zn-Mg-/Cu). A large fraction of cast Al-Si alloys, such as A356, 360 and A380, is also returned from engine blocks. Among these classes, some are incompatible with each other: the high Si content inherited from cast parts is not admissible in wrought alloys, and the high Zn and Cu content returning from the 2xxx and 7xxx alloys is not compatible with 5xxx and 6xxx sheet materials [27,103].

For buildings, the scrap collection scenario is quite different. The average aluminum content of buildings is below 1%, but the total percentage recovered from this is high (about 95%) because many aluminum parts in buildings, such as claddings and sun protection devices, are peripheral and can be easily dismantled. This aluminum can be sold at a good price relative to other materials retrieved from buildings, which are often an economic burden rather than a trading good. The market is very heterogeneous, and there are substantial regional variations. Factories, commercial and office buildings have a much higher aluminum content than residential houses, and building in warm regions use about 20 times more aluminum than those in cold climates. Trends in architecture point to an increase, and the markets for both new aluminum in buildings and the amount returning as scrap are growing. While 5xxx and 6xxx class alloys have traditionally been used in buildings due to their high corrosion resistance paired with high strength, modest cost and good joinability, 3xxx alloys (Al-Mn) and 5xxx alloys containing large amounts of Mg are gaining momentum. While some of these alloys can be mixed to a minor extent, it is economically and ecologically much more sensible to collect them separately, also in view of large and growing transportation, construction and building markets which demand chemically well-controlled high-end alloys [27,39,61,104,105].

3.2. Advanced aluminum scrap sorting and pre-treatment

3.2.1. Brief introduction to scrap sorting

The quality of the input materials in a metallurgical process has a strong influence on both the metal yield and the quality of the final product. This is especially true for aluminum, with its low solubility. Because of this it is very important that treatment of aluminum scrap be high-quality, and therefore the technologies in this area are continually improving. Here, to close the loop in aluminum recycling in the future, increased interplay between scrap sorting and the melting process will be necessary [106].

Because of the growing importance of aluminum as a construction and lightweight material, more alloys and material composites are being produced which guarantee aluminum product functionality. Here sorting and melting processes must be optimized. Of particular importance here, as an essential prerequisite for excellent product properties and high metal yield [106,107], is the reproducible adjustment of a product-specific melt quality with regard to non-metallic and intermetallic inclusions. Due to both

increasing scrap rates and the higher impurity content of input material, it is necessary to optimize scrap sorting and the quality of aluminum melts along the process chain in a secondary aluminum smelter [108,109]. However, legal requirements such as those set out in the European End-of-Life Vehicles Directive or the Reach Regulation also have an impact on the recycling of aluminum. Furthermore, the limited refining possibilities of aluminum smelters demand optimized scrap sorting and collection if high alloy quality is to be achieved [54,72]. In addition, increased mixing of scrap and high organic content are also driving the need to develop new alloying systems [106,110].

The scrap sorting technologies used today are well developed, but are reaching their limit due to the large number of alloys and composites on the market. The following sections explain how the main mechanical and thermal processing techniques are deployed to turn aluminum scrap into high-quality input material for recycling. The aim is on the one hand to facilitate production of high-quality aluminum alloys, and on the other to create the conditions for developing recycling-friendly alloys [110,111].

3.2.2. Types of scrap and valuation

In the recycling of aluminum, only scrap and other materials containing aluminum in metallic form (dross, salt and slag) are considered as input materials [110–112]. Aluminum in non-metallic form, for example oxides, nitrides, chlorides, carbides etc., cannot in principle be reprocessed into metallic aluminum. The main types of scrap are circulating scrap, new scrap and old scrap [110]. Circulating scrap is not usually recorded in statistics and is obtained directly “in-line” during the production process in a clean and unmixed form. If possible, this scrap is immediately remelted in the same factory [110]. Examples are sort-specific scraps from sheet cutting or surface grinding which do not leave the shop floor for any downstream operation but are directly collected for in-house secondary synthesis.

New scrap (pre-consumer scrap) is created during the production and processing of aluminum products, usually at customer sites, which distinguishes it from circulating scrap. New scrap is statistically recorded and is usually remelted into aluminum alloys in smelters (remelters or refiners). In recent years the amount of this type of scrap has increased significantly. In order to guarantee closed-loop recycling of new scrap, the companies involved are required to guarantee complete, sorted scrap collection. The scrap is remelted in the smelters to wrought and cast alloys. New scrap can occur in a variety of forms and ranges from large pieces to highly contaminated, mixed chips. New scrap also includes the dross produced during aluminum production, which is remelted in refiners using salt [110,111].

Old scrap (post-consumer scrap) is produced in all aluminum material applications (automotive, aerospace, construction, food, engineering, packaging, etc.) in widely varying compositions. Some old scrap must be extensively processed to enable its use in subsequent melting processes. Return quantities also depend very much on service life, which can range from weeks to decades (e.g., packaging versus buildings). In addition, collected scrap varies greatly, ranging from packaged beverage cans to shredded scrap from old cars [110].

Scrap is evaluated according to its condition and purity (chemical analysis), type and quantity of foreign components and how they are mixed with the aluminum material [111]. The main parameter for evaluation is purity, i.e. the content of the main alloying elements (Si, Cu, Mg, Zn, Mn), the secondary components (Fe, Cr, Ni, Pb, Sn, Ti etc.) and minor elements (Li, Sr, Sb, Ca, Bi etc.) [110]. Representative sampling is very important for a suitable evaluation. The sample must have a certain minimum size, which is difficult to achieve with heavily mixed scrap. For this reason, adequate sorting technology is also important [110,111].

How scrap is stored plays a decisive role in the output of the melting process and in the purity of the melt. Particularly if there is an unfavorable surface-to-volume ratio (e.g. chips and foils), alloys may have oxide layers and need pre-treatment. Excess moisture may also affect the melting process if scrap has been stored outdoors. At low temperatures, if there are cavities in the scrap ice or water can even get underneath the melt and cause dangerous explosions [110,113]. In principle, dross must always be stored under a roof.

Suitable scrap preparation which generates high-grade products for the melting process is crucial for maintaining high-quality application standards [111,114]. Aluminum recycling treatment, which includes all the processes required to provide high-quality input material, can be both mechanical and thermal.

3.2.3. Mechanical scrap sorting

Mechanical scrap processes mainly include comminution, classification, sorting, agglomeration, and dehydration [106,110]. Comminution plays an important role in the context of aluminum scrap. It enables the separation of foreign substances which can lead to problems in melting. Comminution and/or agglomeration are also beneficial for transport, storage and charging. Non-metallic and metallic components are separated from each other by classification and sorting. There are a wide range of aluminum scrap treatment technologies which are utilised depending on the quality of the raw materials. Fig. 11 shows the various possible processing options and workflows. Comminution is mostly performed by imposing mechanical stresses (tension, pressure, shearing, torsion, bending, cutting, etc.) [111,115].

To sort scrap it is necessary to divide the materials into different size classes. In this sizing process it is possible to remove fine and coarse particles which would be disadvantageous in subsequent processing steps. A sorting process can also be carried out in a sizing procedure if (for example) the metallic aluminum contained in the salt slag remains coarse (deformation process) and the salt and oxidic components break up finely. The materials can then be sorted by subsequent screening [109,111].

Sorting represents an essential step in the processing of scrap for aluminum recycling. The aim is, as far as possible, to separate non-metallic components and other metals (Fe, Mg, Zn, Cu etc.) from scrap which contains aluminum [31,106,111]. Specifically, this involves separating metals from non-metals; light metals from heavy metals; different types of light metal (i.e. aluminum and magnesium); and different aluminum alloys. Various sorting methods are available [106]. The most important are described briefly below.

Density sorting makes use of the difference in mass density between individual materials and a fluid with a certain density (liquid or

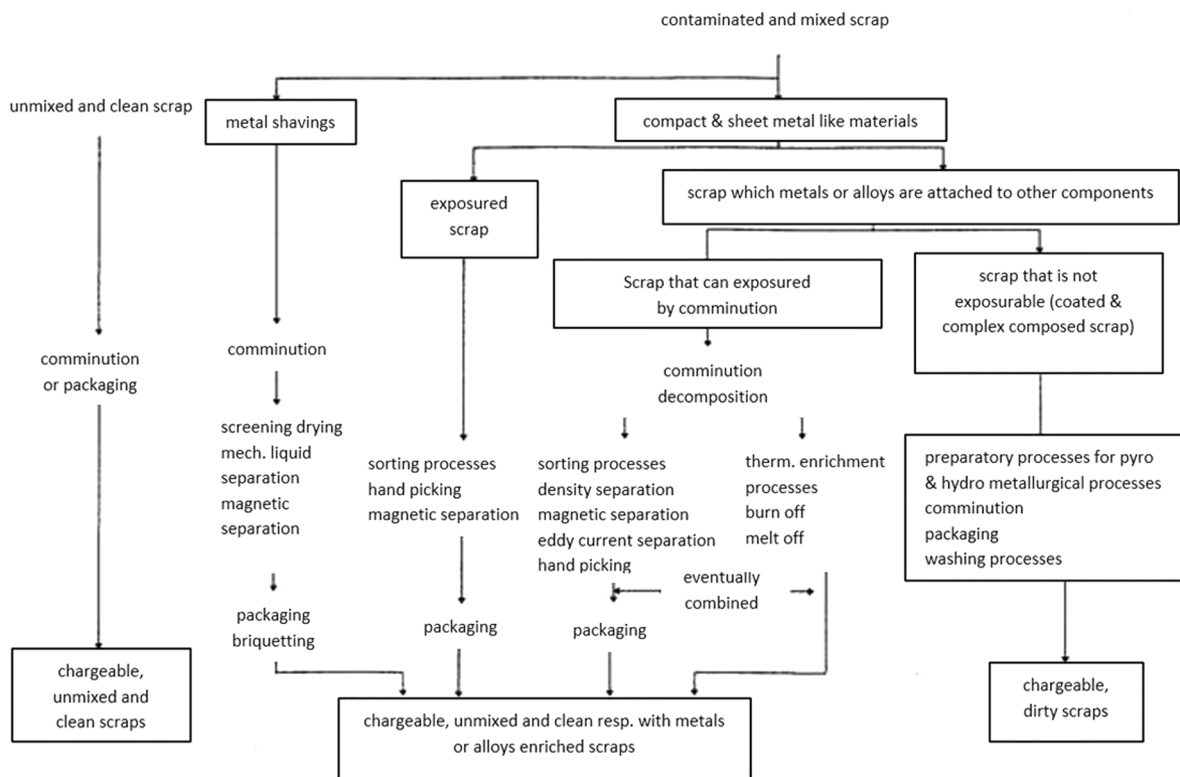


Fig. 11. Processing methods for aluminum scrap. Reprinted with permission from [110].

air) [111,116–118]. Magnetic separation is used to separate ferromagnetic materials from aluminum. Fe plays an important role in aluminum alloy metallurgy through its formation of intermetallic particles, and therefore needs to be controlled carefully. Magnetic sorting is thus often used in the processing of aluminum scrap [111]. A further method for separating metals and non-metals and metals from each other is eddy current separation. A time-variable magnetic field generates electromotive forces, and in a conductive material the induced electromotive forces generate currents in the material. This magnetic field is counter-directed to the inducing magnetic field [75,111], generating repulsion, which depends on the ratio of conductivity/density (see Table 3). This technology is being used more and more frequently, especially for aluminum, because it is an efficient way to sort weakly conducting materials or non-metals.

Manual picking is still used today where there are low volume flows and expensive technologies cannot be economically justified. This applies, for example, to portable batteries, electric motors, etc. In recent years, however, sensor-based sorting has become more common. Originally this addressed visual identification features, but over time has been supplemented or replaced by opto-electronic electromagnetic, X-ray, spectroscopic and other identification methods [106,119]. In sensor-based sorting, determining the exact position is also crucial. Two main identification methods are used for aluminum alloys [106,111]. The first is X-ray transmission measurement (XRT) with spectral resolution (RSA) (reverse saturable absorption), where elements are determined according to their atomic density. This technique is currently used to separate AlCu and AlZn alloys from other aluminum alloys [111]. The second method is laser-induced breakdown spectroscopy (LIBS), where material evaporation and spectral analysis are performed [111].

Table 3
Ratio of conductivity/density for different metals. Reprinted with permission from [111].

Material	Conductivity / density [$\text{m}^2 \cdot 10^3 / \Omega \cdot \text{kg}$]
Aluminum	13
Magnesium	12
Copper	7
Al-alloy	5...23
Zinc	2.4
Gold	2.3
Brass	1.8
Nickel	1.3
Tin	1.2
Lead	1.0
Iron, steel, alloyed steels	1.0...1.3

3.2.4. Thermal pre-treatment

Aluminum scrap may contain large amounts of hydrocarbons, which can enhance emissions, remelting loss and dross formation, and reduce alloy purity. However, scrap with a high organic content is also an energy source which allows fuel savings [120–122].

Not only is the type of scrap (used beverage cans (UBCs), chips, offcuts, used aluminum packaging etc.) important, but also its nature (e.g. loose, compacted, clean, coated) and components. Scrap impurities include non-metallic components, free iron, moisture, and inert, volatile and contaminating substances. The main categories containing them are coated scrap (covered by paint, varnish, printing ink, plastic, paper or metal); scrap containing residual non-metallic substances (such as water, oil, grease, wood, plastic, glass, etc.); scrap containing moisture (with liquid that adheres to the material); and scrap containing volatile substances (which can be removed by appropriate heat treatment before or during melting or by dedusting).

So-called low-grade materials with a non-metallic organic content of >15% by weight are problematic in new scrap. These materials change in the furnace from endothermic to exothermic scrap with an excess of energy in the metallurgical aggregate [121]. Unfortunately, however, the mechanical or thermal treatment required to deal with them is currently either technically inadequate or uneconomical.

Due to the versatility of aluminum as a material, there are many different types of aluminum scrap. The amount of metal each contains can vary considerably. In dry, single-variety raw material, the valuable metal content is largely determined by the weight of the coating. As seen in Table 4, this can vary between 2 and 90% [123,124].

There are different types of coatings on aluminum, and each behaves differently during pyrolysis. The emissions released during this process are related to the compounds contained in the coating. Coatings are mainly composed of plastics, paper, paints, varnishes, inks and various oils, often in the form of multiple layers such as in packaging. If the structure is complex, the aluminum content will be lower. The risk of toxic emissions during pyrolysis increases with higher plastic content [106,124]. Coatings can contain organic and inorganic components. The former comprise carbon compounds, which crack when the temperature is increased [124] while heating has no effect on inorganic components. After heat treatment, this fraction is composed of ashes and metal oxides (pigments) [126], such as titanium or zinc oxides. These substances do not volatilise during thermal pre-treatment. Some substances can be discharged via exhaust gas in the form of dust. When coated material is heated directly in a furnace, waste gas is released, due to the decomposition of the plastics. Besides gas, carbon particles are formed which react with the metallic aluminum and form carbides (Al_4C_3) [126], which tend to accumulate in the salt slag or dross. During intermediate storage or processing of the dross, these carbides can react with water and form methane. Carbides can also enter the aluminum melt and negatively affect alloy properties. These problems can be avoided by thermal treatment (pyrolysis) of the scrap before subjecting it to smelting [127].

To describe the behavior of the input materials in more detail, it is useful to divide the process into two steps: the splitting or thermal decomposition of the hydrocarbons present in the coating, and the combustion of the decomposition products. The first step depends on the type of coating and the metal substrate. During combustion, the coke which is produced during pyrolysis and remains on the surface reacts with the oxygen to form CO and CO_2 [127]. During pyrolysis, a reducing atmosphere is applied, which means that the material is melted without substantial oxidation losses. The gas generated by the thermal treatment contains tars, oils, dust and pollutants, components which can crack during high-temperature treatment, converting the hydrocarbons into CO and H_2 . The gas produced in this way has a calorific value of 4.5 to 5.5 MJ/m³. A typical composition for such a pyrolysis gas is about 22 vol-% H_2 , 14 vol-% CO, 12. Vol.-% CO_2 , 2 vol-% CH_4 and 50 vol-% N_2 [121,128].

3.3. Secondary synthesis: Process steps for aluminum scrap treatment and remelting

3.3.1. Brief introduction to the metallurgical fundamentals

Aluminum reacts with different gases, reducing metal yield and negatively influencing the quality of secondary alloys. The most important reactions and their relation to impurity effects [106,110,111] are briefly discussed in the following.

Aluminum is highly reactive with oxygen and such oxides can no longer be reduced in conventional recycling cycles. Therefore reactions with oxygen plays a special role in the field of recycling. Oxygen itself is practically insoluble as a gas in liquid aluminum [110,111]. Oxidation of an aluminum melt takes place above 727 °C. Due to its high affinity for oxygen, an oxide layer forms instantly on fresh surfaces of solid and liquid aluminum in air. This layer is dense, and protects the aluminum from further oxidation. The reaction takes place with atmospheric oxygen and humidity. However, aluminum oxide can also be formed in a reaction with components in the flame or the combustion gases (CO_2 , H_2O), or arise aluminothermically with other metal oxides, e.g. iron oxide which

Table 4

Properties of different scrap types with organic coating in the field of aluminum recycling. Reprinted with permission from [125].

Scrap Type	Coating	Mass of coating [%]
Foil (blank)	Oil residues from the rolling process	< 10
Printed foil	Color/Varnish	7
Laminated paper	Paper/Ink	50–70
Laminated plastic	Polymer/Ink/Wax	40–90
Laminated tubes	Polymer/Varnish	70
Window frames	Varnish/sheathing	21
U.B.C *	Varnish/Color	2–3

*...Used beverage cans.

Table 5

Free reaction enthalpy of Al and different aluminum compounds to aluminum oxide [110].

Reaction	$\Delta G_{600^\circ\text{C}}^0 \text{ kJ/mol Al}_2\text{O}_3$	$\Delta G_{800^\circ\text{C}}^0 \text{ kJ/mol Al}_2\text{O}_3$
$2\text{Al}^l + 3/2\text{O}_2^g \leftrightarrow \text{Al}_2\text{O}_3^s$	-1402,7	-1336,0
$2\text{Al}^l + 3\text{H}_2\text{O}^g \leftrightarrow \text{Al}_2\text{O}_3^s + 3\text{H}_{2\text{Al}}$	-804,4	-770,9
$2\text{AlN}^l + 3\text{H}_2\text{O}^g \leftrightarrow \text{Al}_2\text{O}_3^s + 3\text{NH}_3^g$	-256,7	-223,5
$\text{Al}_4\text{C}_3^l + 6\text{H}_2\text{O}^g \leftrightarrow 2\text{Al}_2\text{O}_3^s + 3\text{CH}_4^g$	-708,5	-651,6

adheres to tools, or silicon dioxide from (e.g.) the furnace lining. In addition, not only aluminum itself, but also aluminum nitride and carbide formed secondarily in the melt can react to form aluminum oxide (see Table 5) [110,111].

When aluminum oxidizes in the solid state, in dry air the resulting layer consists of amorphous aluminum oxide with a thickness of 2 to 10 nm, which increases only slowly below 300 °C. When exposed to humid air, such layers become much thicker, initially forming a thin non-porous barrier layer on which a porous, hydrous top layer grows, the thickness of which depends on the temperature and can reach a few 0.1 μm. When heated above the aluminum melting point, the amorphous oxide transforms into γ-Al₂O₃. At temperatures above 700 °C the transformation of γ-Al₂O₃ to α-Al₂O₃ (corundum) starts, with a time delay. This causes a decrease in volume, leading to cracks. Oxygen can penetrate through these cracks, causing further oxidation. The speed of oxidation increases with rising temperature and increases very strongly from about 780 °C. For this reason it is essential to avoid overheating, which can be caused by burning dross, a high organic content or incorrectly adjusted burners [110,111].

During the oxidation of alloyed aluminum melts, oxidation can be either selective or non-selective towards aluminum, depending on the oxygen affinity of the respective alloying elements. The alloying constituents thus have a considerable influence on the amount of oxide formed and on the structure and composition of the oxide layers. Selectively oxidizing elements (e.g. Mg, Sr and Ca) have a higher affinity for oxygen than aluminum. They tend to oxidize out of the melt at a high rate and form separate phases, where the oxidation rate increases with the increasing temperature of the melt and with increasing content. In non-selective oxidation (of e.g. Cu, Fe, Zn), which takes place at a low rate, the oxides that form are incorporated into the Al₂O₃ lattice depending on the atomic or ionic size of the element, and generate a change in the oxidation behavior by altering the oxide layer's structure and density [110,111].

In wrought alloys, oxide inclusion and other non-metallic or intermetallic inclusions impair not only the materials' mechanical properties but also influence corrosion, which can lead to problems during pickling, polishing and anodizing [129]. In cast alloys problems can arise during surface treatment, e.g. polishing (as mentioned) and anodic oxidation. Pressure tightness, weldability, corrosion resistance and machinability are also reduced by non-metallic particles. Melts which contain oxides are more viscous, and thus have poorer mold filling and feeding properties. Die casting processes also cause increased mold wear [110].

In order to conduct the entire recycling process of aluminum and produce a high metal yield, the reaction with oxygen must be reduced during storage, transport, smelting (where technique is crucial), holding and casting. The extent of oxidation depends strongly not only on the melt composition but also on temperature and time. The important factors influencing it are oxide, moisture and the impurity content of the input material; temperature control during melting; duration of exposure to atmospheres containing oxygen and moisture; flow conditions during melting, transfer and potting; composition of the fluxes used; and the ratio of the bath surface to the volume of the melt. To melt aluminum scrap with minimum loss, the following conditions must therefore be met [110,111]:

- Oxidation and moisture absorption of the raw materials should be avoided as far as possible (dry storage under a roof, rapid processing, etc.).
- Melting must be carried out at the lowest possible temperature.
- Melting time must be short and unnecessary holding times should be avoided.
- Small and fine material must be stirred into the metal or salt melt quickly to protect it from oxidation.
- Turbulent flows during transfer and casting must be avoided to reduce tearing of the protective oxide layer.
- Bath surface must be small to minimise contact with the atmosphere.
- Optimised fluxes should be used.

Using optimised fluxes is especially important. Here oxide layers must be completely removed from the scrap, and aluminum droplets must be enabled to coalesce in the molten salt [110,111,130].

Oxide layers also play an important role when the material is liquid. This produces dross: a mixture of aluminum, the alloying and impurity elements and their oxides. Halogenides, carbides or nitrides are also found in the dross. The greater the amount of dross produced, the more liquid aluminum is bound within it due to capillary effects. The formation of dross and the associated loss of aluminum can be described in terms of the following steps [123,126]:

- Formation of the oxide skin on the melt
- Breaking of the oxide skin by the bath movement
- Sinking and floating of the oxide particles
- Adhesion of the oxide particles
- Filling of the interstices with metallic Al (capillary action)
- Oxidation of aluminum dispersed in the dross, resulting in additional dross

- Removal of the dross from the molten bath
- Partial dripping of liquid aluminum or further oxidation if no appropriate treatment (rapid cooling) takes place

Oxides also enter the melting process via scrap due to the passive layers. They have a thickness of 4–10 nm in dry air and up to a maximum of 10 µm in moist air. A 2–4 nm thin barrier layer is formed immediately upon contact of the free surface with any oxygen-containing atmosphere. This layer consists of pure Al and amorphous Al₂O₃ and, depending on the aluminum alloy, may also contain mixed oxides such as magnesium oxide. If the humidity is appropriate, a non-porous top layer will form on the porous barrier layer. Here aluminum hydroxide Al(OH)₃ is produced [127]. The structure and growth of this top layer depends on surface impurities or coatings and on air humidity. The growth rate depends on time and temperature. In dry air, the barrier layer has already reached its maximum thickness after about one hour, whereas only increased humidity in the ambient atmosphere will cause the growth of the top layer [79,127,129].

Hydrogen is soluble in aluminum, but little is known about the specific reactions which place except the fact that embrittlement and stress-corrosion cracking can occur in high-strength alloy grades [131–133]. The hydrogen solubility in aluminum increases in the solid and liquid state with temperature and depends on the hydrogen partial pressure [110]. Due to reduced solubility in the solid state compared to that of the liquid state, bubbles and pores form in the material during solidification. However, hydrogen precipitation can be suppressed with the help of a high cooling rate, which is deployed for example in continuous casting or die casting. In subsequent treatment steps (e.g. heat treatment, hot forming, etc.), the forcibly dissolved hydrogen is released and in turn generates annealing bubbles, grain boundary porosity, etc. These greatly impair the mechanical properties of the aluminum alloys, but can be prevented in advance via appropriate melt treatment processes [111].

In castings, any gas porosity that occurs can be used as a measure of hydrogen solubility. However, the tendency towards pore formation depends not only on the hydrogen content, but also, crucially, on the solidification rate, the solidification morphology and the microstructure state.

An equilibrium is established between the aluminum melt and the hydrogen content in the surrounding atmosphere. This defines the proportion of dissolved hydrogen, where environmental water vapour is the main cause of the increased hydrogen content. Water vapour is decomposed by liquid aluminum. The atomic hydrogen formed is quickly dissolved in the molten aluminum, and the oxygen reacts exothermically to form aluminum oxide, which creates a dense oxide layer on the molten aluminum. This reaction increases not only the hydrogen content in the melt, but also reduces the metal yield [110].

Oxide layers on aluminum melts in humid atmospheres provide a certain protection against further reaction with water vapour. However, if this oxide layer is destroyed by turbulent flows (casting and pouring off, gas purging treatment, bath movement, etc.), a reaction with the water vapour of the environment again takes place which is exothermic. This leads to overheating, which favors hydrogen absorption. In the same way, organic substances adhering to the scrap also react with liquid aluminum to form carbon or aluminum carbide, with the resulting hydrogen then being absorbed by the melt. The same reaction takes place in the incomplete combustion of organic compounds. In addition, aluminum carbide can in turn be converted into aluminum oxide in the course of the smelting process [110,111,134].

Hydrogen can also be introduced via the input material. The oxide layer adhering to the scrap is, for example, a source of hydrogen. The naturally formed oxide skin consists of porous aluminum oxide and contains moisture. When using small-sized material (chips, foils, etc.) or dross, the risk of water absorption is particularly high due to capillary effects. The same applies to moist melting salt. Other sources of hydrogen are new crucibles, newly lined furnaces and freshly coated melting tools. In practice, melts with a large hydrogen content also often have a greater oxide content, and vice versa [110,111].

Alloying and trace elements can also influence hydrogen solubility [110]. Elements that increase it are Mg, Ti, Na, Sr and Ca; those that only modestly affect it are Cr and Fe; and elements that decrease it in Al-alloys are Cu, Mn, Ni, Si, Zn and Sn. The aim must therefore be to reduce hydrogen absorption and the associated oxide inclusion. Measures for achieving this include using dry scrap with as little oxidation as possible; rapid melting or submergence of fine scrap; avoiding unnecessary holding times; using dried melting salts and dry gases; and avoiding melt overheating and drying of new linings of furnaces, transfer troughs, ladles, melt treatment and casting equipment.

Nitrogen can also react with solid and liquid aluminum [110] to form aluminum nitride. Similar to oxygen, a thin, dense layer of aluminum nitride is formed on the melt and protects it from further nitrogen absorption. Aluminum nitrides occur not only in the melt, but also in the dross or in salts. The cause of aluminum nitride formation is gas purging treatment with nitrogen and a reaction with atmospheric oxygen, e.g. during local overheating. In dross and salt slags, aluminum nitride reacts with atmospheric humidity or with water during salt slag processing and causes the formation of ammonia (NH₃). AlN can also be present in solid form, suspended in aluminum melts. If no suitable melt treatment is carried out, it will reduce the quality of the resulting products [110].

The high chemical reactivity of liquid aluminum and the alloying elements present in the melts (e.g. Mg) mean that liquid aluminum reacts not only with gases but also with solids. Particularly important are reactions with the refractories (SiO₂, Fe₂O₃ etc.) and alloying additions (master alloys and their impurities), as well as reactions with oxides in (for example) pigments of organic coatings from scrap (TiO₂, ZnO, Pb₃O₄, Fe₂O₃, Cr₂O₃ etc.). The reaction products not only generate impurities in the aluminum melt, but also reduce the yield when aluminum is recycled due to the aluminum oxides that usually form [110,111].

3.3.2. Process and plant technology

Recycling of secondary raw material is carried out for aluminum depending on the degree of impurity. It is necessary to use different furnace systems for efficient recycling of the very different materials involved [110,111,106]. Direct processing of high-purity input materials, which is conducted during production and further downstream processing, can take place in the foundries of the

primary smelters, in semi-finished product plants, recycling plants and foundries. This frequently involves the company's own scrap, which is usually not recorded statistically but treated as a closed-loop contribution [110,111].

Today, new and old scrap are processed in recycling plants, and a distinction is made between remelting for purer scrap and refining for lower-quality scrap. While remelters mostly produce wrought alloys, the products of refiners are cast alloys [110,111,130]. The basic process steps are the same in the production of both [135,110]. They involve preparing the input materials (if necessary); melting; melt treatment (alloying, gas purging treatment, temperature and microstructure adjustment and, if necessary, filtration); and casting.

The main difference in the recycling of aluminum is whether salt is used (refiner) or not (remelter), and this depends on the corresponding input material. The amount of salt depends on the process technology and the material used. An overview of the steps in recycling of aluminum is shown in Fig. 12 [110].

The smelting salts used in the recycling of low-grade scrap comprise mainly sodium chloride (NaCl) and potassium chloride (KCl) with added fluorides, such as fluorspar (CaF_2) or cryolite (Na_3AlF_6) or other alkali fluorides (NaF, KF). The tasks of the salt are (i) to break up the oxide skins; (ii) to absorb the non-metallic impurities (oxides, carbides, nitrides, etc.); (iii) to protect the liquid metal from the furnace atmosphere by covering the melt; and (iv) to improve the coagulation of the metal droplets [110].

Important criteria in commercial smelting technology are high metal yield; low dross formation and low salt input; low energy requirements; high quality of products with a large scrap component (low primary aluminum); low oxidation of aluminum; and low emissions [110,111].

Important improvements have been made to fuel-heated plants via a reduction in the amount of additional materials such as smelting salt; improved burner technology; combustion with oxygen; and waste heat recovery. Controllable medium-frequency induction furnaces are mostly used in electrically heated plants, with high efficiency and improved energy consumption. All melting furnaces are equipped with off gas collection and off gas purification systems, which guarantee compliance with legally prescribed emission values. Off gas purification processes, especially for organically contaminated off gases, have solved former problems associated with the occurrence of PCDD/F (polychlorinated dibenzodioxins and polychlorinated dibenzofurans, often referred to as "dioxins") [54,110,111].

In the context of secondary materials, a distinction can be made between foundries and semi-finished product plants, remelting plants (remelters) and melting plants (refiners) [115]. The individual areas are explained below, with particular reference to furnace technology, melting technology and the materials used. Foundries and semi-finished product plants are often not considered part of the recycling process because they mainly use primary metal or products from secondary smelters (casting ingots or liquid aluminum). In addition, they use sorted scrap which accumulates during production (scrap from foundries, parts of sheet metal, profiles or chips). This type of scrap does not appear on any scrap balance sheet, and quantitative registration usually only takes place within the plant. Nevertheless, because the amount of these high-quality materials has increased in recent years due to the increasing depth of processing and rising production, these furnace systems represent an important part of the overall recycling cycle. The units they use are mostly from tilting or stationary hearth furnaces with a capacity of up to 130 metric tons, although induction furnaces (crucible or

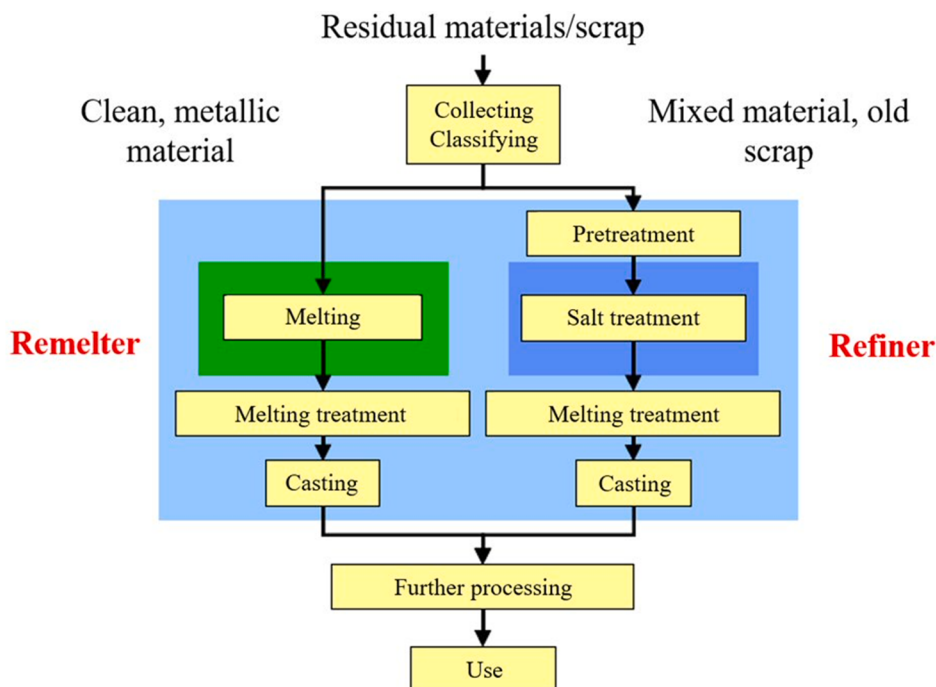


Fig. 12. Process routes (with and without salt) in the recycling of secondary aluminum. Reprinted with permission from [110].

channel furnaces) are also deployed in both recycling plants and foundries.

Remelter plants mainly use low-contaminated, wrought alloy scrap with a low number of alloying elements. Large quantities of sorted scrap with the same composition are usually charged. The treatment of the scrap only consists of making these materials chargeable by cutting or, if necessary, agglomeration. The process sequence in a remelter is shown in Fig. 13 [75,110,111,115,116,135].

Scrap melting usually takes place in fuel-heated single- or multi-chamber furnaces, which increasingly have integrated preheating chambers to smolder adhering organic compounds. These furnaces also have low-temperature carbonization gas and oxygen burners and facilities for heat recovery. In hearth furnaces, the melting process can be accelerated by stirring devices or pumping. Heating is carried out via oil and gas burners to about 950 °C, with the use of oxygen burners on the increase. For more contaminated materials, especially those with higher organic content, multi-chamber furnaces are used. These consist of a reheating and smoldering area, a melting chamber (forehearth) and a heating chamber (main hearth) [115,134,136]. In the smoldering section of the furnace, the off gases from the heating chamber are used to smolder the organic compounds under a reducing atmosphere. These gases heat the scrap and at the same time largely prevent oxidation of the aluminum. In the subsequent charging process, the smoldered scrap is transported by new scrap into the forehearth and melts in the aluminum bath. The main hearth provides the heat necessary for the burning of the smoldered gases from the forehearth.

Other furnace possibilities include rotary drum furnaces without added salt, crucible induction furnaces, and more rarely, channel induction furnaces and hearth shaft furnaces. After the input materials are melted, the liquid aluminum is charged via troughs or by ladle transport in fuel-heated holding furnaces. These are also used as furnaces for the casting process. The gas purging treatment takes place either in the holding furnaces and/or in plants which are arranged “in-line” between the casting furnace and the continuous casting, and where filtration also takes place. In the holding furnaces, which are designed as tilting hearth furnaces, the melt is alloyed, if necessary grain-refined, and cast or delivered in liquid form.

Highly contaminated, oxidized input materials are typically processed by refiners. Mixed scrap from all alloy classes, sometimes with a high organic content, as well as dross, dross and slag grains or scrap with a high surface/volume ratio, are often charged. Melting usually takes place using salt in fuel-fired rotary drum furnaces. Low-salt tilting drum furnaces and hearth or multi-chamber furnaces with a low salt addition are also deployed. After the melting process the liquid aluminum is transferred to holding furnaces, which are also fuel-heated. Here the liquid metal is alloyed, treated for cleaning and microstructure adjustment and finally cast or poured into liquid transport containers. Refiner products are cast alloys in the form of ingots or liquid aluminum. Similarly produced deoxidized aluminum for the steel industry is mainly sold in the form of granules [110,111,130].

Fig. 14 shows the process scheme for producing cast alloys by processing highly contaminated materials in refiners. The criterion which differentiates rotary and tilting drum furnaces is the salt factor [75,110,111,135].

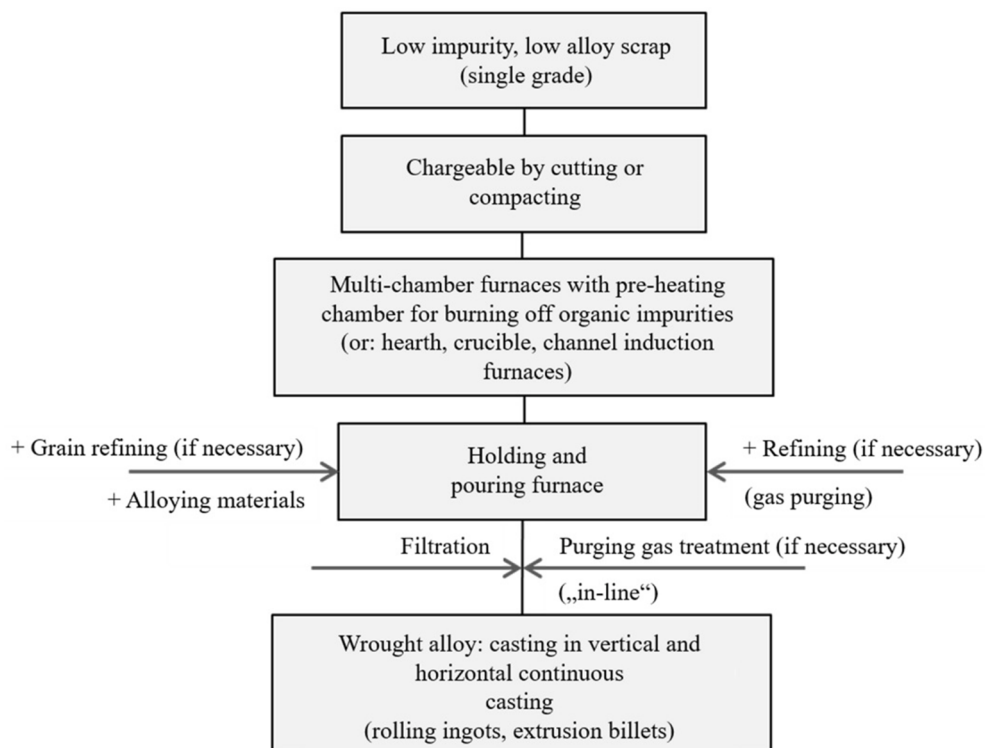


Fig. 13. Illustration of the process steps in aluminum recycling for the production of wrought alloys. Reprinted with permission from [111].

The salt factor (mass of salt / mass of non-metallics) is between 0.5 (tilting drum furnace) and 1.5 (rotary drum furnace), depending on the scrap quality and the furnace system. This correlates to about 300 to 500 kg of salt per metric ton of secondary aluminum produced. The metal content in the salt is between 5 and 20%. The quantities of salt depend on the degree of impurity and the specific surface area of the primary materials [110,137].

A distinction is made between rotary drum and tilt drum furnaces. With a salt factor > 1 , a liquid salt slag is present (salt bath melting). The rotary drum furnaces used are relatively safe and can be operated without complex controls. If the salt factor is significantly below 1 (approx. 0.5), we speak of low-salt smelting. In this case tilting drum furnaces are used. The amount of added salt must be carefully adjusted to the input material, because there is a risk of increased aluminum oxidation as the amount of salt decreases. Drum, hearth and multi-chamber furnaces are also used for salt-free melting in the production of cast alloys [110,111,137,138].

Regardless of which melting concept is used, measures must be taken that enable (i) high energy efficiency; (ii) low salt consumption resulting in a low amount of salt slag and filter dust; and (iv) low environmental pollution. The standard melting unit for contaminated scrap is the rotary drum furnace [75]. It consists of a cylindrical steel vessel, lined with refractory material, which is mounted on two rollers via races on the furnace shell so that it can rotate around a rigid axis of rotation. It is driven electrically by friction-driven rollers, chains or gears, with a stepless speed control typically set to 1–8 revolutions per minute. The furnace capacity is 10–60 t and heating is performed with oil or gas burners. Great improvements in heating are, however, achieved with the help of oxygen burners and additional oxygen lances,. This also makes it possible to completely burn off the smoldering gases of organic fractions that are produced during heating, thus gaining additional heat for melting. Compared to stationary hearth furnaces, rotary drum furnaces have the following advantages [75,110,111,137–139]: (i) The rotating movement enables a mixing and stirring effect between liquid salt, metal and the charged scrap. (ii) The burner heats up the furnace wall, which is then submerged in the molten metal by the rotary movement, thus achieving a very good heat transfer. The scrap is mechanically charged through the furnace door, and the melting process operates at about 800 °C. Tapping openings arranged around the circumference of the furnace shell are used first to recover liquid metal and then to pour off the salt slag. Particularly noteworthy is the improved coagulation of the aluminum droplets due to the rotary motion [110,111,139].

A follow-on of the rotary drum furnace is the tilting drum furnace. Due to the small amount of salt in this furnace operation, a crumbly salt slag (salt cake) is produced which must be emptied by tilting the furnace. The tilting drum furnace operates with a reversing flame, where additional oxygen lances can be used. The principle of the tilting drum furnace is similar to that of a top blow rotary converter, which is often used in the copper industry. Characteristic of these furnaces are their hydraulic tilting mechanism and the use of natural gas-oxygen burners, which are arranged on the front side in the furnace lid. Their capacity is 6–10 t. Their main advantages are less salt slag accumulation and less gas consumption and flue gas volume than those of the rotary drum furnace [12,140,141].

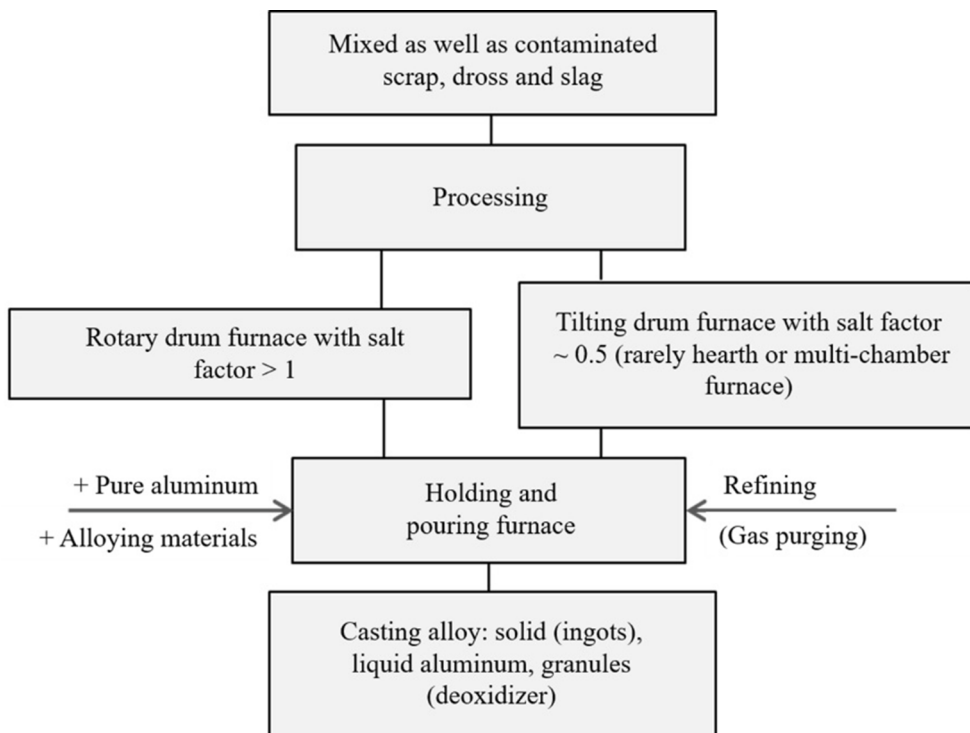


Fig. 14. Illustration of the process sequence for Al recycling with salt slag [110,111]. Reprinted with permission from [111].

When melting with salt, care must be taken to ensure that the off gases are specially treated. The off gases contain not only the combustion products (CO_2 , CO , H_2O , SO_2 , residues of organic materials), but also low-temperature carbonization products, dioxins, evaporated salt (NaCl , KCl , NaF , KF), evaporated MgCl_2 and HF. The resulting filter dust usually has to be disposed of in specialised landfill [137,142].

3.3.3. Residual materials produced in the secondary metallurgy of aluminum

In aluminum secondary metallurgy, a distinction must be made between smelting with and without salt. In all smelting units without the use of a chloride mixture, a dross is produced that can contain up to 80% metallic aluminum. The high degree of metallization shows that this residue is a high-quality raw material. If a salt is used in the melting of Al scrap, then a salt cake or salt slag is produced depending on the amount of salt added. Additionally, many scrap pre-treatment units and the melting processes themselves produce dusts that contain valuable components to be recovered, such as salts and metallic aluminum. Another recoverable residual material is the refractory lining impregnated with the chloride mixture and the Al (furnace spoil) [110,137,143]. Table 6 gives an overview of the residues that occur in the production process of aluminum from scrap.

Drosses are those residues containing aluminum that are produced during smelting, melt treatment and casting of aluminum and its alloys in primary smelters, foundries and recycling works. They are classified as new scrap. In addition to very different degrees of metallic aluminum content, dross contains aluminum oxide, spinels, silicates and the like as well as chlorides and fluorides originating from gas purging and smelting salt treatment (see Table 7). They are processed directly or after prior mechanical treatment in the smelters [110,137,143,144].

Oxidation in the solid and especially in the liquid state of aluminum is the cause of dross. Newly formed oxides in the smelting process or oxides from the input material generate considerable amounts of this residue. Statistically, about 20–30 kg of dross is produced per metric ton of secondary aluminum produced [143,145].

Due to the high metallic content of dross, processing is essential. The residual material produced in primary or secondary production is first subjected to dross treatment, which involves either the processing of hot dross or the mechanical treatment of already cooled dross. The processing of the extracted hot material is performed by shaking out, stirring out, pressing out or centrifuging, whereby a recovery of up to 50% by mass of the metallic aluminum contained is possible. Here the pressing processes are the most effective, as higher metal losses occur due to the initiated movement during the stirring processes. Another possibility in the context of dross preparation is rapid cooling after drossing, such as inert gas cooling with argon [144]. The cooled dross can then be processed by repeated crushing and screening, where the residual materials produced are critical due to their reactivity (formation of H_2 , ammonia, chlorides, etc.) and the low metallic Al content.

Mechanical treatment is a method for material separation. Oxide residues accumulate in the fine material, whereas metal-containing lumps accumulate in the coarse-grained fraction. The metal content differs in the products of the individual processing steps (see Table 8). The further processing of the coarse material (dross, lumps and flakes), which has a higher Al content, is carried out in rotary drum furnaces with the addition of salt. Dross residues can be used as casting powder in the steel industry under limited conditions, but the resulting dusts currently have no subsequent use. Disposing of them in landfill is problematic because gases form if they come into contact with water. Another issue is their high reactivity, as they secrete damaging substances (ammonia, hydrogen, etc.) into the environment when exposed to moisture. This pollutes not only the surrounding air, but also the groundwater. The aim is

Table 6
Presentation of the residues arising in the production of secondary aluminum [110].

	Salt slag	Filter dust	Furnace lining	Dross
Accumulation (in kg/ t_{Al})	300–500	10–40	2–3	20–30
Accumulation point	Smelting in a rotary drum furnace	Exhaust gas treatment Rotary drum and holding furnace	Rotary drum furnace and holding furnace	Melt refining, foundry
Reduction/avoidance	Possible	Hardly possible	Not possible	Hardly possible
Environmental relevance	Gas formation, Elucidability	Elucidability	Elucidability	Gas formation, Elucidability
Utilization	Dissolution-crystallization process	Dissolution-crystallization process	–	Dross processing, melting processes
Removal	Landfill ban	Underground deposition	Deposition	Landfill ban

Table 7
Classification of dross into grain classes with associated metal content and listing of other constituents [110].

Classes	Metallic aluminum	Other components
Unprocessed dross	< 80 wt-%	oxides: Al_2O_3 , $\text{Al}_2\text{O}_3\bullet\text{MgO}$, $\text{Al}_2\text{O}_3\bullet\text{SiO}_2$, $\text{Al}_2\text{O}_3\bullet\text{FeO}$ etc.
Boulders	< 90 wt-%	chlorides: AlCl_3 , NaCl , KCl etc.
Dross skimmings	70 – 50 wt-%	fluorides: CaF_2 , NaF , AlF_3 etc.
Dross residue	50 – 20 wt-%	
Dross dust	< 20 wt-%	

Table 8

Average compositions and exact analyses of accumulating liquid and crumb salt slags [110,140,149,153,155–157].

Component	Salt slag			Salt cake		
	wt.-% ¹⁾	wt.-% ²⁾	wt.-% ²⁾	wt.-% ³⁾	wt.-% ⁴⁾	wt.-% ⁵⁾
NaCl	40–50	45–75	62.9	49.50	23.2 ⁶⁾	20–80
KCl	18–20			10.40		
Other chlorides	< 10		—			
Al ₂ O ₃ , SiO ₂ ·Al ₂ O ₃ , SiO ₂ , MgO·Al ₂ O ₃ and other complex oxides and hydroxides	20–25	20–40	28.0	61.3	67.8	20–60
CaF ₂	1–2		1.6	—	0.7 ⁶⁾	—
Al _{met}	4–10	5–20	7.5	n.a.	8.1	3–10
PCDD/F	20 ng ITE ⁷⁾ /kg	—	—	—	—	—

¹⁾ Specification from Krone and Essafi.²⁾ Specification from Gerke and Boin.³⁾ Specification Gil.⁴⁾ Specification from Prillhofer.⁵⁾ Specification from Peterson.⁶⁾ Specification in Cl und F.⁷⁾ International toxic equivalent.

therefore to develop suitable reprocessing methods that meet all the ecological requirements, or to achieve a chemical composition through targeted treatment which will allow this residual material to be used in alternative industries (e.g. the building materials industry) [75,135,144,146,147].

Dross is mainly processed via the smelting technique. In combination with subsequent salt slag processing, residues destined for landfill can be avoided. The salt slag produced during pyrometallurgical dross recycling is then further processed to close the recycling loop. This generates products such as metallic aluminum and salt, and an alumina-containing residue that is used (e.g.) in the building materials industry. In the context of dross processing, mechanical and pyrometallurgical recycling in combination with salt slag processing should aim for closed-loop recycling [143,148–151].

More advanced processes only introduced into the recycling of aluminum dross in recent years are based on plasma technology. The aims here are to release the metallic aluminum trapped in the dross while producing residues with minimal environmental impact. The advantage of these technologies lies primarily in the elimination of salt additives and the resulting salt slag. In this context, the ALUREC, ECOCENT, DROSRITE and DROSCAR processes are of particular mention [148,149,152].

The processing of low quality scrap or high oxide materials in horizontal or tilting rotary drum furnaces involves the application of smelting salt. The salt requirement depends on the purity of the scrap. The composition of the salt system used in the smelting process is of great importance for the aluminum yield and subsequent slag treatment. In addition to the residues of the salt used, the salt slag after the smelting process contains both metallic aluminum and various products of the chemical reactions between the salt, the metal and impurities. The PCDD/F contents are negligible (see Table 8). Industrial salt slags have an aluminum content of between 5 and 20%, and the recoverable fraction during recycling is 3 to 8% [153,154].

A large part of the aluminum contained in salt slag is in the form of finely dispersed particles and can only be partially recovered. Up to 50% of the metallic Al is contained in particles with a grain size range of 0.5 to 1.6 mm [36]. The coarser components can be separated by mechanical processing. Table 8 shows average compositions of liquid and crumbly salt slags (salt cakes). These essentially contain NaCl and KCl with additions of CaF₂, Na₃AlF₆, NaF, or KF [110,153].

During the solidification of a salt slag, the formation of spinels and silicates depends on the alloy. Metallic silicon and Mg-Al compounds occur in some cases, and magnetite (Fe₃O₄) is also found in some slags [153]. Today the salt slag composition cannot be classified according to specific types of alloy because a complex mix of scrap with unknown alloying element content is generally used in the smelting process [158]. Essential properties of the salt slag are (i) thermochemical and thermal stability at the operating temperatures; (ii) low viscosity; (iii) the highest possible density difference from the liquid metal; (iv) optimal interfacial tension to aluminum or alumina; and (v) the highest possible compatibility with the furnace lining [121,153,156].

The tasks of the smelting salt are to break up the oxide layer; absorb non-metallic impurities and broken oxide skins; promote coagulation of metal droplets to form a melt; and cover the melt to protect it from further oxidation.

The composition of the salt mixture varies depending on the application, scrap type and furnace type. >100 different mixtures are used in the aluminum recycling industry [143]. In Europe a mixture of 70 mass % NaCl and 30 mass % KCl is usual. In the USA and Canada, on the other hand, an equimolar eutectic mixture of 50 mol-% NaCl and 50 mol-% KCl is used, which corresponds to 44 mass-% NaCl and 56 mass-% KCl [121,153,156,157]. The binary phase diagram for the NaCl-KCl system is shown in Fig. 15 [159]. Here a comparison is made between data determined by the thermodynamic calculation program FactSage and previously published data. It can be seen that the eutectic point of the equimolar mixture is below the melting temperature of pure aluminum and the salt mixture therefore begins to melt before the metal, which is why good coverage is ensured. The European mixture, on the other hand, has liquidus and solidus temperatures of 690–712 °C and 644–670 °C, respectively [153,158].

Fluorides are also added to the NaCl-KCl mixture, whereby fluorspar in the range of 2–5 mass % is often used for European applications. This can lead to an increase in the melting point. It should also be noted that the NaCl-KCl-CaF₂ mixture tends to evaporate.

In 1956 the process of detaching the compact oxide layer from the surface of the aluminum was investigated and formulated as a step-by-step process with three stages [146,154,160]. These stages are the formation of defects in the adherent oxide layer, which can

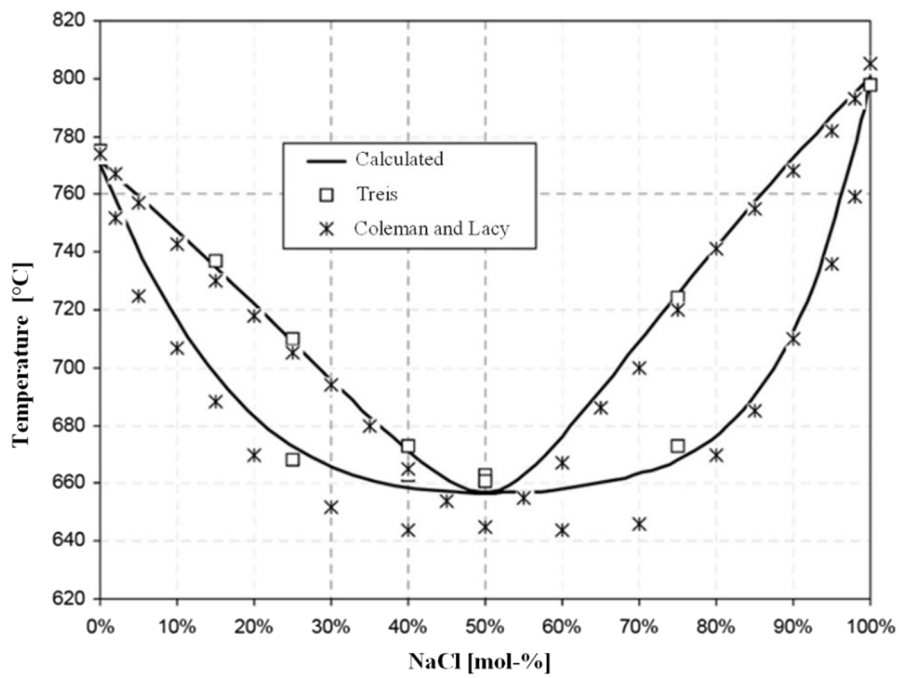


Fig. 15. Binary phase diagram of the NaCl-KCl system. Reprinted with permission from [158].

occur due to thermal stresses and phase transformations; penetration of the molten salt between the oxide layer and the aluminum; and detachment of the oxide layer. The mechanism of oxide layer detachment draws on the fact that the interfacial tension between molten salt and oxide is lower than that between oxide and aluminum. Adding fluorides results in the local accumulation of these surface-active elements, which leads to a reduction of the interfacial tension between salt and aluminum. The resulting tension gradient increases the force for separation. The chlorine anions in the liquid salt also play an essential role in attacking the oxide layer [161]. The stages of oxide layer detachment are shown in Fig. 16. The sub-steps which occur are the contact of molten salt and the oxide layer; the attack of the oxide layer by chlorides; oxide separation by penetration of the liquid salt and separated phases (liquid aluminum and oxide particles) [75,146,161].

The separation of the oxide particles now suspended in the melt takes place by wetting with salt slag. These then rise to the surface and pass into the salt slag phase [162]. After the oxide layer has been stripped off, the aluminum droplets can coagulate and collect at

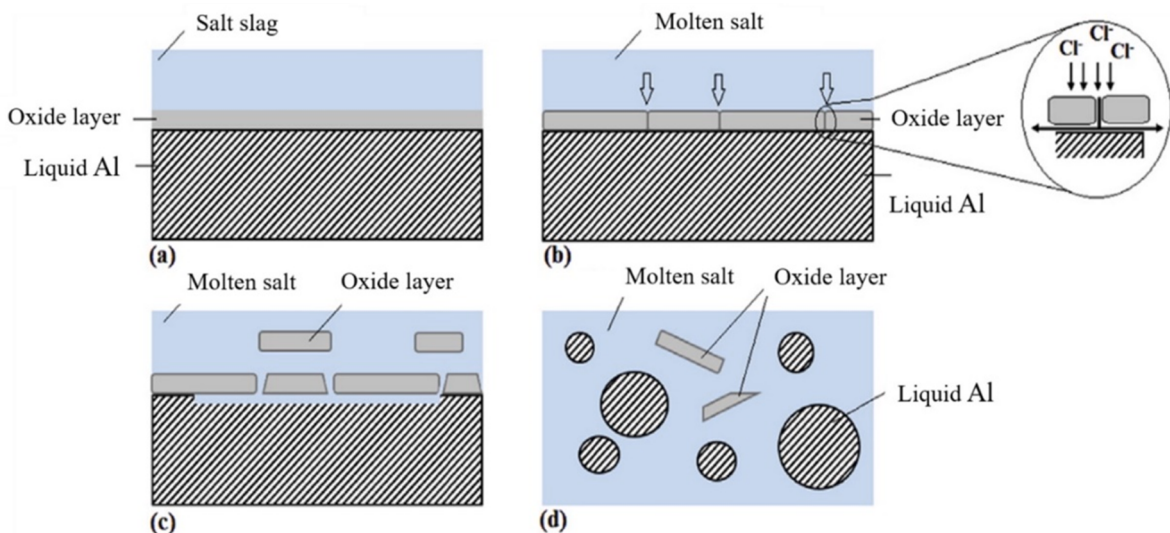


Fig. 16. Schematic representation of the oxide layer separation during the recycling of aluminum using molten salt. Reprinted with permission from [161].

the bottom of the furnace due to the difference in density. Bath agitation, as occurs in rotary and tilting drum furnaces, improves the coalescence of the metal droplets [146,162,163]. The coalescence efficiency depends on the one hand on the density and viscosity of the liquid salt and on the other on interfacial tensions, which play an essential role [164].

The ecological problem associated with salt slag lies in the water-solubility of the chlorides it contains, which can lead to high salt content in groundwater. Here slag also produces harmful gases such as hydrogen, methane, ammonia, hydrogen sulphide and hydrogen phosphide when it comes into contact with water or moisture. However, the valuable materials slag contains, which include metallic aluminum and salt, still make recycling interesting from an economic standpoint [106,110,111]. Salt slag recycling processes that pursue a zero-waste strategy are thus becoming increasingly important due to their economic and sustainability advantages.

The leaching and crystallization process (e.g. the BUS process) is the most widespread technology for the recycling of salt slag. It essentially comprises five process steps. The coarse-grained metallic aluminum is removed in appropriate crushing and classification processes, and the remaining slag is ground in mills. Due to the ductility of the aluminum, it accumulates in the form of finely rolled flakes. The metal obtained is called “coarse” and is returned directly to the smelting process. By leaching the remaining fines (<0.4 mm) with water at elevated temperature (65–80 °C) for a duration of two hours in a multi-stage process, the salts contained dissolve. The metals bound to the halides also go into solution [110,111]. After dedusting of the resulting off gases, treatment with diluted sulphuric acid takes place. In the process the ammonia present reacts to form ammonium sulphate, which is used in fertiliser production. This process is carried out in washing columns. The residual pollutants (e.g. hydrogen sulphide and phosphine) are then adsorbed in a two-stage treatment in an activated carbon adsorption plant. A solid–liquid separation is carried out in lamella thickeners, where the accumulating underflow comprises the oxide residue, and the overflow is fed into evaporation-crystallization plants to recover the salt. The resulting mixed salt has an average residual moisture content of 2–4%. The saturated mother liquor must then be fed to the last two evaporation stages, followed by filtration of the condensate. The BUS process produces metal (80% Al), recycling salt, oxide residue (partly used in the cement industry) and ammonium sulphate (used in the fertiliser industry) [110,111].

Dust which contains aluminum is mainly produced during smelting. However, although the analysis of these varies greatly, corresponding quantities are also produced during treatment of scrap and residual materials. Due to the fineness of the dusts from the secondary aluminum industry and their composition (organics, heavy metals, etc.), developing a suitable processing method is of particular interest. The main types of dust are briefly addressed below [137,145,165].

Filter dust forms during the melting of scrap in recycling furnaces. Here processes involving salt are of particular relevance. In the salt bath process in the rotary drum furnace, dusts occur when volatile components evaporate in the form of (e.g.) chlorides and fluorides; when fine particles are transported with the off gas stream; from CaO added to the off gas; or from organic material. Due to the pyrohydrolysis that takes place, aluminum oxide, hydrogen fluoride and hydrochloric acid are formed from aluminum chloride or fluoride and water. Free chlorine enters the filter dust through the merging of the off gas systems of refining and smelting furnaces. The off gas is treated with calcium hydroxide. Hydrogen fluoride, hydrochloric acid, chlorine and sulphur dioxide (from the fuel) adsorb at 300–500 °C on the sorbent. Calcium chloride, fluoride and sulphate are produced as reaction products. After cooling to below 120 °C, the dust is separated in bag filters [110]. In rotary and tilt drum furnaces operated with salt, the filter dusts consist largely of this chloride-fluoride mixture and unreacted hydrated lime, while those from the salt-free smelting process have lower CaO and salt content. The metallic aluminum nitrate content can be as high as 17.7%. Due to the carbon and the fluctuating oxygen content with the presence of copper as a catalyst, ideal conditions exist for the formation of polychlorinated dibenzodioxins (PCDD) and dibenzofurans (PCDF), plus polycyclic aromatic hydrocarbons (PAH) and polychlorinated biphenyls (PCB) [110,166]. As with salt slag, problems arise with landfill due to water-soluble chlorides, the possible formation of gases (hydrogen, methane, ammonia) when water is added, the fineness of the dust, and PCDD/F contamination [110].

Filter dust comprises waste that is subject to monitoring, which is why such materials may only be deposited in dedicated, specialised landfill. This generates considerable extra costs. Potential recycling processes are therefore being sought, but at present nothing is economically viable and disposal in landfill predominates [110].

In addition to the processes already mentioned, such as BUS technology, there are alternative areas of application where dusts can be utilised. For example, the filter dust produced in rotary drum furnaces can be used as an additive in the pre-filter of exhaust air purification. The fine-particle material from this is in turn used in rotary drum furnaces as cover salt [167]. Another possibility is to add dust to the desulphurization agent (CaO-CaF₂-Al₂O₃) in the steel industry. Here, however, the heavy metals dusts contain are problematic, as they lead to a deterioration in steel quality and generate halide emissions [110,167]. During the treatment (e.g. shredding) of scrap before it is used in the smelting process, dust from scrap processing accumulates to 25 kg/t Al which is composed of organic substances, metallic aluminum, aluminum oxide and free carbon. Currently this fine-scale material also goes to landfill [110].

Finally, residues from refractories need to be considered. These include products made from CaO, MgO, Al₂O₃, ZrO₂, Cr₂O₃, SiO₂ and C [166]. Due to increasingly strict legal requirements and the lack of landfill options, recycling of refractory materials is becoming more and more important. For every metric ton of secondary aluminum, approximately 2 kg of furnace waste is produced, generating a considerable amount of residue on a global scale [110,166]. The refractory industry is trying to minimise the amount of waste destined for landfill, firstly by increasing the service life of the linings, and secondly by recycling the material. The motivation for recycling high-temperature-resistant residual materials lies in the added value through savings in landfill costs, and the reduction of CO₂ emissions in the energy-intensive processes of primary extraction. A further advantage is the familiarity and consistency of the lining composition. It is extremely difficult to collect only one type of material, because diverse refractory products are deployed within one aggregate alone. Further impurities are generated by infiltrations and the attack of slag and metal baths. Approximately 50% of the refractory bricks used in the metallurgical sector are consumed by material conversion, enrichment with foreign substances and mixing with other lining zones, which means that reuse in the form of secondary products is not possible [166]. It is therefore advisable to consider using materials destined for landfill in alternative industrial sectors (e.g. the building materials industry). Appropriate

treatment processes can be deployed to separate valuable metals, and the remaining raw material can be used, for example, as an additive in road construction. Application in cement production and addition to abrasives and slag formers are also conceivable [166].

3.4. Mixing scrap-based melts with primary aluminum in secondary synthesis

If we follow the material flow in the Sankey diagram shown in Fig. 17, we see that only a relatively small proportion of the total end-of-life aluminum scrap from products is returned to secondary processing and used for the subsequent production of wrought aluminum alloys [8]. This reflects the complexity involved in collecting and separating different scrap streams in order to achieve the tight chemical tolerances required for wrought aluminum alloys. There are three ways to use end-of-life scrap: (1) downcycle to fewer alloy-chemistry-sensitive applications; (2) use closed-loop recycling, as in used beverage containers; and (3) dilute “lower grade” scrap by adding primary aluminum.

Aluminum from automotive scrap, for example, has traditionally been downcycled to casting alloys because of the difficulty of separating the alloys it contains, particularly wrought and casting alloys. Based on data collected in 2012 [8] it has been estimated that 6.1 Mt of wrought scrap globally are downcycled every year to cast alloys. Increasingly, however, scrap dealers are forced to deal with the fact that more automotive scrap is available than higher-quality scrap from closed-loop sources. This lower-quality mixed automotive scrap would traditionally have been downcycled to casting alloys, but supply is currently exceeding demand [35]. This trend is exacerbated by the future decrease in demand for automotive aluminum castings, forecast due to the growth in electric vehicle sales [168]. It has been estimated that the way things are going, by 2030 there may be an excess supply of > 6 Mt of scrap which is not recyclable due to the prevalence of alloy scrap collected from open-loop recycling. For this scrap the only option at present is dilution by the addition of primary aluminum. Dilution, or “sweetening”, of scrap in secondary processing by adding primary aluminum, is traditionally performed on a limited basis due to the added expense incurred. This is amplified if we consider the amount of primary aluminum needed to dilute scrap from different sources to render it usable in wrought alloy production. Fig. 18 illustrates the results of a case study [169] which examined the amount (%) of scrap (the scrap source is shown on the periphery) that can be used to generate four specific alloys, two wrought and two cast. If we focus on the two wrought alloys, it is apparent that the 3104 alloy – the alloy used for beverage can bodies – can be produced from 100% scrap. However, apart from this specific combination of alloy and source, it is also apparent that, using the technology available today, generating the wrought alloys will typically require at least 50% primary aluminum in order to achieve the desired wrought alloy chemistries. It is notable that even producing 6061 from 6xxx scrap requires significant dilution due to the significantly different levels of impurity tolerance for minor elements among various alloys within this class [29].

Fig. 18 highlights the significant advantages that might be achieved if aluminum scrap separation could be improved according to scrap source [17]. Taking end-of-life vehicles as an example, the advantages that would arise simply from separating cast components (engine and transmission components) from wrought components are apparent. Owing to the high alloy content of the castings, mixing these two sources otherwise significantly increases the amount of primary aluminum required to achieve wrought alloy chemistries. This would be a motivation for scrap standards that focus on sorting based on product applications [169].

Even in the best-case scenario of closed-loop recycling, as used for beverage cans, a significant proportion of primary aluminum is

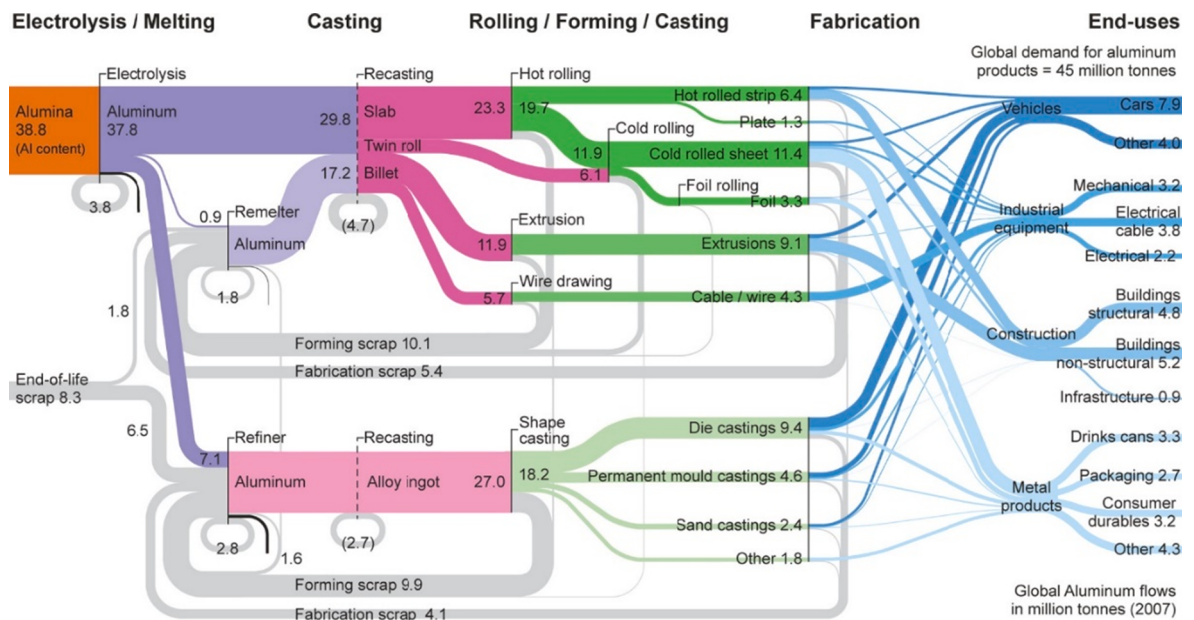


Fig. 17. Sankey diagram (used with permission from [8]) showing materials flow (in millions of metric tons per year; 2007 numbers) showing the flow of aluminum from liquid metal (left) into products (right), including the flow of end-of-life scrap (left, center) into secondary processing.

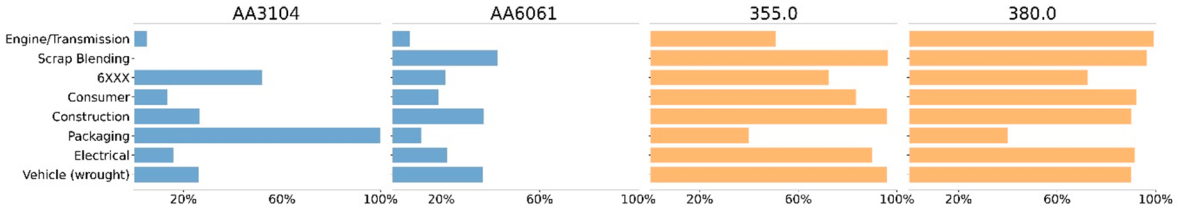


Fig. 18. Case study illustrating an idealized view of maximum scrap utilization (%) for two wrought (3104, 6061) and two cast (355.0, 380.0) aluminum alloys starting from the typical scrap mixes from the sources listed on the periphery of the diagram [169]. Image taken with permission from [169].

still partially required because production outstrips the supply of scrap. The most recent report on aluminum beverage can recycling by the Aluminum Association [170] shows that in the US, 66% of an average aluminum can's weight comprises recycled content (43% from recycled beverage cans and 23% from post-industrial scrap arising from manufacturing); 7% comprises non-beverage can, end-of-life, scrap; and 27% comprises primary aluminum. The repeated recycling of used beverage cans in a closed loop can then lead to the accumulation of minor impurity elements that will eventually exceed alloy tolerances. Løvik and Müller [96] provided a simplified description of such impurity accumulation in the closed-loop recycling of beverage cans. They specifically considered the accumulation of Ti coming from lacquer on the can body, the amount of Ti introduced in each cycle being conservatively estimated to be $x_i \sim 0.1\%$ of the weight of the can body. After n cycles, the concentration of impurity, C_i will have risen from its initial value, $C_i^0 (n = 0)$, to,

$$C_i(n) = (\dot{R})^n C_i^0 + \left[\frac{x_i}{(1 - f_{lid})} \right] \left[\frac{\dot{R}(1 - \dot{R}^n)}{1 - \dot{R}} \right] \quad (3)$$

where f_{lid} is the fraction of the can mass contained in the lid ($\sim 20\%$ [96]) and \dot{R} is the end-of-life recycling rate for beverage cans. In the case of Ti, for which $C_i^0 \approx 0$, the results obtained as a function of the number of cycles is shown in Fig. 19a using different recycling rates to illustrate its effect on Ti accumulation. As $n \rightarrow \infty$ the impurity concentration approaches a saturation value, this saturation level being shown as a function of recycling rate and initial impurity fraction in Fig. 19b. This highly simplified model illustrates the important compromise that must be considered; increasing the scrap intake, even in the case of closed-loop recycling, can lead to undesirable accumulation of impurities that are hard, if not impossible, to remove in secondary processing. This can set an upper limit on the level of recycled content that can be deployed in the manufacture of new products according to current alloy design strategies.

In summary, primary aluminum is still an important mainstay in wrought alloy production today. Compared to wrought alloys, the demand for cast aluminum alloys is decreasing [72,171,172] and this may lead to increased demand for primary aluminum for sweetening. To most effectively use wrought alloy scrap, significant efforts will thus be required in the areas of alloy separation and tramp element removal if we are to recycle automotive wrought alloys in particular [36].

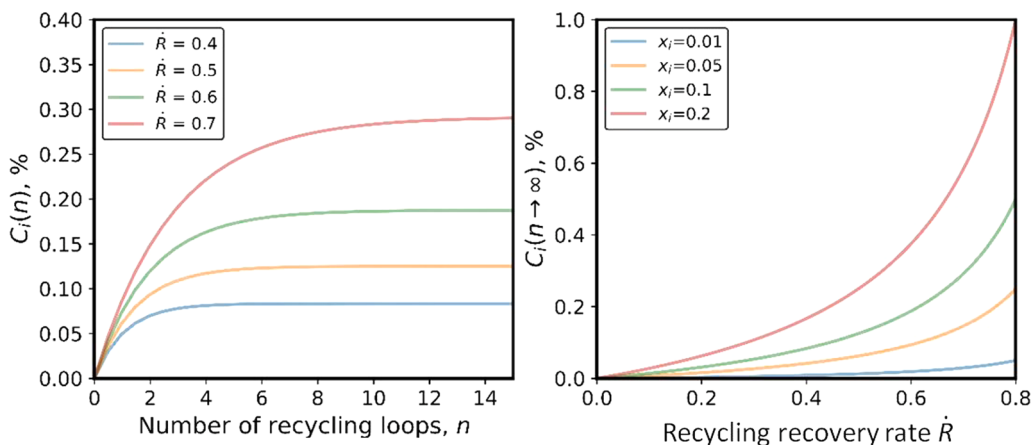


Fig. 19. Prediction of the accumulation of impurity Ti due to recycling of closed-loop beverage cans, reproduced with permission from [96]. (a) The concentration of impurity as a function of the number of recycling loops for different assumptions of the recycling rate of end-of-life beverage cans. (b) In (a) one can see that impurity levels saturate as the number of recycling loops increases. Here this saturation concentration is plotted as a function of the recovery rate for different assumed levels of contamination (% of can weight). The x-axis is truncated at a recovery rate of 80% because the remaining 20% of the recycled can mass comes from the can lids, which do not contribute to Ti contamination via lacquer.

3.4.1. Refining of aluminum melts containing scrap, and casting

3.4.1.1. Brief introduction to the metallurgical fundamentals of the refining process. The reactivity of aluminum with other elements presents refining challenges. These will intensify significantly in the coming years due to the increasing share of low-quality scrap and partially insufficient scrap-sorting quality. Recycling companies will also be confronted with more customer demands with regard to alloy recycling rates, meaning that standard dilution with primary aluminum will no longer be as easy. In the future, besides the usual refining processes such as purging gas technology, filtration and, in some cases, melt settling time, further technologies will have to be deployed to guarantee the quality of materials required. The essential scientific conditions for treating liquid aluminum are explained briefly in the following.

The solubility of almost all metals in aluminum melts and the reduction capacity of base aluminum in oxides each cause an increase in the foreign metal content. Liquid aluminum also has a high affinity to gases, which means that its selective use for melt purification must be restricted to only a few elements, such as Sr, Na, Ca, Li and Mg. Besides the soluble components, solid compounds in the form of oxides, nitrides, chlorides and carbides also cause contamination of the melt and a significant decrease in the quality of the material properties. Many elements form intermetallic compounds (IMCs) with aluminum, especially during the solidification process, which in turn also significantly impair the material properties. Higher quality standards despite the scenario of increasing scrap content coupled with decreasing scrap quality can only be achieved in the future via (i) improved scrap collection and treatment; (ii) optimization of melting technology; (iii) optimization of refining methods; (iv) development of new smelting and refining technologies; and (v) exploitation of casting methods which enable high solidification rates [173–176].

Table 9 and **Table 10** give examples of dissolved and solid impurities and explain their origins, the consequences for quality and possible removal technologies. It should be mentioned, however, that the elements listed only represent a small selection of the potential impurities; main alloying elements such as Cu, Si, and Mn and secondary elements such as Cr, V, Zr, Ti and Cd are not mentioned, but nevertheless enter the melt with the scrap in varying quality. Further elements also enter the melt through low-quality scrap; their effects are not yet known and they are frequently not recorded analytically. Notable examples of such metals are rare earth elements, In, Se, Te, and Bi [110,111,177,178].

The effects of solid impurities can vary greatly according to composition and origin, which is why targeted removal is necessary prior to the solidification process. Otherwise not only the material properties (elongation, toughness, yield strength, corrosion property, surface quality, etc.), but also the subsequent process steps, such as those during forming, can be negatively affected [110,179,180].

Of greater importance are oxides, predominantly aluminum oxide (Al_2O_3). Aluminum oxide can, however, also occur with other oxides: MgO or mixed oxides of aluminum oxide with magnesium oxide (spinel, $\text{MgO}\cdot\text{Al}_2\text{O}_3$), and oxides of other alloying elements, e.g. silicon dioxide (SiO_2). Oxides from the refractory can enter the melt through abrasion of the furnace and channel lining, and are usually silicates or other complex oxides, which may also contain Na, K and Ca. Less frequently, nitrides are present in the metal itself. Similar to oxides, they can be formed by a reaction of the melt with the atmosphere or during gas purging with nitrogen. They mainly occur in the dross or salt slag region, where they largely remain bound. Al carbides play a role in secondary aluminum, for example, when they are introduced via primary metallurgy or input material (organics) and may convert into oxides or other compounds. Chlorides may originate from the salt slags used in smelting or be formed during refining treatment of the melt with chlorine or chlorine-containing gases. They occur as Na, Ca and possibly also Mg chloride inclusions. Intermetallic phases are also present, which either form in high-alloy aluminum melts or are introduced into the melt by master alloys (e.g. Al_3Ti , Al_3Zr) or during grain refining treatment (e.g. TiB_2) [177,181,182].

The sizes of solid particles range from a few micrometres to a few millimetres. The particles often agglomerate, so that oxides are

Table 9

Examples of dissolved elements/impurities, their origins and qualitative effects, plus their refining possibilities in aluminum melts [110].

Element	Origin	Consequences/influence on	Possible removal means
H	Reaction with the atmosphere and combustion gases; moist feed materials and refractory lining; alloying additives	Gas bubbles, gas porosity, annealing bubbles (W); mechanical properties	Steady-state treatment, purge gas treatment (vacuum treatment)
Li	Input materials (Al-Li-alloys)	Dross formation tendency; “blue corrosion” (W)	Treatment with reactive gases and salts
Na	Reaction with refractory materials	Dross formation tendency; edge cracking (W); “pick-up”-formation (W); casting properties	Reaction with reactive gases and salts
Ca	Input materials; reaction with refractory materials	Dross formation tendency; casting properties (C)	Reaction with reactive gases and salts
Sb	Input materials (modified casting alloys)	Analytical tolerance	None
Pb	Input materials (adherent, free-cutting alloy, bearing metal)	Analytical tolerance; casting properties (C)	None (vacuum distillation)
Fe	Input materials (foreign component)	Analytical tolerance	None (crystallization)
Mg	Input materials (alloying element)	Analytical tolerance	Treatment with reactive gases (vacuum distillation)
Bi	Input materials (free-cutting alloy)	Analytical tolerance; casting properties (C)	None
Zn	Input materials (alloying element)	Analytical tolerance	(Vacuum distillation)
Sn	Input materials (adherent, bearing metal)	Analytical tolerance; casting properties (C)	None

C = Casting alloys, W = Wrought alloys.

Table 10

Examples of solid impurities, their origins and the qualitative effects, plus their refining possibilities in aluminum melts [110].

Contamination	Origin	Consequences/influence on	Possible removal means
Oxides Al_2O_3 , MgO Spinelles $\text{Al}_2\text{O}_3\text{-MgO}$ Silicates CaSiO_3 Aluminates CaAl_2O_4	Reaction with the atmosphere; input materials; erosion of refractory lining	Tool damage during processing (W); tool wear during processing (C); mechanical properties; staining, polishing and shining behavior (W); "gray lines" (C)	Steady-state treatment; treatment with reactive gases; filtration
Nitrides AlN	Reaction with the atmosphere; purge gas treatment with N_2		
Silicates CaSiO_3 Aluminates CaAl_2O_4	Refractory lining		
Carbides SiC , TiC	Reaction of the melt with carbon; abrasion of the refractory lining with SiC , master alloys		
Chlorides NaCl , KCl	Melting process with salt; purge gas treatment with Cl_2		
Intermetallic compounds Al_3Zr , Al_3Ti , AlTiZr , etc.	Master alloys; reaction in the melt with unfavorable alloy compositions		(Crystallization, filtration)

C = Casting alloys, W = Wrought alloys.

mainly present in the melt as so-called oxide flakes. In addition to size, the particle concentration (characterized by the inclusion number, i.e. the number of particles per unit area), and above all shape and distribution play a decisive role. Solid impurities are usually removed by means of gas purging in combination with filtration. However, due to the variety and size of the various compounds, existing refining methods are generally not suitable for complete separation.

In aluminum melts, alloying elements which are more noble than aluminum are usually reduced by dilution with primary aluminum because no economical refining processes are available. Hydrogen is removed by gas purging. Salts (described in detail in section 3.3) are also used in the course of smelter purification, sometimes in the form of slags, but also selectively as powders, granules or tablets added during melting. They can be added via immersion bells, via the gas flow or by charging onto the melt surface; they act in the same way as purging gases [106,110,177].

The scrap treatment described in section 3.1 also has an important impact on the purity of the melt. However, the various influencing variables mean that complete grade purity cannot be achieved, and extensive research and development are still needed in the area of refining liquid aluminum for sustainable production of aluminum alloys with high recycling rates. The two common refining methods used to purify molten aluminum are detailed below [110,183].

3.4.2. Gas purging for aluminum melts

In the course of gas purging, a flotation effect brings about the removal of dissolved hydrogen; elements which have a higher affinity to the gas than aluminum; and solid components. In discussing the process a distinction must be made between inert gases (argon and nitrogen) and reactive gases (chlorine and SF_6). Reactive gases are normally used in mixtures (in combination with argon or nitrogen) [177,184]. With inert gases, dissolved hydrogen (H) diffuses into gas bubbles and H_2 is discharged. Here bubble size is an essential factor which depends on the injection system. In gas purging four main process technologies are used to inject the gases. The process can take place in the furnace or in-line in the launder. As the bubble diameter decreases, the specific bubble surface area and thus the mass transfer area increase sharply, greatly increasing the gas purging efficiency. Here not only the removal of hydrogen, but also removal of solid components via a flotation effect play an important role. In gas refining with reactive mixtures (e.g. chlorine-argon with up to 15% chlorine), additional elements such as Sr, Na, Ca, Li and Mg can be removed.

3.4.3. Filtration of impurity-contaminated aluminum melts

Filtration treatments are important for alloys which contain large amounts of scrap. This is mainly due to the intrusion of iron, which is a typical and highly problematic tramp element because of its tendency to form or enrich in ternary or quaternary intermetallic compounds (IMCs) [119]. Advanced filtration strategies are thus gaining momentum for melts with a high fraction of post-consumer (old) scrap, as they typically contain higher iron fractions [185].

Besides binary IMCs Al_3Fe , typical ternary phases containing iron such as Al_3FeSi , $\beta\text{-AlFeSi}$, $\alpha\text{-AlFeSi}$, $\text{Al}_{15}\text{Mn}_3\text{Si}_2$, Al_4FeSi_2 and related compounds have been reported. The literature uses several different notations for some of these phases, which can be confusing. The notations AlFeSi , $\beta\text{-AlFeSi}$ or $\alpha\text{-AlFeSi}$ are actually abbreviations for different types of intermetallic with more complex compositions. For instance, the $\beta\text{-AlFeSi}$ phase is actually stoichiometrically a $\beta\text{-Al}_5\text{FeSi}$ phase, and the $\alpha\text{-AlFeSi}$ phase is stoichiometrically an $\alpha\text{-Al}_8\text{Fe}_2\text{Si}$ phase. Most of these phases are metastable, which means that the specific Fe-rich phase observed depends on cooling rate and heat treatment. For instance, the $\alpha\text{-Al}_8\text{Fe}_2\text{Si}$ phase tends to form at higher cooling rates instead of the $\beta\text{-Al}_5\text{FeSi}$ phase [186–188].

The variety of possible intermetallics naturally increases if other tramp elements such as Mn, Cr, Cu, Ni, Zn Mg, Na and Li also enrich in the scrap and in the melt [37,71]. For instance, as discussed below in more detail, doping with Mn can change the acicular $\alpha\text{-Al}_8\text{Fe}_2\text{Si}$ phase into a more granular-shaped $\alpha\text{-Al}_8(\text{Fe}_2\text{Mn})\text{Si}$ phase or into the $\alpha\text{-Al}_{12}(\text{Fe},\text{Mn})_3\text{Si}$ phase (see Fig. 20).

Scrap-related phases containing Fe, Cu, C and Ni can have a particularly detrimental influence on the alloys' corrosion resistance, as

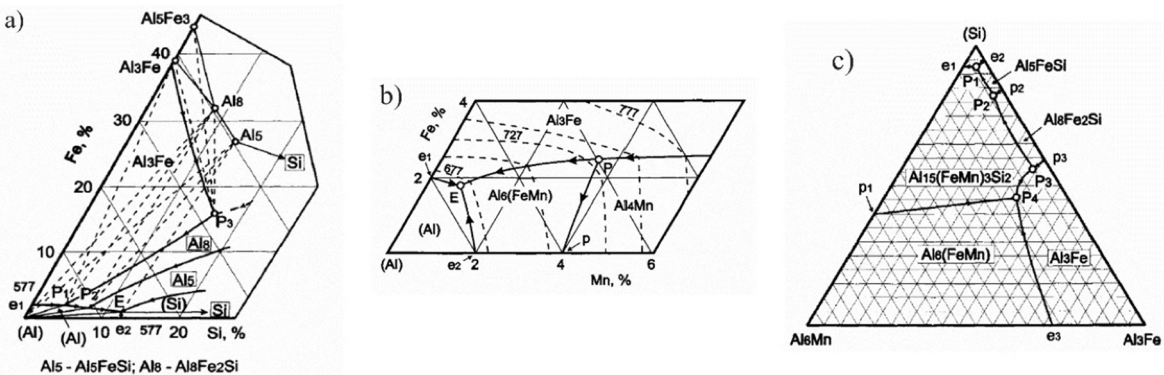


Fig. 20. Aluminum-rich regions of phase-diagram sections and projections for the most important tramp elements Fe, Si and Mn. (a) Aluminum-rich side of the Al-Fe-Si system. (b) Projection of the liquidus lines of an Al-Fe-Mn phase diagram. (c) Polythermal projection of the solidification surface of the quartenary Al-Fe-Mn-Si system. Figures reproduced with permission from [187].

they form local galvanic elements which nucleate and accelerate corrosion. Some IMCs, however, can be beneficial when they act (for instance) as grain refiners. Examples of this effect are some IMCs containing Cr and Zr. Overviews of the phases, their thermodynamics and measures for removing them by filtration, centrifugal separation or electromagnetic (eddy-current) separation were provided by Gnatko et al. [189] and Gaustad et al. [37].

Packed bed filters and ceramic foam filters are used for the filtration of aluminum melts. In applying filter systems a distinction can be made between (i) cake filtration and (ii) deep-bed filtration [190]. In cake filtration a layer of inclusions, the so-called filter cake, is formed on the filter surface through which melt must flow. Cake filtration occurs primarily at high inclusion numbers, with the separation of large inclusions on the surface of the filter cake occurring by mechanical influence [191]. In deep-bed filtration, inclusions are removed from the melt after accumulation and deposition by means of adhesion to the inner surface of the filter medium. Deep bed filtration is particularly effective for the removal of small, low-content inclusions (<20 µm). Surface effects are predominantly responsible for removal [177].

The two filtration mechanisms occur together and/or sequentially. Therefore a filter cake can form on the surface of a deep-bed filter. In cake filtration, however, the filter cake itself acts as a deep-bed filter. The concentration of inclusions in the melt is important in that filter cakes, which improve filtration, only form at high inclusion concentrations. However, very high concentrations can quickly lead to large filter cakes, which result in enhanced filter impermeability to the molten aluminum and, in turn, the necessity for particle pre-separation measures, e.g. gas purging. It is assumed that due to surface effects, particles > 30 µm are isolated mainly by mechanical separation, and particles < 30 µm mainly by adhesion [110,177]. Surface effects are ultimately responsible for the final deposition of particles on the inner filter surface. Particle adhesion is caused by van der Waals and chemical bonding forces, enhanced by hydrodynamic pressure forces. The predominant mechanism in each case depends on (i) particle shape, size, and type; (ii) melt temperature, composition, and flow rate; and (iii) filter material structure, morphology, and composition [192].

Due to the various influencing factors, various types of filter are deployed in aluminum industry gas purging systems: (i) net filters; (ii) packed bed filters; (iii) ceramic foam filters; and (iv) ceramic tube filters. They are frequently used in combination to meet quality requirements, especially in the context of wrought alloys. Due to the challenges inherent in using old scrap, filtration in combination with gas purging technology is likely to receive increased attention in the future [110,177,191].

3.4.4. Alternative refining processes for aluminum melts

Aluminum melts can only be refined to a limited extent, and generally only a few elements (alkali and alkaline earth metals), dissolved hydrogen and solid particles can be removed. To remove higher-content alloying elements and impurity metals, other physical and electrochemical processes can in principle also be considered., these are (i) intermetallic precipitation; (ii) segregation (in combination with centrifuges); (iii) distillation; (iv) ultrasonic treatment for hydrogen removal; and (v) molten salt refining electrolysis (only for very high Al purities). These processes are currently not economically feasible. However, lack of quality scrap, insufficient scrap treatment processes, the limitations of existing refining processes, higher quality standards and increasing recycling rates mean that alternative refining processes for aluminum melts will become ever more pivotal in addressing industry demands and practicalities [193,194].

3.4.5. Continuous casting of aluminum and the roles of solidification rate and scrap-related impurity elements

The invention of today's continuous casting process by Walter Roth in 1936 [195] led to significant developments in the solidification technology of metals, including vertical, horizontal, thin-strip and composite casting (Fig. 21). For aluminum these process technologies are mainly used for the semi-finished product formats of rolling ingots and extruded billets, and for cast ingots. The main differences lie in the mold used and the number of molds [196–200].

Continuous casting is a generic term for a variety of continuous and semi-continuous casting (direct chill casting) processes for metallic materials. It produces elongated castings with a constant cross-section. Continuous casting has many advantages, in particular

(i) high yield; (ii) low energy requirements; (iii) low investment costs; and (iv) high surface and microstructure quality [196–198,201,202].

In addition to affecting the quality of the liquid aluminum (hydrogen, inclusion, alkali metal and alkaline earth metal content), mold technology also has a significant influence on continuous casting quality. This is determined by the mold-length-dependent formation of the strand shell by indirect heat dissipation (which causes edge segregations) and the melt supply, which effects the solidification time, the microstructure and the cooling condition after the mold [196–198].

In semi-continuous direct-chill (DC) casting, water flows directly from the mold to the ingot surface (direct chill). During this process there are three different cooling zones: (i) primary mold cooling; (ii) secondary water cooling; and (iii) bottom block cooling [203].

Vertical continuous (direct chill) casting is the central technology in the aluminum industry. In recent decades, numerous molds have been developed for the purpose. Selected processes and mold technologies are discussed below as examples [204,205]. With the exception of some hot-top molds, in the procedure the metal is fed via a system comprising a pouring nozzle with a plug for metal flow control. The further distribution of the liquid metal in the mold is performed by special glass fiber distributor bags, the structure of which is highly dependent on format and alloy [196,206].

Clad sheets or plates are interesting product alternatives to monolithic material production, particularly if alloys contain large amounts of scrap. Cladding can become necessary because high-strength aluminum alloys contaminated with tramp elements but intended for special applications sometimes lack satisfactory corrosion and/or surface finish properties. Here a thin layer of pure aluminum is applied to ensure a better protective effect [196]. Often the cladding process is carried out by rolling the different materials. This production process is costly and requires high surface purity at the interfaces of the cladding and the core material [207–209]. Novelis and Wagstaff have therefore developed a casting process for the production of already-clad rolling ingots (Fusion™). The main challenges here are the various thermal expansion coefficients and liquidus temperatures of the materials, which require a special cooling regime. Two different melts must also be provided for the casting, each with a separate melt supply. Double-sided cladding therefore needs three melt distribution systems (nozzle, plug, distributor bag, etc.). The control effort and the required degree of automation are also major challenges compared to other casting processes [196,207–209].

The various solidification and casting strategies described above all act on the resulting as-cast microstructures [173–176]. Important features in the context of this paper are the Scheil-type macrosegregation profiles through the cast material; the resulting spatial and size distributions; the particle shapes; the remaining degree of solute supersaturation; and the alignment and morphology of intermetallic phase stringers along cell boundaries. Because the freezing rate changes en route from the surface to the center layer regions, the gradients of features between the center and the near-surface regions also matter.

More specifically, higher cooling rates generate finer dendrite cell sizes and thinner phase morphologies. If cooling rates are too slow, the larger intermetallics in particular become problematic. While these are general trends for all aluminum alloys, a specific challenge in the context of SoDA is how scrap-related tramp elements act and distribute themselves in as-cast slabs. A systematic literature overview and study of the related effects was conducted by Wagstaff et al. [45,210] for a 3104 alloy. They cast ingots with an Fe content higher than that of the commercial standard composition, and investigated the macrosegregation profiles and spatial distribution of the resulting intermetallic particles through the slab thickness. Interestingly, they reported that increased iron content – representative of impurity intrusion from using more recycled material – has a refining effect on the constituent particles. This was particularly true of the center regions of the as-cast ingots. They also suggested that higher particle numbers and reduced particle size improve recrystallization kinetics through particle-stimulated nucleation.

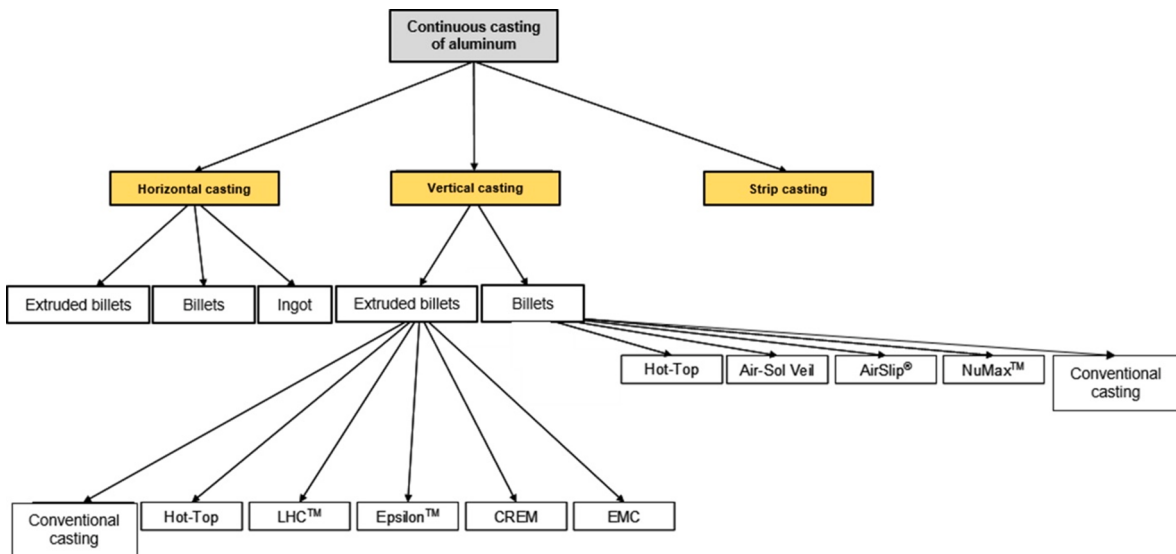


Fig. 21. Continuous casting technologies for the production of aluminum. Reproduced with permission from [196].

Lazaro-Nebreda et al. [173] also studied the solidification of Al-alloys made from scrap containing high levels of Fe, with a special focus on the formation of Fe-rich intermetallic phases and the effects of different melt processing conditions. Their work revealed that the formation and dispersion of Fe-rich IMCs depends not only on cooling rate and holding time prior to solidification, but also substantially on the preceding melt treatment and its effect on IMC nucleation and growth. They also studied the beneficial impact of Mn on IMC dispersion and shape change, and reported that high melt-shearing increased nucleation and thus Fe-rich IMC dispersion.

Jerina et al. [174] studied the solidification behavior of a recycled 7075 alloy using cooling curve analysis and differential scanning calorimetry. They found that a larger specific surface area generates greater melt loss – up to 11 wt% – and a large number of inclusions. They observed the lowest enthalpy of solidification in materials with the largest specific surfaces, and concluded that high-melting inclusions formed.

A detailed review of enhanced solidification rates and their impact on microstructure and mechanical properties was presented by Lavernia et al. [211], who focused on 7XXX aluminum alloys containing differing amounts of tramp elements, e.g. Fe, Ni, Cr and Zr.

3.5. Near-net-shape, thin-strip, belt and chain conveyor casting methods for higher impurity tolerance

In most near-net-shape manufacturing, casting and rolling are closely combined. With the help of a casting nozzle, liquid metal is fed into the roll gap. The rolls subsequently have a double function, i.e. heat extraction for solidification and forming of the solidified strip. This eliminates the need to reheat the semi-finished product for the forming process. Release agents based on water, graphite or emulsions are used to prevent adhesion to the rolls. The main challenges of this casting technology are (i) the melt distribution system; (ii) metal level control; (iii) temperature control; (iv) release agent optimization; (v) roll cooling; and (vi) roll gap control [196,198]. Several reviews have been published of the properties and benefits of aluminum thin slab and sheet production via twin roll and belt casting methods (see Table 11) [212–214].

Belt and twin roll casters produce much thinner slabs than DC casting, in a combined solidification and deformation process with much higher solidification rates and less required in-line and/or downstream deformation, although at smaller overall production rates. Table 11, taken from the overview paper of Sanders [214], gives an overview of the various near-net-shape casting methods.

Twin roll casting involves pouring the melt into the gap between two rotating water-cooled cylindrical rolls, where it solidifies rapidly and produces sheets with a thickness of a few mm. In twin roll casters, the aluminum solidifies almost entirely on the roll surfaces prior to reaching the roll gap, where the hot material is exposed to an in-line deformation step. Compared to conventional DC casting, this method requires less capital, generates lower operating costs and lower energy consumption due to the reduced total thickness reduction, and has a reduced scrap rate – but also has a lower total production rate. Several methods, including varying in-line and downstream deformation and the subsequent heat treatments, have been developed to adjust the crystallographic texture and the microstructure of the sheets.

The attractiveness of the comparably low cost and low deformation work offered by near-net-shape aluminum casting is lessened for some alloy variants by lower surface quality and lower microstructure homogeneity compared to material produced via DC casting and downstream forming. This applies particularly to surface-sensitive can stock and automotive alloy grades. Material of good quality can commonly be produced via the twin roll route for the low-alloyed aluminum grades 1xxx and 8xxx and for 3xxx alloys. Twin-belt machines, mainly of the Hazelett design, are used to produce 3xxx and 5xxx series alloy sheet products with moderate strength, surface requirements and good corrosion resistance. The greater solid solution supersaturation during twin-roll casting leads to finer dispersion of primary phases and finer grains elongated in the casting direction. Therefore – in contrast to the processing routes established for DC cast alloys – processing routes for producing twin-roll cast materials require adjustment.

The solidification rate achieved in twin-roll strip casting depends on the strip thickness and can vary between 10^2 and 10^4 K/s [215], this figure tending to be higher at the surface than at the centerline of the strip [216]. Higher casting rates increase productivity but can cause macro-segregation in the central part of the strip. The two bounding surfaces of the twin roll cast sheets solidify first, inducing the solute enrichment of the liquid. When the two solidification fronts reach the strip center, solute-enriched areas with eutectic structures aligned along the casting direction are formed.

The microstructure and texture of twin roll cast sheets can differ between near-surface and center regions, particularly in particle density and grain size. The number of dispersoids precipitated during heat treatment is usually lower in the near-surface region. Grains in the central region are to a greater or lesser extent equiaxed, while those at the surface may be elongated in the casting direction or are very fine due to the recovery and recrystallization caused by the hot in-line deformation step characteristic of the twin-roll casting process [217].

Table 11

Overview of the various near-net-shape casting methods. Reproduced with permission from [214].

DC Casting	Twin-Belt/Block		Twin-Roll
Ingot casting	450–500 mm	Slab casting	15–20 mm Roll casting 5–6 mm
Scalping	Remove 10–50 mm		None None
Homogenization	500–530 °C		None None
breakdown hot rolling	To 25–40 mm (>430 °C)		None None
Tandem rolling	To 3–8 mm (430 → 300 °C) Annealing (optional)	Tandem rolling Annealing (optional)	To 3 mm (500 → 300 °C) >350 °C Cold rolling To 1 mm Annealing > 350 °C
Cold rolling	To 1 mm	Cold rolling	To 1 mm
Annealing	>350 °C	Annealing	>350 °C

The various casting methods produce different slab dimensions which require specific downstream deformation protocols and heat treatment procedures. The main focus of this article, however, is the specific ability of near net shape casting methods to provide the rapid cooling rates attractive for casting aluminum alloys which contain large amounts of scrap, i.e. those with greater tramp element content. We have therefore reviewed some of the recent work in the field, with attention to the suitability of twin rollers for producing alloys with greater scrap content than commonly feasible in DC casting routes.

Suzuki et al. [218] used a vertical-type high speed twin-roll strip casting device equipped with a symmetrically arranged pair of water-cooled pure copper rolls to produce 6063 alloy base aluminum strips with systematically elevated Fe content, ranging from 0.7 to 6 wt%. The cooling rates were estimated to vary between 4500 K/s at the surface and 100 K/s in the mid-thickness region of the strips. The authors observed a refinement of the primary intermetallic Al-Fe-Si particles in the outer regions of the sheets, but also some coarser precipitates, stemming from a centerline segregation in the sheet center regions. After downstream cold rolling and annealing to T4 condition, or artificial aging to T6 condition, mechanical testing was conducted. The authors reported that no deterioration of bendability was found in materials with up to 3 wt% Fe and no cracking occurred upon hemming. However, age-hardenability was altered for sheets with 1 wt% Fe and above. Good results regarding bendability, increased proof stress and high ultimate tensile strength relative to the reference 6063 alloy with 0.35 wt% Fe were found in both T4 and T6 conditions for a material with 0.7 wt% Fe. This means that with a near-net-shape manufacturing method of this type, it is possible to produce sheets with the same or even better mechanical properties but with twice the Fe content tolerated in DC casting. The authors concluded that due to the high cooling rate provided by their roll caster setup, this production pathway is suitable for reducing the detrimental effects of enhanced impurity Fe content in melts containing large amounts of scrap.

In a similar study, Haga et al. [219] investigated the dependence of the microstructures and properties of 6111 base alloys produced by a high-speed twin roll caster featuring elevated Fe impurity content, in mimicry of using melts prepared from recycled aluminum alloys. They varied the Fe content between 0.14 and 1.02 wt%. They referred to their setup as a high-speed twin roller, as the device was claimed to provide higher cooling rates than conventional twin toll casters with casting speeds of up to 60 m/min. They reported equiaxed or globular microstructure in the as-cast strips. For up to 0.4 wt% Fe no changes to the tensile test results after T6 heat treatment and no cracking after hemming were observed.

In another study, Haga et al. [220] cast strips of recycled 6016 aluminum alloys for auto body sheets at 60 m/min on a vertically arranged high-speed twin roll caster equipped with 1500 mm diameter rolls. The thickness of the as-cast strips was 3.4 mm in both cases. The authors studied two material variants: one standard 6016 alloy with 0.16 wt% Fe as reference material, and another variant with 0.45 wt% Fe, representing the recycled material variant. The authors reported that both types of cast strip could be cold rolled, without any homogenization treatment, to 1 mm sheet thickness, and that T4 heat-treated strips of the 6016 alloy with high Fe content could be deformed by hemming and tensile testing like the reference materials, with no property loss.

Several strip casting studies were also conducted on 5xxx series alloys. Kumar et al. [221] studied twin roll casting and downstream processing of a 5754 alloy with a high added impurity content. The as-cast high-impurity strips generated coarse grains and complex secondary phases. When an Al-Ti-B grain refiner was added, the grain size and centerline segregation decreased significantly. The authors found secondary phases, such as Fe-bearing intermetallics and Mg₂Si, which formed a well interconnected network in the interdendritic regions. Homogenization reduced these networks and modified the secondary phases into a more equiaxed morphology. The equiaxed secondary phases aligned along the direction of rolling. X-ray diffraction showed that the predominating secondary phases produced during casting were α -Al(FeMn)Si and Mg₂Si, and that these phases prevailed during downstream processing. The strip cast and processed high-impurity alloy variant had higher strength and formability relative to the same material processed from standard mold ingot casting. The authors suggested that twin roll casting tolerates higher impurity levels than conventional mold casting.

Komeda et al. [222] and Haga et al. [223] conducted similar investigations on 5xxx series alloys. Both studies cast a recycled 5182 alloy strip using a vertical type high speed twin roll caster at 60 m/min using twin-positioned steel rolls. The authors mimicked a recycled alloy by enhancing its Fe content up to 0.6 wt%, and found properties in the processed strips that were comparable to those of the un-doped reference alloy.

Al-Helal et al. [202,224] conducted several studies of DC cast and strip cast aluminum products, using a 5754 reference alloy. The caster variant they deployed was a continuously operating high-shear melt conditioning twin-roll casting process, which was custom-designed for the production of recycled aluminum alloy strip. They observed that the method provided as-cast sheets with fine and equiaxed grains and a homogenized matrix structure, while the centerline segregation reported in other studies was eliminated. They also found that due to the imposed shear, the cast strip material showed clear recrystallization after thermomechanical treatment at 430 °C for 30 min and had >50% higher elongation and about 4% higher ultimate tensile strength compared to conventionally produced twin-roll cast strips.

Several other studies reporting similar trends for microstructure homogeneity, centerline segregation, mechanical properties and generally improved impurity tolerance of sheets produced via the strip casting route were also published about alloys based on 7050 [225], Al-Mn-Zr (with variations of Si and Fe) [226], Al-Mg-Cu [227], and Al-Mn-Fe (with variations in Mn, Si and Fe content) [228].

3.6. Advanced processing of alloys containing large amounts of scrap

3.6.1. Introduction and overview

The previous sections focused on conventional and thin-strip processing methods and how increased use of mixed scrap aluminum may impact them. However, there are also a few less common processing routes which can have advantages when dealing with material contaminated with scrap.

Two main approaches, namely conventional remelting and solid-state (meltless) recycling [229–231], have been adopted for the recycling of aluminum alloy scrap (Fig. 22). Their respective recycling efficiencies, energy consumption, cost and environmental impact during practical application need to be considered. Solid-state recycling has recently been applied to waste material from machining, chipping and turning [229–234]. This process incorporates annealing and heavy working after initial cold compaction. Large plastic strain was deployed to create metal-to-metal bonding by breaking down the oxide layers, a mechanism referred to as solid welding of scrap [229,232,234]. Such solid-state processes are estimated to reduce environmental impact in terms of energy consumption and carbon emission by 50–70% relative to conventional primary production [230]. The severe deformation and deformation-enhanced diffusion are critical for microstructure control, specifically for grain refinement. The influence of several parameters such as extrusion ratio/rate and temperature on the mechanical properties of solid-state aluminum alloys recycled by hot extrusion has been studied [229,233]. In hot extrusion most of the energy is required to heat the material. Thus, cold solid-state recycling of scrap, specifically cold profile extrusion and cold rolling of swarf material [232], was developed to reduce costs [232,234]. However, if extrusion alone is used, large residual voids remain in the recycled aluminum. A fine dispersion of particles containing Si and a reduction in the number of voids were achieved by combining extrusion and rolling, resulting in a significant increase in the density and strength of recycled Al-Si alloys.

Along similar lines, severe plastic deformation (SPD) can also be utilized for solid-state recycling of aluminum alloys [231]. Several solid-state recovery technologies have been proposed based on SPD, including equal channel angular extrusion (ECAP), cyclic extrusion compression (CEC), friction stir extrusion (FSE) and screw extrusion [231–233]. SPD processes have been successfully applied with the aim of consolidating aluminum scrap by imposing large shear deformation. In addition, SPD processes are capable of producing materials with ultra-fine grains and even nanostructured alloys which in some cases exhibit better mechanical properties than the original ingot.

Subsequent to SPD processing, homogenization and annealing towards precipitation, recovery and recrystallization can be used to control the grain size/morphology and crystallographic texture of the final products [235–237].

When applying such workflows to scrap-based alloys, tramp-element-related brittle intermetallic phases in particular can be harmful. For example the transformation of the needle-like β -Al₅FeSi phase into a more skeleton-like α -Al₁₂(Fe_xMn_{1-x})₃Si is of importance for neutralizing harmful effects resulting from accumulated Fe in recycled aluminum alloys [236,238–240]. The fraction and shape of these and other scrap-related particles is influenced by the heat treatment, and can be understood by using computational thermodynamics, also taking into account integrated solidification and homogenization [238]. Deploying a high solutionizing temperature without initializing the pre-melting of Cu-rich phases results in the fragmentation and dissolution of the Fe-rich phases, an aspect beneficial to the mechanical properties in the recycled AlSi₉Cu₃ cast alloy [240]. Another example is seen in the 7xxx alloys, which were successfully fabricated using recycled beverage cans [241]. Several advanced processing approaches for aluminum alloys

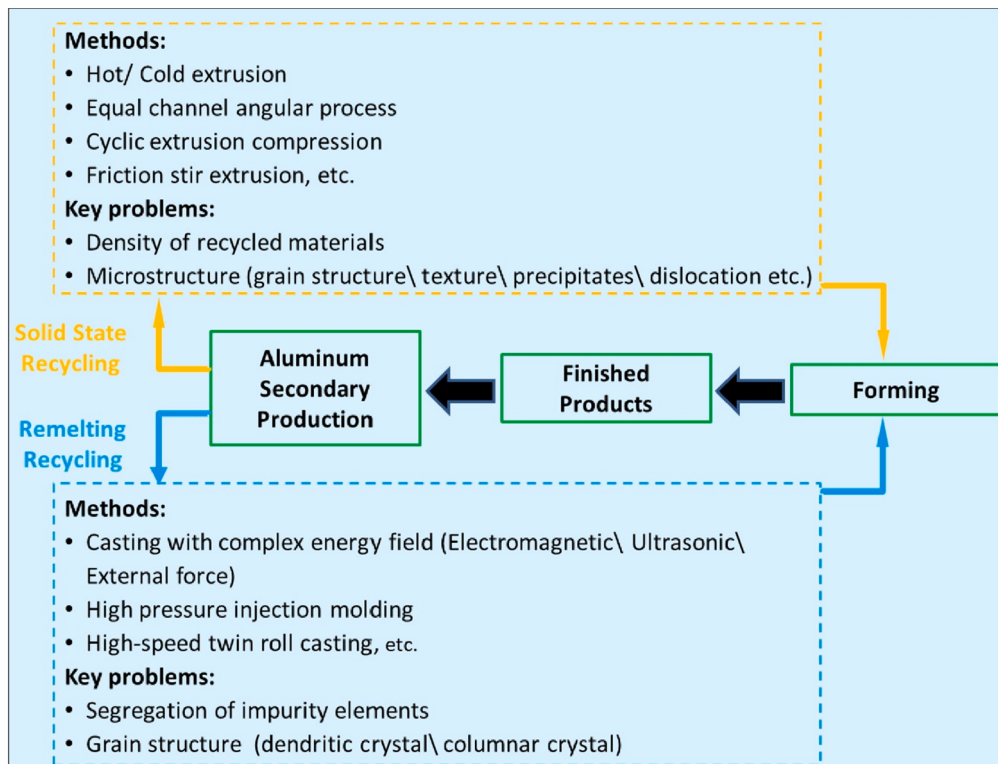


Fig. 22. Microstructure modification of alloys containing large amounts of scrap through processing.

containing large amounts of scrap are discussed in more detail in the next sections.

3.6.2. Liquid-based processing

The traditional practice for aluminum scrap recycling is to either return sorted scrap to secondary processing for smelting and casting or to directly downcycle mixed alloy scrap to cast alloys, where the process and alloys are more tolerant of composition variations. A certain number of impurity elements are thus inevitably introduced into the recycled aluminum alloys, leading to the formation of coarse intermetallic compounds. These compounds can cause excessive shrinkage porosity defects, which may have an adverse effect on mechanical properties (especially ductility) [239,240,242]. Such defects tend to be the source of cracks due to stress concentration, thus damaging fatigue strength and toughness. To mitigate these negative effects, the intermetallic compounds are traditionally modified by adding transition elements (Co, Cr, Mn, V, etc.) [243,244]. Advanced casting methods are also commonly implemented to improve the tolerance limit of the impurity elements in aluminum alloys containing large amounts of scrap [243,245–249].

High-pressure die-casting (HPDC) is widely used in the production of mixed recycled aluminum alloys due to enhanced castability and relatively low cost [245]. Fe normally has a negative effect on the mechanical properties of the cast aluminum alloys, but using HPDC as a casting and forming method can reduce their tendency to form fragile and coarse second phases [245].

Squeeze casting can refine the grain size and the Fe-rich compounds with the formation of a nano-sized Fe-rich α phase [248,249]. For this reason aluminum alloys produced by squeeze casting exhibit excellent tensile properties, especially in terms of elongation. The squeeze-cast 2A16 alloy with 0.5 wt% Fe still meets the requirements of the safety-critical suspension components used in the automotive industry (UTS > 380 MPa, elongation > 7%) [248], aiding the efficient utilization of a secondary aluminum alloy.

The application of external fields, e.g. ultrasonic, electromagnetic and force fields, during the casting process is also effective in controlling the microstructure of the recycled aluminum alloys [250–253]. Ultrasonic melt processing (USP) can not only effectively refine and enhance the peritectic transformation of the Fe-rich phases, but can also reduce the volume fraction of pores in the condensation process [250], thus prospectively modifying the microstructure and improving the mechanical properties of the recycled aluminum alloys. Zhao et. al. [251] used combined fields, i.e. ultrasonic vibration (USP) and applied pressure (squeeze casting), during the solidification of recycled aluminum alloys. They found that using combined fields can significantly refine the α -Al phase and the Chinese-script Fe-rich phases. This method also promotes dendritic fragmentation and reduces solute segregation on grain boundaries.

An intermediate approach under active development is rheoforming [254,255]. Rheoforming is a semi-solid processing technique that involves the controlled cooling of an alloy melt into a semi-solid state [256,257]. This semi-solid alloy is then actively stirred while being injected into a die. Owing to the low temperature and continuous shearing of the semi-solid mix as it is injected into the die, it is possible to achieve a fine microstructure with little macroscopic solute segregation. Unlike thixoforming, rheoforming is less sensitive to minor changes in the liquid fraction. This is beneficial for alloys considered here where small changes in composition and temperature may lead to large changes in liquid fraction [257]. This makes rheoforming feasible for a wide range of alloy types, ranging from traditional cast alloys to wrought alloys such as heat-treatable 2xxx [258], 6xxx [259] and 7xxx [259–261] alloys and non-heat-treatable 5xxx alloys [262]. Solution treatment followed by aging can bring the strength of these alloys close to their expected T6 condition, albeit with lower ductility [257,259,261]. This lower ductility has been attributed to both porosity and to partial remelting due to microsegregation [259]. While rheoforming appears a promising technique worth further exploration, much remains to be done to optimize the process for a wider range of alloys and to achieve properties comparable to those from more conventional processes. Despite this, efforts are underway to produce rheoformed parts to replace parts made by conventional die casting or forging [263].

A second near-net-shape solidification-based process of recent interest for its potential to handle a wide range of recycled alloy scrap is spray forming, alternatively known as liquid dynamic compaction or the Osprey process [264]. In this process, liquid metal is inert-gas atomized (particle sizes of 5 – 250 μm) and the atomized droplets are deposited onto a substrate in a mix of liquid, semi-solid and solid particles. Cooling rates for particles in flight can be very high ($> 10^2 \text{ K/s}$) depending on particle size, while cooling of the densifying deposit occurs much more slowly (0.1 – 10 K/s) [265,266]. Much of the interest in the potential of spray forming as a technique for handling recycled aluminum comes from its ability to refine, modify or even possibly eliminate intermetallic particles deleterious to subsequent formability and produce a fine microstructure [267–271]. A recent study on the spray forming of a 6061 alloy intentionally “contaminated” with 1.4 wt% Fe showed the preferential formation of α -Al₁₅(Fe,Mn)₃Si₂ over the undesirable plate-like β -Al₅FeSi [269]. The as-produced alloy was subsequently hot-extruded and then subjected to homogenization and aging treatments. It was shown that the mechanical properties of the heat-treated material, despite a high Fe content, were very similar to those of conventionally processed 6061. An additional advantage of the spray-forming approach noted by the authors was relatively short homogenization time due to the fine as spray-cast microstructure [269]. Studies on 7xxx series alloys show a similar ability to achieve strengths comparable to those obtained through conventional processing, although with evidence of lower ductility and corrosion resistance [270,271].

3.6.3. Solid-state processing

Rheoforming and spray forming require scrap to be re-melted during processing. The conversion of solid scrap back into liquid comes at a significant cost, both in terms of the energy required for melting (and potentially for sweetening the melt) but also in the pre-treatments required to clean the scrap. In the case of fine scrap (e.g. turnings from machining) there are additional challenges that can result in recycling yields of only approximately 50% [272]. It has been estimated that the energy savings that would arise from a fully solid-state process for aluminum scrap recycling could be as high as 90% [273,274]. This is not a new discovery; the first patent for a fully solid-state-based process for recycling aluminum scrap can be traced to the middle of the last century [273].

A wide variety of solid-state processes for recycling the fine aluminum scrap arising from (e.g.) turnings or extrusions have been

studied; a recent review is found in [231]. These processes can be separated into two groups: those based on powder metallurgy, and those based on deformation. Powder-metallurgy-based processing (milling of turnings followed by sintering, e.g. [275] or direct sintering of recycled turnings [276,277]) remains much less explored than deformation-based processing. In this context a variety of techniques have been explored, such as hot and cold extrusion [231,233,274,278], severe plastic deformation (equal channel angular pressing, high pressure torsion, accumulative roll bonding [279–281]) and friction stir processing [282]. The common feature of these processes is that they take advantage of large plastic strains to cause the fracture of oxide layers and “cold” welding of the individual particles, assisted by the heat generated during the process and, potentially, by heat supplied externally [273]. Among these processes, the most well developed are those based on extrusion. Güley et al. [274] showed the successful hot extrusion of 6061 scrap and mixed 1050 and 6061 scrap starting directly from compacted recycled extrusion pins and turnings from machining. More recent work has produced complex-shaped extrusions made directly from recycled scrap. For example, Chiba and Yoshimura [233] compared two sources of scrap aluminum (milling chips and turnings from machining) in the hot extrusion of parts from an Al-Si alloy. While both source materials could be successfully extruded following cold compaction, two key observations were made. First, fully dense materials required such large strains that it was a challenge to achieve them uniformly given the complex flow pattern through the die. Second, there was a difference in consolidation of the two source materials. While the extrusions made from the milling chips appeared fully dense at the largest extrusion ratio, significant porosity remained in the extrusion manufactured from the turnings. This points to the importance of the handling of the source material prior to consolidation [283].

3.6.4. Processing to achieve hybrid/architected recycling-friendly alloys

Regardless of the process used to convert mixed scrap into new products, concerns about performance in downstream processing or in service remain. For example, one of the problems that rheoforming, spray forming and strip casting aim to circumvent is the formation of coarse, brittle, intermetallics detrimental to ductility. Rather than tackling the issue solely through microstructure manipulation of the alloy, one approach takes into account the material's architecture [284–286]. Aluminum production has long used this approach for clad products. To improve the corrosion resistance of aerospace alloys (e.g. 2024) it is common to roll clad the surface with a thin sheet of a more corrosion-resistant alloy (e.g. 1200), while in for brazing sheets a low melting point alloy (e.g. 4004) is roll bonded onto a high melting point alloy (e.g. 3003) [287]. To address concerns regarding either the corrosion resistance or mechanical performance of recycling-friendly alloys, one solution might therefore be to take a hybrid design approach which combines two or more alloys with a particular spatial arrangement to achieve improved overall performance.

In the case of corrosion resistance, the advantages afforded by roll cladding are obvious. The benefits of a chemically distinct surface layer in controlling mechanical properties can also be quite significant, particularly in the areas of strain localization [288] or fracture [289,290]. In particular, aluminum sheet product performance is often limited by bendability issues. This is the case in automotive applications where hemming operations require a severe 180° bend. Here the most demanding mechanical need exists at the outer surface of the material, where the strains are greatest. Roll cladding made of high-strength, low-ductility aluminum alloys (e.g. 6xxx) combined with a lower strength, ductile alloy (e.g. 8xxx) has been shown to significantly improve hemming performance [290]. In this case, fracture was suppressed for a full 180° bend with a clad layer of 10% of the sheet thickness. Compare this with a monolithic 6016 sheet that exhibited significant surface cracks at bending angles of <120°.

Roll cladding is only one of the possible processes that can be used to manipulate the properties of a material's surface. Another, commercially successful, process involves the direct chill co-casting of two alloys to generate a continuously cast ingot consisting of a core made of one alloy and a surface made of another [287,291].

Roll bonding and co-casting are only two of the potential processes for generating hybrid recycling-friendly alloys. Chemical and/or mechanical treatments of the surface that change the composition or microstructure of the near-surface layer may provide an ideal opportunity to optimize the combination of environmental, mechanical and chemical performance. Taking inspiration from work on the design of architected materials from other fields might also prove highly productive in broadening the commercial appeal of recycling-friendly aluminum alloys.

3.7. Sheet-forming challenges for scrap-based alloys

Flat rolled product (foil, sheet and plate) accounts for ~30%–55% of the Al used today, varying by company, market and region. Of this, ~95% consists of the non-age-hardenable 1xxx, 3xxx and 5xxx grades [292]. In the types of application where these alloys are used, the formability of the sheet is a critical factor during processing. The formability of sheet from age-hardenable alloys (2xxx, 6xxx and 7xxx) is also important, especially for transportation applications, but the forming is usually performed in the naturally aged (T4) state (i.e. before the age-hardening step) so most of the solute is in solid solution. This solute in solution has important effects on the stability of plastic flow and the surface finishes obtained. The microstructural considerations for forming are similar to those for the non-age-hardenable classes, except that one must also consider the effect of the (de)formed microstructure on the subsequent age-hardening reaction, for example during a paint-bake treatment for automotive applications.

Some forming operations for Al-alloys – warm forming or creep forming [293–295] – are performed at elevated temperatures. Apart from the expected effects of temperature on thermally-activated dislocation processes, in the age-hardenable grades one may also observe significant changes in the precipitate state during forming, e.g. [81]. The coupling of plasticity and dynamic precipitation adds an additional layer of complexity to questions surrounding the formability of scrap-based alloys [81,85,296]. The impurity elements accumulated by including scrap can affect both processes together during the forming operation. Such contaminant couplings have not yet been studied in any detail.

There is no one quantitative measure of formability; nor can formability be simply related to any single material property. Different

sheet forming operations are used industrially and each combines different elements of stretching, bending, drawing and ironing. Stampings, such as those used for automotive body panels, are usually stretching-dominated operations, whereas beverage cans are deep drawn.

In general, formability depends on:

- the strain hardening capacity and strain-rate sensitivity of the material (which can be a strong function of the solutes in solution, and hence also of the impurity elements present);
- the crystallographic texture (which depends on the sheet rolling and subsequent recrystallization annealing steps);
- the R-value (which is the ratio of the width to thickness strain and hence is a measure of the resistance to thinning during deformation);
- the resistance to local fracture (which can be sensitive to the constitutive particles present and hence also to the presence of scrap-related impurity elements).

The relative importance of each of the above factors depends on the specific sheet-forming operation, particularly the balance between stretching and drawing. Failure during sheet forming can be of two types: local fracture may occur as a result of reaching a critical local stress or strain (e.g. at a large intermetallic particle), or excessive local thinning (necking) of the sheet may occur due to a mechanical instability in the flow. Both modes of failure can be affected by compositional modifications generated by using scrap.

Forming operations that are dominated by stretching operations (e.g. sheet stampings) often represent formability in terms of a Forming Limit Curve (FLC). FLCs are experimentally generated by stretching a clamped sheet over a hemispherical punch and monitoring the strains at which failure occurs. Fig. 23a shows a schematic FLC which highlights the strain states. Successful forming requires one to remain below the curve for the major and minor strains.

Texture, strain hardening capacity, strain-rate sensitivity, R- and ΔR -values, and resistance to fracture are all properties that can be significantly affected by compositional modifications due to the use of scrap (see Fig. 23b). Examples of these effects are presented in the ensuing sections.

3.7.1. Fracture and the role of constituent particles

The contaminant from scrap that has received the most attention is Fe, and with good reason. Discussed in section 3.7 in the context of twin-roll casting, it is currently an issue for recycling. Al recycling usually leads to Fe accumulation, manifesting as (micron-sized) Fe-containing intermetallic particles in alloys. These large constituent particles can have important effects on fracture, and sheet-forming operations that are fracture-strain-limited can be significantly affected. Bending is particularly sensitive to fracture strain. Fig. 24 shows an example in 6xxx alloys from Lloyd [298]. Here the bendability of the sheet is characterized by the minimum radius to which a sheet of thickness t can be bent without failure. The outside of the sheet surface is in tension and the inside surface is in compression. Failure usually occurs through cracking on the outer surface. Fig. 24 shows data for 6111 with three differing Fe content figures. On average, as the Fe content increases, the minimum bend radius also increases, correlating with decreased bendability. Even though these Fe additions were shown to have little impact on the yield strength, tensile strength, strain hardening or elongation, they do affect the reduction in cross-section during tensile tests. Failure occurs through void formation at the large intermetallic particles, which then coalesce, leading to failure. The correlation between bendability and reduction in thickness (due to the increase in intermetallic particles with increased Fe) is shown in Fig. 24.

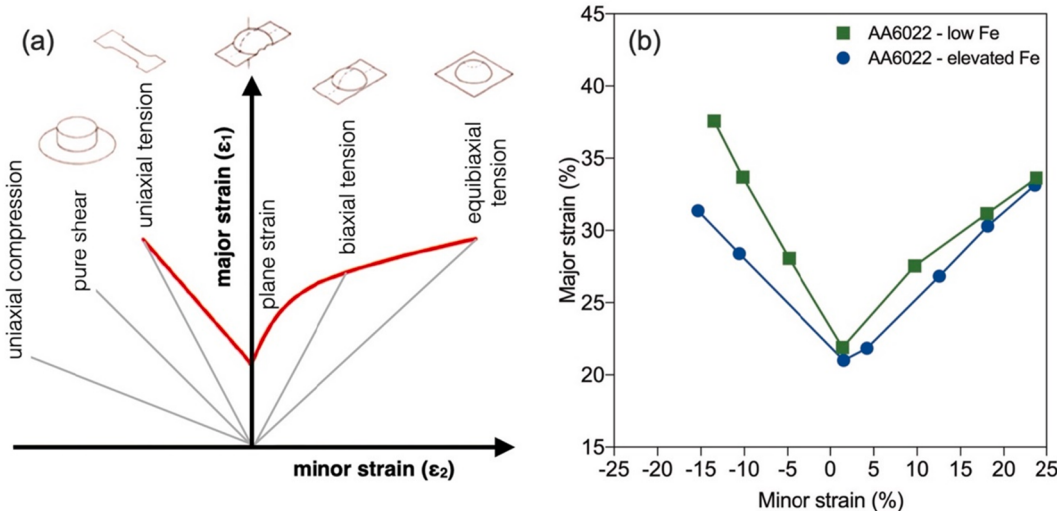


Fig. 23. (a) Schematic Forming Limit Curve (FLC). (b) FLC for two 6022 alloys containing different low and elevated Fe content. Data extracted from [297].

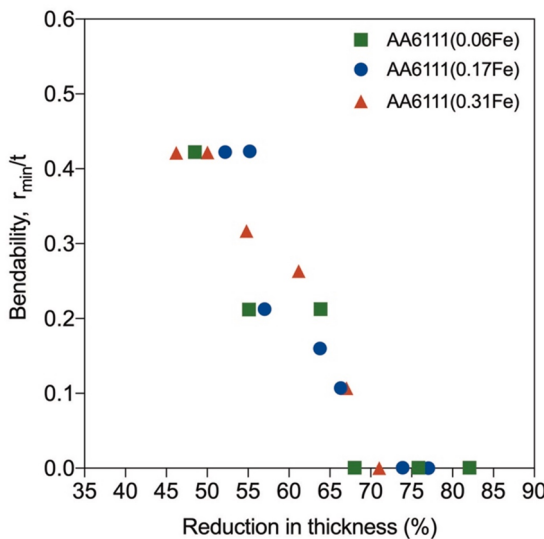


Fig. 24. Bendability of 6111 with differing Fe content as a function of the reduction in thickness measured by tensile tests. Data extracted from [298].

The failure strain is also particularly important in stretching operations. An example from Das et al. [297] of the effects of Fe-containing intermetallics on the FLC is shown in Fig. 23b. Here the FLC was determined for 6022 sheets with both a low Fe content and an elevated Fe content. The FLC for the material with elevated Fe lies below that of the low Fe material. The origin of this reduction in formability is also the Fe-containing intermetallics and their effect on fracture.

However, when considering contaminant effects and intermetallic particle formation it is important to realise that not all intermetallic particles are the same, and that they are not always detrimental. Sillekens et al. observed no significant changes in the FLC for 5017 when they increased the Fe content to 1.4% [299]. Different effects are observed in different alloy systems and for different impurities, depending on the ability of a base alloy to spread plastic deformation during straining. In addition, the critical stress and strain for the initiation of local failure at a particle also depends on its shape. This can be manipulated by adding specific alloying elements. An example is the addition of Mn in the case that the alloy has Fe/Si-containing intermetallics. Mn can change the particles' shape from plate-like to less damaging equiaxed morphologies. Therefore, alloy- and impurity-specific doping strategies can be developed which mitigate potentially damaging effects of the increasing fraction and shapes of intermetallics as a result of recycling. However, as seen below, the effects of intermetallics are not always detrimental.

While the emphasis so far has been the role of intermetallic particles in fracture and the resulting implications for formability, as scrap use increases attention should also be paid to the accumulation of elements that may segregate to grain boundaries and potentially cause embrittlement and intergranular failure. Some elements (such as Ga) are known to generate such effects in Al, but as alloy compositions become more influenced by contaminants we will need knowledge about other embrittling species, and must be able to either control their accumulation or develop mitigation strategies (such as co-segregants).

3.7.2. Grain size, crystallographic texture and R-values

During stretching or drawing operations, the sheet experiences both in-plane and through-thickness strains. The resistance to thinning during forming is the limiting factor in some operations, and this is often characterized by the R-value (the ratio of the in-plane to through-thickness strains). An R-value of 1.0 corresponds to isotropic deformation. Larger values for R correspond to greater resistance to thinning and thus usually translate to better formability of the material. For Al-alloys, the R-value is typically 0.6–0.8. Large values for R are obtained when the texture contains a large fraction of {111} planes parallel to the plane of the sheet, but such textures are difficult to obtain in Al-alloys and this is the reason for the low R-values (compared to steels). Strain within the plane of the sheet is also anisotropic, and the anisotropy is characterized by ΔR , calculated from measurements taken at 0°, 45° and 90° to the rolling direction. It is the ΔR that gives rise to the well-known earing phenomena during the deep drawing of beverage cans. A small ΔR is usually preferable [300–306].

The grain size and shape, and the crystallographic texture, all depend on the thermo-mechanical processing of the sheet; this also involves, in particular, the elevated temperature processes that include recovery and recrystallization. These processes therefore affect the R- and ΔR -values [307–312].

The accumulation of contaminant elements as a result of scrap usage can affect all stages of thermo-mechanical processing. Solute in solution will affect the accumulation of stored energy that drives recovery and recrystallization; intermetallic particles will affect the distribution of stored energy and therefore have an influence on the initiation of recrystallization, for instance through particle stimulated nucleation; tramp elements in solution can strongly affect recovery, hence modifying the competition between recovery and recrystallization; intermetallic particles will affect the migration of grain boundaries through the Zener force and therefore directly

influence the final grain size; and solute in solution can also affect the grain boundary migration through effects on boundary mobility. The final grain size and texture of the sheet will be a result of all these coupled effects – all of which can be affected by contaminant elements [313–321].

Intermetallic particles, such as the Fe-containing particles that can accumulate as a result of recycling, have already been shown to have important effects on limiting grain growth. Sarkar et al. [322] reported that the grain size of their 6111 alloy decreased from 110 μm in an alloy containing 0.06Fe to 40 μm in an alloy containing 0.68Fe. Reductions in grain size can have beneficial effects, such as improving the surface appearance of the sheet after forming by limiting the “orange peel” effect, and they can also affect the Lüders banding. A refined grain size can also give some additional strengthening (although this is not generally a major strengthening mechanism in Al-alloys) and help spread plasticity by limiting slip band length.

Intermetallic particles can, in principle, also affect texture development through potential roles in recrystallization initiation, although this has not yet been studied in detail in alloys contaminated by scrap. In the 6022 studied by Das et al. [297] with two different Fe content figures (Fig. 23b), the alloy containing more Fe actually had a lower ΔR than the lower-content Fe alloy.

Solute in solution can also affect the grain size and texture of the material through effects on both grain boundary motion (solute drag effects) and modifications to the competition between recovery and recrystallization. These have not been studied in scrap-contaminated aluminum alloys, but potential effects probably depend on the elements that accumulate during recycling.

3.7.3. Strain-hardening capacity and strain-rate sensitivity

A high strain-hardening rate and positive strain-rate sensitivity are desired in all forming operations to spread the plasticity at large strains and to prevent, as long as possible, strain localization. Whereas the formation of intermetallic particles was especially important in discussions of local fracture during forming, solute in solution is particularly significant for strain-hardening capacity and strain-rate sensitivity.

Although most solutes improve the strain-hardening rate of Al, some solutes, such as Mg, have an especially strong beneficial effect. This is one of the strategies behind the Mg-rich 5xxx sheet alloys used in applications requiring high formability. Modifications to the solute in solution due to scrap-related contaminants must be monitored carefully, both in terms of adding solute to solution, but also in terms of the formation of intermetallics that may remove valuable solute from solution. A recent study examined the effect of Cu contaminants on 5xxx alloys [323] for exactly this reason – to understand the effects on strengthening and strain hardening from the view of tolerance to recycling. We should expect much more work of this type in the coming years.

While solutes in the matrix are generally beneficial for strain hardening, in alloys containing large solute additions (such as 5xxx series and the age hardenable alloys in T4 state) the dislocation-solute interactions can lead to negative strain-rate sensitivities and the associated instabilities in plastic flow. These can manifest as serrated yielding (PLC effect), stretcher markings or even Lüders bands. All these features are detrimental to formability and can also cause poor surface finish. Some elements are worse than others, and hence an understanding of how the accumulation of scrap-related impurities affect these instabilities is required.

The formability of aluminum sheet material is complex. It depends on the ability of the material to spread plasticity during forming and resist plastic localization. This in turn depends on many features of the microstructure and its plastic response, almost all of which are affected by changes in composition due to contaminants accumulated by recycling. Since flat-rolled product represents such a significant fraction of all the Al used, it is inevitable that scrap use in sheet alloys will continue to increase in the future. It will be necessary to manage the effect of compositional variations in the phenomena discussed above, and also to develop a more in-depth understanding of the roles of all contaminant elements and how they interact with each other and with deliberate additions. Such an understanding will hopefully result in new, more contamination-tolerant sheet alloys in the future.

3.8. Joining of alloys containing scrap-related impurities

The ability to join aluminum alloys with high integrity is a key technology in manufacturing finished products across all industrial sectors. Joints often limit crash worthiness and service durability and are favored sites for fatigue and corrosion initiation. Aluminum is readily weldable by most gas-shielded fusion technologies, including by a range of laser and arc welding processes [324–327]. Of the arc welding processes, Gas-shielded Metal Arc Welding (GMAW) and its more recent lower heat input variant, Cold Metal Transfer (CMT), are generally preferred by the automotive sector to reduce distortion [325]. Al can also be resistance-spot-welded (RSW); however, point joining of Al-alloys in automotive manufacturing currently favors self-piercing rivets (SPR) because RSW with Al-alloys has a high energy requirement and low tolerance to variation in the electrode contact conditions, and produces joints with poorer mechanical performance [326,327]. Aluminum is also readily weldable by solid-state friction stir welding (FSW) which works well with all alloy classes and new variants of FSW, such as stationary shoulder and bobbin welding, offer opportunities for higher surface quality and wider applicability [328–331]. In addition, mechanical joining by SPR and hemming are widely applied to body-in-white assembly in the automotive sector, often together with adhesive bonding [326]. To date, the impact of more recycled Al scrap entering the supply chain on these joining technologies has been the subject of limited systematic research. Specific issues can, however, be anticipated in each class of joining process.

3.8.1. Fusion welding

The main issues associated with fusion welding of recycled Al-alloys are the impact on their high propensity to form gas pores [332,333] and, for certain compositions, the susceptibility to solidification and liquation cracking [334–336]. Due to the significant change in solubility of hydrogen in aluminum between its liquid and solid states, aluminum fusion welds are prone to the formation of H-gas pores [332,333], which can be very detrimental to joint performance. Reuse of scrap with a high surface area could potentially

lead to an increase in hydrogen concentration due to surface contamination from hydrocarbons, moisture, and hydrated surface oxides, as well as the introduction of oxide films into liquid melts. Both of these factors are detrimental to porosity because H-pore formation is very sensitive to the hydrogen concentration and nucleation on oxide bi-films [337]. Fortunately, melt processing technologies are available which can adequately de-gas and filter recycled feedstock if applied correctly.

A further concern associated with fusion welding is that higher Fe and Si levels, and other contaminants present in the scrap supply chain, can affect solidification cracking. Solidification cracking is common in Al-alloys with a wide freezing range (e.g. 7xxx alloys containing Cu) and is caused by a pressure drop developing across the inter-dendritic channels in the mushy zone during the final stages of freezing [336,338]. As such, it is highly sensitive to the freezing range of the last 5–10% fraction of (typically eutectic) liquid, and the ability for liquid to feed through the inter-dendritic channels. Fe and Si on their own do not generally have a great effect on the critical final freezing range of most Al-alloys, but they do promote the formation of complex intermetallic compound (IMC) phases (e.g. α -Al₈Fe₂Si, β -Al₅FeSi, and α -Al₁₅(Fe,Mn)₃Si₂) that can form large, high aspect-ratio IMC particles. These can block feeding channels and can also promote nucleation of H-pores [336,339]. For example, it is known that increased Fe levels can generate higher levels of shrinkage porosity in castings and are expected to aid the nucleation of inter-dendritic gas with negative effects on mechanical performance [336,339]. High solidification rates achievable by laser welding may be beneficial in this regard, as Fe has a low diffusivity in liquid Al and some solute trapping can occur at high welding speeds [340] (see Fig. 25).

Liquation cracking can also occur near the fusion boundary in Al-alloys with low incipient melting points [334,335], but this is not expected to be greatly affected by slightly higher levels of Fe or Si. Other contaminants in Al scrap streams are also of concern to fusion welding. For example, low-melting-point metals like Bi, Pb, Sn and Cd are added to free-machining Al-alloys (e.g. 2011). These elements form soft, low-melting point, phases to promote chip breaking and cutting tool lubrication [341]. In fusion welding, contaminants can also become concentrated at the weld centerline, exaggerating their effect, particularly when welding with a teardrop-shaped melt pool. Care should therefore be taken to exclude materials from the scrap system that contain such elements. Hot cracking issues can also be alleviated by selecting welding conditions and grain refining additions that generate a fine-equiaxed weld zone grain structure, and by avoiding excessive constraint and out-of-plane stresses in recrystallized sheet/plate products [335,336,342].

3.8.2. Friction stir welding technologies

Friction stir welding (FSW) methods have increasingly been adopted to join Al-alloy plate, sheets and extrusions in ship and train building, as well as in specialized automotive and in some aerospace products, particularly for space launch vehicles [328]. FSW is ideally placed to weld more highly contaminated low-grade recycled alloys, as it suffers from none of the liquid-phase-related problems that beset fusion welding. FSW is also very tolerant of the presence of high volume fractions of coarse second-phase particles, and actually refines such particles in the weld zone microstructure by imparting severe deformation to the weld members [328,330]. Indeed, friction stir processing (FSP) has been developed from FSW to specifically refine cast microstructures such as, for example, the primary and eutectic Si particles present in Al-Si castings, bringing significant improvements in mechanical properties [343].

3.8.3. Mechanical joining and adhesive bonding

Self-piercing rivets (SPR) and hemming are common joining technologies used in lightweight Al-alloy car body structures [326,344]. Both processes can be adversely affected by a reduction in the formability of the join members (see Fig. 26). In hemming, Al-alloy closure panels are stretch-bent through a tight radius by rolling or die pressing, giving rise to high surface strains in plane strain where there is a minimum in the sheet forming limit [305,327]. It is already challenging for Al suppliers to meet the cold hemming requirements of vehicle manufacturers [322,327] and any further reduction in ductility could have a significant impact on the ability to form hemmed joints. SPR is also sensitive to poor bottom sheet formability, which can cause cracking in the joint buttons [326]. Forming limits in such scenarios are strongly influenced by the presence of clusters of coarse intermetallic particles that

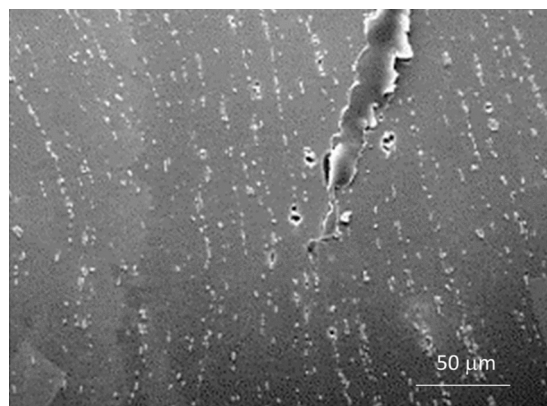


Fig. 25. Cracking following bands of Fe-rich intermetallic particles during bending. Reproduced with permission from [322].

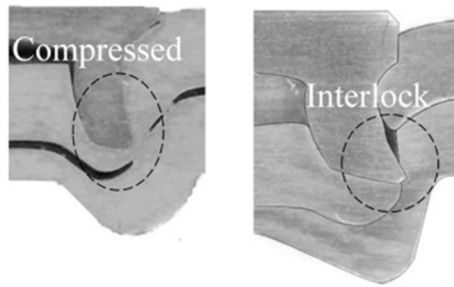


Fig. 26. Joining of aluminum alloy sheets by using self-piercing rivets: (a) conventional; (b) optimized. Reproduced with permission from [347].

prematurely nucleate voids, particularly under triaxial stress states [305,322,345,346]. For example, premature shear cracking has been noted in Al automotive sheets (e.g. 6111) with a high Fe content when bending transverse to bands of Fe-rich stringers [322,345]. The requirement to form mechanical joints is thus probably one of the key factors limiting Fe content in recycled Al for automotive closure sheets.

The high-strength steel rivets currently used in SPR are a known issue with recycling, in that they are difficult to remove from Al scrap and are an increasing source of Fe contamination. Efforts have been made to use high-strength Al-alloy rivets to increase recyclability, but to date this has had limited success due to lower joint strengths and restrictions on the hardness of the materials that can be successfully joined [326,344]. Clinching, while circumventing the requirement for steel rivets, leads to inferior joint performance [327].

Adhesive bonding is frequently applied in conjunction with SPR to assemble aluminum car bodies [326,327]. The chemical conversion treatments used to engineer oxide films on Al-sheets, prior to applying adhesives, are sensitive to the presence of surface second-phase particles, which may not always be removed by the etching step that precedes conversion coating formation. The presence of such residual particles can locally alter the film properties and, due to the cathodic nature of the particles compared to the alloy matrix, may influence the long-term durability of the surface oxide film when exposed to wet or humid environments. However, due to the relatively small particle surface area, it is unlikely that their presence significantly affects surface adhesion.

4. Methods and tools for the investigation and design of aluminum alloys which contain scrap

4.1. Thermodynamics simulation tools for the study of scrap-related impurities and intermetallic phases

The underlying phase diagrams provide tools for understanding and designing scrap-based, impurity-tolerant alloys. These diagrams can be calculated using computational thermodynamics methods which capture and interpolate/extrapolate experimental data. The CALPHAD (CALculation of Phase Diagrams) approach (e.g. [348,349]) has systematized the procedure. Here the excess Gibb's free energy is described using a polynomial expansion which extrapolates the response of pure elements and binary and ternary interactions [350]. Ordered phases are described in the compound energy formalism using multiple sublattices, each with a distinct composition [350,351]. Commercial software packages such as Thermo-Calc [352], Pandat [353] and FactSage [354] provide access to databases which contain free energy-composition descriptions for phases. These can be used to construct estimates for phase fractions as a function of temperature, pressure and composition under stable or metastable equilibrium conditions, also considering tramp-related alloy variations.

Recent CALPHAD solutions and databases suitable for the thermodynamic investigation of Al-alloys are as follows. Thermo-Calc offers the Al-based alloy database TCAL7, which includes 39 elements and contains 267 assessed binary systems, 99 assessed ternary systems, 12 assessed quaternary systems and >600 solution and intermetallic phases [355]. The PanAluminum database from Pandat (PanAl2020) includes 34 elements and 851 phases [356]. The FTlite database from FactSage includes >54 elements for Al-alloy calculations. The FTlite 7.3 database includes 1703 pure compounds with 2104 stoichiometric phases and 265 solution phases [357].

In principle these databases consider the essential, and typical scrap-related contaminants, but they can still neglect some of the associated phases. For instance, in the context of possible incorporation of impurities in recycling, the impact of special minor alloying elements such as rare earth elements in aluminum alloys may be an issue, but small-extent impurities are not always detected by scrap sorting techniques or are overlooked by some databases. The element neodymium is the basis in NdFeB magnets, which provide a significantly higher magnetic field per unit volume compared to ferrite based magnets and are therefore attractive for clean energy applications such as the electric motors found in electric/hybrid vehicles [358]. The FTlite database in FactSage includes neodymium [357]; the databases TCAL7 in Thermo-Calc and PanAl2020 in Pandat do not. The larger number of elements included in the FTlite database are thus an advantage in thermodynamic calculations which include rare earth elements.

Besides the commercial databases, the open database mc_al_v2.029.tdb issued by MatCalc is also available. It is designed for thermo-kinetic simulations for Al-alloys with additions of Cu, Fe, Mg, Mn, Si, Zn and Zr [359]. In a comparative study, DSC experiments were performed to measure the solidus temperature of Al-Zn-Mg-Cu alloys and the experimental results were compared with thermodynamic calculation results obtained by the software packages FactSage, Pandat and MatCalc. The results of the experimental tests matched the results of the thermodynamic calculations, which predicted the trend accurately within a scatter of 49 °C. On the one

hand it is noted that such scatter can occur in the experimental setup due to thermal lag and due to the standard deviation of the DSC measurement results. On the other, the extrapolation of optimized systems in limited thermodynamic datasets and the thermodynamic data itself, which can include measurement errors, may contribute to the observed scatter. Overall it was concluded that CALPHAD can be a useful tool for optimizing specific alloys by predicting the solidus temperature of specific alloy compositions [360].

Pertinent studies depicting the use of the CALPHAD approach to recyclable aluminum alloys have been published in the context of Al-Si cast alloy design [352,361]. These alloys have a higher tolerance for compositional variations compared to wrought alloys, and have long served as sink systems for recycling aluminum scrap [36]. One of the key impurities stemming from such recycled feedstock and needing control is Fe. While Fe is desirable to a small extent because it helps to reduce die soldering and hot tearing, at higher concentrations it reduces ductility. Recycling-friendly wrought aluminum alloys made (e.g.) from automotive scrap are subject to similar challenges, due to increased Fe content and the formation of brittle intermetallic phases. Also requiring consideration is the potential of other tramp elements which generate unwanted brittle phases and alter castability (for strip or direct chill casting) or modify the sequence of precipitation. Here, for example, a quasi-ternary Al-Mg-Si 6xxx series alloy produced from recycled scrap aluminum would need to be viewed as a multicomponent alloy containing non-negligible amounts of Fe, Mn, Cr, Ti, Zn and Cu [3]. The empirical challenge presented by experimentally evaluated alloys which contain up to eight alloying elements, each with compositions in the range 0–10 wt%, is overwhelming. Here up to 10^8 independent alloys would have to be prepared and evaluated in order to assess properties [362].

The CALPHAD approach allows predictions to be made by drawing on a database formulated from a much smaller number of assessments, based on interpolation. The excess free energies are interpolated from the assessment of the pure materials, binary and (sometimes) ternary interactions. Even this strategy, however, leads to combinatorial complexity as the number of elements increases. To fully describe a system with more than three components, we would want to assess all of the binary and ternary systems within it.

An alloy containing 10 elements needs the complete assessment, based on the binomial coefficient, of $\binom{10}{2} = 45$ binary and

$\binom{10}{3} = 120$ ternary systems, while a system containing 15 elements would require 105 binary alloys and 455 ternary system descriptions [363]. While it is often considered sufficient to consider interactions up to ternary, ignoring any higher order terms, in cases where quaternary phases are present they need to be accounted for. The CALPHAD thermodynamic databases are quite extensive as regards classic aluminum alloy compositions, but even there they do not include descriptions for all binary and (particularly) ternary interactions. The lack of experimental studies of ternary systems is often an impediment. For example, the TCAL5 database available from Thermo-Calc was developed in the framework of 35 elements, with the assessment of 258 binaries but only 87 ternary systems [352]. For reference, a complete description of a system containing 35 elements would require the assessment of 595 binaries and 6545 ternaries.

In many cases such a complete description is unnecessary because the assessment can be optimized to focus on specific alloys of interest. Interpolation within the range of alloys close to these are then found to be sufficiently accurate. However, complications arise when using such databases to explore alloying effects where extrapolation is required. Issues of incomplete coverage of binary and ternary systems then become more problematic, as does the possibility of missing phases in the assessment. Recent efforts motivated by multi-principal component alloy design have sought to assess the predictive capability of CALPHAD calculations of phase equilibria based on the fraction of assessed binary (FAB) and ternary (FAT) systems in a given database [363,364]. In a recent study, several 4-component alloys were assessed based on different FAT and FAB values, and compared with the predictions made when the fully assessed database was used [364]. While it was shown that under limited conditions extrapolating from the binary assessments can provide good predictions, this was generally not true across the entire phase diagram. In cases where binary or ternary compounds exist, their omission strongly affects the phase equilibria predictions nearby [364].

In the context of non-traditional alloy chemistries, such as those encountered in aluminum alloys containing a high fraction of scrap-related contaminants, the items outlined above need to be assessed in further detail, particularly for the ternary and higher-order alloy systems and novel binary, ternary and higher-order compounds. The time and effort of conducting experiments have been a traditional bottleneck in this process, but computational techniques help fill such gaps [365–367]. Ab initio electronic structure simulation packages and advanced statistical mechanics tools allow proper sampling of properties at finite temperatures and in disordered phases. Ab initio data in the form of predicted heats of formation for ordered phases have long been used to supplement data in CALPHAD thermodynamic assessments [367]. With the advent of high-throughput tools, the ability to screen a wide range of compositions and crystal structures to identify stable phases and their heat of formation has become essential. For example, in the area of Al-Li-Cu alloys there has been much controversy regarding the composition and structure of the T1 precipitate phase. Using ab initio calculations, Kim et al. [368] were able to compute the heat of formation for five candidate structures proposed in the literature based on experimental observation. From the 0 K heat of formation for the candidate phases and other known stable phases in the alloy system, it was possible to test which phase would be expected to be most stable and to share a tie line with Al. In this case none of the proposed structures was found to be stable, and therefore cluster expansion calculations were used to expand the structures studied. Two were discovered to be stable, and one of them was close to sharing a tie line with Al.

Here one limitation of 0 K heat of formation calculations appears: the possibility of phase stabilization due to the effects of entropy. An example where lack of vibrational entropy effects can cause incorrect predictions is the stability of the equilibrium θ phase relative to that of the metastable θ' phase in Al-Cu binary alloys [369]. The development of effective Hamiltonians to extrapolate 0 K ab initio calculations to include entropic stabilization is progressing, mostly using harmonic or quasi-harmonic approximations [370]. For high temperature predictions, the inclusion of anharmonicity (temperature-dependent phonon softening and broadening beyond the

thermal expansion softening captured in the quasi-harmonic approximation) is becoming more important. While predicting fully anharmonic free energies from density functional theory (DFT) calculations has been computationally taxing up to now, the advent of new techniques is reducing this computational bottleneck significantly. Using machine-learned surrogate interatomic potentials, for example, can make fully anharmonic calculations of free energy by thermodynamic integration from DFT data feasible in multi-component alloys [371]. Anharmonicity can also be important in ab initio predictions of phase stability in another way. In order for ab initio calculations to predict a heat of formation, the phase must be mechanically stable at 0 K [366,370]. There are many examples of phases for which this is not true, but which are stable for $T > 0$ K. Any high throughput approach at 0 K will fail to predict these as a possible phase, leading to incorrect assessments if the results are used as input to CALPHAD databases. Recently a new approach was proposed for handling such cases [372], but it is important not to neglect the potential impact of such phases at finite temperature.

The discussion highlighted examples of ordered phases whose properties were predicted by ab-initio calculations. Fully ordered phases, such as Al₂Cu, where each site is unambiguously occupied by Al or Cu, are well suited to ab initio calculations given the limited number of atoms that can be modelled with current computational limitations. Disordered (or partially disordered) phases with site defects present the challenge of adequately representing the disorder when only a small number of atoms (a few unit cells at most) can be simulated. In this context, there have been significant advances in the development and deployment of special quasi-random structures (SQSs) for the simulation of compositional disorder [373,374]. While such SQSs cannot account for short-range order, and are thus limited to regular solution-like models, their coupling with analytical cluster expansions can be used to correct for this in systems where it is important [365]. This may be the case for many multicomponent aluminum alloys where clustering or ordering are observed to precede precipitation [55].

While the specific technical details described above are instrumental in high-fidelity thermodynamic predictions from ab initio calculations, one must also reflect on the combinatorial challenge in trying to construct a CALPHAD (or CALPHAD-like) representation of the phase equilibria in a multicomponent system. It is here that high-throughput workflows specifically designed to work within a CALPHAD framework show significant promise [365]. A number of systematic and open-source tools for such high throughput calculations have been developed, including the Materials Project, the Open Quantum Materials Database (OQMD) [375], Automatic Flow for Materials Discovery (AFLOW) [376] and the Novel Materials Discovery Laboratory (NOMAD) [377]. The T1 phase predictions described above [368] were performed, for example, within the OQMD database. Such databases, which also collect prior calculations, also allow data mining or the use of search routines to help identify potential alloys of interest [378].

A final consideration is the fact that the above discussion has implicitly focused on classical thermodynamics, where each phase is assumed to be infinite in extent and free of defects. Yet defects play an important role in defining the properties of alloys, and the interaction between chemistry and defects can lead to substantial deviations from the behavior anticipated from an equilibrium phase diagram. The first thermodynamic property that is essential for predictions of microstructure evolution in aluminum alloys is interfacial energy, particularly between the matrix and precipitate phases. How chemistry effects surface energy can have a significant impact on the progression of decomposition of a solid solution. Ab initio calculations in this case are possible in some cases, but require many more computational resources because relatively large supercells are needed to allow one phase to be embedded into the other. The possible equilibrium arrangement of solute around grain boundaries, free surfaces and at dislocations is a topic of increasing importance, requiring an assessment of chemical equilibrium. Recent work has illustrated how chemical equilibrium between solute, a solid solution and a grain boundary can generate solute ordering induced by segregation and the structure of the boundary. Computation of “defect phase diagrams” is necessarily complicated by the fact that supercell sizes need to be large to incorporate the defect; for example, in the case of a dislocation one must properly account for the long-range elastic strain field if one wishes to predict equilibrium. This may preclude “brute force” ab initio calculations, but techniques such as quantum mechanics/molecular mechanics (QM/MM) or machine-learned interatomic potentials with accuracies for formation energies which approach those from direct ab initio calculations show promise for the further exploration of this topic.

4.2. Theory and simulation for the study of scrap-related impurity effects on precipitation kinetics and microstructure evolution

The impact of impurity elements on the thermo-mechanical response during production and on the properties of the finished product is many-sided, and the consequences of even minor amounts of impurity elements can be substantial. For instance, if a certain element accelerates or decelerates the formation of a particular precipitate, or if it modifies the sequence of precipitation or changes the crystal structure (e.g., Cu- additions [379]), this will affect many other (subsequent) processes, such as (i) the further formation of (strengthening) precipitates due to the availability of precipitate-forming elements (Cu, Mg, Si, Zn etc.); (ii) the annihilation or generation of structural vacancies at the precipitate/matrix interfaces during heat treatment and thus the diffusion-controlled kinetics of subsequent precipitation reactions (quench-sensitivity); (iii) the amount of solute present in the matrix, which will affect electrical and thermal conductivity; and (iv) the mobility of grain boundaries and dislocations, which are influenced by the (precipitation-related) Zener drag or the solute drag / dynamic strain aging effect caused by segregation of dissolved atoms into interfaces/dislocations, which will impact the degree and continuity of the stress-strain response of the material (Portevin-Le Chatelier effect), grain growth and recrystallization kinetics during heat treatment [55]. Impurity atoms in solid solution can also (v) modify recrystallization textures (as has been shown for (e.g.) Fe additions [236]); or (vi) change the strain hardening behavior of alloys (e.g. Cu [380] or Mg [381]), stimulate precipitate/dispersoid nucleation, (e.g. Cd [382], Sn [383], Au [384] or Ag and Si [385]), or generally influence heat treatments, such as homogenization (as shown for Fe and Sc additions [386,387]).

4.2.1. General considerations about microstructure and precipitation modeling

When designing a computational framework for the modeling and simulation of scrap effects in Al-alloys, one is confronted with

the fundamental question of which models and mechanisms should be considered. Simulations can only deliver useful predictions if the relevant mechanisms are properly reflected in the constitutive formulations. For instance, quench sensitivity and natural aging kinetics can only be properly described if the evolution of excess vacancies is taken into account in the simulation together with the precipitation kinetics of dispersoids and the trapping of vacancies at solute atoms or within atomic clusters [388]. Otherwise the impact of alloy composition and/or thermo-mechanical treatment on the processing and properties of the alloy will not be reflected in the necessary depth, meaning that their effects cannot be correctly predicted; and the model will remain incomplete and of limited value.

A major aspect of such simulations of precipitation and microstructure evolution is that the individual metallurgical mechanisms never operate independently, but are coupled; i.e., they interact and are often competitive [55]. The more complex the simulation, the more the individual models need to be incorporated into the framework and properly connected to each other. Fig. 27 shows a rough sketch of fundamental models for precipitation kinetics and microstructure evolution, with their interactions and relevance for Al-alloy processing. For instance, precipitation kinetics will determine the amount and type of solutes that are dissolved in the matrix. This will directly influence the mobility of dislocations and grain boundaries and, thus, impact recrystallization kinetics and stress-strain response during plastic deformation. The latter processes will, in turn, influence the precipitation process by providing the heterogeneous nucleation sites (dislocations, subgrain boundaries and cells, grain boundaries) and deformation-induced vacancies. In addition, the number of dissolved impurities impacts the availability of vacancies through the mechanism of solute trapping, which is a major factor in all kinds of diffusion-controlled processes, such as precipitation, recovery, recrystallization or creep. Table 12 displays an overview of the metallurgical mechanisms that are triggered by scrap-related impurities and their possible impact.

4.2.2. Precipitation kinetics modeling

The formation of precipitates is a process that is governed by nucleation of particles within a supersaturated matrix [389,390], followed by the subsequent growth of the precipitates [390,391] and, eventually, overaging/coarsening [392,393]. Although sometimes treated in a separate manner, all three processes can overlap [394]. The following sections briefly review precipitation modeling and outline the advantages and potential drawbacks of the respective approaches.

Constitutive models

A mean field model for describing phase transformation kinetics is the Kolmogorov-Johnson-Mehl-Avrami (KJMA) approach [395-397], which can be written [398].

$$V(t) = 1 - e^{-V_e(t)} \quad (4)$$

where $V(t)$ is the transformed volume and $V_e(t)$ is called the extended volume. The latter quantity is formulated in terms of suitable nucleation and growth expressions, and the well-known sigmoidal curves are obtained for the particular phase transformation

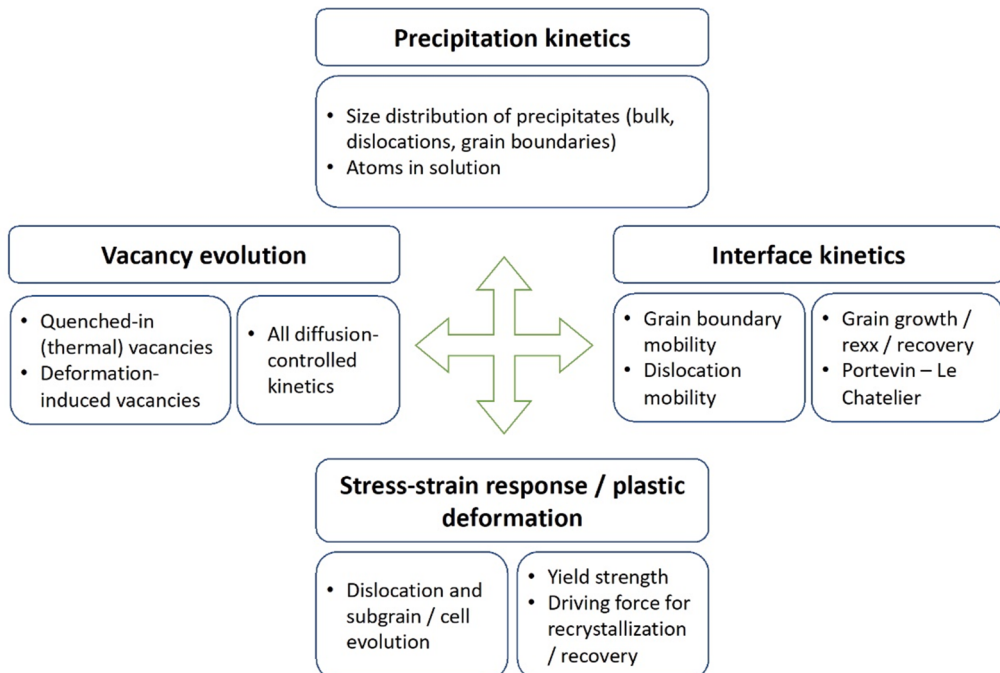


Fig. 27. Interaction of models for microstructure evolution and precipitation kinetics.

Table 12

Overview of the possible impact of scrap elements on processing and properties.

	Mechanism	Consequence	Effect on
Trace elements (impurities)	Segregation to grain boundaries	Modify grain boundary energy Modify heterogeneous nucleation energy Modify grain boundary mobility (solute drag)	Grain growth Precipitate nucleation Grain growth Recrystallization
	Segregation to dislocations	Dislocation pinning / cross-core diffusion effect	Plastic response / Portevin-Le Chatelier effect
	Trapping of vacancies	Reduce/increase effective diffusion coefficient Change lattice concentration of vacancies	Precipitation / clustering kinetics
Precipitate-forming elements	Heterogeneous nucleation	Increased nucleation rates	Extension of precipitation free zones
	Precipitate/dispersoid formation	Capture other alloying elements	Precipitate/dispersoid density Precipitate formation / change of precipitation sequence
	Enter into precipitates	Change its crystal structure	Change thermodynamic stability

considered [396]. The extended volume is often written as $V_e(t) = kt^n$, where k is a rate constant and n is the Avrami exponent. The KJMA approach has been used at various times to describe precipitation in Al-alloys. Sekhar et al. [399] used the KJMA model to describe the underaging kinetics in 6063 and combined it with the classical LSW [392,393] model for coarsening to take into account overaging. The information on volume fraction and radius was then used to describe the Vickers hardness and yield strength of the alloy. Sha [400] also used the KJMA approach to model the Vickers hardness evolution in several 6xxx alloys. In the same way, Pogatscher et al. [388] fit Avrami equations to their experimental hardness data from artificial aging of a 6061. Earlier modeling activities date to the 1990 s, where Shercliff and Ashby [401,402] developed a precipitation kinetics model to predict the yield strength in 6082. This model was later adopted by Rometsch and Schaffer [403] in an Al-7Si-Mg alloy. Eivani and Taheri [404] applied the KJMA model to simulate the age-hardening kinetics in an Al-Mg-Si-Cu alloy, and Guo et al. [405] investigated the effect of Zn-additions on precipitation kinetics. Yazdanmer et al. [406] applied the KJMA model to precipitation-hardening for non-isothermal aging of Al-Mg-Si alloys. Esmaeili et al. [407,408] developed their KJMA model for the 6111 alloy. Starink [409] introduced a model for diffusion-controlled precipitation that was later utilized (e.g.) in the analysis of cooling DSC curves in Al-Cu [410], Al-Mg-Si [411], Al-Mg-Mn-Cu [412] and Al-Zn-Mg-Cu [413] alloys. Another interesting example of DSC curve modeling is the approach by Hersent et al. [414], who used the regular solution model to represent the thermodynamics in the Al-Mg-Cu system. Further constitutive models for precipitation kinetics are (e.g.) [415–419].

Although computationally efficient, applying the original KJMA approach to the entire precipitation reaction is not straightforward in more complex heat treatments, because a single transformation variable, i.e., the volume fraction of the transformed phase, $V(t)$, cannot usually describe processes that occur after reaching the peak hardness [84]. This applies to (e.g.) Ostwald ripening/overaging and to the dissolution of metastable phases during prolonged heat treatment, or the dissolution of precipitates following a reheating treatment, for instance during homogenization. Possible solutions to this are offered by multi-phase KJMA models, as shown in [420,421] for precipitation in steel.

To predict mechanical properties, however, at least a minimum of information on (morphological) parameters is necessary, such as the mean radius of the precipitates, their number density and also often their shape. Models that incorporate evolution equations for radius and number density of precipitates are now commonly used.

Nucleation, growth and coarsening models

Models characterized by evolution equations for the radius and number density of the precipitates, involving the elementary processes of nucleation, growth and coarsening, are generally termed Classical Nucleation and Growth Theories (CNGT). A first category of the corresponding models involves the “mean radius approach” [422], where the evolution of a size distribution of precipitates is reduced to the evolution of its mean radius and precipitate number density. Models of this type exhibit good computational efficiency. The classical representative of this type of approach is the Langer-Schwartz (LS) model [423], which has been taken as starting point in numerous works.

In a practical sense, the most essential ingredient of the LS-type models is the nucleation model, because the nucleation process determines the number of precipitates that will form and, by extension, dictates the maximum size of the precipitates as determined by soft impingement (overlap of diffusion fields) and the evolution of the precipitate volume fraction. A lower number density of particles means, on the one hand, that each precipitate can grow to a larger size because its individual growth volume is larger. On the other, the overall reaction will take more time to reach the maximum phase fraction because the diffusion distances become wider. The precipitation kinetics can differ by many orders of magnitude depending on the nucleation rate, whereas the overall reaction is much less sensitive to variations in the growth rate of precipitates at constant particle number density.

Nucleation is commonly expressed in terms of the nucleation rate, J , which is the number of nuclei of the new phase that will form per unit volume and unit time. It is commonly written as [389,424].

$$J = N_0 \beta^* Z e^{-\frac{G^*}{k_B T}} e^{-\frac{\tau}{t}} \quad (5)$$

where N_0 is the number of potential nucleation sites, β^* is the atomic attachment rate, Z is the Zeldovich factor, G^* is the critical nucleation energy, k_B is the Boltzmann constant, t is the incubation time and T and t have their usual meanings. From Classical

Nucleation Theory (CNT), the nucleation barrier assuming homogeneous nucleation is given by.

$$G^* = \frac{16\pi}{3} \frac{\gamma^3}{d^2} \quad (6)$$

where γ is the interfacial energy (J/m^2) and d is the effective driving force (J/m^3). The latter quantity can be estimated from computational approaches, such as, CALPHAD [425]. Multi-component expressions for the quantities appearing in the nucleation rate are summarized, for example, in [390].

Interfacial energies can also be calculated from thermodynamic databases using, for example, the Generalized Broken Bond (GBB) model [426]. However, for estimates of the interfacial energies and, thus, reasonable estimates of nucleation rates, it is necessary to go beyond the planar sharp interface approximation of the GBB model and to treat the interface energy, γ , as a function of the nucleus size (interface energy size effect) [427] and temperature (diffuse interface effect) [428]. In multi-component precipitation systems with solution phases, i.e. precipitates with a certain compositional range of stability, the chemical composition of the nucleus also plays a decisive role; see e.g. [429,430].

Once the precipitate nucleus has reached supercritical size, its further evolution is usually described by the diffusion-controlled transport of atoms towards and away from the particle. The evolution of (mean) radius, r , as function of time can be written in a general form as.

$$\frac{dr}{dt} = \alpha_g \frac{D}{r}, \quad (7)$$

where D is an effective diffusion coefficient and α_g is a growth rate coefficient. Various expressions for α_g are reported in literature, e.g. in Zener [391], where the local equilibrium (LE) hypothesis is used to obtain an approximate solution of the moving boundary problem at the precipitate matrix interface [350,431,432]. Integrating eq. (7) delivers the well-known parabolic growth law for diffusion-controlled growth.

Alternatively, growth rate equations can be derived from the thermodynamic extremum principle [433–435], which was first demonstrated by Svoboda et al. [436] and which has recently also attracted the attention of other researchers [437,438]. Evolution equations for grain boundary precipitation have been developed; see e.g. [439,440] and the works cited therein.

Most coarsening / overaging models used in CNGT with mean precipitation quantities are based on the mean-field solution of the classical LSW treatment [392,393]. The general form of the coarsening rate equation for the mean radius evolution is.

$$\frac{dr}{dt} = \alpha_c \frac{D}{r^2} \quad (8)$$

where α_c is a coarsening rate coefficient. The literature on this topic is exhaustive and various extensions of the original LSW model are discussed, e.g., in [441–443]. With reference to Al-alloys, coarsening of Al_3Sc particles was investigated, for instance, by Novotny and Ardell [444].

The models introduced above are valid for stationary and/or known size distribution of particles. For instance, the LSW model predicts a self-similar left-skewed distribution, also known as LSW-distribution, which remains stationary throughout coarsening. The distribution that is assumed to be present in the LS-model [423] is a-priori undefined; however, it is approximately fixed by the assumption that it coincides with the LSW-distribution in the long-term limit. Alternatively, the LS-model can also be derived assuming a log-normal distribution [445].

In the models discussed below, these assumptions are relaxed because the precipitate size distribution is discretized and the evolution of the distribution is governed by the evolution equations for the individual size classes or the fluxes prescribed between the size classes.

Class precipitation models and software

The second group of CNGT precipitation kinetics approaches [422] comprises “class” models, where the actual particle size distribution is discretized in several size classes. The time evolution of each class is calculated either by evaluating the fluxes between neighbouring classes (Euler-type integration scheme) or by the size evolution of each individual class (Lagrange-type integration scheme). Both approaches deliver the evolution of the size distribution of precipitates over time as well as the evolution of mean precipitate quantities, radius, number density and volume fraction. A major advantage of these class models is that no separate model for overaging/coarsening is required. This is because the possible dissolution of precipitates is an inherent part of class models for spherical precipitates, provided that the mathematical formalism incorporates the Gibbs-Thomson effect [446].

The classical simulation approach for class precipitation kinetics modeling was introduced by Kampmann and Wagner [447] and it is known as the Numerical Kampmann Wagner (NKW) model. It is an extension of the original LS approach, where the evolution of the mean precipitation parameters, i.e. number density and mean radius, are replaced by the evolution of discretized precipitate size classes.

The available NKW models can be roughly categorized into (i) general-purpose precipitation kinetics and microstructure evolution software and (ii) special-purpose software/approaches, developed for particular application to certain groups of Al-alloys. Reviews on precipitation kinetics models and software are available from (e.g.) Hutchinson [84], Sigli et al. [448] and Robson et al. [449]. A summary of NKW models and software is shown in Table 13.

Precipitate shape effects

An explicit feature of Al-alloys is that many of their important (strengthening) precipitates can be highly non-spherical. The reasons

Table 13

Overview of numerical Kampmann Wagner models and corresponding software for the simulation precipitation kinetics and microstructure evolution, including information about specific alloying / tramp elements.

Name	Model	Publ.	Comment	Al-Applications
Cinkilic et al.	[450]	2020	PK,YS; TDC: PanEngine ¹	[450]
ClaNG	[451,452]	2002	PK,YS; Al-Mn-Mg-Fe-Si, 8xxx alloys	[314,315,453-458]
Du et al.	[459-461]	2012	PK; TDC: Gibbs energy lookup Table 2	[462]
Khan & Starink	[463,464]	2008	PK,YS; Al-Cu-Mg	[465]
Larouche et al.	[466-468]	2015	PK,YS; Mixed-mode growth; Al-Cu	[469,470]
MatCalc*	[436]	2004	PK,MS,YS; TDC: CALPHAD databases + MatCalc engine ³	[471-477]
multipreci	[478]	2005	M(C,N) precipitates in steel	–
NAMO	[479-483]	2000	PK,MS,YS; Al-Mg-Si alloys	[484-488]
Nicolas and Deschamps	[489]	2003	No nucleation, reversion treatments; Al-Mg-Zn	
PanPrecipitation*	[490,491]	2009	PK; TDC: PanEngine/PanDat ¹	–
PrecipiCalc	[492]	2004	PK,YS; Ni-base alloys	–
Preciso	[422,493,494]	1998	PK; various Al-alloys	[495,496]
Robson et al.	[497-499]	2001	PK; TDC: pre-calculated chemical potentials ⁴	[500-502]
Samaras	[503]	2006	PK,YS; population balance approach	
Sarafoglu et al.	[188]	2019	Dual-grain model + NKW	
TC-Prisma*	[504-506]	2014	PK; alloys with precipitates	–

*General purpose software; PK: Precipitation kinetics; MS: Microstructure evolution; YS: Yield strength; TDC: Thermodynamic coupling.

¹ PanEngine: CompuTherm LLC. (Madison, WI, USA); ²from ThermoCalc AB, Sweden; ³MatCalc: <https://matcalc.at>; ⁴From MT-DATA, National Physical Laboratory, UK.

for this may be [448] (i) anisotropy of interfacial energy or mobility; (ii) anisotropy of elastic constants; and/or (iii) strain incompatibility of precipitate and matrix. Precipitate plates with aspect ratios of 10–100 are common in Al-Cu-based alloys, e.g. Θ' (Al_2Cu) or T_1 (Al_2CuLi). The modeling of precipitation processes discussed above is well developed for spherical particles, and coarsening processes can only be modelled analytically for spherical particles. In some cases, such as 7xxx alloys, the precipitates have an aspect ratio generally only up to ~ 3 . In these cases the spherical particle assumption still seems to work well, and there are many examples where state-of-the-art CNGT precipitation modeling was applied with success to 7xxx alloys, e.g. [449,489,507].

However, in alloys such as 6xxx, where precipitates usually adopt rod shapes, and 2xxx, where particles often have plate shapes, the spherical approximation in modeling is no longer suitable. In the simplest configuration of dilute solutions, non-spherical precipitate shapes mainly modify the diffusion fields around the particles, and thus lead to changes in the growth kinetics of these particles. A pragmatic solution which accounts for the growth kinetics of elongated or flat cylinders to represent needles and plates has been derived by Kozeschnik et al. [508]; the geometrical assumptions for the shape factor $h = H/D$ are shown in Fig. 28.

The central prediction of this model [508] is an accelerated growth rate for disc-shaped precipitates and a deceleration of diffusional growth for needle-shaped particles. In more recent work Holmedal et al. [461] arrived at partially contradictory results, which these authors attribute to different model assumptions. In their analysis they observe rather similar growth kinetics for needle-shaped precipitates compared to spheres of equivalent volume, but a deceleration in coarsening rates. The implementation of the Holmedal et al. model in the NKW framework is described in [462]. There are several other general treatments of non-spherical precipitate growth kinetics [466,494,509–513], some of them focusing specifically on Al-alloys [461,514,515].

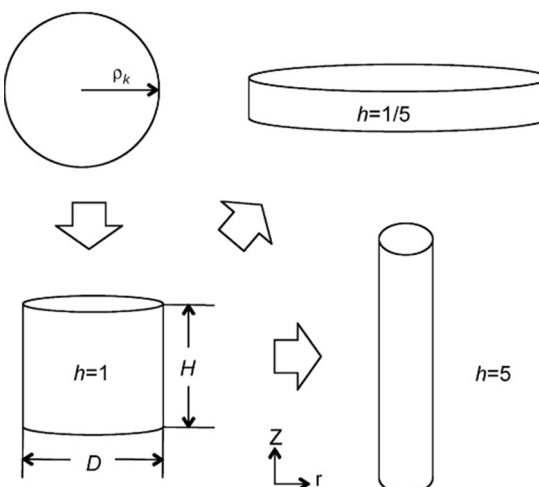


Fig. 28. Definition of a simple shape factor to represent needles and plates based on a cylindrical shape. Reproduced with permission from [508].

A number of new factors must be incorporated into an even minimum ingredients model for precipitation if the precipitates are highly non-spherical. The first is that in the case of rod- or plate-shaped precipitates, the evolution of particles is no longer well described by a single growth rate at each point in time. For a precipitate plate the lengthening rate will have one value, and the thickening rate will have a different, much lower value. The time dependence of these growth rates also differs from that of spherical particles: diffusion-controlled lengthening is usually linear in time (i.e. there is a constant lengthening rate), and thickening is interface-controlled. Consequently the whole time dependence of the precipitation growth phase is modified, and this in turn affects the time evolution of the solute content in solution. The second consequence of highly anisotropic precipitate shapes is that soft-impingement of the ends of precipitates can occur far earlier than soft impingement at other interfaces. A schematic example is shown in Fig. 29 for plate-shaped θ' particles forming on {100} planes in the Al matrix [516]. Both the particle itself and the surrounding solute diffusion field are shown. As seen in Fig. 29c, soft impingement occurs at the ends of the particles long before it is seen at the broad faces.

The consequence of the geometry effects shown in Fig. 29 are that coarsening processes begin at the ends of the plates long before they do so at the broad faces. This means that there is an extreme overlap in the growth and coarsening processes, specific to Al-alloys, that must be taken into account in CNGT models.

The third factor that must be addressed is the coarsening behavior of non-spherical particles. Analytical expressions of this have not yet been developed. Some authors have described the coarsening of such structures using LSW and spheres of equivalent volume, but the results are not fully satisfactory [516]. General solutions for precipitate coarsening based on simple shape factors are also rare (see for example Kim and Voorhees [517]), and asymptotic analysis shows that the temporal exponents for the coarsening law for prolate spheroidal particles are identical to those for a system of spherical particles. However, the amplitudes of the power laws depend on the particle aspect ratio. The coarsening rate constant for the equivalent mean radius of a particle decreases as the aspect ratio increases [518].

Two approaches have been suggested to model highly non-spherical particles. The low computational cost approaches described above, e.g. those of Holmedal et al. [461] or da Costa Teixeira et al. [516], consider the lengthening rate of plates using a Zener-Hillert diffusion-controlled approximation and combine it with LSW mean-field coarsening kinetics. The medium computational cost approach by Bardel considers rod-shaped precipitates in 6xxx in a coupled multi-class and phase field model approach [494]. This type of model is discussed in more detail below.

Phase-field modeling of precipitation

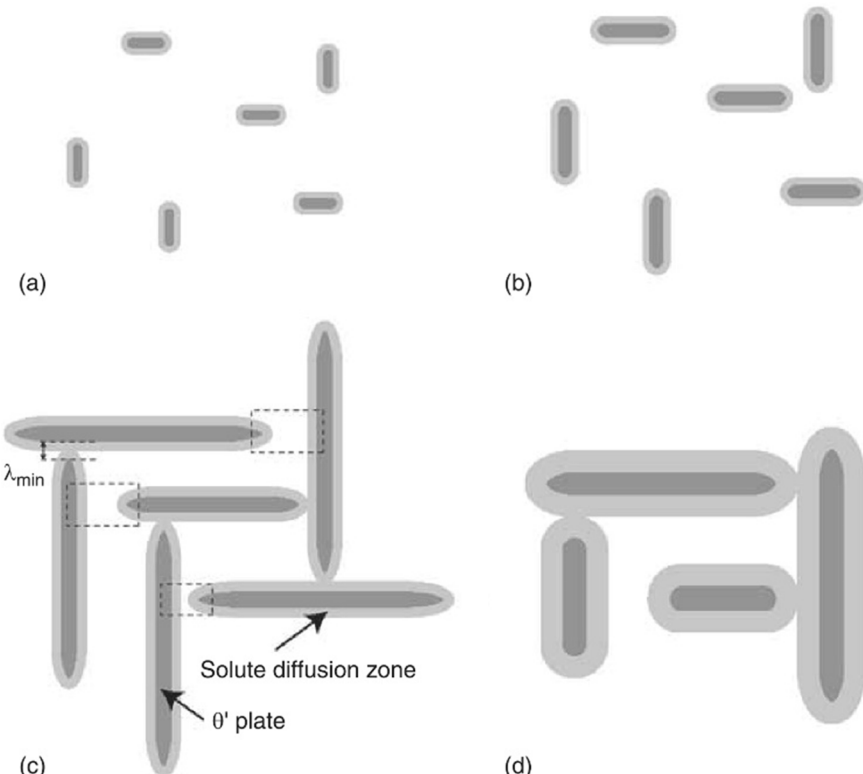


Fig. 29. Schematic representation of the diffusional growth and coarsening of a distribution of plate-shaped precipitates on {100} planes of an Al matrix viewed in a {100} direction. (a) Rapid nucleation and early growth of the θ' precipitates; (b) diffusional precipitate growth; (c) soft impingement of adjacent plates at different times (dotted rectangles). The white regions represent the untransformed supersaturated matrix. (d) Coarsening during which a decrease in the number density is observed. Reproduced with permission from [516].

Common approaches to modeling of precipitation kinetics utilize either spherical or shape-conserving approximations in a mean-field environment. If the precipitation analysis should extend to the impact of precipitate morphology on growth and coarsening rates, the phase-field technique [519–521] offers a versatile tool for expanding into the analysis of orientation-dependent kinetics and nucleation [522].

The nucleation process can be incorporated into the phase-field technique [424] either by using the phase-field simulation to calculate spatial variations in chemistry and then applying the classical nucleation rate equation to place seeds into the simulation domain, as in [523–525] for nucleation in Ni-base superalloys; or by incorporating a stochastic term in the phase-field equations and modeling the nucleation process in this manner, as in [526,527] for nucleation involving elastic stress. An interesting work on predicting the equilibrium shape of O' (Al_2Cu) particles based on the combination of ab-initio simulations with Density Functional Theory is that by Kim et al. [528], where the theory predicts a plate-like morphology for the strengthening precipitate in Al-Cu systems utilizing the first-principles-calculated interface energy anisotropy and the phase-field method, in agreement with experience.

In the context of scrap-related elemental contamination, impurities can influence the interface energy, which can affect nucleation, shape anisotropy and the size of the precipitation-free zones [529,530]. In such cases the phase-field method is a method of choice to account for these effects; see e.g. [522].

Atomistic models

CNGT models generally utilize Classical Nucleation Theory to model the nucleation process, and they are limited to the capabilities of this theory and its extensions. In some cases, however, alternative approaches can provide additional insights into the nucleation process [449]. Examples are atomistic approaches, such as (kinetic) Monte Carlo with Cluster Expansion of Density Functional Theory (DFT) energies [531–535], or cluster dynamics [536].

Although this type of simulation approach delivers results of significant physical depth, present limitations in computational resources limit atomistic techniques as a method of choice mainly to fundamental studies of metallurgical mechanisms. The calculation of segregation energies for solutes at dislocations or grain boundaries is an example. Although typical engineering applications commonly involve simulation systems too large and complex to be handled by these methods, atomistic models are a highly valuable means of gaining insights into fundamental mechanisms and can provide physical quantities that may be used as input parameters for larger-scale simulation approaches, as in [537].

Applications of precipitation kinetics modeling

Many applications of constitutive and CNGT-type models have been reported in literature. An example is the analysis of quench-sensitivity of Al-alloys [538], which documents the degradation of mechanical properties as a result of decreasing cooling rates after solution annealing. The main reason for this is the precipitation of coarse particles that bind certain elements and make them unavailable for later strengthening heat treatments. For a computational treatment of quench sensitivity, it is necessary to simulate the heterogeneous precipitation of particles during the quench process. In earlier studies based on cooling Differential Scanning Calorimetry DSC experiments, the kinetic model, developed originally by Zahra and Starink [539] for Al-Si alloys and developed further by Rometsch et al. [419], was utilized to investigate, for instance, the quench sensitivity of Al-Si alloys [540]. In more recent work, a KJMA-based model from Starink [409] is applied to study quench sensitivity in Al-Mg-Si [411] and Al-Zn-Mg-Cu [413].

A similar application for precipitation modeling is the identification of precipitation sequences and deconvolution of DSC curves [541]. Examples for corresponding studies are, for instance, the analysis of precipitation reactions performed by Lang et al. in Al-Mg-Si [473] and in Al-Zn-Mg [472] alloys in the framework of an NKW approach. These authors utilized the software package MatCalc to simulate the precipitation sequence during DSC heating experiments and to derive the corresponding enthalpy change accompanying the phase changes from the simulations. The experimental and computed DSC signals are compared and the peaks of the DSC signal are correlated to the formation or dissolution of the corresponding precipitate types. The measured and calculated heat flow for one of the alloys in Lang et al. [473] is shown in Fig. 30, and the corresponding phase fraction evolution in Fig. 31. Formation peaks of precipitates produce an exothermic reaction in the DSC; dissolution of precipitates show an endothermic signal. By comparing calculation and experiment, each peak can be assigned to the formation/dissolution of a specific precipitate type and the integral DSC signal can be deconvoluted into individual reactions.

A particularly interesting application of precipitation modeling with relation to scrap-related effects is the analysis of dispersoid evolution during 8xxx alloy heat treatments. Simulations performed with CLaNG [451] have been presented which were performed in the Al-Mn-Mg-Fe-Si system, including a number of dispersoid phases such as Mg_2Si , $\text{Al}_3(\text{Fe},\text{Mn})$, $\text{Al}_6(\text{Mn},\text{Fe})$, and others. The interactions between these precipitate phases alongside the homogenization and solution annealing treatments is of particular importance for the number of atoms remaining in solid solution after the treatments.

A recent work by Engler and Miller-Jupp [453] analyzes the evolution of dispersoids in the course of various heat treatment schedules; see the example in Fig. 32. The plots show the evolution of the volume fractions of dispersoids and the number of elements in solid solution for the heat treatment indicated by the temperature profile. The CLaNG simulations demonstrate a complex interaction of precipitate types, with formation of new dispersoids and dissolution of existing ones as a function of temperature. The experimentally measured solute contents and the simulations are in good agreement, thus demonstrating the predictive capabilities of the simulations and their potential in alloy development.

In the context of scrap elements, it is interesting to note that one key publication on the CLaNG model, [452], already bears the expression "... for recycled commercial aluminum alloys" in its title. The thermodynamic data in this work are reported to stem from a database which contains 15 elements. With most of the impurity elements of recycled Al-alloys in their database, the authors claim that the model can be applied to practically all commercial Al-alloys.

Another Al-alloy system is treated in NaMo ("nanostructure model"), which is described in refs. [479–483]. This model is focused on 6xxx alloys and their typical processing route, which is depicted in Fig. 33. The basic thermo-mechanical treatment involves the

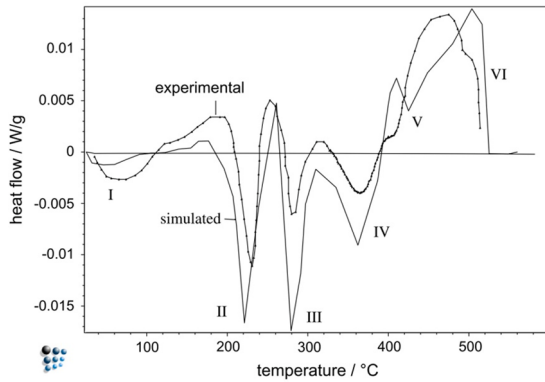


Fig. 30. Measured and calculated heat flow during heating DSC experiment in alloy A. Reproduced with permission from [473].

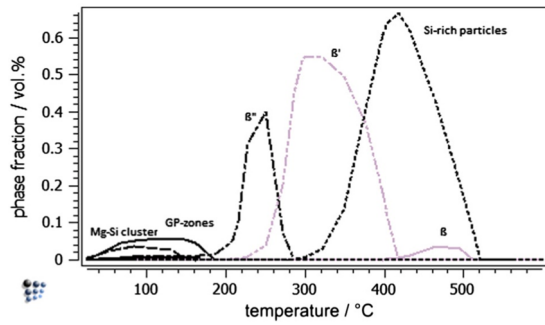


Fig. 31. Calculated phase fractions of precipitates during heating DSC experiment in alloy A. Reproduced with permission from [473].

solution heat treatment, followed by a quench and holding at room temperature before cold rolling. After a period of room temperature aging, the model accounts for an artificial aging treatment, where the supersaturated solid solution decomposes into the precipitation sequence of ss – nuclei – β'' – β' and the stable β –phase. The final part of the model involves a prediction of the stress–strain response of the material as a function of processing steps and schedule. In their study, Myhr et al. [482] compute the evolution of microstructure

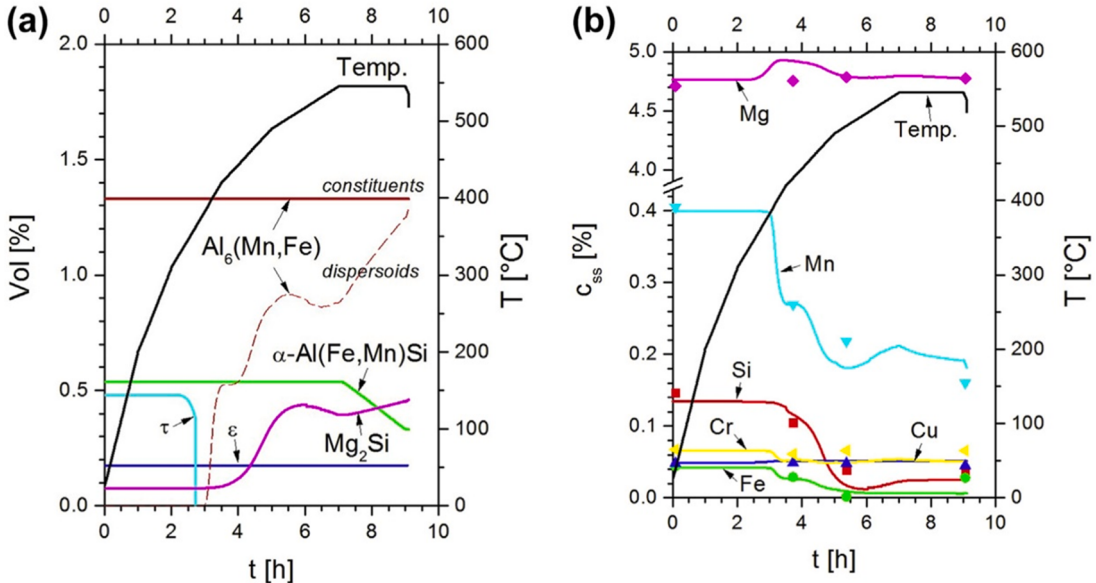


Fig. 32. ClaNG simulations showing the evolution of (a) volume of second-phase particles and (b) solutes c_{ss} during homogenization practice “HT” (symbols: experimental data). Reproduced with permission from [453].

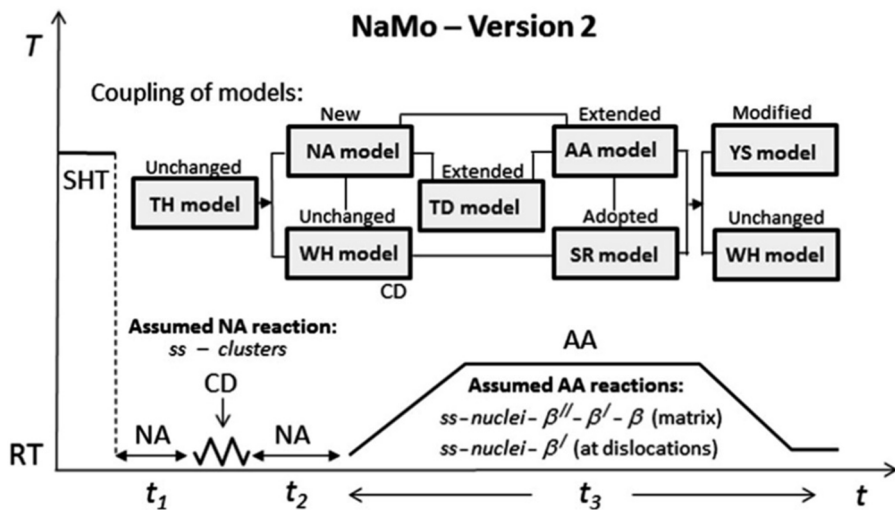


Fig. 33. Schematic outline of the NaMo software. SHT: solution heat treatment; NA: natural aging; AA: artificial aging; CD: cold deformation; TH: thermal; WH: work hardening; TD: thermodynamic; SR: static recovery; YS: yield strength; ss: solid solution. Reproduced with permission from [482].

and precipitates over the entire production route and finally compare the predicted and measured yield strength of various 6xxx alloys with good accuracy. The corresponding diagram is shown in Fig. 34.

4.2.3. Vacancy trapping and interaction with scrap-related tramp elements

Precipitation processes in Al-alloys are diffusion-controlled, and vacancies are the carriers of this mechanism. For most metals their concentration approaches 10^{-4} close to the melting point. This is important in Al processing, because homogenization and solution treatments are often carried out in this temperature range. When the alloy is quenched to lower temperature, a considerable portion of the thermal vacancies can be quenched-in and remain in the crystal. Diffusion is thus accelerated and the kinetics of diffusion-controlled reactions can occur orders of magnitude faster when compared to a crystal which contains only thermally equilibrated vacancies.

Vacancies are created at sources such as free surfaces, grain boundaries, dislocation jogs or incoherent precipitate/matrix interfaces (e.g. those of tramp-element-related IMPs). The same microstructural features will act as sinks for vacancies. The impact of excess vacancies on diffusion in aluminum alloys has been investigated by many groups [542–549]. Robson [550] recently showed that the concentration of excess vacancies due to deformation can even exceed the maximum thermal vacancy concentration close to the melting point.

Vacancies can have attractive or repulsive interactions with many solute atoms within an Al matrix [551,547]. This is relevant for trace elemental concentrations, which are introduced via recycling. Therefore such effects will prospectively become more relevant in future.

If a vacancy travels through the crystal lattice and encounters a corresponding trap with attractive interaction, it will remain in the vicinity of this trap for a characteristic time determined by the value of the interaction energy. As a consequence, the average travel distances during diffusion will decrease and the effective diffusion coefficients become smaller. This effect is well documented as the retarding effect of Sn- or In- micro alloying on natural aging kinetics in 2xxx alloys [552] and 6xxx alloys [545,553–555] or as a major effect determining hydrogen diffusion in steel in the presence of microstructural traps [556]. Fischer et al. [557] investigated the impact of element trapping on diffusion and derived the effective diffusion coefficient in the presence of traps. Using this approach, Lang et al. [558,559] investigated the impact of vacancy trapping for various types of element in Al-0.5 Mg-1Si with and without addition of 0.05Sn (wt%). With interaction energies calculated from Density Functional Theory ($\Delta E_{\text{Mg}} = 2510$; $\Delta E_{\text{Si}} = 3180$; $\Delta E_{\text{Mg}} = 27100$ J/mol), these authors obtain a significant reduction in vacancy diffusion, particularly if the effect of Sn is taken into account. This demonstrates quite a strong interaction with vacancies. Some of their results are shown in Fig. 35 and Fig. 36. The study indicates that trapping of vacancies is particularly efficient for elements with high binding energy, such as Sn, and that trapping increases strongly with decreasing temperature. Consequently certain impurities, which may also be impurities introduced via recycling, make it possible to trap vacancies at room temperature to suppress fast natural aging and release vacancies again at higher temperature to accelerate artificial aging kinetics, in line with experimental evidence [555].

The preceding paragraphs discussed the impact of vacancy trapping on an effective diffusion coefficient, which ultimately determines the kinetics of diffusion-controlled reactions. The main impact of vacancy trapping is thereby exhibited on the remaining concentration of lattice vacancies that are available to enable the diffusion processes. The examples shown involve situations where the effective traps are provided by individual atoms with attractive vacancy-solute interactions. In some alloys, for example in the Al-Mg-Si system, the atomic clusters that are formed in the precipitation process can act as strong vacancy traps by themselves, thus leading to significantly altered precipitation kinetics. Pogatscher et al. [388] have denoted this phenomenon as the “vacancy prison”

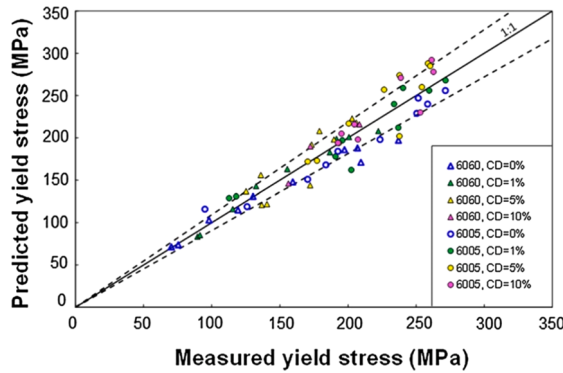


Fig. 34. Strength prediction with NaMo for various 6xxx alloys. Reproduced with permission from [482].

mechanism, proposing that vacancies can be efficiently trapped in solute clusters during natural aging, but can escape the clusters again during heating to artificial aging temperature and thus improve the age-hardening response of the alloy.

Zurob and Seyedrezai [560] provide a theoretical investigation of the concurrent trapping of vacancies and growth of solute clusters, obtaining a model that predicts a severe deviation from the classical parabolic growth law for diffusion-controlled reactions. Although a direct observation of growth kinetics appears to be difficult, these authors provide indirect evidence for a log-based growth kinetics utilizing electrical resistivity measurements. Fig. 37 shows a sketch of a vacancy trapped in a solute cluster.

In the Zurob and Seyedrezai model [560], the cluster growth rate, i.e., the evolution of the number of atoms in the cluster, n_{cl} , is assumed to be proportional to the escape rate of vacancies from the cluster as:

$$\frac{dn_{\text{cl}}}{dt} \propto e^{-\frac{m_{\text{cl}} \Delta E_{\text{cl}}}{k_B T}}, \quad (9)$$

where α is a constant and ΔE_{cl} is the binding energy between the vacancy and a solute atom in the cluster. Separating variables and integration leads to the result that the number of atoms in the clusters evolves in proportion to the logarithm of time as.

$$n_{\text{cl}}(t) = \frac{k_B T}{\alpha \Delta E_{\text{cl}}} \ln \left(\frac{K \alpha \Delta E_{\text{cl}}}{k_B T} \right) + \frac{k_B T}{\alpha \Delta E_{\text{cl}}} \ln(t), \quad (10)$$

where K is the proportionality constant from eq. (9).

The logarithmic growth rate also seems to agree well with experimental evidence regarding the growth kinetics of clusters obtained via atom probe tomography. The clusters commonly show a statis in their growth behavior when observed over long periods during natural aging [561]. Direct experimental confirmation of this growth characteristic is sparse. Some evidence for logarithmic growth characteristics in clusters is available from positron annihilation experiments, e.g. Lay et al. [543]. In their review on clustering in age-hardenable aluminum alloys, Dumitraschkewitz et al. [562] also conclude that Mg-Si-rich clusters stagnate in size evolution even at small sizes, again supporting the prediction of logarithmic growth behavior.

4.2.4. Microstructure evolution modeling

In the present context, the term “microstructure modeling” refers to mechanisms that alter the grain, subgrain/cell and dislocation structure of the metallic matrix as well as its corresponding stress-strain response (strain hardening). The particular mechanisms that are important for green Al production are the segregation of impurities into, and their interactions with, dislocations and grain/

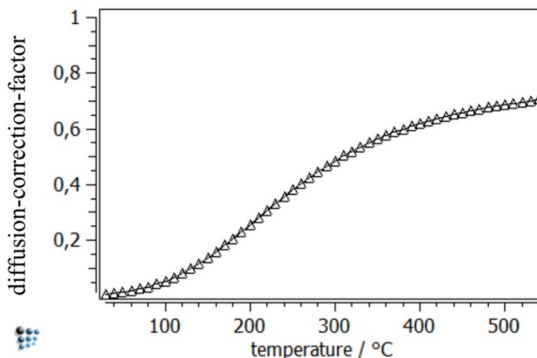


Fig. 35. Vacancy trapping in Al-0.5 Mg-1Si-0.05Sn and corresponding deceleration of diffusion kinetics. Reproduced with permission from [558].

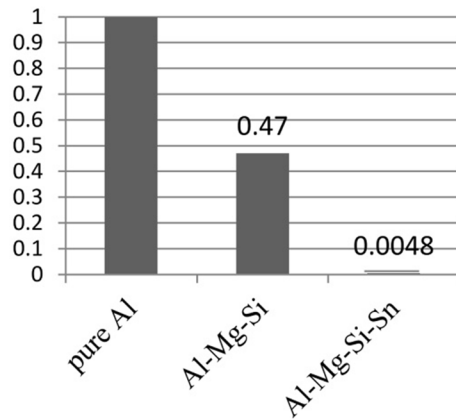


Fig. 36. Vacancy trapping and relative deceleration of diffusion kinetics in pure Al, Al-0.5 Mg-1Si and Al-0.5 Mg-1Si-0.05Sn. Numbers refer to the fraction of diffusivity with solute trapping in comparison with pure Al. Reproduced with permission from [558].

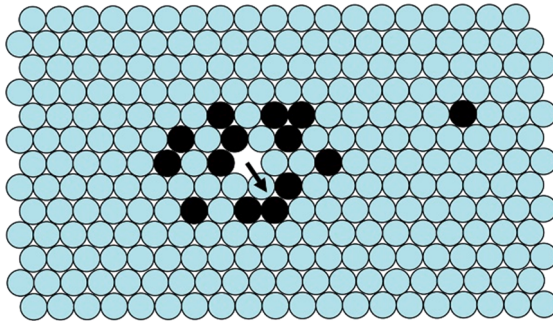


Fig. 37. Illustration of a solute cluster with gray and black circles representing solvent and solute atoms, respectively. The arrow illustrates a vacancy jump, which will free the vacancy from some solute atoms but place it next to other solute atoms within the cluster. Reproduced with permission from [560].

subgrain boundaries. Some areas where scrap elements might potentially impact microstructure evolution are briefly outlined below.

It is well known that impurities have a certain tendency to diffuse to the stress field of dislocations. On the one hand, these atoms then influence the mobility of the dislocations by forming Cottrell atmospheres, an effect that is familiar in steel with respect to carbon atoms. Numerous publications deal with the phenomenon and modeling of this effect [563–568]. In Al-alloys it has been shown that the effect of cross-core diffusion can have a significant impact, and it is well documented that Mg is a crucial element in this context. Soare and Curtin [569,570] developed a rate theory for dynamic strain aging, a mechanism that is made responsible for the Portevin – Le Chatelier effect in aluminum alloys containing Mg [571,572]. The Soare and Curtin model was recently utilized by Kreyca et al. [573,574] to simulate stress-strain curves in Al-Mg alloys and to predict regions of negative strain rate sensitivity. Kabirian et al. [575] use a constitutive approach to model the same phenomenon.

Dissolved impurities also tend to segregate to grain boundaries, and thus impact the mobility of planar defects by solute drag. It has been demonstrated that even small amounts of solute can have severe effects, for instance on grain growth and recrystallization. A classic study in this context is the analysis by Huang and Humphreys [319,320], which investigates the impact of Mg, Mn and Si on grain boundary mobility. The information on mobility was recently deployed by Buken and Kozeschnik [474] in a simulation of recrystallization in Al-Mg alloys, where the significant impact of Mg on the kinetics of recrystallization is observed both experimentally and in simulations. Fig. 38 shows grain boundary mobility from this analysis as function of temperature and Mg content. A particularly strong effect can emerge when the Mg content increases substantially, for instance where there are high levels of contamination from scrap.

4.2.5. Future challenges for green aluminum modeling and simulation

The models reviewed above can be used in simulations of scrap-related alloying effects. However, several pieces of the green aluminum puzzle are missing, and some represent mechanisms which have a severe impact.

One topic is the question of the exact nature of interaction between solute atoms and quenched-in excess vacancies. What is the nature of the vacancy trapping in 6xxx alloys that makes the kinetics of natural aging insensitive to cooling rates after solution annealing? Why is the kinetics of natural aging similar, independently of how the quenching process is performed? Why do water quenching, cooling with ventilated air and still air cooling result in natural aging kinetics occurring within one order of magnitude of

time [576–578], while simulations of excess vacancies (see model of Fischer et al. [579]) deliver excess lattice vacancy concentration differences of several orders of magnitude? A detailed analysis and overview of the role of excess vacancies in natural and artificial aging which addresses many of these questions, particularly for the Al-Mg-Si system, was recently provided by Yang and Banhart [544].

What is the role of atomic pairs and couples in this context? Madanat et al. [577] speculate that vacancies can be very efficiently trapped at Si-Si pairs and that the corresponding trapping enthalpies should be significantly higher than those of individual Si atoms. The modeling of this effect is possible in principle using the models for couple and pair formation recently developed by Svoboda et al. [580,581], combined with the vacancy trapping approach reported here. Corresponding analyses are still lacking in literature, and conclusive models describing the mechanism of vacancy trapping during quenching of 6xxx alloys are needed. In 6xxx alloys with a high level of dispersoids the effect also seems much less pronounced, as demonstrated for instance by Strobel et al. [582]. This has immediate relevance for green aluminum alloys, where elevated levels of Fe can be expected. Here the quenching rate may assume renewed importance.

What, exactly, happens during natural aging? How can the thermodynamics of cluster formation be described properly, keeping in mind that thermodynamics is a theory involving systems large enough to allow statistical averaging? Clusters consist of a very limited number of atoms. Can atomistic modeling deliver correct answers, and can the associated approaches be extended to sufficiently large systems? Reports on successful applications exist, but these do not properly describe the observed compositional variations of of 6xxx alloy clusters during natural aging. These clusters can be Si-rich, Mg-rich, or anything in between [561,583].

Can the application of Classical Nucleation Theory be justified in precipitation modeling in systems at high supersaturation, which are typical for quenched Al-alloys? The driving forces are often so high that the sizes of critical nuclei fall below the dimensions of a single atom, and clusters form homogeneously in the undisturbed crystal with no conceivable nucleation barrier. Can compositional gradients around near-critical nuclei be neglected [584]?

What is the exact nature of the transformation of clusters and precursor phases into precipitates with distinct crystal structures, e.g. Mg₅Si₆ (β'') particles in 6xxx alloys, η' in 7xxx alloys [585] or Θ' in Al-Cu [542]? What about particle-into-particle transformation versus independent classical nucleation of the same phases (without precursor phases) in the bulk volume of the Al matrix, for instance during direct aging treatments?

What is the role of heterogeneous nucleation sites? In continuous cooling DSC experiments with medium to slow cooling rates, the stable Mg₂Si seems to form very close to its thermodynamic solvus. Classical Nucleation Theory predicts that a necessary undercooling of >100 K will take place before this phase nucleates, in clear contrast to experimental evidence. The energy of heterogeneous nucleation sites, e.g. grain boundary corners and edges, must also be taken into account.

Is precipitate growth controlled by diffusion, while precipitate dissolution is controlled by the interface or reaction rate? There is some evidence that these mechanisms may be important in the evolution of clusters and other particles [467].

There is also a need to further investigate the impact of solutes on the mobility of linear and planar defects. Solute drag may potentially play an important role in alloys containing (uncontrolled) amounts of impurities that show strong segregation tendencies towards grain boundaries and dislocations. Variations in grain boundary mobility can require the adaptation of entire alloy processing regimes to achieve stable production of green aluminum products.

4.3. Combinatorial metallurgical methods to study the effects of tramp elements

The processing parameter scope of classical aluminum alloys has many dimensions. These comprise chemical composition in the

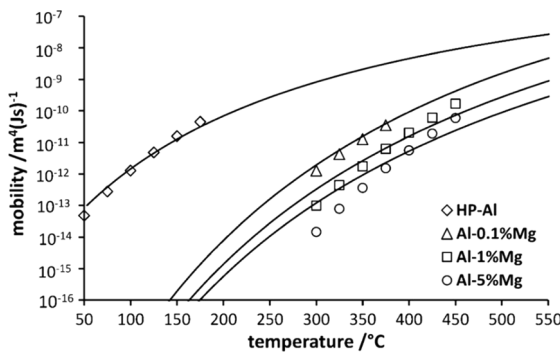


Fig. 38. Mobility of grain boundaries in Al-Mg alloys as function of temperature and Mg content. The HP-Al line was calculated for an Mg content of $X_{Mg} = 10^{-8}$. Reproduced with permission from [474].

multi-component alloys (typically 4 to 5 different species that have a first-order influence on alloy properties), and processing parameters, whose number can be very large if the entire processing route of the alloy is considered and typically consist of temperatures (of rolling, heat treatment); heating and quenching rates; heat treatment duration; amount of plastic deformation, etc. All of these parameters affect final properties via differences in microstructure at different scales: grain size, morphology and texture; intermetallics and dispersoid distribution; and nanosized precipitate nature, shape, size, density, distribution and dislocation density. When dealing with recycled alloys the diversity of the parameters to be investigated is potentially even greater, with new chemical species added to the classical ones, guiding us into regions of the alloy design space which are essentially unexplored. Innovative processes such as additive manufacturing or severe plastic deformation (see section 3.6) are also frequently required to mitigate the negative effects of adding impurity elements, and are also mostly uncharted in the alloy design sense.

Finding optimal solutions within such a large design space is an immense task. The traditional route would combine an understanding of the physical and mechanical processes that govern microstructure development and the resulting properties with predictive integrated modeling and a few experimental validations. However, in corners of the design space where little knowledge and data are available, such as the area of recycled Al-alloys, the predictive capability of existing knowledge and models is likely to be insufficient. There is a strong need for extensive experimental data to improve matters and identify optimal solutions.

Obtaining extensive datasets on microstructure and properties requires us to develop specific high-throughput methodologies. These can be grouped under the generic name “combinatorial methods” [586,587], although in metallurgy such methods are seldom truly combinatorial (in the sense of randomly combining many parameters). The objective is to quasi-continuously vary a few alloy design parameters (whether compositional or processing-related), and be able to measure, also quasi-continuously, the relevant microstructure parameters and properties of interest [588]. Possible strategies for these two steps are detailed below.

4.3.1. Methods for high-throughput material fabrication

It is possible to systematically vary alloy design parameters either continuously, by establishing materials with gradients of composition or processing materials [83,589], or discretely, by quickly fabricating a large number of samples in a controlled manner [590]. When dealing with gradient materials, the magnitude of the gradients is important. Too-small gradient sizes in variation may impact the transformations to be studied. For instance, a very steep composition gradient (e.g., a few μm) may influence diffusion-controlled phase transformations and (even more) the transferability of results on microstructure evolution (e.g. recrystallization and grain growth) to larger scales. Thus the range of parameter variation within a gradient sample should be much greater than the characteristic size scale of the microstructure to be studied. The microstructure of the graded material should also be representative of the microstructure in bulk alloys, especially if mechanical properties are to be measured. This imposes particular requirements on the fabrication process of samples. For example, combinatorial studies of functional properties (thermoelectric efficiency, shape-memory effect, etc.) have often focused on fabricating compositionally graded materials using physical vapor deposition [591,592], which enables ternary planar gradients to be achieved in a straightforward manner. This method, however, is ill-suited for the study of metallurgical processes because the fabricated materials have a very limited thickness. The dimension of the gradient should also be of the appropriate scale with respect to the characterization methods applied to evaluate the microstructure or the properties as a function of the local parameter value. This depends on the phenomenon to be characterized and the technique used, but as a rule of thumb the resolving capability of high-throughput characterization is on the order of 100 μm , demanding gradients of several millimeters in order to resolve a sufficient number of parameter values. This requirement means limitations for fabrication methods that imply solid-state diffusion to create the gradient, especially where the influence of slow-diffusing elements (such as Fe for the study of recycling) is to be investigated.

Compositionally graded aluminum alloys have been fabricated mostly by making diffusion couples between two alloys of the end compositions in the gradient [593–595]. Successfully achieving the required continuous gradient requires an additional criterion: a temperature must exist where the alloy is in a single (solid) phase for all compositions within the gradient, so that the interdiffusion heat treatment can be realized without composition partitioning. When joining aluminum alloys in the solid state, a difficulty is the presence of the oxide layer, which prevents good metallurgical bonding. However, interdiffusion can still be achieved by simple hot pressing [593]. Due to time limitations, large gradients cannot be obtained in this way, and extending the gradient is hard due to the brittleness of the joining interface. An alternative is to use a solid-state joining technique which removes the oxide layer at the junction. Dissimilar friction stir welding is a widely available technique, but has the disadvantage of a very complex 3-D distribution of the two joined materials. This is complicated to transform into a smooth gradient by diffusion. Linear friction welding has been successfully applied to generate planar oxide-free dissimilar joints, which could then be extended by interdiffusion and plastic deformation (rolling) [594,595], as illustrated in Fig. 39. The advantage of this strategy is that the graded material is made from wrought alloys, which are representative of the bulk end alloys.

Powder metallurgy has also been used to fabricate compositionally graded material. By mixing different powders, several end alloy compositions can be targeted and then placed in a crucible before sintering, e.g. using spark plasma sintering [596]. Compositionally graded materials can be fabricated in this way, although the methodology has yet to be validated in the context of aluminum alloys. Because sintering breaks the oxide layers, the compacts thus obtained can be further processed by interdiffusion heat treatments and plastic deformation in order to reach the appropriate scale of the gradient.

Combinatorial thin-film synthesis techniques, for instance magnetron sputtering, may be suitable methods for efficiently screening and exploring a large variety of chemical compositions with respect to changes in microstructure. Compositionally graded films sputtered on one substrate can consist of 5 elements [597], which may include elements familiar in aluminum scrap such as Fe and Si. The screening of such compositionally graded samples may inspire a focus on interesting specific chemical compositions, which can be further investigated with the corresponding bulk material.

However, due to the high solidification rate of energetic particles, the conditions of thin film growth may be unbalanced [598]. Magnetron sputtering is considered a far-from-equilibrium technique [599], and films produced by it might not be directly comparable with bulk samples produced by conventional casting techniques. During the magnetron sputtering process it may be possible to reduce the solidification rate by heating the substrate, as shown during plasma-spraying [600]. To obtain thermodynamically stable phases and to mitigate the effects of defects, annealing treatments are often applied to co-sputtered thin films [597]. Compositinally graded material might also be developed by casting techniques using one chemical composition. It has been shown that the Fe content in 3104 ingots can vary between the surface and the center of the ingot produced by DC casting [45].

An alternative to using samples with gradients of composition or processing parameters is to fabricate a large number of samples, each with different parameters (e.g. of composition). This may be achieved by direct metal deposition, although the obtained materials may not show microstructures representative of bulk wrought alloys. A large set of bulk samples were shown to be made with the DC casting method [210]. 950 industrial ingots within the compositional limits of 6008 alloy were produced and processed to study the effects of the main impurity elements Fe and Si on mechanical properties such as yield strength and tensile strength [210]. While an increase in the Fe content without increasing the Si content can reduce mechanical properties, a high Si content combined with low Fe content can increase them. It may be necessary to compensate a high Fe content with an increase in the Si content to balance the Fe-Si reaction [210]. Bulk samples can also be made using traditional casting and processing methods, miniaturized and automatized in order to facilitate duplication in large numbers. This Rapid Alloy Prototyping strategy has been used to design steels [590,601,602]. Although the number of parameters that can be reached is more limited when compared to gradient materials, this strategy has the advantage of making it possible to evaluate bulk properties such as fracture stress or even fracture toughness.

4.3.2. Methods for high-throughput microstructure and property characterization

Resolving microstructure features and properties with a high throughput capability is the next challenge. Both direct observation and indirect methods can be used for microstructure evaluation. High throughput necessarily means automated data analysis. In addressing large particles or grain size, optical or scanning electron microscopy may be used [603], where data acquisition and analysis can be automated if the contrast is sufficiently uniform. The situation is more complicated with nanometer-scale microstructure features, such as nanoscale precipitates. Spatially-resolved observation of graded alloys in a transmission electron microscope has been achieved for Ni based alloys [589], but with a compositional gradient scale which is necessarily of the same order of magnitude as the characteristic distance of precipitation. The alternative is to use indirect measuring techniques such as X-ray diffraction, small-angle X-ray scattering (see section 4.6), differential scanning calorimetry (DSC), or spatially resolved conductivity measurements. Some methods need development or adaptation (such as robotic sample handling for DSC) to approach high throughput. With DSC it is difficult to obtain more than a few hundred measurements in a reasonable amount of time (weeks!). Using X-ray methods, on the other hand, it is possible to obtain $10^3\text{-}10^4$ results easily in a few hours if using synchrotron sources and appropriately prepared graded samples [83,604]. X-ray methods are also adapted to in-situ measurement, making it possible to study the kinetics of microstructure evolution in graded material by simultaneously performing space- and time-resolved experiments. Fig. 40 illustrates this for an Al-Cu-Li alloy with variable Mg.

In terms of mechanical properties, the feature that can be spatially most easily resolved with high throughput is hardness, with a resolving power of $\sim 100\text{ }\mu\text{m}$ for microhardness and $\sim 1\text{ }\mu\text{m}$ for nano-indentation. It is reasonably possible to obtain datapoints on the order of $10^3\text{-}10^4$ in a few hours [605]. However, hardness is only a rough indication of mechanical properties and it is usually desirable to characterize them more precisely. When dealing with graded samples, it is possible to spatially resolve the yield stress by applying a tensile test parallel to the gradient of the composition / processing parameter, while measuring the strain distribution by digital image correlation. A requirement for achieving this is that the gradient of yield stress should be sufficiently modest for the measurement in the hardest zones of the gradient not to be affected by the plasticity in the softest zones (change in cross-section and possibly fracture). Measurement of fracture properties is much more challenging, as these properties have a strong size dependence and measurement is difficult to achieve on graded samples. But inspiration can be taken from other alloy families, where, for instance, the forming ability of

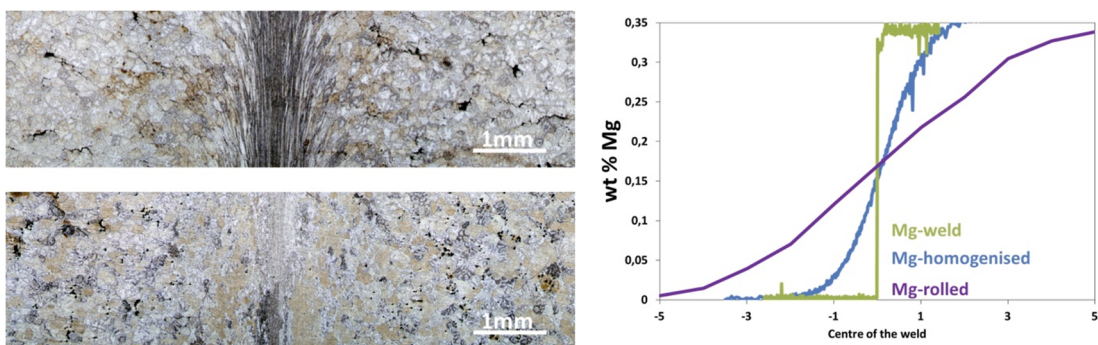


Fig. 39. Diffusion couple made by linear friction welding from two Al-Cu-Li alloys of variable Mg content. (Top left) Micrograph after welding. (Bottom left) Micrograph after homogenization. (Right) Composition profile after the different processing steps. Figure used with permission from [594].

metallic glasses has been mapped in compositional space using innovative arrays of holes made in a two-dimensional composition gradient [592]. Other properties related to alloy durability can be also mapped; this is the case for electrochemical properties using Kelvin Force microscopy [606]. Local electrochemical properties can also be obtained by using a scanning droplet cell (SDC). It has been shown that SDC microscopy can be successfully combined with an automatic robotic system, which can provide an efficient automated characterization of co-sputtered thin film surfaces [607]. Multi-SDC microscopy can be applied to conduct electrochemical measurements on several (e.g. 8) local surface spots at the same time [608].

4.4. Chemically highly-resolved characterization of tramp elements

Understanding the metallurgical influence of impurity elements on the solid solution and precipitation state of recycled Al-alloys requires that these elements be observed with high chemical and spatial detection sensitivity. Standard techniques used for this purpose are the various chemical sensing methods used in Scanning and Auger Electron Microscopy; Glow Discharge Optical and Mass Emission Spectroscopy; Secondary Ion Mass Spectrometry; X-ray Photoelectron Spectroscopy; and Rutherford Backscattering. When aiming at the characterization of tramp elements at near-atomic scale, spatial and chemical resolution typically involve a combination of more advanced techniques, often culminating in the various imaging, diffraction and spectroscopic methods available in the (scanning) transmission-electron microscope ((S)TEM) and atom-probe tomography (APT). Each of these two techniques has its strengths, limitations, and idiosyncrasies, but they offer a combination of the highest possible spatial resolution and compositional accuracy, specifically when performed in combination on a single specimen [609,610]. The operation and challenges associated with each technique are explored in the following sections. APT is addressed first, including opportunities to link it with atomistic simulations. Second comes (S)TEM. Finally, we discuss examples and challenges associated with both techniques as regards the chemically highly-resolved characterization of impurity elements in Al-alloys.

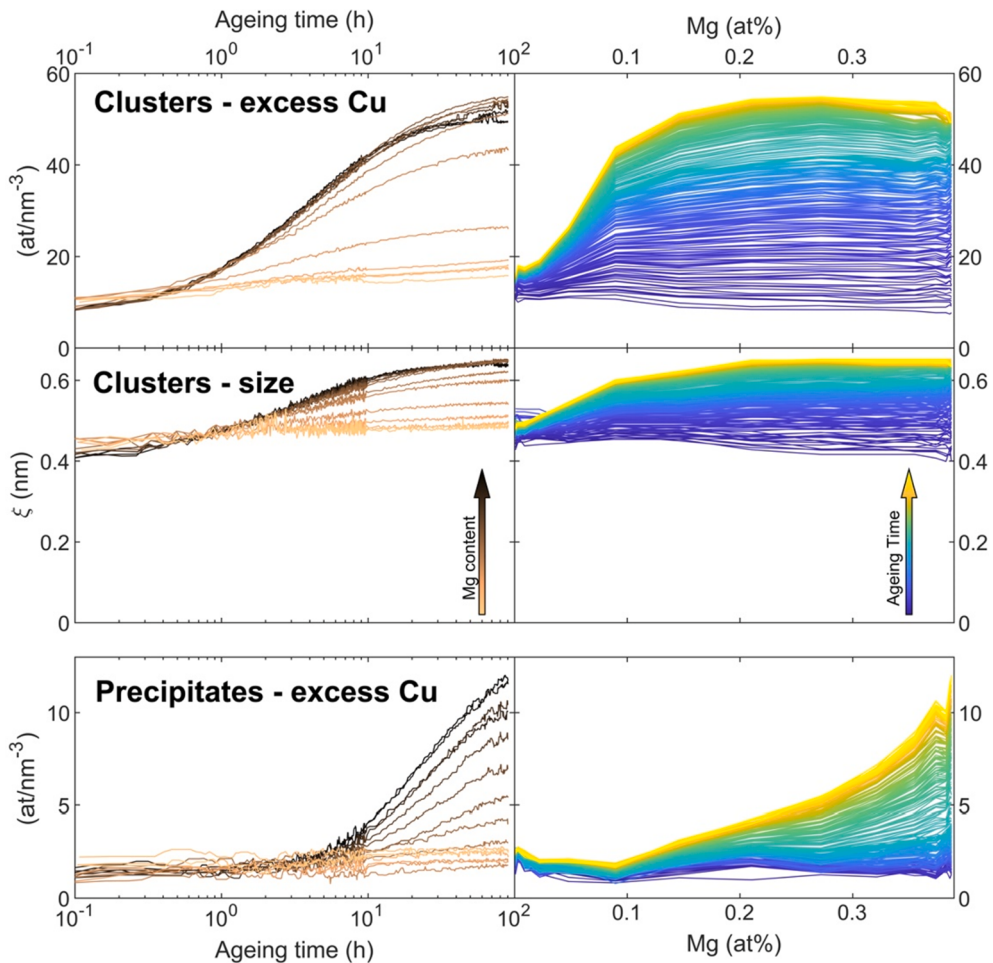


Fig. 40. Parameters of the nanoscale cluster and precipitate microstructure obtained by simultaneous time- and space-resolved SAXS experiments performed during natural aging of an Al-Cu-Li-Mg compositionally graded alloy of varying Mg content. Figure used with permission from [595].

4.4.1. Atom probe tomography

APT relies on the time-controlled removal (evaporation) and projection of individual atoms, in the form of low-charge state ions, from a needle-shaped specimen (a nanotip) onto a position-sensitive detector, as depicted in Fig. 41a. The ions are created by the process of field evaporation; that is, under the influence of an intense electric field generated by subjecting a sharp needle-shaped nanotip to high voltage of a few kilovolts (for tungsten, for example, the evaporation field is 40 V/nm). The ion trajectories are defined mostly by the distribution of the electrostatic field surrounding a sharply pointed nanotip [611], but also by the shape of the nanotip and the geometry of the APT itself [612]. The measurement of the time-of-flight (ToF) of each ion proceeds via nanosecond high-voltage pulses or ultraviolet picosecond laser pulses (sometimes femtosecond laser pulses) superimposed on the static electrostatic field. The pulses provide time-control of the departure of each ion. Thus it is possible to field evaporated atoms essentially one

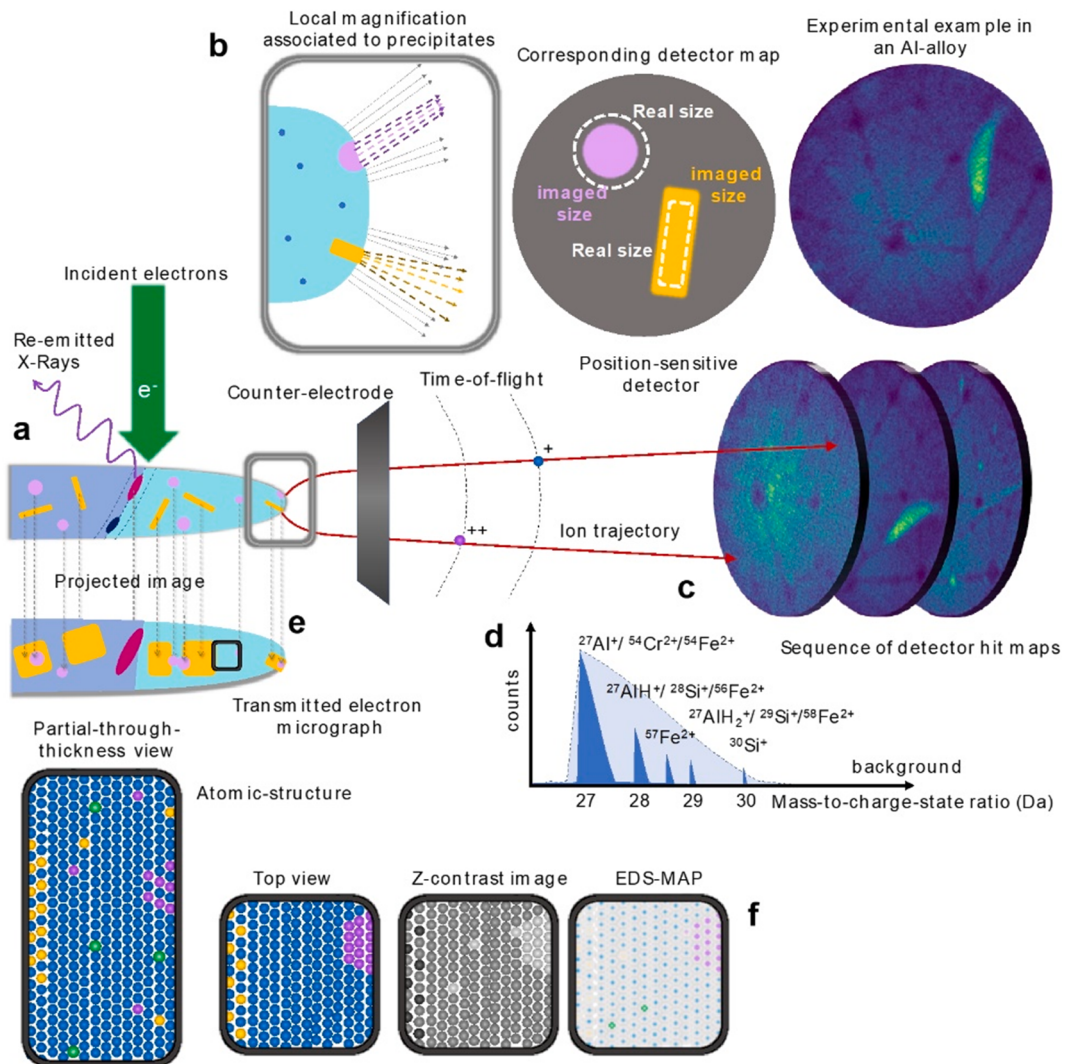


Fig. 41. Schematic overview of atom probe and transmission-electron microscopy in combination. (a) Needle-shaped atom probe specimen containing a grain boundary and a range of second-phase precipitates both intragranular (in yellow and pink) and intergranular (dark blue and magenta). The specimen is located in front of the counter-electrode enhancing the intensity of the electrostatic field. Ions emitted by the specimen fly towards the position-sensitive detector and their time-of-flight is recorded, along with the impact position. (b) Because phases require different electric field to be field evaporated, different curvatures develop, generating either compression or dilation of the ion trajectory that affects the imaged size of the particles and causes changes in the impact density on the detector maps. (c) A cumulative histogram of the impact positions shows a pattern that can reveal symmetries of the crystal and differences in the density which typically indicate different phases. (d) Cartoon view of a section of a mass spectrum highlighting some of the possible isobaric and charge-state-related overlaps, or issues associated with background levels or mass resolution. (e) Projected image of the corresponding microstructure within the atom probe specimen obtained by the transmitted electrons. (f) The through-thickness and corresponding top view of the atomic arrangement inside the specimen and examples of a Z-contrast image and possible X-ray energy dispersive spectroscopy map obtained from the corresponding top view. (For interpretation of the references to color in this figure legend, the reader is referred to the web version of this article.)

atom at a time and atomic layer by atomic layer. During post-processing of this metadata, the times-of-flight are converted into a mass-to-charge-state ratio for each ion, and the impact position on the detector is reverse-projected by assuming a certain projection law onto a virtual model of the emitting nanotip specimen [613,614].

A number of challenges are generally encountered during APT analyses, and these can be more critical in the case of Al-alloys. First, as indicated in Fig. 41b, the surface of the emitter can develop local radii of curvatures. In addition, the critical electric field necessary to trigger field evaporation depends on the composition, and probably also the structure, of each of the phases [615–617]. Subtle roll-up-type, short-range displacements of atoms on a specimen's surface prior to their departure cause the spatial precision of the measurement to degrade [618–620]. Because a second phase precipitate intersects a specimen's emitting surface, a different radius of curvature also develops locally according to the magnitude of the electric field (and local work function) required to initiate field evaporation, i.e. the so-called evaporation field. The magnification of the ion's projection depends directly on the local radius of curvature of an emitter; therefore a change in the local radius of curvature leads to either compression or dilation of an ion's trajectory if the evaporation field is respectively greater or smaller than that of the matrix [621]. This effect is referred to as the local magnification, which causes an artificial expansion or compression of the imaged dimensions of a precipitate [622,623]. This can also be observed as a variation in the impact density on the detector maps, as suggested by a series of detector hit maps obtained during an analysis near a grain boundary in a 7xxx-series alloy, Fig. 41c. Changes in the local point density are also typically observed at grain boundaries and more generally at crystalline imperfections [624,625]. They are associated with the shaping of a specimen's surface or end form, which permits retrieval of information pertaining to the local crystalline structure and orientation [626]. This latter aspect has been utilized efficiently in the case of Al-alloys [627–629]. Fig. 41d displays a cartoon of a portion of a mass spectrum, showing a series of peaks, often observed in the analysis of Al-alloys, which highlight some of the possible isobaric and charge-state-related overlaps. These effects are discussed in greater detail below.

APT has been used extensively for the analysis of precipitation in Al-alloys [531,630–638]. However, in these materials local magnification effects are critical. Examples for high-field precipitates, which are imaged larger than their real size, are Cu-rich GP zones, θ' [639] or T_1 precipitates in the 2XXX-series [640], β' -precipitates in the 6xxx-series [641]; Al_3Zr and Al_3Sc precipitates. Low-field precipitates, which are imaged smaller, are for example the η' -precipitates in the 7xxx-series or $Al-Ag$ or $Al-Li \delta'$ precipitates [642].

Trajectory aberrations lead to a crossing of the ions' trajectories, resulting in an intermixing of atoms from within precipitates and the matrix which affects the accuracy of the composition measurements [643]. The precision of the spatial and compositional measurements in APT is hence extremely complex because it is determined by the details of the field-evaporation process and the local environment of each atom at a specimen's surface. Recent reports state that even segregated, first-nearest-neighbour (NN) atoms at a specimen's surface before departure are not reconstructed as NN atoms after analysis [644], raising questions about a number of literature analyses of the early stages of clustering in Al-alloys [562,645–647]. These aspects are discussed extensively by De Geuser et al. [641].

4.4.2. Analysing tramp-related solute atoms and precipitates in atom probe tomography data from aluminum alloys

Analyses of solute atoms in aluminum-based alloys start with atomic scale fluctuations in solid solution, which lead to the formation of short-range order (SRO) or clustering of atoms to form ultimately stable precipitates or nuclei (in the language of classical nucleation theory (CNT)) [648]. An unstable nucleus is referred to as an embryo in CNT. One approach to this problem is to apply partial radial distribution functions (p-RDFs) [649–651]; a sub-routine for this analysis is readily found in most data analysis programs [652]. This permits one to distinguish between clusters of solute atoms (embryos) and stable precipitates (nuclei); a specimen may contain both embryos and nuclei simultaneously. Stable precipitates may also exhibit a certain degree of SRO, which increases as the mean radius, $\langle R(t) \rangle$, of precipitates grows with increasing aging time. Partial RDFs also permit us to distinguish between repulsive versus attractive interactions between different species [653]. The identification of precipitates (nuclei) can sometimes be accomplished using cluster-finding algorithms [654] and, when larger, via iso-concentration surfaces and proximity histograms [655,656]. No specific approaches need to be developed for SoDA, i.e. to detect effects associated with scrap-related tramp elements, but for elements with low concentrations care must generally be taken with parameter selection [657,658].

4.4.3. Combination of atom probe tomography with atomistic simulations

In the context of scrap-related contaminants, the scale of volumes imaged by APT and the fine scale resolution make the technique particularly useful in combination with atomistic simulations: the simulations help to interpret experimental atom-probe tomographic data, while APT helps inform the simulations. Here multiple techniques have been deployed, including Monte Carlo [647,659,660], molecular dynamics [661,662] and density-functional theory [663,664], particularly in the area of Al-alloys [665–669]. Many efforts have involved vacancy-mediated lattice kinetic Monte Carlo (LKMC) simulations. LKMC allows the modeling of diffusive processes in alloys mediated by a vacancy mechanism. Here a mono-vacancy changes places with the nearest NN atoms [392], and the necessary energy interaction parameters can be obtained from density-functional theory. Specifically, LKMC is capable of studying nucleation, growth, and coarsening of precipitates in great detail [660,670–672], while allowing comparison with coarsening models [673–675]. In the area of Al-alloys, precipitation in binary and ternary alloys, $Al-Sc$, $Al-Zr$, $Al-Sc-Zr$ and $Al-Sc-Mg$ have been studied extensively [676–680], especially the core / double-shell nanoprecipitates produced by solid-state precipitation [681,682]. Correlations from LKMC and cluster dynamics were drawn by for such systems by Clouet et al. [531,536,683–685], revealing many details of the phase separation mechanisms. Up to now such studies utilizing APT in conjunction with atomistic simulations have been performed for intentional, controlled alloying additions and for mixtures of small numbers of species. They have not yet been directly applied to the SoDA concept.

4.4.4. Scanning transmission electron microscopy

The following (scanning) transmission-electron microscopy (STEM) processes are well documented in the literature [686]: (i) an electron-beam is generated and accelerated, typically to 80–300 keV; and (ii) a thin specimen, usually of between 10 and 150 nm for metallic samples, is placed in the beam. This beam can be a large parallel beam flooding the sample as in TEM (see Fig. 41f), or a finely focused probe that can be scanned over the specimen (STEM) or kept stationary (see Fig. 42). The interaction between the incident beam of electrons and the specimen generates many different signals, the most useful containing the transmitted electrons. These can be collected to form images and diffraction patterns and yield spectroscopic data. X-rays are also generated, and can provide chemical information. To characterize metallic alloys at high spatial resolution, HAADF (high angle annular dark field) STEM and energy dispersive X-ray spectroscopy (EDXS) in STEM mode (STEM-EDXS) have been the techniques most commonly used in the last decade, because they can provide atomic resolution of the projected two-dimensional structure and chemistry. Many further (S)TEM techniques are available, and are becoming increasingly relevant to the characterization of alloying elements; these are also discussed briefly below. A schematic illustration of these techniques is displayed in Fig. 42 and Fig. 41f.

HAADF-STEM collects electrons scattered at high angles and thus provides contrast approximately proportional to the atomic number Z^n , where $n \sim 1.7$, depending on many factors such as specimen thickness, local atomic environment, probe size, etc. [687]. Although HAADF-STEM was first developed in the 1970 s [687], it is only since the mid to late 2000s that it has become the technique of choice for characterizing the structure of materials at the atomic scale. This revolution has been enabled by major improvements in electronics which permit the accurate scanning of atomically-sized electron probes. It has been accelerated by the advent of aberration correctors [688], which have further improved spatial resolution to sub-angstrom levels. HAADF-STEM is particularly advantageous for embedded particles or interfaces. This contrasts with high-resolution TEM, where the image contrast is generally much more difficult to interpret (compare for instance, the images of Ag-rich interfaces in [689,690]).

The Z contrast in HAADF-STEM images is a form of chemical characterization and is especially useful when imaging chemical elements with very disparate atomic numbers. Examples relevant to aluminum alloys and other light alloys include the characterization of atomic clusters [85,691], the chemical segregation of elements at precipitate interfaces [383,384,690,692,693] and lattice defects [694]. In some cases, atomic clusters or interfaces containing only a handful of atoms [85,383,691] can be detected. Even for materials containing elements with widely spaced Z numbers, HAADF-STEM does not always provide unambiguous characterization of the chemistry and atomic structure. For example, features buried in the sample rather than near its top surface will not be imaged

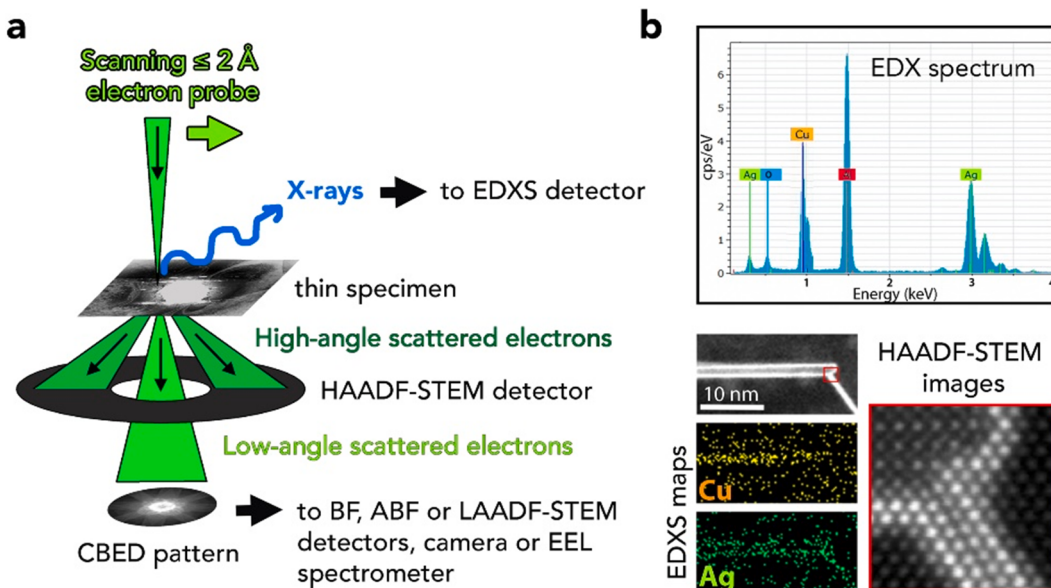


Fig. 42. Schematic overview of scanning transmission electron microscopy (STEM). (a) A focused electron beam incident on a thin specimen is scanned laterally. Transmitted electrons which have interacted with the specimen are detected at different angles and locations, where they form images, diffraction patterns and provide spectroscopic information. Electrons scattered at high angles are detected by a high angle annular dark field (HAADF) STEM detector, which will result in images dominated by atomic number (Z) contrast. Electrons scattered at lower angles pass through the hole of the HAADF-STEM detector and may be used to form other signals which can provide additional structural or chemical information: STEM images in bright field (BF), annular bright field (ABF) or low-angle annular dark field (LAADF) modes; convergent beam electron diffraction (CBED) patterns; and electron energy loss spectra (EELS). X-rays are also generated and can be analysed through energy dispersive X-ray spectroscopy (EDXS). (b) A schematic EDX spectrum shows the characteristic X-ray peaks associated with specific chemical elements. If some of the peaks are selected, elemental maps can be generated in conjunction with images in HAADF-STEM (or other STEM image modes). At high resolution, the projected atomic structure of the specimen may be visible, with brighter regions indicative of greater Z density in projection. The case shown here comprises an Al-Cu-Ag alloy with Cu-rich and Ag-rich precipitates. Ag atoms segregate to the Cu-rich precipitate-matrix interfaces, as revealed by HAADF-STEM imaging and EDXS maps for Cu and Ag [690].

clearly due to broadening of the electron probe as it travels through the specimen [695]. Although this may lead to significant errors in interpreting the images, simple strategies are available for avoiding these pitfalls. They involve recording electron diffraction patterns and simulating images, and are similar to the strategies required (e.g.) to ascertain the validity of the interpretation of most (S)TEM images.

It is important to mention that STEM imaging modes other than HAADF are easily accessible in modern instruments and can provide extremely useful and complementary information. For instance, bright-field (BF) and annular bright field (ABF) STEM can image light elements (e.g. Li) [696,697], while low or medium angle annular dark field (LAADF, MAADF) STEM can image strain fields and lattice defects [85]. The following fact should also be stressed, as it is often poorly appreciated: in ADF-STEM modes the electron diffraction pattern at each pixel can be recorded simultaneously (four-dimensional (4D)-STEM) [698] or as an average (position averaged convergent beam electron diffraction, PACBED) [699]. These reasonably new techniques will become powerful tools for multiscale characterization of structure and chemistry [698], including that of light alloys.

Obtaining direct chemical information in the TEM requires spectroscopic data. This can be acquired using EDXS or electron energy loss spectroscopy (EELS). EDXS is preferred for most applications involving metal alloys because it can be used on the typically thicker specimens (>20 nm) of alloy samples; it also discriminates well between different chemical elements with $Z > 5$. EDXS detects characteristic X-rays emitted from the sample when electrons from the atomic inner shells of the material excited by the electron beam return to their original states. When used in the STEM, atomically-resolved EDXS maps can be obtained which provide information which is complementary to HAADF-STEM results. Examples relevant to aluminum and other light alloys are currently limited to precipitate structure [700] or segregants in significant quantities along the electron beam direction (i.e. several nanometres), such as at planar defects [701]. This is because only a small fraction of the X-rays emitted is collected, even in current state-of-the art X-ray detectors, where it is $\sim 8\%$ at best [702]. It should also be emphasized that as in HAADF-STEM images, the EDX signals may not come from an atomic column which was hit by the electron probe on the sample's top surface. Therefore, without detailed simulations great caution must be exercised when interpreting atomically resolved EDXS maps [703]. Another important limitation of EDXS is its inability to detect light elements such as Li or H, which are important alloying or trace elements in Al-alloys. If a TEM is employed, however, EELS can be used to detect Li, and this has been applied to Mg-alloys [704]. In fact, EELS can be extremely useful depending on the elements of interest, because in contrast to EDXS most of the EELS signal is detected and can be attributed to single atomic columns. To date the application of atomic-resolution EELS to light alloys has been limited to probing internal and interfacial precipitate chemistry [705,706]. However, the success of EELS in probing atomic clusters or even single dopant atoms in non-metallic materials [707,708] offers the prospect that this technique might be employed to characterize the chemistry of trace elements near the atomic scale in metallic alloys.

As seen above, one of the main limitations of (S)TEM is the difficulty of accessing the third dimension of a sample. Three-dimensional structural and chemical information can be obtained by deploying the sophisticated techniques of electron tomography [709,710], atom counting in its different forms [384,711,712] and quantitative convergent beam electron diffraction (QCBED) [713]. Although they currently require significant experimental and computational effort to achieve trustworthy results, these techniques are extremely powerful. For example, the size and location along the incident electron beam direction of nanovoids in aluminum can be determined with sub-nanoscale accuracy [714].

Another substantial limitation of (S)TEM at the nanoscale and sub-nanoscale is the poor statistics it provides due to the relatively small volumes it can examine. However, this limitation may cease to apply in the near future thanks to the application of different electron diffraction methods together with new-generation electron detectors and powerful computational tools [698]. For instance, scanning precession electron diffraction (SPED) has recently been used in a statistical analysis of nanoscale precipitates in 6xxx alloys [715].

Other potential problems associated with (S)TEM are sample preparation artefacts and electron beam damage. Luckily, aluminum alloy specimens for (S)TEM can generally be prepared relatively easily by electropolishing or ion beam thinning. Beam damage can be mitigated by applying lower accelerating voltages (as low as 30 kV in the latest off-the-shelf (S)TEM instruments) and specimen stage cooling, or lower electron doses thanks to the more sensitive detectors currently available. In fact, many technological and technique developments from the last decade have not yet been exploited for the characterization of trace elements in light alloys at high spatial and chemical resolution.

4.4.5. Examples and challenges associated with the chemically highly resolved characterization of impurity elements

Both APT and (S)TEM have been extensively applied to characterize Al-alloys. APT, in particular, has been used to study the distribution of minor alloying additions [716,717]. However, only a few studies have focused on the role of actual scrap-related impurities [718–721], e.g. Mn, Fe or Si integrated within precipitates or in intermetallics, as commonly seen in alloys in the SoDA field. This is in part due to challenges inherent in analysing impurity elements by APT and TEM. Let us consider two key aspects.

First, impurity elements typically exhibit low solubility in the FCC-Al matrix, and hence tend to be more highly concentrated within secondary phases or segregated at crystalline defects. These include grain boundaries, where significant segregation and consequently precipitation often occurs. Segregation is often the precursor to precipitation. It is driven by a decrease in the Gibbs free energy of a grain boundary (GB) according to the Gibbs adsorption isotherm. Yet from a characterization standpoint, GBs pose significant challenges. They are typically considered as two-dimensional structures, although they can assume complex shapes in three-dimensions. High-resolution characterization of these GBs typically requires dedicated approaches to prepare specimens suitable for both TEM or APT. Site-specific GB preparation is hindered in Al and its alloys due to the use of gallium in the liquid–metal-ion source of the focused-ion beam used to perform targeted specimen preparation for APT [722]. Ga is known to be a strong segregant in Al [720], in particular at GBs, and can cause severe embrittlement [723]. This can be overcome by using other types of ions, e.g. xenon from a plasma (PFIB)

source [724]. Recently Lilensten et al. demonstrated that these issues can be overcome by using a cryogenic stage to form an APT specimen [725], and similar results can probably be obtained for TEM-lamellae based on observations in other alloy systems [726]. These advances in the preparation of specimens from bulk model alloys [727], including those intended for high-resolution imaging [728], and of industrial alloys [729], are important.

Second, there is an issue with the sensitivity limit of each technique. Sensitivity in STEM-EDXS is at best 0.05% [702], depending on the elements being considered and the microstructural feature being investigated [703]. For dilute elements within the matrix the effect of the through projection further reduces the signal from the element of interest, because most of the X-rays are generated by the matrix atoms. This is also true for the imaging, as discussed above: light elements tend to go undetected. When considering impurity elements, if segregated at second-phase precipitates or at crystalline defects their concentration may not be sufficient enough to be detected. In APT, the issues are different. Fig. 41 showcases some of them. There are isobaric overlaps, and molecular ions may form at the surface of the specimen with the residual hydrogen in an APT vacuum chamber which overlap with (for example) Si. This makes identifying the presence of some of the key impurity elements, such as Cr, Mn or Fe, extremely challenging. The volume analysed by APT is also relatively small; and numerous property-controlling microstructural features are on a larger scale or scarce, making them difficult to analyse by APT in particular, despite the possibility of target specimen preparation.

Despite these limitations, and the possible problems associated with APT, and to a lesser extent TEM, one must bear in mind that the combination of sub-nanometre resolution and high elemental sensitivity still makes APT an amazing and truly unique materials characterization technique, especially for analysing Al-alloys. Similarly, TEM remains unrivalled in the local, structural analysis of materials, even though substantial challenges require great care in the analysis and interpretation of the data. Efforts are ongoing to overcome many of these limitations, including the search for better ways to process the data originating from these techniques. An interesting perspective on the TEM side at least was recently provided by some of the experts in this in this field [730].

4.5. Advanced *in-situ* diffraction methods to study the effects of tramp elements on precipitation kinetics and thermodynamics

4.5.1. Introduction to small-angle X-ray scattering for the investigation of aluminum alloys

Monitoring the precipitation kinetics in age-hardenable aluminum alloys is of great importance in developing advanced alloy design strategies which optimize the heat treatments and thermo-mechanical processes of alloy variants with high scrap-related impurity content. This is because these alloys are strengthened by a fine intragranular distribution of precipitates which are usually metastable [720,731,732].

Because impurity elements do not normally change the nature of the main alloying elements, their effect on the age-hardenability of aluminum alloys should not drastically alter the precipitation “sequence” and the nature of the main stable and metastable phases that are expected to form within the grains. However, their effect on the kinetics of precipitation of those phases, and on their distribution (size and density), can be very significant. The kinetics of precipitation can be monitored by indirect means, e.g. via hardness, resistivity, dilatometry, calorimetry, etc. [413,544,554,636,733–735]. The relationship between the measurements and the actual precipitation reaction is, however, far from trivial and can lead to ambiguous interpretations. In addition, no information can be gained on the size and density of precipitates.

Transmission electron microscopy and atom probe tomography enable direct measurement of precipitation (see the preceding section), but not *in-situ* measurement in general (see the additional discussion and references in section 4.4) [385,636,645,736–739]. Scattering experiments are a good alternative, as they allow direct and *in-situ* monitoring of precipitation. X-ray diffraction (XRD) has often been deployed to study precipitates, but this is usually limited to coarse particles (grain-boundary precipitates, dispersoids, etc.) because strengthening precipitates are frequently coherent with the host matrix and generally too small to give an exploitable signal.

The technique of choice is thus small-angle X-ray scattering (SAXS). A more detailed description of SAXS principles can be found in [740,741]. SAXS is a diffraction experiment for which only the signal very close to the transmitted beam is collected. Because it focuses on small scattering angles SAXS, is sensitive to composition fluctuations at scales larger than the interatomic distances, so that the samples can be described by a continuous function $\rho(\vec{r})$ representing the local electron density. Small-angle scattering can thus be seen as a measure of the homogeneity of the sample, i.e. a homogeneous sample does not give rise to a SAXS signal. Interpreting SAXS data requires the construction of a model for electron density fluctuations. A widely used interpretation model for precipitation in alloys is the “2-phase” model which assumes precipitates of homogeneous composition in a matrix of likewise homogeneous composition, separated by a sharp interface [742,743]. Errors of the method are usually associated with the model used for signal interpretation, where the decisive parameters are the shape of the particles, the size distribution function, etc. It is thus important to associate SAXS analysis with complementary techniques such as TEM or APT to confirm the model’s assumptions.

4.5.2. SAXS monitoring of the precipitation kinetics in aluminum alloys

Because of the high contrast in atomic numbers between Al-Cu, Al-Zn, Al-Li, Al-Zr, Al-Ag, Al-Fe and Al-Mn, SAXS is well adapted for studying precipitation in most of the widely used aluminum alloy series, such as the 2xxx series or the 7xxx series. This is particularly true for typical impurity elements (such as Cu, Fe or Mn). The 6xxx series alloys, on the other hand, which are common in the automotive industry, require the use of small-angle neutron scattering (SANS) rather than SAXS, due to the lack of sufficient electron contrast between Al, Mg and Si [494,744,745]. SANS requires longer counting times, which is less favorable for *in-situ* studies, although some successful *in-situ* SANS experiments have been performed [746].

Guinier-Preston zones (GP zones) are at the origin of the small-angle X-ray scattering technique, as we know from the seminal work of André Guinier [747]. However, only a comparatively low number of studies have addressed this because of the difficulties of coping

with the anisotropic signal due to the large aspect ratio of the particles. Some recent works [748] used both small and wide angle scattering to monitor the archetypal precipitation sequence of metastable phase GP zones, θ'' , θ' and θ , which can be found in most textbooks. The body of literature concerning spherical precipitation in aluminum alloys studied *in situ* by SAXS is much more substantial, mostly because the isotropies of the precipitates and of the signal allow easier interpretation. The Al-Li system, with the formation of ordered coherent L₁₂ δ' precipitates, has been the subject of many studies assessing the classical theories of nucleation, growth and coarsening [13–15]. This alloy system has also triggered studies of complex non-isothermal or multi-step aging processes and has provided evidence for the clear complementarity of *in-situ* SAXS studies of precipitation kinetics with thermo-kinetics precipitation modeling [16]. This is shown in Fig. 43, where the regression of a pre-existing population of precipitates during an isothermal high temperature treatment is excellently reproduced by a Kampmann-Wagner-type class model for precipitation [17,18]. Other spherical L₁₂ precipitates in aluminum such as Al₃(Sc,Zr) have also been characterized by SAXS.

Among the aluminum alloys of industrial interest, the 7xxx Al-Zn-Mg-(Cu) series has received much attention in terms of SAXS analysis. This series features high contrast; the early GP zones can be considered as spheres; and the metastable η' MgZn₂ phases, while they are faceted and their aspect ratio increases with time, can usually be approximated as spheroidal. These convenient interpretation conditions have motivated several SAXS studies, addressing effects of composition [749–751], pre-deformation [752], cooling rate [753,754], multi-step aging treatment [755] and severe plastic deformation [756].

The 7xxx alloy series is also suited for *anomalous* small-angle scattering (ASAXS), or resonant SAXS experiments, where energies close to the X-ray absorption edge of a specific element are used to modify the apparent electron density contrast $\Delta\rho$ and gain information on the chemistry of the precipitates formed. *In-situ* ASAXS experiments can probe the evolution of the chemistry of the precipitates as a function of aging time [755].

Some researchers have also used SAXS to map the precipitation state in heterogeneous samples of 7xxx alloys, such as in welds involving either MIG welding [757], electron beam welding [758,759], or friction-stir welding [760], but also after surface treatments [761]. This microstructure mapping of heterogeneous samples, together with combinatorial strategies, can generate high-throughput characterization methods, as discussed in section 4.3.

Other important Al-alloy families have been studied, but present interpretation challenges. These are mostly due to the anisotropic shape of precipitates and simultaneous addition of multiple contributions, in combination. This is true of the wide 2xxx series, which includes both Al-Cu-Mg-based alloys and Al-Cu-Li alloys. These alloys are strengthened by precipitates of high-aspect-ratio, with orientation relationships with the aluminum matrix. While these might be easily dealt with theoretically via either a perfectly aligned single crystal, or a perfect “powder” in the powder diffraction sense (i.e. grains which are small compared with the beam size, and random orientation), in real samples the 2D scattering patterns are much more complex and difficult to interpret.

In samples prepared from rolled sheets with a strong brass texture, this texture can be used and full modeling of the scattering signal of the platelet precipitates can proceed, depending on their habit planes [763]. The result can be a complete description of the precipitation kinetics, in particular including a separate assessment of the length and thickness of the strengthening objects to provide a better understanding of strengthening by non-spherical precipitates. Fig. 44 illustrates this, showing the precipitation kinetics of T₁ Al₂CuLi, which forms platelets in the {111} planes of the Al matrix, and in a 2198 Al-Li-Cu alloy during aging at 155 °C and 190 °C

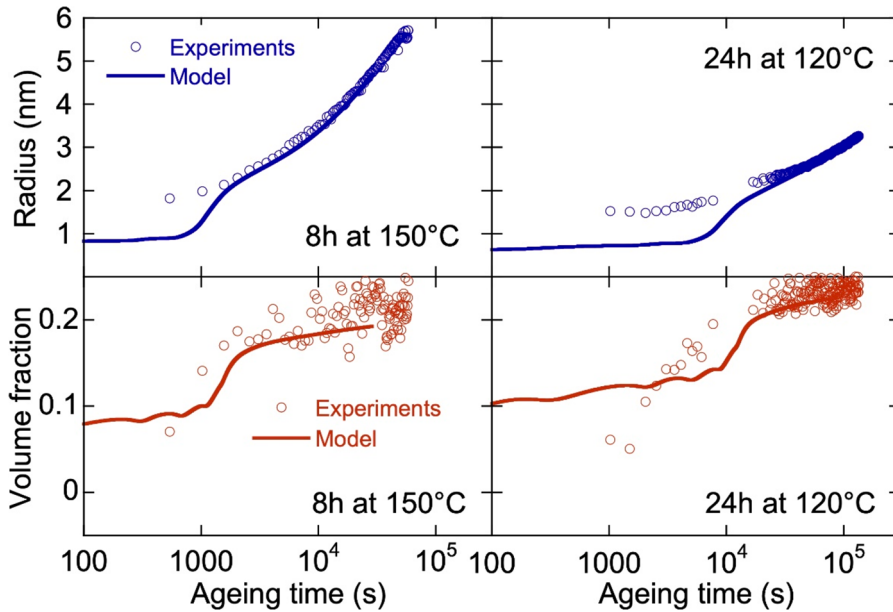


Fig. 43. Comparison between SAXS experiments and precipitation modeling in two isothermal reversion experiments at 180 °C on Al-2 wt%Li-5 wt %Mg. The starting microstructures were created by isothermal treatments of 8 h at 150 °C (left) and 24 h at 120 °C (right). Reproduced with permission from [507].

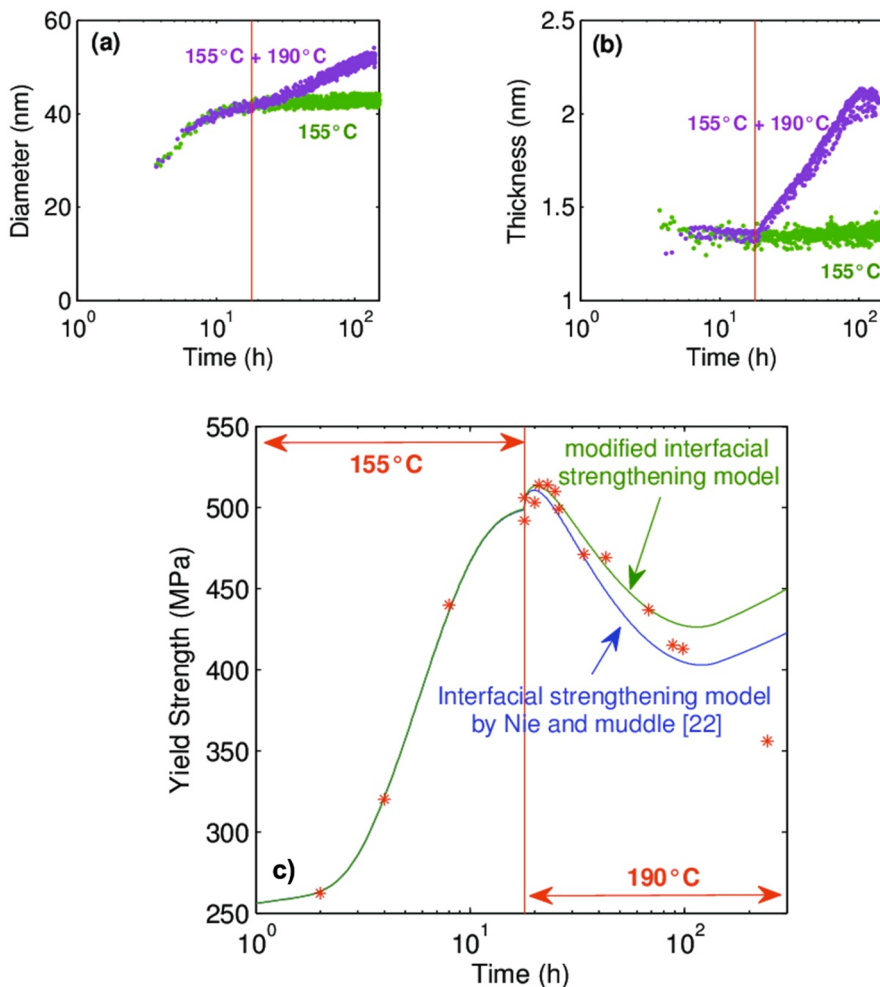


Fig. 44. T_1 precipitate morphology measurements during aging at 155 °C and 190 °C of a 2198 Al-Li-Cu alloy: (a) diameter; (b) thickness. The morphology can be used to better model the strengthening of non-spherical precipitates, as shown in (c). Reproduced with permission from [762].

[762]. Precipitate length and thickness are measured simultaneously and can be used to model the strengthening mechanism, as shown by the evolution of yield strength plotted together with the strengthening model.

This is, however, not always practical, and is impossible in heterogeneously textured samples. There, it is necessary to make assumptions and approximations, which generate a quantification that is potentially less complete, but is still unique in the kinetics information it can give [605,764–766].

4.6. Machine-learning approaches for the development of sustainable aluminum alloys

4.6.1. Brief introduction to machine learning and the architecture of an artificial neural network

Machine learning refers to the ability of computer programs to learn something about the features and effects of an input system and its projection to an output or response. Computer programs in machine learning are usually staggered workflow arrays of mathematically rather plain algorithms that apply certain rules, often in the form of matrix-shaped filters, to individual nodes referred to as artificial neurons, which in turn are assembled in layers to mathematically mimic mutual connectivity.

The interesting feature of machine learning is that it learns about input–output relations without having explicitly been programmed with the underlying balance and conservation laws from physics and chemistry that would otherwise describe such systems in forward simulations (for instance in the form of differential equations, which can be solved with adequate initial values and boundary conditions). The training of machine-learning programs using reference data – i.e. (usually large) data sets that carry experience of the problem at hand, and specifically some output features that can be empirically related to the input data – generates improvements in predictive or recognition performance.

Machine learning is a sub-discipline of artificial intelligence, which describes any set of techniques that enable computers to imitate human cognitive behavior. When we refer to machine learning nowadays, by implication we mostly mean so-called deep learning

techniques. These involve artificial neural networks which are capable of extracting information (meaningful output/predictions) from complex, large and often high-dimensional input data sets containing apparent or hidden patterns.

Artificial neural networks are algorithms made up of at least two mathematical layers: an input and an output layer. Usually they have multiple other layers sandwiched between them, which are referred to as hidden layers. The more complex the problem to be solved with the help of the artificial neural network, the more the layers required. A large number of specialized artificial (mathematically mimicked) neurons lie on each layer of the network. Information processing in the neural network always follows the same sequence: information in the form of patterns or signals hits the neurons in the input layer, where it is processed and disseminated further to other neurons in the next layer. Usually, neurons are fed the output of multiple other neurons in the previous layer. Each neuron is assigned a weight so that neurons can have different levels of importance. The weight value of a neuron is calculated by adding up all the respective input or output values from all the neurons in the preceding layer that are connected to it. This additive value is then modified by a neuron transfer function. This function usually has a sigmoidal shape so that low input values remain below a certain threshold value. This means that the artificial neuron would not produce a notable output value for the next layer when it has not been sufficiently excited while moderate input values get amplified. This means that the additive effects of the input values, the neuron weights and the activation or transfer function, together with their respective excitation threshold values, calculate and weight the output value that is passed on to the neuron in the next step. Depending on the evaluation and weighting of the information, further neurons are linked and activated to a greater or lesser extent. This combination and weighting are used to create an algorithm (which is actually a layered set of fitting procedures) that generates a result for each input. Using penalty functions that quantify mismatch between known sets of inputs and outputs, used for training, the variables of the neurons such as the weights and threshold values are adjusted so that the network delivers ever more accurate and better results with more detailed training, provided that the training data are of sufficient quality and richness.

Besides the field of classical forward simulation (e.g. Calphad based thermodynamic predictions, phase-field simulations or crystal plasticity homogenization), machine learning has emerged as a data-driven scientific discovery method and useful statistical analysis tool in materials science that is capable of making predictions essentially on the basis of trained pattern recognition, i.e. without referring to established thermodynamic or mechanical structure–chemistry–property relations. This is particularly interesting in the highly complex field of metallurgy (many chemical elements, lattice defects, processing conditions, environmental conditions, etc.) which is often challenging to comprehend using simple laws.

A typical workflow in a machine learning application involves (i) collecting clean and reliable data with both input and output features that are detailed and rich enough to be a suitable training basis for a software code which usually contains no underlying physics model linking output to input; (ii) performing feature identification to extract relevant attributes that represent the data numerically; (iii) applying a set of staggered analyses and feature detection and prediction algorithms, usually formulated as artificial convolutional neural networks, that map the features with the property of interest; and (iv) fine-tuning the model parameters by adjusting the neuron weight factors through adequate penalty or loss functions to achieve better performance using previously unseen data.

4.6.2. Use of machine learning in aluminum scrap sorting

One of the biggest challenges in scrap sorting is not the availability of scrap, or collection logistics, but rather scrap quality, i.e. the degree of mutual alloy mixing. This applies particularly to the recycling of post-industrial and post-consumer scrap. Mixing renders this scrap less valuable and less useful for turning into alloy-specific high-value products, where compositional cleanliness is important.

Collection and recycling pathways for aluminum have existed for a long time. Scrap is substituted for primary raw material at levels of 30%–>90% in some aluminum products (see details in the preceding sections), but repeated recycling, and mixing with less pure scrap, can lead to the gradual accumulation or sudden poisoning of alloys by tramp elements such as Cu, Fe, Mg, Mn, Si, Zn und Cr and produce lower-quality scrap grades.

As described in section 3.1, separation technologies already exist that can, in principle, differentiate between different scrap types. One common method for identifying specific metals and even related alloys of the same material family is laser-induced plasma spectroscopy (LIBS) [59]. Here a high-intensity laser beam is focused on the surface of a small portion of the surface of the scrap alloy of interest. Through the energy input from the laser, part of the sample material is ablated and converted into a plasma. As the plasma cools, element-specific radiation is emitted which provides information on the composition of the sample. The radiation is fed into a spectrometer via an optical fiber and recorded as an atomic emission spectrum. Each peak in the spectrum can be assigned to an element based on its associated wavelength. Qualitative information on the analysed sample is obtained from the position of the peaks. Quantitative information can be determined from the peak height or peak area. To do this, a matrix-adapted calibration procedure must first be conducted using suitable reference materials. Using LIBS probing, the characteristic spectroscopic fingerprint of the scrap material, representative of its chemical composition, can in principle be determined.

By evaluating this spectrum it is possible to identify the exact alloy of a metal and thus not only differentiate between different metals such as aluminum, steel or copper, but between aluminum of the 5xxx alloy group and aluminum of the 6xxx alloy group. It is even possible to differentiate within alloy classes: the technique will discern between a 6010 aluminum alloy and a 6016 alloy. Improved results are obtained when the surfaces of the scrap chips are cleaned prior to actual LIBS probing, by removing surface impurities such as oil residues and oxides using a pre-ablation laser treatment [767].

The smaller the chemical differences among related alloys, the more challenging it is to differentiate them in terms of the underlying multi-peak spectra. These spectra have a certain scatter, as do the sometimes contaminated surfaces of the scrap pieces being probed. This is a particularly important challenge for the huge quantities of scrap from the >50 million vehicles that reach the ends of their lives every year. This mixed automotive scrap represents an essential market asset, but it also contains a number of aluminum

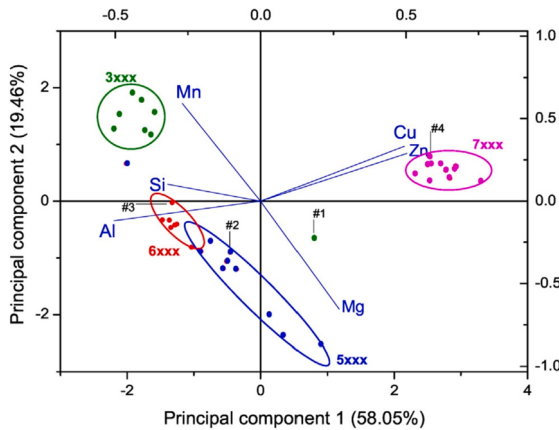


Fig. 45. Principal component analysis and classification of 35 Al-alloy specimens according to their nominal chemical compositions, obtained from the machine-learning-based analysis and classification of the LIBS spectra. The numbers #1–#4 refer to the four samples predicted by the artificial neural network. Figure used with permission from [769].

alloys which are closely related chemically. If these alloys are not separated, they lose substantial value.

This is a task where machine learning has proven especially valuable [768]. For example, Campanella et al. [769] successfully developed a classification scheme for the identification of different types of wrought aluminum alloy scrap chips by training an artificial neural network, which also contained elements from classical fuzzy logic, with LIBS spectra taken from known, well-defined aluminum alloys. The approach enabled robust and reproducible findings, with an alloy-specific recognition rate above 99%: a good result considering the unavoidable signal variations stemming from the modest reproducibility of the LIBS signals. Interestingly, this study showed that although the principal component analysis (see Fig. 45) would suggest that separating 3xxx alloys containing Mn from 5xxx alloys containing Mg and Mg-Si blended 6xxx alloys should not be critical, the highest identification rate was obtained for 7xxx alloys, probably due to the multiple peaks produced from LIBS (see Fig. 46). Good results were also achieved in the classification of industrial and post-consumer aluminum scrap, when applied to well averaged and calibrated spectral data sets by combining classical partial least squares regression methods with artificial neural networks trained by multi-billion iterations [767].

4.6.3. Use of machine learning for the design of scrap-tolerant aluminum alloys

Another field relevant to the theme of this paper is the use of artificial neural networks for (scrap-tolerant) alloy design. Similar to scrap sorting, designing aluminum alloys with tramp element content inherited from secondary synthesis is a multi-parameter challenge that cannot be readily understood in simple chemistry-structure-property terms. However, the challenge might be addressable with machine learning methods. In every respect materials containing large amounts of scrap compete with (potentially cleaner) alloys made from primary synthesis. As primary production based on renewable energy sources gains momentum globally, even the “green branding” advantage associated with alloys made from scrap may in some cases not be a sufficiently strong argument for alloys which feature slightly worse performance. Hence, aluminum alloys with high tramp element content must meet a wide set of quality requirements if they are to improve their mechanical, electro-chemical, surface, optical, electrical, haptic, machining and manufacturing behavior.

Using conventional thermodynamics and kinetics simulations alone to develop crossover or less pure aluminum alloys under these constraints may be too slow and/or insufficient. This section therefore presents recent progress in the use of machine learning for alloy design that might become useful for sustainability and a circular metallurgical economy. Chaudry et al. [770] discussed various machine-learning methods and their respective suitability for the compositional design and age-hardening heat treatment of better-performing aluminum alloys based on the age-hardening concept. They targeted the Al-Cu-Mg alloy class, with variations in Zn and Zr content. The composition and heating variants were correlated with literature data on hardness for training. The result was that the so-called gradient-boosting decision tree algorithm was in particular capable of identifying unexplored alloys with increased hardness. Gradient-boosted decision trees use an amplification method, also referred to as boosting, to combine individual decision trees. The term boosting refers here to combining learning algorithms in the form of a series to achieve a strong learning method out of many sequentially connected weak learning methods. For the gradient-boosted decision tree method the weak learning methods are, for instance, classical Boolean decision trees.

Vahid et al. [771] applied a Bayesian optimization method directly to an important pending aluminum recycling problem, namely the development of 7xxx aluminum alloys using high-strength recycled aerospace-grade material. Their motivation was the expected availability of high-strength 7075 aluminum alloy scrap from airplanes reaching the ends of their lives. The authors re-melted the material and mixed it with different amounts of new primary aluminum. They successfully used Bayesian optimization as a method for most efficiently identifying suitable alloy compositions and processing workflows. Bayesian optimization methods are efficient when solving global optimization problems. They work by building a probabilistic model of the objective function, called a surrogate function, which is first searched efficiently with an acquisition function prior to subjecting candidate samples for evaluation by the real objective function. With their approach, the authors were able to identify new variants of the 7075 alloy with modified composition

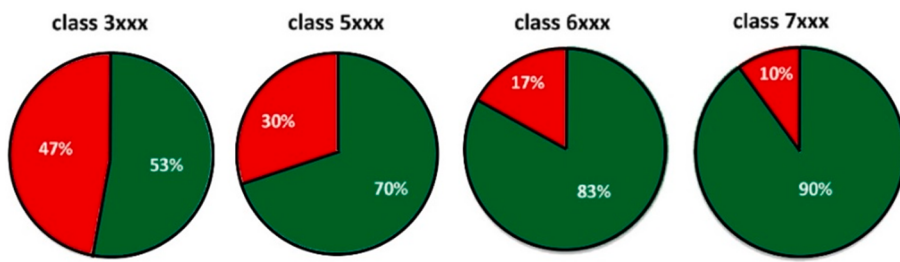


Fig. 46. Machine-learning-based classification findings for mixed aluminum scrap chips, probed by considering the chips' LIBS spectra. Classification of these measurements into aluminum alloy groups proceeded by using a modified artificial neural network. Green: correct; red: incorrect. Figure used with permission from [769]. (For interpretation of the references to color in this figure legend, the reader is referred to the web version of this article.)

and heat treatment, yielding a material with maximum yield strength and ultimate tensile strength values of 729 MPa and 761 MPa, respectively.

In their machine-learning study of Al-Zn-Mg alloys, Cao et al. [772] included the search for both improved mechanical properties and enhanced corrosion resistance, with special attention to the role of heat treatment. They used a generalized regression neural network and a support vector machine to model both the mechanical and the corrosion properties, and the more conventional multiple linear regression method to predict mechanical properties. The support vector machine algorithm is an efficient multi-dimensional regression method that enables fast classification of high-dimensional data point arrays. The authors also evaluated the effect of the quality of the training data. One result of the study was that both, a single-stage aging heat treatment and retrogression re-aging can produce a material with higher strength than conventional double-stage aging, but at reduced corrosion resistance. The support vector machine method was also successfully used by Ampazis et al. [773] to predict the change in tensile strength brought about by surface corrosion of aerospace aluminum grade 2024. Training data were generated by tensile testing, targeted corrosion and imaging of the corroded surfaces, mapping several types of surface pitting features.

Several related studies have explored similar ways to use machine learning for the efficient prediction of (mainly) the mechanical, functional and corrosion properties of several types of aluminum alloy [774–778].

4.6.4. Further application areas of machine learning and artificial intelligence in the field of aluminum recycling

In the context of sustainable aluminum design, processing and manufacture, further areas where artificial intelligence and big-data-driven analysis methods may be of substantial future benefit are: tramp-element-sensitive through-process modeling; surface-quality control and improvement; corrosion analysis; and microstructural-damage phenomena [773,774,776–783].

The first area, through-process modeling based on analysing and using big data, is a general trend in metallurgical processing due to modern, fully automated and highly synchronised processing lines [285,784–786] which already feature large numbers of sensors. A very promising future approach would be to correlate all of the sensor data available with the corresponding variations in the chemical composition of the material that enters via scrap. From these correlations it should be possible to uncover trends in the impurity elements and properties of the material, particularly in the context of high-end sheet products.

Similar arguments apply to the second area, surface-quality control [787]. Customer requirements mean that most advanced aluminum products are very surface-sensitive. Examples here are outer automotive sheet materials, the alloys used for notebook computers and mobile phones, and sheets used for decorative purposes in architecture. In all of these cases the surface appearance of the material is of the highest priority. Scrap-related impurities and variations among batches can therefore be a substantial problem for manufacturers. For this reason it is a sensible option to take the sensor data from the corresponding processing lines (particularly from those processing steps that play an important role in final surface appearance, such as finish rolling, heat treatment, surface cleaning and etching) and correlate these data with fully automated surface-pattern recognition techniques that provide information about the state of the surface at the end of a manufacturing line. The connection of these two types of data through suitable machine learning techniques can help to identify impurity-sensitive correlations.

A very similar rationale applies to corrosion properties, which can react very sensitively to the chemical state of the material; and also to pattern-based precipitation-related damage analysis, including cracking during rolling and forming or the more microscopic cracking phenomena when (for instance) the final sheet material is bent [772,773,776,783,788]. In all of these cases a classical forward simulation technique is often a cumbersome or even hopeless undertaking, as the many influencing factors in real manufacturing lines are simply too influential for all to be properly considered on solid scientific grounds. Instead, the vast availability of sensor data should be exploited. Although as a rule these data may have little immediate relevance for classical structure–property relations, they can be suitable for classical convolutional neural network analysis: provided that sufficiently large data sets are

available, the associated techniques can identify trends without being fed with classical forward models.

5. Physical metallurgy of scrap-related tramp elements in aluminum alloys and effects on mechanical properties

Recycling aluminum alloys from end-of-life components often generates undesired composition features due to the accumulation of impurities beyond the tolerance limit and the mixing of different alloys [789,790]. In certain cases this harms product properties. To circumvent impurity-related issues it is usually helpful to reduce the impurity level in the alloys. However, it is challenging and/or energy-consuming to remove specific impurity elements (e.g. Fe or Si) during the remelting of aluminum scrap [43,791,792]. For this reason the conventional way to suppress impurity concentration in recycled aluminum is dilution by adding a large fraction of the associated alloys, and/or metals of high purity. This obviously undermines the added value of recycled aluminum alloys, and a more efficient strategy of using scrap is urgently needed.

To guide the design of recycled aluminum alloys and the optimum use of scrap, it is crucially important to fully understand the metallurgical effects of tramp elements. In this section we do not address the problems associated with primary casting and processing (please refer to [790,793,794] for these issues), but review studies of the effects of different impurities on microstructure evolution and key properties. We also summarise the consequences if the elemental concentration exceeds that of normal aluminum alloys.

The properties of aluminum alloys are determined by the matrix defect structure and a plethora of elemental segregation/precipitation components of different sizes, e.g. intermetallic compounds, grain boundary precipitates (GBPs), stable precipitates, intermediate meta-stable precipitates and solute clusters (see Fig. 47). Impurities' effects on the recovery, recrystallization, grain growth and texture evolution during annealing can also be determined through precipitation processes. Therefore we present impurity-induced modification of the microstructure at different scales to build a full physical metallurgical picture of recycling aluminum alloy scrap. The fact that compositional deviation does not necessarily have a detrimental effect is highlighted.

The aim of this section is also to inspire the development of novel aluminum alloys and processing technologies that counteract the harmful effects of impurity elements in recycled aluminum alloys.

5.1. Influence of scrap-related tramp elements on precipitates and forming properties

As shown in Fig. 48, the compositional deviation in recycled age-hardenable aluminum alloys compared to standard aluminum alloys has two main causes: (i) mixing of two or more types of alloy series; and (ii) impurities from scrap-related tramp elements. In this section we first summarize the common precipitates in conventional aluminum alloys, and then discuss the effects of the above factors on the precipitates formed in recycled aluminum alloys. (For some of the basics and main microstructure variables which affect aluminum sheet forming in conjunction with scrap-related impurities, see section 3.7.).

5.1.1. Possible precipitate types in age-hardenable aluminum alloys

The age-hardenable wrought alloy systems are based on the Al-Mg-Si-Cu 6xxx, Al-Cu-Mg 2xxx and Al-Zn-Mg-Cu 7xxx series. Minor alloying elements, e.g. Sc, Zr, Cr, Ag, are intentionally added to modify the associated microstructures [794–797], furthering the development of commercial aluminum alloys. High-performance aluminum alloy products can then be manufactured through well-controlled thermomechanical processing and heat treatment. Here precipitates play a key role in strength due to a precipitation-hardening effect. The solutes dissolved in the matrix undergo a complex precipitation process involving transformation from metastable phases to thermodynamically stable variants. To acquire the desired precipitate size and morphology and thus the maximum hardening effect, alloys' composition and thermal-mechanical history need to be strictly controlled. The rational design of alloy compositions requires an understanding of how alloying elements aggregate and grow into strengthening phases. However, it is usually very difficult to accurately determine the structure and composition of reinforcing particles because they are very small and are embedded in the aluminum matrix [795,798,799]. Over the past decade, advanced techniques such as aberration-corrected transmission electron microscopy (TEM) and three-directional atom probe tomography (APT) have made it possible to identify the structural and compositional determinations of numerous precipitates responsible for the critical performance of precipitation-hardened aluminum alloys at different stages in the processing chain [542,795,798–801]. In the following sections we summarise the current understanding of precipitation sequences in current alloy systems, which can help us to understand the effects of impurity elements on precipitates in recycled aluminum alloys. While various aluminum alloy series can be used to manufacture cast products, the common cast alloys are based on Al-Si-(Cu) and can be sorted relatively easily at the recycling stage. The non-age-hardenable wrought Al-alloys are 1xxx (Al-Fe-Si), 3xxx (Al-Mn) and 5xxx (Al-Mg). Table 14 summarizes the primary strengthening precipitates of main age-hardenable Al-alloys identified in the literature.

The precipitation sequence in ternary Al-Mg-Si alloys can be described as follows [795,798,802]: SSSS (super-saturated solid solution) → atomic clusters/GP zones → $\beta'' \rightarrow \beta' \rightarrow \beta$, Si, while U1, U2 and B' also occur, accompanying β' in alloys when the Mg/Si ratio is low. The atomic clusters are also known as Mg-Si-vacancy complexes [824]; their configuration and ordering are still poorly understood. GP zones generally form at the initial aging stage and are fully coherent with the α -Al matrix. The needle-like β'' phase usually

appears in the peak-aged state and is regarded as the primary strengthening phase in the Al-Mg-Si alloy system [798]. When a small amount of Cu (0.1–1 wt%) is added to form the quaternary alloy, the precipitation sequence is modified as follows [808,809,811]: SSSS → Clusters/GP zones → β'' , L, C → β' , Q' → Q, where L and C are precursors to Q'. Alloys with higher Cu content usually have larger hardness, with the main strengthening phases L and C [808,809]. The C phase possesses a rectangular cross-section with a broad coherent interface along the $\langle 001 \rangle$ α plane. The Q' and C phases share the same triangle sub-unit [811], implying their inherent structural similarity. In general, the precipitation process in the Al-Mg-Si-(Cu) alloy is strongly dependent on the Mg/Si ratio and the Cu content [795,808,811].

The precipitation sequence in Al-Cu-(Mg) alloys takes the following two routes [542,800,812,814,816,818,825,826]: SSSS → GP I → GP II → θ'' → θ' (high Cu/Mg ratio) and SSSS → GP → S (gradual thickening by an even number of Cu-Mg layers) (low Cu/Mg ratio). GP I/II are planar structures of Cu layer lying on the $\{002\}$ Al plane [812]. The tetragonal θ' phase (Al_2Cu) possesses a plate-like morphology [816] and is considered to be the most effective strengthening precipitate in the binary alloy system (e.g. the 2219 alloy). To improve the age-hardening potential in Al-alloys, a certain amount of pre-strain can be applied prior to artificial aging [812,814]. This temper is also designated as T8. The introduced dislocations have a significant influence on the phase selection and precipitation pathways in important commercial alloys. A recent study reports that the precipitation at dislocations in Al-Cu alloys evolves according to at least three paths [812,814]: (i) the direct precipitation of thick θ' ; (ii) the pre- θ' -1 first forms and then transforms to θ' with a thickness of $2 c_{\theta'}$ (please see the c parameter of the θ' phase in Table 14); and (iii) the pre- θ' -2 first forms and then transforms to θ' with a thickness of $1.5 c_{\theta'}$. Note that the pre- θ' and θ' phases have the same interfacial structure, which is a coherent and continuous Cu layer. In the Al-Cu-Mg alloy with a low Cu/Mg ratio (e.g. the 2024 alloy), the major strengthening S phase (Al_2CuMg) is lath-shaped and grows along $\langle 001 \rangle$ Al with a habit plane of $\{012\}_{\text{Al}}$ [818]. The Guinier-Preston-Bagaryatsky (GPB) zones composed of 1D rod-like sub-nanometre units ($\text{Mg}_4\text{Cu}_4\text{Al}$) only occur upon aging at elevated temperatures [821]. The orthorhombic Ω - Al_2Cu phase prefers to form on $\{111\}$ Al planes in the Al-Cu-Mg alloys with additions of silver [693,795]. This phase generates excellent thermal stability in the Al-alloys. When Li is further added in the multi-component Al-Cu-Li-Mg-Ag alloys (e.g. 2195 and 2050), the major hardening precipitate changes into thin plate-like T1 phases on the $\{111\}$ planes of the matrix [796,820].

The generic precipitation sequence of an Al-Zn-Mg-(Cu) alloy under artificial aging is well-known as [822,823,827]: SSSS → GP zone → η' → η (MgZn_2). The precise transition mechanisms involved in this process have been elucidated by advanced TEM and density-functional theory (DFT) calculations. Atomic-resolution TEM observations reveal that η_2 (one common variant of the η phase) initially consists of rhombohedral (R) units and orthorhombic (O) units [799]. The η_2 phase grows by the stacking of R units and R¹ (rotated R) units, with the artificial aging progressing toward a peak-aged state [799,828]. The experimentally observed $\eta' \rightarrow \eta_p \rightarrow \eta$ sequence is also rationalized by the solute substitution process calculated by DFT [823]. Although the theoretical study supports the premise that Cu/Mg and Zn respectively prefer to dissolve into the bulk interior of η and segregate to the broad interface, the elemental segregation of Cu at the Al matrix proximate to η has been observed in a 7050 alloy [829].

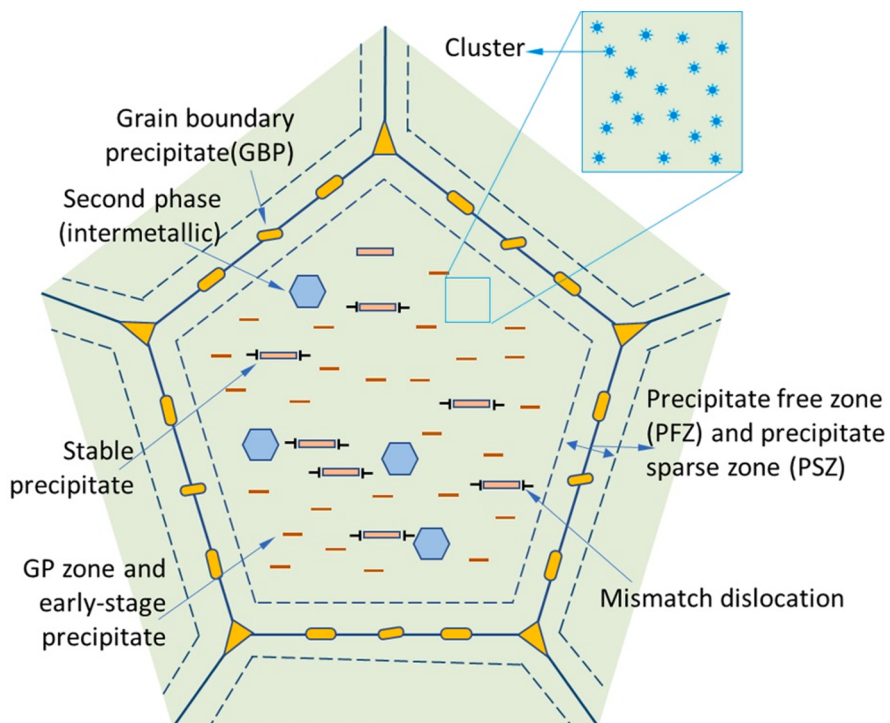


Fig. 47. Schematic of the multiscale elemental segregation in aluminum alloys.

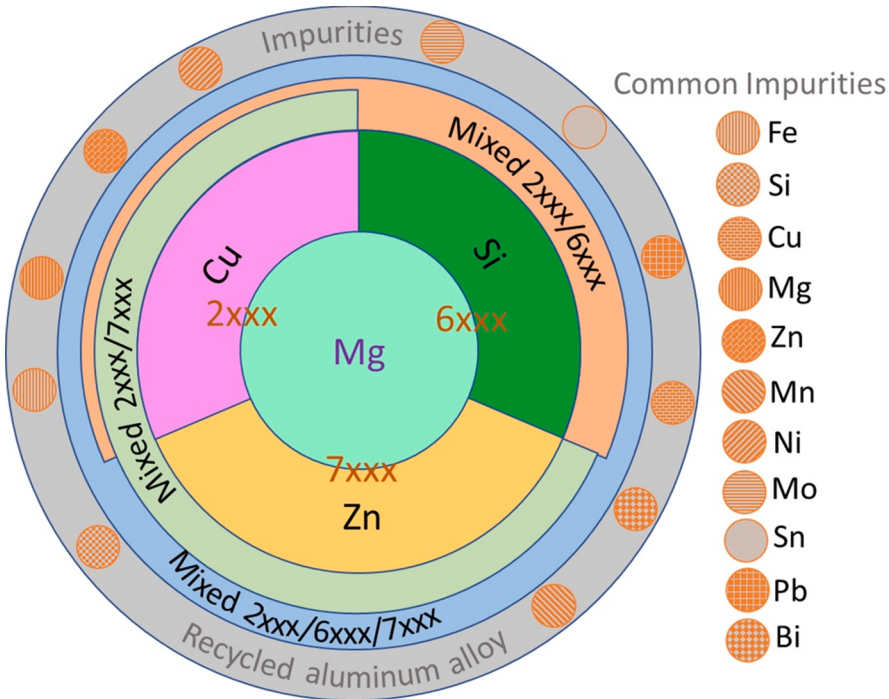


Fig. 48. Element radar chart for age-hardenable recycled wrought aluminum alloys, where deviation from the standard compositions of the current aluminum alloy occurs due to the mixing of different grades of aluminum alloy and the impurities introduced from the contaminated scrap [43,790,791].

5.1.2. Impurity effects on precipitation reactions

The major impurity elements vary according to scrap source [789–791]. The most common are Fe, Si, Cu, Zn, Sn and Mg. Most of these can cause detrimental effects in alloys and – except for Mg and Zn – are often difficult to remove [43]. Therefore, one of the core issues in the physical metallurgy of recycling aluminum alloys is to understand and control the metallurgical effect of impurities on processing and properties. In this section we briefly review the current understanding of the role of impurity effects on precipitation during final aging. Several papers on this subject have been published. They address both the effects of impurities on IMCs [789,794,830] and methods for removing such tramp elements [43,791,792].

Several minor impurity elements have subtle effects on nano-sized particles, particularly in Al-Mg-Si-(Cu) alloys [379,831]. Cu and Zn, which are often present in mixed aluminum alloys, also appear as impurities in cables and engine block parts containing Al scrap [791,794]. They normally improve the precipitation-hardening response, albeit alongside a loss in corrosion resistance due to grain boundary precipitation [379,809]. A small amount of Sn (0.02–0.08 wt%) could suppress natural clustering [555], which is responsible for the lessened press forming ability of automobile body panels made from 6xxx alloys, without reducing hardening from artificial aging. The microalloying of Sn also considerably enhances precipitation hardening at elevated artificial aging temperatures by inducing the formation of composite β'' precipitates on modified β' ($Mg_9Si_{5-x}Sn_x$) [832]. Sn has a strong binding tendency with vacancies and thus fundamentally affects initial precipitation [555]. However, it also acts as a surface-active element and can promote corrosion.

Ag has an effect similar to that of Cu in terms of both age-hardening behavior and precipitation process [833]. Solute Ag can influence the whole precipitation stage and profoundly alter the phase transformation. Cd is considered a biologically harmful tramp element, but as an impurity in aluminum alloys (~0.25 wt%) it can appreciably improve the age-hardening response of Al-Mg-Si-(Cu) alloys [834]. Cd-rich particles form in such materials and facilitate the formation of needle-like Mg-Si-Cu precipitates containing Q'/C-like sub-units [834]. Transition metals (TM) such as Cr and Fe often reduce the precipitation-hardening response in 6xxx alloys [835]. The precipitate types remain almost unchanged, but are coarser and unevenly distributed at the dispersoids/Al interfaces. AlSi(Fe, Cr) and the different types of AlSiFe dispersoids and IMCs also consume the main alloying element Si [835]. Al-Mg-Si alloys have an extremely low tolerance limit for Ca, because 60 ppm Ca can cause measurable loss in age-hardening response [836]. Ca absorbs Si to form micro-meter-sized $CaAl_2Si_2$ particles, leading to a deficiency in the Si content, which is critical for forming Mg-Si coherent precipitates. Solute Ca does not accumulate in the Mg-Si precipitates [836], possibly due to its repulsion of solutes Mg and Si.

A variety of micro-alloying effects on precipitation in Al-Cu-(Mg) alloys have been investigated in the literature [383,837–842]. Many micro-alloying elements tend to accumulate in recycled Al-Cu-(Mg) alloys as impurities. The 0.3 wt% Si added in the binary Al-Cu alloy generally has a positive effect on the age-hardening response [837]; this is ascribed to the greater number density of the θ''/θ' phases. Si is believed to promote the heterogeneous nucleation of precipitates based on the observation of Si partitioning and

Table 14

Common precipitate types in current age-hardenable aluminium alloy series: 6xxx\Al-Mg (0.5–1 wt%)-Si(0.5–1 wt%) -Cu(0–1 wt%), 2xxx\Al-Cu (4–6 wt%)-Mg (0.0–2 wt%), 7xxx\Al-Zn(4–8 wt%)-Mg (1–3 wt%).

Alloy	Phase	Shape	Space group	Lattice parameters (nm)	Composition	Ref.
6xxx	Pre- β''	Needle	Monoclinic $C2/m$	$a = 1.478, b = 0.405, c = 0.674, \beta = 105.8^\circ$	(Al + Mg) ₅ Si ₆	[802]
	β''	Needle	Monoclinic $C2/m$	$a = 1.516, b = 0.405, c = 0.674, \beta = 105.3^\circ$	Mg ₅ Si ₆	[798]
	β'	Rod	Hexagonal $P6_3/m$	$a = b = 0.715, c = 1.215, \gamma = 120^\circ$	Mg ₉ Si ₅	[803]
	U1 (typeA)	Lath	Trigonal $P\bar{3} m1$	$a = b = 0.405, c = 0.674, \gamma = 120^\circ$	Mg ₂ Al ₂ Si ₂	[804]
	U2(typeB)	Lath	Orthorhombic $Pnma$	$a = 0.675, b = 0.405, c = 0.794$	Mg ₂ Al ₂ Si ₂	[805]
	B' (type C)	Lath	Hexagonal $P\bar{6}$	$a = b = 1.04, c = 0.405, \gamma = 120^\circ$	Mg ₉ Al ₃ Si ₇	[802,806]
	β	Plate	Cubic $Fm\bar{3} m$	$a = 0.635$	Mg ₂ Si	[802,806,807]
	C	Lath	Monoclinic $P21/m$	$a = 1.032, b = 0.81, c = 0.405, \gamma = 101^\circ$	Mg ₈ Si ₆ Cu ₂ Al ₂	[808,809]
	Q'	Lath	Hexagonal $P\bar{6}$	$a = b = 1.032, c = 0.405, \gamma = 120^\circ$	Al ₃ Cu ₂ Mg ₉ Si ₇	[810,811]
	GP I	plate	–	Single Cu layer	Cu layer	[797,812]
2xxx	θ'' (GP II)	plate	–	Cu layer separated by 0.81	Al ₃ Cu	[813]
	pre- $\theta'-1$	plate	Tetragonal	$a = b = 0.405, c = 0.608$	Al ₂ Cu	[800,812]
	pre- $\theta'-2(\eta')$	plate	Orthorhombic $Cmmm$	$a = 0.412, b = 1.216, c = 0.880$	AlCu	[542,814]
	θ'	plate	Tetragonal $I\bar{4} m2$	$a = b = 0.58, c = 0.405$	Al ₂ Cu	[815,816]
	θ	plate	Tetragonal $I4/mcm$	$a = b = 0.599, c = 0.481$	Al ₂ Cu	[795,817]
	S	plate	Orthorhombic $Cmcm$	$a = 0.401, b = 0.926, c = 0.712$	Al ₂ CuMg	[818]
	Ω	plate	Orthorhombic	$a = 0.496, b = 0.856, c = 0.848$	Al ₂ Cu	[693,819]
	T1	plate	Hexagonal $D6h$	$a = 0.496, c = 1.390$	Al ₂ LiCu	[801,820]
	GPB	needle	–	1D periodic ($c = 0.405$)	AlMg ₄ Cu ₄	[821]
	η'	plate	Hexagonal $P6_3/mmc$	$a = 0.504, c = 1.303$	Mg ₂ Zn _{5-x} Al _{2+x} ($x = 2–4$)	[822,823]
7xxx	$\eta_2(\eta_p)$	plate	Hexagonal	$a = 0.504, c = 0.828$	MgZn ₂ Al	[799,823]
	η	plate	Hexagonal $P6_3/mmc$	$a = 0.521, c = 0.849$	MgZn ₂	[799]

interfacial segregation in these phases [837]. Si still plays an advantageous role when it is co-doped with a small amount of Mg [842]. However, the mechanism changes: a C phase containing Si, Mg and Cu forms first, and then catalyses the heterogeneous growth of θ''/θ' [842]. When a small amount of Fe is added together with Si, Si with a content of below 1.0 wt% slightly reduces the mechanical properties, while higher Si content can significantly decrease them due to the occurrence of excessive Si particles [840]. Sn is another possible impurity, and was found to considerably promote and refine the θ' precipitates [383,838], leading to enhanced precipitation hardening in Al-Cu alloys. Sn solutes present at the rim interface may reduce the misfit strain and promote the nucleation of the θ' phase [383]. Conversely, Sn has an adverse influence on the precipitation-hardening effect when introduced with Mg (0.35 wt%) [838]. The formation of stable Mg₂Sn phases consumes solute Mg and reduces its concentration in the alloy. Au has an effect similar to that of Sn on the precipitate morphology and hardening response [841]. Nevertheless, Au refines the precipitates by replacing Cu in the middle of θ' and modifying its growth mechanism [841]. These studies demonstrate that impurity effects on precipitation hardening vary with content. Na is an undesirable impurity and has a negative effect on the performance of Al-Cu alloys [839]. It dramatically impairs the hardening potential in artificially aged Al-Cu alloys, as it can segregate at and weaken the interface between the Al₂Cu phase and the matrix. Na also tends to segregate to grain boundaries and embrittles Al-Cu alloys [839].

High-strength Al-Zn-Mg-(Cu) alloys are mainly used to produce high-performance, load-bearing components, such as those in airplanes. They normally have a very low tolerance limit for impurities, such as Fe, Si and some transition metals that form notoriously insoluble intermetallics [789,794,843]. Therefore it is very challenging to recycle 7xxx alloys from scrap [844]. It was found that rare earth metal elements (REM) do not influence the morphology of the η -type hardening precipitates [843]. Adding minor elements such as Mn can refine grains and thus reduce hot tearing during the casting of 7xxx alloys with high solute content [845]. However, the age-hardening response can then become significantly suppressed and larger precipitation-free zones (PFZs) can be formed around the grain boundaries [845]. Small amounts of Sn and Ag may markedly reduce the PFZ and thus cause the precipitation-hardening response in fine-grained 7xxx alloys to recover. This has been attributed to the strong interaction of Sn/Ag with the main solutes [845,846], but it may also result from the interaction of these elements with vacancies. In an Al-Zn-Mg-Cu alloy with low Zn and Mg content (with low strength but excellent formability), Ag induces pronounced enhancement of the age-hardening response [847]. Ag aggregates with other alloying elements at the very early aging stage and increases the number density of fine clusters.

When producing cast Al-Si-Mg-Cu alloys from scrap, the situation is very similar to that of 6xxx alloys and special attention must be paid to the consumption of the main alloying elements by unavoidable formation of IMCs [848]. For example, the amount of Ni is controlled to be below 0.16 wt%; otherwise the decrease in mechanical properties would be obvious [849]. However, it is known to be a beneficial alloying element in heat-resistant Al-Si casting alloys [850]. Current studies on the effects of impurities in commercial Al-Cu-Li-Mg-Ag alloys are very limited. It would be very demanding to produce this kind of alloy, considering the strict control of alloying elements and the complex interaction of Li with other phases [851].

Based on above analysis, multiple interactions between impurities and main alloying elements determine the variety of impurities' effects on precipitation hardening in Al-alloys. Several representative interactions are illustrated in Fig. 49. Beneficial impurities can usually aggregate with or replace the alloying elements in precipitation phases. They promote heterogeneous nucleation and growth of

fine hardening precipitates. DFT and Monte Carlo simulations reveal that beneficial impurities generally prefer to bind with vacancies and main alloying elements [846,852]. In contrast, the most harmful impurities are those that tend to form (coarse) intermetallics with the alloying elements during casting.

5.1.3. Multiple precipitation reactions in mixed aluminum alloys made from scrap

When different types of aluminum alloy are mixed together in the same melt, the recycled aluminum alloys obtained contain multiple components which can affect precipitation reactions in multiple ways [853–856]. When crossing established composition bounds, new phases can form. Knowledge about the interactions among them is of great significance, particularly for mechanical and corrosion properties. From a structural and compositional perspective, the precipitation interaction between different phases in the mixed alloy can be categorized into three types: (i) replacement of alloying elements which usually occupy atomic sites with impurity elements; (ii) interfacial segregation of impurity elements; and (iii) composite and “backpack” precipitates composed of different phases.

Various alloys of the same alloy system, targeted for different applications, have been developed by altering the ratio and total content of the differing alloying elements. The Mg/Si ratio changes the Mg:Si ratio in the pre- β'' precipitates [855] and thus the peak hardness in the Al-Mg-Si alloy (e.g. 6061 and 6016). The Cu level has a substantial effect on the precipitation of Cu-containing phases in Al-Mg-Si-Cu alloys [379,809]. HAADF-STEM observations [379,809] reveal Cu substitution of Mg1 and/or Si3/Al sites in the β'' phase (Fig. 50a-b) in the Cu-augmented Al-Mg-Si alloy (e.g. 6013 and 6056). Periodic Cu segregation at the habit plane of the lath-like β' precipitates has also been observed in the over-aged stage [857], indicating a strong interaction between the Cu atoms and the precipitates. When the Cu content is higher (still usually remaining below 1.0 wt% in the 6xxx alloy specification), C and Q phase [858] and their precursors are formed [809,811]. Another prominent feature of the interaction between precipitates is the formation of composite (or hybrid) precipitates containing different precipitate types [379,809]. These composite or backpack precipitates usually appear disordered and incorporate several sub-structures of different well-defined phases in Al-Mg-Si-Cu alloys. The precipitates characterized by a disordered structure with β'' substructure (low density cylinder, LDC) and Q' substructure (Cu triangle sub-structural unit) are frequently observed in under-aged Al-Mg-Si-Cu alloys [809]. The composite precipitates including β'' and precursors of Q'/C phases form in the peak-aged state [809,855].

These precipitation scenarios in the Al-Mg-Si-Cu alloy reflect the precipitation reactions that may occur in the 6xxx alloy when mixed with a small portion of 2xxx alloy. The influence of Zn on the precipitates and age hardening in the Al-Mg-Si-(Cu) alloys have also been reported recently [831,859,860], and is helpful in understanding the possible precipitation reactions in mixed 6xxx and 7xxx alloys. Saito et. al. [831] found that adding Zn (up to 1 wt%) slightly improved the age-hardening response due to the increased number densities of needle-like precipitates in Al-Mg-Si alloy. Zn atoms tend to occupy different sites in the atomic columns of the precipitates rather than form the precipitates of the Al-Zn-Mg alloy system. Zn atoms also prefer to segregate and form a continuous Zn film along grain boundaries, leading to the high intergranular corrosion (IGC) susceptibility in peak-aged Zn-augmented alloys (~1 wt %). HAADF-STEM imaging and DFT calculations suggest the favorability of incorporation of Zn at Si3/Al sites into the β'' phase (Fig. 50c) [860], similar to what was observed for Cu. However, the Zn-Zn interaction is relatively weak, explaining the random distribution of Zn along the growth direction of the particles. Clarifying the amount of foreign solute atoms that a precipitate can accommodate is important if we are to understand these kinds of precipitation interaction in impurity-contaminated alloys. When the added Zn content reaches up to 3.0 wt% in an Al-Mg-Si-Cu alloy with a high Mg/Si ratio, the yield strength increases by 50 MPa, while the elongation remains almost unchanged [859]. This is due to the refined size of needle-like precipitates and the increased number density of solute-rich particles. The tendency of Zn to partition in these particles occurs because of the strong interaction of Zn with other solutes, like Mg, Si and Cu.

In an Al-Cu-Mg-Si alloy with a Cu content of ~ 5 wt% (similar to the 2xxx alloy mixed with a small portion of a 6xxx alloy), the hybrid precipitates include fragments of the C phase, the Q' phase, GPB and the θ' phase [856]. This observation suggests that the precipitates formed in such mixed alloys, stemming from different scrap sorts, do not just contain simple mixtures of phases from the Al-Mg-Si-(Cu) and Al-Cu-(Mg) alloy systems. Different configurations of various phases and their sub-structural units, e.g. the LDC of β'' surrounded by GPB zone and monoatomic Cu layer (GP I), have been identified (Fig. 50d), and the stabilities of these structures have been rationalized by DFT calculations [856]. Such types of interaction between various phases may markedly affect the morphology of the main strengthening phase, e.g. the θ'' phase formed on the broad interface of C-type precipitates (Fig. 50e) [842].

A systematic investigation of the effect of 1–4 wt% Zn on the peak-aged precipitation in a mixed Al-Cu-Mg (2xxx) and Al-Zn-Mg (7xxx) model alloy, which mimics the use of scrap from different alloys groups, was performed by Wenner et. al. [854]. Alloys with 1% and 4% Zn contain mainly S (2xxx system) and η -type (7xxx system) precipitates, respectively. The alloy with a medium Zn content (2.5 wt%) is hardened by both S and η -type phases. Although these phases maintain their original native structures, compositional modification was identified by high resolution elemental mapping. DFT calculations show that replacement of Zn by Cu in the η -type phase is preferred if the substituted Zn is below 25%, while the substitution of Al by Zn in the S phase was observed to be the most favorable configuration [854]. The interaction of the precipitation is manifested in the non-stoichiometric compositions of the hardening phases.

An attempt to study the precipitation system in an Al-Zn-Cu-Mg-Si alloy (which mimics a blend of 2xxx, 6xxx and 7xxx alloys) has also been reported [853]. The precipitates encompass phases from three main classes of age-hardening alloy [48,55,494,861,862]: Al-Cu(-Mg), Al-Mg-Si-Cu, and Al-Zn-Mg. Si-containing disordered precipitates composed of substructures of the C phase and GPB form first and grow along the (001) Al lattice direction. These needle-like precipitates are dominant until peak-aging. During over-aging, a variety of phases including S, θ' , η and Ω occur concomitantly. The combined C/ θ'' phase was revealed (see Fig. 50f), and the segregation of Zn at the broad interface of Ω (Fig. 50g), demonstrating the interaction between various phases. η -type precipitates were

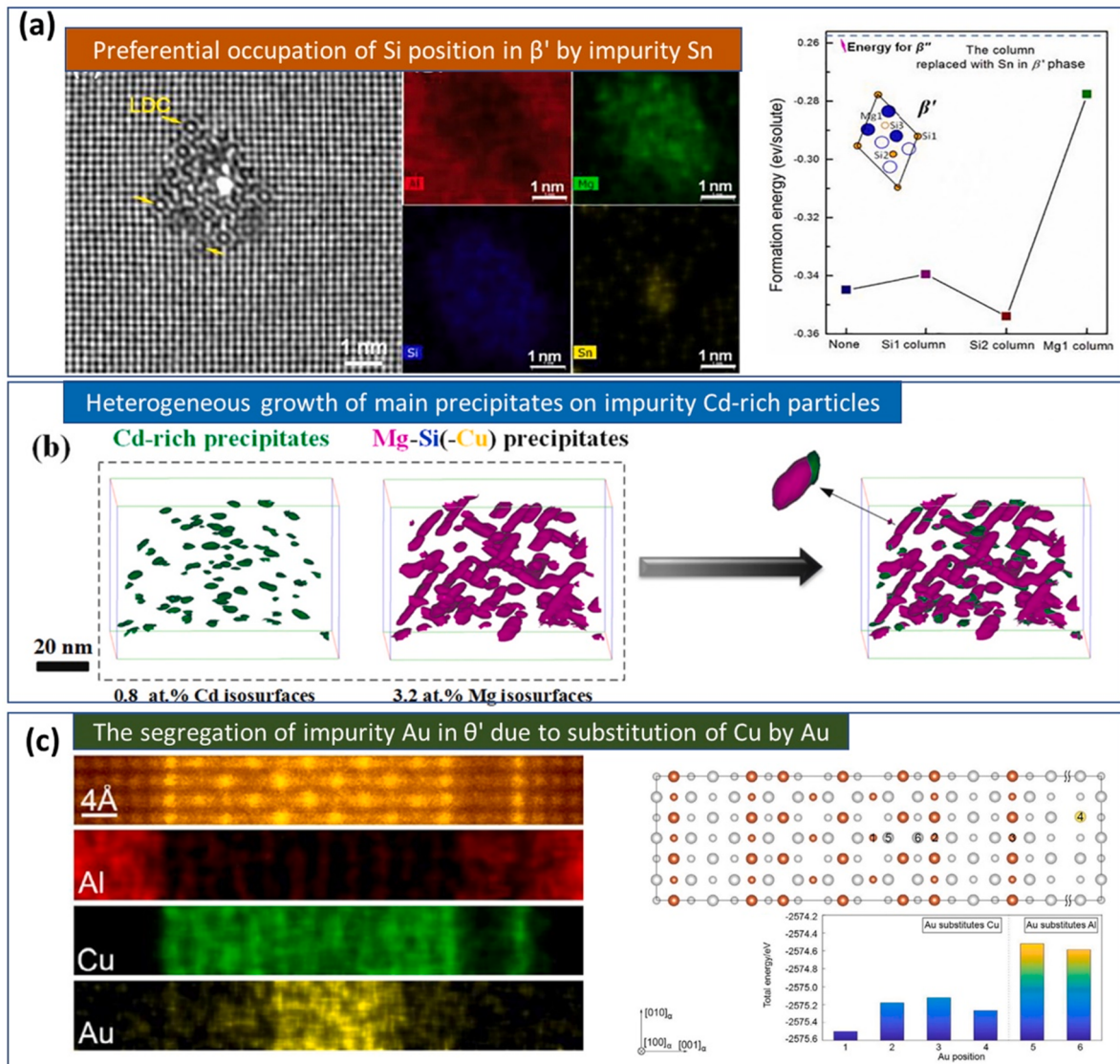


Fig. 49. Characteristic interactions between precipitation phases and minor impurities in recycled Al-alloys. (a) High-resolution HAADF-STEM images displaying the composite β'/β'' phase containing Sn in the Sn-added Al-Mg-Si alloy, as confirmed by elemental mapping [832]. The right-hand panel shows the formation energy calculation result revealing the favorable substitution of Si in β' by Sn. (b) Atom probe tomography (APT) elemental concentration iso-surface results showing the distribution of precipitates in the 6082 alloy with added Cd [834]. (c) High-resolution HAADF-STEM images and elemental maps showing the Au segregation in the hardening θ' phase [841]. The preferential anchoring positions of Au are confirmed by first-principles calculations. TEM images in (a, c) were taken along $\langle 001 \rangle$ Al. The images are reproduced with permission.

only rarely observed despite the high Zn content (4 wt%). This may be explained by the fact that Zn prefers to locate in the Cu-containing phases and that there is a high solubility of Zn in the Al matrix. Previous studies have demonstrated that small changes in alloy composition can alter precipitation significantly [863]. Producing Al-alloys from mixed scrap / composition origin can lead to backpack-like phase agglomerates and phases different from those observed in the established classical alloy systems [55]. A multitude of intergrown precipitate phases already reflect the complex precipitation reaction in the mixed alloys, not to mention those in the Li-containing mixed Al-alloy (Al-Cu-Li alloy and other alloy series). In addition, their growth and strengthening mechanisms remain to be explored.

5.2. Mitigation of scrap related issues by alloying

While some impurity additions can have beneficial effects on properties such as strength, one of the biggest challenges in recycling aluminum alloys is suppressing the harmful effects of impurity elements (e.g. Fe and Si). It is well recognized that the high Fe content in aluminum alloys can cause a significant decrease in tensile properties, especially in ductility [864]. Fe has a low solubility in aluminum

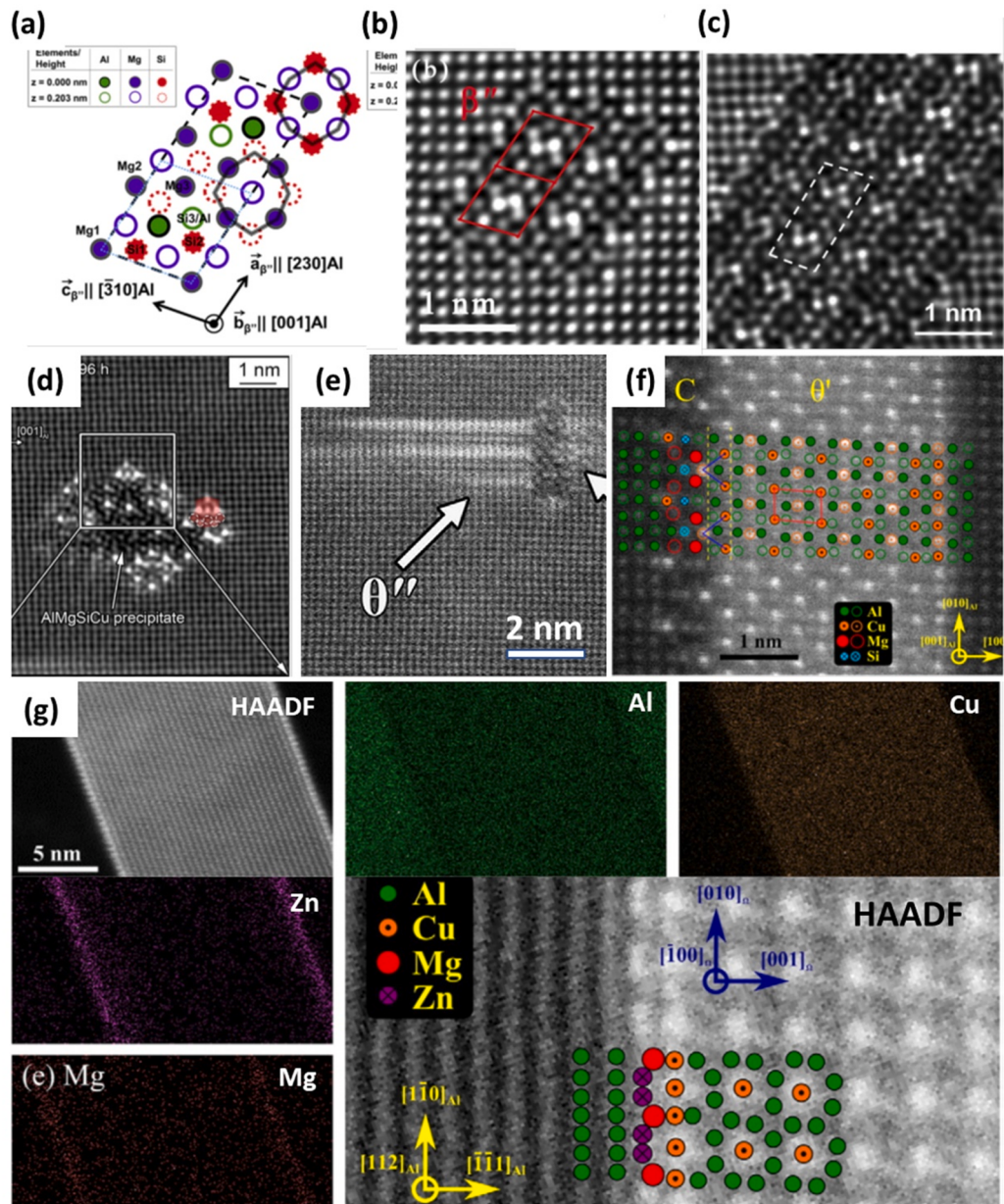


Fig. 50. Characteristic interactions between a precipitation phase and another phase or foreign solutes in mixed aluminum alloys: (a) native atomic structure of the β' phase projected along the b-axis [860]; HAADF-STEM images of the cross-section of the β'' phase with the Mg1 and/or Si3/Al sites replaced by Cu (b) [860] and Zn (c) [860]; (d) substructures of the C phase decorated by units of GPB [856]; (e) the inter-connected θ'' and C phases [842]; (f) the combined θ' -C plate [853]; (g) elemental maps and high-resolution STEM image showing the Zn enrichment at the interfacial layer between the Ω phase and the Al matrix [853]. The HAADF-STEM images in (b-f) are taken along $\langle 001 \rangle$ Al while that in (g) is along $\langle 112 \rangle$ Al. The images are reproduced with permission.

alloys and often precipitates in the form of Fe-rich intermetallic compounds during solidification [249]. These intermetallic compounds usually have a plate-like or needle-like morphology, which are harmful to castings due to stress concentration. In addition, they are unstable and prone to breakage, which can damage the integrity of the castings and increase the processing cost. In order to produce high-quality recycling aluminum alloys, measures must be taken to eliminate or reduce the negative effects of Fe. In this regard, the most common approach is to alloy with neutralizing elements as shown in Fig. 51 [865–869]. Previous studies have demonstrated that adding trace elements, such as Mn, Ce, Y, can change the nucleation and growth kinetics of Fe-rich intermetallic compounds, e.g. facilitate their heterogeneous nucleation [865,866]. The trace elements may segregate in the alloy prior to nucleation and growth, thus affecting the formation kinetics of Fe-rich intermetallic compounds. Adding appropriate trace elements (e.g. Mn and Y) in that context not only helps to promote the refinement of the otherwise coarser needle-like $\beta\text{-Al}_5\text{FeSi}$ phase in the recycled alloy,

but also helps to reduce the volume fraction of that phase significantly. Simultaneously, it can also transform the α -Al₈Fe₂Si phase into an α -Al₈(Fe₂Mn)Si phase variant with a fine, rounded shape. The occurrence of α -Al₁₂(Fe,Mn)₃Si has also been reported.

Direct chill casting simulations have been used to study the effect of different amounts of Ni and V on the intermetallic second phases in aluminum alloys containing Fe [249,731,867]. Adding Ni promotes the formation of Al₃Fe and α -Al₈Fe₂Si and inhibits the nucleation and growth of metastable Al_mFe [867], while a new Ni-rich Al₉FeNi phase is observed at high Ni content. These alloying effects have been observed in different Al-alloy systems containing large amounts of Fe, including Al-Cu [248,249], Al-Mg [867] and Al-Si [731]. In contrast, adding V strongly promotes the precipitation of Al_mFe and reduces the critical cooling rate for its formation [867]. Adding Sc and Cu is also effective in improving the properties of the alloys [870,871]. Sc can transform the needle-like β -Al₅FeSi phase into a relatively harmless spherical Sc-Fe phase. Because the hardness and elastic modulus of the Sc-Fe phase are lower than those of the β -Al₅FeSi phase, the cracking propensity in the Al matrix is evidently lowered. In addition, the spherical Sc-Fe phase can improve the fluidity of the Al-alloy during solidification, thereby reducing the dendritic shrinkage [870,871].

Si is another harmful impurity in many recycled aluminum alloys, but contradictory results exist regarding the influence of Si on the recycled alloys [840,872]. Questions surround (i) whether Si is an impurity or a beneficial alloying element; and (ii) the range in which Si can improve the mechanical properties of Al-alloys. On one hand, Si can transform the morphology of Fe-rich intermetallic compounds from a harmful lath-like to a less harmful Chinese script shape. On the other, the Si may reduce ductility. In order to eliminate the negative effect of Si in recycled Al-alloys, small amounts of chemical modifiers, e.g. Na, Sr, Ca, Ba and Eu, are usually added to melt the recycled Al-Si based alloy [866,873]. Adding chemical modifiers can change the morphology of the eutectic Si phase and affect the nucleation of the eutectic grains. It also promotes the morphological transformation of the eutectic Si phase from coarse plate to fine fiber.

Al-Cu based alloys have relatively good fatigue properties, high specific strength and good heat resistance. However, their casting properties, such as hot crack sensitivity and fluidity in cast Al-Cu alloys, are relatively poor [874]. Alloying Si in Al-Cu alloys can reduce thermal cracking sensitivity [840]. However, the Si content needs to be strictly controlled to obtain optimized properties. The mechanical properties of the Al-Cu-Mn-Fe alloy decreases slightly for an Si content below 1.0 wt% [840]. This has been attributed to the coupling effects between the increase in nano-scale α -Al₈Fe₂Si particles, the grain size coarsening and the formation of a grain boundary Al₂Cu phase. When the Si content is 1.5%, the mechanical properties of the Al-Cu alloy are significantly reduced, mainly due to the formation of excessive Si particles and the aggregation of the second phases. As the most widely used cast aluminum alloy, the Al-Si alloy has been widely used in automotive components. Here, in order to improve the strength of Al-Si castings, a small amount of Mg is added to improve age hardening. Adding Mg can also effectively modify some of the Fe-rich phases and improve the alloy's performance [864]. When a small amount of Mg is added, a fraction of the α -Al₈Fe₂Si particles in the alloy will be transformed into the flake-like Al₁₃Fe₄ phase. With a further increase in Mg, the morphology of the Al₁₃Fe₄ phase evolves from flake-like to petal-like. This evolution mechanism is possibly related to the Mg/Si combination and the increase in undercooling [864].

In order to design new alloys without impairing the properties of recycling alloys, aluminum scrap needs to be remelted and alloyed during secondary production. However, various alloying elements and many processing steps make it difficult to design the alloy on demand. Bayesian optimization has recently been used as the basis for adaptive experimental optimization to explore and optimize multivariate problems [771]. The optimization of composition to maximize alloy strength and reduce the overall heat treatment time to maintain cost-effectiveness has been achieved. The experimentally designed 7xxx alloy features maximum yield and ultimate tensile strengths of 729 MPa and 761 MPa, respectively. Its mechanical properties are equivalent to or exceed those of current high-strength 7xxx series Al-alloys. Exploiting advances in the understanding of thermodynamics and diffusion kinetics, Kampmann-Wagner numerical simulations of precipitation (see also section 4.5) have been used to study the effect of adding alloying elements (e.g. Cr and Zn) [876]. Such simulations can help to reveal the behavior of each element during nucleation, growth and coarsening. With the further improvement of the nucleation model, the proposed model has the potential to guide the design or optimization of chemical composition and heat treatment processes for recycling Al-alloys.

5.3. Damage initiation through precipitates related to tramp elements

Deterioration of the toughness and ductility in alloys is attributed to the nucleation and propagation of damage. To study damage initiation, one needs to address damage-susceptible regions in alloys' microstructure. Coarse particles are important in this regard, because void/crack nucleation is more likely to start at the largest inclusions due to the localized stress concentration. The largest constituents in Al 6xxx alloys are usually Al-Fe-Si-based intermetallic phases (IMPs), which occupy a considerable volume fraction of the microstructure (~1%) and have an average size of 1 ~ 20 μm [100,877]. During the age-hardening of Al 6xxx alloys, different precipitates with a wide range of length scales, ranging from a few nm-sized Guinier-Preston (GP) zones to microscale-sized platelet-like β -Mg₂Si precipitates, are also found [877,878]. In addition to IMPs, microscale Mg₂Si particles are therefore regarded as possible damage initiation regions in the microstructure of these alloys [877,879,880]. Besides the size of precipitates, their morphology; their alignment and its angle relative to the loading axis; the particle-matrix interface, and their distribution also can influence damage initiation [346,879,881,882]. In the following, the major characteristics of the above-mentioned precipitates and inclusions are addressed in the context of damage initiation in Al 6xxx alloys.

Hannard et al. [883] investigated the fracture behavior of three 6xxx alloys, 6005A, 6061, and 6056, processed using different heat treatments. The volume fraction of the secondary phase particles was kept almost constant for all materials. They found that the particle size distribution is the predominant factor in the decrease of fracture strain with an enhancement of yield strength. The best result was obtained for the alloy with the smallest average distribution of particles. Particles of comparable sizes >5 μm are mostly prone to fracture (around 80% of the particles), while in contrast those of smaller sizes ($\leq 1 \mu\text{m}$) do not break at the same strain level,

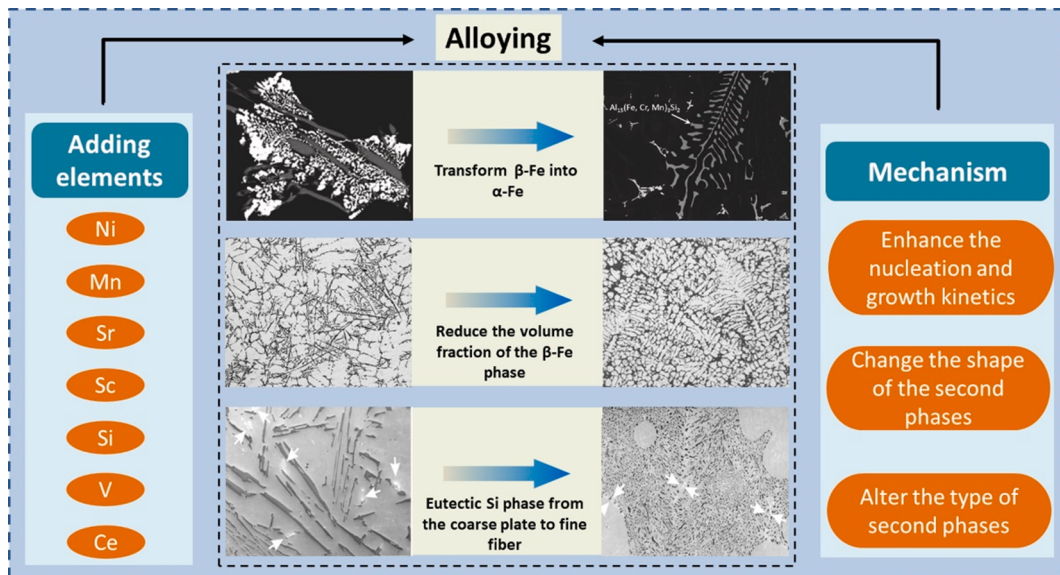


Fig. 51. The effect of adding trace elements on the microstructure of recycled casting alloys. The micrographs in the middle are selected from [866,873,875] and reproduced with permission [865–869].

but at higher strains [884]. The authors also found that coarser particles ($>3 \sim 4 \mu\text{m}$) tend to break more than once. This becomes more detrimental because the local density of the cracks will increase and their interaction will generate faster propagation of damage.

The damage mechanism, from the perspective of particle failure, is either fracture of the particle or its decohesion from the matrix [879,883,884]. This depends on many factors including morphology, size, alignment around the applied load, mismatch stress between the inclusion and the matrix. Babout et al. [885] have shown that the damage mechanism is also related to matrix hardness. For a soft matrix, particle–matrix debonding is the main damage mechanism, while if matrix strength is greater the same particles tend to break rather than debond. The number of damage events caused by both particle decohesion and cracks increase with plastic strain. However, in the case of a hard matrix the particles break at lower strains, and the number of cracked particles increases sharply with plastic strain. The morphology of the particles plays an important role in the localization of the strain and consequently in the damage mechanism. Two of the most common IMPs in Al 6xxx alloys are plate-like $\beta\text{-Al}_5\text{FeSi}$ and round $\alpha\text{-Al}_{12}(\text{Fe},\text{Mn})_3\text{Si}$ particles [881,886,887]. The first is more detrimental due to its elongated morphology. The effect of loading direction associated with the morphology shows that $\beta\text{-Al}_5\text{FeSi}$ particles aligned parallel to the loading direction break into fragments, while those particles (either $\alpha\text{-Al}_{12}(\text{Fe},\text{Mn})_3\text{Si}$ or $\beta\text{-Al}_5\text{FeSi}$) perpendicular to the loading direction generate void nucleation through particle debonding from the matrix [881]. In general, when the angle between the long axis of the particle and the loading direction is $>45^\circ$, particles tend to undergo interface decohesion. Otherwise, they fail by cracking. The cracks are normal to the main loading direction and the larger plate-like particles ($\beta\text{-Al}_5\text{FeSi}$) tend to break into several fragments [881,883,884].

In the literature, ductile fracture is reported to be the main mechanism in the failure of 6xxx alloys [877,883]. This is characterized by the nucleation of voids, followed by their growth and coalescence. Petit et al. [877] showed that the coarse particles do not localize at the grain boundaries, but rather are distributed inside the grains. However, the particles also tend to form along the subgrain boundaries. As the damage initiation is dominated by failure of coarse Mg_2Si or Fe-rich IMPs and these are distributed mostly within the grains, the main mechanism for the fracture is shown to be transgranular (see Fig. 52). In contrast, Shen et al. [879] have shown that the coarse particles are distributed along the grain boundaries, and since the damage nucleates and propagates through these precipitates along grain boundaries the fracture is assumed to be dominated by intergranular crack propagation. These different observations may be attributed to the use of different alloys and heat treatments. It is shown in [877,879] that large Mg_2Si particles break at lower strains compared to other IMPs, even though their mean size is lower than that of IMPs. This can be seen in Fig. 53, where the damage originates from Mg_2Si particles. Upon higher plastic strains, the cracks propagate through large IMPs. As a result, the fracture surfaces of 6061 samples are found to include many dimples caused by the breakage of Mg_2Si particles. Only a few other IMPs are shown to be fractured, generating what are thought as of secondary cracks.

The Fe content in these alloys is a decisive parameter for the damage mechanism because, on the one hand, it contributes to the formation of Fe-containing IMPs, and on the other, it determines which Fe-containing phase will form in the microstructure. The increase in Fe significantly reduces ductility, while slightly enhancing yield strength [100]. One of the earliest studies by Blind et al. [888] showed that toughness increases due to the higher volume fraction of dispersoids in low-Fe alloys ($<0.06 \text{ wt\%}$), but decreases as the Fe content becomes higher ($\sim 0.30 \text{ wt\%}$). This is attributed to formation of coarse IMPs [100,888]. Sweet et al. [886] showed that at lower Fe content ($\sim 0.1 \text{ wt\%}$) $\beta\text{-Al}_5\text{FeSi}$ particles are dominant in the microstructure, while $\alpha\text{-Al}_{12}(\text{Fe},\text{Mn})_3\text{Si}$ particles become the major type of intermetallic at increased Fe content ($\sim 0.5 \text{ wt\%}$) (see Fig. 54). Substitution of plate-like particles with a more compact $\alpha\text{-Al}_{12}(\text{Fe},\text{Mn})_3\text{Si}$ phase in the form of round or Chinese-script-shaped particles improves ductility. Adding Mn has been found to

suppress the development of β -Al₅FeSi particles and to promote the formation of the more spherical-shaped α -Al₁₂(Fe,Mn)₃Si precipitates. This transformation can be triggered by homogenization at relatively high temperatures [887,889,890]. A reduced Si level has also been reported to enhance the spheroidization of intermetallic particles containing Al-Fe-Si [889]. It has also been observed that in order to enforce transformation of the β -Al₅FeSi phase into the α -Al₈Fe₂Si phase, a Mn:Fe ratio of 0.5 is particularly desirable, producing an α -Al₈(Fe₂Mn)Si phase or an α -Al₁₂(Fe,Mn)₃Si phase in the material [100]. When considering IMPs as damage initiation spots, the concentration of Fe and Mn becomes important. The magnesium content of 6xxx alloys has no significant effect on the formation of Fe-rich IMPs, but rather on the formation of Mg₂Si particles. There is also evidence that Mg addition can promote the formation of π -Al₈FeMg₃Si₆ particles with a hexagonal structure that forms at lower temperatures than β -Al₅FeSi [886]. These particles also have Chinese-script morphology. Ji et al. [100] found that the size and morphology of the α -Al₁₂(Fe,Mn)₃Si particles can be altered by the cooling rate. At higher cooling rates (over 10³ K/s), Chinese-script-like particles form and assume a fine compact morphology, and their particle size is almost insensitive to variations in Fe content, with average particle sizes around 0.75 μ m. However, their volume fraction increases by approximately 30% if the Fe content is altered from 0.5 to 1.5 wt% [100]. In contrast, at lower cooling rates (below 10² K/s) particle size and the volume fraction of α -Al₁₂(Fe,Mn)₃Si particles both increase notably with Fe content, with a maximum average size of ~60 μ m observed for 1.8 wt% Fe.

Formation of precipitate-free zones (PFZ) adjacent to grain boundaries can also decrease toughness and facilitate damage propagation in this class of aluminum alloys [891–893]. Moregeneyer et al. [891] studied the quench sensitivity of toughness in 6156 alloys, and found that the energy required for crack propagation drops substantially in air-cooled samples with relatively large PFZs compared to those which are water-cooled. In air-cooled samples the cracks are also observed to be thoroughly intergranular, and most cracking occurs parallel to the loading direction. By conducting compression tests with different strains, Christiansen et al. [894] showed that PFZs and grain interiors in 6060 alloys can exhibit different orientations. The misorientation between the grain interior and PFZs becomes more pronounced at larger strains. The grain-like PFZs are expected to inhibit void nucleation at grain boundaries, but their boundary with interior grain will be susceptible to damage initiation [891].

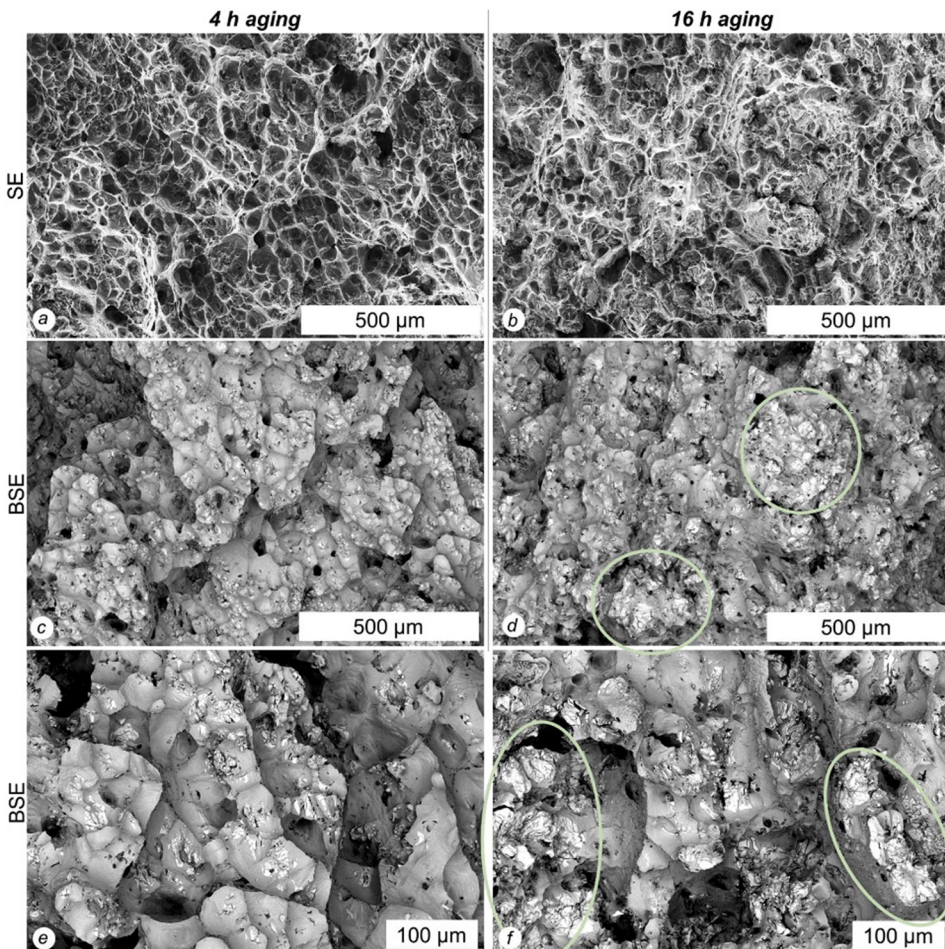


Fig. 52. Fracture surfaces of two 6061-T6 alloys subjected to different aging times of 4 and 16 h. The fracture mechanism in both cases is transgranular. Dimples correspond to broken Mg₂Si precipitates and circled areas correspond to very large IMPs. Reproduced with permission from [877].

5.4. Influence of scrap-related contaminant elements on the quench sensitivity of aluminum alloys

Thermal treatment of precipitate-strengthened alloys usually involves three steps: solution treatment, quenching and aging [895]. The purpose of solution heat treatment is to fully dissolve the soluble alloying elements into the aluminum matrix. After rapid quenching, a supersaturated solid solution (SSSS) begins to form and finally decomposes during artificial aging. The quenching rate strongly affects the supersaturation degree and thus subsequent age hardening. Quench sensitivity refers to the reduction in final properties (e.g. strength, ductility/toughness) due to the reduction in the quenching cooling rate [538,896]. The effect of quench sensitivity on the final properties of aluminum alloys and the characterization methods of quench sensitivity are summarized in Fig. 55.

The quenching rate changes the width of the PFZ by affecting the concentration of as-quenched-in vacancies. A low quenching rate allows more vacancies to become annihilated at sinks like the nearest grain boundaries (or dislocation jogs), favoring a greater PFZ width. Thereby the quenching rate substantially affects many critical damage properties, including stress corrosion cracking (SCC) susceptibility, fatigue and fracture. A faster quenching rate often corresponds to higher peak-aged hardness and greater SCC resistance. Quench sensitivity can also be measured by two indicators: (i) the upper critical cooling rate (UCCR) (higher than which a fully supersaturated solid solution can be reached); and (ii) the corresponding relationship between the strength and the cooling rate [538]. More attention has been paid to the quench sensitivity of thick plates [897–900]. The quench rate is relatively low in the center but high at the surface, resulting in different solute precipitation sizes [896]. The cooling rate near the core is lower than the UCCR. After solution treatment, the solute atoms precipitate during quenching to form coarse particles, which greatly reduces solute supersaturation and precipitation strengthening during subsequent aging.

The effect of quench sensitivity should also be considered in aluminum alloy sheets used for hot stamping. Because of the high forming temperature, the equipment must be specially designed to achieve rapid cooling of quench-sensitive alloys to avoid the formation of coarse secondary phases at grain boundaries and dislocations [901,902].

Quench sensitivity depends on alloy composition [896,905]. Therefore, it is important to study the effect of contaminant elements on the quench sensitivity of recycled aluminum alloys. There are three types of alloying element in the different aluminum alloy systems [904]: (i) the major alloying elements; (ii) the impurity elements; (iii) deliberately-added minor elements. Taking 7xxx alloys

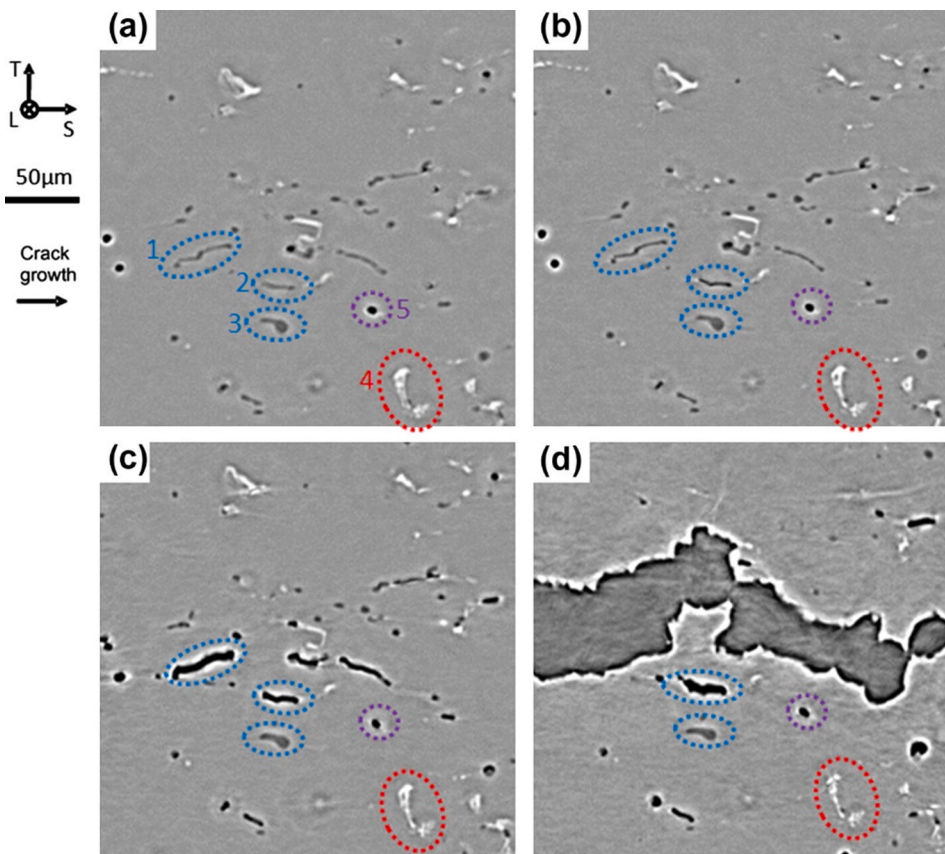


Fig. 53. Nucleation and propagation of the damage in a 6061 aluminum alloy in T6 condition. The damage initiates from the decohesion of Mg_2Si particles (e.g. number 1, circled in blue) and then continues by propagation and coalescence with other voids until it travels through the captured region. The circled regions correspond to Mg_2Si precipitates (blue), Fe-containing IMPs (red), and pre-existing voids (purple). Reproduced with permission from [879]. (For interpretation of the references to color in this figure legend, the reader is referred to the web version of this article.)

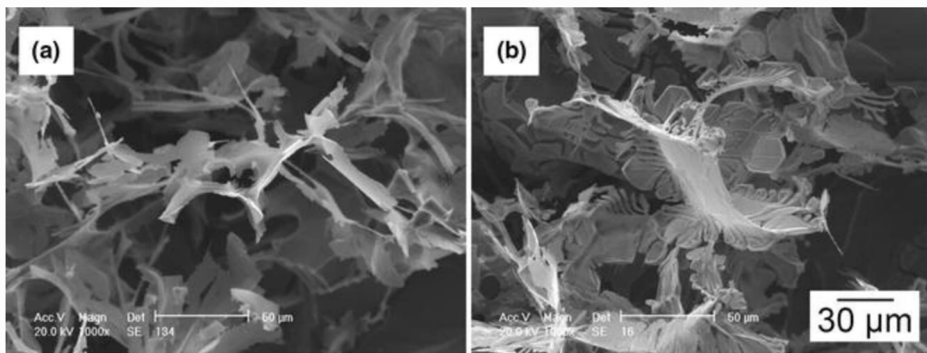


Fig. 54. Morphology (deep etched) of two different intermetallic phases by variation of Fe content in a 6060 aluminum alloy: (a) the plate-like β - Al_5FeSi phase with 0.1 wt% Fe; and (b) the Chinese-script α - $\text{Al}_{12}(\text{Fe},\text{Mn})_3\text{Si}$ phase with 0.5 wt% Fe. Reprinted with permission from [886].

as an example, Zn, Mg and Cu are the major alloying elements, Mn, Cr, Zr, and Sc are the minor elements, and Fe, Si, etc. are the impurity elements. The Al-Zn-Mg-(Cu) aluminum alloy is considered to be the most sensitive to quenching rate because it usually contains a high concentration of alloying elements [538]. For this reason the quench sensitivity of 7xxx aluminum alloys has been studied extensively [413,896,897,900,906]. Quench sensitivity increases with the total content of alloying elements ($\text{Zn} + \text{Mg} + \text{Cu}$) due to the enhanced tendency of the supersaturated solid solution to decompose during the cooling process [899,905]. The increase in Mg content in 7085 aluminum alloys may reduce the solubility of the other main alloying elements, leading to an increase in the driving force for η phase precipitation during quenching [897]. It is believed that the 7xxx series aluminum alloy with a higher Zn/Mg ratio has relatively low quench sensitivity [905]. The possible explanations for this are (i) the decelerated decomposition rate of the solid solution to a stable phase [907] and (ii) the significant suppression of the precipitation of the S phase (Al_2CuMg) during continuous cooling [904]. In consequence more Cu and Mg can be retained in solid solution, resulting in reduced quench sensitivity. Adding Cu results in higher quench sensitivity [749]. However, Livak and Papazian [908] demonstrated that a small addition of Cu to an Al-Zn-Mg alloy could decrease the quench sensitivity by promoting the formation of solute-vacancy complexes. In 6xxx alloys, changes in the content and ratio of the main alloying elements also seriously affect quench sensitivity. Milkereit et al. [411] pointed out that increasing the total content while keeping the Mg/Si ratio unchanged increases quench sensitivity. A comparative study also reveals that higher Mg and Si content induces a faster critical cooling rate and thus greater quench sensitivity [909]. In 2xxx aluminum alloys increasing the Cu content will also increase quench sensitivity [910,911]. For example, compared with 2024, 2219 with a higher Cu content is more sensitive to the cooling rate and is more likely to generate an θ phase during cooling [538]. Therefore both the content and the proportion of alloying elements must be controlled to avoid unacceptable quench sensitivity.

Adding minor elements such as Mn, Cr and Zr to the aluminum alloy can increase the latter's recrystallization temperature and inhibit the occurrence of recrystallization [896,905]. The reduction in grain size will increase the alloy's quench sensitivity by increasing the number of both nucleation sites for particles during cooling and sites where excess vacancies can annihilate. In 7xxx series alloys, the minor elements added usually accumulate in the matrix in the form of second phases, e.g. $\text{Al}_{18}\text{Cr}_2\text{Mg}_3$ (E phase) and an AlMgMn phase [905], which can act as nucleation sites for the equilibrium η phase. Zr has been reported to inhibit recrystallization through the presence of Al_3Zr dispersoids and to reduce the alloy's quench sensitivity [497,896]. The crystallographic orientation relationship plus the interfacial energy between the dispersoid phase and the precipitate play a substantial role in quench sensitivity. In Al-Zn-Mg alloys Ge can significantly inhibit quench-induced coarse precipitates [896,912]. The Al-Zn-Mg-Cu alloy containing both Ag and Ge has a lower coarse equilibrium phase density after slow quenching. It is believed that Ag/Ge trap free vacancies and reduce the amount of coarse precipitation on particles containing either Cr or Zr during quenching, leading to the lower quench sensitivity [896]. Fe and Si are common impurities in 7xxx series aluminum alloys, and their content should be controlled to remain at very low levels [913,914]. The mechanism underlying the effect of Fe and Si on quench sensitivity is still a subject of debate. Si may combine with Mg to form the Mg_2Si phase, while Fe can promote the formation of $\text{Al}_{15}(\text{FeMn})_3\text{Si}_2$ with Mn. These primary intermetallic phases are insoluble coarse particles which may cause premature cracks and failure [915]. The traditional belief is that adding Fe and Si will increase quench sensitivity due to the presence of dispersoids and such intermetallic phases [905]. However, the impurity elements Fe and Si mainly exist in Al-Zn-Mg-Cu alloys such as the $\text{Al}_{17}\text{Cu}_2\text{Fe}$ phase and the Mg_2Si phase [916]. The formation of these phases consumes large amounts of Cu and Mg, reducing the solutes supersaturation and the equilibrium phase precipitation during slow quenching.

Adding Mn and Cr will increase the quench sensitivity of 6xxx aluminum alloys [917–919]. In a way similar to 7xxx alloys, the dispersoids containing Mn or Cr formed during the cooling process promote β/β' precipitation. Taking the 6063 alloy as an example, a cooling temperature of $0.8^\circ\text{C}/\text{s}$ followed by artificial aging can obtain 90% strength in T6 state. When the alloy contains excessive Mn/Cr, the cooling rate needs to be increased to $25^\circ\text{C}/\text{s}$ to reach the same level [917–919]. Saito et al. [920] found that a small amount of Cu (~0.1%) will not change the quench sensitivity in an Al-Mg-Si alloy. The average precipitate size reduces significantly, while the precipitate number density increases after subsequent artificial aging in the copper-containing alloy after either air cooling or water quenching [920]. However, Kassner et al. pointed out that when too much Cu is introduced, it increases quench sensitivity [921]. Tzeng et al. [922] reported that adding a small amount of Sc (0.04 wt%) can reduce the quench sensitivity in Al-Mg-Si alloys. They

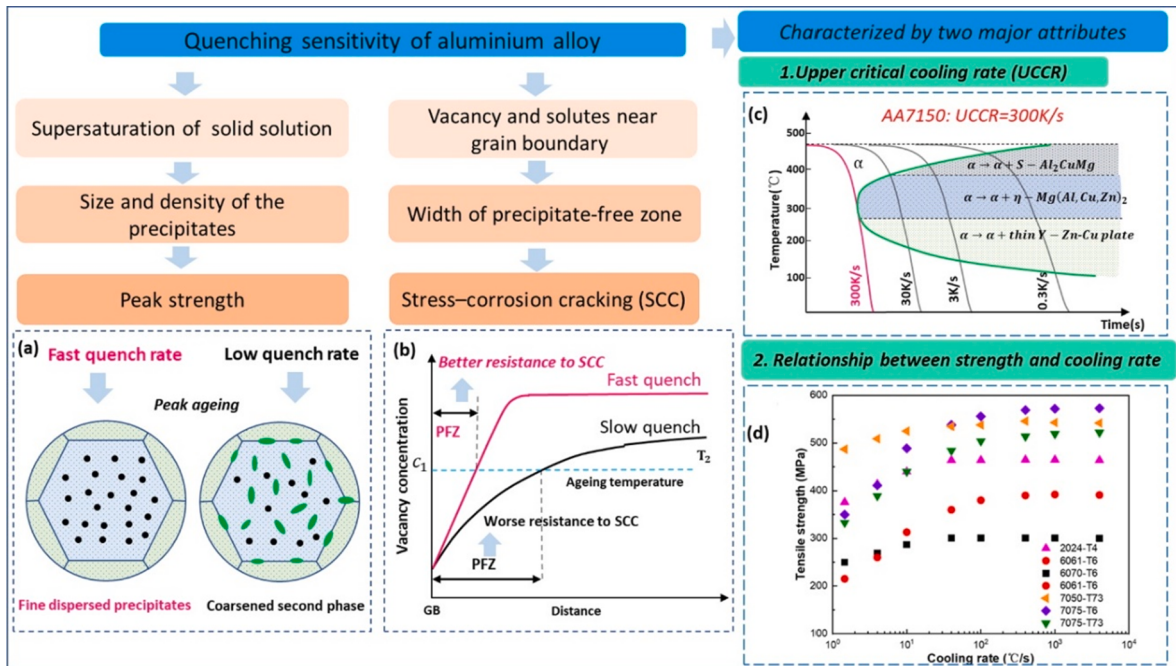


Fig. 55. The effect of quench sensitivity on the final properties of aluminum alloys and characterization methods for the material's quench sensitivity: (a) the effect of quenching rate on the peak aging microstructure; (b) the effect of quenching rate on the vacancy concentration adjacent to a grain boundary and the width of PFZ [903]; (c) continuous cooling precipitation diagram for 7150 [538]; (d) tensile strengths of eight aluminum alloys as a function of average cooling rate during cooling [904]. The diagrams in (c) and (d) are reproduced with permission.

believe that Sc atoms have the ability to preferentially trap vacancies and form Al_3Sc during the cooling process, effectively hindering the movement of Mg atoms and thereby delaying the formation of Mg_2Si . In 2xxx aluminum alloys, adding trace elements such as Mg and Mn also affects quench sensitivity [538,910,923,924]. During cooling, S phase Al_2CuMg and T phase $Al_{20}Cu_2Mg_3$ tend to precipitate at the grain boundaries along with a PFZ, all of this having a negative impact on the strength of the alloy. Fig. 56 summarizes the effects of various elements on the quench sensitivity of three heat-treatable aluminum alloys.

5.5. Influence of scrap-related contaminant elements on the fatigue behavior of aluminum alloys

Scrap-related elements such as Si, Fe, Mn and Cu are commonly present in commercial aluminum alloys as precipitates or secondary phases, and they accumulate during recycling. The influence of Si on the fatigue behavior of hypo-eutectic Al-Si cast alloys is twofold. On the one hand, the eutectic Si particles can cause crack deflections, and slow down crack propagation [925,926]. On the other, large eutectic Si particles can increase the probability of crack nucleation and promote formation of crack networks [925,927]. Which mechanism dominates depends strongly on the stress or strain levels. Under low stress conditions with only minor plastic deformation (i.e. high cycle fatigue (HCF)), the number of cracks is very small and normally only a single main fatigue crack dominates. In such scenarios a higher Si content would be very harmful, because the eutectic Si particles would then be the main reason for crack nucleation [927]. At higher fatigue deformations (i.e. low cycle fatigue (LCF)), cracks can nucleate nearly everywhere in the eutectic structure, and the number of crack nucleation events is usually sufficiently high to enable the further growth of cracks. At the early stage of fatigue with relatively high local plastic strain, when many cracks form and propagate, they can be deflected by hard eutectic Si particles. Here only a few cracks grow further and cause fatigue damage.

In cast aluminum alloys Fe usually causes the formation of Fe-Al based intermetallic compounds, e.g. β - Al_5FeSi in needle- or plate-like shapes, which can have a detrimental effect on mechanical properties [339,928]. The effect of Fe content on the fatigue life of a cast Al-7 %Si-0.7 %Mg (A357) alloy with secondary dendrite arm spacing (SDAS) of 20–80 μm was studied by Wang et al. [929] with a sinus load frequency of 55 Hz. They found that an increase in Fe content from 0.08 to 0.14 wt% generates a decrease in the fatigue life of the cast alloy for larger SDAS ($>60 \mu m$), while its influence at small and intermediate SDAS values ($<60 \mu m$) is insignificant [929]. Horng et al. [930] studied Al-7 %Si-0.3 %Mg (A356) alloys with an Fe content varying from 0.14 to 0.97 wt%. They found that the primary Fe-rich IMCs are π - $Al_8Mg_3FeSi_6$ and α - $Al_{15}Fe_3Si_2$ at an Fe content of below 0.57 wt%, while β - Al_5FeSi is formed where there is higher Fe content, e.g. 0.97 wt% [930]. Compared to π - $Al_8Mg_3FeSi_6$ and α - $Al_{15}Fe_3Si_2$, the β - Al_5FeSi IMC is more detrimental to fracture resistance, and has an increasing effect on the mechanical properties of the materials with increasing Fe content [930]. It has also been observed that fatigue cracks propagate along Si particles and Fe-rich IMCs [930]. Gall et al. [931] investigated the fatigue crack paths in a cast Al-7 %Si-0.3 %Mg (A356) alloy containing modified IMCs, and found that during the later stage of fatigue the cracks propagate preferentially along Fe-rich ($Al_{15}(Fe,Mn)_3Si_2$) IMCs and Si particles.

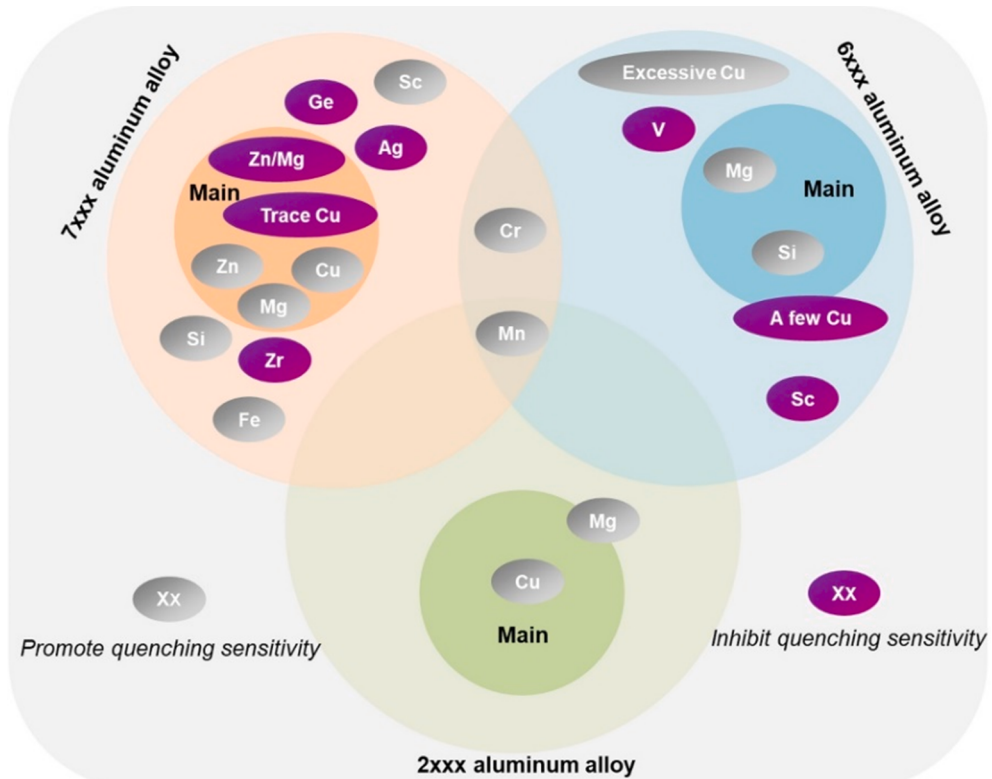


Fig. 56. The influence of various alloying elements on the quench sensitivity of 2xxx, 6xxx and 7xxx aluminum alloys.

The effect of Fe on fatigue behavior also depends strongly on stress and cycling time. Yi et al. [932] found that in the short lifetime regime ($<10^5$ cycles) of the conventional cast Al–7 %Si–0.3 %Mg (A356) alloy the influence of Fe is insignificant, but that Fe-rich IMCs generate a remarkable decrease in fatigue life in the long lifetime regime ($>10^6$ cycles) (see Fig. 57). With high levels of applied stress in the short lifetime regime, crack propagation dominates fatigue life. The growth of small cracks can be hampered by the large plate-like Fe-rich particles via crack branching and meandering in the high Fe content cast A356 alloy [932]. However, in the long lifetime regime with relatively low levels of applied stress, the large Fe-rich particles stimulate crack initiation by increasing the stress-strain concentration [932].

When Fe and Mn accumulate together during recycling, their joint effect on fatigue behavior is particularly interesting. Ceschin et al. [933] studied the effects of Fe and Mn content on the fatigue properties of an Al–10 %Si–2 %Cu casting alloy. The needle-like β -Al₅FeSi was the main intermetallic phase in the high-Fe content (0.5 wt%) alloy samples, while α -Al₁₅(Fe,Mn)₃Si₂ and π -Al₈Mg₃FeSi₆ intermetallic phases with a Chinese-script morphology were also present in the alloy samples containing Mn [933]. It was found that the α -Al₁₅(Fe,Mn)₃Si₂ and π -Al₈Mg₃FeSi₆ intermetallic compounds increased the fatigue resistance at high applied stress, while they decreased the cycles to failure at low applied stress [933]. These findings relate to the following facts. Dislocation movement is more effectively blocked by intermetallic compounds than by eutectic silicon particles under low applied stress, and thus the accumulation of dislocations at the interface between the alloy matrix and the intermetallic compounds leads to stress concentrations and consequently promotes crack nucleation with the matrix-particle decohesion or the cracking of particles. However, under high applied stress microcrack propagation determines the fatigue life [929,930,933]. Because Mn could modify the morphology of the needle-like β -Al₅FeSi and promote the formation of α -Al₁₅(Fe,Mn)₃Si₂ with a Chinese-script-like morphology (less harmful shape) [933], the overall fatigue and other mechanical properties could be optimized.

The influence of Sr (~0.2 wt%) on the fatigue behavior of an AlSi₆Cu₄ alloy was investigated by Huter et al. [927]. They observed a significantly longer fatigue lifetime for the Sr-modified alloy in both the high- and low-cycle fatigue regimes. Sr enables the eutectic silicon particles to assume smoother shapes and smaller sizes by promoting phase nucleation, thus acting as a refinement or modifying agent in the alloys [927,934]. It was found that the elastic strain energy necessary for interface cracking in the AlSi₆Cu₄ alloy without Sr modification is lower than that required in the Sr-modified alloy; thus crack nucleation in the former starts earlier during fatigue [927]. This suggests that Sr has a beneficial effect on preventing fatigue crack initiation. Moreover, because by adding Sr it was possible to induce more internal eutectic Si particles as barriers to fatigue crack propagation, average crack propagation speed could be reduced compared to the AlSi₆Cu₄ alloy without Sr modification.

The influence of Cu on the fatigue endurance limit of an AlSi₇Mg(Sr) alloy was also reported by Huter et al. [927]. In the initially solidified state, some primary Al₂Cu precipitates (the θ phase) can be present, and they can evolve into the coherent θ'' phase and the

partially incoherent θ' phase upon solution annealing treatment and artificial aging. Accordingly, Cu generates enhanced strength in the alloy due to precipitation. The Cu-induced precipitation-hardening effect can also increase the fatigue limit under HCF [927]. One possible explanation was that the fatigue load can be internally shed onto the precipitates, and the fatigue endurance can be enhanced via the Orowan mechanism [927]. However, when fatigue proceeds in the plastic regime, alloys with lower Cu content have higher ductility and hence show higher fatigue life [927].

Fig. 58 summarizes the above discussions about the effects of some scrap-related elements (Si, Fe, Mn, Sr and Cu) on the fatigue behavior of aluminum alloys. The scrap-related elements influence the fatigue properties mainly by precipitation and/or modification of intermetallic compounds or secondary phases. The related effects are strongly dependent on the stress and plasticity levels involved in fatigue. The shape of the precipitates is also important for the fatigue properties, e.g., the Chinese-script-like α -Al₁₅(Fe,Mn)₃Si₂ is less harmful than the needle-like β -Al₅FeSi₃, as discussed above.

Zhang et al. [935] recently suggested an alternative, or additional, method of making high-strength Al-alloys more resistant to fatigue. This involves a specific microstructure design that exploits the mechanical energy imparted during the initial cycles of fatigue to dynamically heal the weak points inherent in the microstructure. This concept substantially improved the fatigue life of ultrahigh-strength Al-alloys and may also work in impurity-contaminated alloy variants.

5.6. Influence of scrap-related contaminant elements on the corrosion of aluminum alloys

Aluminum and its alloys feature high chemical activity, but they usually exhibit excellent corrosion resistance owing to the formation of a thin, uniform and stable oxide film [936]. Modifying the alloying elements can alter the microstructure and affect the anti-corrosion performance of recycled aluminum alloys, as summarized in Fig. 59. The impurity elements accumulated in the recycled aluminum alloys usually promote the formation of intermetallic compounds, which can induce micro-galvanic cells due to the electrochemical potential difference between the compounds and the matrix. If the electrochemical potential of intermetallic compounds is higher than that of the aluminum matrix, these compounds (e.g., Al₂Cu) will become cathodic with respect to the anodic aluminum matrix, causing localized corrosion [937,938]. For instance, Fe contamination in aluminum alloys promotes electrochemical corrosion due to the formation of local electrochemical cells [939]. As the Fe content increases, a large number of anodically acting needles (i.e., Al₆Fe, Al₃Fe and Al₁₂Fe₃Si₂ intermetallics) form and produce more potential corrosion sites on the surfaces. Therefore, enhanced Fe content lowers the corrosion performance of recycled aluminum alloys [67,940]. Adding Mn or Cr can help to neutralize the adverse effect of Fe on corrosion resistance due to the formation of Al₆(Mn,Cr,Fe) and Al₁₂(Mn,Cr,Fe)₃Si IMCs, whose electrochemical potentials are similar to those of aluminum [941,942].

The size of the intermetallic compounds is also important, affecting the alloys' formability and their corrosion resistance in particular due to the formation of micro-galvanic elements. More specific, large intermetallic compounds with micrometre dimensions usually cause corrosion performance to degrade substantially, while sometimes no corrosion attack at all can be found on or around nanometre-sized intermetallics [943,944]. For instance, if Zr is added to an 1070 Al-alloy as a model impurity this can trigger refinement and improved dispersion of Fe-containing intermetallics, an effect which mitigates the negative influence of the Fe-containing intermetallics in the alloy [732]. In general, the following aspects related to these beneficial elements contribute to neutralizing intermetallics' negative effects on corrosion [732,941,942]: (i) enhanced passivation performance, which slows the formation of corrosion pits; (ii) reduced potential difference between intermetallic compounds and the matrix; (iii) the refinement and improved dispersion of particles to prevent localized corrosion due to propagation. Note that non-metallic impurities (e.g., Al₄C₃ particles and entrapped oxides) generally cause corrosion resistance to deteriorate, as they may react with water at the surface

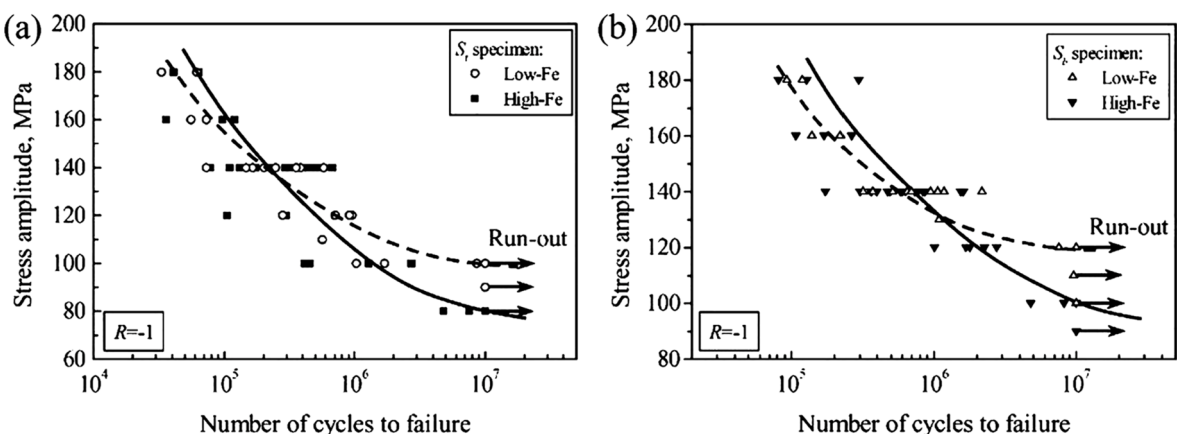


Fig. 57. Stress cycle number curves for a cast Al-7 %Si-0.3 %Mg (A356) alloy with low Fe content (<0.1 wt% Fe, denoted as “Low-Fe”) and high Fe content (>0.55 wt% Fe, denoted as “High-Fe”). S_t and S_b specimens refer to specimens taken from the top and bottom positions of the wedge A356 ingot, respectively. Diagrams reproduced with permission from [932].

[941,942].

Impurity elements also exert an influence on the corrosion behavior of aluminum alloys through their interaction with precipitations, either inside grains or at grain boundaries [945–947]. Examples of such interaction are seen in 6xxx alloys. In these materials the Zn content has to be strictly controlled to values below 0.03 wt% in recycled Al-Mg-Si ternary alloys, because larger amounts can cause corrosion attack on grains and interfaces in alkaline solutions which would be harmful to the anodized surface appearance.

Tolerance to Zn levels in 6xxx alloys made from scrap can be increased if a similar level of Cu (e.g., 0.1 wt%) is added. Preferential grain boundary corrosion attack rather than grain surface attack then occurs due to the segregation of Cu or the formation of precipitates (e.g. the Q phase) at grain boundaries. The accumulation of Zn was observed to increase the Zn/Cu ratio in the Q phase. This effect seems to change the potential difference of the Q phase relative to the neighbouring matrix [149].

In Al-Mg-Si-Cu-Zn alloys (i.e. modified 6xxx and most 7xxx alloys) with relatively high Zn/Cu content, intergranular corrosion (IGC) resistance first degrades with an increase of the Zn level to 1 wt%, and then improves with its increase to values above 2.0 wt% [946]. This effect is related to the compositional states of the Zn-containing grain boundary precipitates and the precipitation free zones (PFZs).

Ag was found to reduce the severe IGC susceptibility in the Si-excess Al-Mg-Si alloys. However, an accumulation of Ag above 0.3 wt % reverses this trend due to the more significant formation of intergranular anode β' phases [947].

In addition to scrap-related impurity elements (Fe, Zn, etc.) and microstructure-modifying elements (Mn, Zr, Cr, etc.), the main alloying elements Cu, Si, Mg can also affect the corrosion performance of recycled aluminum alloys [948] if they deviate from standard specifications. For example, adding Cu can cause the formation of Cu-containing phases or the segregation of Cu at grain boundaries, thereby reducing the corrosion resistance of these alloys [945,949,950]. Even trace levels of Cu (as low as 0.06 wt%) can induce substantial IGC sensitivity in Al-Mg-Si alloys, due to the formation of Cu-containing precipitates at high-angle grain-boundaries [950]. Enhanced scrap-related Si content in recycled alloys can be beneficial, as it generates (e.g.) higher strength, but it also increases corrosion tendency [951]. Because the concentration of Si atoms in PFZs is lower than that in grain interiors and in Si-containing grain boundary precipitates, the corrosion potential of the Si depletion layer (PFZ) is not only lower than that of the adjacent precipitates, but also lower than that of the adjacent grain interior. This can have severe anodic dissolution effects and lead to corrosion of the PFZs around the Si particles, thus increasing the material's overall IGC sensitivity [952]. This Si effect is important, because future scrap will probably have a higher overall Si content due to the massive number of cast vehicle parts from the automotive sector which will be returned in the next two decades.

In many cases adding Mg serves to enhance the corrosion resistance of aluminum alloys. However, too much Mg inherited from scrap can lead to the precipitation of anodically active Al_3Mg_2 IMCs at grain boundaries, creating the sensitization problem characteristic of 5xxx alloys. Therefore care must be taken to control the compositions of alloys made from 5xxx scrap or from mixed light metal scrap, to prevent them from triggering the unwanted grain boundary precipitation of Mg-rich IMCs.

Mg has a strong affinity with almost all of the other major alloying elements, e.g., Si, Cu and Zn, and can promote precipitation of unwanted phases that contain these elements in the grain interior [952,953]. The grain interiors then become less noble, leading to a smaller potential difference between the grain boundaries and the adjacent grain interiors. This effect reduces the material's IGC sensitivity [949].

The scrap-related tramp elements discussed above primarily act on specific microstructural and galvanic features. However, there are also impurity elements that are surface-sensitive and influence corrosion through a mechanism referred to as anodic activation [954,955]. Components pertaining to this group are, for example, the low-melting elements Pb, Sn, Bi and In. Most of the detailed

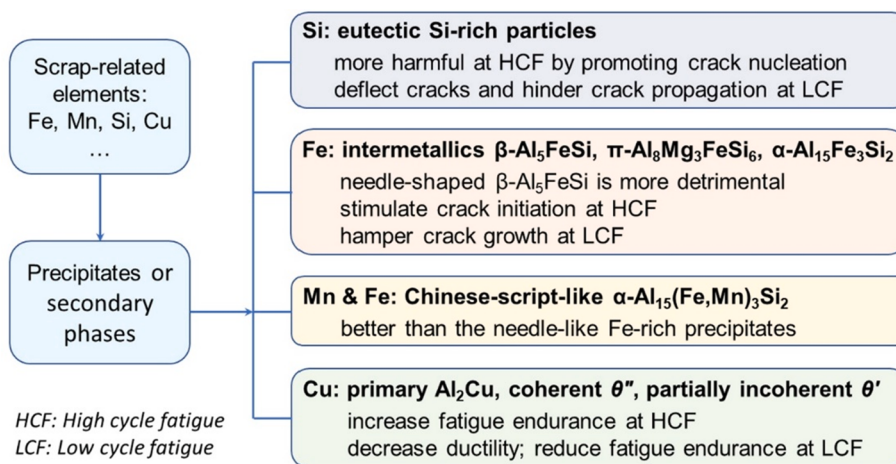


Fig. 58. Diagram summarizing the influences of some scrap-related elements on the fatigue behavior of aluminum alloys.

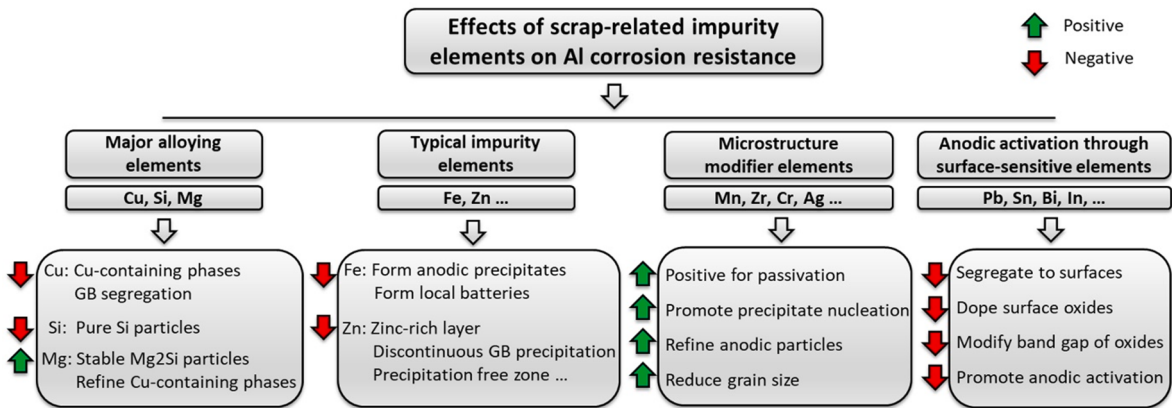


Fig. 59. Effect of various scrap-related tramp elements on the corrosion of recycled alloys.

studies have been conducted on the role of Pb [956,957].

When these elements accumulate above their solubility limits they segregate to the alloys' surfaces and can generate impurity-enriched metal-oxide films, for instance when the alloys are exposed to processing steps where these elements are sufficiently mobile. This changes the band-gap of the oxides, which leads to anodic activation, meaning that the oxides are destabilised, particularly under the effect of chloride ions. The phenomenon can appear in the form of enhanced pitting and even activate the entire oxide surface. Countermeasures include additional doping with noble elements such as Cu to change the surface potential [958].

Reviewing these different types of mechanism shows that a better understanding of the effects on corrosion of scrap-related composition deviation is crucial for the design of recycling-friendly aluminum alloys [959]. It is important to mention that advanced processing technologies, e.g. high pressure die-casting [960], solid-state recycling [940], severe plastic deformation [279] and casting methods featuring higher solidification rates can also lessen the difference between the behavior of secondary-synthesis alloys and primary-synthesis alloys in terms of corrosion resistance [936]. The modification of microstructure in recycled aluminum alloys with scrap-related contaminant elements through processing was discussed in more detail in section 3.6.

5.7. Trapping of contaminant elements at defects and in precipitates

Aluminum alloys generally show high sensitivity to embrittlement induced by impurities. For example, alkaline impurities such as Na and Ca which intrude into the material during the aluminum recovery process, can cause high-temperature embrittlement [961]. They segregate to grain boundaries and reduce their cohesive strength.

Another examples is hydrogen and the associated hydrogen embrittlement (HE) [962] which can have catastrophic impact on the mechanical properties of materials made from contaminated scrap. Organic matter in particular, which is inevitably introduced by post-consumer scrap into recycled aluminum alloys, acts as a hydrogen source. Therefore the hydrogen content in some recycled aluminum alloys may in certain cases be higher than that in aluminum alloys made entirely from primary materials. The potential of low-temperature atom probe tomography to observe the distribution of hydrogen (and deuterium) at various structural defects in metal alloys was demonstrated recently by Chen et al. [963], Breen et al. [964–966] and Zhao et al. [133]. Hydrogen trapped at defects (vacancies, dislocations, grain boundaries, sub-grain boundaries) and precipitates [963,967,968] can reduce stress corrosion resistance [133] and enhance the HE propensity of recycled aluminum alloys [131,967]. At room temperature, the solubility of hydrogen in aluminum is below 0.1×10^{-6} wt%. Excessive hydrogen intrusion affects the mechanical properties of aluminum alloys in two ways: (i) segregated hydrogen induces interfacial decohesion at grain boundaries (HE) and (ii) micropores composed of hydrogen molecules cause ductile fracture [962,969]. Oger et al. [131] studied the segregation of hydrogen in 7xxx aluminum alloys in different artificial aging stages. They proposed that the interface between the precipitates and the Al matrix is an effective trap site for hydrogen, and that the presence of precipitates can effectively reduce hydrogen trapping by grain boundaries. Their findings thus emphasize that strictly controlling precipitates may aid resistance to HE [131]. Tsuru et al. [967] confirmed by first-principles calculation that the interface between MgZn₂ and the Al matrix is a more favorable site for trapping hydrogen compared to the grain boundaries in an Al-Mg-Zn alloy. Chao et. al. [968] found that the θ phase in 2xxx aluminum alloys is also capable of trapping hydrogen. Therefore, refinement of grains, introduction of dislocations/vacancies and the control of H-trapping precipitates are strategies that can be employed to effectively reduce HE in recycled aluminum alloys.

Trapping of scrap-related tramp elements also occurs in precipitates. It was observed that traces of Zn can introduce precipitates into an Al-Mg-Si alloy enhanced with Zn, resulting in a change in the precipitate's structure but without changing its sequence [831]. If the Zn content exceeds 1 wt% Zn will segregate to grain boundaries under peak aging conditions, leading to high IGC sensitivity. These observations suggest that trapping contaminant Zn in precipitates is an effective way to avoid the segregation of Zn at grain boundaries. Contaminants can also get trapped by their preferential enrichment around precipitates. For example, when Ag is added to an Al-Cu alloy some portion of the Ag will partition to the coherent interface at the θ' precipitates to form an Ag-rich double-layer structure [690], which is believed to reduce the interfacial energy between θ' and the matrix. Some Ag also segregates to the semi-

coherent θ' -matrix interface and acts as an obstacle to Cu diffusion. This interfacial trapping may hinder or prevent the lateral growth of θ' precipitates. Fig. 60 summarizes the distribution of various minor contaminant elements at defects/precipitates and their associated influence on the macroscopic properties of recycled aluminum alloys.

6. Effects of scrap-related impurities in cast alloys: Constitution, microstructure, processing and properties

6.1. Brief introduction to cast alloys

Given their high fluidity, low tendency to hot cracking and good as-cast surface quality, aluminum casting alloys offer good castability. Like wrought alloys, they are divided into alloy series according to their main alloying elements: Si, Cu, Mg, Zn and Sn [970,971] (see Table 15). Unfortunately, however, no globally recognized designation system exists. Many countries use specific alloy names. In the following reference is therefore made to the system of the Aluminum Association (AA), but where necessary a designation according to the chemical composition is also provided. The AA uses a four-digit numerical system. The first digit indicates the alloy group; the following two digits identify the different aluminum alloys in the group; and the digit that follows the decimal indicates the product form. Variations in specified compositions are denoted by the prefix letters A, B, C or D to define differences in impurity limits, in particular relating to Fe content. For example, the upper limit for Fe in A356 is 0.15 wt%, but in C356 it is only 0.07 wt%.

Castability is best with the 3xx and 4xx series and decreases on the order of 5xx, 2xx and 7xx.

Besides the major alloying elements, (i) minor elements, (ii) microstructure-modifying elements; and (iii) impurities must also be considered, as follows:

- (i) *Minor elements*: Ni for enhancement of the elevated temperature service strength
- (ii) *Microstructure-modifying elements*: Ti and B for refining primary aluminum grains; Sr, Na, Ca, Sb for modifying the morphology of the eutectic silicon phase in Al-Si alloys; Mn, Cr, V, Mo for changing the structure and morphology of the monoclinic β -Al₅FeSi phase to the cubic α -Al₁₅(MnFe)₃Si₂ phase, which is much less harmful to ductility
- (iii) *Impurities*: e.g. Fe, Cr and Zn

Various commercial alloys are subject to tight restrictions on a number of different elements that may negatively affect material properties. However, with regard to the influence of scrap-related impurities on property profiles, it is basically true that aluminum casting alloys are much more tolerant and less sensitive than wrought alloys [72]. This is mainly due to two things: aluminum casting alloys' generally higher alloying element content, and the significantly wider tolerance range of these alloying elements [972].

The alloys of the 3xx-series are the most popular in the casting industry because of their superior casting characteristics and good strength properties [973]. Secondary Al-Si-Cu-Mg alloys dominate the market for powertrain components and die-cast parts, where strength at elevated temperature and wear resistance are more important than ductility. Al-Si-Mg alloys – mostly primary alloys – are used for wheels, structural castings and suspension parts, which require medium to high strength and good ductility [972]. The 4xx-series alloys are used when good castability in combination with particularly good ductility (Mg-free) or particularly good corrosion resistance (Cu-free) is required [970].

Cast alloys of the 5xx-series are characterized by high resistance to corrosion, weathering and seawater. They are well suited for decorative anodic oxidized components. Conventional Al-Mg alloys have medium strength values, but exhibit good ductility properties. However, their castability is comparatively limited, i.e. they lack fluidity and are sensitive to hot cracking. Therefore they are not often used for die-cast components [971]. Contaminants and impurities should be avoided, as many applications involve surface finishing (polishing). Alloys suitable for die-casting typically contain about 1 wt% Si to form an Al-Mg₂Si eutectic. Their mechanical properties are rather modest, with yield strength values around 90–120 MPa and elongation at fracture of roughly 5% [974]. More recent developments in the 5xx family concern alloy type AlMg5Si2Mn. They enable the die-cast production of large thin-walled structural parts with improved ductility. Depending on the wall thickness, good mechanical properties are achieved without heat treatment, i.e. in the “naturally hard” state (yield strength 140–170 MPa, elongation to fracture 9 – 14% for wall thickness 5 mm). However, high ductility requires the use of low-iron primary alloys with Fe < 0.2 wt% [975].

2xx-series cast alloys have been used in various industrial sectors such as the automotive and aerospace industries due to their high strength and good elevated temperature properties. The age-hardenable Al-Cu-Mg variants exhibit the highest strength levels of all aluminum casting alloys. With carefully controlled levels of impurities, excellent ductility is also achieved. The alloy A206 (AlCu4.5Mg0.25), for example, reaches yield strength values of 350 MPa at 12% elongation to fracture, but the Fe content is limited to 0.15 wt% and the Si content to 0.05 wt% [976]. The corrosion resistance of 2xx alloys is not very high, and certain compositions may be susceptible to stress corrosion cracking in the high-strength state. Generally the alloys of the 2xx series are not preferred candidates for die-casting due to their poor fluidity and relatively high tendency to hot cracking, but they are increasingly being used in squeeze casting [971,972].

The alloys of the 7xx-series usually contain Mg and minor additions of one or more of the elements Cu, Fe, Cr and Mn. The alloys in the as-cast state exhibit a pronounced tendency for natural aging, but artificial aging is only used in special cases. Yield strength values of over 250 MPa can be achieved, but ductility is modest. The casting properties are relatively poor and they show a strong tendency to hot cracking [977]. On the whole, the alloys can be regarded as special and are not considered further in the next section.

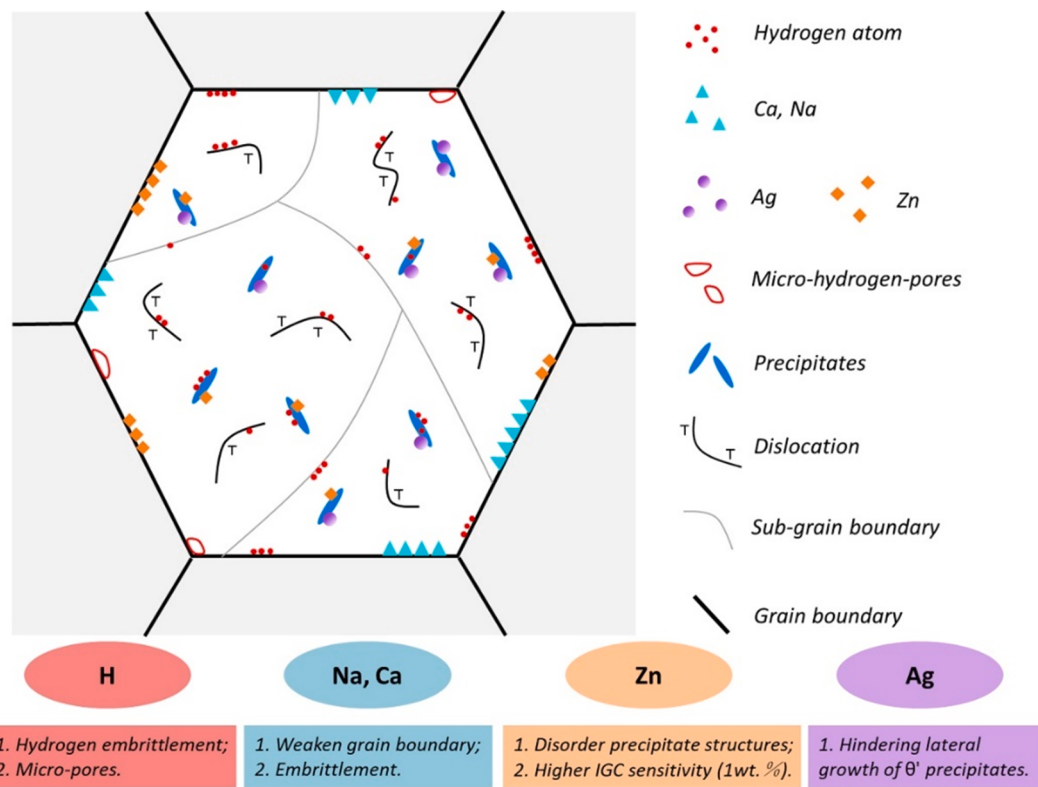


Fig. 60. Schematic diagram summarizing potential trapping sites for contaminant elements at defects and precipitates. The influences of contaminant elements on macroscopic performance are also included.

6.2. Main contaminants and contaminant effects in cast alloys

Cast alloys are sometimes more suitable for absorbing material from mixed alloy scrap streams than wrought alloys, which mostly have little tolerance for impurity elements and scrap-related compositional variations.

While a number of contaminating elements cause property changes which are comparable in all alloy groups, specific elements have particularly detrimental effects on some alloys. In the following, the most important alloy series are considered individually; where there are generally applicable impacts, this is explicitly pointed out. It is important to note that cast components frequently undergo post-processing heat-treatment operations which bring the microstructure from a non-equilibrium state to a state closer to thermodynamic equilibrium. In consequence, the effects of the contaminants may change (see Table 16).

By far, the most important contaminant introduced by scrap is Fe. However, Cu and Si can also have considerable contamination effects. It must therefore always be kept in mind that major elements in some alloys may be impurity elements in others. An important example is Cu, as Cu-free 3xx-series cast alloys for structural applications are often regarded as more corrosion-resistant than Cu-containing counterparts. However, Fragner et al. [978,979] pointed out that even a small increase in tolerable Cu content could lead to a considerable increase in potential scrap input – without any noticeable influence on corrosion properties. Si is Janus-faced in the 5xxx series. While in binary die-cast alloys it is considered a harmful element even in relatively low amounts if it forms Mg_2Si precipitates at grain boundaries, it can contribute to better castability if it is present in sufficient quantity to form an Al-Mg₂Si eutectic. Zinc is generally considered an acceptable impurity element in many scrap-based alloys. It is quite neutral in small concentrations, and neither improves nor diminishes the properties of an alloy.

Possible measures for reducing or eliminating property deterioration due to contamination and optional alloy design possibilities outside the standard compositions are discussed below. They address only the most important alloy series: 3xx, 5xx and 2xx. The assessment of Fe contamination is accorded the greatest importance.

The 3xx-series alloys 319 (AlSi6Cu3.5Zn) and A380 (AlSi9Cu3.5FeZn) are the most important scrap-based secondary alloys, and are primarily used in engine blocks and cylinder heads. Their usage volume equals over 80% of all die-cast alloys [971]. Because their impurity tolerance is significantly greater than that of other alloys, they are currently the most important sinks for scrap. Despite their wide compositional tolerance, these alloys are easy to process and exhibit good strength properties, even at higher temperatures up to 180 °C. However, their wide tolerance range is accompanied by great variations in strength and elongation values. In addition, a significant susceptibility to corrosion makes these alloys unsuitable for use in safety-critical components. Pucher et al. [99,980,981] systematically investigated the options for microstructure design and the associated property changes in AlSi9Cu3FeZn. The tolerance

Table 15

Aluminum Association four-digit numerical system for identification of aluminum alloys. The examples highlighted in color were considered in the preceding sections.

Number series	Major alloying elements	Example alloy
1xx.x	99% minimum Al content	Al99.7
2xx.x	Al + Cu	AlCu4Mg0.25 (206)
3xx.x	Al + Si + Mg, Al + Si + Cu, Al + Si + Mg + Cu	AlSi10.5Mg0.4 AlSi9Cu3MgFeZn (A380) AlSi7Mg (A356)
4xx.x	Al + Si	AlSi10FeCuNi (A413)
5xx.x	Al + Mg	AlMg5Si2MnTi AlMg5Zn3.5Cu0.5
7xx.x	Al + Zn	AlZn5.5Mg0.5
8xx.x	Al + Sn	AlSn6

range defined by the standards for all alloying elements presents wide scope for specific adaptations to the alloy composition to meet increased requirements, both for as-cast and age-harden conditions. Depending on the chemical composition within the tolerance band chosen ($8 < \text{Si} < 11$; $2 < \text{Cu} < 3.5$; $0.1 < \text{Mg} < 0.5$, $0.15 < \text{Mn} < 0.55$, $0.4 < \text{Fe} < 1.2$; in wt.%), the yield strength and elongation to fracture of permanent mold and high pressure die-cast components in the as-cast state range from 100 MPa to 200 MPa and 0.35% to 3.9% respectively, and in the T6 state from 135 MPa to 400 MPa and 0.15% to 7% respectively (see Fig. 61).

As far as ductility is concerned, the morphology of the intermetallic phases which contain Fe is the decisive aspect, just as it is in wrought alloys (see section 8). The occurrence of the monoclinic β -Al₅FeSi phase must be prevented in favor of the cubic α -Al₁₅(MnFe)₃Si₂ phase. This can be achieved by adding so-called Fe-corrector elements, with Mn and Cr being the most important and effective ones [971].

Fig. 62 shows for the quaternary Al-Si-Fe-Mn system the effect of Mn on the Fe-containing IMCs for the case of a non-equilibrium solidification according to Scheil (as-cast condition) and for the equilibrium state at 495 °C (after solution heat treatment).

The tolerance bands for Mn and Fe of alloys 319 (Mn < 0.5 wt%, Fe < 1 wt%) and A380 (Mn < 0.5 wt%, Fe < 2% wt.%) mean that greater Fe content will lead to the formation of the unfavorable primary β -Al₅FeSi phase there. It may be expected that at greater Mn content outside the tolerance band the preference for the α -Al₁₅(MnFe)₃Si₂ phase over the β -Al₅FeSi phase will result in improvements in ductility, although the total volume of IMCs which contain Fe will increase.

Hwang et al. [983] investigated the influence of Mn on the mechanical properties of alloy 319 containing 0.5 wt% Fe. They varied the Mn content in steps from 0.02 to 0.85 wt% and showed that the content of the β -Al₅FeSi phase was 0.5 vol% at 0.3% Mn but that no β -Al₅FeSi phase was present at 0.65% Mn (note that this is outside the tolerance range for Mn). Despite an overall higher volume fraction of IMCs of 0.29 vol% (α -Al₈Fe₂Si phase) versus 0.2 vol% (α -Al₈Fe₂Si + β -Al₅FeSi phase), the alloy with 0.65% Mn was significantly more ductile. Jin et al. [984] investigated the influence of the combined addition of Mn and Mo on the formation of β -Al₅FeSi and α -Al₈Fe₂Si phases in alloy 319, with 0.3 and 0.7 wt% Fe. They showed that adding Mo strongly promotes the formation of α -Al₈Fe₂Si and suppresses the precipitation of the β -Al₅FeSi phase in alloys containing both small and large amounts of Fe. However, the effect of Mo on the suppression of the β -Al₅FeSi phase depends on the Fe content. In alloys containing low Fe content, as little as 0.37% Mo completely suppresses the formation of the β -Al₅FeSi phase, whereas in alloys containing high Fe content only the pre-eutectic β -Al₅FeSi phase can be reduced as the Mo content increases, while the eutectic β -Al₅FeSi phase remains unchanged. Only the combined addition of Mn (0.24 wt%) and Mo (0.41 wt%) completely suppresses the β -Al₅FeSi phase in this case.

The influence of Cr and Co on the formation of α -Al₈Fe₂Si and β -Al₅FeSi phases in alloy A413 (AlSi10FeCuNi) with Fe content ranging from 0.5 to 2.5 wt% was investigated in [985]. The authors showed that an Fe/Cr ratio of 3 should be aimed for to eliminate the β -Al₅FeSi phase. For Co, an effect similar to that of Cr was observed, but a higher alloy content was identified in the formation of an α -Al₈Fe₂Si Chinese script instead of a β -Al₅FeSi phase. An optimal ratio of Fe/Co amounts to ≈ 1.0 .

A team at Brunel University [986] investigated the effect of solution and aging on the microstructure and mechanical properties of AlSi9Cu3.5 die-cast alloys with ≈ 0.5 wt% Mn and a modified Fe content of 0.1 and 1.0 wt%. In the as-cast state the microstructures of the low-Fe alloy contained the intermetallic α -Al₈Fe₂Si phase, θ -Al₂Cu and Q-Al₂Cu₂Mg₈Si₆. The Fe-rich alloy also contained a β -Al₅FeSi phase and a higher α -Al₈Fe₂Si phase content. In the as-cast state the elongation to fracture of the Fe-rich alloy was reduced. The solution heat treatment caused the Cu-rich phases to dissolve and the eutectic Si phase to become spheroidized, resulting in significant improvement in mechanical properties after an additional aging treatment. Assuming that the Mn content of the alloys is higher, such that the Fe-rich variant would be in the sector of the β -Al₅FeSi transformation in Fig. 62, then an even more significant

Table 16

Influence of specific tramp elements on cast aluminum alloys.

Impurity element	Undesired influence on alloy and processing
Cu	Lowers corrosion resistance, Lowers weldability
Fe	Forms coarse intermetallic phases, Embrittling effect
Zn	Embrittling effect Promotes oxidation of the liquid
Mg, Ca, Na	Promote oxidation of the liquid, Lead to mold sticking

improvement in properties might be expected from high temperature annealing.

Pucher et al. [99] evaluated A380 alloys outside the tolerance band for Cu. As mentioned above, at high Si and Cu content not only α -Al₈Fe₂Si and β -Al₅FeSi phases determine the ductility level, but also the intermetallic phases Q-Al₂Cu₂Mg₈Si₆ and θ -Al₂Cu. Systematic tests with Cu content reduced to slightly below 2.0 wt% generate a significant improvement in ductility. Permanent mold castings in the as-cast state exhibit an elongation to fracture of \approx 10% at yield strength of 120 MPa.

These examples show that it is possible to increase the property profile of alloys 319 and A380 by partially bypassing the tolerance limitation. This potential for property improvement is particularly important for the following reason. Alloys 319 and A380 are the most important secondary alloys, for the synthesis of which almost all wrought alloys are ideally suited. This is best illustrated by Modaresi et al. [987] in Fig. 63. It shows the clear potential for recycling of many wrought alloy series into alloys 319 and A380 (this is indicated by the lighter shades in the red frame). However, the demand for alloys for internal combustion engines will decrease in the near future due to the electrification of vehicles (this topic is addressed in more detail in section 7.3). If variants are designed based on alloys 319 and A380, but with a balanced content of the main alloying elements and thus improved properties, they may however find applications outside of the field of combustion engines.

Of particular importance in the automotive industry are not only the casting alloys for aggregates described, but also those used in car bodies. Here the high ductility of the castings is absolutely essential for structural applications. The reference alloy for such applications is the primary alloy AlSi10MnMg, which is subject to challenging quality requirements (die-cast, T7 condition: yield strength > 120 MPa, elongation to fracture > 12%) and restrictions regarding the main impurity elements from scrap-iron, copper and zinc permitted. Consequently, the casting alloys used today are mostly based on primary aluminum. In all of them, Fe content is limited to values below 0.15 wt% to prevent the formation of the ductility-reducing β -Al₅FeSi phase. Because increased use of secondary aluminum inevitably leads to increased Fe content, alloy design focuses primarily eliminating this IMP.

Boesch et al. [988] evaluated the optimum Mn content in age-hardenable AlSi10Mg0.4 alloys with \approx 0.55 wt% Fe which would

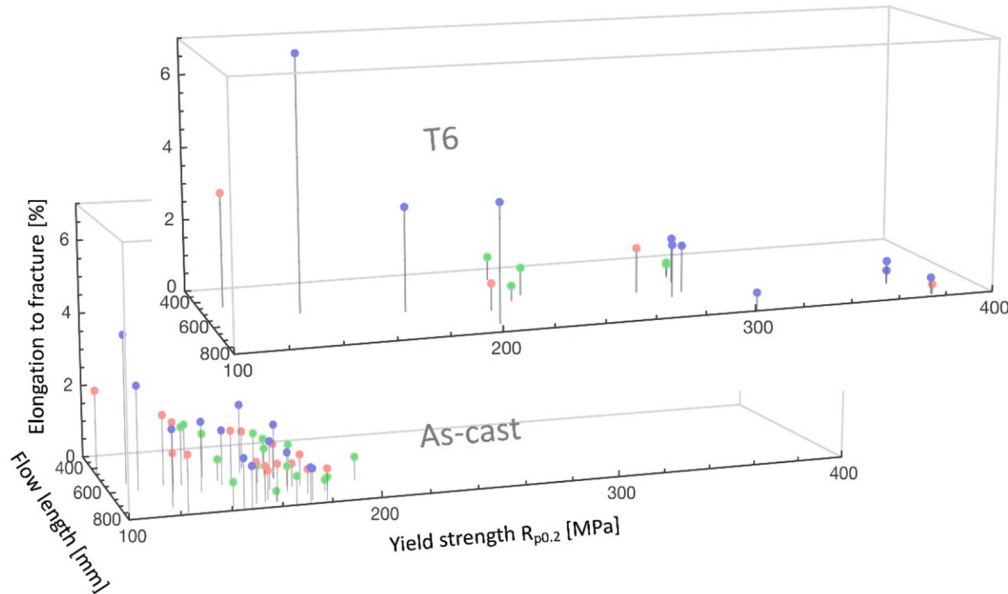


Fig. 61. Mechanical properties and flow length of AlSi9Cu3(Fe,Zn) in as-cast and T6 states as a result of systematic variation of chemical composition within the alloy limitations. The range of properties is greatly extended by applying a heat treatment (solid solution treatment at 495 °C/8 h + 160 °C/10 h). Blue: 0.4% Fe; red: 0.8% Fe; green: 1.2% Fe. Adapted from [981]. (For interpretation of the references to color in this figure legend, the reader is referred to the web version of this article.)

allow a high fraction of secondary aluminum. According to their systematic study, the Mn concentration most promising for neutralizing 0.55 wt% Fe in AlSi10Mg HPDC alloys is in the range of 0.4–0.6 wt%. A Fe/Mn ratio of slightly above 1 is particularly recommended, since an Mn content of 0.6 wt% leads to the formation of a finer morphology of the α phase compared to 0.4 wt% Mn. The associated mechanical properties are very satisfactory and meet requirements, with $R_{p0.2} \approx 150$ MPa and $\epsilon_f = 13\%$.

In [989] the influence of Mn and combined Mn plus Cr on the tensile properties of AlSi7Mg (A356) with 0.20 wt% Fe were investigated. With the addition of 0.20 wt% Mn, the acicular β -Al₅FeSi phase is replaced by the granular α -Al₈Fe₂Si phase with the effect of a slight increase in strength and doubling of the elongation to fracture. Simultaneous addition of 0.13 wt% Mn and 0.13 wt% Cr also generates the transformation of the β -Al₅FeSi phase but causes an almost threefold improvement in ductility. The mechanical properties of this Mn + Cr-modified Fe-enriched alloy variant exceed those of the commercial reference alloy A356 containing < 0.15 wt% Fe.

Basaz and Babu [871] investigated the effect of Cu on the microstructure and properties of a recycled AlSi6 cast alloy with 2 wt% Fe, i.e. the upper limit for the content of Fe impurities in recycled Al-Si alloys. They reported that the harmful β -Al₅FeSi phase was destabilized by the addition of Cu, thereby apparently providing an alternative to traditional Mn addition. Solution annealing of variants with a Cu content > 4 wt% at 500 °C leads to the formation of the ω -Al₇Cu₂Fe phase instead of the β -Al₅FeSi phase, which in turn decomposes into the θ -Al₂Cu phase at lower temperatures. Although the mechanical properties obtained are rather modest – yield strength ≈ 100 MPa at elongation to fracture < 3% – the study points towards interesting options for the modification of secondary alloys with high Fe content.

Lin et al. [990] investigated the formation of IMCs and the mechanical properties of vanadium-modified AlSi7Mg cast alloys (A356) with 1.5 wt% Fe. Experiments which systematically varied V-content up to 1 wt% showed that an increasing V-content promotes the formation of an α -Al₁₅(Fe,V)₃Si₂ phase and reduces the size of the β -Al₅FeSi phase. With regard to mechanical properties, a V content of 0.8 wt% proves particularly favorable. A yield strength of almost 160 MPa is achieved at an elongation at break of just above 5%.

The above-mentioned scrap-related modifications of 3xx-series cast alloys have one aspect in common: they aim to prevent the formation of the plate/needle-shaped monoclinic β -Al₅FeSi phase by adding transition metals in well balanced amounts. However, such alloy modifications have two further significant effects, firstly the reduction or elimination of “die soldering”, and secondly the formation of “sludge” particles.

Die soldering is a casting defect which is of considerable importance in high-pressure die-casting. It is caused by an interfacial reaction between the liquid aluminum alloy and the ferrous die-casting material [991]. A boundary layer is formed with various intermetallic compounds that adhere to the tool surface. This leads on the one hand to permanent damage of the tool surface, and on the other to the sticking of the castings to the mold, with negative consequences for process time and product quality. The tendency towards die soldering is clearly dependent on the chemical composition of the casting alloy. Increased content of Fe and Mn, but also of Cr and other Fe correctors, reduces the risk of die soldering [992–994]. In this respect, all measures for increasing ductility by transforming β -Al₅FeSi into the α -Al₈Fe₂Si phase are also beneficial to the prevention of die soldering. This in turn implies that “chemically corrected” 3xx-series casting alloys may be particularly suitable for HPDC.

Fe correction (i.e. the addition of Mn and Cr to secondary cast alloys and their incorporation into the α -Al₈Fe₂Si phase), however,

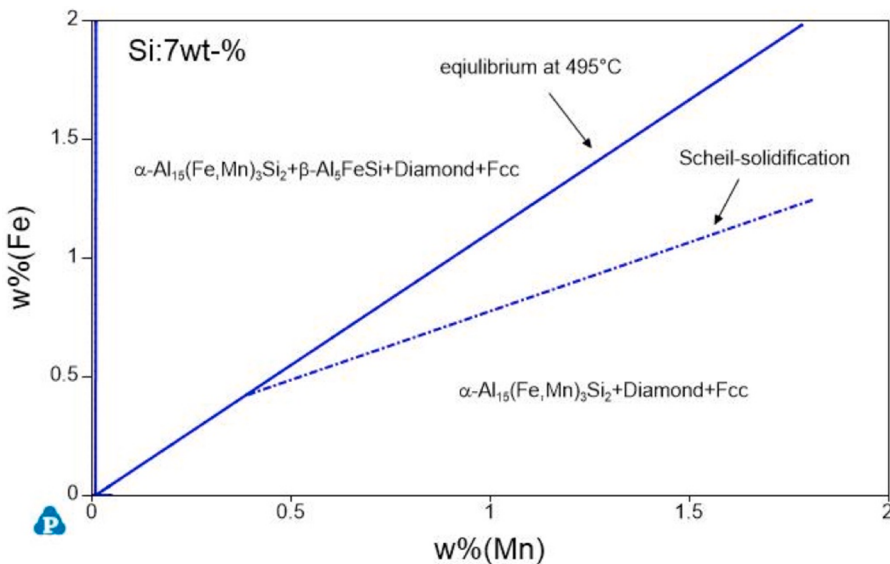


Fig. 62. The isothermal section at 495 °C in the Al-Si7-Fe-Mn system illustrates the border between microstructures free of the β -Al₅FeSi phase and β -containing structures depending on Fe and Mn content (solid line). In addition, the demarcation of areas with the primary β phase after non-equilibrium solidification according to Scheil is shown (calculated with the Pandat software using the database PanAl2019 [982]).

increases the total fraction of IMCs and their thermal stability. Their liquidus temperature may exceed the casting temperature [995,996], with the result that large, primary α -Al₁₅(FeMnCr)₃Si₂ phase particles with polyhedral and star-like morphologies are already formed in the holding furnace [997,998]. Due to their high density ($\rho \approx 3.6 \text{ g cm}^{-3}$) they fall to the bottom of the furnace as sediment, which in the long term creates process-related problems, or they are transported with the melt into the castings and create ductility-reducing inclusions [988,999]. To evaluate the tendency of alloys to form sludge and to avoid undesired phase formation, a segregation factor sludge factor was derived by Jorstad [999] ($SF = Fe + 2 Mn + 3 Cr$ [wt.%]) which should not exceed a value of 1.8. Thus, the content of Fe, Mn and Cr in an alloy cannot be increased arbitrarily, because with sludge factor > 1.8 the occurrence of a coarse α -Al₈Fe₂Si phase becomes increasingly more likely [999]. The result is a significant reduction in ductility [988]. This effect should be taken into account when designing scrap-tolerant 3xx-series casting alloys.

The contaminant effects in 5xx-series alloys must be considered separately in the context of conventional binary alloys, conventional complex die-cast alloys, and recently developed die-cast variants for use in thin-walled structural components. As mentioned above, impurities should be avoided in corrosion-resistant binary alloys intended for decorative applications. These alloys usually have a polished surface whose optical quality is unacceptably reduced by second-phase particles. Thus Fe should be kept to a minimum, and Si content also requires particular attention. Thermodynamic calculations for solidification in non-equilibrium show that AlMg4.5 alloys with an Si content of 0.25 wt% already precipitate approx. 0.5 mol.% Mg₂Si from the residual melt [982], reducing ductility and corrosion resistance.

However, if increased strength with acceptable ductility is more important than high corrosion resistance, which is the case in many applications, increased scrap content may be considered. For this reason, Zhu et al. [1000] investigated the influence of Fe on the structure and properties of AlMg5 and AlMg5Mn0.6 alloys. The Fe content was varied systematically from 0 to 3.5 wt%. The Fe-rich intermetallics – monoclinic Al₁₃Fe₄ in AlMg5 and orthorhombic Al₆(Fe, Mn) in AlMg5Mn0.6 – influence the mechanical properties of the casting alloys significantly. Adding Fe increases the yield strength from ≈ 130 to 150 MPa, but significantly reduces elongation from 20 to 5%, independent of the Mn content. Nevertheless, elongations of $> 15\%$ are achieved at an Fe content of 1 wt%.

The available industrial secondary 5xx die-cast alloys feature a very wide range of compositions, which are defined in country-specific specifications. At an average Mg and Mn content of 4.5 wt% and 0.5 wt% respectively, the concentrations of Si, Fe and Cu vary considerably in the range of $0.3 < Si < 1.5$, $0.35 < Fe < 1.2$, $0.03 < Cu < 1.0$. The mechanical properties are accordingly rather modest. For example, for the alloy GK-AlMg5Si with an Si content between 0.9 and 1.5 wt% and an Fe content of 0.4 wt%, yield strength of 110–150 MPa and elongation to fracture of 2–5% were reported [1001].

Significantly more ductile variants of alloy type AlMg5Si2Mn have been successfully developed over the last few years [974,1002],

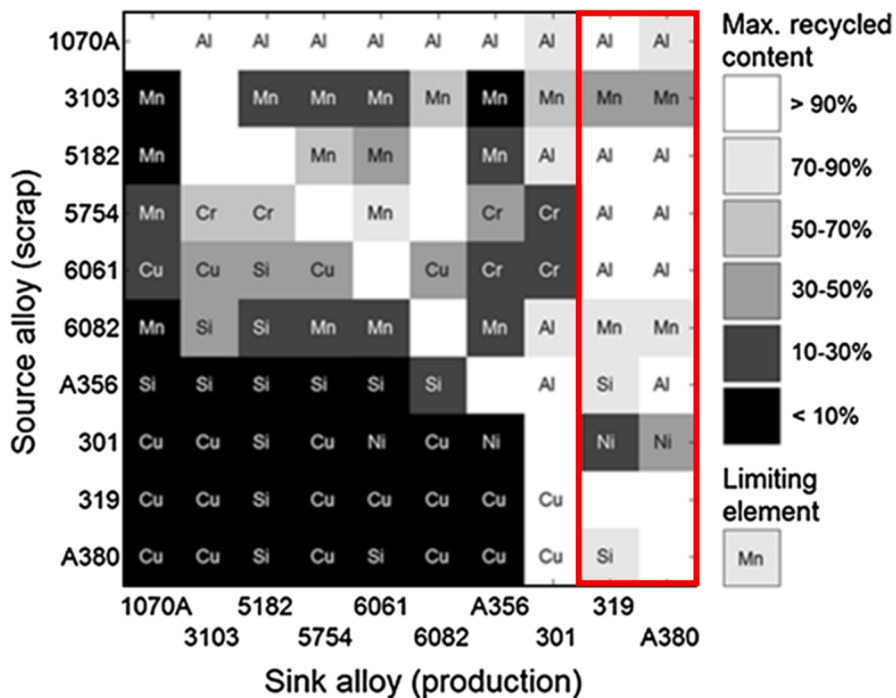


Fig. 63. Options for and restrictions on recycling paths of aluminum alloy series due to differing alloy content. The shades of gray indicate the percentage of a source alloy (scrap) that could be used in the production of the sink alloy. Reprinted with permission from [987].

with the aim of enabling the production of large thin-walled structural parts. The optimum composition of the alloy is specified as 5.0–5.5 wt% Mg, 1.5–2.0 wt% Si, 0.5–0.7 wt% Mn, 0.15–0.2 wt% Ti. Rods of 6.4 mm diameter produced by HPDC achieve yield strength values of 140 MPa at 18% elongation. Cu increases the tendency towards hot cracking and affect ductility. A content of 0.4 wt % already reduces the elongation to fracture by a factor of 2. An Fe content of up to 0.25 wt%, however, can be tolerated, because the increased Mn content enables the formation of a compact α -Al₈Fe₂Si phase [974]. At higher content the elongation to fracture decreases unacceptably. Adding 0.1–0.3 wt% Cr hinders the tendency towards die soldering [1003]. Higher contents should be avoided, as otherwise an Al₇Cr phase is formed, which significantly reduces ductility [1004]. In general, the effect of contaminants on the properties of alloy AlMg5Si2Mn can be regarded as rather moderate. However, during smelting it is important to reduce the content of alkali and alkaline earth elements as much as possible. Calcium and sodium are limited to a maximum of 15 ppm, as these increase the tendency of castings towards hot cracking and lead to reduced fluidity [975]. When using recycled material, monitoring the calcium and sodium content is strongly recommended.

Alloy design based on the crossover principle is proving an interesting method (see section 8.4). One example is new high-pressure die-casting alloys based on Al-Mg-Zn-(Cu) for structural cast components [1005]. Compared to the binary AlMg4.5 variants, the scrap-relevant elements Zn and Cu are also taken into account here as main alloying elements. A decisive advantage of these alloys is their potential for artificial aging. The experimental alloy with 4.8 %Mg, 3.4 %Zn, 0.8 %Mn and 0.5 %Cu is a good example. After pre-aging at 100 °C/3h, an aging treatment at temperatures in the range of 150 to 175 °C leads to a considerable increase in hardness within an industrially relevant time range of 2 to 20 h. The formation of T-phase (Mg₃₂(Al, Zn)₄₉) precursors is responsible for the age hardening [1005,1006].

The influence of Fe and Si contamination on the structure and properties of 2xx-series alloys can be best illustrated using the example of alloy 206 (AlCu4.5Mg0.25). Again, Fe is a property-determining impurity and is normally limited to 0.15 wt%. In addition, Si content is restricted to < 0.1 wt%. A study by Liu et al. [1007] showed how the Fe-containing IMCs are modified when alloys containing 0.15 wt% Fe are treated with Mn and Si. Adding either Mn or Si or both promotes the formation of the α -Al₈Fe₂Si phase and inhibits the occurrence of the β -Al₅FeSi phase. The cooling rate also has a positive effect on β - to α -Al₈Fe₂Si phase conversion. At 0.3 wt % Mn and 0.3 wt% Si the formation of the β -Al₅FeSi phase is completely prevented. In a further work [1008], the same group is examining Al-Cu 206 cast alloys with different Fe content in the range of 0.15 to 0.5 wt% at Si and Mn content of 0.1–0.3 wt% and 0.1–0.5 wt%, respectively. At comparable Si and Mn content the elongation to fracture decreases with increased Fe content due to the increasing volume and size of the Fe-rich intermetallic compounds. With a simultaneous Si and Mn content of 0.3 wt% each, quite good mechanical properties are achieved in condition T4, with a yield strength of 260 MPa and an elongation to fracture of ≈8%. Zhang et al. investigated the influence of Fe in the range 0.1 – 1.5 wt% for AlCu5 alloys with 0.6 wt% Mn and 0.1 wt% Si. In the squeeze-casting process, very good properties are achieved with an Fe content of 0.5 wt% ($R_{p0.2} \approx 220$ MPa, A≈18%). The latter two studies may serve as incentives in the development of contaminant-compliant 2xx-series casting alloys.

6.3. End-of use recycling of engine block alloys and gearbox housings

It can be assumed that the demand for cast components as aggregates of passenger cars will decrease as the electrification of private transport progresses [62]. Engine blocks and gearbox housings, for example, are nowadays made from composition-tolerant recycling alloys, mainly from the aforementioned alloys 319 and A380, for which there is no other relevant use requiring large quantities. If such cast components are returned to the scrap cycle at the end of the vehicles' lives, it is predictable that there will no longer be any direct recycling use for them due to their high Si, Cu and Fe content. This brings up the question of possibilities for metallurgical modification with the aim of alternative use in structural components subject to increased demands on mechanical and electrochemical properties. Three options can be mentioned here: (i) alloy and process design of scrap-tolerant alloys; (ii) alternative manufacturing processes which allow rapid solidification; and (iii) removal of contaminants by physical methods with reuse of the purified fraction.

(i) Alloy and process design were already mentioned above, and demonstrated with two examples. The first suggestion was to reduce the Cu content of A380 while balancing the Fe/Mn ratio. Such measures, however, require a willingness of industry and customers to break away from traditional standardization constraints. The second measure was the use of thermal treatment with the aim of dissolving a portion of the IMCs and spheroidizing the eutectic Si [98,986]. A prerequisite for this, however, is low gas content in the components to avoid blistering, which would require a vacuum-supported high-pressure die-casting process.

(ii) Alternative manufacturing processes which allow rapid solidification offer the advantage of refining the IMCs, which with their smaller size and reduced aspect ratio have fewer ductility-reducing effects. Examples are processes for additive manufacturing (AM) and the spray forming technique. The possibilities of AM are described in detail in section 9.1. In particular, a study by Suchy et al. [1009] is referred to there in which A380 powder was compacted by laser powder bed fusion, resulting in good mechanical properties. Here a brief reference is made to the experience with spray forming (Osprey). The recycling of contaminated casting alloys using the spray-forming technique is not a new approach. A series of publications show that the spray-forming production of Al-alloys with acceptable mechanical properties can be achieved even where there is high iron content [269]. Ferrarini et al. [268] investigated the structural and property changes of spray-compacted A380 and show that the spray-forming process can strongly suppress the formation of the β -Al₅FeSi phase. However, increased porosity levels are an inherent problem in spray forming, necessitating subsequent treatment by extrusion or forging to achieve ductility properties for structural applications [1010]. This significantly reduces the attractiveness of the process.

(iii) On the subject of removal of contaminants by physical methods, two techniques are addressed below which enable significant reduction in harmful contaminants. The first covers the separation of the solid phase and melt of alloy A380 in the semi-solid state, and the second the separation of sludge-forming IMCs by means of gravity or supergravity segregation.

In hypoeutectic alloys 319 and A380 in the semi-solid state, the chemical composition of the solid fcc-Al phase differs significantly from the basic composition, since the majority of the IMCs are precipitated in the melt. For example, for an AlSi8Cu3.5Mn0.55Mg0.5 alloy with 0.8 wt% Fe, the fcc-Al phase at 560 °C would have a mass fraction of ≈ 0.5 and a chemical composition of 1.38 wt% Si, 1.12 wt% Cu, 0.17 wt% Mg, 0.02 wt% Mn and only 0.003 wt% Fe (calculated with Pandat software using database PanAl2019 [982]). If the solid fcc phase is mechanically separated from the melt and the IMCs, considerable cleaning performance is achieved. Such a method is described in the Austrian patent specification AT412348B [1011]. It is based on the principle of mechanical squeezing of a liquid-filled sponge.

Sludge removal by gravity separation is based on the difference in density between sludge and melt. The literature reports on Fe reduction in Al-Si alloys by the intentional addition of Mn and Cr to form sludge (see section 6.2), which is then separated from the melt by physical sedimentation or centrifugation, but also by electromagnetic sedimentation or filtration [1012–1016]. At this point, instead of detailing the various processes, an estimation of the purification potential of sludge removal in alloy A380 is useful. It is based on thermodynamic calculations using Pandat with the database PanAl2019 [982]. For alloy A380 (AlSi8Cu3.5Mn0.55Mg0.5Fe0.8) at 620 °C, which is about 30 °C above the liquidus temperature of the fcc-Al phase, Table 17 shows the calculated values for the mass fraction of the α -Al₈Fe₂Si phase (V_α , sludge to be removed) and for the composition of the melt (without the α -Al₈Fe₂Si phase). The data are given for the original alloy with 0.8 wt% Fe and 0.55 wt% Mn, and after addition of 1.0 wt% Mn and 1.5 wt% Mn. The calculated data indicate that optimal process control of the sludge removal may enable the Fe level of the secondary alloy to approach that of a primary alloy.

7. Effects of scrap-related impurities in wrought alloys: Constitution, microstructure, processing and properties

7.1. Brief introduction to wrought alloys

Unlike cast aluminum alloys, wrought alloys have narrow and sometimes low compositional limits. This means that wrought alloys do not easily absorb mixed alloy scrap streams and that primary aluminum remains an important backbone for them [72,171,172].

The alloying elements used in the wrought aluminum alloy series 1xxx to 8xxx are listed in Fig. 64. For typical alloys within the different classes, major, common minor and less common minor alloying elements according to [1017,1018] are indicated. Elements are considered to be intentionally added if there are a lower and an upper limit in the composition range of the standard. Based on the allowable compositional ranges, some critical elements can be specified (Fig. 64) and these can give a first indication of whether or not a wrought alloy series is easy to recycle and tolerates impurities. The 1xxx, 7xxx and 8xxx series are considered “tough” (to produce from scrap) due to the compositional restrictions set by current standards. The 2xxx and 6xxx series can be judged as “challenging”. Only the 3xxx and 4xxx wrought alloys exhibit a “moderate” challenge for production from scrap. The most problematic elements according to this evaluation are Fe, Si, and Cu, and these are well known in the aluminum recycling community [51].

Ashkenazi et al. [1019] provide a rather long list of problematic impurities from recycling which includes Cr, Cu, Fe, Mg, Mn, Ni, Pb, Si, V and Zn. Their list is consistent with Fig. 64, but also includes minor common alloying elements as critical (here Pb, Ni, V). From this it is important to acknowledge that not only the main elements present in the different alloy classes can cause problems upon recycling; even trace elements present in specific alloys can have drastic effects on other wrought alloys. For example, adding a few parts per million of Sn can dramatically suppress or accelerate aging behavior in 6xxx [553,555] and 2xxx series alloys [383] respectively. Nowadays Sn is used as a substitute for poisonous Pb in some alloys for machining operations, to enhance chip breaking [341,1020]. Other exotic elements are also often used in 8xxx-series alloys, which are sometimes referred to as miscellaneous alloys [970]. However, the introduction of new or exotic alloying elements in alloy development needs to consider their impact on other alloy classes and the implications for recycling. Most recent studies have considered such impacts from a very general perspective without examining the detailed metallurgical effects such elements may have [71,1021]. In the recycling of scrap from the automotive sector a comprehensive analysis was in fact performed to examine whether Ce, which may be used in some new casting alloys, will impact the future properties of alloys produced from recycling [1022]. However, up to now this type of study seems to be the exception rather than the rule.

Fig. 65 displays the tensile properties covered by wrought aluminum alloys. A broad range of properties are covered by classes 1xxx to 8xxx. Alloys where the properties are most sensitive to contamination by tramp elements are indicated by colored group contours.

There is no obvious direct correlation between the properties presented in Fig. 65 and sensitivity to tramp elements. However, it is clear that the alloys providing the extreme values for yield strength or elongation are subject to “tough” compositional restrictions in the context of recycling. With decreasing yield strength and elongation values, the compositional restrictions change from “tough” to “challenging” and finally to “moderate”. In other words, the most-developed alloys from the material point of view are also the most difficult to recycle. This may indicate an inherent connection, or simply that recyclability was not explicitly considered by materials scientists in alloy design over the last few decades.

The alloy series where the impurity content is critical comprises the high-strength alloys often used in aircraft [78]. The content of Fe and Si as tramp elements is especially crucial in the 7xxx series, but also in the 2xxx series of alloys frequently applied in the aircraft industry [1017]. Besides the high-strength alloys, very soft alloys like the 1xxx series are also highly sensitive to elements such as Mg (see Fig. 64). Those alloys are typically used in foils (e.g. for food equipment), decorative and gloss applications, heat shielding plates or electric applications [1017,1018]. Some alloy series exhibiting medium strength and elongation values are less sensitive to tramp elements (Fig. 64). These mostly involve 3xxx-series alloys, which are used heavily in beverage cans [1017,1018]. 3xxx-series alloys are also utilized in architecture and as the core material in heat exchangers, where 4xxx series alloys are often applied as clad material for soldering applications [1018]. In contrast, other lower-to-medium-strength alloys such as the 5xxx series alloys feature tight Si

Table 17

Thermodynamically calculated values for the mass fraction of the α -Al₈Fe₂Si phase, V_a, and the chemical composition of the purified melt [in wt.%]; alloy A380 with 8 %Si, 3.5 %Cu, 0.5 %Mg, 0.55 %Mn and 0.8 %Fe at 620 °C.

	V _a	Si	Cu	Mg	Mn	Fe
A360 (0.8%Fe, 0.55%Mn)	0.0153	7.97	3.55	0.51	0.30	0.60
+ 1.0 at.% Mn	0.054	7.88	3.70	0.53	0.50	0.28
+ 1.5 at.% Mn	0.071	7.83	3.77	0.54	0.57	0.20

limits and, in several cases, tight Cu limits. These alloys are typically deployed for inner panels in automotive applications or for other structural parts in transportation, pressure vessels, boat hulls and ballistic armour plates [1024–1026]. The 6xxx-alloy class is judged to be moderate according to Fig. 64, but actually shows diverse tolerance limits if examined in more detail. Fortunately Si is a major alloying element in 6xxx-series alloys and thus tight compositional control is not critical. However, some alloys exhibit strict Fe tolerance limits, and others strict Mn tolerance limits. This strongly depends on the actual alloy application, which ranges widely for the 6xxx series and encompasses transportation, automotive industry and mechanical engineering [1017,1027,1028].

Combinations of different wrought alloys series are deployed in several fields of application. In the following we discuss how wrought-alloy diversity impacts potential recycling in three specific cases: beverage cans, automobiles and aircraft.

Recycling of old scrap for aircraft alloys seems very difficult, because the alloys involved are typically in use for a long period and tolerance limits are very strict (especially in the 7xxx series, but also in some 2xxx wrought alloys), excluding nearly all impurity elements (Fig. 64). One reason for the low tolerance of Fe and Si impurities, which can form brittle IMCs, are aircraft applications' stringent fracture toughness requirements [1029,1030]. Manufacturing for the aircraft industry usually involves complex machining operations, and typically a high proportion of the material is lost during production (this is known as the “buy to fly ratio”) [3,1031]. Here closed-loop recycling may be an option [1032]. There the challenge is more logistical than metallurgical. Nevertheless, the issue of old-scrap recycling will also arise in this area, and solutions must be found to the problem of narrow tolerance limits for tramp elements.

Aluminum beverage cans present an extreme contrast to the situation described above. Today packaging is the second-largest source of aluminum scrap, and here cans are a well suited example to the transition towards a circular economy [30]. Can usage time is relatively short, and the recycling of used beverage cans (UBC) is well established [30,299]. In some countries with dedicated collection systems (i.e. Finland [30]) the recycling rate is as high as 97%. The composition of UBCs is very suitable for recycling because few alloys are involved (i.e. 3004 for the body and 5182 for the lid [30]). Therefore recycling is simple as to composition; the fact that the main alloy system (3xxx) is moderately tolerant of foreign elements (Fig. 64) is also helpful. Other types of packaging scrap may even be deployed for cans. However, according to recent work can-to-can recycling seems the better option with regard to climate change [30].

ALLOYING ELEMENTS					
Alloys	Major	Minor (common)	Minor (less common)	Critical limits	
1xxx	Al	Si, Fe	-	Mg, Mn, Zn, Cu, Ti	
2xxx	Al, Cu	Mg, Mn	Si, Fe, Zr, Li, Ni, Cr, Zn, Pb, Bi	Fe, Si (some alloys)	
3xxx	Al, Mn	Mg, Cu	Fe, Si	Cu (some alloys)	
4xxx	Al, Si	Mg	Mn	Mn, Mg (some alloys)	
5xxx	Al, Mg	Mn	Cr, Zr, Cu, Zn	Si, Cu (most alloys)	
6xxx	Al, Mg, Si	Cu, Mn, Cr	Fe, V, Zn, Bi, Pb	Fe, Cu, Mn (some alloys)	
7xxx	Al, Zn, Mg	Cu, Mn, Cr, Zr	-	Si, Fe	
8xxx	Al	Fe, Si, Cu	Sn, Ni	Mg	

Compositional restrictions:

- tough
- challenging
- moderate

Fig. 64. Alloying elements in wrought aluminum alloys and their critical limits (sorted according to the most common alloys given in [1017,1018]).

The third complex, challenging and most important example of aluminum in terms of recycling is automotive. Today's automotive industry is already the largest consumer of secondary aluminum due to the huge number of used castings that are relatively easily recycled into other castings [72]. All car manufacturers have increased their use of aluminum over the last few years because it is lightweight, and this is forecast to increase further (see Fig. 66) [72].

At the same time, however, vehicles' wrought alloy content (sheets, forging and extrusion) is strongly increasing [44,71,72,987,1033]. This is illustrated in Fig. 67, which shows the tremendous growth in scrap potentially available from automotive body sheet (ABS) material [36]. This colossal wave of ABS scrap requires us to think carefully about appropriate recycling strategies. This is even truer if we consider that Zhu et al. [36,113] calculated that in the best-case scenario in 2017, only 70% of aluminum scrap could be recycled domestically in the US due to compositional constraints. Currently the issue is partially masked by scrap exports (in particular to China, and concerning mainly shredded auto scrap). A further increase in demand for wrought alloys, to produce power-supply boxes in electric vehicles, is predicted [168].

Without a technological leap, the huge increase in wrought products in the automotive sector may become incompatible with current casting-focused recycling of end-of-life vehicles (ELVs), or even generate excess scrap by reducing automotive casting demand (at present the automotive industry is the biggest consumer of secondary castings) [35,72]. The complexity of the problem is amplified because data is lacking on the alloy quantities and types needed in future ELVs [72]. This is a general problem, because most data sources list only the total amount of aluminum produced in wrought, cast or extruded form, and data on specific alloys are seldom available [72]. Table 18 shows some typical alloys used in various different aluminum components in cars [72].

In Table 18, while the problem of mixed cast and wrought alloys is not addressed, the large number of different wrought alloys used in cars is immediately apparent. 1xxx, 2xxx, 3xxx, 4xxx, 5xxx, 6xxx and 7xxx alloys have all been deployed there. However, the most frequent automotive wrought alloys are the 6xxx, 5xxx and 3xxx series [72]. Besides the fact that contamination from cast alloys is problematic for most wrought alloys, recycling the wrought material from cars into new wrought alloys is a great challenge [36]. This can be deduced by comparing alloying limits (Fig. 64). A good example considers the mix of 6xxx and 5xxx series alloys, which are typically tightly joined as inner (e.g. 5182) and outer (e.g. 6016) car door parts [1034]. Although Mg is a major alloying element in 6xxx alloys, the Mg content limit can be more than one order of magnitude lower in 6016 series alloys than in 5182 series alloys [1017,1018]. Even more problematic is the very low Si limit in 5xxx series alloys: Si content can be >7 times higher in 6016 than in 5182 [1017,1018]. The metallurgical origins of these tight controls are discussed in subsequent sections.

Drastic improvements in sorting technology are clearly mandatory if wrought alloys are to be recycled efficiently to new wrought alloys in ELVs. Full separation of alloys is not currently possible, because shredder-based recycling practices show natural limits when faced with complex product designs and the various associated joining means [1035]. Hence impurity levels will rise along with the increase in the number of different alloying elements, because of the various types of wrought alloys used [72]. The growing number of alloys used in cars will generate a concurrent increase in joining means such as screws, rivets and adhesive bonding, while welding will decrease [116]. The trend towards multi-material design will reduce the potential of higher-purity wrought alloy recycling streams and increase the proportion of material with a higher Fe content [116,1036,1037].

IMCs which contain Fe can be present in most wrought alloys in the form of brittle needles or plates, and are known to cause detrimental effects such as crack initiation [78,252], reduced ductility and bendability [322], reduced fracture toughness [1017] and

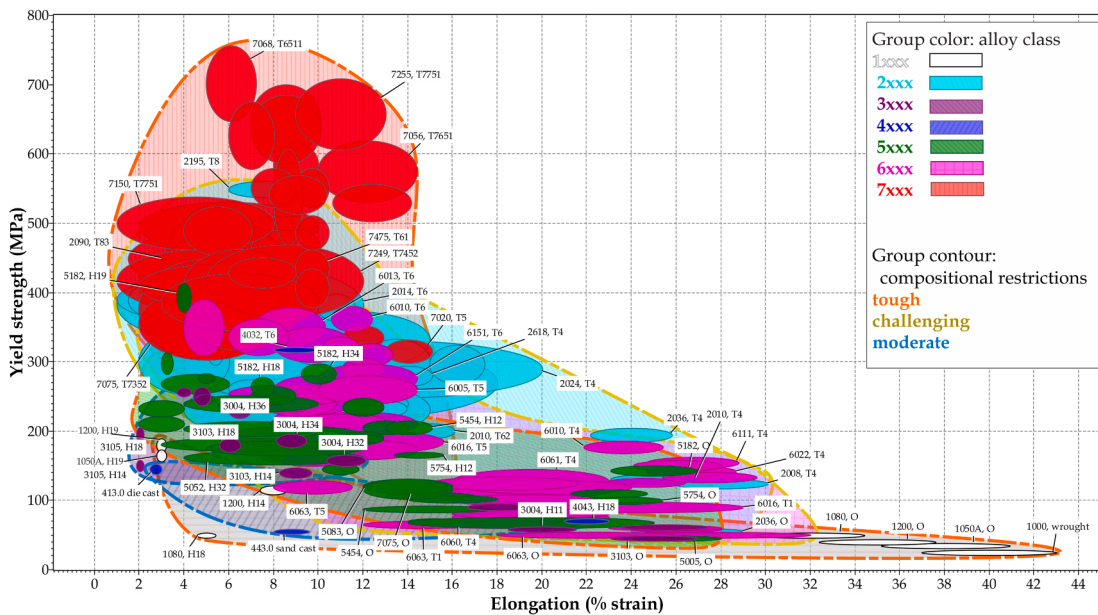


Fig. 65. Comparison of tensile properties for 1xxx to 8xxx wrought aluminum alloys. Alloys where properties are most sensitive to contamination by tramp elements according to the evaluation in Fig. 64 are indicated [1023].

deteriorated surface finish [1038]. However, in wrought aluminum alloys Fe is not solely detrimental. In 1xxx and (especially) 8xxx series alloys, the situation is reversed: high fractions of Fe-containing IMCs are required to control the grain size and properties of foil [1039].

Despite their importance, the effects of Fe-containing IMCs have not been studied as intensively in wrought alloys as in cast alloys, because most contaminated old scrap usually goes for the production of cast alloys. This section briefly addresses only wrought alloys or the basic principles of Fe-containing IMCs. Details on the effects of specific Fe-containing IMCs can be found in the corresponding sections on specific wrought alloy classes.

Fundamental research on Fe-containing IMCs, such as the recent first-principles study by Fang et al. [1040] on the solubility of Si in some Fe-containing IMCs, is gaining increasing importance in light of the implications for recycling. Feng et al. [1041] also recently studied the formation of primary Fe-containing IMCs using in-situ X-ray radiography. They report a correlation between inoculation by TiC and TiB₂, the solidification conditions and an increased number density of Fe-containing IMCs [1041]. Similar to the basic studies of the Al-Fe system in [1041–1043], there have been attempts to better control the size, distribution and morphology of Fe-containing IMCs [1044–1047] by understanding the fundamentals of nucleation, growth and phase selection, in order, potentially, to facilitate better toleration of higher Fe content in wrought alloys [1044–1050]. Efforts have also been made to search for potent nuclei for primary Fe-containing IMCs, at least for cast alloys [175]. However, while some authors reported a weak inoculation effect of α -Al₂O₃, TiC and TiB₂ [1049] in experimental alloys near the 1xxx series, Lui et al. [1046] suggested that TiB₂ might be associated with nucleation of Fe-containing IMCs in 6xxx alloys. Many questions remain in this important field of phase selection.

Another element whose limit is often considered critical in wrought alloys is Si (Fig. 64). Si is present as a major element in cast alloys to improve casting properties. It is also seen in the 6xxx series of wrought alloys, but can have severe negative effects in other classes. Highly sensitive alloys include the 7xxx and 5xxx series, because there Si can generate large, brittle IMCs. For example, if Mg content is high, the primary Mg₂Si phase will form even at low Si content [78]. Primary Mg₂Si particles have been shown to initiate fracture even at low strains [877].

A third element that is critical in some wrought alloys is Cu (Fig. 64). Cu is the main element for age hardening in 2xxx series wrought alloys, and also promotes strength in other alloy classes such as the 6xxx and 7xxx series. However, Cu can negatively affect corrosion properties [1017]. This problem is often discussed in the context of the automotive applications of 5xxx and 6xxx series alloys. However, many 6xxx series alloys used in the automotive sector contain Cu as an alloying element. Even incorporation of Cu in automotive 5xxx series alloys to mitigate strength loss upon paint baking has recently been examined [1051]. It is true that some corrosion properties can deteriorate here, but they can also be kept above a level satisfactory for the application; and Cu can even improve performance in the area of specific corrosion types [1052]. A similar effect is known in 7xxx series alloys, where adding Cu mitigates stress corrosion cracking [1053]. Nevertheless, it is a fact that many wrought alloy standards place tight restrictions on Cu.

In conclusion, it must be emphasized that in general there is no such thing as a “bad element” in wrought aluminum alloys. All

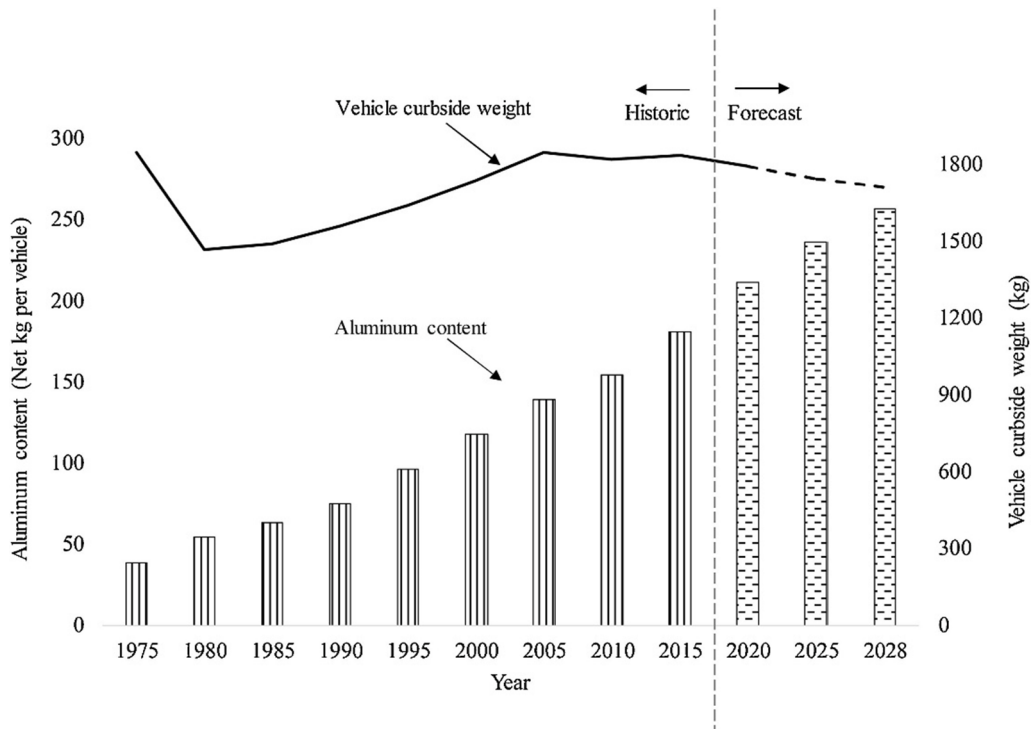


Fig. 66. Average vehicle curbside weight and the aluminum content in cars in North America. Reprinted with permission from [72].

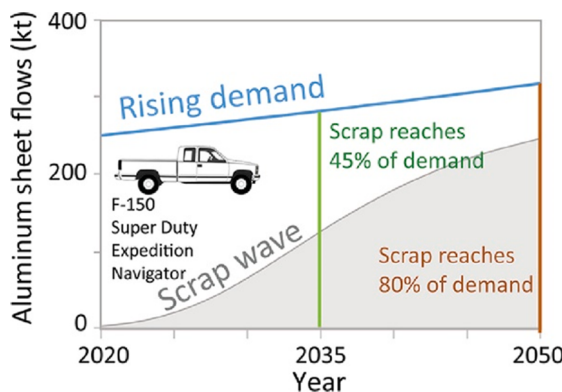


Fig. 67. Estimation of the ABS scrap generated by vehicles with the highest US sales: Ford F-150, Super Duty, Expedition, and Lincoln Navigator. Reprinted with permission from [36].

Table 18

Typical alloys utilised by the automotive industry. Reprinted with permission from [72].

Body & Inner Panel	Body Closures	Heat Exchangers	Heat Shields	Misc. Engine
2008, 5030, 5052, 5182, 5454, 6009, 6016, 6111 Cradles & Frames	2008, 2036, 6009, 6016, 6010, 6383, 6061, 6111 Wheels	6060, 6061, 6063, 6106, 5049, 7072, 1145, 4047, 4004, 4045, 4343, 3003, 8079, 6006, 1200, 1050, 1100 Steering System	1056, 3003, 5052, 5182 Fuel System	226, AlSn20Cu, AlZn5Bi4 Engine/ Cylinders
	5182	6082, 7108, 7021	6063, 3103, 5049, 5754	380, 319, Al-Si
Collision 6013, 7021, 7029	Brake System 359 or 360 + SiC	Suspension Parts AlSi7Mg, 6013, 6082	Trans 380.2	Pistons 4032

elements introduced by recycling can have positive effects. Even the impurity most often discussed in the literature, Fe, is beneficial in 8xxx series alloys. It is, rather, the combination of a certain wrought alloy with a certain tramp element that causes problems. A holistic view of the effects of elements in alloys can help to allay the specific problems caused by some currently unavoidable tramp elements in wrought alloys.

7.2. Use of scrap in 1xxx and 8xxx alloys for electric, decorative, chemical and packing products

As Fig. 65 indicated, the 1xxx and 8xxx series alloys for electrical, decorative, chemical and packaging products are very sensitive to many accompanying elements. Table 19 shows their typical compositions and respective uses. 1xxx alloys are subject to very tight limits on most of the important alloying elements used in other wrought alloy classes. These alloys include Mg, Cu, Mn and Zn, which are often kept below 0.05 wt% in alloys used in food equipment, decorative and shiny applications and heat protection plates [1018,1054]. It is thus immediately clear that given such strong restrictions on impurities, no other wrought alloys recycled from old scrap can be used in these types of product. Hence production is highly dependent on primary aluminum, and only alloy-to-alloy recycling (e.g. from production scrap) is an option. This also applies to some electrical and electronic products which use 1xxx alloys with high-purity aluminum (e.g. 1199 with 99.99 wt% Al) [1054].

In the past, alloys of the 1xxx series (e.g. 1145, 1100, and 1200) were widely used for foil stock [1054]. However, due to increased demands on strength and ductility higher levels of Fe (up to 2 wt%), Si (up to 1.1 wt%) and sometimes Mn (up to 1.0 wt%) are now often used in foils to control the microstructure during recovery and recrystallization via IMCs, which turned those alloys from 1xxx to 8xxx series alloys [1039,1054]. High levels of Fe increase the strength of foils (unlike that of all other wrought products), and generates ductile material behavior via IMCs. Fe acts as effective grain refiner (highly important in thin foils) [1039]. Fig. 68 shows one of the rare cases where Fe is a welcome element. Here Fe acts in exactly the opposite way than it does in aluminum alloys used for structural applications. Instead of limiting ductility, it increases elongation when its amount is increased. However, this is an indirect effect and results mainly from the increase in the volume fraction of IMCs acting as grain refiners upon recrystallization, as the maximum Fe content in the solid solution is only 0.05 wt% [1039].

In the recycling of 8xxx alloys used for foils, the situation is essentially the same as for 1xxx alloys. The limits on elements other than Si and Fe are only in rare cases slightly less stringent than in 1xxx alloys, and production from old scrap via recycling is difficult.

A more differentiated picture emerges when considering the use of these 1xxx and 8xxx alloys in recycling for the production of other alloys. The high-purity and 1xxx alloys are the ideal starting material in terms of composition and are comparable to primary aluminum in terms of composition. However, recycling then takes place as downcycling in a cascade recycling chain, with such low-

alloy aluminum at the top of the cascade [169]. However, with increased amounts of Fe and Si, using 1xxx and especially 8xxx alloys becomes more challenging (compare with Fig. 65). Although mixed packaging waste might be deployed in (e.g.) can bodies, Niero et al. saw can-to-can recycling as more sustainable [30]. In this context, it is important to know that the EU has a target of recycling > 75% of packaging waste in the next few years [30].

Packaging scrap from households is typically sorted into ferrous and non-ferrous alloys, resulting in a mixture of cast and wrought alloys which is mostly absorbed in cast alloy production. This results in continuous downcycling of the wrought scrap fraction [31]. According to Paraskevas et al. [169], container and packaging scrap might theoretically be managed using a separate closed-loop recycling strategy for the same applications, which may solve the problem.

Different alloys are often used in rather similar products, increasing recycling complexity and making scrap separation in particular more challenging. A good example are wrought alloys used for heat exchangers, where (among others) both 1xxx and 8xxx alloys are deployed. The variety of alloy types in heat exchanger components shown as an example in Fig. 69 necessarily produces a large number of tramp elements [72].

The 1xxx and (even more) the 8xxx alloys intentionally contain Fe, an element which is typically detrimental to most other wrought alloy series. Allen et al. [1048] summarized the various stable and metastable phases which can be present in 1xxx alloys. Although only the phase FeAl_3 (often denoted as FeAl_3 , but structurally complex with 100 atoms / unit cell) exists at dilute conditions in binary Al-Fe in the thermodynamically stable state, [1048] lists at least 6 structurally distinct phases in that form under industrially standard non-equilibrium solidification conditions. The presence of Si further increases the phase complexity of the compositionally simple 1xxx alloys. Eight structurally different phases are listed for the common α - and β - Al_5FeSi phases [1048]. Fig. 70 shows the composition ranges of some of the most common phases in dilute Al-Fe-Si alloy systems.

It is significant that the phase selection can be influenced by varying the casting conditions (local solidification velocity, cooling rate, grain refinement). In compositionally simple systems the underlying mechanisms of nucleation and growth in Fe-containing IMCs have been much investigated. Because it is important to control the size and change the morphology and distribution of Fe-containing IMCs [1048,1049,1055,1056], existing basic information on 1xxx alloys may be an interesting source of knowledge in the effort to better control Fe-containing IMCs in other wrought alloys with high recycling content. Further properties such as corrosion have also been investigated in these alloys. For example, Dorin et al. [1057] showed that an increased cooling rate upon solidification has a positive influence on corrosion properties. Therefore direct strip casting was concluded to be an interesting candidate technology for improving the recyclability of Fe-containing Al-alloys, as it enables high solidification rates.

Several more exotic manufacturing and industrially less-common methods were studied in the context of Al-Fe alloys with high Fe content. This includes work on rapid solidification [1058–1060], mechanical alloying [1061–1063] and severe plastic deformation [1064,1065]. Such work may also provide useful knowledge for the future recycling of high-Fe aluminum scrap.

7.3. Use of scrap in 2xxx alloys intended for high-strength components

7.3.1. Introduction

With the development of the duralumin alloy, the Al-Cu-based 2xxx alloy family gained the first age-hardenable aluminum alloys used in high-strength aerospace applications [1066]. Today this alloy family comprises three main sub-types, based on their combination of solute elements: (i) Al-Cu based alloys, strengthened by the θ - Al_2Cu precipitation sequence including GP zones, θ and θ' phases (typical alloys: 2219, 2017) [1067]; (ii) Al-Cu-Mg alloys, strengthened by the S- Al_2CuMg precipitation sequence including clusters, GPB zones, and the S phase (typical alloys 2024 and its variations 2124, 2524, 2624) [1068,1069]; and (iii) Al-Cu-Li-(Mg) alloys, strengthened by combinations of phases, including $\text{T}_1\text{-Al}_2\text{CuLi}$, δ' - Al_3Li , and the phases of the two aforementioned sequences (typical alloys 2195, 2198, 2099, 2070) [1070–1072].

7.3.2. The role of impurities in 2xxx alloys: Chemistry effects

2xxx series alloys are generally used in high-strength components. The Li-containing alloys reach strengths comparable to those of 7xxx alloys. Al-Cu-Mg-based alloys are frequently used in tension, so their damage tolerance is of paramount importance. The fatigue resistance of these alloys is also one of their key properties in such conditions. Al-Cu-based alloys are used primarily at elevated temperatures, with high Cu levels (up to 6 wt%).

In all these alloys, evidence has shown that coarse intermetallic particles are the primary cause of fracture [891,1073–1075] both during initiation (short crack nucleation) and final fracture (toughness-controlled). The damage tolerance has been shown to be degraded when the amount of Fe in particular is increased [1076–1078]. This effect may be linked to the phase diagram of the Al-Cu-Fe

Table 19

Typical compositions and uses of 1xxx and 8xxx wrought alloys [1054].

Designation	Si	Fe	Cu	Mn	Mg	Zn	Cr	Ti	Comments/Typical application
1100	1 (Fe + Si)		0.05–0.20	0.05		0.10			Al > 99/Foils, sheets, plates, tubes, wires spun hollowware, food equipment
1200	1 (Fe + Si)		0.05	0.05		0.10		0.05	Al > 99/Foils,
1145	0.55 (Fe + Si)		0.05	0.05	0.05	0.05		0.03	Al > 99.45/Foils, sheet, semi-rigid containers
1199	0.006	0.006	0.006	0.002	0.006	0.006		0.002	Al > 99.99/Electrical and electronic foil
8011	0.50–0.9	0.6–1.0	0.10	0.10	0.05	0.10	0.05	0.08	Household foils, bottle caps,
8006	0.40	1.2–2.0	0.30	0.30–1.0	0.10	0.10			Foils, finstock for heat exchangers

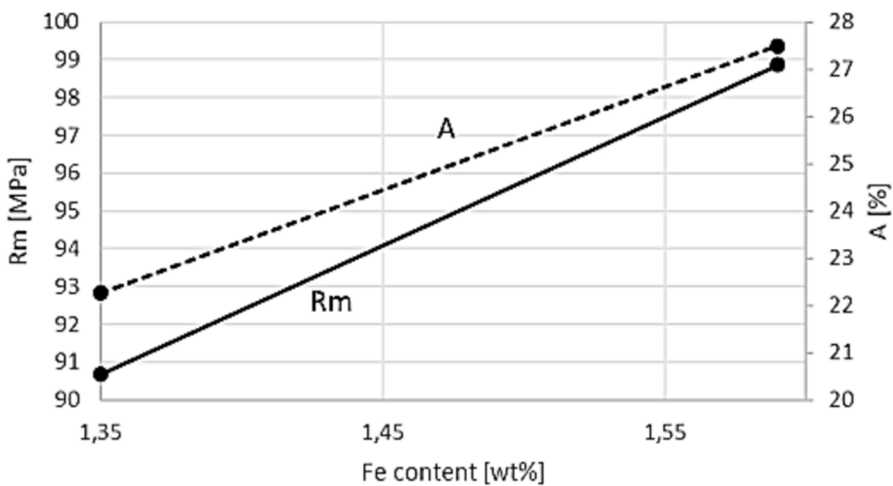


Fig. 68. Effect of Fe content on strength and elongation of 8021 foil in the O-temper. Reprinted with permission from [1039].

system [1079,1080]. Adding Fe in the presence of Cu induces the formation of the $\text{Al}_7\text{Cu}_2\text{Fe}$ phase (denoted as β or ω) in the form of elongated, brittle platelets [1081] during solidification. In addition, the presence of Fe-containing intermetallics may reduce the alloy's corrosion resistance [943].

The effect of adding Si has mostly been investigated in tandem with the addition of Fe, because the two are usually added or removed together when the alloy's purity is modified. However, Si has a more complex effect: it can be associated with some of the hardening precipitates, such as the S phase in the 2024 alloy [1082], or change the precipitation sequence with the appearance of the Q phase and its precursors, as well as induce the formation of complex multi-component intermetallic phases [1083].

Other impurities may enter the alloys if mixed with other families by recycling. Adding Mn is a useful way to modify the nature of intermetallic particles, favoring phases such as $\text{Al}_6(\text{Fe},\text{Mn})$ or $\text{Al}_3(\text{Fe},\text{Mn})$ and changing the $\beta\text{-Al}_5\text{FeSi}$ phase into the less detrimental α phase (in association with Si) [1084]. When coupled with Zr, Mn can be a very useful addition to an Al-Cu binary alloy to stabilize θ' precipitates through interfacial segregation, providing exceptional thermal stability and high-temperature strength [719,1085]. Adding Ni may also change the nature and morphology of Fe-rich intermetallic particles [249].

If mixed with 7xxx scrap, 2xxx alloys may end up with some Zn content. This addition was shown to be favorable, strength-wise, for

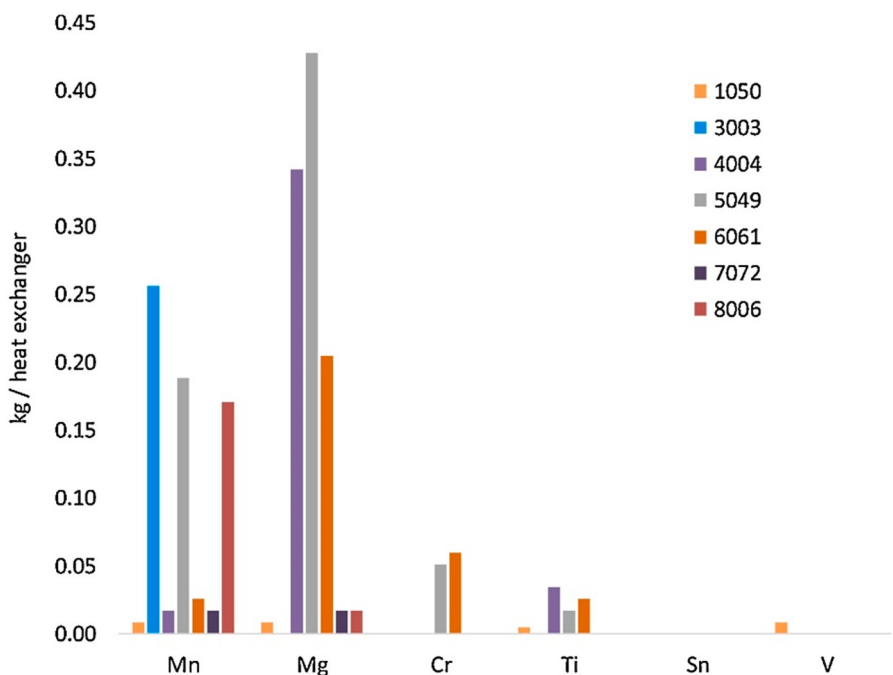


Fig. 69. Range of elements in different heat exchanger alloys. Reprinted with permission from [72].

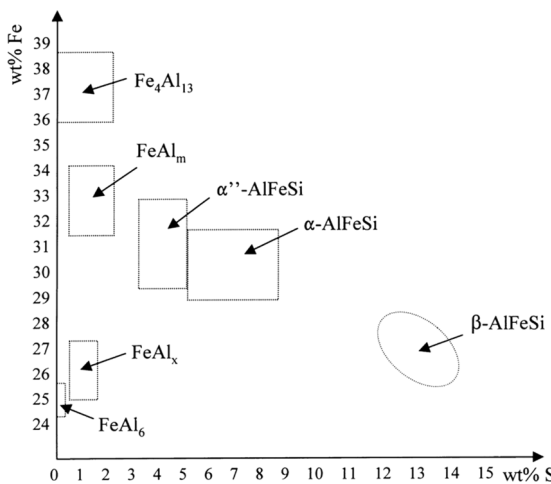


Fig. 70. Compositions of common IMCs in dilute Al-Fe-Si systems. Reprinted with permission from [1048].

the Al-Cu-Mg-based 2024 alloy [1086] and for Al-Cu-Li-Mg-based alloys [1087,1088], due in both cases to the incorporation of Zn into the strengthening precipitates. The affinity between Li-containing alloys and 7xxx alloys was confirmed by the discovery in 7xxx alloys of the Y phase [1089], which shows a striking similarity to the highly beneficial T1 phase in Al-Cu-Li [801,1090].

Other minor additions have been used to improve the properties of 2xxx alloys, in particular Sc, which in conjunction with Mg was shown to improve the elevated temperature strength of the 2219 alloy [1091,1092]. However, these are unlikely to be added through recycling.

7.3.3. Mitigating the role of impurities by processing

The detrimental effect of Fe-rich intermetallics on Al-Cu alloys is (besides their brittle nature) largely due to their size, which often exceeds 10 µm in some directions. Some of the detrimental effects of these phases can be mitigated by specific processing techniques.

When processing in the liquid phase, squeeze casting under pressure was investigated with Fe amounts of up to 1.5 wt% [1084,1093]. It was shown that the applied pressure promotes the formation of less detrimental phases, improving ductility in comparison with conventional casting routes. However, the degradation of fracture properties is still clear, at above 0.5 wt%.

Another processing approach is to cast under in conjunction with ultrasonic treatment. This method has been shown to promote higher dispersion of intermetallic particles and therefore lead to higher ductility in the final product [1094].

Fine-scale microstructures can be obtained by additive manufacturing, although Al-Cu alloys are prone to hot cracking and thus difficult to process in this way [1095]. However, Al-Cu and Al-Cu-Mg alloys have been processed successfully by laser power bed fusion, with a microstructure comprising fine-scale intermetallics [1096–1098].

The other possibility for reducing the size and improving the dispersion of intermetallics is to deploy plastic deformation. Very high-strain processes such as high-pressure torsion or equal angle channel processing are the most efficient, but are not very practical. Among more scalable processes, multi-directional forging was shown to be an efficient way to induce the spheroidization of intermetallics in alloy 2219 [1099], and friction stir processing was shown to cause a similar effect [1100].

7.4. Use of scrap in 3xxx and 4xxx alloys intended for packaging, buildings and infrastructure

Wrought aluminum alloys of the 3xxx series use Mn as a major alloying element, usually in the range of between 0.5 and 2 wt% (see Table 20). They can also contain Mg, Cu and Si as minor alloying ingredients. Interestingly, Mn is – among all the conventional alloying elements used in Al – the most sustainable in terms of emission and energy footprint. Additional Mg doping (0.8–1.3 wt%) increases solid solution strength and strain hardening. 3xxx alloys are usually not heat-treatable and are strengthened by cold working. Al-Mn alloys have moderate mechanical strength, weldability, very high formability and excellent corrosion resistance. They are used predominantly in products such as thin sheets for beverage cans and similar rigid containers, foils, roof sheets, cooking utensils and radiators. The fine dispersoids in 3xxx alloys tend to decorate grain boundaries and stabilize the alloys against grain coarsening during annealing, providing Hall-Petch strengthening and maintaining high formability. Mn also improves castability and reduces shrinkage during solidification [1101].

Recycling of 3xxx alloy materials is an important topic due to their sometimes very short lifetimes, particularly when serving in packaging. However, 3xxx alloys used in buildings (such as for roofs) have very long lifetimes and often enter the recycling stream only after several decades.

In the context of packaging it must be considered that cans consist of 2 different alloys: the lid is made of a slightly different alloy than the aluminum used for the base and sides. The body of the container is generally made of 3004 or 3104 alloys, which have similar chemical compositions (about 1 wt% Mn, 1 wt% Mg, up to 0.25 wt.%Cu). Some variants can even tolerate quite high Fe content (up to

0.7–0.8%). The lids consist of the 5182 alloy, with about 4–5 wt% Mg and only 0.20–0.50% Mn. The third alloy, usually 5042 with less Mg but similar Mn content, is used for the opening bank, and makes the smallest contribution to the total bank weight. Because these 3 alloy groups are chemically quite compatible, the whole product can essentially be remelted. This also applies to the minor alloy ingredients, i.e. the Cu, Si, Fe and Mn values in the 5182 alloy are in principle all below those of the 3004 alloy. This means that the joint remelting of the two introduces no impurity incompatibilities. The only exception here is Mg, which is considerably higher in the 5182 alloy than in the 3004 alloy. However, owing to its higher oxidation tendency compared to the base metal, Mg is substantially reduced in the remelting process and also during fluxing and purification [1102].

Recent developments in machine-learning-enhanced LIBS-based scrap sorting are currently improving alloy separation even among these rather closely related materials (i.e. 3xxx and 5xxx alloys) [59,769,781,1103,1104].

Another aspect of high relevance for recycling of packing alloys is the use of paint. It was observed that Ti in particular can intrude as a paint debris contaminant into melts produced from secondary sources [119,123,127]. This suggests that such contamination should be prevented by removing any paint by adequately pre-treating the scrap and properly adjusting the melting temperature.

Wrought Al-Si silicon alloys of the 4xxx alloys series form only a small group in the overall alloy market. They include both heat-treatable and non-heat-treatable materials, although most of them (except alloy 4032 with 1 % Mg and alloy 4145 with 4% of copper) are non-heat-treatable. Besides their major alloying element, Si, they may contain Cu, Mg, Ni and Be as minor alloying ingredients. Si is blended in these materials at up to 13.5% (alloy 4032) to reduce the liquidus temperature and increase fluidity, because these alloys are mainly used in filler materials such as welding wires or brazing rods. Some are also used in buildings for architectural reasons owing to their characteristic gray color in the anodized state.

7.5. Use of scrap in 5xxx alloys intended for automotive, buildings and infrastructure

The classic alloys of the 5xxx series generally have narrow Si tolerance limits and are therefore rated as “tough” with regard to recycling. Compositions and uses of typical 5xxx wrought alloys are shown in Table 21. Even at low concentrations, Si can react with the Mg present in the melt in 5xxx alloys to form the primary Mg₂Si phase, which is usually undesirable [78]. This is illustrated in Fig. 71, where the Mg content is comparable to that of the common alloy 5182. It can be seen that at elevated Si content, formation of Mg₂Si occurs, and there is no option to dissolve Si into the matrix by homogenization or solution annealing. Only at below 0.1% Si does a gap begin to appear between the Mg₂Si solvus and the solidus temperature of the alloy, providing an opportunity to dissolve Mg₂Si. Even in the 5xxx series of wrought alloys made mainly from primary aluminum (e.g. 5182), primary Mg₂Si can be found which has survived homogenization treatments [1105]. Mg₂Si was seen to form fractured stringer-like particle structures in rolled sheets of 5754 [1106]. Moreover, it is known from observations in other wrought alloys that primary Mg₂Si particles fracture at even lower strains than Fe-containing IMCs [877], highlighting the detrimental effect of primary Mg₂Si.

Although there are some 5xxx alloys where Cu is used for precipitation hardening [1051,1052,1109], there are usually also strict limits on Cu in the important 5xxx alloys (see Table 21). Besides the effect of hardening due to low Cu addition, Cu together with added Zn can also reduce the volume fraction of β -Al₃Mg₂. This introduces a less anodic phase and thereby mitigates intergranular cracking, which can be problematic in 5xxx alloys at elevated temperature [1110]. This illustrates the fact that sometimes elements that are subject to tight restrictions can in some cases be used to generate beneficial properties. Not only Cu exhibits such effects on certain types of corrosion in 5xxx series alloys; many other minor elements have also been studied in this context [1111,1112]. Interestingly, Ce has recently been shown to be beneficial [1113], and may appear in some automotive scrap in the future [1022].

In addition to Si and Cu, Fe is set to relatively low values in specific alloys. This has to do with the common issue of reduced formability at increased Fe content in aluminum alloys. For example, a twin-roll-casted (TRC) Al-Mg alloy with a high impurity content (0.72 wt% Si, 0.58 wt% Fe) was investigated and exhibited a fine distribution of Fe-containing intermetallics and Mg₂Si at higher cooling rates ($\approx 10^3$ K/s), and hence improved tensile and fracture properties. Although the secondary phase particles in the as-cast TRC strip were shown to be fine and discrete by 2D analysis, 3D analysis showed that these particles were arranged in intact networks [221]. Hence, 2D evaluation of particles can lead to misleading assumptions and should be carefully scrutinized. However, after homogenization treatment, these networks were broken up into clusters and Fe-bearing intermetallics and Mg₂Si spheroidized [221]. These aspects will be discussed in detail later in this section in the context of 5xxx series alloys.

5xxx series alloys are typically used in structural plates or sheets and in extrusions for transportation and engineering, where their high ductility (even at cryogenic temperatures), good weldability and high corrosion resistance is important. Typical products are marine applications, tanks and pressure vessels, and ballistic armour plates [970,1018]. In transport applications where high formability is required, especially in the automotive sector, 5xxx series alloys are the exclusive choice among non-heat-treatable wrought alloys because of their superior strain hardening behavior [1018,1114]. However, a drawback of the 5xxx series alloys is the

Table 20

Chemical compositions of some wrought 3xxx aluminum alloys (wt.%).

Alloy designation	Cu	Mn	Mg
3003	0.05–0.20	1.0–1.5	–
3004	0.25 max	1.0–1.5	0.8–1.3
3005	0.30 max	1.0–1.5	0.2–0.6
3105	0.30 max	0.3–0.8	0.2–0.8

appearance of Lüders elongation, dynamic strain aging, and deteriorating surface quality via formation of strain localization upon forming [86,87,1115]. In addition to processing-related measures, it appears that less-pure alloys may improve this behavior. It has been shown that adding Cu and Zn can reduce Lüders elongation and dynamic strain aging [87]. Interestingly, large IMCs can also help to suppress Lüders elongation [86]. Ebenberger et al. [86] showed that the differences in thermal expansion behavior between IMCs and the aluminum matrix can be utilized to introduce mobile dislocations via quenching that are not blocked by dissolved Mg atoms (illustrated in Fig. 72), thus eliminating detrimental Lüders elongation. In [86] IMCs of type $\text{Al}_{13}(\text{Mn},\text{Fe})_6$ were studied in alloy 5182, but this basic mechanism is applicable to other IMCs with different thermal expansion coefficients than Al. This can be seen as a potentially beneficial side-effect of introducing tramp elements through recycling, which often generate coarse IMCs.

In most 5xxx series alloys used today for forming and automotive applications, impurities are still typically kept to a minimum [78]. Nevertheless, an automotive alloy of the 5xxx series with a high content of recycled material already exists. Novelis UK and Jaguar Land Rover have developed a 5754 alloy with up to 75% recycled scrap, called RC5754. In the context of such alloys, twin-roll casting has also been investigated as a method of achieving high cooling rates, which favor the formation of less-harmful Fe-containing IMCs [224]. Recently Al-Helal et al. [202] showed that even 100% scrap can be used. However, in this study Taint Tabor scrap (a special clean wrought alloy scrap from the UK which includes a large fraction of production scrap [202]) was used. This scrap was shredded further, thoroughly re-sorted, and cast via melt conditioned direct chill casting (MC-DC) [1116]. 5754 billets produced from 100% Taint Tabor scrap were then extruded, cold rolled to sheets and annealed [202]. In the best-case scenario, the industrial limits for 5754 were reached directly. Here it can be noted that the MC technique can also be used in twin-roll casting [224]. Recently, Das et al. [1117] concluded that to make a 5754 alloy recycling-friendly the processing conditions need to be adjusted, because additional IMCs and dispersoids affect microstructure formation. Modified heat treatments should be applied to improve properties such as self-piercing riveting performance, where a high level of formability through a combination of optimised grain size and balanced texture is required.

Que et al. [1118] made the important point that “understanding the formation of Fe-rich IMCs during solidification of Al-alloys is essential for developing effective approaches to mitigate their harmful effect on mechanical properties.” Here it is important to recognise that appropriate grain refinement was also shown to be significant in obtaining a good distribution of primary IMCs when casting recycled 5xxx series wrought alloys [175]. Although the literature mainly addresses Fe-containing IMCs, it must be considered that in 5xxx series alloys with increased impurity content, one is dealing with an array of particles, not just Fe-containing IMCs (e.g. Mg_2Si , the S phase (Al_2CuMg), and the Q phase (AlMgSiCu) [175,1044].

Table 21

Composition [970,1018] (if no range is given, the values are upper limits) and typical application of 5xxx alloys.

Designation	Si	Fe	Cu	Mn	Mg	Zn	Cr	Ti	Typical application
5182	0.20	0.35	0.15	0.2–0.5	4.0–5.0	0.25	0.15	0.1	Packaging products, automotive body panels and reinforcements
5083	0.40	0.40	0.10	0.4–1.0	4.0–4.9	0.25	0.05–0.25	0.15	Transportation equipment, marine parts, pressure vessels
5754	0.40	0.40	0.10	0.50	2.6–3.6	0.30	0.20	0.15	Vehicle bodies, tread plates, shipbuilding, rivets
5251	0.40	0.50	0.15	0.1–0.5	1.7–2.4	0.15	0.15	0.15	Panelling and pressings, vehicle panels, furniture
5005	0.30	0.70	0.20	0.20	0.5–1.1	0.25	0.1	–	Architectural facades, furniture, high-strength foils, HVAC equipment
5052	0.25	0.40	0.10	0.10	2.2–2.8	0.10	0.15–0.35	–	Architectural facades, tread plates, fence systems, furniture
5086	0.40	0.50	0.10	0.2–0.7	3.5–4.5	0.25	0.05–0.25	0.15	Pressure vessels, transportation equipment

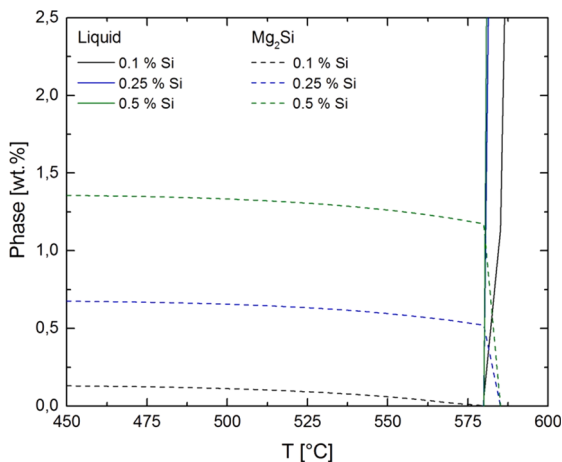


Fig. 71. Evolution of Mg_2Si and the liquid phase in an Al-4.5 %Mg-x%Si system as a function of temperature when increasing Si content from 0.1% to 0.5% Si in thermodynamic equilibrium (calculated with FactSage 8.0 [1107] software using the FACT light-metal alloy database FTlite 2020 [1108]).

For all these IMCs, solidification rate plays an important role. High-speed twin roll casting was shown to be beneficial for an Fe-containing 5xxx series alloy [222]. Liu et al. [1119] also showed that cooling rate plays a critical role and that the $\text{Al}_6(\text{Fe},\text{Mn})$ IMCs can be given fine Chinese-script morphology by near-rapid cooling (e.g. continuous strip casting). The same group also investigated the effect of increasing Fe and Si content in 5083 as a function of the cooling rate during solidification [1120,1121]. An increase in Fe content leads to an increase in the amount and size of the $\text{Al}_6(\text{Fe},\text{Mn})$ phase. An increase in Si content generates an increase in the Mg_2Si phase, which forms a network structure. Increasing the cooling rate at high Fe and Si content not only significantly refines the IMCs, but also changes their type to a quaternary $\text{Al}_{15}(\text{Fe},\text{Mn})_3\text{Si}$ phase with a fish-bone or Chinese-script structure, which is claimed to be beneficial for the strip casting of recycling-based 5xxx series wrought alloys.

The currently high usage of Si in casting alloys, together with the usage of other impurities, will make the production of conventional 5xxx series alloys via ELV recycling difficult. In particular, a mix with 6xxx wrought alloys from ABS is problematic here [1122]. Hence, at present 5xxx series alloys are only easily converted into specific 5xxx series alloys, or are fed into some 6xxx series alloys in ABS recycling by removing Mg through oxidation [1122].

Que et al. demonstrated one way to address this problem. They intensively studied an Al-5Mg-2Si-0.7Mn-1.1Fe alloy [1118,1123-1127], which is an interesting model system for highly contaminated 5xxx-series alloys from ELVs. Originally they studied the alloys from the perspective of cast alloys. However, [1118] investigated the formation of Fe-containing IMCs during solidification in twin-roll casting of strips for automotive applications made of this alloy. In their model alloys the authors obviously considered high Si content and also addressed high Fe contamination. Unfortunately, no reports on the mechanical properties of the sheets made from this alloy seem to be available so far.

Although high-pressure die casting was used for processing in the work of Zhu et al. [1000] and Liu et al. [1128], the base alloy composition resembles a typical wrought 5xxx series alloy. From Fig. 73 it can be estimated that there is potential for significantly increasing the Fe content tolerated in 5xxx series alloys that do not require superior ductility under rapid solidification conditions [1000].

Algendi et al. [1129] showed that the formation of Fe-containing IMCs depends not only on the commonly studied elements Fe, Mn and Si. The range of Mg content in the 5xxx series alloys must also be taken into account, and different IMCs can form. Que et al. [1130] also demonstrated that the morphology of the formed eutectic $\text{Al}_6(\text{Fe},\text{Mn})$ changed from needle- and plate-like to Chinese script in Al-1.4Fe-0.7Mn-xMg if the Mg content is increased from 0 to 3%, even though Mg is not found in the $\text{Al}_6(\text{Fe},\text{Mn})$ IMCs. They also reported that an increase in Mg content also leads to grain refinement via heterogeneous nucleation of α -Al on naturally formed MgAl_2O_4 particles. Interestingly, they observed the accumulation of Mg on the surface of $\text{Al}_6(\text{Fe},\text{Mn})$ particles, with the likely formation of an $\text{Al}_{12}\text{Mg}_{17}$ phase a few nanometres thick. The authors concluded that growth rates along different growth directions in $\text{Al}_6(\text{Fe},\text{Mn})$ particles are changed by Mg segregation in such way that growth becomes two-dimesional at low Mg and three-dimensional at high Mg content, generating the morphologies observed. These results may be of interest when using new alloying elements that indirectly influence the morphology of Fe-containing IMCs.

Of course, the formation of Fe-containing IMCs in 5xxx wrought alloys also depends on the solidification conditions, and hence, in conventional DC-casting, on the local position in the cast ingot. Li and Arnborg [1131] reported in the context of an Fe-containing 5182 alloy that as a function of the distance from the skin of the ingot, the type of IMC changed from $\text{Al}_m(\text{Fe},\text{Mn})$ with skeletal morphology to $\text{Al}_3(\text{Fe},\text{Mn})$ with plate-like or rod-like morphology. They explained the tendency to form $\text{Al}_m(\text{Fe},\text{Mn})$ in the eutectic reaction at higher cooling rates by the higher growth temperature at higher growth velocity compared to $\text{Al}_3(\text{Fe},\text{Mn})$. In a further work [1132] they found that the primary $\text{Al}_m(\text{Fe},\text{Mn})$ can be transformed, by homogenization via a eutectoid transformation, to a lamellar mixture of $\text{Al}_3(\text{Fe},\text{Mn})$ and Al. The authors linked this with an easy break-up of primary particles during further hot rolling. Interestingly, they found no $\text{Al}_6(\text{Fe},\text{Mn})$ in 5182, and explain this by the high Mg and low Mn content in the alloys. It should be noted that other elements, such as Cr, are also important for IMC formation in some industrial 5xxx alloys [1133].

All these findings indicate that 5xxx series wrought alloys feature complex relationships between casting conditions, chemical composition, phase selection and the phase morphology of Fe-containing and other IMCs introduced by recycling. Only systematically analyzed and understood relationships can be used to develop 5xxx series alloys that are more suitable for recycling.

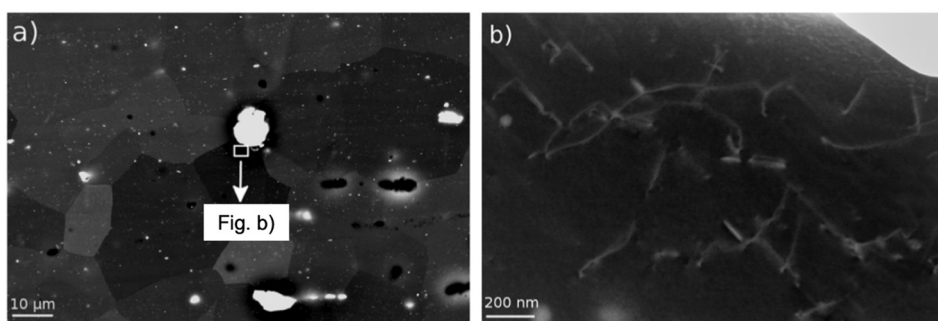


Fig. 72. Electron Channelling Contrast Image reevaling large IMCs (a) and mobile dislocations (b) in a 5182 alloy after quenching. Electron Channelling Contrast Imaging is a technique which reveals lattice defects such as dislocations directly in a scanning electron microscope. Reprinted with permission from [86].

7.6. Use of scrap in 6xxx alloys intended for automotive and mobile communication applications

The 6xxx series wrought alloys are not extremely sensitive to impurities from recycling, but production from scrap can still be a challenge (see Fig. 84, section 7.1). Bearing this in mind, it is important to appreciate that 6xxx wrought alloys are frequently used [1134] and are expected to comprise the major part of recycling scrap in the future – even though today only 20% of 6xxx series scrap is recycled into 6xxx wrought alloys [3,252]. Table 22 illustrates the compositions and common uses of typical 6xxx alloys. The main restrictions in some alloys concern Fe and Cu, or Mn and Zn, which are all potential cross-contaminants from the recycling of aluminum scrap. Other elements (e.g. Cr) are also subject to tight limits in certain alloys, but are only minor alloying elements in specific alloys which usually represent minimal contamination in typical scrap streams. The fields of application for 6xxx alloys are wide and include the construction, automotive, marine and aircraft industries in rolled, extruded, drawn and forged form [1018]. This is due to their interesting combination of properties such as good formability (especially for extrusion), high corrosion resistance, excellent surface properties and weldability, combined with relatively low price [1054,1135]. The wide range of the 6xxx series alloys is also shown in Fig. 65 in section 7.1, where it is seen that only the extreme strength and elongation limits cannot be reached in the field of wrought aluminum alloys.

A 6xxx alloy that is particularly well suited for recycling is 6061 [51,171,269]. This is mainly due to the fact that this alloy can absorb a considerable amount of Mg, Si, Fe and Cu (see Table 22). It is one of the most commonly used 6xxx alloys. Some other alloys of the 6xxx series are much more limited in the concentration of impurities they tolerate. This is especially true of 6xxx alloys used as automotive body sheets (ABS), such as 6022.

However, from a plot of dilution-quality-losses for 6061 (Fig. 74) derived from a Monte Carlo-based decision support tool in [171] it becomes clear that even the production of the impurity-tolerant alloy 6061 can require significant dilution with primary aluminum if it is produced by recycling the material from scrap. This is even the case if scrap of superior quality from the wrought aluminum products of vehicles (SC2) is used. If scrap of other qualities is deployed, e.g. that from engines and vehicle transmissions (SC1) or used beverage cans (UBC) (SC3), the demand for primary aluminum is enormous. Mixing these scrap classes helps, but does not solve the problem. This example shows clearly that the recycling of used wrought alloys into new 6xxx series wrought alloys is currently a challenge.

Dilution losses can be only reduced at the moment by using compositionally similar grades (i.e. the same alloys) [171,1122]. This type of recycling is called “tolling” and is applicable in closed-loop systems directly during production, such as stamping scrap. The

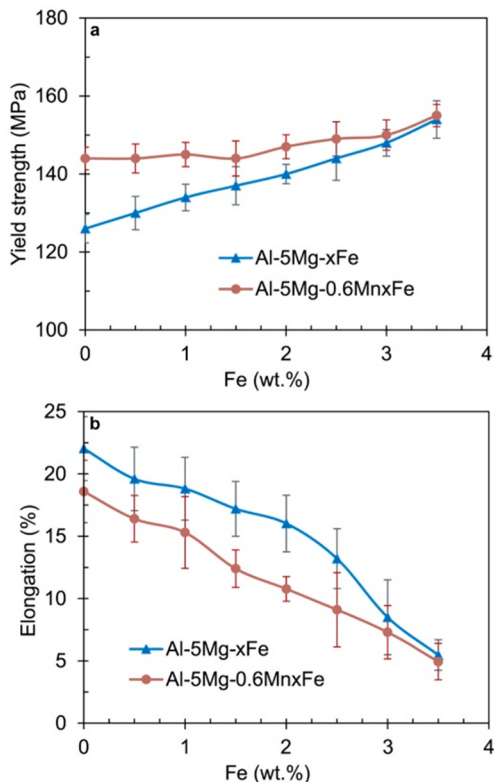


Fig. 73. Yield strength and elongation of Al-5Mg-xFe and Al-5Mg-0.6MnxFe alloys. Reprinted with permission from [1000].

Ford Motor Company used it for the F-series pickup truck, where up to 33% of primary aluminum can be saved with the strategy [78]. However, for end-of-life products and complex systems the approach does not seem very accessible at the moment.

The complex compositional challenge arises not only from the mixture of different alloy series from wrought and cast alloys and other metals typical of ELV recycling. Arowosola et al. [72] noted that over the last few decades several different 6xxx series alloys (6005, 6009, 6010, 6111, 6014, 6016, 6022 and 6451) have been registered for automotive skin applications alone. This makes for more complexity even within a single series of wrought alloys used for a single purpose, without taking into account that in reality the compositional space of a single standard cannot be fully exploited for the industrial production of high-performance alloys for many products. This is particularly true of automotive applications, where alloy composition requirements are generally very tough.

The following section examines the main metallurgical effects of critical elements introduced into 6xxx series alloys by recycling. Although many other elements can exceed standard limits and such considerations depend on the specific case (e.g. Mg from 5xxx series alloys can also be a problem in recycling), in this section we concentrate primarily on Fe and to a lesser extent on Cu, as these elements are the most widely discussed in the literature.

The Fe content in 6xxx alloys is limited due to the formation of primary Fe-containing IMCs [78], which can cause crack initiation, especially when present as brittle needles or plates [78,252]. The negative effects of these Fe-containing IMCs can be reduced during wrought alloy processing, i.e. via an appropriate homogenization practice and/or plastic deformation to break large Fe-containing IMCs into smaller ones [78]. However, it is not just Fe-containing IMCs which need to be considered in the context of fracture initiation in 6xxx series alloys. In studying a 6061 alloy, Petit et al. [877] showed that large Mg₂Si particles can fracture at low plastic strains. In addition, reduced ductility and bendability have been associated with increased Fe content in 6xxx series alloys [322] (see also Section 3.7). However, they are not always linearly connected with this Fe content. Lu et al. [1136] indicated that hemming and bending properties in 6xxx series alloys may result from a complex interdependence between Fe content and processing conditions such as the degree of hot rolling and quenching parameters, and that there can be sweet spots which do not require the lowest Fe content. The surface finish of 6xxx alloys can also be affected by Fe-containing IMCs [1137,1038].

Besides these Fe effects, the formation of primary Fe-containing IMCs also removes Si from solid solution [78]. This can significantly affect artificial aging kinetics, as shown in Fig. 75 [735], and needs to be considered if high Fe content is introduced via recycling. Interestingly, the effect of reduced Si super-saturation on aging kinetics is much stronger when novel aging strategies based on direct artificial aging are deployed [735].

Modification via Fe in the dissolved Si concentration in the aluminum matrix also depends on which IMC phase is actually formed [78]. In 6xxx series alloys, as-cast IMCs often exhibit an Si-rich composition around β -Al₅FeSi, which can be transformed into α -Al₁₂(Fe,Mn)₃Si by homogenization [887,1038,1138,1139]. This transition can release Si into the aluminum matrix [78]. Mn plays an important role in this transition [78]. Fig. 76 illustrates the effects that can be achieved through heat treatment and compositional measures. The metastable β phase in as-cast condition shown can be transformed into α by suitable homogenization.

Besides its effect on the Si supersaturation, the morphology of the Fe-containing IMCs formed is crucial for the properties of these alloys. For the often-discussed impurity-tolerant 6061 alloy, the most important IMCs are α -Al₈Fe₂Si, α -Al₁₅(Fe,Mn)₃Si₂ and β -Al₉Fe₂Si₂ [269]. The α phases can show Chinese-script or polyhedral morphology, while the β phase comprises unfavorable plates or needles [269]. As discussed above, the detrimental β phase can be transformed by long-term, high-temperature treatments which generate spheroidization [78]. According to Wang et al. [1140], this was shown to significantly improve elongation and fatigue strength in an extruded 6060 alloy. Moreover, after exposing the material to a slightly corrosive environment its surface appearance can be improved,

Table 22

Typical composition and uses of 6xxx wrought alloys [1018,1054].

Designation	Si	Fe	Cu	Mn	Mg	Zn	Cr	Ti	Typical application
6016	1.0–1.5	0.50	0.20	0.20	0.25–0.6	0.20	0.10	0.15	Automobile body sheets widely used in Europe
6022	0.8–1.5	0.05–0.2	0.01–0.11	0.02–0.1	0.45–0.7	0.25	0.1	0.15	Automobile body sheets
6014	0.30–0.6	0.35	0.25	0.05–0.20	0.40–0.8	0.10	0.20	0.10	+0.05–0.20 Vanadium
6005	0.60–0.9	0.35	0.10	0.10	0.40–0.6	0.10		0.10	automobile body sheets, profiles
									General-purpose extrusions, rail vehicles, construction
6111	0.60–1.1	0.40	0.50–0.9	0.20	0.10–0.45	0.15	0.10	0.10	Automobile body sheets
6060	0.30–0.60	0.10–0.3	0.10	0.10	0.35–0.6	0.15	0.05	0.10	General-purpose extrusions, rail vehicles, construction, forgings
6063	0.20–0.6	0.35	0.10	0.10	0.45–0.9	0.10	0.10	0.10	Casing for electronic devices, architectural extrusions, pipes, door and window frames, heat exchanges, rail vehicles, bumpers
6061	0.40–0.80	0.70	0.15–0.40	0.15	0.8–1.2	0.25	0.04–0.35	0.15	Higher-strength applications, welded structures, rail vehicles, construction, bumpers
6082	0.70–1.3	0.50	0.10	0.40–1.0	0.6–1.0	0.20	0.25	0.10	Higher-strength applications widely used in Europe, extrusions
									Plates, chassis components, forgings, rail vehicles, construction, bumpers
6013	0.40	0.50	0.10	0.2–0.7	3.5–4.5	0.25	0.05–0.25	0.15	Aircraft sheets, fuselages

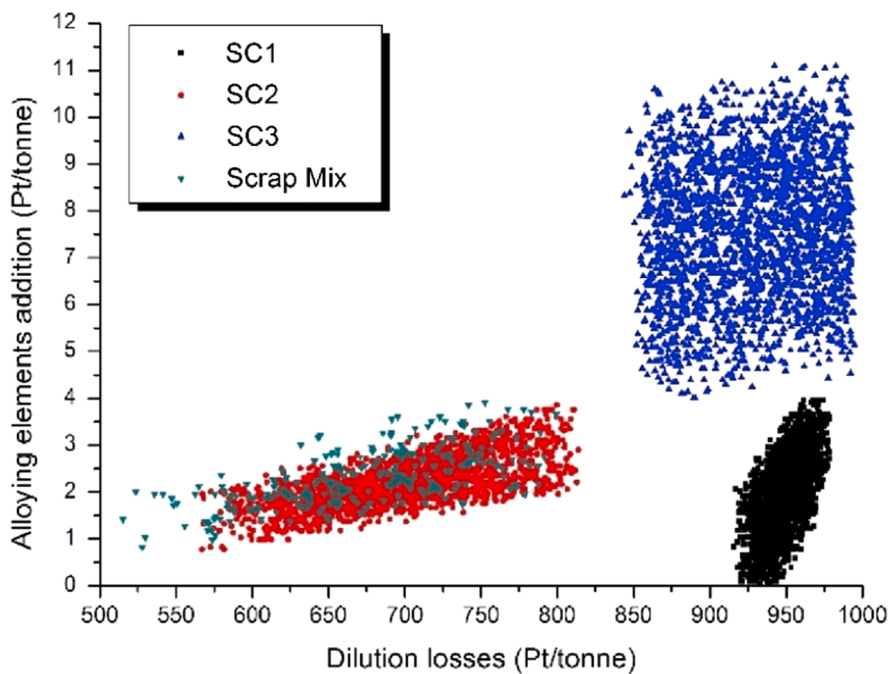


Fig. 74. Dilution-quality-losses plot for the production of 6061 from different types of scrap: Al engines and transmissions (SC1), wrought products from vehicles (SC2), UBC (SC3) and a mix of these. All model solutions are shown as scatter diagram for the addition of primary Al (dilution losses) and required alloying elements. The best case for recycling is at the lowest dilution losses and where there are small amounts of additional alloying elements. Reprinted with permission from [171].

because micro surface defects due to the debonding of β -particles from the Al matrix can be averted by a suitable heat treatment [1140]. This is illustrated in Fig. 77.

The adverse impact of the α phase can be mitigated in 6xxx alloys with increased Mn content (a ratio of Mn/Fe > 0.5 is often suggested) [78]. This promotes α -type IMCs (see Fig. 76), which do not cause ductility to deteriorate as much. Hence, promotion of the α phase by adding Mn makes it possible to accept higher Fe content, while maintaining good tensile elongation [1141]. Adding Cr has a comparable effect [78]. However, these compositional measures also have their limitations: too much added Mn increases porosity and sludge formation, decreases machinability [252,339,1142,1143] and reduces strength and ductility [1144].

The type of IMC formed during casting also depends on Fe content. Sweet et al. [886] showed that in 6060 an increase from 0.1 wt% to 0.5 wt% Fe shifted the cast microstructure from β -Al₅FeSi to a Chinese-script cubic α_c -Al(Fe,Mn)Si phase (see Fig. 54). This observation may support the above-mentioned non-linear effect of Fe content on bending and hemming properties. In general, there are several Fe-containing IMCs (only in the lean 6060 alloys described in [886] have four different phases been found in as-cast conditions) which may form in 6xxx series alloys. The phase depends strongly on composition (involving many transition metals or even Mg for the π -Al₈FeMg₃Si₆ phase) and the highly complex formation progression upon solidification, which includes a series of peritectic reactions [886,1145].

It seems very significant that the array of phases in 6xxx alloys depends on the solidification conditions. As already shown, the β phase is of a metastable nature, and its formation depends on the growth rate. Sha et al. [1050] demonstrated in 6xxx model alloys made by Bridgman furnace solidification that high growth rates above 120 mm/min strongly favor formation of the beneficial α phase. Consequently, various novel casting techniques are being utilized to improve the morphology and distribution of Fe-containing IMCs. Al-Helal [1146] et al. used high shear melt conditioning to create less-harmful Fe-containing IMCs in twin roll cast recycled 6111 strips. In this context, Wang et al. [1147] studied an alloy with 0.8 wt% Mg, 0.8 wt% Si and 0.7 wt% Fe which they produced by direct chill casting, and reported a refinement of Fe-containing IMCs, Al-grains and an increased fraction of small α -dispersoids in billets cast at high speeds. There are complex links between the microstructure, morphology, type and interconnectivity of the Fe-containing IMCs in the cast state which also influences the formation of other IMCs during processing. This includes Mg₂Si, as this phase tends to nucleate at β -Al₅FeSi [1044]. Inoculation and its interdependence with Fe-containing IMCs upon solidification has also been investigated in the literature [1046,1047].

It should be noted that high levels of Fe content also influence the conventional casting process of 6xxx series alloys. In the context of direct chill casting of a 6xxx series alloy, Nagaumi et al. [1148] reported that increased Fe content can significantly degrade hot cracking behavior.

Sweet et al. [1149] studied hot tear susceptibility in DC cast 6060 aluminum alloys with various amounts of Fe. They observed that materials with an Fe content ranging from 0.02 to 0.5 wt% had a substantial influence on load response during solidification and on the

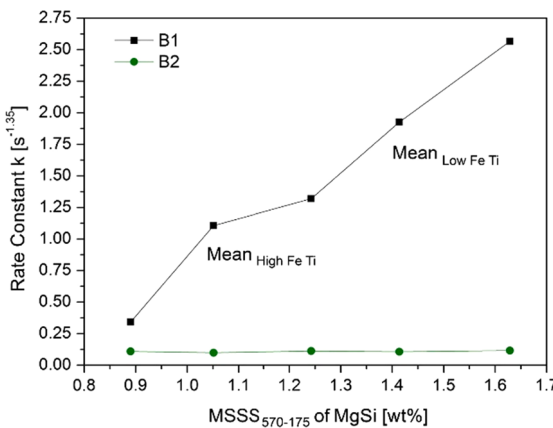


Fig. 75. Dependence of age-hardening kinetics on the super-saturation of Mg plus Si (MSSS₅₇₀₋₁₇₅ of MgSi) expressed by a rate constant k according to the model used in [735] within the standard compositional limits of 6061. The results for direct artificial aging and artificial aging with storage at RT are shown. The effect of Fe (and in this case Ti) which form IMCs and trap Si is clearly shown (“mean” denotes a similar nominal Si and Mg content in the 6061 alloy used). Reprinted with permission from [735].

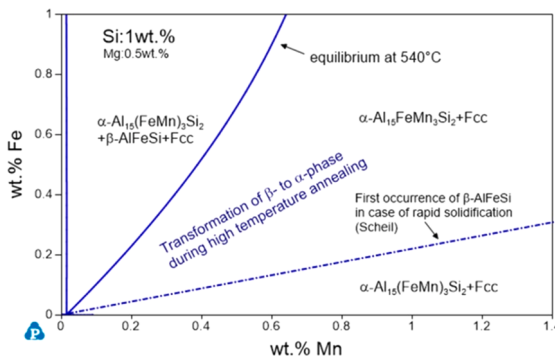


Fig. 76. Isothermal section at 540 °C in an alloy with 1 wt% Si and 0.5 wt% Mg indicating the fields of existing IMCs in dependence on the Mn and Fe content. The effect of Scheil-cooling and the resulting extended metastable β phase field in as-cast condition are shown. This can be brought into equilibrium via homogenization (calculated with Pandat software using database PanAl2019 [982]).

resulting hot tear susceptibility. They interpreted their observations in terms of the influence of Fe content on the frequency, size and morphology of β-Al₅FeSi and α-AlFeSi IMCs and their influence on the coherency and coalescence of the microstructure.

In the same context, Sree et al. [1150] recently introduced an in-situ microstructural control method for changing the dispersion and distribution of second-phase particles via a mechanically melt conditioned direct chill (MC-DC) casting process, operated only 2–7 °C above liquidus. The approach makes use of a rotor-stator high-shear device. These authors successfully applied the method to an 6082 alloy containing 0.27 wt% Fe. The results show that the approach improves particle dispersion and thus helps to reduce or even suppress the need for subsequent expensive, time-consuming homogenization operations. The method thus clearly increases flexibility in the use of higher scrap fractions in such alloys, where second-phase dispersion is otherwise a challenge.

The second element to be considered is Cu, which shows two faces in the 6xxx series. It is strongly restricted in many alloys (often to below 0.1 wt%), but there are also 6xxx wrought alloys that contain >1 wt% Cu. This becomes important when we consider the 6xxx alloys used together in similar products, e.g. cars. A good example of misfit affecting recycling is seen in the frequently used ABS alloys 6022 and 6111, where compositional differences in Cu are extreme and complicate recycling [1122]. Cu acts in these alloys as follows. High Cu content (e.g. in 6111) is used to generate additional strengthening because it introduces the Q phase and its precursors [808]. The rationale for tight limits on Cu in 6022 (and many other primary alloys), however, is a bit less clear. One reason may be the deteriorative influence that Cu may have on various types of corrosion in 6xxx series alloys, even though this also depends in very complex ways on the composition and processing conditions affecting the different types of corrosion [1151,1152].

The Cu content of Al-alloys used in enclosures for electronic devices (such as 6063) is controlled carefully (<0.1 wt%), because it can have an impact on cosmetic appearance by affecting the color of the enclosure after anodizing. Fe can influence the appearance of Al-alloys and generate grayish colors [1153], possibly due to the disappearance of Fe-rich IMCs after anodizing, which leaves etching pits which reduce surface gloss [1154]. The formation of “foggy” oxides in Fe-containing alloys may also contribute to their unattractive appearance. Gray coloring can also arise from the presence of Si in the alloy. Anodization of pure aluminum generates the brightest anodic oxides compared to Al-alloys [1155]. The challenge of reproducing a defined compositional range to achieve

consistent cosmetic appearance increases with the degree of recycling and is related to the source and amount of recycling material. Cosmetic aspects are often linked to corrosion behavior. The effects of scrap-related tramp elements on corrosion are discussed in more detail in section 5.6.

In conclusion, we will mention some new recycling-based concepts for 6xxx alloys addressed in recent literature. In [252] Kotadia et al. explored extending the current composition limits of 6xxx alloys, particularly with regard to Si, Fe and Mg content, but they also considered further tramp elements. As a first step, they showed that ultrasonication upon casting can significantly refine grain structure and effectively modify Fe-containing IMCs in a beneficial way. Other new technologies, such as spray forming, are also being investigated to produce starting material for forming operations that can tolerate higher Fe content. Pereira et al. [269] showed in the context of wrought alloy 6061 that IMCs with detrimental morphologies can be avoided even at 1.4 wt% of Fe. The formation of the primary α -Al₁₅(Fe,Mn)₃Si₂ phase with polyhedral morphology and homogeneous distribution can generate significant ductility and enable the hot extrusion of such 6xxx material enriched with Fe [269].

To summarize, a major feature of current literature on the development of recyclable 6xxx series alloys is acceptance of higher levels of Fe contamination. This applies to research on novel casting technology, solidification and inoculation, heat treatments and alloy solidification techniques other than conventional casting.

7.7. Use of scrap in 7xxx alloys intended for high-strength applications

Al-alloys in the 7xxx series are heat-treatable, and those in the quaternary system Al-Zn-Mg-Cu in particular have the potential to reach very high strength levels (tensile strength up to 850 MPa [1156], and up to 1 GPa with ultrafine grain structures [629]) in comparison with the other Al-alloy classes. These high strength levels are primarily achieved by the precipitation of precursors of the η phase (MgZn₂) during heat treatment. Further increases in strength can arise by adding significant amounts of Cu, as in most modern aerospace alloys. This can alter precipitates into Mg(Zn,Cu)₂ [102] compounds.

7.7.1. The role of Fe and Si impurities in 7xxx series alloys

Historically, the widest application field of the 7xxx alloy series has been in structural components for the aircraft industry. This is due to their high strength-to-weight ratio and relatively low cost [913,1157]. Fracture-critical design concepts led to the development of special high-toughness alloys, such as 7150, 7175 and 7475 [1157]. The latter involves modification of the high-strength 7075 alloy to improve ductility. By limiting the total amount of Fe and Si content to max. 0.22 wt% in 7475 (compared to a limit of max. 0.9 wt% in 7075), both fracture toughness properties and strength were improved [913]. Reducing impurity elements, such as Fe and Si, is a common way to improve fracture toughness properties, not only in the aircraft industry. While impurity content is limited to 0.10–0.15 wt% Fe and 0.15–0.25 wt% Si in superior, high-toughness aerospace alloys, Fe and Si levels are typically limited to max. 0.40 wt% in wrought premium automotive alloys such as 7116 and 7129 (both max. 0.30 wt% Fe), used for bumpers. The amount of Fe and Si tends to increase the more frequently an Al-alloy is recycled [29], mainly because it is picked up by scrap handling equipment [1158]. An increase in Fe in recycled Al-alloys during automotive recycling is considered unavoidable, and presumably arises from the

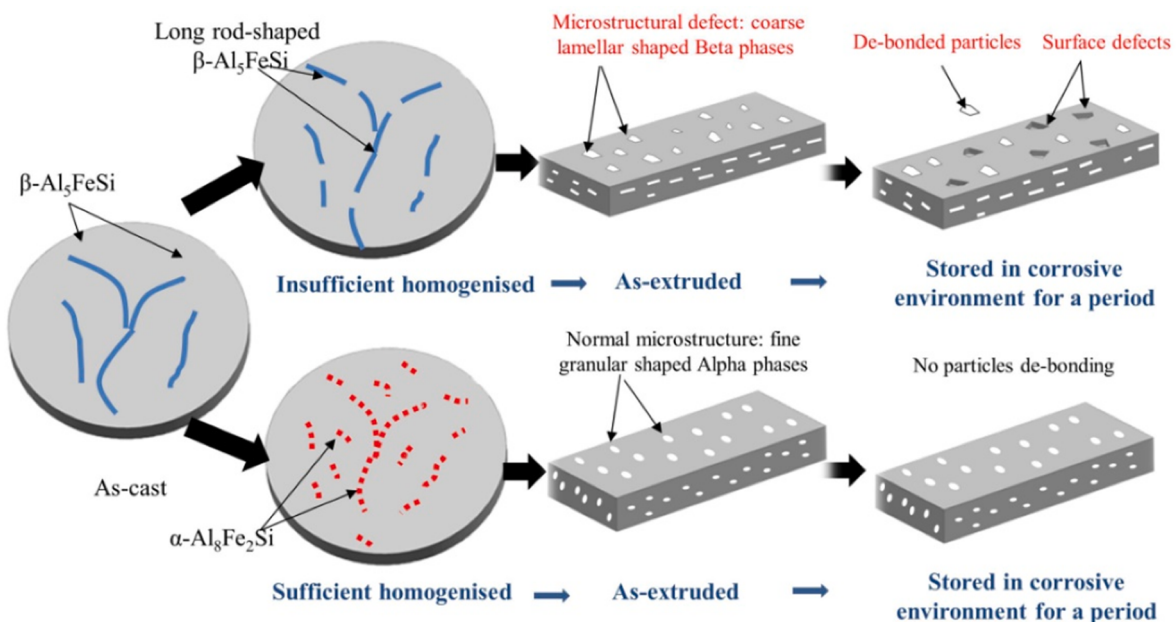


Fig. 77. Schematic illustration of α - and β -particles during processing and the impact on surface properties of 6060 extrusions. Reprinted with permission from [1140].

unintended mixing of steel parts in these alloys due to non-prompt sorting [1159]. Because Fe is highly soluble in molten Al [1257], abrasion from the steel machining tools used in melting production processes can increase the Fe content in Al products [1258]. Fe is in fact the most common impurity element in Al-alloys. Due to its low solubility in the solid state (≈ 0.05 wt% [1257]) it can form intermetallic particles, which can impair mechanical properties [1162] and corrosion resistance [102].

The presence of impurities may be unavoidable, and is to be expected in scrap material. Therefore we will address the effects of impurities in 7xxx series alloys and similar alloys. Several studies focus on the effects on microstructure caused by higher impurity content in 7xxx series alloys. Micropillar compression tests conducted on constituent particles in a 7075 alloy showed the completely brittle nature of $\text{Al}_7\text{Cu}_2\text{Fe}$ particles, which had a higher compressive strength compared to Mg_2Si particles and the 7075 alloy matrix [1163]. Microstructures of 7475 and 7081 alloys after potentiodynamic polarization tests in 3.5% NaCl solution revealed corrosion pits around $\text{Al}_7\text{Cu}_2\text{Fe}$ particles, indicating the cathodic behavior of these particles relative to the matrix [1164]. $\text{Al}_7\text{Cu}_2\text{Fe}$ particles were shown to be insoluble during heat treatment due to the high melting point [1165–1168]; subsequent mechanical processing leads to the cracking and re-allocation of these particles [1168]. In another study, the 7075 alloy, with 0.23 wt% Fe, was successfully produced by TRC. It exhibited a homogeneous distribution of small particles ($\approx 1 \mu\text{m}$) due to the higher solidification rate, compared to the same alloy fabricated with a permanent mold casting (PMC) technique, which generated a large number of finer particles ($\approx 0.1 \mu\text{m}$), but also a few much larger particles ($>5 \mu\text{m}$) (Fig. 78). While the small particles in the TRC alloy induced a fine-grained microstructure with enhanced ductility, the fine particles in the PMC alloy induced an inhomogeneous microstructure and decreased elongation at high temperatures during hot tensile deformation. Cracks were observed inside large Fe-bearing particles ($>5 \mu\text{m}$) and also at the interface between particles and matrix, lowering fracture elongation [1169].

The susceptibility of 7xxx series alloys to hot tearing has been shown in the context of DC casting. A DC-cast 7055 alloy exhibits a wider temperature range between solidus and liquidus than pure Al and an Al-4.5 wt%Cu alloy, leading to a higher temperature range in the sump. Due to the higher temperature range, cracks initiate and propagate more easily in 7xxx series alloys than in the other alloys investigated. Hot tearing occurred in the center of the ingot due to the formation of a shrinkage cavity [1170].

Several strategies can be used to overcome hot cracking in Al-Zn-Mg-Cu alloys during processing through SLM. Al_3Zr particles have been shown to be particularly effective, serving as solidification nuclei and thus helping to refine grain size, thereby reducing hot cracking susceptibility. These particles can be introduced as Zr nanoparticles added to the Al powder [1171], in the form of zirconia powders mixed with the Al powders or added to the respective master alloy used to produce the alloy powder [1172]. Submicron Si and TiB_2 can also be added to the alloy. While the Al-Zn-Mg-Cu alloy exhibited macrocracks and poor fracture strength and elongation, the alloy with the addition of submicron Si and TiB_2 revealed no hot cracking and showed improved fracture toughness. Adding Si increased fluidity and reduced solidification shrinkage [1173].

Al-Si cast alloys (e.g. AlSi7CuMg) are widely used in the automotive industry for engine block applications [1174]. Mixing them as aluminum cast scrap with 7xxx wrought alloys is not favorable due to the large amount of Si they contain, which will be detrimental due to the formation of coarse brittle Si-rich IMCs in the microstructure.

The detrimental effect of brittle IMCs on the mechanical properties of 7xxx series alloys can also be mitigated by severe plastic deformation. Large-strain-constrained plastic deformation breaks the intermetallics into smaller particles of smaller aspect ratio, and randomizes their distribution. All these effects may combine to improve the fracture properties of Al-alloys, as shown for friction stir processing [884]. In the processing by high-pressure torsion (HPT) of an alloy similar to 7449 supplemented with various levels of Fe up to 1.2 wt%, it was shown that a combination of tensile strength $>850 \text{ MPa}$ and of ductility $>5\%$ could be maintained independently of Fe content [1175]. In simpler Al-Fe binary alloys, processing by HPT can dissolve a significant portion of the Fe intermetallics into a supersaturated solid solution [1176]. Upon subsequent heat treatment, this solid solution decomposes into extremely fine Fe-rich precipitates, thus providing high strength, high thermal stability (due to the slow diffusion of Fe), and an absence of large intermetallic particles.

Nevertheless, the profound effects of intermetallics may be weakened by producing Al 7xxx wrought alloys with higher solidification rates or by modifying the composition to incorporate elements such as Mn into Fe-bearing intermetallics. Once coarse intermetallic particles are present in the 7xxx wrought microstructure, these not only tend to impair mechanical properties and corrosion resistance but may also generate difficulties in processing.

High-strength 7xxx series alloys are susceptible to hot tearing during extrusion due to large precipitated particles, which can raise the flow stress. An increase in the flow stress during extrusion can increase the actual temperature of the extrudate to above the solidus temperature, causing local melting and crack formation. The multiplication of the two factors (presence of large particles and local melting) may result in hot tearing. The applicable speed of extrusion is therefore determined by alloy composition and the microstructure, which can be modified by homogenization treatment. In the 7xxx series alloys, Al-Fe-Mn-Si particles located at grain boundaries and Al-Mg-Zn-Cu eutectic phases can lower the extrusion speed. Al-Fe-Mn-Si particles located at the grain boundaries (GB particles) are brittle and hard, and are therefore detrimental to mechanical properties and extrudability [1177]. The effectiveness of further processing, in terms of time consumption and the energy required for hot working and cooling, might therefore also be considered when choosing appropriate 7xxx recycling alloys with (preferably) higher local solidus temperatures and fewer large particles.

7.7.2. Recycling of 7xxx series alloys with and without pre-sorting

Das and Kaufman [1158] discussed the possible recycling of aerospace alloys, mainly the 2xxx and 7xxx alloy series. The pre-sorting of alloys within the 7xxx series and 2xxx series from aircraft sitting in graveyards may generate composition R7XXX, which is similar to the 7075 alloy after recycling (Table 23). Such an alloy may be usable in non-fracture-critical aircraft parts. No pre-sorting of 2xxx series alloys with 7xxx series alloys can result in composition R2 + 7XX, which is shown in Table 23 [1158]. Although the pre-

sorting of 2xxx series alloys and 7xxx series alloys should be technically achievable due to the higher Cu-content in 2xxx series alloys and higher Zn content in 7xxx series alloys [844], lack of proper pre-sorting (e.g. due to possible shredding inaccuracy) should also be addressed.

The Zn content in the recycled alloy without pre-sorting (3.0 wt%, R2 + 7XX) is expected to be approximately half of that in the resulting recycled alloy after pre-sorting (6.0 wt%, R7XXX).

7.7.3. The role of Zn and Mg in 7xxx series alloys

The 7xxx alloy series is the only Al-alloy series in which Zn is used as an intended alloying element in amounts of 1 to 8 wt% [1257]. This can explain a dilution of Zn after mixing 7xxx series alloys with Al-alloys of other series, as shown in the composition of R2 + 7XX compared to R7XXX. From composition R2 + 7XX it can also be observed that the Mg content is lower (1.8 wt%) than in composition R7XXX (2.5 wt%), because the Mg content of many 2xxx series alloys is lower compared to 7xxx series alloys [1158]. Since Zn in combination with Mg or Mg + Cu provides the high levels of strength in the 7xxx series, lower Zn/Mg ratios may influence the final properties of the product.

It has been shown that – among alloys with Zn + Mg content of \approx 7 wt% – a decrease in the Zn/Mg weight ratio from 13 to 5 leads to an increase in both ultimate tensile strength and yield strength of about 30%. This was ascribed to a higher density of precipitates in the matrix [1178]. Electrochemical cyclic polarization tests in 3.5% NaCl solution revealed a higher corrosion potential and lower corrosion current density in low-Zn/Mg-ratio alloys than in high-Zn/Mg-ratio alloys, and hence higher corrosion resistance and higher stress corrosion cracking (SCC) resistance. Both are explained by the lower Zn content in the matrix and the narrower precipitate-free zones (PFZ) [1178]. Experimental Al-Zn-Mg-Cu alloys with a total Zn + Mg content of \approx 4.8 wt% and Zn/Mg ratios between 2.3 and 0.9 exhibited the same peak hardness level after heat treatment. High-Zn/Mg-ratio alloys achieved peak hardness faster during heat treatment compared to low-Zn/Mg-ratio alloys. This was attributed to the nucleation of a larger number of GP II zones and their transformation to the η' phase in high-Zn/Mg-ratio alloys. However, after reaching peak-aged condition the rate of hardness reduction increased with higher-Zn/Mg ratios during overaging [1179]. The 7xxx series alloys are often used in a slightly overaged temper to achieve a trade-off between strength, corrosion resistance, and fracture toughness [1257]. Hence the Zn/Mg ratio should be considered during the production of recycled 7xxx series alloys and preferably kept in a tolerance range where similar applied heat treatments will lead to comparable material properties required for designated applications.

Zn may be removable from the melt by vaporization due to the high vapour pressure, and Mg can be removed by chlorination using Cl₂ gas [844], so it may be technically possible to decrease the Zn or Mg content to adjust the Zn/Mg ratio.

7.7.4. The role of Cu in 7xxx series alloys

The 7xxx alloy series can be divided into Cu-free alloys and alloys with Cu addition. The latter can have a significant influence on

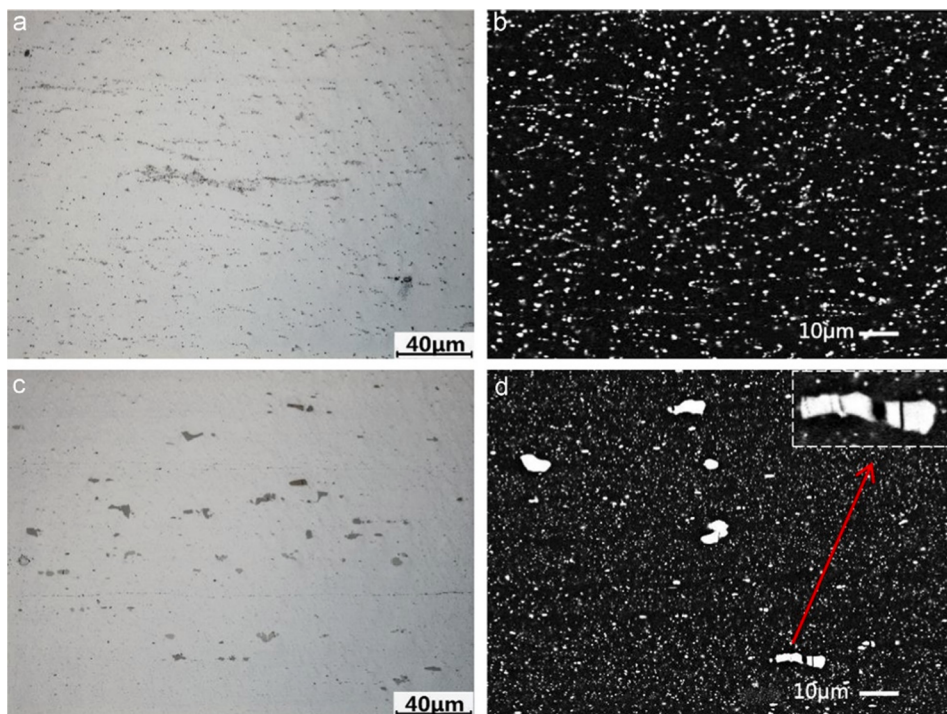


Fig. 78. Distribution of second-phase particles of cold-rolled 7075 alloy samples produced by TRC (a,b) and PMC (c,d). Reprinted with permission from [1169].

final strength and corrosion resistance. An increase in Cu content from 0 to 1.6 wt% in a 7xxx series alloy can generate an increase in tensile strength from 515 MPa to 574 MPa, presumably due to a greater amount of the main strengthening η' phase [1180]. Because they provide both mechanical strength and high corrosion resistance, Cu-rich 7xxx series alloys are a more appropriate choice for structural materials for aircraft than Cu-free alloys. However, it has been shown that Cu in intermetallic particles, the solid solution in the matrix and precipitates at grain boundaries can have differing effects on corrosion behavior, which might be adjustable by heat treatment. In under-aged condition the 7055 alloy showed a decrease in Zn in the matrix, leading to a more noble matrix and hence decreasing the galvanic coupling between $\text{Al}_7\text{Cu}_2\text{Fe}$ particles and the matrix. In overaged temper condition, however, a higher pitting corrosion trend was observed, presumably due to the reduction of Cu in the matrix, which enhances the galvanic effect between $\text{Al}_7\text{Cu}_2\text{Fe}$ particles and the matrix. While a higher Cu content in the matrix would therefore lead to higher pitting corrosion resistance, less Cu in grain boundary precipitates would increase the susceptibility to SCC and intergranular corrosion [1181]. Alloys with higher Cu and Zn content, such as 7050, show more S phase (Al_2CuMg) to be dissolved in homogenization heat treatments. The presence of the S phase in combination with high heating rates can result in overheating, causing the formation of rosettes. An almost complete dissolution of the S phase should therefore be aimed for, since pre-melting could otherwise take place in the following hot working processes at temperatures below 480° C [1182]. Several studies focus on suitable homogenization treatments for 7xxx series alloys to dissolve phases such as the S phase. These have led to the development of multi-step homogenization treatments [1183,1184]. In addition, Cu in combination with Zn and Mg in the 7xxx series alloys generates enhanced susceptibility to weld cracking [1185]. Hence, mechanical and corrosion properties may to a certain extent be adjustable via specific heat treatments, and lead to a higher compositional tolerance range for possible Cu dilution or Cu addition during the recycling of Al scrap material in the 7xxx alloy series.

7.7.5. The role of transition elements in 7xxx series alloys

In 7xxx series alloys transition element additions such as Cr and Zr can be present in small quantities, primarily to inhibit recrystallization during processing and to maintain the resulting grain structure after solution heat treatment. Elongated grain structures in a 7xxx series alloy after hot rolling may increase resistance to SCC in extrusions, because the propagation of intergranular SCC cracks perpendicular to the elongated grains is difficult [1182]. It may be necessary to apply a two-step homogenization treatment to achieve an improved Al_3Zr dispersoid distribution to almost completely inhibit recrystallization with < 0.09 wt% Zr [1186]. The potential accumulation of grain-refining elements such as Cr or Zr during recycling needs further investigation [1158]. However, removal of Ti and Zr might be possible with an addition of B to generate TiB_2 and ZrB_2 stable precipitates, which could be filtered [844].

7.7.6. "Green" 7xxx series alloys

While recycled high-strength 7xxx series alloys may not achieve the properties required for critical parts in the aircraft or automotive industries, they may be applicable in less critical applications such as consumer electronic devices, and easier to introduce. Because customers expect authentic materials, TVs are being developed with thinner profiles and the size of tablet computers is increasing. The use of Al-alloys could be increased further compared to plastic materials. Anodizing 7xxx series alloys does not generally produce the appearance desired. Nevertheless, a pure Al-clad material with a better surface finish around a 7xxx series core alloy bonded by hot rolling may be appropriate in consumer electronics [1187], and may have potential as a herald of "green" high-strength Al products even as recycled old scrap.

8. Future alloys, products and processes designed for high levels of scrap usage

8.1. Sustainable aluminum alloys and powder recycling procedures in additive manufacturing

8.1.1. Introduction

Additive manufacturing (AM) comprises fabrication processes that are characterized by a layer-by-layer build-up of 3-D objects, whose geometrical information is provided in the form of computer-aided design models. In Powder Bed Fusion (PBF), a laser (L-PBF) or an electron beam (Electron Beam Melting (EBM)) is used to melt and consolidate a powder. Here we focus mainly on L-PBF, which is currently the most common technique in metal AM.

The geometrical freedom provided by L-PBF allows optimization of lightweight parts with better design and functionality than existing components. This in turn offers the potential to reduce energy consumption in the aerospace and automotive sectors [1188–1190]. On-demand production of parts reduces transportation in the supply chain [1188] and waste associated with large inventories [1188]. Because unmelted powder can be reused for subsequent building jobs, less waste material is produced during the

Table 23

The 7075 alloy and potential compositions in wt.% of recycled aircraft alloys, assuming both pre-sorting (R7XXX) and no pre-sorting (R2 + 7XX) [1158].

Alloy	Al	Zn	Mg	Cu	Fe	Mn	Si	Others
7075	≈ 90	5.6	2.5	1.6	max. 0.5	max. 0.4	max. 0.4	
R7XXX	≈ 90	6.0	2.5	2.0	0.4	0.2	0.2	0.2
R2 + 7XX	≈ 92	3.0	1.8	3.0	0.4	0.4	0.4	

layer-by-layer construction of the part [1188,1191]. This contrasts with traditional subtractive manufacturing, where material is selectively removed in order to produce a component. Particularly striking examples include components of complex geometries such as those used in aerospace applications, where buy-to-fly ratios (i.e. the ratio between the weight of the raw material and the weight of the final component) of > 95% are common [1192]. A decrease in the amount of waste material results in a reduced CO₂ footprint. The specific energy consumption of an efficient AlSi10Mg build in which extensive utilization of the available space on the building platform was realized was measured by Faludi et al. at 566 MJ/kg [1193]. In primary production, the embodied energy of bulk AlSi10Mg (currently the most-used aluminum alloy in additive manufacturing [1194]) is ~ 189 MJ/kg [1195], while atomization adds an additional ~ 8 MJ/kg to the embodied energy of the material [1195]. A non-significant proportion of the CO₂ footprint associated with parts produced by L-PBF therefore arises from steps preceding the AM process. This highlights the importance of powder recycling.

8.1.2. Powder recycling

Metal powders can be reused in PBF in a variety of ways [1196]. Used powder can be sieved and reused without mixing with other powders; this is currently the most commonly employed strategy documented in the scientific literature [1196]. Used powder can also be sieved and mixed with virgin powder or mixed with used powder of the same age [1197]. In the latter context Lutter-Günther et al. [1197] modelled the maximum number of powder reuse cycles as a function of powder batch size, build volume utilization, powder coating dosage factor and powder loss. The build volume utilization was found to have the greatest impact on the maximum life cycle, which varied between 1 and 117 cycles for all combinations of parameters tested [1197]. The average maximum number was calculated at 35 cycles for batch sizes of 100 – 1000 kg [1197]. This provides a reference value up to which powder recycling should be assessed for typical L-PBF applications [1196]. During the fabrication process, however, several mechanisms can affect the properties of metal powders [1198], leading to potential quality degradation and therefore to fewer achievable reuse cycles.

A well-documented phenomenon is the formation of laser spatter. The evaporation of material resulting from intense local interaction of the laser with the metal powder is associated with substantial recoil pressure, which can lead to melt pool instabilities and ejection of material from the melt pool [1199]. Spatter can also be formed if powder particles surrounding the melt pool are ejected due to the intense vapour flow or by the entrainment of particles within the inert gas flow present inside the building chamber [1200]. Individual spatter particles are typically spherical [1201]. If liquid spatter particles collide with other particles either during their flight or after contact with the powder bed, aggregates can form [1202]. In addition to the relatively coarse spatter particles, the partial evaporation of metal powder causes condensate to form, consisting of submicron particles deposited on the walls of the building chamber and on the surface of spatter particles [1202]. Apart from changes in granulometry and morphology, i.e. in the particle size distribution and morphology of the metal powders used, the chemical composition of spatter may differ from that of virgin powder. This was observed by Simonelli et al., who found surface oxides on laser spatter of an AlSi10Mg powder [1201]. While large agglomerates can be effectively filtered out during sieving, the majority of laser spatter particles, as well as most metal condensate, will be transferred to subsequent build jobs when recycled, potentially having negative effects on built parts. This is mainly because laser absorption and heat transfer, which govern the formation of melt pools [1203], are strongly dependent on the properties of the powders used. The absorptivity of metal powders is generally higher in comparison to flat surfaces due to multiple scattering [1204], with the absolute value for the absorption coefficient depending on the powder size distribution and the resulting packing density [1204]. Similarly, the thermal conductivity of metal powders is dependent on their size and shape [1205]. In the powder size ranges typical for L-PBF (<100 µm), densely spaced solid-to-solid contact points contribute significantly to thermal resistance [1206]. Conductivity therefore depends on the nature of contact points and voids between the powder particles. Similarly, surface oxides may affect both the thermal conductivity of the powder feedstock [1207] and the phase constitution of the final alloy due to the incorporation of oxides, thereby affecting reproducibility with an increasing number of powder reuse cycles.

Tradowsky et al. fabricated specimens of AlSi10Mg by L-PBF and subsequently analyzed them [1208]. After initial processing, the leftover powder was reused in a separate build job without prior sieving [1208]. The void content increased drastically, from 0.26% for a specimen made from virgin powder to 2.00% for a sample made from the recycled powder. The increased presence of irregularly shaped voids in the sample produced from the recycled powder was ascribed to the formation of significant amounts of oxides. Yield strength and ultimate tensile strength decreased by approximately 8%, while the elongation at fracture decreased by roughly 14% [1208].

In another study, Asgari et al. investigated the effect of one powder reuse cycle on the properties of AlSi10Mg powder and the properties of built parts [1210]. In contrast to the study by Tradowsky et al. [1208], the powder was sieved after the first use cycle. No statistically significant difference in the average particle size was found between virgin and recycled powders [1210]. Moreover, the yield strength, ultimate tensile strength and elongation at fracture of a specimen made from recycled powder showed no significant variations from published values for samples made from virgin powders [1210], indicating that using a recycled powder did not negatively affect the quality of the built parts. Similarly, Hadadzadeh et al. investigated the effect of one powder reuse cycle on AlSi10Mg powder characteristics and the resulting part properties [1211], employing the same recycling strategy of sieving and reusing without mixing with virgin powder. Only minor variations were found in the average powder particle size (standard deviation ≈ 9 µm in the virgin powder and ≈ 10 µm in the recycled powder), solidification cell size and dislocation density. While the difference in yield strength between vertically-built virgin and recycled powder samples was found to be negligible, the latter exhibited a lower elongation to fracture [1211].

The experimental studies mentioned above only covered one reuse cycle. To quantify the effect of multiple reuse cycles on the mechanical properties of AlSi10Mg, Del Re et al. measured the powder properties and mechanical properties of L-PBF-processed parts for a total of 9 subsequent build jobs using the same powder batch, which was sieved after each build [1209] (see Fig. 79). Notably, the

chemical composition, apparent density, tap density and particle sphericity of the AlSi10Mg powder were found to remain approximately constant for the full duration of 8 reuse cycles [1209]. The oxygen content was not measured. The particle size distribution exhibited a shift towards smaller particle sizes, especially during the first cycles (see Fig. 79a and b) [1209]. This behavior was attributed to comparatively coarse particles being gradually removed from the powder batch due to sieving [1209]. The results of tensile tests are displayed in Fig. 79c and d. No significant effect of the powder recycling on elongation at fracture was observed. In contrast, a statistically significant reduction in yield strength with an increasing number of reuses was observed. However, the total extent to which the yield strength decreased over 8 reuse cycles was small. In addition to the decrease in strength, high cycle fatigue strength decreased by approximately 12% [1209]. According to the authors, the changes in mechanical properties observed still conform to the alloy specifications [1209]. The results of Del Re et al. [1209] regarding multiple reuse were largely confirmed in a separate study by Maamoun et al. [1212], who investigated the characteristics of AlSi10Mg powder subjected to 18 prior build jobs (see Fig. 80). Relative to the virgin powder, the recycled powder exhibited a shift towards smaller particle diameters. The overall degree to which the particle size distribution shifted was small, as values for the 10th (D10) and 90th (D90) percentiles only decreased from 11.8 and 54.1 μm for the virgin powder to 10.7 and 52.6 μm for the recycled powder, respectively.

The findings of the studies presented suggest that powder recycling is a viable solution for improving the eco-efficiency of additively manufactured components, provided that used powder is sieved after each build job. However, more research is needed to quantify the maximum numbers of reuse cycles up to which properties of build parts will continue to retain their respective specifications. Because certain applications, e.g. in the aerospace industry [1194], require mechanical properties beyond those offered by AlSi10Mg, it is also necessary to investigate the effects of powder recycling using different aluminum alloys, as recycling behavior may differ according to the chemical composition of the powder.

8.1.3. Sustainable aluminum alloys for additive manufacturing

The vast majority of aluminum powder is produced from primary aluminum [1213]. Apart from reusing powders, the CO₂ footprint associated with typical AM processing might be further reduced by employing secondary aluminum as the raw material. Due to the currently high price of spherical metal powder [1198] and the inability to process many commercial high-strength aluminum alloys [1194], comparatively little attention has so far been paid to developing sustainable aluminum alloys for AM.

In general, impurities can exert harmful effects on aluminum alloys in a variety of ways, some of which are universal among manufacturing methods. More specifically, the interaction between impurities and other solute species can cause drastic changes in phase equilibria. In high-strength Al-Cu-Mg-Ag alloys, for instance, the addition of only 0.2 wt% Si is sufficient to fully suppress the formation of the desirable Ω phase [1215]. Interactions between different solute species depend on the chemical composition and need to be considered for the various alloy systems individually. However, L-PBF provides cooling rates on the order of 10^4 – 10^6 K/s [1216], and some mechanisms by which impurities adversely affect the properties of aluminum alloys can be mitigated or even fully eliminated because rapid solidification is known to increase the effective solubilities of alloying elements in aluminum and decrease the size of second-phase particles [1217]. Clear examples of this are provided by studies on the AM of Fe-bearing aluminum alloys.

Suchy et al. [1009] compared the microstructure and mechanical properties of L-PBF-produced and as-cast AlSi9Cu3, an alloy frequently used in the production of die-cast engine blocks in the automotive industry [1218]. The microstructure of the as-cast alloy containing 0.65 wt% Fe was characterized by coarse eutectic Si and intermetallic Fe- and Cu-rich phases [1009]. The intermetallic phases in the L-PBF-processed material had a significantly finer dispersion, despite the higher Fe content of 1.01 wt% [1009]. This microstructural refinement was accompanied by a significant improvement in mechanical properties. The elongation at fracture increased from approximately 0.6% in the cast specimen to 5.3% in the sample produced by L-PBF. Moreover, the yield strength almost doubled. A similar improvement in mechanical properties was noted by Yamasaki et al. [1214], who produced AlSi12CuNiMg with a nominal Fe concentration of 0.1 wt% via both casting and L-PBF. Two modified alloys with nominal Fe concentrations of 3 and 5 wt% were also processed by L-PBF. All specimens were annealed at 300 °C [1214]. One group of alloys was heat-treated to the T6 condition prior to this step. High-temperature tensile tests were performed at 300 °C; the results are displayed in Fig. 81. Among the samples annealed at 300 °C, those produced by L-PBF exhibited enhanced strength and elongation at fracture at all Fe concentrations. Similarly, the elongation at fracture was drastically increased in the additively manufactured samples of the T6 group, indicating that Fe addition can be deployed to improve the strength-ductility relationship in L-PBF-processed Al-Si-based cast alloys.

Remarkably, an improvement in mechanical properties when Fe is added has not only been observed in alloys of the Al-Si system. An AM-related patent application published by AMAG casting GmbH and AUDI AG [1220] discloses the chemical compositions of commercial aluminum alloys modified by adding Mn and Fe, and presents the properties of L-PBF-processed materials. Adding 0.5–1 wt% Fe to Mn-modified wrought alloys of the 5xxx series (Al-4.9 Mg-0.6Mn-0.5Sc-0.5Zr-0.1Fe), the 6xxx series (Al-1.2 Mg-0.8Si-0.7Mn-0.2Fe), and the 7xxx series (Al-6Zn-1.6Cu-2.7 Mg-0.3Mn-0.1Fe) generated increased ultimate tensile strength, elongation at fracture, reduced porosity and hot cracking susceptibility in all alloys [1220].

Even higher Fe concentrations can be found in the rapid solidification alloy 8009 with the composition Al-8.5Fe-1.3 V-1.7Si (wt.%) [1219], originally developed by Skinner et al. [1221]. Fig. 82 provides a direct comparison between cast and L-PBF-produced 8009 [1219]. Despite the high Fe content, no coarse intermetallic phases can be observed in the additively manufactured alloy. It achieves an ultimate tensile strength of 454 MPa and an elongation at break of 7.2% [1222]. This provides a notable example of how high concentrations of otherwise deleterious alloying additions can be exploited to create high-strength alloys for AM.

The available literature suggests that many of the commercial aluminum alloys currently in use exhibit high impurity tolerance to Fe during additive manufacturing. This clearly illustrates the potential of using secondary aluminum as raw material in the production of aluminum-based powders.

Future research should aim at quantifying the effects of different levels and combinations of impurity elements (e.g. Fe and Mn) –

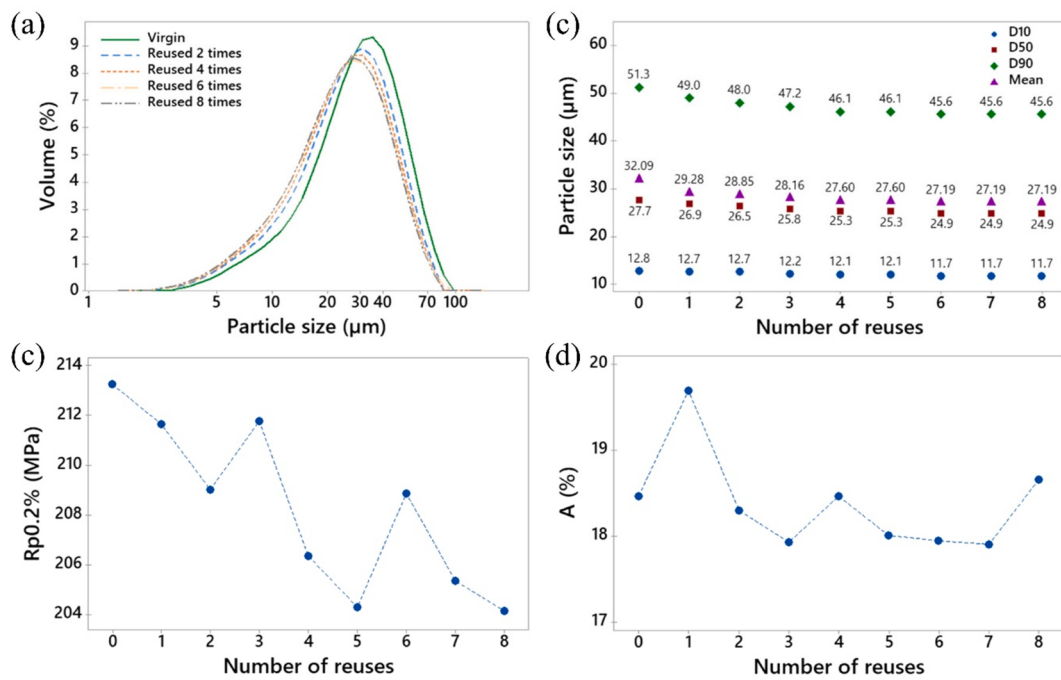


Fig. 79. Evolution of (a) particle size distribution in an AlSi10Mg powder; (b) average particle size; (c) tensile yield strength of AlSi10Mg in the as-built state; and (d) elongation at fracture with an increasing number of reuse cycles. The powder was sieved after each build job. Adapted with permission from [1209].

not only on mechanical properties, but also on corrosion behavior and the processability of aluminum alloys. This will be a step towards determining the grade-specific maximum tolerable concentrations of these impurities.

8.2. Uni-alloys, crossover alloys and multi-purpose alloys

First, we will define what we mean by the terms uni-alloys, multi-purpose alloys and crossover alloys [48]. A uni-alloy addresses a single composition space and targets a reduced number of alloy compositions for different parts and components of a system made from it. In the simplest example, this can be the use of a single composition for can bodies and lids [31,299]. Its current extreme is a uni-alloy car, which is currently far from being realized. However, an interesting example that actually exists is car doors. Currently, the inner part of car doors is often made of non-hardenable, highly formable 5xxx wrought alloys [1223]. Unfortunately, these alloys are soft and their surfaces after forming is not decorative. Therefore wrought 6xxx alloys, which show good surface quality after being shaped but are more limited in formability compared to the 5xxx alloys, are often used for the outer part of the door [1223]. However, the combined recycling of these materials is problematic because the alloys cannot be recycled in the same scrap stream due to elemental incompatibilities (see section 7.5 and 7.6 for details). Although it is obvious that a uni-alloy strategy can reduce compositional complexity in future structures, it should be noted that in very simple cases, such as beverage cans, it does not always provide environmental benefits if certain boundary conditions apply [31]. However, in many complex structures and systems the strategy is indeed beneficial. A uni-alloying concept could remedy this situation and provide more sustainable, simplified recycling.

In this context it is very important to recognize that such concepts can only be realized if the properties of an alloy can be meaningfully changed via microstructure adjustment. To a small extent, this has been investigated in the area of 6xxx alloys in cars. Some 6xxx series alloys have been promoted as uni-alloy in the automotive sector (e.g. 6022 for outer and inner body panels [29,1224]). In reality, however, a mixture of alloys is still often used due to the varying demands of today's automotive designs and the lack of studies and development work on 6xxx-based automotive uni-alloys.

Uni-alloy concepts exist in the area of AlSiMg structural castings. These concepts mainly apply to the use of single compositions which provide a broad property range via adjustments to the heat treatment condition. For example, Müller et al. [1225] developed a high-pressure die-cast alloy for various car components classified as “crash-relevant”, “strength-relevant” and “high-strength”. At present different near-eutectic AlSi alloys are deployed in such components depending on the application, but in the future the new Si-

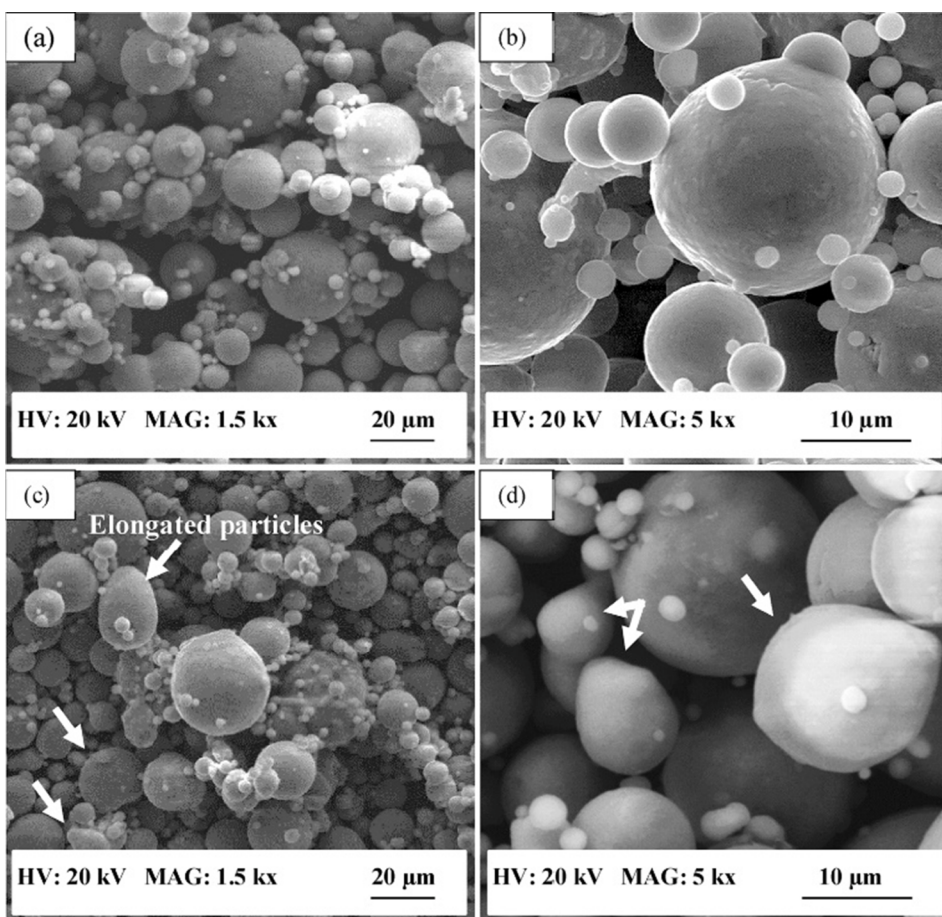


Fig. 80. SEM images showing the morphology of AlSi10Mg powder in the (a, b) virgin state and (c, d) after 18 prior uses. The powder was sieved after each build job. Reprinted with permission from [1212].

reduced AlSi7Mg variant should meet all requirements. For this purpose, the heat treatment of the alloy was redesigned. Adjusting the solution heat treatment and increasing the quenching rate generates a high-strength condition. To be “crash-relevant”, where increased ductility is required, a share of the component’s strength is sacrificed by applying an overaging treatment. This procedure is further associated with an increase in necking elongation and a simultaneous improvement in the multiaxial deformability of the material, resulting in an improvement of the often application-critical self-pierce riveting properties [1225].

The aspect of setting different properties by modifying process parameters also applies to multi-purpose alloys. Multi-purpose alloys are particular alloys which can be deployed in several applications. In addition, one alloy composition can be subjected to different production methods (e.g. castings and wrought products are made from the same alloy). To a small extent multi-purpose alloys already exist today: for example, the wrought alloy 5182 overlaps closely with the casting alloy EN AC-AlMg5. Other examples include the use of both casting and wrought alloys in additive manufacturing, for example AlSi10Mg [1226] or 6061 [1227]. These have in common that due to a high solidification rate and the associated fine formation of IMCs, they tolerate a higher trace element content.

The term “crossover alloy” [48] implies that the compositional classifications usually in place for the different alloy classes are neglected for bridging properties. This applies to both the uni-alloy and the multi-purpose concepts. The aim of the crossover approach is to expand the property range to reduce the number of alloys required in complex systems [3,1228].

Production and design often require the use of several different alloy systems, limiting recyclability at the end of a product’s service life [3]. One example is a complicatedly shaped component in a vehicle. Although it is possible to improve the formability of 6xxx alloys without loss of strength [1229–1231], this development direction has natural limits because strain hardening of these alloys cannot be easily modulated over a wide range. Hence, 6xxx alloys do not yet meet some of the requirements for complex forming operations (especially stretch forming), even though these alloys offer good age-hardening potential. Today’s wrought 5xxx alloys offer high uniform elongation and work hardening due to their inherently high Mg content [1018], which is beneficial for complex forming operations. However, Lüders elongation, dynamic strain aging and low strength are disadvantages of these alloys [86,87].

One approach to solving this problem is to introduce additional alloying elements into 5xxx alloys to promote age hardening. The addition of small amounts of Cu to 5xxx wrought alloys to prevent softening due to recovery of automotive 5xxx alloys during paint

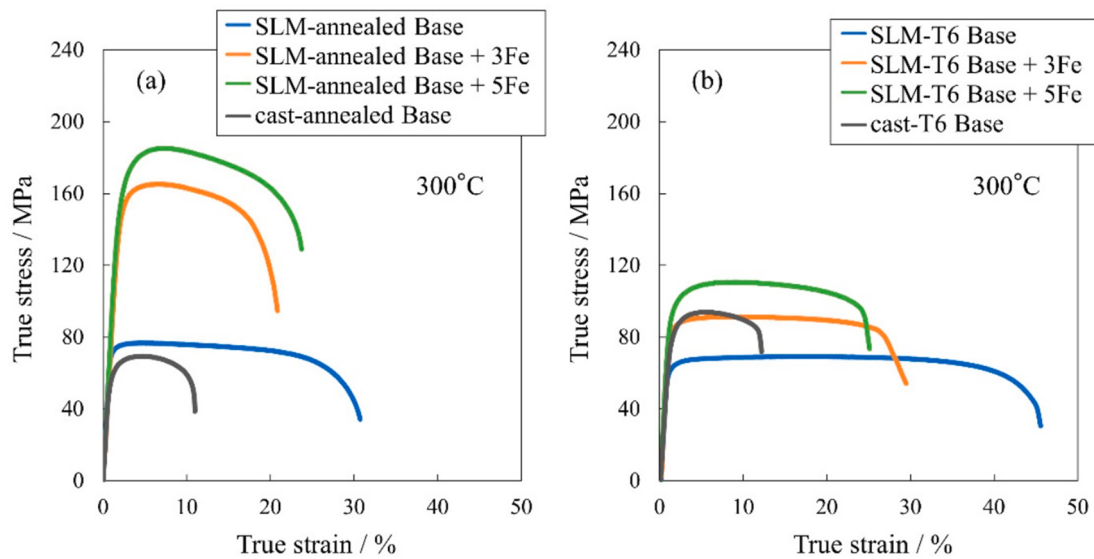


Fig. 81. True stress–strain curves of an AlSi12CuNiMg alloy with varying Fe content, produced by casting and L-PBF (denoted here as Selective Laser Melting (SLM)), and measured at 300 °C. Reprinted with permission from [1214].

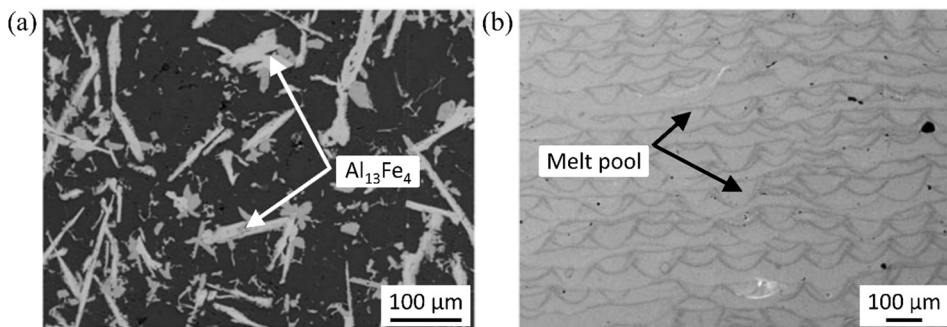


Fig. 82. SEM micrographs of (a) as-cast and (b) L-PBF-produced 8009. Adapted with permission from [1219].

baking was first seen in Japan at the beginning of the 1990 s [1232], and has attracted further interest since [1052,1109,1233]. This research may involve the first exploitation of the extensive work hardening of 5xxx alloys combined with the age-hardening potential of another alloy class (Cu from the 2xxx series) and the crossover of properties. As in 2xxx series alloys, the typical precipitation sequence in such crossover systems includes clusters, precursors and finally the equilibrium S phase (Al_2MgCu) [1233].

While the Cu additions to wrought 5xxx alloys investigated were generally rather small, other studies addressed Zn addition to 5xxx alloys of up to several percent. Compositionally the results can be regarded as crossovers of 5xxx and 7xxx series alloys. Their aim is not only increased strength, but also reduced serrated flow behavior and enhanced corrosion resistance. In recent years, an increasing trend towards adding Zn [1051,1234–1238] has been observed, although with an even stronger focus on the combined adding of Zn and Cu [87,1006,1239–1245]. Note that this concept has also been applied to casting alloys [1005].

It is now accepted that in equilibrium, the T phase ($\text{Mg}_{32}(\text{Al},\text{Zn})_{49}$) is formed in these systems. However, the precipitation sequence utilized in aging treatments is complex and still under debate. It depends on thermal history and composition. This is illustrated in Fig. 83.

Fig. 84 demonstrates the potential of this type of 5xxx to 7xxx crossover concept. The combination of high strain hardening caused by high Mg content and a rapid, superior age-hardening response within a short time, typically applied upon paint-baking in the automotive industry, proves to be feasible [1239]. Although the concept is promising, it has not yet reached industrial scale due to the recent nature of intensive research in this field.

Compositionally, crossovers between 6xxx and 7xxx series wrought alloys also exist. The main aim with these crossover alloys is to improve the age-hardening potential of 6xxx alloys via Zn addition and to add the aging characteristics of 7xxx series alloys to 6xxx alloys [405,831,861,862,1246–1249]. As can be seen from the literature on it, this research was not undertaken to reduce the number of alloys required via an expansion of the property profile, but the results may well serve this goal.

In general, the environmental benefits of the above-mentioned crossover alloys have not been studied in depth. There are also no studies on their recyclability, apart from the general argument – which should be noted by product designers – that reducing the

number of alloys can be beneficial. In this context another meaning for the term “crossover” was brought to light by Haga et al. [1250]. They studied a compositional crossover between 6xxx wrought alloys and AlSi-based casting alloys processed by high speed twin roll casting. This involved a true compositional blend resulting from mixed scrap streams rather than an overlap in material properties. Similar research was conducted on a crossover of 5xxx wrought alloys and AlSi-based casting [1251]. The alloy 5182 was contaminated with up to 2 wt% of Si and processed by vertical high-speed twin-roll casting. The final cold-rolled and annealed sheets showed promising properties, with a limiting draw ratio of 1.8 and elongation above 20% at 2 wt% of Si. Haga et al. [1251] concluded that the alloys could be used for die casting and sheet forming – evoking multipurpose alloys.

Finally, it should be mentioned that the crossover concept is also being applied in new processing routes such as additive manufacturing [1252]. In this area in particular, but also in general, we see that composition classifications that have been common for decades are beginning to break down, leaving plenty of room for alloy development.

9. Conclusions, outlook and future research

This article has reviewed the state of the art and the scientific challenges involved in making aluminum alloys more sustainable through transitioning to a more circular system of material recovery and reuse. It was motivated by the huge discrepancies between primary synthesis and secondary synthesis (i.e. recycling) in terms of energy consumption, GHG emissions and environmental pollution associated with mining and by-product management. The energy needed to melt aluminum scrap is 5% of that needed to reduce ore, a difference which – where exploited – translates into reduced CO₂ emissions. The amount of available aluminum scrap is also estimated to double by 2050, which indicates the urgency of this topic.

The key challenge here is the large-scale intrusion and accumulation of impurity elements in alloys, in terms of both the number of different elements and their concentrations. Here two main tasks emerge. One is to develop mature engineering alloys which are more scrap-compatible, i.e. more tolerant of certain tramp elements that intrude from scrap so as to make them more robust under conditions of both higher impurity content and higher composition variability. This would render alloys fit for the maximised use of scrap. The other task is to reduce both the number of alloys and their chemical complexity and, wherever possible, achieve consistent properties by replacing composition tuning by microstructure tuning.

These two tasks comprise research directions that address an overall future need: to establish a “science of dirty alloys” which encompasses a set of approaches that will equip aluminum alloys with higher impurity tolerance [3].

The article has reviewed and evaluated the metallurgical mechanisms behind the topics involved, including such things as the influence of scrap-related contaminants on the thermodynamics and kinetics of precipitation reactions, plus their mechanical and electrochemical effects; precipitation-free zones around grain boundaries; casting microstructures; and adjustment of processing parameters, plus the resulting mechanical, functional and chemical properties.

In the second section a few guiding questions were formulated, to which we now return. With regard to both controlling potential negative effects and realizing great benefits, what main factors require our attention?

(i) What effects do contaminants have?

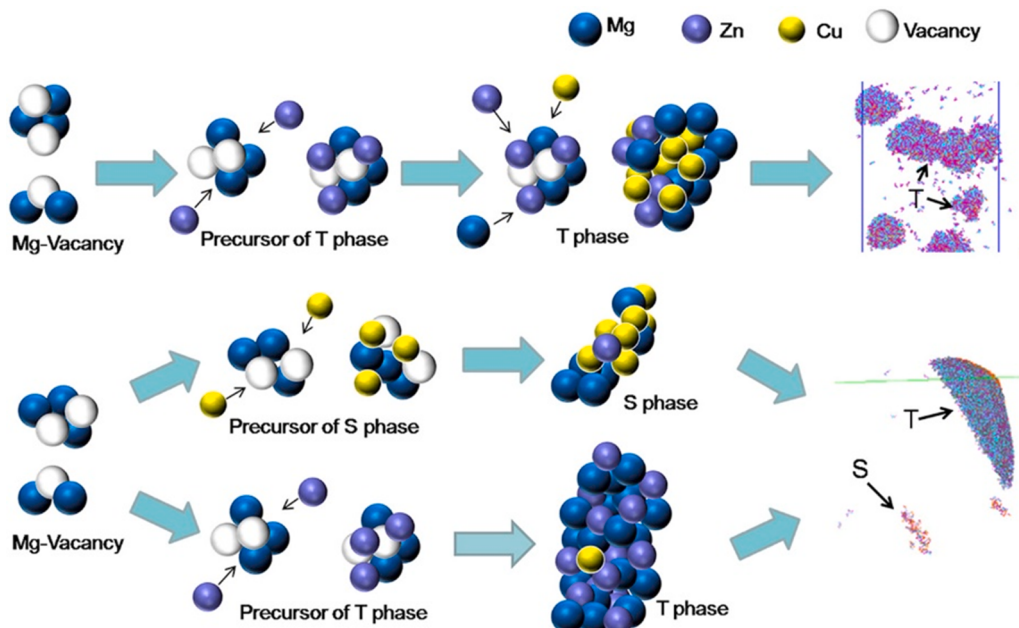


Fig. 83. Schematic illustration of the proposed precipitation sequence by Cao et al. [1241] for alloy AlMg5.2Zn2.0Cu0.45 (in wt.%) upon aging at 180 °C with (a) and without (b) prior pre-aging (80 °C/12 h). Reprinted with permission from [1241].

Due to their usually low solubility, most impurity elements promote the formation of intermetallic phases. These phases can affect castability, ductility, fracture toughness, fatigue, various forming limits, surface finish, corrosion, age-hardening capability and precipitation free zones. The associated effects can be positive (e.g. by controlling recrystallization during homogenization, or refining grain size during casting) or negative (e.g. for fracture properties if the particle size, shape and distribution is not well controlled). Well known in this respect is Fe, which can cause morphologically unfavorable intermetallic phases to form in many alloys. However, the nature and properties of the phases formed are highly dependent on processing and constitution, and there are many possibilities for optimization. In addition to forming intermetallics, impurity elements can also significantly modify existing intermetallics (through changes in intermetallic type or shape). A well-known example is the addition of Mn to FeSi-containing intermetallics. Here Mn can change the shape, which is very beneficial. Another effect of impurities can be segregation at interfaces, weakening mechanical properties or corrosion properties (e.g. Cu at grain boundaries). In addition to the formation of intermetallic phases, elements in the solid solution can also have effects, e.g. on the precipitation kinetics. Knowing more about how impurity elements might be used in such areas would be a useful aim in the science of dirty alloys. Another important impact of impurity elements is on the precipitation process itself, either directly through effects on phase selection and the trajectory of metastable and stable phases that form, or indirectly through interactions with vacancies that subsequently affect precipitation.

(ii) Are thermodynamic and kinetic databases sufficiently detailed and reliable as foundations for the development of “dirty alloys”, in particular in the areas of spinodal, metastable and intermetallic phases and contaminant effects on vacancies?

Detailed thermodynamic information about some of the relevant impurity elements, and specifically their interactions with the base alloy composition, is sparse when it comes to the prediction (and avoidance) of their occurrence and associated intermediate states. This is true not only for the underlying Gibbs free energy or Landau potential landscape curves, but also for the mobility coefficients, their effects on vacancies, and the nucleation barriers or respective spinodal decomposition windows.

Much more development work is required in the future on free energy descriptions of intermetallics as a function of different scrap alloying element additions. The pending questions here are: how is the competition between different intermetallics affected by impurity addition? What scrap elements are soluble in the various intermetallics? How do scrap additions modify the shapes of intermetallics?

The effect of vacancy binding due to impurity elements and the subsequent effect on diffusion and precipitation needs more investigation. Excess vacancy content during precipitation is non-constant due to such effects. Phenomena such as the “vacancy pump” have been proposed to explain some of the unusual time dependence of diffusion-controlled processes in Al-alloys (such as the logarithmic time dependence of resistivity changes). It is clear that mass transport under conditions of vacancy trapping and binding requires much work. This strongly influences the kinetics of precipitation in aluminum alloys.

(iii) Can scrap-related contaminants get trapped at lattice defects and inside precipitates? Could such trapping be used to render them harmless? Which types of thermal treatment should be applied to this end? Are all contaminant-related phases that form harmful, or are there beneficial features associated with any of the tramp elements?

Impurities are often found to become enriched in dispersoids, in intermetallics, in the bulk and at grain boundaries. Investigations are thus needed to detail which of these nano-alloying elements are harmless and which are not, e.g. in terms of embrittlement, precipitation-free zones, age-hardening kinetics, hydrogen embrittlement and/or micro-galvanic corrosion. In some well-studied scrap-related intermetallic precipitates, modest alloy modifications can be a suitable pathway for mitigating harmful effects from such precipitation states.

Some impurity elements can be deployed to segregate to precipitate interfaces and beneficially affect thermal stability; this has been done in Al-Cu based alloys. More work in this direction is required. Some tramp elements can be bad, however, and finding ways to immobilise them at trapped sites is worth considering. Can reservoirs be built into the alloy design to trap detrimental species so that

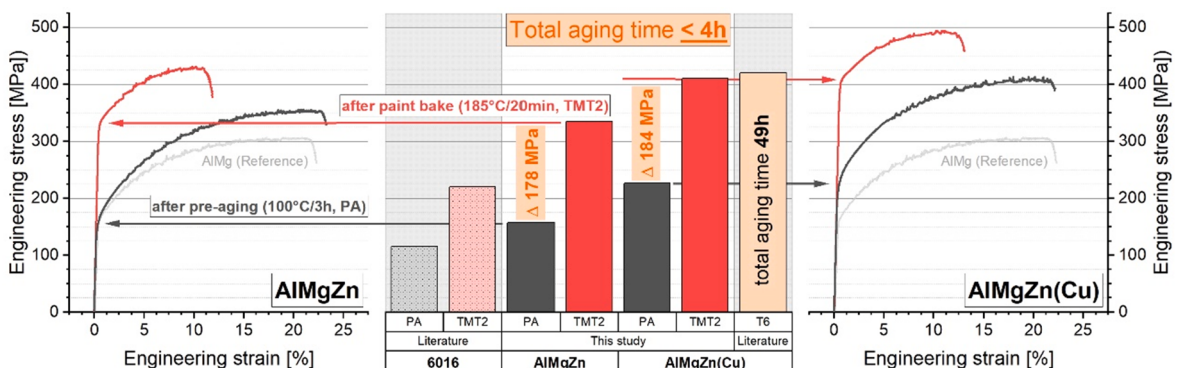


Fig. 84. Demonstration of the potential of an 5182 base alloy (denoted as AlMg) with the addition of 3.5 wt% Zn (denoted as AlMgZn) and 3.5 wt% Zn and 0.5 wt% Cu (denoted as AlMgZnCu). Data after pre-aging (typical forming condition) and after a paint-bake treatment (typical application condition) are shown. The forming properties deducible from the tensile tests (elongation, strain hardening) are comparable to 5182 for the alloys with added Zn and Zn + Cu. The strength after a paint-bake treatment is superior. A comparison with a common automotive 6xxx alloy for automotive applications is also shown. Reprinted with permission from [1239].

they cannot damage other processes?

(iv) How impurity-tolerant can we make green near-commercial Al-alloys, and which contaminants are most relevant? What upper limits apply to contaminants in near-engineering Al-alloys?

The most important contaminants are Fe, Mn, Cr, Cu and Si, depending on the alloy class and the product application targeted. It was shown that with regard to some of these scrap-related contaminants, alloy tolerance can already be increased in existing alloys without any substantial loss of properties. It is important to understand that through advanced casting processes and higher quench rates, higher levels of impurities (e.g. Fe) might be made possible. Most work concerns alloys for automotive applications (5xxx, 6xxx series alloys and casting alloys), but increased impurity levels are also being discussed in the context of aircraft alloys. In general there is much scope for research into improving the impurity tolerance of established alloys, either through processing or through minor compositional measures (e.g. modification of deleterious intermetallic phases).

(v) Which crossover alloys are the most promising for combining beneficial mechanisms across established alloy families?

Such broad-band, multi-purpose alloys must be designed as universal and not as niche alloys. They should be broad in their composition tolerance and application range. This field is relatively new, but there have already been attempts to combine excellent forming properties and high strength in new AlMgZn(Cu) alloys in order to cover more automotive applications with one alloy [48,1006]. Attempts are also being made to extend the properties of existing wrought (6xxx) and cast alloys (AlSiMg) within one compositional range to broaden their applicability. Although the overall concept of such crossover alloys is very appealing, it must be considered that most of the Al produced thus far is still in use, and that the accumulation of Al out there falls into composition ranges that are roughly defined by the existing classes. Making those existing classes more robust in the face of impurities would probably be of greater benefit to the field because it would encompass the Al already in use.

(vi) What combinatorial high-throughput methods are suitable for revealing scrap-related composition-microstructure-kinetics-property trends and ranges? How can we probe damage-tolerance in the associated experiments?

Recent work suggests that the combinatorial screening of alloys for effects associated with scrap-related impurities requires the use of at least mm-thick sample sizes which can be cast, homogenised and quenched-in under conditions that approximate macroscopic processing conditions, at least roughly. Thin film combinatorial methods, or compositional alloy gradients produced by additive manufacturing or related methods which utilise rapid quenching, create microstructures that are not really comparable to those observed under real manufacturing conditions.

(vii) For which phases is it necessary to use atomistic simulation methods to understand phase (meta-) stability, impurity trapping, sublattice occupancy and phase stoichiometry ranges? In general, are there sufficiently suitable modeling techniques available by which we can analyse the effects of tramp elements on aluminum alloys?

Few reliable thermodynamic data are available on phases with > 4 components. When such phases become important in the context of contaminants from scrap, it may be expedient to study their exact composition and structure by electron microscopy and atom probe tomography and to use the results for thermodynamic calculations. If only a small fraction of tramp elements enters dispersoids or transient phases, ab initio calculations become challenging because they need a certain minimum stoichiometry to fit supercell simulations. A better thermodynamic understanding of impurity-related phases is generally important, because in some cases a suitable strategy may be to add further doping elements that render some of these intermetallic cases less harmful (i.e. Fe-containing phases become less harmful if they are doped with Mn).

(viii) How does deploying meso- and near atomic-scale characterization methods address these challenges? How can the main effects associated with tramp elements be observed and identified?

High-resolution probing techniques such as scanning transmission electron microscopy and atom probe tomography can reveal even near-ppm-range impurity effects and the associated structures of nano-precipitates. Ideally these techniques are applied to the same portion of the material in question, a technique that is referred to as correlated microscopy. Corresponding additional information on size distributions, which gives such studies statistical relevance, can be obtained using advanced synchrotron methods. In some cases, it may be necessary to conduct these studies together with ab initio calculations. A remaining weakness lies in analyzing the interaction between impurity elements and vacancies, an effect which can be particularly important in aluminum alloys.

(ix) Can supervised, knowledge-informed machine learning identify suitable nanostructure-composition-processing-property relations for the field of sustainability alloy design?

The currently most promising, valuable application of artificial intelligence methods in this area is in scrap separation and sorting, mainly applied in LIBS analysis. Future benefits for recycling and the related alloys may also come from exploiting the massive amounts of processing data provided today by the many sensors that exist in current processing lines – data gathered over many processing steps and analysed in dependence on chemical composition variations. Here, discovering trends with the help of machine learning may be a very fruitful way to use scrap in aluminum alloys efficiently in future, and also to screen composition-property relationships for scrap-compatible alloy design [1253,1254].

(x) How do processes have to be adjusted to deal with the effects of contaminant elements?

Besides improved scrap sorting, techniques for advanced casting techniques including flow optimization and more rapid cooling are gaining momentum. For instance, high solidification rates in near-net-shape casting lead to reduced through-thickness compositional gradients, higher dispersion of contaminant-affected precipitates, reduced Scheil segregation profiles, and smaller grain and dendrite sizes, and thus generate greater homogeneity in the cast material overall. The extreme case here is additive manufacturing, where high solidification rates allow the use of high concentrations of typical impurity elements (e.g. Fe) to further improve the property portfolio. Later procedures in the process chain such as heat treatments may also require adjustment (e.g. advanced homogenization for fragmentation of intermetallic phases).

It is also worthwhile in general to consider being less reliant on thermally induced precipitation to make high-strength aluminum

alloys. The reason these alloys are so sensitive to compositional variation is because the thermally induced precipitation process is also very sensitive to composition. What if we did not need to use thermally induced precipitation but could instead force the decomposition of the solid solution by external means? We could, instead, consider forcing precipitation via a “driven system”. One example of such external forcing is seen in the recently published approach of deploying cyclic plasticity to continually inject vacancies into the material to drive the decomposition of the solid solution by dynamic precipitation at room temperature [85]. This approach is very effective and much less sensitive to impurity effects. While industrializing such new processes is a challenge, they should definitely be considered in making alloys more composition-robust. High-powered ultrasonics or forms of irradiation might be interesting sources for such excitation. These and other different approaches to processing may completely change precipitation sensitivity to impurities [296,935].

(xi) What measures and approaches promise to be the most effective in improving the sustainability of secondary synthesis?

In processing, a significant impact is to be expected from scrap avoidance, streamlined scrap collection and improved scrap sorting, including the associated producer and downstream manufacturer workflows. These things will clearly have the greatest effects. The origin of scrap also matters: when expressed as global warming potential (GWP, in kgCO₂eq per metric ton), primary smelters where the material is synthesized from ores have a GWP footprint of 12.2, production from old (post-consumer) scrap have a GWP footprint of only 1.4, and production from new (in-production) scrap have a GWP footprint as low as 0.4. Further effects come from replacing all fuels used for furnace heating with renewable electrical and/or green hydrogen sources. Generally, electrification of processes should have high priority. In casting, rolling and heat treatment efforts should be directed at enhancing the dispersion of dispersoids and precipitates, including intermetallic particles that can occur when a higher impurity content enters the alloys. Incentives for establishing some of these measures might be tax regulations and/or sustainability labels that make them, and improved scrap streams, visible to customers. Ideally, high market prices would result. On the metallurgical side, all measures that enhance alloy tolerance to impurity elements have a significant effect, particularly in alloys traded in large quantities. One example is the increase in the Fe content of 6xxx sheet alloys used for vehicles. For more examples see the bulk text.

In the context of all these measures it is important to calibrate metallurgical and processing adjustments to the scrap-based alloys which are the most sustainable.

From a conceptual perspective it would surely be desirable in the future to reduce the number of alloy variants on the market, and even to develop certain standards to govern which alloys should be used for certain parts so as to avoid the often-observed wide variation in alloy types used in the same product, which makes subsequent scrap separation a challenge. Also, microstructure tuning should generally be preferred over composition tuning when adjusting and developing materials for new products. Microstructure tuning requires state-of-the-art processing equipment and both knowledge-based and machine-learning-based access to the underlying processing-structure–property relationships of alloys which contain impurities. Another very promising avenue lies in developing multi-purpose and crossover alloys. These could generally help to reduce the number of alloy variants on the market.

Product design will also have to be adjusted on the customer side where sustainable alloys made from scrap are involved. In the future, customers who use alloys with a high recycling content will more frequently have to adjust downstream processing instead of sticking to established operations. It follows that their awareness of the issues which arise when they use alloys made from scrap needs to be improved. In any case, the best results of all will generally be achieved by improving scrap separation and establishing closed producer-customer scrap cycles.

Author contributions

Dierk Raabe, Stefan Pogatscher, Helmut Antrekowitsch, Christopher Hutchinson und Peter J. Uggowitzer designed the article's concept.

Content dealing with scrap-based aluminum alloys was contributed mainly by Dierk Raabe, Stefan Pogatscher and Chad W. Sinclair, and was revised by all other authors.

The discussion of the sustainability of aluminum alloys was conceptually designed by Dierk Raabe, Stefan Pogatscher, Helmut Antrekowitsch, Peter J. Uggowitzer and Chad W. Sinclair and was revised by all other authors.

The sections dealing with scrap-related production steps and their sensitivity to tramp elements, types and flows of aluminum scrap, secondary synthesis, recycling rates and their consequences for alloys, advanced aluminum scrap sorting, pre-treatment methods, process technology and plant technology were authored mainly by Helmut Antrekowitsch, Stefan Pogatscher and Dierk Raabe and were revised by all other authors.

The sections on near-net-shape, thin-strip, belt and chain conveyor casting methods were contributed mainly by Dierk Raabe, Stefan Pogatscher and Mario Paolantonio.

The sections on sheet-forming challenges for scrap-contaminated alloys were authored mainly by Christopher Hutchinson, Dierk Raabe, Stefan Pogatscher, Peter J. Uggowitzer, Chunhui Liu and Zhiming Li.

The section on joining scrap-contaminated alloys was authored by Philip Prangnell and Joseph Robson.

The sections on thermodynamics simulation tools for the study of scrap-related impurities and intermetallic phases and simulation methods for the study of scrap-related impurity effects on precipitation kinetics and microstructure evolution were authored mainly by Chunhui Liu, Zhiming Li, Chad W. Sinclair, Mario Paolantonio, Christopher Hutchinson, Pratheek Shanthraj, Samad Vakili, Philip Prangnell and Ernst Kozeschnik.

The section on combinatorial metallurgical methods for studying the effects of tramp elements was developed and written by Alexis Deschamps, Mario Paolantonio, Dirk Ponge and Dierk Raabe.

The section on advanced analysis tools related to the highly-resolved characterization of tramp elements was written mainly by

David Seidmann, Baptiste Gault, Frédéric De Geuser, Alexis Deschamps and Laure Bourgeois.

The section on machine-learning approaches for the development of sustainable aluminum alloys was developed by Dierk Raabe and Chad Sinclair.

The sections on powder metallurgy, additive manufacturing and recycling-friendly and contaminant-tolerant near-engineering Al-alloys was written by Moritz Roscher, Stefan Pogatscher, Peter J. Uggowitzer and Dierk Raabe.

Reflections on all of these different aspects and discussions, and summarizing thoughts on a wide range of aluminum alloys, were contributed by all authors.

Declaration of Competing Interest

The authors declare that they have no known competing financial interests or personal relationships that could have appeared to influence the work reported in this paper.

Acknowledgments

C.H.L. acknowledges financial support from the National Natural Science Foundation of China (No. U2032117). Z.L. would like to acknowledge special funding from the Construction of Innovative Hunan Province of China (2019RS1001). D.N.S. acknowledges the support of the Northwestern University Center for Atom-Probe Tomography (NUCAPT). The LEAP tomograph at NUCAPT was purchased and upgraded with grants from the NSF-MRI (DMR-0420532) and ONR-DURIP (N00014-0400798, N00014-0610539, N00014-0910781, N00014-1712870) programs. NUCAPT received support from the MRSEC program (NSF DMR-1720139) at the Materials Research Center, the SHYNE Resource (NSF ECCS-2025633), and the Initiative for Sustainability and Energy (ISEN) at Northwestern University. The research on aluminum alloys was supported by the Office of Naval Research, Dr. William M. Mullins, grant officer. D.N. S. is grateful to D. Isheim for managing the atom probe tomography center at Northwestern University. P.B.P. and J.D.R. thank the EPSRC, LightForm Programme grant, (EP/R001715/1) for supporting aspects of this work. S.P. gratefully acknowledges financial support from the Austrian Federal Ministry for Digital and Economic Affairs, the National Foundation for Research, Technology and Development and the Christian Doppler Research Association. E.K. gratefully acknowledges financial support from the Austrian Federal Government (in particular from Bundesministerium für Verkehr, Innovation und Technologie and Bundesministerium für Wissenschaft, Forschung und Wirtschaft) represented by Österreichische Forschungsförderungsgesellschaft mbH and the Styrian and the Tyrolean Provincial Government, represented by Steirische Wirtschaftsförderungsgesellschaft mbH and Standortagentur Tirol, within the framework of the COMET Funding Programme. L.B. acknowledges the use of the instruments and scientific and technical assistance at the Monash Centre for Electron Microscopy, a Node of Microscopy Australia. This research used equipment funded by Australian Research Council grant LE0454166.

Several of the authors express their sincere thanks for inspiring discussions about sustainable aluminum with companies such as AMAG, Hydro and Alcoa.

References

- [1] International Aluminium Institute. Global Aluminium Cycle 2019. Alucycle 2020. <https://alucycle.international-aluminium.org/public-access/>.
- [2] Bertram M, Ramkumar S, Rechberger H, Rombach G, Bayliss C, Martchek KJ, et al. A regionally-linked, dynamic material flow modelling tool for rolled, extruded and cast aluminium products. *Resour Conserv Recycl* 2017;125:48–69. <https://doi.org/10.1016/j.resconrec.2017.05.014>.
- [3] Raabe D, Tasan CC, Olivetti EA. Strategies for improving the sustainability of structural metals. *Nature* 2019;575:64–74. <https://doi.org/10.1038/s41586-019-1702-5>.
- [4] Cann JL, De Luca A, Dunand DC, Dye D, Miracle DB, Oh HS, et al. Sustainability through alloy design: Challenges and opportunities. *Prog Mater Sci* 2020. <https://doi.org/10.1016/j.pmatsci.2020.100722>.
- [5] Allwood JM, Cullen JM, Milford RL. Options for achieving a 50% cut in industrial carbon emissions by 2050. *Environ Sci Technol* 2010;44:1888–94. <https://doi.org/10.1021/es902909k>.
- [6] Gutowski TG, Sahni S, Allwood JM, Ashby MF, Worrell E. The energy required to produce materials: Constraints on energy-intensity improvements, parameters of demand. *Philos Trans R Soc A Math Phys Eng Sci* 2013;371. <https://doi.org/10.1098/rsta.2012.0003>.
- [7] Ritchie H, Roser M. CO₂ and greenhouse gas emissions. OurWorldInDataOrg 2020;1. <https://ourworldindata.org/co2-and-other-greenhouse-gas-emissions>.
- [8] Cullen JM, Allwood JM. Mapping the global flow of aluminum: From liquid aluminum to end-use goods. *Environ Sci Technol* 2013;47:3057–64. <https://doi.org/10.1021/es304256s>.
- [9] Daehn K, Basu R, Gregory J, Berlinger M, Somjit V, Olivetti EA. Innovations to decarbonize materials industries. *Nat Rev Mater* 2021. <https://doi.org/10.1038/s41578-021-00376-y>.
- [10] OECD. OECD Green Growth Studies Material Resources, Productivity and the Environment. 2015.
- [11] Gupta A, Basu B. Sustainable primary aluminium production: technology status and future opportunities. *Trans Indian Inst Met* 2019;72:2135–50. <https://doi.org/10.1007/s12666-019-01699-9>.
- [12] Brough D, Jouhara H. The aluminium industry: A review on state-of-the-art technologies, environmental impacts and possibilities for waste heat recovery. *Int J Thermofluids* 2020;1–2. <https://doi.org/10.1016/j.ijft.2019.100007>.
- [13] International Aluminium Institute. Prim Alum Smelt Power Consum 2020. <https://www.world-aluminium.org/statistics/primary-aluminium-smelting-power-consumption/>.
- [14] IAI. International Aluminium Institute Historical Statistics. Stat Part 2011;Accessed M. <https://www.world-aluminium.org/statistics/primary-aluminium-smelting-power-consumption/>.
- [15] Allwood JM, Cullen JM, Carruth MA, Cooper DR, McBrien M, Milford RL, Moynihan MC, Patel ACH, Bauer S. Sustainable materials: With both eyes open. vol. 15. Cambridge, England: UIT Cambridge Ltd; 2012. Doi: 10.1016/s1369-7021(12)70169-4.
- [16] Holtzhausen HJ. Embodied energy and its impact on architectural decisions. *WIT Trans Ecol Environ* 2007;102:377–85. <https://doi.org/10.2495/SDP070361>.
- [17] Allwood JM, Ashby MF, Gutowski TG, Worrell E. Material efficiency: A white paper. *Resour Conserv Recycl* 2011;55:362–81. <https://doi.org/10.1016/j.resconrec.2010.11.002>.
- [18] Ashby M. Materials and the Environment: Eco-informed Material Choice: Second Edition. 2012. Doi: 10.1016/C2010-0-66554-0.

- [19] Gutowski T, Allwood JM, Sahni S, Herrmann C. A Global Assessment of Manufacturing: Economic Development, Energy Use, Carbon Emissions, and the Potential for Energy Efficiency and Materials Recycling. 2013. Doi: 10.1146/annurev-environ-041112-110510.
- [20] Venkatarama Reddy BV, Jagadish KS. Embodied energy of common and alternative building materials and technologies. *Energy Build* 2003;35:129–37. [https://doi.org/10.1016/S0378-7788\(01\)00141-4](https://doi.org/10.1016/S0378-7788(01)00141-4).
- [21] Graedel TE, Allwood J, Birat JP, Buchert M, Hagelüken C, Reck BK, et al. What do we know about metal recycling rates? *J Ind Ecol* 2011;15:355–66. <https://doi.org/10.1111/j.1530-9290.2011.00342.x>.
- [22] Graedel TE, Harper EM, Nassar NT, Reck BK. On the materials basis of modern society. *Proc Natl Acad Sci U S A* 2015. <https://doi.org/10.1073/pnas.1312752110>.
- [23] Reck BK, Graedel TE. Challenges in metal recycling. *Science* (80-) 2012;337:690–5. <https://doi.org/10.1126/science.1217501>.
- [24] Dahmus JB, Gutowski TG. What gets recycled: An information theory based model for product recycling. *Environ Sci Technol* 2007;41:7543–50. <https://doi.org/10.1021/es062254b>.
- [25] Schlesinger M. The Recycling Industry. *Alum Recycl* 2006;163–70. <https://doi.org/10.1201/9781420006247.ch11>.
- [26] Schlesinger ME. Aluminum recycling: Second edition 2013. <https://doi.org/10.1201/b16192>.
- [27] Das SK, Green JAS, Kaufman JG, Emadi D, Mahfoud M. Aluminum recycling—An integrated, industrywide approach. *JOM* 2010;62:23–6. <https://doi.org/10.1007/s11837-010-0026-6>.
- [28] Gaustad G, Olivetti E, Kirchain R. Design for Recycling: Evaluation and Efficient Alloy Modification. *Ssrn* 2010;14. Doi: 10.1111/j.1530-9290.2010.00229.x.
- [29] Das SK, Green JAS, Kaufman JG. The development of recycle-friendly automotive aluminum alloys. *JOM* 2007;59:47–51. <https://doi.org/10.1007/s11837-007-0140-2>.
- [30] Niero M, Olsen SI. Circular economy: To be or not to be in a closed product loop? A Life Cycle Assessment of aluminium cans with inclusion of alloying elements. *Resour Conserv Recycl* 2016;114:18–31. <https://doi.org/10.1016/j.resconrec.2016.06.023>.
- [31] Stotz PM, Niero M, Bey N, Paraskevas D. Environmental screening of novel technologies to increase material circularity: A case study on aluminium cans. *Resour Conserv Recycl* 2017;127:96–106. <https://doi.org/10.1016/j.resconrec.2017.07.013>.
- [32] Kelly JC, Sullivan JL, Burnham A, Elgowainy A. Impacts of Vehicle Weight Reduction via Material Substitution on Life-Cycle Greenhouse Gas Emissions. *Environ Sci Technol* 2015;49:12535–42. <https://doi.org/10.1021/acs.est.5b03192>.
- [33] Kawajiri K, Kobayashi M, Sakamoto K. Lightweight materials equal lightweight greenhouse gas emissions?: A historical analysis of greenhouse gases of vehicle material substitution. *J Clean Prod* 2020. <https://doi.org/10.1016/j.jclepro.2019.119805>.
- [34] Miller WS, Zhuang L, Bottema J, Wittebrood AJ, De Smet P, Haszler A, et al. Recent development in aluminium alloys for the automotive industry. *Mater Sci Eng A* 2000;280:37–49. [https://doi.org/10.1016/S0921-5093\(99\)00653-X](https://doi.org/10.1016/S0921-5093(99)00653-X).
- [35] Modaresi R, Müller DB. The role of automobiles for the future of aluminum recycling. *Environ Sci Technol* 2012;46:8587–94. <https://doi.org/10.1021/es300648w>.
- [36] Zhu Y, Chappuis LB, De Kleine R, Kim HC, Wallington TJ, Luckey G, et al. The coming wave of aluminum sheet scrap from vehicle recycling in the United States. *Resour Conserv Recycl* 2021;164. Doi: 10.1016/j.resconrec.2020.105208.
- [37] Gaustad G, Olivetti E, Kirchain R. Improving aluminum recycling: A survey of sorting and impurity removal technologies. *Resour Conserv Recycl* 2012;58:79–87. <https://doi.org/10.1016/j.resconrec.2011.10.010>.
- [38] Buchner H, Laner D, Rechberger H, Fellner J. Potential recycling constraints due to future supply and demand of wrought and cast Al scrap—A closed system perspective on Austria. *Resour Conserv Recycl* 2017;122:135–42. <https://doi.org/10.1016/j.resconrec.2017.01.014>.
- [39] Rombach G. Raw material supply by aluminium recycling—Efficiency evaluation and long-term availability. *Acta Mater* 2013;61:1012–20. <https://doi.org/10.1016/j.actamat.2012.08.064>.
- [40] Bertram M, Martchek KJ, Rombach G. Material flow analysis in the aluminum industry. *J Ind Ecol* 2009;13:650–4. <https://doi.org/10.1111/j.1530-9290.2009.00158.x>.
- [41] Paraskevas D, Kellens K, Renaldi Dewulf W, Duflou JR. Closed and open loop recycling of aluminium: A Life Cycle Assessment perspective. *Proc 11th Glob Conf Sustain Manuf - Innov Solut* 2013:302–7.
- [42] Gaustad G, Li P, Kirchain R. Modeling methods for managing raw material compositional uncertainty in alloy production. *Resour Conserv Recycl* 2007;52:180–207. <https://doi.org/10.1016/j.resconrec.2007.03.005>.
- [43] Nakajima K, Takeda O, Miki T, Matsubae K, Nakamura S, Nagasaka T. Thermodynamic analysis of contamination by alloying elements in aluminum recycling. *Environ Sci Technol* 2010;44:5594–600. <https://doi.org/10.1021/es9038769>.
- [44] Løvik AN, Modaresi R, Müller DB. Long-term strategies for increased recycling of automotive aluminum and its alloying elements. *Environ Sci Technol* 2014;48:4257–65. <https://doi.org/10.1021/es405604g>.
- [45] Wagstaff SRR, Wagstaff RBB, Allanore A. Tramp Element Accumulation and Its Effects on Secondary Phase Particles. In: Ratvik AP, editor. Miner. Met. Mater. Ser., Cham: Springer International Publishing; 2017, p. 1097–103. Doi: 10.1007/978-3-319-51541-0_132.
- [46] Kevorkian V. Challenges and Advantages of Recycling Wrought Aluminium Alloys From Lower Grades of Metallurgically Clean Scrap Recikiranje Gnetnih Aluminijevih Zlitin Iz Nizkocenovnih Vrst Metalur[Ko "Istega Odpadnega Aluminija. Mater Tehnol 2013;47.
- [47] Pogatscher S, Antrekowitsch H, Werinos M, Rank G, Kais A, Prillhofer R, et al. Statistical and thermodynamic optimization of trace-element modified Al-Mg-Si-Cu alloys. *Light Met* 2015;2015:263–70. <https://doi.org/10.1002/9781119093435.ch45>.
- [48] Stemer L, Tunes MA, Tosone R, Uggowitzer PJ, Pogatscher S. On the potential of aluminum crossover alloys. *Prog Mater Sci* 2021. <https://doi.org/10.1016/j.pmatsci.2021.100873>.
- [49] Sverdrup HU, Ragnarsdottir KV, Koca D. Aluminium for the future: Modelling the global production, market supply, demand, price and long term development of the global reserves. *Resour Conserv Recycl* 2015;103:139–54. <https://doi.org/10.1016/j.resconrec.2015.06.008>.
- [50] Rombach G, Modaresi R, Müller DB. Aluminium recycling - raw material supply from a volume and quality constraint system. *World Metall - ERZMETALL* 2012;65:157–62.
- [51] Soo VK, Peeters JR, Compston P, Doolan M, Duflou JR. Economic and environmental evaluation of aluminium recycling based on a belgian case study. *Procedia Manuf*, vol. 33, Elsevier BV; 2019, p. 639–46. Doi: 10.1016/j.promfg.2019.04.080.
- [52] Frees N. Crediting aluminium recycling in LCA by demand or by disposal. *Int J Life Cycle Assess* 2008;13:212–8. <https://doi.org/10.1065/lca2007.06.348>.
- [53] Wagstaff SR, Wagstaff RB, Allanore A. Light Metals 2017:2017. <https://doi.org/10.1007/978-3-319-51541-0>.
- [54] Boin UMJ, Bertram M. Melting standardized aluminum scrap: A mass balance model for Europe. *JOM* 2005;57:26–33. <https://doi.org/10.1007/s11837-005-0164-4>.
- [55] Deschamps A, Hutchinson CR. Precipitation kinetics in metallic alloys: Experiments and modeling. *Acta Mater* 2021;220:117338. <https://doi.org/10.1016/j.actamat.2021.117338>.
- [56] Ashby MF. What a “Sustainable Development”? *Mater. Sustain Dev* 2015:27–38. <https://doi.org/10.1016/b978-0-08-100176-9.00002-5>.
- [57] Kümmeler K, Clark JH, Zuin VG. Rethinking chemistry for a circular economy. *Science* (80-) 2020;367:369–70. <https://doi.org/10.1126/science.aba4979>.
- [58] Haas W, Krausmann F, Wiedenhofer D, Heinz M. How circular is the global economy?: An assessment of material flows, waste production, and recycling in the European union and the world in 2005. *J Ind Ecol* 2015. <https://doi.org/10.1111/jiec.12244>.
- [59] Rombach G, Bauerschlag N. LIBS based sorting—a solution for automotive scrap. *Miner Met Mater Ser* 2019;1351–7. https://doi.org/10.1007/978-3-030-05864-7_167.
- [60] Gaustad G, Arowosola A, Leader A, Brooks L. Dissipative use of critical metals in the aluminum industry. *Miner Met Mater Ser* 2018;Part F4:1137–9. Doi: 10.1007/978-3-319-72284-9_148.
- [61] Efthymiou E, Cocen ON, Ermolli SR. Sustainable aluminium systems. *Sustainability* 2010;2:3100–9. <https://doi.org/10.3390/su2093100>.
- [62] Stahel WR. The circular economy. *Nature* 2016;531:435–8. <https://doi.org/10.1038/531435a>.
- [63] Brunner PH, Rechberger H. Practical handbook of material flow analysis. *Int J Life Cycle Assess* 2004. <https://doi.org/10.1007/bf02979426>.

- [64] De Schrynmakers P. Life cycle thinking in the aluminium industry. *Int J Life Cycle Assess* 2009;14. Doi: 10.1007/s11367-009-0072-x.
- [65] Gusberti V, Severo DS, Welch BJ, Skyllas-Kazacos M. Modeling the mass and energy balance of different aluminium smelting cell technologies. *Light Met* 2012;2016:929–34. https://doi.org/10.1007/978-3-319-48179-1_161.
- [66] Allanore A, Yin L, Sadoway DR. A new anode material for oxygen evolution in molten oxide electrolysis. *Nature* 2013;497:353–6. <https://doi.org/10.1038/nature12134>.
- [67] Kuchariková L, Tillová E, Bokůvká O. Recycling and properties of recycled aluminium alloys used in the transportation industry. *Transp Probl* 2016;11:117–22. <https://doi.org/10.20858/tp.2016.11.2.11>.
- [68] Müller DB, Liu G, Bangs C. Stock Dynamics and Emission Pathways of the Global Aluminum Cycle. *REWAS* 2013 Enabling Mater Resour Sustain 2013;2:178. Doi: 10.1002/9781118679401.ch46.
- [69] International Aluminum Institute. Global Aluminium Recycling : A Cornerstone of Sustainable Development. *Int Alum Inst* 2009:1–36.
- [70] Olivetti EA, Cullen JM. Toward a sustainable materials system. *Science* (80-) 2018;360:1396–8. <https://doi.org/10.1126/science.aat6821>.
- [71] Arowosola A, Gaustad G, Brooks L. Aluminum alloys in automobiles: sources and sinks. *Miner Met Mater Ser* 2019;1:381–3. https://doi.org/10.1007/978-3-030-05864-7_171.
- [72] Arowosola A, Gaustad G. Estimating increasing diversity and dissipative loss of critical metals in the aluminum automotive sector. *Resour Conserv Recycl* 2019;150. Doi: 10.1016/j.resconrec.2019.06.016.
- [73] Krainikov AV. Effect of the structure and chemical inhomogeneity of rapidly solidified powders on the properties of aluminum alloys. *Powder Metall Met Ceram* 2010;49:397–409. <https://doi.org/10.1007/s11106-010-9250-4>.
- [74] Kammer C. Aluminum and Aluminum Alloys. In: Warlimont H, Martienssen W, editors. Springer Handb. Mater. Data. Springer Handbooks, Springer, Cham; 2018. Doi: 10.1007/978-3-319-69743-7_6.
- [75] Josef Domagala PHCS, Schmitz C. *Handbook of aluminium recycling mechanical preparation | metallurgical processing | heat treatment*. Essen: Vulkan-Verlag; 2014.
- [76] Staley JT, Lege DJ. Advances in aluminium alloy products for structural applications in transportation. *Le J Phys IV* 1993;03:C7-179-C7-190. Doi: 10.1051/jp4:1993728.
- [77] European Aluminium Association. *Aluminium in Cars. Alum Automot Man* 2011.
- [78] Poznak A, Freiberg D, Sanders P. Automotive wrought aluminium alloys. *Fundam Alum Metall* 2018;333–86. <https://doi.org/10.1016/b978-0-08-102063-0.00010-2>.
- [79] Zapp P, Rombach G, Kuckshinrichs W. The future of automotive aluminium. *Light Met Proc Sess TMS Annu Meet* (Warrendale, Pennsylvania) 2002;2040.
- [80] Hirsch J. Recent development in aluminium for automotive applications. *Trans Nonferrous Met Soc China* (English Ed 2014. [https://doi.org/10.1016/S1003-6326\(14\)63305-7](https://doi.org/10.1016/S1003-6326(14)63305-7).
- [81] Deschamps A, Fribourg G, Bréchet Y, Chemin JL, Hutchinson CR. In situ evaluation of dynamic precipitation during plastic straining of an Al-Zn-Mg-Cu alloy. *Acta Mater* 2012;60:1905–16. <https://doi.org/10.1016/j.actamat.2012.01.002>.
- [82] Hutchinson CR, Gouné M, Redjaïmia A. Selecting non-isothermal heat treatment schedules for precipitation hardening systems: An example of coupled process-property optimization. *Acta Mater* 2007;55:213–23. <https://doi.org/10.1016/j.actamat.2006.07.028>.
- [83] De Geuser F, Styles MJ, Hutchinson CR, Deschamps A. High-throughput in-situ characterization and modeling of precipitation kinetics in compositionally graded alloys. *Acta Mater* 2015;101:1–9. <https://doi.org/10.1016/j.actamat.2015.08.061>.
- [84] Lumley RN. *Fundamentals of aluminium metallurgy: Production, processing and applications*. Woodhead Publishing Limited 2010. <https://doi.org/10.1533/9780857090256>.
- [85] Sun W, Zhu Y, Marceau R, Wang L, Zhang Q, Gao X, et al. Precipitation strengthening of aluminum alloys by room-temperature cyclic plasticity. *Science* (80-) 2019;363:972–5. <https://doi.org/10.1126/science.aav7086>.
- [86] Ebenberger P, Uggowitzer PJ, Kirnštötter S, Gerold B, Zaeferer S, Pogatscher S. Processing-controlled suppression of Lüders elongation in AlMgMn alloys. *Scr Mater* 2019;166:64–7. <https://doi.org/10.1016/j.scriptamat.2019.02.047>.
- [87] Ebenberger P, Uggowitzer PJ, Gerold B, Pogatscher S. Effect of compositional and processing variations in new 5182-type AlMgMn alloys on mechanical properties and deformation surface quality. *Materials (Basel)* 2019;12:1645. <https://doi.org/10.3390/ma12101645>.
- [88] Jarfors AEW, Du A, Yu G, Zheng J, Wang K. On the sustainable choice of alloying elements for strength of aluminum-based alloys. *Sustain* 2020;12:1–12. <https://doi.org/10.3390/su12031059>.
- [89] Saevarsdottir G, Kvande H, Welch BJ. Aluminum production in the times of climate change: the global challenge to reduce the carbon footprint and prevent carbon leakage. *JOM* 2020;72:296–308. <https://doi.org/10.1007/s11837-019-03918-6>.
- [90] Kvande H, Haupin W. Inert anodes for Al smelters: Energy balances and environmental impact. *JOM* 2001;53:29–33. <https://doi.org/10.1007/s11837-001-0205-6>.
- [91] Sai Krishna P, Andrey SY, Peter VP. Progress of inert anodes in aluminium industry: review. *J Sib Fed Univ Chem* 2018;11:18–30. <https://doi.org/10.17516/1998-2836-0055>.
- [92] Yasinskiy AS, Padamata SK, Polyakov PV, Shabanov AV. An update on inert anodes for aluminium electrolysis. *Non-Ferrous Met* 2020;48:15–23. <https://doi.org/10.17580/nfm.2020.01.03>.
- [93] Solheim A. Inert Anodes—The Blind Alley to Environmental Friendliness? *Miner. Met. Mater. Ser., vol. Part F4*, 2018, p. 1253–60. Doi: 10.1007/978-3-319-72284-9_164.
- [94] ELYSIS Exclusive. *Alum Int Today* 2019;32.
- [95] Soo VK, Compston P, Doolan M. Life cycle modelling of end-of-life products: Challenges and opportunities towards a circular economy. *Procedia CIRP* 2019;80:607–12. <https://doi.org/10.1016/j.procir.2019.01.092>.
- [96] Løvik AN, Müller DB. A material flow model for impurity accumulation in beverage can recycling systems. *Light Met* 2014;9781118889(2014):907–11. <https://doi.org/10.1002/9781118888438.ch151>.
- [97] Kah P, Rajan R, Mvola B, Martikainen J. Trends in Al alloy development and their joining methods. *Rev Adv Mater Sci* 2016;44:383–97.
- [98] Hurtalová L, Tillová E, Chalupová M. The structure analysis of secondary (Recycled) AlSi9Cu3 cast alloy with and without heat treatment. *Eng Trans* 2013;61:197–218.
- [99] Pucher P, Böttcher H, Kaufmann H, Antrekowitzsch H, Uggowitzer PJ. Influence of the chemical composition on the ductility of an AlSiCuZnFe recycling foundry alloy. *Light Met* 2014;9781118889(2014):189–93. <https://doi.org/10.1002/9781118888438.ch33>.
- [100] Ji S, Yang W, Gao F, Watson D, Fan Z. Effect of iron on the microstructure and mechanical property of Al-Mg-Si-Mn and Al-Mg-Si diecast alloys. *Mater Sci Eng A* 2013. <https://doi.org/10.1016/j.msea.2012.11.095>.
- [101] Association EA. Materials – Microstructure and properties. *Alum Automot Manual, Eur Alum Assoc* 2002:1–29.
- [102] Sukiman NL, Zhou X, Birbilis N, Hughes AE, Mol JMC, Garcia SJ, et al. Durability and corrosion of aluminium and its alloys: overview, property space, techniques and developments. *Alum Alloy - New Trends Fabr Appl* 2012. <https://doi.org/10.5772/53752>.
- [103] Das SK. Designing aluminium alloys for a recycling friendly world. *Mater Sci Forum* 2009;519–521:1239–44. <https://doi.org/10.4028/www.scientific.net/msf.519-521.1239>.
- [104] Marks J, Bayliss C. Aluminum-meeting the challenges of climate change. *JOM* 2010;62:33–6. <https://doi.org/10.1007/s11837-010-0122-7>.
- [105] Radlbeck C, Dienes E, Kosteas D. Sustainability of aluminium in buildings. *Struct Eng Int J Int Assoc Bridg Struct Eng* 2004;14:221–4. <https://doi.org/10.2749/10168604477963838>.
- [106] Capuzzi S, Timelli G. Preparation and melting of scrap in aluminum recycling: A review. *Metals (Basel)* 2018;8:249. <https://doi.org/10.3390/met8040249>.
- [107] Castro MBG, Remmerswaal JAM, Reuter MA, Boin UJM. A thermodynamic approach to the compatibility of materials combinations for recycling. *Resour Conserv Recycl* 2004;43:1–19. <https://doi.org/10.1016/j.resconrec.2004.04.011>.

- [108] Mutz S, Meier-Kortwig J, Pretz T. Recycling activities for aluminium packaging in Germany including the preparation for the re-melting process. *Light Met Proc Sess TMS Annu Meet (Warrendale, Pennsylvania)* 2001;1139–44.
- [109] Schubert G. Aufbereitung metallischer Sekundärrohstoffe. Leipzig: Springer-Verlag Wien; 1984. doi: 10.1007/978-3-7091-9512-3.
- [110] Krone K. Vereinigung Deutscher Schmelzhütten e.V. Aluminiumrecycling - Vom Vorstoff bis zur fertigen Legierung. Düsseldorf: Aluminiumverlag 2000.
- [111] Martens H. Recyclingtechnik Fachbuch für Lehre und Praxis. vol. 11. Wiesbaden: Springer Fachmedien Wiesbaden; 2011. doi: 0.1007/978-3-658-02786-5.
- [112] Green, John A.S.E. Aluminum recycling and processing for energy conservation and sustainability. Materials Park: ASM International. Ohio: ASM International; 2007.
- [113] Zhu Y, Cooper DR. An optimal reverse material supply chain for U.S. Aluminum scrap. *Procedia CIRP*, vol. 80, 2019, p. 677–82. doi: 10.1016/j.procir.2019.01.065.
- [114] Kelly S, Apelian D. Grave-to-gate: Automotive aluminum recycling at end-of-life. *Light Met Age* 2017;75:40–3.
- [115] Kevorkjian VV. The recycling of standard quality wrought aluminum alloys from low-grade contaminated scrap. vol. 62. 2010. doi: 10.1007/s11837-010-0123-6.
- [116] Soo VK, Peeters J, Paraskevas D, Compston P, Doolan M, Duflou JR. Sustainable aluminium recycling of end-of-life products: A joining techniques perspective. *J Clean Prod* 2018;178:119–32. <https://doi.org/10.1016/j.jclepro.2017.12.235>.
- [117] Rossel H. Physikalische Aufbereitung von Aluminiumschrotten. Aufbereit. Im Hüttenwesen, Schriftenr Der GDMB 1989;54.
- [118] Schubert G. Aufbereitung der NE-Metallschrotte und NE-metallhaltigen Abfällen. *Aufbereit* 1991;32(7):78–89.
- [119] David E, Kopac J. Use of separation and impurity removal methods to improve aluminium waste recycling process. *Mater. Today Proc.*, vol. 2, Elsevier Ltd; 2015, p. 5071–9. doi: 10.1016/j.mtproc.2015.10.098.
- [120] Krone K. Ökologische Aspekte der Primär- und Sekundäraluminumerzeugung in der Bundesrepublik Deutschland. *Metall* 1990;6:559–67.
- [121] Schwalbe M. Grundlagen und Möglichkeiten der Verarbeitung von höher kontaminierten Aluminiumschrotten. *World Metall - ERZMETALL* 2011;64:157–64.
- [122] Rossel H, Mackenstedt D, Fillon B, Bertaud Y, Blanc B, Templier JC, et al. Investigations about thermal separation of aluminium packaging. *Light Met Proc Sess TMS Annu Meet (Warrendale, Pennsylvania)* 1996;1049–60.
- [123] Kvithyld A, Engh TA, Illés R. Decoating of aluminium scrap in various atmospheres. *Light Met Proc Sess TMS Annu Meet (Warrendale, Pennsylvania)* 2002; 1055–60.
- [124] Bateman W, Guest G, Evans R. Decoating of aluminum products and the environment. *Light Met. Proc Sess TMS Annu Meet (Warrendale, Pennsylvania)* 1999; 1099–106.
- [125] Kvithyld A, Gaal S, Kowalewski P, Engh TA. Gases evolved during decoatng of aluminium scrap in inert and oxidizing atmospheres. *TMS Light Met* 2003; 1091–5.
- [126] Rombach G. Untersuchungen zum Verhalten mineralischer Pigmente beim Aluminiumrecycling. *RWTH Aachen* 1997.
- [127] Kvithyld A, Meskers CEM, Gaal S, Reuter M, Engh TA. Recycling light metals: Optimal thermal de-coating. *JOM* 2008;60:47–51. <https://doi.org/10.1007/s11837-008-0107-y>.
- [128] Escherle A. Application of pyrolysis in aluminium recycling. *Erzmetall J Explor Min Metall* 2002;55:471–8.
- [129] Das SK. Emerging trends in aluminum recycling: Reasons and responses. *Light Met* 2006;4:911–6. <https://doi.org/10.1361/arpe2007p147>.
- [130] Pirker A. Optimierung des Al-Recyclingprozesses von verunreinigten Schrotten. *Montanuniversität Leoben* 2015.
- [131] Oger L, Lafouresse MC, Odemer G, Peguet L, Blanc C. Hydrogen diffusion and trapping in a low copper 7xxx aluminium alloy investigated by Scanning Kelvin Probe Force Microscopy. *Mater Sci Eng A* 2017;706:126–35. <https://doi.org/10.1016/j.msea.2017.08.119>.
- [132] Pouillier E, Gourgues AF, Tanguy D, Bussé EP. A study of intergranular fracture in an aluminium alloy due to hydrogen embrittlement. *Int J Plast* 2012;34: 139–53. <https://doi.org/10.1016/j.ijplas.2012.01.004>.
- [133] Zhao H, Chakraborty P, Ponge D, Hickel T, Sun B, Wu C-H, et al. Hydrogen trapping and embrittlement in high-strength Al-alloys. *Nature* 2022;602:437–41. <https://doi.org/10.1038/s41586-021-04343-z>.
- [134] Antrekowitsch H, Paulitsch H, Pirker A. Einsatz minderwertiger Schrotte und Reststoffsituation beim Recycling von Aluminium. *Recycl Und Rohstoffe* 2013;6: 433–53.
- [135] Rombach G. Recycling aus der Sicht eines integrierten Aluminiumkonzerns - Rohstoffe, Technologie, Qualität. In: Goldmann D, editor. *Recycl. und Rohstoffe*, Berlin, Deutschland: Thomé-Kozmiensky; 2010, p. 527–37.
- [136] Wibner S, Antrekowitsch H. Recycling of aluminium with variation of the scrap processing techniques. *Eur. Metall. Conf.*, Düsseldorf, Deutschland: 2019, p. 1151–61.
- [137] Wibner S. Verhalten aluminiumhaltiger Reststoffe und minderwertiger Schrotte beim Recycling unter Berücksichtigung von Sondermetallen. *Montanuniversität Leoben* 2021.
- [138] Nieckele AO, Naccache MF, Gomes MSP. Combustion performance of an aluminum melting furnace operating with natural gas and liquid fuel. *Appl Therm Eng* 2011;31:841–51. <https://doi.org/10.1016/j.applthermaleng.2010.11.003>.
- [139] Zhou B, Yang Y, Reuter MA, Boin UMJ. CFD-based process modelling of a rotary furnace for aluminium scrap melting. *Prog Comput Fluid Dyn* 2007;7: 195–208. <https://doi.org/10.1504/pcfd.2007.013012>.
- [140] Linsmeyer T, Winter B. STAND DER TECHNIK IN DER SEKUNDÄRALUMINUMERZEUGUNG IM HINBLICK AUF DIE IPPC-RICHTLINIE. Band: 120. Wien: 2000.
- [141] Maiwald D. Advanced control of a rotary drum furnace in a secondary smelter. *TMS Annu Meet* 2009;615–9.
- [142] Schemberg S, Rudig S, Müller M. Reduzierung von CO-Emissionen durch Erdgas/Sauerstoff-Brennertechnologien. *Prozesswärme*, 1, Online Proceedings: 2018.
- [143] Antrekowitsch H, Paulitsch H. Reststoffe aus der Aluminium-Sekundärindustrie. *Berliner Schlackenkonferenz*, Berlin, Deutschland: 2013, p. 615–38.
- [144] Peterson RD, Newton L. Review of aluminum dross processing. *Light Met Proc Sess TMS Annu Meet (Warrendale, Pennsylvania)* 2002;1029–37.
- [145] Becker E. Reststoffe des Aluminium-Recyclings. *RWTH Aachen*, 1993.
- [146] Gisbertz K, Friedrich B. VeMRec – Metallurgische Herausforderungen beim Recycling von NE-Metallkonzentraten aus Abfallverbrennungs-Rostasche. Miner Nebenprodukte Und Abfälle Aschen, Schlacken, Stäube Und Baurestmassen 2012:227–53.
- [147] Peel AM, Herbert J, Roth D, Collins MJ. Furnace operations to reduce dross generation. *Mater Sci Forum* 2010;630:45–52. <https://doi.org/10.4028/www.scientific.net/MSF.630.45>.
- [148] Meshram A, Singh KK. Recovery of valuable products from hazardous aluminum dross: A review. *Resour Conserv Recycl* 2018;130:95–108. <https://doi.org/10.1016/j.resconrec.2017.11.026>.
- [149] Prillhofer R, Prillhofer B, Antrekowitsch H. Verwertung von Reststoffen beim Aluminium-Recycling. *BHM Berg- Und Hüttenmännische Monatshefte* 2008;153 Jg.:103–8.
- [150] David E, Kopac J. Aluminum recovery as a product with high added value using aluminum hazardous waste. *J Hazard Mater* 2013;261:316–24. <https://doi.org/10.1016/j.jhazmat.2013.07.042>.
- [151] Zhang L. State of the art in aluminum recycling from aluminum dross. *TMS Light Met* 2006;2006:931–6.
- [152] Ünlü N, Drouet MG. Comparison of salt-free aluminum dross treatment processes. *Resour Conserv Recycl* 2002;36:61–72. [https://doi.org/10.1016/S0921-3449\(02\)00010-1](https://doi.org/10.1016/S0921-3449(02)00010-1).
- [153] Gerke M. Untersuchungen zum Einsatz von Schmelzsäulen bei der Vearbeitung spezieller Aluminiumschrotte und Kräzen. *RWTH Aachen* 2002.
- [154] Paulitsch P. Verwertungsstrategien für Reststoffe aus der Aluminiumsekundärmetallurgie. *Montanuniversität Leoben* 2012.
- [155] Kammer C. Aluminiumtaschenbuch - 1. Teil. Düsseldorf, Deutschland: Aluminiumverlag; 2002.
- [156] Prillhofer R, Prillhofer B, Antrekowitsch H. Treatment of residues during aluminum recycling. *TMS Annu Meet* 2009;857–62.
- [157] Prillhofer R, Antrekowitsch H. Einsatzmöglichkeiten prozessbedingter Reststoffe beim Al-Recycling. *Proc Depotech* 2008;231–6.
- [158] Zhou B, Yang Y, Reuter MA. Process modeling of aluminum scraps melting in molten salt and metal bath in a rotary furnace. *TMS Light Met* 2004;919–24.
- [159] Alfaro I. Technische und wirtschaftliche Gesichtspunkte der Entstehung und der Verarbeitung von Aluminiumkräze. *Aluminium* 1986;62:259–66.

- [160] Milke E, Friedrich B, Sydykov A, Arnold A. Solubility of CaF₂ in NaCl-KCl salt flux for Al-recycling and its effect on Al-loss. *Proc - Eur Metall Conf EMC* 2005;4 (2005):1537–48.
- [161] Mahinroosta M, Allahverdi A. Hazardous aluminum dross characterization and recycling strategies: A critical review. *J Environ Manage* 2018;223:452–68. <https://doi.org/10.1016/j.jenvman.2018.06.068>.
- [162] Wan B, Li W, Liu F, Lu T, Jin S, Wang K, et al. Determination of fluoride component in the multifunctional refining flux used for recycling aluminum scrap. *J Mater Res Technol* 2020;9:3447–59. <https://doi.org/10.1016/j.jmrt.2020.01.082>.
- [163] Tenorio JAS, Espinosa DCR. Effect of salt/oxide interaction on the process of aluminum recycling. *J Light Met* 2002;2:89–93. [https://doi.org/10.1016/S1471-5317\(02\)00027-5](https://doi.org/10.1016/S1471-5317(02)00027-5).
- [164] Besson S, Pichat A, Xolin E, Chartrand P, Friedrich B. Improving coalescence in Al-Recycling by salt optimization. *Proc - Eur Metall Conf EMC* 2011;5(2011):1852–3.
- [165] Zähr J. Einfluss des Oberflächenzustandes auf das thermische Fügen von Aluminium. *Dresdner fügetechnische Berichte*, vol. Band: 21, Dresden, Deutschland: TUDPress Verl. der Wiss; 2011.
- [166] Horn V, S. P. Recycling von Nichteisenmetallen aus Feuerfestausbruch. 2006.
- [167] Urbach R. Aufarbeitungsmöglichkeiten dioxinhaltiger Filterstaube aus Aluminiumschmelzwerken. *Metall* 1993;47:810–6.
- [168] Hatayama H, Daigo I, Matsuno Y, Adachi Y. Evolution of aluminum recycling initiated by the introduction of next-generation vehicles and scrap sorting technology. *Resour Conserv Recycl* 2012;66:8–14. <https://doi.org/10.1016/j.resconrec.2012.06.006>.
- [169] Paraskevas D, Kellens K, Dewulf W, Dufoulo JR. Environmental modelling of aluminium recycling: A Life Cycle Assessment tool for sustainable metal management. *J Clean Prod* 2015;105:357–70. <https://doi.org/10.1016/j.jclepro.2014.09.102>.
- [170] The Aluminum Can Advantage: Key Sustainability Performance Indicators 2019. 2019.
- [171] Paraskevas D, Ingarao G, Deng Y, Dufoulo JR, Pontikes Y, Blanpain B. Evaluating the material resource efficiency of secondary aluminium production: A Monte Carlo-based decision-support tool. *J Clean Prod* 2019;215:488–96. <https://doi.org/10.1016/j.jclepro.2019.01.097>.
- [172] Martinsen K, Gulbrandsen-Dahl S. Use of post-consumer scrap in aluminium wrought alloy structural components for the transportation sector. *Procedia CIRP*, vol. 29, Elsevier B.V.; 2015, p. 686–91. Doi: 10.1016/j.procir.2015.02.072.
- [173] Lazarro-Nebreda J, Patel JB, Chang ITH, Stone IC, Fan Z. Solidification processing of scrap Al-alloys containing high levels of Fe. *IOP Conf Ser Mater Sci Eng* 2019;529:11–7. <https://doi.org/10.1088/1757-899X/529/1/012059>.
- [174] Jerina L, Medved J, Godec M, Vončina M. Influence of the specific surface area of secondary material on the solidification process and microstructure of aluminium alloy AA7075. *J Therm Anal Calorim* 2018;134:455–62. <https://doi.org/10.1007/s10973-018-7425-2>.
- [175] Kumar S, Babu NH, Scamans GM, Eskin DG, Fan Z. Solidification behaviour of an AA5754 Al alloy ingot cast with high impurity content. *Int J Mater Res* 2012;103:1228–34. <https://doi.org/10.3139/146.110760>.
- [176] Li DM, Bakker A. Shear fracture mechanism in a rapidly-solidified aluminium scrap alloy. *J Mater Sci* 1997;32:259–66. <https://doi.org/10.1023/A:1018572509835>.
- [177] Prillhofer B. Verbesserung der Stranggussqualität von hochlegierten Al-Walzbarren. *Montanuniversitaet Leoben* 2009.
- [178] Prillhofer B, Antrekowitsch H, Böttcher H, Enright P. Nonmetallic inclusions in the secondary aluminum industry for the production of aerospace alloys. *TMS Light Met* 2008:603–8.
- [179] Prillhofer B, Antrekowitsch H. Abscheidung von nichtmetallischen Einschlüssen bei der Raffination von AluminiumlegierungenSeparation of Nonmetallic Inclusions in Aluminium Alloy Refining. *BHM Berg- Und Hüttenmännische Monatshefte* 2007;152:53–61. <https://doi.org/10.1007/s00501-007-0274-0>.
- [180] Prillhofer BF, Böttcher H, Antrekowitsch H. Mögliche Einschlussbildung bei der Herstellung von Walzbarren der Legierung EN AW-7075. *Aluminium* 2008;6:1–10.
- [181] Roy R, Sahai Y. The role of salt flux recycling of aluminium. *Light Met* 1993:1237–43.
- [182] Thiele W. Die oxidation von aluminium- und aluminiumlegierungs-schmelzen. *Aluminium* 1962;38:780–6.
- [183] Prillhofer B, Antrekowitsch H, Böttcher H. Optimisation of the melt quality in casting/holding furnaces. *TMS Light Met* 2008:627–32.
- [184] Chen XG, Engler S. Wasserstoff und Porosität in Aluminium-Silizium Legierungen (Teil I). *Metall* 1991;45:995–1000.
- [185] Görner H. Removal of dissolved elements in aluminium by filtration. Norwegian University of Science and Technology Faculty of Natural Sciences and Technology, 2009.
- [186] Vončina M, Kresník K, Volšák D, Medved J. Effects of homogenization conditions on the microstructure evolution of aluminium alloy EN AW 8006. *Metals* (Basel) 2020;10:419. <https://doi.org/10.3390/met10030419>.
- [187] Belov NA, Eskin DG, Aksenen AA. Alloys of the Al-Mg–Mn–Si–Fe System. *Multicomponent Phase Diagrams* 2007:133–57. <https://doi.org/10.1016/b978-008044537-3/50004-4>.
- [188] Sarafoglou PI, Serafeim A, Fanikos IA, Aristeidakis JS, Haidemenopoulos GN. Modeling of microsegregation and homogenization of 6xxx Al-alloys including precipitation and strengthening during homogenization cooling. *Materials* (Basel) 2019;12. Doi: 10.3390/ma12091421.
- [189] Gnatok M, Li C, Arnold A, Friedrich B. Purification of aluminium cast alloy melts through precipitation of fe-containing intermetallic compounds. *Metals* (Basel) 2018;8:796. <https://doi.org/10.3390/met8100796>.
- [190] Instone S, Buchholz A, Gruen GU. Inclusion transport phenomena in casting furnaces. *TMS Light Met* 2008:811–6.
- [191] Courtenay JH, Instone S, Reusch F, Instone S, Reusch F. A review of the development of new filter technologies based on the principle of multi stage filtration with grain refiner added in the intermediate stage. *Light Met TMS* 2011;769–74. <https://doi.org/10.1002/9781118061992.ch133>.
- [192] Velasco E, Proulx J. Metal quality of secondary alloys for Al castings. *TMS Light Met* 2006;2006:721–4.
- [193] Utigard TA, Roy RR, Friesen K. Properties of fluxes used in molten aluminium processing. *High Temp Mater Process* 2001;20:303–7. <https://doi.org/10.1515/HTMP.2001.20.3-4.303>.
- [194] Wiredu Damoah LN, Zhang L. High frequency electromagnetic separation of inclusions from aluminum. *Light Met* 2012;2016:1069–76. https://doi.org/10.1007/978-3-319-48179-1_185.
- [195] Roth W. *Stranggießkokille*. 813755, 1949.
- [196] Bührig-Polaczek A, Michaeli W, Spur G. *Handbuch Urformen*. München: Carl Hanser Verlag; 2013. Doi: 10.3139/9783446434066.
- [197] Schneider W. *Stranggießen von Aluminium-Werkstoffen*. Oberursel: DGM Informationsgesellschaft; 1995.
- [198] Schneider WDC. Casting of aluminium alloys - past, present and future. *Light Met* 2002:534–41.
- [199] Roller E. Vertikales und horizontales kontinuierliches stranggiessen von kupferlegierungen. *Metall* 1984;38:720–9.
- [200] Bletschacher M, Vosskuhler H. Kontinuierliches giessen von ne-metallen und ne -metall - legierungen mittels durchlaufkokillen. *Zeit Fuer Met* 1969;60:684–93.
- [201] Krall HA. Horizontal-stranggiessanlagen zur vollkontinuierlichen herstellung von pressbolzen aus kupfer und kupferlegierungen. *Metall* 1979;33:1247–57.
- [202] Al-Helal K, Patel JB, Scamans GM, Fan Z. Melt conditioned direct chill (MC-DC) casting and extrusion of AA5754 aluminium alloy formulated from recycled tabor scrap. *Materials* (Basel) 2020;13:2711. <https://doi.org/10.3390/ma13122711>.
- [203] Key to Metals AG. Direct-Chill Casting 2016.
- [204] Wagstaff RB, Bowles KD. Practical low head casting (LHC) mold for aluminum ingot casting. *Light Met. Proc Sess TMS Annu Meet (Warrendale, Pennsylvania) 1995:1071–5*.
- [205] Wagstaff FE, Wagstaff WG, May PH. Direct Chill Casting. United States 2008:1–18. <https://doi.org/10.1201/9781420062823.ch1>.
- [206] Založník M, Kumar A, Combeau H, Bedel M, Jarry P, Waz E. The coupling of macrosegregation with grain nucleation, growth and motion in DC cast aluminum alloy ingots. *Essent Readings Light Met* 2013;3:848–53. <https://doi.org/10.1002/9781118647783.ch106>.
- [207] Anderson M, Bruski R, Groszkiewicz D, Wagstaff B. NETCAST™ shape casting technology: a technological breakthrough that enhances the cost effectiveness of aluminum forgings. *Essent Readings Light Met* 2013;3:612–8. <https://doi.org/10.1002/9781118647783.ch75>.

- [208] Bischoff TF, Hudson LG, Wagstaff RB. Novelis fusion™: A novel process for the future. *Essent Readings Light Met* 2013;3:628–32. <https://doi.org/10.1002/9781118647783.ch77>.
- [209] Davisson TL, Hudson LG, Wagstaff RB. Direct chill casting of heat exchanger material via the novelis fusion™ process. *TMS Light Met* 2007;739–43.
- [210] Samuel RW, Wagstaff SR. The impact of recycling on the mechanical properties of 6XXX series aluminum alloys. *J Sib Fed Univ Eng Technol* 2018;11:409–18. <https://doi.org/10.17516/1999-494x-0063>.
- [211] Lavernia E, Rai G, Grant NJ. Rapid solidification processing of 7XXX aluminium alloys: A review. *Mater Sci Eng* 1986;79:211–21. [https://doi.org/10.1016/0025-5416\(86\)90406-4](https://doi.org/10.1016/0025-5416(86)90406-4).
- [212] Haga T, Tkashiki K, Ikawaand M, Watari H. Twin roll casting of aluminum alloy strips. *J Mater Process Technol* 2004;153–154:42–7. <https://doi.org/10.1016/j.jmatprotec.2004.04.018>.
- [213] Haga T, Suzuki S. Study on high-speed twin-roll caster for aluminum alloys. *J Mater Process Technol* 2003;143–144:895–900. [https://doi.org/10.1016/S0924-0136\(03\)00400-X](https://doi.org/10.1016/S0924-0136(03)00400-X).
- [214] Sanders RE. Continuous casting for aluminum sheet: A product perspective. *JOM* 2012;64:291–301. <https://doi.org/10.1007/s11837-012-0247-y>.
- [215] Sahoo S. Review on vertical twin-roll strip casting: a key technology for quality strips. *J Metall* 2016;2016:1–13. <https://doi.org/10.1155/2016/1038950>.
- [216] Sun N, Patterson BR, Suni JP, Simielli EA, Weiland H, Allard LF. Microstructural evolution in twin roll cast AA3105 during homogenization. *Mater Sci Eng A* 2006;416:232–9. <https://doi.org/10.1016/j.jmsea.2005.10.018>.
- [217] Pokov M, Cieslar M, Lacaze J. Enhanced AW3003 aluminum alloys for heat exchangers. *WDS'11 Proc. Contrib Pap Part III - Phys* 2011:141–6.
- [218] Suzuki K, Kumai S, Saito Y, Haga T. High-speed twin-roll strip casting of Al-Mg-Si alloys with high iron content. *Mater Trans* 2006;46:2602–8. <https://doi.org/10.2320/matertrans.46.2602>.
- [219] Haga T, Ikawa M, Watari H, Suzuki K, Kumai S. High-speed twin roll casting of thin aluminum alloy strips containing Fe impurities. *Mater Trans* 2005;46:2596–601. <https://doi.org/10.2320/matertrans.46.2596>.
- [220] Haga T, Kumai S, Watari H. Strip casting of recycled aluminum alloys by a twin roll caster. *Waste and Biomass Valorization* 2012;3:419–24. <https://doi.org/10.1007/s12649-012-9153-3>.
- [221] Kumar S, Hari Babu N, Scamman GM, Fan Z, O'Reilly KAQ. Twin roll casting of Al-Mg alloy with high added impurity content. *Metall Mater Trans A Phys Metall Mater Sci* 2014;45:2842–54. <https://doi.org/10.1007/s11661-014-2229-x>.
- [222] Komeda K, Haga T. Casting of recycled A5182 alloy strip by high speed twin roll caster. *Nihon Kaiki Gakkai Ronbunshu, A Hen/Transactions Japan Soc. Mech. Eng. Part A*, vol. 76, Japan Society of Mechanical Engineers; 2010, p. 694–5. Doi: 10.1299/kikaia.76.694.
- [223] Haga T, Komeda K, Mtsuoka K, Kumai S, Watari H. Roll casting of recycled AA5182. *Appl Mech Mater* 2012;121–126:4667–70. <https://doi.org/10.4028/www.scientific.net/AMM.121-126.4667>.
- [224] Al-Helal K, Chang I, Patel JB, Fan Z. Thermomechanical treatment of high-shear melt-conditioned twin-roll cast strip of recycled AA5754 alloy. *JOM* 2019;71:2018–24. <https://doi.org/10.1007/s11837-018-3190-8>.
- [225] Wang H, Zhou L, Zhang Y, Cai Y, Zhang J. Effects of twin-roll casting process parameters on the microstructure and sheet metal forming behavior of 7050 aluminum alloy. *J Mater Process Technol* 2016;233:186–91. <https://doi.org/10.1016/j.jmatprotec.2016.02.016>.
- [226] Karifli M, Mánik T, Lauschmann H. Influence of Si and Fe on the distribution of intermetallic compounds in twin-roll cast Al-Mn-Zr alloys. *J Alloys Compd* 2012;515:108–13. <https://doi.org/10.1016/j.jallcom.2011.11.101>.
- [227] Cheon BH, Han JH, Kim HW, Lee JC. Asymmetric rolling of twin-roll cast Al-5.5Mg-0.3Cu alloy sheet: Mechanical properties and formability. *J Korean Inst Met Mater* 2011;49:243–9. <https://doi.org/10.3365/KJMM.2011.49.3.243>.
- [228] Slámová M, Sláma P, Cieslar M. The influence of alloy composition on phase transformations and recrystallization in twin-roll cast Al-Mn-Fe alloys. *Mater Sci Forum* 2006;519–521:365–70. <https://doi.org/10.4028/www.scientific.net/msf.519-521.365>.
- [229] Ab Rahim SN, Lajis MA, Ariffin S. A review on recycling aluminum chips by hot extrusion process. *Procedia CIRP*, vol. 26, Elsevier B.V.; 2015, p. 761–6. Doi: 10.1016/j.procir.2015.01.013.
- [230] Dufoulo JR, Tekkaya AE, Haase M, Welo T, Vanmeensel K, Kellens K, et al. Environmental assessment of solid state recycling routes for aluminium alloys: Can solid state processes significantly reduce the environmental impact of aluminium recycling? *CIRP Ann - Manuf Technol* 2015;64:37–40. <https://doi.org/10.1016/j.cirp.2015.04.051>.
- [231] Wan B, Chen W, Lu T, Liu F, Jiang Z, Mao M. Review of solid state recycling of aluminum chips. *Resour Conserv Recycl* 2017;125:37–47. <https://doi.org/10.1016/j.resconrec.2017.06.004>.
- [232] Chiba R, Nakamura T, Kuroda M. Solid-state recycling of aluminium alloy swarf through cold profile extrusion and cold rolling. *J Mater Process Technol* 2011;211:1878–87. <https://doi.org/10.1016/j.jmatprotec.2011.06.010>.
- [233] Chiba R, Yoshimura M. Solid-state recycling of aluminium alloy swarf into c-channel by hot extrusion. *J Manuf Process* 2015;17:1–8. <https://doi.org/10.1016/j.jmapro.2014.10.002>.
- [234] Haase M, Tekkaya AE. Cold extrusion of hot extruded aluminum chips. *J Mater Process Technol* 2015;217:356–67. <https://doi.org/10.1016/j.jmatprotec.2014.11.028>.
- [235] Alvarez-Antolín JF, Segurado-Frutos E, Neira-Castaño H, Asensio-Lozano J. Heat treatment optimization in Al-Cu-Mg-Si alloys, with or without prior deformation. *Metals (Basel)* 2018;8. <https://doi.org/10.3390/met8100739>.
- [236] Bunkholt S, Nes E, Marthinsen K. The effect of iron and the precipitation behavior of iron during annealing of a cold deformed commercial purity aluminium alloy. *Mater Charact* 2017;129:18–23. <https://doi.org/10.1016/j.matchar.2017.04.014>.
- [237] Mikhaylovskaya AV, Portnoy VK, Mochugovskiy AG, Zadorozhny MY, Tabachkova NY, Golovin IS. Effect of homogenisation treatment on precipitation, recrystallisation and properties of Al - 3% Mg - TM alloys (TM = Mn, Cr, Zr). *Mater Des* 2016;109:197–208. <https://doi.org/10.1016/j.matdes.2016.07.010>.
- [238] Haidemenopoulos GN, Kamoutsi H, Zervaki AD. Simulation of the transformation of iron intermetallics during homogenization of 6xxx series extrudable aluminum alloys. *J Mater Process Technol* 2012;212:2255–60. <https://doi.org/10.1016/j.jmatprotec.2012.06.026>.
- [239] Basak CB, Hari Babu N. Morphological changes and segregation of β -Al9Fe2Si2 phase: A perspective from better recyclability of cast Al-Si alloys. *Mater Des* 2016;108:277–88. <https://doi.org/10.1016/j.matdes.2016.06.096>.
- [240] Tillova E, Chalupova M, Hurtalova L. Evolution of the Fe-rich phases in recycled AlSi9Cu3 cast alloy during solution treatment. *Komunikacie* 2010;12:95–101.
- [241] Kazeem A, Badarulzaman NA, Fahmin Faiz Wan Ali W. Effect of heat treatment on modulus hardening and phase transformation in experimental 7xxx stir-cast alloy from recycled beverage cans. *Mater Today Proc* 2020. Doi: 10.1016/j.matpr.2020.05.615.
- [242] Torres JT, Valdés AF, Rivera NMT, Robles JMA. Analysis of the formation of intermetallic compounds in foams Al-Cu-Ni obtained from recycled aluminum cans. *Mater. Today Proc*, vol. 10, Elsevier Ltd; 2019, p. 355–9. Doi: 10.1016/j.matpr.2018.10.417.
- [243] Canté MV, Lima TS, Brito C, Garcia A, Cheung N, Spinelli JE. An alternative to the recycling of Fe-contaminated Al. *J Sustain Metall* 2018;4:412–26. <https://doi.org/10.1007/s40831-018-0188-y>.
- [244] Xavier MGC, Souza TMG, Cheung N, Garcia A, Spinelli JE. Effects of cobalt and solidification cooling rate on intermetallic phases and tensile properties of a -Cu, -Zn, -Fe containing Al-Si alloy. *Int J Adv Manuf Technol* 2020;107:717–30. <https://doi.org/10.1007/s00170-020-05077-4>.
- [245] Zhang Y, Wang S, Lordan E, Wang Y, Fan Z. Improve mechanical properties of high pressure die cast Al9Si3Cu alloy via dislocation enhanced precipitation. *J Alloys Compd* 2019;785:1015–22. <https://doi.org/10.1016/j.jallcom.2019.01.278>.
- [246] Nouri Z, Sedighi M. Effect of powder thixoforging process on microstructural and mechanical properties of recycled 520 aluminum alloy. *J Mech Sci Technol* 2018;32:2003–9. <https://doi.org/10.1007/s12206-018-0408-1>.
- [247] Otani LB, Matsuo MM, Freitas BJM, Zepon G, Kiminami CS, Botta WJ, et al. Tailoring the microstructure of recycled 319 aluminum alloy aiming at high ductility. *J Mater Res Technol* 2019;8:3539–49. <https://doi.org/10.1016/j.jmr.2019.06.030>.
- [248] Lin B, Xu R, Li H, Xiao H, Zhang W, Li S. Development of high Fe content squeeze cast 2A16 wrought Al alloys with enhanced mechanical properties at room and elevated temperatures. *Mater Charact* 2018;142:389–97. <https://doi.org/10.1016/j.matchar.2018.06.009>.

- [249] Lin B, Zhang W, Zheng X, Zhao Y, Lou Z, Zhang W. Developing high performance mechanical properties at elevated temperature in squeeze cast Al-Cu-Mn-Fe-Ni alloys. *Mater Charact* 2019;150:128–37. <https://doi.org/10.1016/j.matchar.2019.01.022>.
- [250] Easton MA, Qian M, Prasad A, StJohn DH. Recent advances in grain refinement of light metals and alloys. *Curr Opin Solid State Mater Sci* 2016;20:13–24. <https://doi.org/10.1016/j.cossms.2015.10.001>.
- [251] Zhao Y, Lin B, Song D, Zheng D, Sun Z, Xie C, et al. Effect of compound fields of ultrasonic vibration and applied pressure on the 3D microstructure and tensile properties of recycled Al-Cu-Mn-Fe-Si alloys. *Materials (Basel)* 2019;12:1–17. <https://doi.org/10.3390/ma122333904>.
- [252] Kotadia HR, Qian M, Das A. Microstructural modification of recycled aluminium alloys by high-intensity ultrasonication: Observations from custom Al-2Si-2Mg-1.2Fe-(0.5,1.0)Mn alloys. *J Alloys Compd* 2020;823. <https://doi.org/10.1016/j.jallcom.2020.153833>.
- [253] Li YZ, Mangelinck-Noël N, Zimmermann G, Sturz L, Nguyen-Thi H. Modification of the microstructure by rotating magnetic field during the solidification of Al-7 wt.% Si alloy under microgravity. *J Alloys Compd* 2020;836. <https://doi.org/10.1016/j.jallcom.2020.155458>.
- [254] Atkinson HV. Alloys for semi-solid processing. *Solid State Phenom* 2013;192:193–16. <https://doi.org/10.4028/www.scientific.net/SSP.192-193.16>.
- [255] Fan Z. Semisolid metal processing. *Int Mater Rev* 2002;47:49–86. <https://doi.org/10.1179/09566001225001076>.
- [256] Rogal. Critical assessment: opportunities in developing semi-solid processing: aluminium, magnesium, and high-temperature alloys. *Mater Sci Technol (United Kingdom)* 2017;33:759–64. <https://doi.org/10.1080/02670836.2017.1295212>.
- [257] Li G, Lu H, Hu X, Lin F, Li X, Zhu Q. Current progress in rheoforming of wrought aluminum alloys: A review. *Metals (Basel)* 2020;10. Doi: 10.3390/met10020238.
- [258] Möller H, Curle UA, Masuku EP. Characterization of surface liquid segregation in SSM-HPDC aluminium alloys 7075, 2024, 6082 and A201. *Trans Nonferrous Met Soc China (English Ed)* 2010;20. Doi: 10.1016/S1003-6326(10)60593-6.
- [259] Curle UA. Semi-solid near-net shape rheocasting of heat treatable wrought aluminum alloys. *Trans Nonferrous Met Soc China (English Ed)* 2010;20:1719–24. [https://doi.org/10.1016/S1003-6326\(09\)60364-2](https://doi.org/10.1016/S1003-6326(09)60364-2).
- [260] Bolouri A, Zhao QF, Côté P, Chen XG. Microstructure and rheological properties of semi-solid 7075 slurries using SEED rheocasting process. *Solid State Phenom* 2016;256:288–93. <https://doi.org/10.4028/www.scientific.net/SSP.256.288>.
- [261] GUO H min, YANG X jie, WANG J xuan, HU B, ZHU G lei. Effects of rheoforming on microstructures and mechanical properties of 7075 wrought aluminum alloy. *Trans Nonferrous Met Soc China (English Ed)* 2010;20:355–60. Doi: 10.1016/S1003-6326(09)60146-1.
- [262] Lü S, Wu S, Wan L, An P. Microstructure and tensile properties of wrought Al alloy 5052 produced by rheo-squeeze casting. *Metall Mater Trans A Phys Metall Mater Sci* 2013;44:2735–45. <https://doi.org/10.1007/s11661-013-1637-7>.
- [263] Qi M, Kang Y, Zhou B, Liao W, Zhu G, Li Y, et al. A forced convection stirring process for Rheo-HPDC aluminum and magnesium alloys. *J Mater Process Technol* 2016;23:4353–67. <https://doi.org/10.1016/j.jmatprotec.2016.04.003>.
- [264] Raju K, Ojha SN, Harsha AP. Spray forming of aluminum alloys and its composites: An overview. *J Mater Sci* 2008;43:2509–21. <https://doi.org/10.1007/s10853-008-2464-x>.
- [265] Pariona MM, Bolfarini C, Dos Santos RJ, Kiminami CS. Application of mathematical simulation and the factorial design method to the optimization of the atomization stage in the spray forming of a Cu-6% Zn alloy. *J Mater Process Technol* 2000;102:221–9. [https://doi.org/10.1016/S0924-0136\(00\)00482-9](https://doi.org/10.1016/S0924-0136(00)00482-9).
- [266] Kiminami CS, Botta WJ, Bolfarini C. Processing of glass former alloys by spray forming. *Materwiss Werksttech* 2010;41:513–23. <https://doi.org/10.1002/mawe.201000637>.
- [267] Godinho HA, Beletati ALR, Giordano EJ, Bolfarini C. Microstructure and mechanical properties of a spray formed and extruded AA7050 recycled alloy. *J Alloys Compd* 2014;586. <https://doi.org/10.1016/j.jallcom.2012.12.122>.
- [268] Ferrarini CF, Bolfarini C, Kiminami CS, Botta FWJ. Microstructure and mechanical properties of spray deposited hypoeutectic Al-Si alloy. *Mater Sci Eng A* 2004;375–377:577–80. <https://doi.org/10.1016/j.msea.2003.10.062>.
- [269] Pereira LH, Asato GH, Otani LB, Jorge AM, Kiminami CS, Bolfarini C, et al. Changing the solidification sequence and the morphology of iron-containing intermetallic phases in AA6061 aluminum alloy processed by spray forming. *Mater Charact* 2018;145:507–15. <https://doi.org/10.1016/j.matchar.2018.09.006>.
- [270] Qu Y dong, Su R ming, You J hua, Li R de. Study on microstructure, mechanical properties and corrosion behavior of spray formed 7075 alloy. *Mater Today Commun* 2015;4:109–15. Doi: 10.1016/j.mtcomm.2015.06.003.
- [271] Mazzer EM, Afonso CRM, Bolfarini C, Kiminami CS. Microstructure study of Al 7050 alloy reprocessed by spray forming and hot-extrusion and aged at 121 C. *Intermetallics* 2013;43:182–7. <https://doi.org/10.1016/j.intermet.2013.08.004>.
- [272] Gronostajski JZ, Kaczmar JW, Marciniak H, Matuszak A. Direct recycling of aluminium chips into extruded products. *J Mater Process Technol* 1997;64:149–56. [https://doi.org/10.1016/S0924-0136\(96\)02563-0](https://doi.org/10.1016/S0924-0136(96)02563-0).
- [273] Cooper DR, Allwood JM. The influence of deformation conditions in solid-state aluminium welding processes on the resulting weld strength. *J Mater Process Technol* 2014;214:2576–92. <https://doi.org/10.1016/j.jmatprotec.2014.04.018>.
- [274] Güley V, Ben Khalifa N, Tekkaya AE. Direct recycling of 1050 aluminum alloy scrap material mixed with 6060 aluminum alloy chips by hot extrusion. *Int J Mater Form* 2010;3:853–6. <https://doi.org/10.1007/s12289-010-0904-z>.
- [275] Fuziana YF, Wariikh ARM, Lajis MA, Azam MA, Muhammad NS. Recycling aluminium (Al 6061) chip through powder metallurgy route. *Mater Res Innov* 2014;18:S6-354-S6-358. Doi: 10.1179/1432891714Z.00000000981.
- [276] Cislo CN, Kronthaler B, Buchmayr B, Weiß C. Solid state recycling of aluminum alloy chips via pulsed electric current sintering. *J Manuf Mater Process* 2020;4. <https://doi.org/10.3390/jmmp4010023>.
- [277] Paraskevas D, Vanmeensel K, Vleugels J, Dewulf W, Deng Y, Duflou JR. Spark plasma sintering as a solid-state recycling technique: The case of aluminum alloy scrap consolidation. *Materials (Basel)* 2014;7:5664–87. <https://doi.org/10.3390/ma7085664>.
- [278] Rady MH, Mustapa MS, Wagiman A, Shamsudin S, Lajis MA, Al Alimi S, et al. Effect of the heat treatment on mechanical and physical properties of direct recycled aluminium alloy (AA6061). *Int J Integr Eng* 2020;12:82–9. <https://doi.org/10.30880/ijie.2020.12.03.011>.
- [279] Taha MA, Abbas AT, Benyahia F, Alharbi HF, Guitián B, Novoa XR. Enhanced corrosion resistance of recycled aluminum alloy 6061 chips using hot extrusion followed by ECAP. *J Chem* 2019;2019. <https://doi.org/10.1155/2019/3658507>.
- [280] Takahashi T, Kume Y, Kobashi M, Kanetake N. Solid state recycling of aluminum machined chip wastes by compressive torsion processing. *Keikinzoku/Journal Japan Inst Light Met* 2009;59:354–8. <https://doi.org/10.2464/jilm.59.354>.
- [281] Cui J, Guo W, Roven HJ, Wang Q, Chen Y, Peng T. Recycling of aluminum scrap by severe plastic deformation. *Mater Sci Forum* 2011;667–669:1177–82. <https://doi.org/10.4028/www.scientific.net/MSF.667-669.1177>.
- [282] Tang W, Reynolds AP. Production of wire via friction extrusion of aluminum alloy machining chips. *J Mater Process Technol* 2010;210:2231–7. <https://doi.org/10.1016/j.jmatprotec.2010.08.010>.
- [283] Lui EW, Palanisamy S, Dargusch MS, Xia K. Effects of chip conditions on the solid state recycling of Ti-6Al-4V machining chips. *J Mater Process Technol* 2016;238:297–304. <https://doi.org/10.1016/j.jmatprotec.2016.07.028>.
- [284] Bouaziz O, Bréchet Y, Embury JD. Heterogeneous and architectured materials: A possible strategy for design of structural materials. *Adv Eng Mater* 2008;10:24–36. <https://doi.org/10.1002/adem.200700289>.
- [285] Estrin Y, Beygelzimer Y, Kulagin R. Design of Architectured Materials Based on Mechanically Driven Structural and Compositional Patterning. *Adv Eng Mater* 2019;21. Doi: 10.1002/adem.201900487.
- [286] Ashby MF, Bréchet YJM. Designing hybrid materials. *Acta Mater* 2003;51:5801–21. [https://doi.org/10.1016/S1359-6454\(03\)00441-5](https://doi.org/10.1016/S1359-6454(03)00441-5).
- [287] Wagstaff RB, Lloyd DJ, Bischoff TF. Direct chill casting of CLAD ingot. *Mater Sci Forum* 2006;519–521:1809–14. <https://doi.org/10.4028/www.scientific.net/msf.519-521.1809>.
- [288] Azizi H, Zurob HS, Embury D, Wang X, Wang K, Bose B. Using architectured materials to control localized shear fracture. *Acta Mater* 2018;143:298–305. <https://doi.org/10.1016/j.actamat.2017.10.027>.

- [289] Roumina R, Bruhis M, Masse JP, Zurob HS, Jain M, Bouaziz O, et al. Bending properties of functionally graded 300M steels. *Mater Sci Eng A* 2016;653:63–70. <https://doi.org/10.1016/j.msea.2015.12.012>.
- [290] Muhammad W, Kang J, Brahma AP, Ali U, Hirsch J, Brinkman HJ, et al. Bendability enhancement of an age-hardenable aluminum alloy: Part I — relationship between microstructure, plastic deformation and fracture. *Mater Sci Eng A* 2019;753:179–91. <https://doi.org/10.1016/j.msea.2019.03.053>.
- [291] Caron EJFR, Pelayo REO, Baserinia AR, Wells MA, Weckman DC, Barker S, et al. Direct-chill Co-casting of AA3003/AA4045 aluminum ingots via fusionTM technology. *Mater. Trans. B Process Metall. Mater. Process. Sci.*, vol. 45, 2014, p. 975–87. Doi: 10.1007/s11663-013-0016-5.
- [292] Polmear I, St. John D, Nie J-F, Qian M. Light Alloys: Metallurgy of the Light Metals: Fifth Ed. 2017.
- [293] Zhan L, Lin J, Dean TA, Huang M. Experimental studies and constitutive modelling of the hardening of aluminium alloy 7055 under creep age forming conditions. *Int J Mech Sci* 2011;53:595–605. <https://doi.org/10.1016/j.ijmecsci.2011.05.006>.
- [294] Zhang J, Deng Y, Zhang X. Constitutive modeling for creep age forming of heat-treatable strengthening aluminum alloys containing plate or rod shaped precipitates. *Mater Sci Eng A* 2013;563:8–15. <https://doi.org/10.1016/j.msea.2012.10.055>.
- [295] Lin YC, Xia YC, Jiang YQ, Zhou HM, Li LT. Precipitation hardening of 2024-T3 aluminum alloy during creep aging. *Mater Sci Eng A* 2013;565:420–9. <https://doi.org/10.1016/j.msea.2012.12.058>.
- [296] Hutchinson CR, De Geuser F, Chen Y, Deschamps A. Quantitative measurements of dynamic precipitation during fatigue of an Al-Zn-Mg-(Cu) alloy using small-angle X-ray scattering. *Acta Mater* 2014;74:96–109. <https://doi.org/10.1016/j.actamat.2014.04.027>.
- [297] Das SK, Yin W, Wen X, Liu Y, Ningler S. Formability evaluation of recycle-friendly automotive aluminum alloys. *SAE Int J Mater Manuf* 2008;1:503–10. <https://doi.org/10.4271/2008-01-1095>.
- [298] Lloyd DJ. Ductility and bendability in 6000 Series Automotive Alloys. *Alum. Alloy.* 1999 TMS Symp. Proc., 2000, p. 211–21.
- [299] Sillekens WH, Sano T, Terasaki M, Matsuno K, Kals JAG. Formability of recycled aluminium alloy 5017. *J Mater Process Technol* 1997;65:252–60. [https://doi.org/10.1016/S0924-0136\(96\)02278-9](https://doi.org/10.1016/S0924-0136(96)02278-9).
- [300] Ma A, Roters F, Raabe D. Numerical study of textures and Lankford values for FCC polycrystals by use of a modified Taylor model. *Comput Mater Sci* 2004;29:353–61. <https://doi.org/10.1016/j.commatsci.2003.10.011>.
- [301] Tikhovskiy I, Raabe D, Roters F. Simulation of earing during deep drawing of an Al-3% Mg alloy (AA 5754) using a texture component crystal plasticity FEM. *J Mater Process Technol* 2007;183:169–75. <https://doi.org/10.1016/j.jmatprotec.2006.10.006>.
- [302] Zhang H, Diehl M, Roters F, Raabe D. A virtual laboratory using high resolution crystal plasticity simulations to determine the initial yield surface for sheet metal forming operations. *Int J Plast* 2016;80:111–38. <https://doi.org/10.1016/j.ijplas.2016.01.002>.
- [303] Han F, Diehl M, Roters F, Raabe D. Using spectral-based representative volume element crystal plasticity simulations to predict yield surface evolution during large scale forming simulations. *J Mater Process Technol* 2020;277:116449. <https://doi.org/10.1016/j.jmatprotec.2019.116449>.
- [304] Roters F, Eisenlohr P, Hantcherli L, Tjahjanto DD, Bieler TR, Raabe D. Overview of constitutive laws, kinematics, homogenization and multiscale methods in crystal plasticity finite-element modeling: Theory, experiments, applications. *Acta Mater* 2010;58:1152–211. <https://doi.org/10.1016/j.actamat.2009.10.058>.
- [305] Pradeau A, Thuillier S, Yoon JW. Prediction of failure in bending of an aluminium sheet alloy. *Int J Mech Sci* 2016;119:23–35. <https://doi.org/10.1016/j.ijmecsci.2016.09.033>.
- [306] Banabic D, Balan T, Comsa DS. A new yield criterion for orthotropic sheet metals under plane stress conditions. 7th Cold Met Form Conf 2000:217–24. Doi: 10.1016/S0020-7403(03)00139-5.
- [307] Winther G. Effect of grain orientation dependent microstructures on flow stress anisotropy modelling. *Scr Mater* 2005;52:995–1000. <https://doi.org/10.1016/j.scriptamat.2005.01.029>.
- [308] Sidor J, Petrov RH, Kestens LAI. Deformation, recrystallization and plastic anisotropy of asymmetrically rolled aluminum sheets. *Mater Sci Eng A* 2010;528:413–24. <https://doi.org/10.1016/j.msea.2010.09.023>.
- [309] Delannay L, Kalidindi SR, Van Houtte P. Quantitative prediction of textures in aluminium cold rolled to moderate strains. *Mater Sci Eng A* 2002;336:233–44. [https://doi.org/10.1016/S0921-5093\(01\)01966-9](https://doi.org/10.1016/S0921-5093(01)01966-9).
- [310] Delannay L, Melchior MA, Signorelli JW, Remacle JF, Kuwabara T. Influence of grain shape on the planar anisotropy of rolled steel sheets - evaluation of three models. *Comput Mater Sci* 2009;45:739–43. <https://doi.org/10.1016/j.commatsci.2008.06.013>.
- [311] Zhao Z, Mao W, Roters F, Raabe D. A texture optimization study for minimum earing in aluminium by use of a texture component crystal plasticity finite element method. *Acta Mater* 2004;52:1003–12. <https://doi.org/10.1016/j.actamat.2003.03.001>.
- [312] Raabe D, Zhao Z, Mao W. On the dependence of in-grain subdivision and deformation texture of aluminum on grain interaction. *Acta Mater* 2002;50:4379–94. [https://doi.org/10.1016/S1359-6454\(02\)00276-8](https://doi.org/10.1016/S1359-6454(02)00276-8).
- [313] Godfrey A, Juul Jensen D, Hansen N. Recrystallisation of channel die deformed single crystals of typical rolling orientations. *Acta Mater* 2001;49:2429–40. [https://doi.org/10.1016/S1359-6454\(01\)00148-3](https://doi.org/10.1016/S1359-6454(01)00148-3).
- [314] Engler O, Liu Z, Kuhnke K. Impact of homogenization on particles in the Al-Mg-Mn alloy AA 5454-Experiment and simulation. *J Alloys Compd* 2013;560:111–22. <https://doi.org/10.1016/j.jallcom.2013.01.163>.
- [315] Engler O, Löchte L, Hirsch J. Through-process simulation of texture and properties during the thermomechanical processing of aluminium sheets. *Acta Mater* 2007;55:5449–63. <https://doi.org/10.1016/j.actamat.2007.06.010>.
- [316] Vatne HE, Furu T, Ørsund R, Nes E. Modelling recrystallization after hot deformation of aluminium. *Acta Mater* 1996;44:4463–73. [https://doi.org/10.1016/1359-6454\(96\)00078-X](https://doi.org/10.1016/1359-6454(96)00078-X).
- [317] Vandermeer RA, Juul Jensen D. Recrystallization in hot vs cold deformed commercial aluminum: A microstructure path comparison. *Acta Mater* 2003;51:3005–18. [https://doi.org/10.1016/S1359-6454\(03\)00112-5](https://doi.org/10.1016/S1359-6454(03)00112-5).
- [318] Juul Jensen D. Growth rates and misorientation relationships between growing nuclei/grains and the surrounding deformed matrix during recrystallization. *Acta Metall Mater* 1995;43:4117–29. [https://doi.org/10.1016/0956-7151\(95\)00111-8](https://doi.org/10.1016/0956-7151(95)00111-8).
- [319] Huang Y, Humphreys FJ. Measurements of grain boundary mobility during recrystallization of a single-phase aluminium alloy. *Acta Mater* 1999;47:2259–68. [https://doi.org/10.1016/S1359-6454\(99\)00062-2](https://doi.org/10.1016/S1359-6454(99)00062-2).
- [320] Huang Y, Humphreys FJ. The effect of solutes on grain boundary mobility during recrystallization and grain growth in some single-phase aluminium alloys. *Mater Chem Phys* 2012;132:166–74. <https://doi.org/10.1016/j.matchemphys.2011.11.018>.
- [321] Humphreys FJ. The nucleation of recrystallization at second phase particles in deformed aluminium. *Acta Metall* 1977;25:1323–44. [https://doi.org/10.1016/0001-6160\(77\)90109-2](https://doi.org/10.1016/0001-6160(77)90109-2).
- [322] Sarkar J, Kutty TRG, Wilkinson DS, Embury JD, Lloyd DJ. Tensile properties and bendability of T4 treated AA6111 aluminum alloys. *Mater Sci Eng A* 2004;369:258–66. <https://doi.org/10.1016/j.msea.2003.11.022>.
- [323] Medrano S, Zhao H, Gault B, De Geuser F, Sinclair CW. A model to unravel the beneficial contributions of trace Cu in wrought Al-Mg alloys. *Acta Mater* 2021;208:116734. <https://doi.org/10.1016/j.actamat.2021.116734>.
- [324] Zhao H, White DR, Debroy T. Current issues and problems in laser welding of automotive aluminum alloys. *Int Mater Rev* 1999;44:238–66. <https://doi.org/10.1179/095066099101528298>.
- [325] Selvi S, Vishvakarman A, Rajasekar E. Cold metal transfer (CMT) technology - An overview. *Def Technol* 2018;14:28–44. <https://doi.org/10.1016/j.dt.2017.08.002>.
- [326] Li D, Chrysanthou A, Patel I, Williams G. Self-piercing riveting-a review. *Int J Adv Manuf Technol* 2017;92:1777–824. <https://doi.org/10.1007/s00170-017-0156-x>.
- [327] Mori K ichiro, Abe Y. A review on mechanical joining of aluminium and high strength steel sheets by plastic deformation. *Int J Light Mater Manuf* 2018;1:1–11. Doi: 10.1016/j.ijlmm.2018.02.002.
- [328] Threadgill PL, Leonard AJ, Shercliff HR, Withers PJ. Friction stir welding of aluminium alloys. *Int Mater Rev* 2009;54:49–93. <https://doi.org/10.1179/174328009X411136>.

- [329] Wu H, Chen YC, Strong D, Prangnell P. Stationary shoulder FSW for joining high strength aluminum alloys. *J Mater Process Technol* 2015;221:187–96. <https://doi.org/10.1016/j.jmatprotec.2015.02.015>.
- [330] Nandan R, DebRoy T, Bhadeshia HKDH. Recent advances in friction-stir welding - Process, weldment structure and properties. *Prog Mater Sci* 2008;53: 980–1023. <https://doi.org/10.1016/j.pmatsci.2008.05.001>.
- [331] Goebel J, Reimann M, Norman A, dos Santos JF. Semi-stationary shoulder bobbin tool friction stir welding of AA2198-T851. *J Mater Process Technol* 2017; 245:37–45. <https://doi.org/10.1016/j.jmatprotec.2017.02.011>.
- [332] Mazur M. Porosity in aluminium welds *Weld Int* 1992;6:929–31. <https://doi.org/10.1080/09507119209548317>.
- [333] Devletian JH, Wood WE. *Buletin Welding Research Council*. New York, N.Y.: Buletin Welding Research Council; 1983. p. 1–18.
- [334] Mishra S, Chakraborty S, Debroy T. Probing liquation cracking and solidification through modeling of momentum, heat, and solute transport during welding of aluminum alloys. *J Appl Phys* 2005;97. <https://doi.org/10.1063/1.1886272>.
- [335] Hermann R, Birley SS, Holdway P. Liquation cracking in aluminium alloy welds. *Mater Sci Eng A* 1996;212:247–55. [https://doi.org/10.1016/0921-5093\(96\)10198-2](https://doi.org/10.1016/0921-5093(96)10198-2).
- [336] Böllinghaus T, Herold H, Cross CE, Lippold JC. Hot cracking phenomena in welds II 2008. <https://doi.org/10.1007/978-3-540-78628-3>.
- [337] Tirayakoglu M. The effect of hydrogen on pore formation in aluminum alloy castings: Myth versus reality. *Metals (Basel)* 2020;10. <https://doi.org/10.3390/met10030368>.
- [338] Rappaz M, Drezet JM, Gremaud M. A new hot-tearing criterion. *Metall Mater Trans A Phys Metall Mater Sci* 1999;30:449–55. <https://doi.org/10.1007/s11661-999-0334-z>.
- [339] Taylor JA. Iron-containing intermetallic phases in Al-Si based casting alloys. *Procedia Mater Sci* 2012;1:19–33. <https://doi.org/10.1016/j.mspro.2012.06.004>.
- [340] Gremaud M, Carrard M, Kurz W. The microstructure of rapidly solidified AlFe alloys subjected to laser surface treatment. *Acta Metall Mater* 1990;38:2587–99. [https://doi.org/10.1016/0956-7151\(90\)90271-H](https://doi.org/10.1016/0956-7151(90)90271-H).
- [341] Koch S, Antrekowitsch H. Free-Cutting Aluminium Alloys with Tin as Substitution for LeadSubstitution von Blei durch Zinn in zerspanbaren Aluminiumlegierungen. *BHM Berg- Und Hüttenmännische Monatshefte* 2008;153:278–81. <https://doi.org/10.1007/s00501-008-0390-5>.
- [342] Löveborn D, Larsson JK, Persson KA. Weldability of aluminium alloys for automotive applications. *Phys Procedia* 2017;89:89–99. <https://doi.org/10.1016/j.phpro.2017.08.011>.
- [343] Ma ZY. Friction stir processing technology: A review. *Metall Mater Trans A Phys Metall Mater Sci* 2008;39 A:642–58. Doi: 10.1007/s11661-007-9459-0.
- [344] Hoang NH, Porcaro R, Langseth M, Hanssen AG. Self-piercing riveting connections using aluminium rivets. *Int J Solids Struct* 2010;47:427–39. <https://doi.org/10.1016/j.ijсолstr.2009.10.009>.
- [345] Lievers WB, Pilkey AK, Lloyd DJ. The influence of iron content on the bendability of AA6111 sheet. *Mater Sci Eng A* 2003;361:312–20. [https://doi.org/10.1016/S0921-5093\(03\)00535-5](https://doi.org/10.1016/S0921-5093(03)00535-5).
- [346] Hannard F, Simar A, Maire E, Pardo T. Quantitative assessment of the impact of second phase particle arrangement on damage and fracture anisotropy. *Acta Mater* 2018;148:456–66. <https://doi.org/10.1016/j.actamat.2018.02.003>.
- [347] Mori K, Abe Y, Kato T, Sakai S. Self-pierce riveting of three aluminium alloy and mild steel sheets. *AIP Conf Proc* 2010;1252:673–80. <https://doi.org/10.1063/1.3457620>.
- [348] Kattner UR. The thermodynamic modeling of multicomponent phase equilibria. *JOM* 1997;49. <https://doi.org/10.1007/s11837-997-0024-5>.
- [349] L. K, Bernstein H. Computer Calculation of Phase Diagrams. Academic Press NY; 1970.
- [350] Hillert M. Phase Equilibria. Phase Diagrams and Phase Transformations 2007. <https://doi.org/10.1017/cbo9780511812781>.
- [351] Hillert M. The compound energy formalism. *J Alloys Compd* 2001;320. Doi: 10.1016/S0925-8388(00)01481-X.
- [352] Chen HL, Chen Q, Engström A. Development and applications of the TCAL aluminum alloy database. *Calphad Comput Coupling Phase Diagrams Thermochem* 2018;62. <https://doi.org/10.1016/j.calphad.2018.05.010>.
- [353] Chen SL, Daniel S, Zhang F, Chang YA, Yan XY, Xie FY, et al. The PANDAT software package and its applications. *Calphad Comput Coupling Phase Diagrams Thermochem* 2002;26. [https://doi.org/10.1016/S0364-5916\(02\)00034-2](https://doi.org/10.1016/S0364-5916(02)00034-2).
- [354] Bale CW, Béolis E, Chartrand P, Deckerov SA, Eriksson G, Gheribi AE, et al. FactSage thermochemical software and databases, 2010–2016. *Calphad Comput Coupling Phase Diagrams Thermochem* 2016;54. Doi: 10.1016/j.calphad.2016.05.002.
- [355] Thermocalc Software. TCS Al-based Alloy Database (TCAL7) 2020.
- [356] CompuTherm LLC. PanAluminum 2020.
- [357] FactSage. FTlite Database for FactSage 7.3 2020. http://www.crct.polymtl.ca/fact/documentation/FTlite/FTlite_documentation.pdf.
- [358] Jin H, Afifun P, Dove S, Furlan G, Zakotnik M, Yih Y, et al. Life cycle assessment of neodymium-iron-boron magnet-to-magnet recycling for electric vehicle motors. *Environ Sci Technol* 2018;52:3796–802. <https://doi.org/10.1021/acs.est.7b05442>.
- [359] MatCalc Engineering GmbH. mc_al_v2.032.tdb 2018.
- [360] Kolb G, Scheiber S, Antrekowitsch H, Uggowitzer P, Pöschmann D, Pogatscher S. Differential scanning calorimetry and thermodynamic predictions—a comparative study of Al-Zn-Mg-Cu alloys. *Metals (Basel)* 2016;6:180. <https://doi.org/10.3390/met6080180>.
- [361] Shi R, Luo AA. Applications of CALPHAD modeling and databases in advanced lightweight metallic materials. *Calphad Comput Coupling Phase Diagrams Thermochem* 2018;62. <https://doi.org/10.1016/j.calphad.2018.04.009>.
- [362] Reed RC, Tao T, Warnken N. Alloys-By-Design: Application to nickel-based single crystal superalloys. *Acta Mater* 2009;57:5898–913. <https://doi.org/10.1016/j.actamat.2009.08.018>.
- [363] Wert KN, Miller JD, Senkov ON. Toward multi-principal component alloy discovery: Assessment of CALPHAD thermodynamic databases for prediction of novel ternary alloy systems. *J Mater Res* 2018;33. <https://doi.org/10.1557/jmr.2018.61>.
- [364] Gorsse S, Senkov ON. About the reliability of CALPHAD predictions in multicomponent systems. *Entropy* 2018;20. Doi: 10.3390/e20120899.
- [365] Van De Walle A, Asta M. High-throughput calculations in the context of alloy design. *MRS Bull* 2019;44. Doi: 10.1557/mrs.2019.71.
- [366] Pollock TM, Van Der Ven A. The evolving landscape for alloy design. *MRS Bull* 2019;44:238–46. <https://doi.org/10.1557/mrs.2019.69>.
- [367] Turchi PEA, Abrikosov IA, Burton B, Fries SG, Grimvall G, Kaufman L, et al. Interface between quantum-mechanical-based approaches, experiments, and CALPHAD methodology. *Calphad Comput Coupling Phase Diagrams Thermochem* 2007;31. <https://doi.org/10.1016/j.calphad.2006.02.009>.
- [368] Kim K, Zhou BC, Wolverton C. First-principles study of crystal structure and stability of T1 precipitates in Al-Li-Cu alloys. *Acta Mater* 2018;145. <https://doi.org/10.1016/j.actamat.2017.12.013>.
- [369] Wolverton C, Ozoliņš V. Entropically favored ordering: The metallurgy of Al2Cu revisited. *Phys Rev Lett* 2001;86:5518–21. <https://doi.org/10.1103/PhysRevLett.86.5518>.
- [370] Van Der Ven A, Thomas JC, Puchala B, Natarajan AR. First-principles statistical mechanics of multicomponent crystals. *Annu Rev Mater Res* 2018;48. <https://doi.org/10.1146/annurev-matsci-070317-124443>.
- [371] Grabowski B, Ikeda Y, Srinivasan P, Körmann F, Freysoldt C, Duff AI, et al. Ab initio vibrational free energies including anharmonicity for multicomponent alloys. *Npj Comput Mater* 2019;5. <https://doi.org/10.1038/s41524-019-0218-8>.
- [372] Van De Walle A, Hong Q, Kadkhodaei S, Sun R. The free energy of mechanically unstable phases. *Nat Commun* 2015;6. <https://doi.org/10.1038/ncomms8559>.
- [373] Zunger A, Wei SH, Ferreira LG, Bernard JE. Special quasirandom structures. *Phys Rev Lett* 1990;65. <https://doi.org/10.1103/PhysRevLett.65.353>.
- [374] Van De Walle A, Tiwary P, De Jong M, Olmsted DL, Asta M, Díez A, et al. Efficient stochastic generation of special quasirandom structures. *Calphad Comput Coupling Phase Diagrams Thermochem* 2013;42. <https://doi.org/10.1016/j.calphad.2013.06.006>.
- [375] Kirklin S, Saal JE, Meredig B, Thompson A, Doak JW, Aykol M, et al. The Open Quantum Materials Database (OQMD): Assessing the accuracy of DFT formation energies. *Npj Comput Mater* 2015;1. <https://doi.org/10.1038/npjcompumats.2015.10>.
- [376] Gossett E, Toher C, Oses C, Isayev O, Legrain F, Rose F, et al. AFLOW-ML: A RESTful API for machine-learning predictions of materials properties. *Comput Mater Sci* 2018;152. <https://doi.org/10.1016/j.commatsci.2018.03.075>.

- [377] Draxl C, Scheffler M. The NOMAD laboratory: from data sharing to artificial intelligence. *J Phys Mater* 2019;2:036001. <https://doi.org/10.1088/2515-7639/ab13bb>.
- [378] Kirklin S, Saal JE, Hegde VI, Wolverton C. High-throughput computational search for strengthening precipitates in alloys. *Acta Mater* 2016;102.. <https://doi.org/10.1016/j.actamat.2015.09.016>.
- [379] Sunde JK, Marioara CD, Holmestad R. The effect of low Cu additions on precipitate crystal structures in overaged Al-Mg-Si(-Cu) alloys. *Mater Charact* 2020;160:110087. <https://doi.org/10.1016/j.matchar.2019.110087>.
- [380] da Costa Teixeira J, Bréchet Y, Estrin Y, Hutchinson C. The Strain Hardening Behaviour of Supersaturated Al-Cu Alloys. *Proc 12th Int Conf Alum Alloy* 2010; 536–41.
- [381] Sherby OD, Anderson RA, Dorn JE. Effect of alloying elements on the elevated temperature plastic properties of alpha solid solutions of aluminum. *JOM* 1951; 3:643–52. <https://doi.org/10.1007/bf03397360>.
- [382] Qian F, Jin S, Sha G, Li Y. Enhanced dispersoid precipitation and dispersion strengthening in an Al alloy by microalloying with Cd. *Acta Mater* 2018;157: 114–25. <https://doi.org/10.1016/j.actamat.2018.07.001>.
- [383] Bourgeois L, Dwyer C, Weyland M, Nie JF, Muddle BC. The magic thicknesses of θ' precipitates in Sn-microalloyed Al-Cu. *Acta Mater* 2012;60:633–44. <https://doi.org/10.1016/j.actamat.2011.10.015>.
- [384] Li J, Bourgeois L, Tsalanidis A, Weyland M, Medhekar NV, Bourgeois L, et al. The enhanced theta-prime (θ') precipitation in an Al-Cu alloy with trace Au additions. *Acta Mater* 2017;125:340–50. <https://doi.org/10.1016/j.actamat.2016.12.012>.
- [385] Raviprasad K, Hutchinson CR, Sakurai T, Ringer SP. Precipitation processes in an Al-2.5Cu-1.5Mg (wt. %) alloy microalloyed with Ag and Si. *Acta Mater* 2003; 51:5037–50. [https://doi.org/10.1016/S1359-6454\(03\)00351-3](https://doi.org/10.1016/S1359-6454(03)00351-3).
- [386] Gao YH, Kuang J, Liu G, Sun J. Effect of minor Sc and Fe co-addition on the microstructure and mechanical properties of Al-Cu alloys during homogenization treatment. *Mater Sci Eng A* 2019;746:11–26. <https://doi.org/10.1016/j.msea.2018.12.099>.
- [387] Suresh M, Sharma A, More AM, Nayan N, Suwas S. Effect of Scandium addition on evolution of microstructure, texture and mechanical properties of thermo-mechanically processed Al-Li alloy AA2195. *J Alloys Compd* 2018;740:364–74. <https://doi.org/10.1016/j.jallcom.2017.12.045>.
- [388] Pogatscher S, Antrekowitsch H, Leitner H, Ebner T, Uggowitzer PJ. Mechanisms controlling the artificial aging of Al-Mg-Si Alloys. *Acta Mater* 2011;59: 3352–63. <https://doi.org/10.1016/j.actamat.2011.02.010>.
- [389] Russell KC. Nucleation in solids: The induction and steady state effects. *Adv Colloid Interface Sci* 1980;13:205–318. [https://doi.org/10.1016/0001-8686\(80\)80003-0](https://doi.org/10.1016/0001-8686(80)80003-0).
- [390] Kozeschnik E. Modeling Solid-State Precipitation. New York: Momentum Press, LLC, New York; 2012. Doi: 10.5643/9781606500644.
- [391] Zener C. Theory of growth of spherical precipitates from solid solution. *J Appl Phys* 1949;20:950–3. <https://doi.org/10.1063/1.1698258>.
- [392] Lifshitz IM, Slyozov VV. The kinetics of precipitation from supersaturated solid solutions. *J Phys Chem Solids* 1961;19:35–50. [https://doi.org/10.1016/0022-3697\(61\)90054-3](https://doi.org/10.1016/0022-3697(61)90054-3).
- [393] Wagner C. Theorie der Alterung von Niederschlägen durch Umlösen (Ostwald-Reifung). *Zeitschrift Für Elektrochemie, Berichte Der Bunsengesellschaft Für Phys Chemie* 1961;65:581–91.
- [394] Robson JD. Modelling the overlap of nucleation, growth and coarsening during precipitation. *Acta Mater* 2004;52:4669–76. <https://doi.org/10.1016/j.actamat.2004.06.024>.
- [395] Kolmogorov A. The statistics of crystal growth in metals. *Izvestia Acad Nauk SSSR - Seria Mat* 1937;1:333–9.
- [396] Johnson WA, R.F. Mehl. Reaction Kinetics in Processes of Nucleation and Growth. *Trans Am Inst Minning Metall Eng* 1939;135:416–58.
- [397] Avrami MM. Kinetics of phase change. I: General theory. *J Chem Phys* 1939;7:1103–12. <https://doi.org/10.1063/1.1750380>.
- [398] Fanfoni M, Tomellini M. The Johnson-Mehl-Avrami-Kolmogorov model: A brief review. *Nuovo Cim Della Soc Ital Di Fis D - Condens Matter, At Mol Chem Physics, Biophys* 1998;20:1171–82. <https://doi.org/10.1007/BF03185527>.
- [399] Sekhar AP, Nandy S, Ray KK, Das D. Prediction of Aging Kinetics and Yield Strength of 6063 Alloy. *J Mater Eng Perform* 2019;28:2764–78. <https://doi.org/10.1007/s11665-019-04086-z>.
- [400] Sha W. Application of simple practical models for early stage ageing precipitation kinetics and hardening in aluminium alloys. *Mater Des* 2007;28:528–33. <https://doi.org/10.1016/j.matdes.2005.08.012>.
- [401] Shercliff HR, Ashby MF. A process model for age hardening of aluminium alloys-I. The model. *Acta Metall Mater* 1990;38:1789–802. [https://doi.org/10.1016/0956-7151\(90\)90291-N](https://doi.org/10.1016/0956-7151(90)90291-N).
- [402] Shercliff HR, Ashby MF. A process model for age hardening of aluminium alloys-II. Applications of the model. *Acta Metall Mater* 1990;38:1803–12. [https://doi.org/10.1016/0956-7151\(90\)90292-O](https://doi.org/10.1016/0956-7151(90)90292-O).
- [403] Rometsch PA, Schaffer GB. An age hardening model for Al-7Si-Mg casting alloys. *Mater Sci Eng A* 2002;325:424–34. [https://doi.org/10.1016/S0921-5093\(01\)01479-4](https://doi.org/10.1016/S0921-5093(01)01479-4).
- [404] Eivani AR, Taheri AK. Modeling age hardening kinetics of an Al-Mg-Si-Cu aluminum alloy. *J Mater Process Technol* 2008;205:388–93. <https://doi.org/10.1016/j.jmatprotec.2007.11.195>.
- [405] Guo MX, Zhang XK, Zhang JS, Zhuang LZ. Effect of Zn addition on the precipitation behaviors of Al-Mg-Si-Cu alloys for automotive applications. *J Mater Sci* 2017;52:1390–404. <https://doi.org/10.1007/s10853-016-0433-3>.
- [406] Yazdanmehr M, Bahrami A, Anijdan SHM. A precipitation-hardening model for non-isothermal ageing of Al-Mg-Si alloys. *Comput Mater Sci* 2009;45:385–7. <https://doi.org/10.1016/j.commatsci.2008.10.013>.
- [407] Esmaili S, Lloyd DJ. Modeling of precipitation hardening in pre-aged AlMgSi(Cu) alloys. *Acta Mater* 2005;53:5257–71. <https://doi.org/10.1016/j.actamat.2005.08.006>.
- [408] Esmaili S, Wang X, Lloyd DJ, Poole WJ. On the precipitation-hardening behavior of the Al-Mg-Si-Cu alloy AA6111. *Metall Mater Trans A Phys Metall Mater Sci* 2003;34:751–63. <https://doi.org/10.1007/s11661-003-1003-2>.
- [409] Starink MJ. A new model for diffusion-controlled precipitation reactions using the extended volume concept. *Thermochim Acta* 2014;596:109–19. <https://doi.org/10.1016/j.tca.2014.09.016>.
- [410] Starink MJ, Gao N, Davin L, Yan J, Cerezo A. Room temperature precipitation in quenched Al-Cu-Mg alloys: A model for the reaction kinetics and yield strength development. *Philos Mag* 2005;85:1395–417. <https://doi.org/10.1080/1478643041233133374>.
- [411] Milkereit B, Starink MJ. Quench sensitivity of Al-Mg-Si alloys: A model for linear cooling and strengthening. *Mater Des* 2015;76:117–29. <https://doi.org/10.1016/j.matdes.2015.03.055>.
- [412] Zhu Z, Starink MJ. Age hardening and softening in cold-rolled Al-Mg-Mn alloys with up to 0.4 wt% Cu. *Mater Sci Eng A* 2008;489:138–49. <https://doi.org/10.1016/j.msea.2007.12.019>.
- [413] Starink MJ, Milkereit B, Zhang Y, Rometsch PA. Predicting the quench sensitivity of Al-Zn-Mg-Cu alloys: A model for linear cooling and strengthening. *Mater Des* 2015;88:958–71. <https://doi.org/10.1016/j.matdes.2015.09.058>.
- [414] Hersent E, Driver JH, Piot D. Modelling differential scanning calorimetry curves of precipitation in Al-Cu-Mg. *Scr Mater* 2010;62:455–7. <https://doi.org/10.1016/j.scriptamat.2009.12.009>.
- [415] Ji K, Li G, Sun Y, Xu J, Chen H, Chen K, et al. A constitutive model for yield strength and work hardening behaviour of aluminium alloys during artificial ageing. *Metals (Basel)* 2020;10:1–14. <https://doi.org/10.3390/met10081094>.
- [416] Li Y, Shi Z, Lin J. Experimental investigation and modelling of yield strength and work hardening behaviour of artificially aged Al-Cu-Li alloy. *Mater Des* 2019;183:108121. <https://doi.org/10.1016/j.matdes.2019.108121>.
- [417] Zheng JH, Lin J, Lee J, Pan R, Li C, Davies CM. A novel constitutive model for multi-step stress relaxation ageing of a pre-strained 7xxx series alloy. *Int J Plast* 2018;106:31–47. <https://doi.org/10.1016/j.ijplas.2018.02.008>.
- [418] Robson JD, Sullivan A. Process model for strength of age hardenable aluminium alloy welds. *Mater Sci Technol* 2006;22:146–52. <https://doi.org/10.1179/174328406X81603>.

- [419] Rometsch PA, Starink MJ, Gregson PJ. Improvements in quench factor modelling. *Mater Sci Eng A* 2003;339:255–64. [https://doi.org/10.1016/S0921-5093\(02\)00110-7](https://doi.org/10.1016/S0921-5093(02)00110-7).
- [420] Matsuda H, Bhadeshia HKDH. Avrami theory for transformations from non-uniform austenite grain structures. *Mater Sci Technol* 2003;19:1330–4. <https://doi.org/10.1179/026708303225002055>.
- [421] Robson JD, Bhadeshia HKDH. Modelling precipitation sequences in power plant steels Part 1 - Kinetic theory. *Mater Sci Technol* 1997;13:631–9. <https://doi.org/10.1179/mst.1997.13.8.631>.
- [422] Perez M, Dumont M, Acevedo-Reyes D. Implementation of classical nucleation and growth theories for precipitation. *Acta Mater* 2008;56:2119–32. <https://doi.org/10.1016/j.actamat.2007.12.050>.
- [423] Langer JS, Schwartz AJ. Kinetics of nucleation in near-critical fluids. *Phys Rev A* 1980;21:948–58. <https://doi.org/10.1103/PhysRevA.21.948>.
- [424] Clouet E. Modeling of Nucleation Processes. In: D. U. Furrer and S. L. Semiatin, editor. *Fundam. Model. Met. Process.*, vol. 22A, 2018, p. 203–19. Doi: 10.31399/asm.hb.v22a.a0005410.
- [425] Lukas HL, Fries SG, Sundman B. Computational thermodynamics: The Calphad method 1868;978052:2007. <https://doi.org/10.1017/CBO9780511804137>.
- [426] Sonderegger B, Kozeschnik E. Generalized nearest-neighbor broken-bond analysis of randomly oriented coherent interfaces in multicomponent Fcc and Bcc structures. *Metall Mater Trans A Phys Metall Mater Sci* 2009;40:499–510. <https://doi.org/10.1007/s11661-008-9752-6>.
- [427] Sonderegger B, Kozeschnik E. Size dependence of the interfacial energy in the generalized nearest-neighbor broken-bond approach. *Scr Mater* 2009;60:635–8. <https://doi.org/10.1016/j.scriptamat.2008.12.025>.
- [428] Sonderegger B, Kozeschnik E. Interfacial energy of diffuse phase boundaries in the generalized broken-bond approach. *Metall Mater Trans A Phys Metall Mater Sci* 2010;41:3262–9. <https://doi.org/10.1007/s11661-010-0370-8>.
- [429] Kozeschnik E, Svoboda J, Fischer FD. On the role of chemical composition in multi-component solid-state nucleation. In: Howe JM, Laughlin DE, Lee JK, Dahmen U, Soffa WA, editors. *Proc. an Int. Conf. Solid-Solid Phase Transform. Inorg. Mater.* 2005, vol. 2, Phoenix, AZ, USA: TMS (The Minerals, Metals and Materials Society); 2005, p. 301–10.
- [430] Kozeschnik E. Thermodynamic prediction of the equilibrium chemical composition of critical nuclei: Bcc Cu precipitation in α -Fe. *Scr Mater* 2008;59:1018–21. <https://doi.org/10.1016/j.scriptamat.2008.07.008>.
- [431] Hillert M. Nature of local equilibrium at the interface in the growth of ferrite from alloyed austenite. *Scr Mater* 2002;46:447–53. [https://doi.org/10.1016/S1359-6462\(01\)01257-X](https://doi.org/10.1016/S1359-6462(01)01257-X).
- [432] Hillert M, Odqvist J, Ågren J. Interface conditions during diffusion-controlled phase transformations. *Scr Mater* 2004;50:547–50. <https://doi.org/10.1016/j.scriptamat.2003.10.027>.
- [433] Svoboda J, Turek I, Fischer FD. Application of the thermodynamic extremal principle to modeling of thermodynamic processes in material sciences. *Philos Mag* 2005;85:3699–707. <https://doi.org/10.1080/14786430500267760>.
- [434] Fischer FD, Svoboda J, Petryk H. Thermodynamic extremal principles for irreversible processes in materials science. *Acta Mater* 2014;67:1–20. <https://doi.org/10.1016/j.actamat.2013.11.050>.
- [435] Svoboda J, Fischer FD, Kozeschnik E. Thermodynamic modelling of irreversible processes. *Eur Mineral Union Notes Mineral* 2017;16:181–214. <https://doi.org/10.1180/EMU-notes.16.7>.
- [436] Kozeschnik E, Svoboda J, Fratzl P, Fischer FD. Modelling of kinetics in multi-component multi-phase systems with spherical precipitates II: Numerical solution and application. *Mater Sci Eng A* 2004;385:157–65. <https://doi.org/10.1016/j.msea.2004.06.016>.
- [437] Kuang W, Wang H, Zhang J, Liu F. Application of the thermodynamic extremal principle to diffusion-controlled phase-transformations in multi-component substitutional alloys: Modeling and applications. *Acta Mater* 2016;120:415–25. <https://doi.org/10.1016/j.scriptamat.2016.08.078>.
- [438] Bonvalet-Rolland M, Philippe T, Ågren J. Kinetic theory of nucleation in multicomponent systems: An application of the thermodynamic extremum principle. *Acta Mater* 2019;171:1–7. <https://doi.org/10.1016/j.actamat.2019.03.031>.
- [439] Jiang H, Faulkner RG. Modelling of grain boundary segregation, precipitation and precipitate-free zones of high strength aluminium alloys - I. The model. *Acta Mater* 1996;44:1857–64. [https://doi.org/10.1016/1359-6454\(95\)00317-7](https://doi.org/10.1016/1359-6454(95)00317-7).
- [440] Kozeschnik E, Svoboda J, Radis R, Fischer FD. Mean-field model for the growth and coarsening of stoichiometric precipitates at grain boundaries. *Model Simul Mater Sci Eng* 2010;18:015011. <https://doi.org/10.1088/0965-0393/18/1/015011>.
- [441] Ardell AJ. The effect of volume fraction on particle coarsening: theoretical considerations. *Acta Metall* 1972;20:61–71. [https://doi.org/10.1016/0001-6160\(72\)90114-9](https://doi.org/10.1016/0001-6160(72)90114-9).
- [442] Wang KG, Glicksman ME, Rajan K. Modeling and simulation for phase coarsening: A comparison with experiment. *Phys Rev E - Stat Physics, Plasmas, Fluids, Relat Interdiscip Top* 2004;69:9. <https://doi.org/10.1103/PhysRevE.69.061507>.
- [443] Voorhees PW. The theory of Ostwald ripening. *J Stat Phys* 1985;38:231–52. <https://doi.org/10.1007/BF01017860>.
- [444] Novotny GM, Ardell AJ. Precipitation of Al3Sc in binary Al-Sc alloys. *Mater Sci Eng A* 2001;318:144–54. [https://doi.org/10.1016/S0921-5093\(01\)01326-0](https://doi.org/10.1016/S0921-5093(01)01326-0).
- [445] Zhao D, Xu Y, Gouttebroze S, Friis J, Li Y. Modelling the Age-Hardening Precipitation by a Revised Langer and Schwartz Approach with Log-Normal Size Distribution. *Metall Mater Trans A Phys Metall Mater Sci* 2020;51:4838–52. <https://doi.org/10.1007/s11661-020-05879-x>.
- [446] Perez M. Gibbs-Thomson effects in phase transformations. *Scr Mater* 2005;52:709–12. <https://doi.org/10.1016/j.scriptamat.2004.12.026>.
- [447] Kampmann R, Wagner R. KINETICS OF PRECIPITATION IN METASTABLE BINARY ALLOYS - THEORY AND APPLICATION TO Cu-1.9 AT % Ti AND Ni-14 AT % Al. *Acta Scr Met Ser "Decomposition Alloy early stages"* 1984;91–103. <https://doi.org/10.1016/b978-0-08-031651-2.50018-5>.
- [448] Sigli C, De Geuser F, Deschamps A, Lépinoux J, Perez M. Recent advances in the metallurgy of aluminum alloys. Part II: Age hardening. *Comptes Rendus Phys* 2018;19:688–709. <https://doi.org/10.1016/j.crhy.2018.10.012>.
- [449] Robson JD, Engler O, Sigli C, Deschamps A, Poole WJ. Advances in Microstructural Understanding of Wrought Aluminum Alloys. *Metall Mater Trans A Phys Metall Mater Sci* 2020;51:4377–89. <https://doi.org/10.1007/s11661-020-05908-9>.
- [450] Cinkilic E, Yan X, Luo AA. Modeling precipitation hardening and yield strength in cast Al-Si-Mg-Mn alloys. *Metals (Basel)* 2020;10:1–14. <https://doi.org/10.3390/met10101356>.
- [451] Schneider M, Gottstein G, Löchte L, Hirsch J. A statistical model for precipitation - Applications to commercial Al-Mn-Mg-Fe-Si alloys. *Mater Sci Forum* 2002;396–402:637–42. <https://doi.org/10.4028/www.scientific.net/msf.396-402.637>.
- [452] Liu Z, Monles V, Engler O, Gottstein G, Mohles V, Engler O, et al. Statistical Model of Precipitation Kinetics for Recycled Commercial Aluminum Alloys. *Suppl. Proc. Mater. Fabr. Prop. Charact. Model.*, vol. 2, Hoboken, NJ, USA: John Wiley & Sons, Inc.; 2011, p. 449–56. Doi: 10.1002/9781118062142.ch54.
- [453] Engler O, Miller-Jupp S. Control of second-phase particles in the Al-Mg-Mn alloy AA 5083. *J Alloys Compd* 2016;689:998–1010. <https://doi.org/10.1016/j.jallcom.2016.08.070>.
- [454] Afshar M, Mao F, Jiang H, Mohles V, Schick M, Hack K, et al. Modelling of differential scanning calorimetry heating curves for precipitation and dissolution in an Al-Mg-Si. *Comput Mater Sci* 2019;158:235–42. <https://doi.org/10.1016/j.commatsci.2018.11.023>.
- [455] Liu Z, Mohles V, Engler O, Gottstein G. Thermodynamics based modelling of the precipitation kinetics in commercial aluminium alloys. *Comput Mater Sci* 2014;81:410–7. <https://doi.org/10.1016/j.commatsci.2013.08.049>.
- [456] Crumbach M, Neumann L, Goerdeler M, Aretz H, Gottstein G, Kopp R. Through-process modelling of texture and anisotropy in AA5182. *Model Simul Mater Sci Eng* 2006;14:835–56. <https://doi.org/10.1088/0965-0393/14/5/003>.
- [457] Engler O, Laptyeva G, Wang N. Impact of homogenization on microchemistry and recrystallization of the Al-Fe-Mn alloy AA 8006. *Mater Charact* 2013;79:60–75. <https://doi.org/10.1016/j.matchar.2013.02.012>.
- [458] Lenz M, Laptyeva G, Engler O. Characterization of second-phase particles in two aluminium foil alloys. *J Alloys Compd* 2016;660:276–88. <https://doi.org/10.1016/j.jallcom.2015.11.111>.
- [459] Du Q, Poole WJ, Wells MA. A mathematical model coupled to CALPHAD to predict precipitation kinetics for multicomponent aluminum alloys. *Acta Mater* 2012;60:3830–9. <https://doi.org/10.1016/j.actamat.2012.02.050>.

- [460] Du Q, Tang K, Marioara CD, Andersen SJ, Holmedal B, Holmestad R. Modeling over-ageing in Al-Mg-Si alloys by a multi-phase CALPHAD-coupled Kampmann-Wagner Numerical model. *Acta Mater* 2017;122:178–86. <https://doi.org/10.1016/j.actamat.2016.09.052>.
- [461] Holmedal B, Osmundsen E, Du Q. Precipitation of non-spherical particles in aluminum alloys part I: generalization of the kampmann-wagner numerical model. *Metall Mater Trans A Phys Metall Mater Sci* 2016;47:581–8. <https://doi.org/10.1007/s11661-015-3197-5>.
- [462] Du Q, Holmedal B, Friis J, Marioara CD. Precipitation of non-spherical particles in aluminum alloys part II: Numerical simulation and experimental characterization during aging treatment of an Al-Mg-Si alloy. *Metall Mater Trans A Phys Metall Mater Sci* 2016;47:589–99. <https://doi.org/10.1007/s11661-015-3196-6>.
- [463] Khan IN, Starink MJ, Yan JL. A model for precipitation kinetics and strengthening in Al-Cu-Mg alloys. *Mater Sci Eng A* 2008;472:66–74. <https://doi.org/10.1016/j.msea.2007.03.033>.
- [464] Khan IN, Starink MJ. Microstructure and strength modelling of Al-Cu-Mg alloys during non-isothermal treatments Part 1 - Controlled heating and cooling. *Mater Sci Technol* 2008;24:1403–10. <https://doi.org/10.1179/174328408X317020>.
- [465] Khan IN, Starink MJ, Sinclair I, Wang SC. Microstructure and strength modelling of Al-Cu-Mg alloys during non-isothermal treatments Part 2 - Welds. *Mater Sci Technol* 2008;24:1411–8. <https://doi.org/10.1179/174328408X317048>.
- [466] Larouche D. Mixed mode growth of an ellipsoidal precipitate: Analytical solution for shape preserving growth in the quasi-stationary regime. *Acta Mater* 2017;123:188–96. <https://doi.org/10.1016/j.actamat.2016.10.031>.
- [467] Naseri T, Larouche D, Martinez R, Breton F, Massinon D. Analytical modeling of the mixed-mode growth and dissolution of precipitates in a finite system. *Metals (Basel)* 2019;9:889. <https://doi.org/10.3390/met9080889>.
- [468] Martinez R, Larouche D, Cailletaud G, Guillot L, Massinon D. Simulation of the concomitant process of nucleation-growth-coarsening of Al₂Cu particles in a 319 foundry aluminum alloy. *Model Simul Mater Sci Eng* 2015;23. doi: 10.1088/0965-0393/23/4/045012.
- [469] Naseri T, Larouche D, Heugue P, Martinez R, Breton F, Massinon D. Multiphase modelling of the growth kinetics of precipitates in Al-Cu alloys during artificial aging. *Philos Mag* 2021;101:1–24. <https://doi.org/10.1080/14786435.2020.1808255>.
- [470] Heugue P, Larouche D, Breton F, Martinez R, Chen XG. Evaluation of the growth kinetics of θ' and α-Al₂Cu precipitates in a binary Al-3.5 Wt pct Cu alloy. *Metall Mater Trans A Phys Metall Mater Sci* 2019;50:3048–60. <https://doi.org/10.1007/s11661-019-05227-8>.
- [471] Falahati A, Povoden-Karadeniz E, Lang P, Warczok P, Kozeschnik E. Thermo-kinetic computer simulation of differential scanning calorimetry curves of AlMgSi alloys. *Int J Mater Res* 2010;101:1089–96. <https://doi.org/10.3139/146.110396>.
- [472] Lang P, Wojcik T, Povoden-Karadeniz E, Falahati A, Kozeschnik E. Thermo-kinetic prediction of metastable and stable phase precipitation in Al-Zn-Mg series aluminium alloys during non-isothermal DSC analysis. *J Alloys Compd* 2014;609:129–36. <https://doi.org/10.1016/j.jallcom.2014.04.119>.
- [473] Lang P, Povoden-Karadeniz E, Falahati A, Kozeschnik E. Simulation of the effect of composition on the precipitation in 6xxx Al alloys during continuous-heating DSC. *J Alloys Compd* 2014;612:443–9. <https://doi.org/10.1016/j.jallcom.2014.05.191>.
- [474] Buken H, Kozeschnik E. Modeling static recrystallization in Al-Mg alloys. *Metall Mater Trans A Phys Metall Mater Sci* 2021;52:544–52. <https://doi.org/10.1007/s11661-020-06100-9>.
- [475] Vierenstein B, Kozeschnik E. Integrated physical-constitutive computational framework for plastic deformation modeling. *Metals (Basel)* 2020;10:1–13. <https://doi.org/10.3390/met10070869>.
- [476] Weisz T, Warczok P, Ebner T, Falahati A, Kozeschnik E. Simulation of natural aging in Al-Mg-Si alloys. *Mater Sci Forum* 2015;828–829:468–73. <https://doi.org/10.4028/www.scientific.net/MSF.828-829.468>.
- [477] Lang P, Weisz T, Ahmadi MR, Povoden-Karadeniz E, Falahati A, Kozeschnik E. Thermo-kinetic simulation of the yield strength evolution of AA7075 during natural aging. *Adv Mater Res* 2014;922:406–11. <https://doi.org/10.4028/www.scientific.net/AMR.922.406>.
- [478] Maugis P, Gouné M. Kinetics of vanadium carbonitride precipitation in steel: A computer model. *Acta Mater* 2005;53:3359–67. <https://doi.org/10.1016/j.actamat.2005.03.036>.
- [479] Myhr OR, Grong Ø. Modelling of non-isothermal transformations in alloys containing a particle distribution. *Acta Mater* 2000;48:1605–15. [https://doi.org/10.1016/S1359-6454\(99\)00435-8](https://doi.org/10.1016/S1359-6454(99)00435-8).
- [480] Myhr OR, Grong Ø, Andersen SJ. Modelling of the age hardening behaviour of Al-Mg-Si alloys. *Acta Mater* 2001;49:65–75. [https://doi.org/10.1016/S1359-6454\(00\)00301-3](https://doi.org/10.1016/S1359-6454(00)00301-3).
- [481] Myhr OR, Grong Fjær HG, Marioara CD. Modelling of the microstructure and strength evolution in al-mg-si alloys during multistage thermal processing. *Acta Mater* 2004;52:4997–5008. <https://doi.org/10.1016/j.actamat.2004.07.002>.
- [482] Myhr OR, Grong Ø, Schäfer C. An extended age-hardening model for Al-Mg-Si alloys incorporating the room-temperature storage and cold deformation process stages. *Metall Mater Trans A Phys Metall Mater Sci* 2015;46:6018–39. <https://doi.org/10.1007/s11661-015-3175-y>.
- [483] Myhr OR, Schäfer C, Grong Ø, Engler O, Brinkman HJ, Hirsch J. Modelling the combined effect of room temperature storage and cold deformation on the age-hardening behaviour of Al-Mg-Si alloys-part 1. *Mater Sci Forum* 2014;794–796:670–5. <https://doi.org/10.4028/www.scientific.net/MSF.794-796.670>.
- [484] Myhr OR, Hopperstad OS, Borvik T. A combined precipitation, yield stress, and work hardening model for Al-Mg-Si alloys incorporating the effects of strain rate and temperature. *Metall Mater Trans A Phys Metall Mater Sci* 2018;49:3592–609. <https://doi.org/10.1007/s11661-018-4675-3>.
- [485] Myhr OR, Borvik T, Marioara CD, Wenner S, Hopperstad OS. Nanoscale modelling of combined isotropic and kinematic hardening of 6000 series aluminium alloys. *Mech Mater* 2020;151. <https://doi.org/10.1016/j.mechmat.2020.103603>.
- [486] Schäfer C, Myhr OR, Brinkman HJ, Engler O, Hirsch J. Modelling the combined effect of room temperature storage and cold deformation on the age-hardening behaviour of Al-Mg-Si alloys-part 2. *Mater Sci Forum* 2014;794–796:722–7. <https://doi.org/10.4028/www.scientific.net/MSF.794-796.722>.
- [487] Engler O, Marioara CD, Aruga Y, Koizuka M, Myhr OR. Effect of natural ageing or pre-ageing on the evolution of precipitate structure and strength during age hardening of Al-Mg-Si alloy AA 6016. *Mater Sci Eng A* 2019;759:520–9. <https://doi.org/10.1016/j.msea.2019.05.073>.
- [488] Engler O, Schäfer C, Myhr OR. Effect of natural ageing and pre-straining on strength and anisotropy in aluminium alloy AA 6016. *Mater Sci Eng A* 2015;639:65–74. <https://doi.org/10.1016/j.msea.2015.04.097>.
- [489] Nicolas M, Deschamps A. Characterisation and modelling of precipitate evolution in an Al-Zn-Mg alloy during non-isothermal heat treatments. *Acta Mater* 2003;51:6077–94. [https://doi.org/10.1016/S1359-6454\(03\)00429-4](https://doi.org/10.1016/S1359-6454(03)00429-4).
- [490] Cao W, Zhang F, Chen SL, Zhang C, Chang YA. An integrated computational tool for precipitation simulation. *JOM* 2011;63:29–34. <https://doi.org/10.1007/s11837-011-0106-2>.
- [491] Cao W, Chen SL, Zhang F, Wu K, Yang Y, Chang YA, et al. PANDAT software with PanEngine, PanOptimizer and PanPrecipitation for multi-component phase diagram calculation and materials property simulation. *Calphad Comput Coupling Phase Diagrams Thermochem* 2009;33:328–42. <https://doi.org/10.1016/j.calphad.2008.08.004>.
- [492] Jou H-JJ, Voorhees P, Olson GB. Computer simulations for the prediction of microstructure/property variation in aeroturbine disks. In: Green KA, Pollock TM, Harada H, Howson TE, Reed RC, Schirra JJ, et al., editors. Proc. Int. Symp. Superalloys, TMS (The Minerals, Metals & Materials Society); 2004, p. 877–86. doi: 10.7449/2004/superalloys_2004.877_886.
- [493] Deschamps A, Brechet Y. Influence of predeformation and ageing of an Al-Zn-Mg Alloy-II. Modeling of precipitation kinetics and yield stress. *Acta Mater* 1998;47:293–305. [https://doi.org/10.1016/S1359-6454\(98\)00296-1](https://doi.org/10.1016/S1359-6454(98)00296-1).
- [494] Bardel D, Perez M, Nelias D, Deschamps A, Hutchinson CR, Maisonneuve D, et al. Coupled precipitation and yield strength modelling for non-isothermal treatments of 6061 aluminium alloy. *Acta Mater* 2014;62:129–40. <https://doi.org/10.1016/j.actamat.2013.09.041>.
- [495] Deschamps A, Perez M. Mesoscopic modelling of precipitation: A tool for extracting physical parameters of phase transformations in metallic alloys. *Comptes Rendus Phys* 2010;11:236–44. <https://doi.org/10.1016/j.crhy.2010.07.005>.
- [496] Chen R, Xu Q, Guo H, Xia Z, Wu Q, Liu B. Modeling the precipitation kinetics and tensile properties in Al-7Si-Mg cast aluminum alloys. *Mater Sci Eng A* 2017;685:403–16. <https://doi.org/10.1016/j.msea.2016.12.042>.
- [497] Robson JD, Prangnell PB. Dispersoid precipitation and process modelling in zirconium containing commercial aluminum alloys. *Acta Mater* 2001;49:599–613. [https://doi.org/10.1016/S1359-6454\(00\)00351-7](https://doi.org/10.1016/S1359-6454(00)00351-7).

- [498] Robson JD, Jones MJ, Prangnell PB. Extension of the N-model to predict competing homogeneous and heterogeneous precipitation in Al-Sc alloys. *Acta Mater* 2003;51:1453–68. [https://doi.org/10.1016/S1359-6454\(02\)00540-2](https://doi.org/10.1016/S1359-6454(02)00540-2).
- [499] Robson JD. A new model for prediction of dispersoid precipitation in aluminium alloys containing zirconium and scandium. *Acta Mater* 2004;52:1409–21. <https://doi.org/10.1016/j.actamat.2003.11.023>.
- [500] dos Santos JF, Staron P, Fischer T, Robson JD, Kostka A, Colegrave P, et al. Understanding precipitate evolution during friction stir welding of Al-Zn-Mg-Cu alloy through in-situ measurement coupled with simulation. *Acta Mater* 2018;148:163–72. <https://doi.org/10.1016/j.actamat.2018.01.020>.
- [501] Larráyoz Izcarra X, Guiaro Blank A, Pyczak F, Staron P, Schumann S, Huber N. Characterization and modeling of the influence of artificial aging on the microstructural evolution of age-hardenable AlSi10Mg(Cu) aluminum alloys. *Mater Sci Eng A* 2014;610:46–53. <https://doi.org/10.1016/j.msea.2014.04.031>.
- [502] Kamp N, Sullivan A, Tomasi R, Robson JD. Modelling of heterogeneous precipitate distribution evolution during friction stir welding process. *Acta Mater* 2006;54:2003–14. <https://doi.org/10.1016/j.actamat.2005.12.024>.
- [503] Samaras SN. Modelling of microstructure evolution during precipitation processes: A population balance approach of the KWN model. *Model Simul Mater Sci Eng* 2006;14:1271–92. <https://doi.org/10.1088/0956-0393/14/8/001>.
- [504] Chen Q, Jeppsson J, Ågren J. Analytical treatment of diffusion during precipitate growth in multicomponent systems. *Acta Mater* 2008;56:1890–6. <https://doi.org/10.1016/j.actamat.2007.12.037>.
- [505] Chen Q, Wu K, Sternier G, Mason P. Modeling precipitation kinetics during heat treatment with calphad-based tools. *J Mater Eng Perform* 2014;23:4193–6. <https://doi.org/10.1007/s11665-014-1255-6>.
- [506] Sheng Z, Bonnalet Rolland M, Zhou T, Odqvist J, Hedström P. Langer-Schwartz-Kampmann-Wagner precipitation simulations: assessment of models and materials design application for Cu precipitation in PH stainless steels. *J Mater Sci* 2021;56:2650–71. <https://doi.org/10.1007/s10853-020-05386-9>.
- [507] Deschamps A, Sigli C, Mourey T, De Geuser F, Lefebvre W, Davo B. Experimental and modelling assessment of precipitation kinetics in an Al-Li-Mg alloy. *Acta Mater* 2012;60:1917–28. <https://doi.org/10.1016/j.actamat.2012.01.010>.
- [508] Kozeschnik E, Svoboda J, Fischer FD. Shape factors in modeling of precipitation. *Mater Sci Eng A* 2006;441:68–72. <https://doi.org/10.1016/j.msea.2006.08.088>.
- [509] Ham FS. Theory of diffusion-limited precipitation. *J Phys Chem Solids* 1958;6:335–51. [https://doi.org/10.1016/0022-3697\(58\)90053-2](https://doi.org/10.1016/0022-3697(58)90053-2).
- [510] Ham FS. Diffusion-limited growth of precipitate particles. *J Appl Phys* 1959;30:1518–25. <https://doi.org/10.1063/1.1734993>.
- [511] Wu K, Chen Q, Mason P. Simulation of precipitation kinetics with non-spherical particles. *J Phase Equilibria Diffus* 2018;39:571–83. <https://doi.org/10.1007/s11669-018-0644-1>.
- [512] Horvay G, Cahn JW. Dendritic and spheroidal growth. *Acta Metall* 1961;9:695–705. [https://doi.org/10.1016/0001-6160\(61\)90008-6](https://doi.org/10.1016/0001-6160(61)90008-6).
- [513] Ferrante M, Doherty RD. On the precipitate growth kinetics in aluminium-silver alloys. *Scr Metall* 1976;10:1059–64. [https://doi.org/10.1016/0036-9748\(76\)90025-9](https://doi.org/10.1016/0036-9748(76)90025-9).
- [514] Anjabin N. Modeling the age-hardening process of aluminum alloys containing the prolate/oblate shape precipitates. *Met Mater Int* 2020. <https://doi.org/10.1007/s12540-019-00579-7>.
- [515] Doherty RD, Ferrante M, Chen YH. On the growth kinetics of plate-shaped precipitates. *Scr Metall* 1978;12:885–91. [https://doi.org/10.1016/0036-9748\(78\)90176-X](https://doi.org/10.1016/0036-9748(78)90176-X).
- [516] da Costa Teixeira J, Cram DG, Bourgeois L, Bastow TJ, Hill AJ, Hutchinson CR. On the strengthening response of aluminum alloys containing shear-resistant plate-shaped precipitates. *Acta Mater* 2008;56:6109–22. <https://doi.org/10.1016/j.actamat.2008.08.023>.
- [517] Kim K, Voorhees PW. Ostwald ripening of spheroidal particles in multicomponent alloys. *Acta Mater* 2018;152:327–37. <https://doi.org/10.1016/j.actamat.2018.04.041>.
- [518] Aaronson HI, Enomoto M, Lee JK. Mechanisms of diffusional phase transformations in metals and alloys. CRC Press 2016. <https://doi.org/10.1201/b15829>.
- [519] Steinbach I. Phase-field model for microstructure evolution at the mesoscopic scale. *Annu Rev Mater Res* 2013;43:89–107. <https://doi.org/10.1146/annurev-matsci-071312-121703>.
- [520] Steinbach I. Phase-field models in materials science. *Model Simul Mater Sci Eng* 2009;17:073001. <https://doi.org/10.1088/0956-0393/17/7/073001>.
- [521] Liu H, Nie JF. Phase field simulation of microstructures of Mg and Al alloys. *Mater Sci Technol (United Kingdom)* 2017;33:2159–72. <https://doi.org/10.1080/02670836.2017.1375749>.
- [522] Heo TW, Chen L-QQ. Phase-field modeling of nucleation in solid-state phase transformations. vol. 66. 2014. Doi: 10.1007/s11837-014-1033-9.
- [523] Simmons JP, Shen C, Wang Y. Phase field modeling of simultaneous nucleation and growth by explicitly incorporating nucleation events. *Scr Mater* 2000;43:935–42. [https://doi.org/10.1016/S1359-6462\(00\)00517-0](https://doi.org/10.1016/S1359-6462(00)00517-0).
- [524] Wen YH, Simmons JP, Shen C, Woodward C, Wang Y. Phase-field modeling of bimodal particle size distributions during continuous cooling. *Acta Mater* 2003;51:1123–32. [https://doi.org/10.1016/S1359-6454\(02\)00516-5](https://doi.org/10.1016/S1359-6454(02)00516-5).
- [525] Shen C, Simmons JP, Wang Y. Effect of elastic interaction on nucleation: II. Implementation of strain energy of nucleus formation in the phase field method. *Acta Mater* 2007;55:1457–66. <https://doi.org/10.1016/j.actamat.2006.10.011>.
- [526] Wang Y, Wang H-Y, Chen L-Q, Khachaturyan AG. Microstructural development of coherent tetragonal precipitates in magnesium-partially-stabilized zirconia: a computer simulation. *J Am Ceram Soc* 1995;78:657–61. <https://doi.org/10.1111/j.1151-2916.1995.tb08228.x>.
- [527] Le Bouar Y, Loiseau A, Khachaturyan AG. Origin of chessboard-like structures in decomposing alloys. Theoretical model and computer simulation. *Acta Mater* 1998;46:2777–88. [https://doi.org/10.1016/S1359-6454\(97\)00455-2](https://doi.org/10.1016/S1359-6454(97)00455-2).
- [528] Kim K, Roy A, Gururajan MP, Wolverton C, Voorhees PW. First-principles/Phase-field modeling of θ' precipitation in Al-Cu alloys. *Acta Mater* 2017;140:344–54. <https://doi.org/10.1016/j.actamat.2017.08.046>.
- [529] Shanthraj P, Liu C, Akbarian A, Svendsen B, Raabe D. Multi-component chemo-mechanics based on transport relations for the chemical potential. *Comput Methods Appl Mech Eng* 2020;365:113029. <https://doi.org/10.1016/j.cma.2020.113029>.
- [530] Liu C, Garner A, Zhao H, Prangnell PB, Gault B, Raabe D, et al. CALPHAD-informed phase-field modeling of grain boundary microchemistry and precipitation in Al-Zn-Mg-Cu alloys. *Acta Mater* 2021;214:116966. <https://doi.org/10.1016/j.actamat.2021.116966>.
- [531] Clouet E, Laé L, Épicier T, Lefebvre W, Nastar M, Deschamps A, et al. Complex precipitation pathways in multicomponent alloys. *Nat Mater* 2006;5:482–8. <https://doi.org/10.1038/nmat1652>.
- [532] Zhang X, Sluiter MHF. Cluster expansions for thermodynamics and kinetics of multicomponent alloys. *J Phase Equilibria Diffus* 2016;37:44–52. <https://doi.org/10.1007/s11669-015-0427-x>.
- [533] Müller S, Wolverton C, Wang LW, Zunger A. Predicting the size- and temperature-dependent shapes of precipitates in Al-Zn alloys. *Acta Mater* 2000;48:4007–20. [https://doi.org/10.1016/S1359-6454\(00\)00209-3](https://doi.org/10.1016/S1359-6454(00)00209-3).
- [534] Gorbatov OI, Stroev AY, Gornostyrev YN, Korzhavyi PA. Effective cluster interactions and pre-precipitate morphology in binary Al-based alloys. *Acta Mater* 2019;179:70–84. <https://doi.org/10.1016/j.actamat.2019.08.011>.
- [535] Kleiven D, Ødegård OL, Laasonen K, Akola J. Atomistic simulations of early stage clusters in Al-Mg alloys. *Acta Mater* 2019;166:484–92. <https://doi.org/10.1016/j.actamat.2018.12.050>.
- [536] Clouet E, Barbu A, Laé L, Martin G. Precipitation kinetics of Al₃Zr and Al₃Sc in aluminum alloys modeled with cluster dynamics. *Acta Mater* 2005;53:2313–25. <https://doi.org/10.1016/j.actamat.2005.01.038>.
- [537] Kleiven D, Akola J. Precipitate formation in aluminium alloys: Multi-scale modelling approach. *Acta Mater* 2020;195:123–31. <https://doi.org/10.1016/j.actamat.2020.05.050>.
- [538] Milkereit B, Starink MJ, Rometsch PA, Schick C, Kessler O. Review of the quench sensitivity of aluminium alloys: Analysis of the kinetics and nature of quench-induced precipitation. *Materials (Basel)* 2019;12:4083. <https://doi.org/10.3390/MA12244083>.
- [539] Starink MJ, Zahra AM. Kinetics of isothermal and non-isothermal precipitation in an Al-6 at.% Si alloy. *Philos Mag A Phys Condens Matter. Struct Defects Mech Prop* 1998;77:187–99. <https://doi.org/10.1080/01418619808214237>.

- [540] Schumacher P, Pogatscher S, Starink MJ, Schick C, Mohles V, Milkereit B. Quench-induced precipitates in Al-Si alloys: Calorimetric determination of solute content and characterisation of microstructure. *Thermochim Acta* 2015;602:63–73. <https://doi.org/10.1016/j.tca.2014.12.023>.
- [541] Starink MJ. Analysis of aluminium based alloys by calorimetry: Quantitative analysis of reactions and reaction kinetics. *Int Mater Rev* 2004;49:191–226. <https://doi.org/10.1179/095066004225010532>.
- [542] Bourgeois L, Zhang Y, Zhang Z, Chen Y, Medhekar NV. Transforming solid-state precipitates via excess vacancies. *Nat Commun* 2020;11.. <https://doi.org/10.1038/s41467-020-15087-1>.
- [543] Lay MDH, Zurob HS, Hutchinson CR, Bastow TJ, Hill AJ. Vacancy behavior and solute cluster growth during natural aging of an Al-Mg-Si alloy. *Metall Mater Trans A Phys Metall Mater Sci* 2012;43:4507–13. <https://doi.org/10.1007/s11661-012-1257-7>.
- [544] Yang Z, Banhart J. Natural and artificial ageing in aluminium alloys – the role of excess vacancies. *Acta Mater* 2021;215:117014. <https://doi.org/10.1016/j.actamat.2021.117014>.
- [545] Wernitos M, Antrekowitsch H, Kozeschnik E, Ebner T, Moszner F, Löffler JFF, et al. Ultrafast artificial aging of Al-Mg-Si alloys. *Scr Mater* 2016;112:148–51. <https://doi.org/10.1016/j.scriptamat.2015.09.037>.
- [546] Swiatek R, Zehetbauer M, Mikulowski B. Work hardening by deformation induced vacancies in low temperature deformed aluminium single crystals. *Mater Sci Eng A* 1997;234–236:441–4. [https://doi.org/10.1016/s0921-5093\(97\)00166-4](https://doi.org/10.1016/s0921-5093(97)00166-4).
- [547] Peng J, Bahl S, Shyam A, Haynes JA, Shin D. Solute-vacancy clustering in aluminum. *Acta Mater* 2020;196:747–58. <https://doi.org/10.1016/j.actamat.2020.06.062>.
- [548] Liu M, Klobes B, Maier K. On the age-hardening of an Al-Zn-Mg-Cu alloy: A vacancy perspective. *Scr Mater* 2011;64:21–4. <https://doi.org/10.1016/j.scriptamat.2010.08.054>.
- [549] Hutchinson CR. Modeling the kinetics of precipitation in aluminium alloys. *Fundam Alum Metall Prod Process Appl* 2010:422–67. <https://doi.org/10.1533/9780857090256.2.422>.
- [550] Robson JD. Deformation enhanced diffusion in aluminium alloys. *Metall Mater Trans A Phys Metall Mater Sci* 2020;51:5401–13. <https://doi.org/10.1007/s11661-020-05960-5>.
- [551] Wolverton C. Solute-vacancy binding in aluminum. *Acta Mater* 2007;55:5867–72. <https://doi.org/10.1016/j.actamat.2007.06.039>.
- [552] Noble B. Precipitation in aluminium-copper alloys containing additions of indium and tin. *Met Sci J* 1968;2:117–20. <https://doi.org/10.1179/030634568790443503>.
- [553] Schmid F, Uggowitzer PJ, Schäublin R, Wernitos M, Ebner T, Pogatscher S. Effect of thermal treatments on Sn-alloyed Al-Mg-Si alloys. *Materials (Basel)* 2019;12:1801. <https://doi.org/10.3390/ma12111801>.
- [554] Wernitos M, Antrekowitsch H, Ebner T, Prillhofer R, Uggowitzer PJ, Pogatscher S. Hardening of Al-Mg-Si alloys: Effect of trace elements and prolonged natural aging. *Mater Des* 2016;107:257–68. <https://doi.org/10.1016/j.matdes.2016.06.014>.
- [555] Pogatscher S, Antrekowitsch H, Wernitos M, Moszner F, Gerstl SSAA, Francis MF, et al. Diffusion on demand to control precipitation aging: Application to Al-Mg-Si alloys. *Phys Rev Lett* 2014;112:10–4. <https://doi.org/10.1103/PhysRevLett.112.225701>.
- [556] Zamberger S, Lang P, Klösch G, Klarner J, Kozeschnik E. Long-range diffusion of H in the presence of traps in a microalloyed steel. *Comput Mater Sci* 2016;113:266–74. <https://doi.org/10.1016/j.commatsci.2015.11.014>.
- [557] Fischer FD, Svoboda J, Kozeschnik E. Interstitial diffusion in systems with multiple sorts of traps. *Model Simul Mater Sci Eng* 2013;21:025008. <https://doi.org/10.1088/0965-0393/21/2/025008>.
- [558] Lang P, Povoden-Karadenez E, Mayer W, Falahati A, Kozeschnik E. The bustling nature of vacancies in A1 alloys. In: Marquis F, editor. 8th Pacific Rim Int. Congr. Adv. Mater. Process. 2013, PRICM 8, vol. 4, TMS (The Minerals, Metals & Materials Society); 2013, p. 3181–8. doi: 10.1007/978-3-319-48764-9_392.
- [559] Lang P, Shan YV, Kozeschnik E. The life-time of structural vacancies in the presence of solute trapping. *Mater Sci Forum* 2014;794–796:963–70. <https://doi.org/10.4028/www.scientific.net/MSF.794-796.963>.
- [560] Zurob HS, Seyedrezai H. A model for the growth of solute clusters based on vacancy trapping. *Scr Mater* 2009;61:141–4. <https://doi.org/10.1016/j.scriptamat.2009.03.025>.
- [561] Aruga Y, Kozuka M, Takaki Y, Sato T. Evaluation of solute clusters associated with bake-hardening response in isothermal aged Al-Mg-Si alloys using a three-dimensional atom probe. *Metall Mater Trans A Phys Metall Mater Sci* 2014;45:5906–13. <https://doi.org/10.1007/s11661-014-2548-y>.
- [562] Dumitraschkewitz P, Gerstl SSA, Stephenson LT, Uggowitzer PJ, Pogatscher S. Clustering in age-hardenable aluminum alloys. *Adv Eng Mater* 2018;20. <https://doi.org/10.1002/adem.201800255>.
- [563] Takeuchi S, Argon AS. Glide and climb resistance to the motion of an edge dislocation due to dragging a Cottrell atmosphere. *Philos Mag A Phys Condens Matter, Struct Defects Mech Prop* 1979;40:65–75. <https://doi.org/10.1080/01418617908234833>.
- [564] Kozeschnik E, Buchmayr B. A contribution to the increase in yield strength during the bake hardening process. *Steel Res* 1997;68:224–30. <https://doi.org/10.1002/srin.199701783>.
- [565] Svoboda J, Zickler GA, Kozeschnik E, Fischer FD. Kinetics of interstitial segregation in Cottrell atmospheres and grain boundaries. *Philos Mag Lett* 2015;95:458–65. <https://doi.org/10.1080/09500839.2015.1087652>.
- [566] Cottrell AH, Bilby BA. Dislocation theory of yielding and strain ageing of iron. *Proc Phys Soc Sect A* 1949;62:49–62. <https://doi.org/10.1088/0370-1298/62/1/308>.
- [567] Harper S. Precipitation of carbon and nitrogen in cold-worked alpha-iron. *Phys Rev* 1951;83:709–12. <https://doi.org/10.1103/PhysRev.83.709>.
- [568] Epperly EN, Sills RB. Transient solute drag and strain aging of dislocations. *Acta Mater* 2020;193:182–90. <https://doi.org/10.1016/j.actamat.2020.03.031>.
- [569] Soare MA, Curtin WA. Solute strengthening of both mobile and forest dislocations: The origin of dynamic strain aging in fcc metals. *Acta Mater* 2008;56:4046–61. <https://doi.org/10.1016/j.actamat.2008.04.027>.
- [570] Soare MA, Curtin WA. Single-mechanism rate theory for dynamic strain aging in fcc metals. *Acta Mater* 2008;56:4091–101. <https://doi.org/10.1016/j.actamat.2008.04.030>.
- [571] Klusemann B, Fischer G, Böhle T, Svendsen B. Thermomechanical characterization of Portevin-Le Chatelier bands in AlMg3 (AA5754) and modeling based on a modified Estrin-McCormick approach. *Int J Plast* 2015;67:192–216. <https://doi.org/10.1016/j.ijplas.2014.10.011>.
- [572] Kang J, Mishra RK, Wilkinson DS, Hopperstad OS. Effect of Mg content on Portevin-Le Chatelier band strain in Al-Mg sheet alloys. *Philos Mag Lett* 2012;92:647–55. <https://doi.org/10.1080/09500839.2012.714082>.
- [573] Kreycja J, Kozeschnik E. State parameter-based constitutive modelling of stress strain curves in Al-Mg solid solutions. *Int J Plast* 2018;103:67–80. <https://doi.org/10.1016/j.ijplas.2018.01.001>.
- [574] Kreycja J, Kozeschnik E. Temperature-dependent strain hardening, precipitation and deformation-induced microstructure evolution in AA 6061. *Mater Sci Eng A* 2017;708:411–8. <https://doi.org/10.1016/j.msea.2017.10.027>.
- [575] Kabirian F, Khan AS, Pandey A. Negative to positive strain rate sensitivity in 5xxx series aluminum alloys: Experiment and constitutive modeling. *Int J Plast* 2014;55:232–46. <https://doi.org/10.1016/j.ijplas.2013.11.001>.
- [576] Strobel K, Lay MDH, Easton MA, Sweet L, Zhu S, Parson NC, et al. Effects of quench rate and natural ageing on the age hardening behaviour of aluminium alloy AA6060. *Mater Charact* 2016;111:43–52. <https://doi.org/10.1016/j.matchar.2015.11.009>.
- [577] Madanat M, Liu M, Zhang X, Guo Q, Čížek J, Banhart J, et al. Co-evolution of vacancies and solute clusters during artificial ageing of Al-Mg-Si alloys. *Phys Rev Mater* 2020;4:043608. <https://doi.org/10.1103/PhysRevMaterials.4.043608>.
- [578] Yang Z, Jiang X, Zhang X, Liu M, Liang Z, Leyvraz D, et al. Natural ageing clustering under different quenching conditions in an Al-Mg-Si alloy. *Scr Mater* 2021;190:179–82. <https://doi.org/10.1016/j.scriptamat.2020.08.046>.
- [579] Fischer FD, Svoboda J, Appel F, Kozeschnik E. Modeling of excess vacancy annihilation at different types of sinks. *Acta Mater* 2011;59:3463–72. <https://doi.org/10.1016/j.actamat.2011.02.020>.
- [580] Svoboda J, Shan YV, Kozeschnik E, Fischer FD. Couples and pairs formation - Thermodynamic and kinetic modelling applied to Al-Mg-Si. *Model Simul Mater Sci Eng* 2017;25:065011 (15pp). doi: 10.1088/1361-651X/aa76cf.

- [581] Svoboda J, Shan Y V, Kozeschnik E, Fischer FD. A thermokinetic model for Mg-Si couple formation in Al-Mg-Si alloys. *Model Simul Mater Sci Eng* 2016;24. Doi: 10.1088/0965-0393/24/3/035021.
- [582] Strobel K, Easton MA, Lay MDH, Rometsch PA, Zhu S, Sweet L, et al. Quench sensitivity in a dispersoid-containing Al-Mg-Si alloy. *Metall Mater Trans A Phys Metall Mater Sci* 2019;50:1957–69. <https://doi.org/10.1007/s11661-019-05130-2>.
- [583] Poznak A, Thole V, Sanders P. The natural aging effect on hardenability in Al-Mg-Si: A complex interaction between composition and heat treatment parameters. *Metals (Basel)* 2018;8. Doi: 10.3390/met8050309.
- [584] Diao J, Salazar R, Kelton KF, Gelb LD. Impact of diffusion on concentration profiles around near-critical nuclei and implications for theories of nucleation and growth. *Acta Mater* 2008;56:2585–91. <https://doi.org/10.1016/j.actamat.2008.01.044>.
- [585] Bendo A, Matsuda K, Nishimura K, Numomura N, Tsuchiya T, Lee S, et al. The possible transition mechanism for the meta-stable phase in the 7xxx aluminium. *Mater Sci Technol (United Kingdom)* 2020;36:1621–7. <https://doi.org/10.1080/02670836.2020.1821323>.
- [586] Potyrailo R, Rajan K, Stoeke W, Takeuchi I, Chisholm B, Lam H. Combinatorial and high-throughput screening of materials libraries: Review of state of the art. *ACS Comb Sci* 2011;13:579–633. <https://doi.org/10.1021/co200007w>.
- [587] Green ML, Takeuchi I, Hattrick-Simpers JR. Applications of high throughput (combinatorial) methodologies to electronic, magnetic, optical, and energy-related materials. *J Appl Phys* 2013;113. <https://doi.org/10.1063/1.4803530>.
- [588] Miracle D, Majumdar B, Wertz K, Gorse S. New strategies and tests to accelerate discovery and development of multi-principal element structural alloys. *Scr Mater* 2017;127:195–200. <https://doi.org/10.1016/j.scriptamat.2016.08.001>.
- [589] Miyazaki T. Development of “macroscopic Composition Gradient Method” and its application to the phase transformation. *Prog Mater Sci* 2012;57:1010–60. <https://doi.org/10.1016/j.pmatsci.2011.11.002>.
- [590] Springer H, Raabe D. Rapid alloy prototyping: Compositional and thermo-mechanical high throughput bulk combinatorial design of structural materials based on the example of 30Mn-1.2C-xAl triplex steels. *Acta Mater* 2012;60:4950–9. <https://doi.org/10.1016/j.actamat.2012.05.017>.
- [591] Buenconsejo PJS, Siegel A, Savan A, Thienhaus S, Ludwig A. Preparation of 24 ternary thin film materials libraries on a single substrate in one experiment for irreversible high-throughput studies. *ACS Comb Sci* 2012;14:25–30. <https://doi.org/10.1021/co2001263>.
- [592] Ding S, Liu Y, Li Y, Liu Z, Sohn S, Walker FJ, et al. Combinatorial development of bulk metallic glasses. *Nat Mater* 2014;13:494–500. <https://doi.org/10.1038/nmat3939>.
- [593] Marceau RKW, Qiu C, Ringer SP, Hutchinson CR. A study of the composition dependence of the rapid hardening phenomenon in Al-Cu-Mg alloys using diffusion couples. *Mater Sci Eng A* 2012;546:153–61. <https://doi.org/10.1016/j.msea.2012.03.043>.
- [594] Gumbmann E, De Geuser F, Deschamps A, Lefebvre W, Robaut F, Sigli C. A combinatorial approach for studying the effect of Mg concentration on precipitation in an Al-Cu-Li alloy. *Scr Mater* 2016;110:44–7. <https://doi.org/10.1016/j.scriptamat.2015.07.042>.
- [595] Ivanov R, Deschamps A, De Geuser F. High throughput evaluation of the effect of Mg concentration on natural ageing of Al-Cu-Li-(Mg) alloys. *Scr Mater* 2018;150:156–9. <https://doi.org/10.1016/j.scriptamat.2018.03.024>.
- [596] Yongming L, Wei P, Shiqin L, Ruigang W, Jianqiang L. A novel functionally graded materials in the Ti-Si-C system. *Mater Sci Eng A* 2003;345:99–105. [https://doi.org/10.1016/S0921-5093\(02\)00400-8](https://doi.org/10.1016/S0921-5093(02)00400-8).
- [597] Li Z, Ludwig A, Savan A, Springer H, Raabe D. Combinatorial metallurgical synthesis and processing of high-entropy alloys. *J Mater Res* 2018;33:3156–69. <https://doi.org/10.1557/jmr.2018.214>.
- [598] Han Z, Tian J, Lai Q, Yu X, Li G. Effect of N₂ partial pressure on the microstructure and mechanical properties of magnetron sputtered CrNx films. *Surf Coatings Technol* 2003;162:189–93. [https://doi.org/10.1016/S0257-8972\(02\)00667-9](https://doi.org/10.1016/S0257-8972(02)00667-9).
- [599] Dias L, Trindade B, Coelho C, Patankar S, Draney C, Sam Froes FH. Ti-Mg-Si alloys produced by non-equilibrium processing methods: Mechanical alloying and sputtering. *Mater Sci Eng A* 2004;364:273–80. <https://doi.org/10.1016/j.msea.2003.08.029>.
- [600] Pershin V, Lufitha M, Chandra S, Mostaghimi J. Effect of substrate temperature on adhesion strength of plasma-sprayed nickel coatings. *J Therm Spray Technol* 2003;12:370–6. <https://doi.org/10.1361/105996303770348249>.
- [601] Springer H, Belde M, Raabe D. Bulk combinatorial design of ductile martensitic stainless steels through confined martensite-to-austenite reversion. *Mater Sci Eng A* 2013;582:235–44. <https://doi.org/10.1016/j.msea.2013.06.036>.
- [602] Springer H, Belde M, Raabe D. Combinatorial design of transitory constitution steels: Coupling high strength with inherent formability and weldability through sequenced austenite stability. *Mater Des* 2016;90:1100–9. <https://doi.org/10.1016/j.matdes.2015.11.050>.
- [603] Contreras-Piedras E, Dorantes-Rosales HJ, López-Hirata VM, Hernández Santiago F, González-Velázquez JL, López-Monroy FI. Analysis of precipitation in Fe-rich Fe-Ni-Al alloys by diffusion couples. *Mater Sci Eng A* 2012;558:366–70. <https://doi.org/10.1016/j.msea.2012.08.013>.
- [604] Gregoire JM, Van Campen DG, Miller CE, Jones RJR, Suram SK, Mehta A. High-throughput synchrotron X-ray diffraction for combinatorial phase mapping. *J Synchrotron Radiat* 2014;21:1262–8. <https://doi.org/10.1107/S1600577514016488>.
- [605] Malard B, De Geuser F, Deschamps A. Microstructure distribution in an AA2050 T34 friction stir weld and its evolution during post-welding heat treatment. *Acta Mater* 2015;101:90–100. <https://doi.org/10.1016/j.actamat.2015.08.068>.
- [606] Collins L, Kilpatrick JI, Kalinin SV, Rodriguez BJ. Towards nanoscale electrical measurements in liquid by advanced KPFM techniques: A review. *Reports Prog Phys* 2018;81. <https://doi.org/10.1088/1361-6633/aab560>.
- [607] Fan M, Sliozberg K, La Mantia F, Miyashita N, Nagymási M, Schnitter C, et al. Characterization of Ta-Ti thin films by using a scanning droplet cell in combination with AC linear sweep voltammetry. *ChemElectroChem* 2014;1:903–8. <https://doi.org/10.1002/celc.201300153>.
- [608] Kollender JP, Mardare AI, Hassel AW. Multi-Scanning Droplet Cell Microscopy (multi-SDCM) for truly parallel high throughput electrochemical experimentation. *Electrochim Acta* 2015;179:32–7. <https://doi.org/10.1016/j.electacta.2015.04.103>.
- [609] Herbig M. Spatially correlated electron microscopy and atom probe tomography: Current possibilities and future perspectives. *Scr Mater* 2018;148:98–105. <https://doi.org/10.1016/j.scriptamat.2017.03.017>.
- [610] Liebscher CH, Stoffers A, Alam M, Lymparakis L, Cojocaru-Mirédin O, Gault B, et al. Strain-induced asymmetric line segregation at faceted Si grain boundaries. *Phys Rev Lett* 2018;121:15702. <https://doi.org/10.1103/PhysRevLett.121.015702>.
- [611] Gillott L, Sugden J. Ion trajectories in the field-ion microscope. *J Phys E* 1973;6:1218–20. <https://doi.org/10.1088/0022-3735/6/12/025>.
- [612] Loi ST, Gaul B, Ringer SP, Larson DJ, Geiser BP. Electrostatic simulations of a local electrode atom probe: The dependence of tomographic reconstruction parameters on specimen and microscope geometry. *Ultramicroscopy* 2013;132:107–13. <https://doi.org/10.1016/j.ultramic.2012.12.012>.
- [613] Vurpillot F, Gaul B, Geiser BP, Larson DJ. Reconstructing atom probe data: A review. *Ultramicroscopy* 2013;132:19–30. <https://doi.org/10.1016/j.ultramic.2013.03.010>.
- [614] Larson DJ, Gaul B, Geiser BP, De Geuser F, Vurpillot F. Atom probe tomography spatial reconstruction: Status and directions. *Curr Opin Solid State Mater Sci* 2013;17:236–47. <https://doi.org/10.1016/j.cossms.2013.09.002>.
- [615] Tsong TT. Field ion image formation. *Surf Sci* 1978;70:211–33. [https://doi.org/10.1016/0039-6028\(78\)90410-7](https://doi.org/10.1016/0039-6028(78)90410-7).
- [616] Marquis EA, Vurpillot F. Chromatic aberrations in the field evaporation behavior of small precipitates. *Microsc Microanal* 2008;14:561–70. <https://doi.org/10.1017/S1431927608080793>.
- [617] Ge XJ, Chen NX, Zhang WQ, Zhu FW. Selective field evaporation in field-ion microscopy for ordered alloys. *J Appl Phys* 1999;85:3488–93. <https://doi.org/10.1063/1.369706>.
- [618] Waugh AR, Boyes ED, Southon MJ. Investigations of field evaporation with a field-desorption microscope. *Surf Sci* 1976;61:109–42. [https://doi.org/10.1016/0039-6028\(76\)90411-8](https://doi.org/10.1016/0039-6028(76)90411-8).
- [619] Schmidt WA, Erns N, Suchorski Y. Local electric fields at individual atomic surface sites: field ion appearance energy measurements. *Appl Surf Sci* 1993;67:101–10. [https://doi.org/10.1016/0169-4332\(93\)90300-Z](https://doi.org/10.1016/0169-4332(93)90300-Z).
- [620] Ashton M, Mishra A, Neugebauer J, Freysoldt C. Ab initio description of bond breaking in large electric fields. *Phys Rev Lett* 2020;124:176801. <https://doi.org/10.1103/PhysRevLett.124.176801>.

- [621] Vurpillot F, Bostel A, Blavette D. Trajectory overlaps and local magnification in three-dimensional atom probe. *Appl Phys Lett* 2000;76:3127–9. <https://doi.org/10.1063/1.126545>.
- [622] Miller MK, Hetherington MG. Local magnification effects in the atom probe. *Surf Sci* 1991;246:442–9. [https://doi.org/10.1016/0039-6028\(91\)90449-3](https://doi.org/10.1016/0039-6028(91)90449-3).
- [623] Miller MK. THE EFFECTS OF LOCAL MAGNIFICATION AND TRAJECTORY ABERRATIONS ON ATOM PROBE ANALYSIS. *Le J Phys Colloq* 1987;48:C6-565-C6-570. Doi: 10.1051/jphyscol:1987692.
- [624] Oberdorfer C, Eich SM, Schmitz G. A full-scale simulation approach for atom probe tomography. *Ultramicroscopy* 2013;128:55–67. <https://doi.org/10.1016/j.ultramic.2013.01.005>.
- [625] Tang F, Gault B, Ringer SP, Martin P, Bendavid A, Cairney JM. Microstructural investigation of Ti-Si-N hard coatings. *Scr Mater* 2010;63:192–5. <https://doi.org/10.1016/j.scriptamat.2010.03.050>.
- [626] Gault B, Moody MP, Cairney JM, Ringer SP. Atom probe crystallography. *Mater Today* 2012;15:378–86. [https://doi.org/10.1016/S1369-7021\(12\)70164-5](https://doi.org/10.1016/S1369-7021(12)70164-5).
- [627] Moody MP, Tang F, Gault B, Ringer SP, Cairney JM. Atom probe crystallography: Characterization of grain boundary orientation relationships in nanocrystalline aluminium. *Ultramicroscopy* 2011;111:493–9. <https://doi.org/10.1016/j.ultramic.2010.11.014>.
- [628] Breen AJ, Babinsky K, Day AC, Eder K, Oakman CJ, Trimby PW, et al. Correlating atom probe crystallographic measurements with transmission kikuchi diffraction data. *Microsc Microanal* 2017;23:279–90. <https://doi.org/10.1017/s1431927616012605>.
- [629] Liddicoat PV, Liao XZ, Zhao YH, Zhu YT, Murashkin MY, Lavernia EJ, et al. Nanostructural hierarchy increases the strength of aluminium alloys. *Nat Commun* 2010;1:63. <https://doi.org/10.1038/ncomms1062>.
- [630] Marquis EA, Seidman DN, Asta M, Woodward C. Composition evolution of nanoscale Al3Sc precipitates in an Al-Mg-Sc alloy: Experiments and computations. *Acta Mater* 2006;54:119–30. <https://doi.org/10.1016/j.actamat.2005.08.035>.
- [631] Van Dalen ME, Gyger T, Dunand DC, Seidman DN. Effects of Yb and Zr microalloying additions on the microstructure and mechanical properties of dilute Al-Sc alloys. *Acta Mater* 2011;59:7615–26. <https://doi.org/10.1016/j.actamat.2011.09.019>.
- [632] Edwards GA, Stiller K, Dunlop GL, Couper MJ. The precipitation sequence in Al-Mg-Si alloys. *Acta Mater* 1998;46:3893–904. [https://doi.org/10.1016/S1359-6454\(98\)00059-7](https://doi.org/10.1016/S1359-6454(98)00059-7).
- [633] Stiller K, Warren PJ, Hansen V, Angenete J, Gjønnes J. Investigation of precipitation in an Al-Zn-Mg alloy after two-step ageing treatment at 100° and 150°C. *Mater Sci Eng A* 1999;270:55–63. [https://doi.org/10.1016/S0921-5093\(99\)00231-2](https://doi.org/10.1016/S0921-5093(99)00231-2).
- [634] De Geuser F, Lefebvre W, Blavette D. 3D atom probe investigation of the early stages of precipitation in an Al-Mg-Si alloy. *Proc an Int Conf Solid-Solid Phase Transform Inorg Mater* 2005;1(2005):295–300.
- [635] Dumont M, Lefebvre W, Doisneau-Cottignies B, Deschamps A. Characterisation of the composition and volume fraction of η' and η precipitates in an Al-Zn-Mg alloy by a combination of atom probe, small-angle X-ray scattering and transmission electron microscopy. *Acta Mater* 2005;53:2881–92. <https://doi.org/10.1016/j.actamat.2005.03.004>.
- [636] Ringer SP, Hono K. Microstructural evolution and age hardening in aluminium alloys: atom probe field-ion microscopy and transmission electron microscopy studies. *Mater Charact* 2000;44:101–31. [https://doi.org/10.1016/S1044-5803\(99\)00051-0](https://doi.org/10.1016/S1044-5803(99)00051-0).
- [637] Sha G, Wang YB, Liao XZ, Duan ZC, Ringer SP, Langdon TG. Influence of equal-channel angular pressing on precipitation in an Al-Zn-Mg-Cu alloy. *Acta Mater* 2009;57:3123–32. <https://doi.org/10.1016/j.actamat.2009.03.017>.
- [638] Aruga Y, Nako H. Experimental and theoretical measurements of the evolution of embryos before and during the nucleation stage. *Metall Mater Trans A Phys Metall Mater Sci* 2012;43:1102–8. <https://doi.org/10.1007/s11661-011-0950-2>.
- [639] Marceau RKW, Stephenson LT, Hutchinson CR, Ringer SP. Quantitative atom probe analysis of nanostructure containing clusters and precipitates with multiple length scales. *Ultramicroscopy* 2011;111:738–42. <https://doi.org/10.1016/j.ultramic.2010.12.029>.
- [640] Gault B, de Geuser F, Bourgeois L, Gabble BM, Ringer SP, Muddle BC. Atom probe tomography and transmission electron microscopy characterisation of precipitation in an Al-Cu-Li-Mg-Ag alloy. *Ultramicroscopy* 2011;111:683–9. <https://doi.org/10.1016/j.ultramic.2010.12.004>.
- [641] De Geuser F, Gault B. Metrology of small particles and solute clusters by atom probe tomography. *Acta Mater* 2020;188:406–15. <https://doi.org/10.1016/j.actamat.2020.02.023>.
- [642] Gasnier V, Gault B, Nako H, Aruga Y, Sha G, Ringer SPSP. Influence of experimental parameters on the composition of precipitates in metallic alloys. *Ultramicroscopy* 2013;132:199–204. <https://doi.org/10.1016/j.ultramic.2013.02.005>.
- [643] Blavette D, Vurpillot F, Pareige P, Menand A. A model accounting for spatial overlaps in 3D atom-probe microscopy. *Ultramicroscopy* 2001;89:145–53. [https://doi.org/10.1016/S0304-3991\(01\)00120-6](https://doi.org/10.1016/S0304-3991(01)00120-6).
- [644] Katnagallu SS, Stephenson LT, Mouton I, Freysoldt C, Subramanyam APAPA, Jenke J, et al. Imaging individual solute atoms at crystalline imperfections in metals. *New J Phys* 2019;21:1–18. <https://doi.org/10.1088/1367-2630/ab5cc4>.
- [645] Marceau RKW, Sha G, Lumley RN, Ringer SP. Evolution of solute clustering in Al-Cu-Mg alloys during secondary ageing. *Acta Mater* 2010;58:1795–805. <https://doi.org/10.1016/j.actamat.2009.11.021>.
- [646] Takaki Y, Aruga Y, Kozuka M, Sato T. Effects of pre-aging and natural aging on bake hardening behavior in Al-Mg-Si alloys. *Mater. Sci. Forum*, vol. 794–796, Trans Tech Publications Ltd; 2014, p. 1026–31. Doi: 10.4028/www.scientific.net/MSF.794-796.1026.
- [647] Sha G, Cerezo A. Kinetic Monte Carlo simulation of clustering in an Al-Zn-Mg-Cu alloy (7050). *Acta Mater* 2005;53:907–17. <https://doi.org/10.1016/j.actamat.2004.10.048>.
- [648] Christian JW. The theory of transformations in metals and alloys. Elsevier 2002. <https://doi.org/10.1016/b978-0-08-044019-4.x5000-4>.
- [649] Sudbrack CK, Noebe RD, Seidman DN. Direct observations of nucleation in a nondilute multicomponent alloy. *Phys Rev B - Condens Matter Mater Phys* 2006;73:212101. <https://doi.org/10.1103/PhysRevB.73.212101>.
- [650] De Geuser F, Lefebvre W, Blavette D. 3D atom probe study of solute atoms clustering during natural ageing and pre-ageing of an Al-Mg-Si alloy. *Philos Mag Lett* 2006;86:227–34. <https://doi.org/10.1080/09500830600643270>.
- [651] Zhao H, Gault B, Ponge D, Raabe D, De Geuser F. Parameter free quantitative analysis of atom probe data by correlation functions: Application to the precipitation in Al-Zn-Mg-Cu. *Scr Mater* 2018;154:106–10. <https://doi.org/10.1016/j.scriptamat.2018.05.024>.
- [652] Kühbach M, Bajaj P, Zhao H, Celik MH, Jägle EA, Gault B. On strong-scaling and open-source tools for analyzing atom probe tomography data. *Npj Comput Mater* 2021;7:1–10. <https://doi.org/10.1038/s41524-020-00486-1>.
- [653] Marquis EA, Seidman DN, Asta M, Woodward C, Ozolins V. Mg segregation at [formula presented] heterophase interfaces on an atomic scale: experiments and computations. *Phys Rev Lett* 2003;91. <https://doi.org/10.1103/PhysRevLett.91.036101>.
- [654] Keutgen J, London AJ, Cojocaru-Mirédin O. Solving peak overlaps for proximity histogram analysis of complex interfaces for atom probe tomography data. *Microsc Microanal* 2020;1–8. <https://doi.org/10.1017/S1431927620024800>.
- [655] Hellman OC, Vandenbroucke JA, Rüsing J, Isheim D, Seidman DN. Analysis of three-dimensional atom-probe data by the proximity histogram. *Microsc Microanal* 2000;6:437–44. <https://doi.org/10.1007/s100050010051>.
- [656] Rüsing J, Sebastian JT, Hellman OC, Seidman DN. Three-dimensional investigation of ceramic/metal heterophase interfaces by atom-probe microscopy. *Microsc Microanal* 2000;6:445–51. <https://doi.org/10.1007/s100050010050>.
- [657] Serizawa A, Miller MK. Radius dependence of solute concentration estimates of simulated ultrafine precipitates. *Microsc Res Tech* 2013;76:1196–203. <https://doi.org/10.1002/jemt.22285>.
- [658] Jägle EA, Choi P-PP, Raabe D. The maximum separation cluster analysis algorithm for atom-probe tomography: Parameter determination and accuracy. *Microsc Microanal* 2014;20:1662–71. <https://doi.org/10.1017/S1431927614013294>.
- [659] Pareige-Schmuck C, Soisson F, Blavette D. Ordering and phase separation in low supersaturated Ni-Cr-Al alloys: 3D atom probe and Monte Carlo simulation. *Mater Sci Eng A* 1998;250:99–103. [https://doi.org/10.1016/S0921-5093\(98\)00543-7](https://doi.org/10.1016/S0921-5093(98)00543-7).
- [660] Mao Z, Sudbrack CK, Yoo KE, Martin G, Seidman DN. The mechanism of morphogenesis in a phase-separating concentrated multicomponent alloy. *Nat Mater* 2007;6:210–6. <https://doi.org/10.1038/nmat1845>.

- [661] Prakash A, Guénolé J, Wang J, Müller J, Spiecker E, Mills MJ, et al. Atom probe informed simulations of dislocation-precipitate interactions reveal the importance of local interface curvature. *Acta Mater* 2015;92:33–45. <https://doi.org/10.1016/j.actamat.2015.03.050>.
- [662] Kirchmayer A, Lyu H, Pröbstle M, Houillé F, Förner A, Huenert D, et al. Combining experiments and atom probe tomography-informed simulations on γ' precipitation strengthening in the polycrystalline Ni-base superalloy A718Plus. *Adv Eng Mater* 2020;22:2000149. <https://doi.org/10.1002/adem.202000149>.
- [663] Dey P, Nazarov R, Dutta B, Yao M, Herbig M, Friák M, et al. Ab initio explanation of disorder and off-stoichiometry in Fe-Mn-Al-C k carbides. *Phys Rev B* 2017;95:104108. <https://doi.org/10.1103/PhysRevB.95.104108>.
- [664] Yao MJ, Dey P, Seol JB, Choi P, Herbig M, Marceau RKW, et al. Combined atom probe tomography and density functional theory investigation of the Al off-stoichiometry of κ -carbides in an austenitic Fe-Mn-Al-C low density steel. *Acta Mater* 2016;106:229–38. <https://doi.org/10.1016/j.actamat.2016.01.007>.
- [665] Gault B, Cui XY, Moody MP, De Geuser F, Sigli C, Ringer SP, et al. Atom probe microscopy investigation of Mg site occupancy within δ' precipitates in an Al-Mg-Li alloy. *Scr Mater* 2012;66:903–6. <https://doi.org/10.1016/j.scriptamat.2012.02.021>.
- [666] Moody MP, Ceguerra AV, Breen AJ, Cui XY, Gault B, Stephenson LT, et al. Atomically resolved tomography to directly inform simulations for structure-property relationships. *Nat Commun* 2014;5:1–10. <https://doi.org/10.1038/ncomms6501>.
- [667] Gault B, Cui XY, Moody MP, Ceguerra AV, Breen AJ, Marceau RKW, et al. A nexus between 3D atomistic data hybrids derived from atom probe microscopy and computational materials science: A new analysis of solute clustering in Al-alloys. *Scr Mater* 2017;131:93–7. <https://doi.org/10.1016/j.scriptamat.2017.01.011>.
- [668] Cui XY, Ringer SP. On the nexus between atom probe microscopy and density functional theory simulations. *Mater Charact* 2018;146:347–58. <https://doi.org/10.1016/j.matchar.2018.05.015>.
- [669] Liu L, Cui XY, Jiang JT, Zhang B, Nomoto K, Zhen L, et al. Segregation of the major alloying elements to Al₃(Sc, Zr) precipitates in an Al-Zn-Mg-Cu-Sc-Zr alloy. *Mater Charact* 2019;157:109898. <https://doi.org/10.1016/j.matchar.2019.109898>.
- [670] Plotnikov EY, Mao Z, Nobe RD, Seidman DN. Temporal evolution of the γ (fcc)/ γ (L1₂) interfacial width in binary Ni-Al alloys. *Scr Mater* 2014;70:51–4. <https://doi.org/10.1016/j.scriptamat.2013.09.016>.
- [671] Mao Z, Booth-Morrison C, Sudbrack CK, Martin G, Seidman DN. Kinetic pathways for phase separation: An atomic-scale study in Ni-Al-Cr alloys. *Acta Mater* 2012;60:1871–88. <https://doi.org/10.1016/j.actamat.2011.10.046>.
- [672] Plotnikov EY, Mao Z, Il Baik S, Yıldırım M, Li Y, Cecchetti D, et al. A correlative four-dimensional study of phase-separation at the subnanoscale to nanoscale of a Ni-Al alloy. *Acta Mater* 2019;171:306–33. <https://doi.org/10.1016/j.actamat.2019.03.016>.
- [673] Philippe T, Voorhees PW. Ostwald ripening in multicomponent alloys. *Acta Mater* 2013;61:4237–44. <https://doi.org/10.1016/j.actamat.2013.03.049>.
- [674] Wagner C. Theorie der Alterung Niederschlägen durch Umlosen. *Zeitschrift Für Electrochem* 1961;65:581–91. <https://doi.org/10.1002/BBPC.19610650704>.
- [675] Ardell AJ, Bellor P. Radiation-induced solute segregation in metallic alloys. vol. 20. 2016. Doi: 10.1016/j.cossms.2015.11.001.
- [676] Marquis EA, Seidman DN. Nanostructural evolution of Al₃ Sc precipitates in an Al-Sc-Mg alloy by three-dimensional atom probe microscopy. *Surf Interface Anal* 2004;36:559–63. <https://doi.org/10.1002/sia.1699>.
- [677] Seidman DN, Marquis EA, Dunand DC. Precipitation strengthening at ambient and elevated temperatures of heat-treatable Al(Sc) alloys. *Acta Mater* 2002;50:4021–35. [https://doi.org/10.1016/S1359-6454\(02\)00201-X](https://doi.org/10.1016/S1359-6454(02)00201-X).
- [678] Marquis EA, Seidman DN. Nanoscale structural evolution of Al₃Sc precipitates in Al(Sc) alloys. *Acta Mater* 2001;49:1909–19. [https://doi.org/10.1016/S1359-6454\(01\)00116-1](https://doi.org/10.1016/S1359-6454(01)00116-1).
- [679] Fuller CB, Seidman DN, Dunand DC. Mechanical properties of Al(Sc, Zr) alloys at ambient and elevated temperatures. *Acta Mater* 2003;51:4803–14. [https://doi.org/10.1016/S1359-6454\(03\)00320-3](https://doi.org/10.1016/S1359-6454(03)00320-3).
- [680] Fuller CB, Murray JL, Seidman DN. Temporal evolution of the nanostructure of Al(Sc,Zr) alloys: Part i - Chemical compositions of Al₃(Sc_{1-x}Zr_x) precipitates. *Acta Mater* 2005;53:5401–13. Doi: 10.1016/j.actamat.2005.08.016.
- [681] Monachon C, Dunand DC, Seidman DN. Atomic-scale characterization of aluminum-based multishell nanoparticles created by solid-state synthesis. *Small* 2010;6:1728–31. <https://doi.org/10.1002/smll.201000325>.
- [682] Monachon C, Krug ME, Seidman DN, Dunand DC. Chemistry and structure of core-double-shell nanoscale precipitates in Al-6.5Li-0.07Sc-0.02Yb (at.%). *Acta Mater* 2011;59:3398–409. <https://doi.org/10.1016/j.actamat.2011.02.015>.
- [683] Clouet E, Nastar M, Sigli C. Nucleation of Al₃Zr and Al₃Sc in aluminum alloys: From kinetic Monte Carlo simulations to classical theory. *Phys Rev B - Condens Matter Mater Phys* 2004;69:064109. <https://doi.org/10.1103/PhysRevB.69.064109>.
- [684] Clouet E, Hin C, Gendt D, Nastar M, Soisson F. Kinetic Monte Carlo simulations of precipitation. *Adv Eng Mater*, vol. 8, John Wiley & Sons, Ltd; 2006, p. 1210–4. Doi: 10.1002/adem.200600183.
- [685] Clouet E, Barbu A. Using cluster dynamics to model electrical resistivity measurements in precipitating AlSc alloys. *Acta Mater* 2007;55:391–400. <https://doi.org/10.1016/j.actamat.2006.08.021>.
- [686] Hawkes P, Spence J. Springer Handbook of Microscopy. vol. 108. Cham: Springer International Publishing; 2019. Doi: 10.1007/978-3-030-00069-1.
- [687] Sugawara E, Nikaido H. Properties of AdeABC and AdeJK efflux systems of *Acinetobacter baumannii* compared with those of the AcrAB-ToIC system of *Escherichia coli*. *Antimicrob Agents Chemother* 2014;58:7250–7. <https://doi.org/10.1128/AAC.03728-14>.
- [688] Erni R. Aberration-Corrected imaging in transmission electron microscopy: An Introduction. Imperial College Press; 2010. Doi: 10.1142/P703.
- [689] Rosalie JM, Bourgeois L, Muddle BC. Precipitate assemblies formed on dislocation loops in aluminium-silver- copper alloys. *Philos Mag* 2009;89:2195–211. <https://doi.org/10.1080/14786430903066959>.
- [690] Rosalie JM, Bourgeois L. Silver segregation to 0' (Al₂Cu)-Al interfaces in Al-Cu-Ag alloys. *Acta Mater* 2012;60:6033–41. <https://doi.org/10.1016/j.actamat.2012.07.039>.
- [691] Nie JF, Wilson NC, Zhu YM, Xu Z. Solute clusters and GP zones in binary Mg-RE alloys. *Acta Mater* 2016;106:260–71. <https://doi.org/10.1016/j.actamat.2015.12.047>.
- [692] Saito T, Mörtzell EA, Wenner S, Marioara CD, Andersen SJ, Friis J, et al. Atomic structures of precipitates in Al-Mg-Si alloys with small additions of other elements. *Adv Eng Mater* 2018;20:1800125. <https://doi.org/10.1002/adem.201800125>.
- [693] Kang SJ, Kim YW, Kim M, Zuo JM. Determination of interfacial atomic structure, misfits and energetics of Ω phase in Al-Cu-Mg-Ag alloy. *Acta Mater* 2014;81:501–11. <https://doi.org/10.1016/j.actamat.2014.07.074>.
- [694] Nie JF, Zhu YM, Liu JZ, Fang XY. Periodic segregation of solute atoms in fully coherent twin boundaries. *Science* (80-) 2013;340:957–60. <https://doi.org/10.1126/science.1229369>.
- [695] Nguyen DT, Findlay SD, Etheridge J. A menu of electron probes for optimising information from scanning transmission electron microscopy. *Ultramicroscopy* 2018;184:143–55. <https://doi.org/10.1016/j.ultramic.2017.08.020>.
- [696] Findlay SD, Kohno Y, Cardamone LA, Ikuhara Y, Shibata N. Enhanced light element imaging in atomic resolution scanning transmission electron microscopy. *Ultramicroscopy* 2014;136:31–41. <https://doi.org/10.1016/j.ultramic.2013.07.019>.
- [697] Zhu Y, Withers RL, Bourgeois L, Dwyer C, Etheridge J. Direct mapping of Li-enabled octahedral tilt ordering and associated strain in nanostructured perovskites. *Nat Mater* 2015;14:1142–9. <https://doi.org/10.1038/nmat4390>.
- [698] Ophus C. Four-Dimensional Scanning Transmission Electron Microscopy (4D-STEM): From Scanning Nanodiffraction to Ptychography and Beyond. *Microsc Microanal* 2019;25:563–82. <https://doi.org/10.1017/S1431927619000497>.
- [699] Lebeau JM, Findlay SD, Allen LJ, Stemmer S. Standardless atom counting in scanning transmission electron microscopy. *Nano Lett* 2010;10:4405–8. <https://doi.org/10.1021/nl102025s>.
- [700] Wenner S, Jones L, Marioara CD, Holmestad R. Atomic-resolution chemical mapping of ordered precipitates in Al alloys using energy-dispersive X-ray spectroscopy. *Micron* 2017;96:103–11. <https://doi.org/10.1016/j.micron.2017.02.007>.
- [701] Zhao X, Chen H, Wilson N, Liu Q, Nie JF. Direct observation and impact of co-segregated atoms in magnesium having multiple alloying elements. *Nat Commun* 2019;10:1–7. <https://doi.org/10.1038/s41467-019-10921-7>.

- [702] Zaluzec NJ. Improving the sensitivity of X-ray microanalysis in the analytical electron microscope. *Ultramicroscopy* 2019;203:163–9. <https://doi.org/10.1016/j.ultramic.2018.11.008>.
- [703] Spurgeon SR, Du Y, Chambers SA. Measurement error in atomic-scale scanning transmission electron microscopy-energy-dispersive X-ray spectroscopy (STEM-EDS) mapping of a model oxide interface. *Microsc Microanal* 2017;23:513–7. <https://doi.org/10.1017/S1431927617000368>.
- [704] Yan Y, Qiu Y, Gharbi O, Birbilis N, Nakashima PNH. Characterisation of Li in the surface film of a corrosion resistant Mg-Li(-Al-Y-Zr) alloy. *Appl Surf Sci* 2019;494:1066–71. <https://doi.org/10.1016/j.apsusc.2019.07.167>.
- [705] Wenner S, Marioara CD, Ramasse QM, Kepaptsoglou DM, Hage FS, Holmestad R. Atomic-resolution electron energy loss studies of precipitates in an Al-Mg-Si-Cu-Ag alloy. *Scr Mater* 2014;74:92–5. <https://doi.org/10.1016/j.scriptamat.2013.11.007>.
- [706] Li J, An Z, Hage FS, Wang H, Xie P, Jin S, et al. Solute clustering and precipitation in an Al-Cu-Mg-Ag-Si model alloy. *Mater Sci Eng A* 2019;760:366–76. <https://doi.org/10.1016/j.msea.2019.06.021>.
- [707] Rossell MD, Ramasse QM, Findlay SD, Rechberger F, Erni R, Niederberger M. Direct imaging of dopant clustering in metal-oxide nanoparticles. *ACS Nano* 2012;6:7077–83. <https://doi.org/10.1021/nn3021212>.
- [708] Ramasse QM, Seaboume CR, Kepaptsoglou DM, Zan R, Bangert U, Scott AJ. Probing the bonding and electronic structure of single atom dopants in graphene with electron energy loss spectroscopy. *Nano Lett* 2012;13:4989–95. <https://doi.org/10.1021/nl304187e>.
- [709] Midgley PA, Weyland M. 3D electron microscopy in the physical sciences: The development of Z-contrast and EFTEM tomography. *Ultramicroscopy*, vol. 96, Elsevier; 2003. p. 413–31. Doi: 10.1016/S0304-3991(03)00105-0.
- [710] Xiong X, Weyland M. Microstructural characterization of an Al-Li-Mg-Cu alloy by correlative electron tomography and atom probe tomography. *Microsc Microanal* 2014;20:1022–8. <https://doi.org/10.1017/S1431927614000798>.
- [711] Van Aert S, Batenberg KJ, Rossell MD, Erni R, Van Tendeloo G. Three-dimensional atomic imaging of crystalline nanoparticles. *Nature* 2011;470:374–7. <https://doi.org/10.1038/nature09741>.
- [712] Lebeau JM, Findlay SD, Allen LJ, Stemmer S. Position Averaged Convergent Beam Electron Diffraction 2021. <https://doi.org/10.1017/S1431927609096743>.
- [713] Zuo JM. Electron nanodiffraction. Springer Handbooks, Springer; 2019, p. 905–69. Doi: 10.1007/978-3-030-00069-1_18.
- [714] Zhu Y, Nakashima PNH, Funston AM, Bourgeois L, Etheridge J. Topologically enclosed aluminum voids as plasmonic nanostructures. *ACS Nano* 2017;11:11383–92. <https://doi.org/10.1021/acsnano.7b05944>.
- [715] Sunde JK, Johnstone DN, Wenner S, van Helvoort ATJ, Midgley PA, Holmestad R. Crystallographic relationships of T-/S-phase aggregates in an Al-Cu-Mg-Ag alloy. *Acta Mater* 2019;166:587–96. <https://doi.org/10.1016/j.actamat.2018.12.036>.
- [716] Poon I, Marceau RKW, Xia J, Liao XZ, Ringer SP. Precipitation processes in Al-Cu-Mg-Sn and Al-Cu-Mg-Sn-Ag. *Mater Des* 2016;96:385–91. <https://doi.org/10.1016/j.matdes.2016.02.048>.
- [717] Money AI, Zandbergen MW, Cerezo A, Smith GDW. The effect of pre-ageing and addition of copper on the precipitation behaviour in Al-Mg-Si alloys. *Mater. Sci. Forum*, vol. 519–521, Trans Tech Publications Ltd; 2006, p. 543–8. Doi: 10.4028/www.scientific.net/msf.519-521.543.
- [718] Beeri O, Dunand DC, Seidman DN. Roles of impurities on precipitation kinetics of dilute Al-Sc alloys. *Mater Sci Eng A* 2010;527:3501–9. <https://doi.org/10.1016/j.msea.2010.02.027>.
- [719] Poplawsky JD, Milligan BK, Allard LF, Shin D, Shower P, Chisholm MF, et al. The synergistic role of Mn and Zr/Ti in producing $\theta'/\text{L}12$ co-precipitates in Al-Cu alloys. *Acta Mater* 2020;194:577–86. <https://doi.org/10.1016/j.actamat.2020.05.043>.
- [720] Tang F, Gianola DS, Moody MP, Hemker KJ, Cairney JM. Observations of grain boundary impurities in nanocrystalline Al and their influence on microstructural stability and mechanical behaviour. *Acta Mater* 2012;60:1038–47. <https://doi.org/10.1016/j.actamat.2011.10.061>.
- [721] Barrirero J, Engstler M, Mücklich F. Atom probe analysis of Sr distribution in alsi foundry alloys. *Miner Met Mater Ser*, Springer International Publishing 2016: 291–6. https://doi.org/10.1007/978-3-319-65136-1_50.
- [722] Hartshorne MI, Isheim D, Seidman DN, Taheri ML. Specimen preparation for correlating transmission electron microscopy and atom probe tomography of mesoscale features. *Ultramicroscopy* 2014;147:25–32. <https://doi.org/10.1016/j.ultramic.2014.05.005>.
- [723] Benson BA, Hoagland RG. Crack growth behavior of a high strength aluminum alloy during LME by gallium. *Scr Metall* 1989;23:1943–8. [https://doi.org/10.1016/0036-9748\(89\)90487-0](https://doi.org/10.1016/0036-9748(89)90487-0).
- [724] Fisher K, Marquis E. Comparing Plasma-FIB and Ga-FIB Preparation of Atom Probe Tomography Samples. *Microsc Microanal* 2016;22:692–3. <https://doi.org/10.1017/s1431927616004311>.
- [725] Liliensten L, Gault B. New approach for FIB-preparation of atom probe specimens for aluminum alloys. *PLoS One* 2020;15. <https://doi.org/10.1371/journal.pone.0231179>.
- [726] Chang Y, Lu W, Guénolé J, Stephenson LT, Szczepaniak A, Kontis P, et al. Ti and its alloys as examples of cryogenic focused ion beam milling of environmentally-sensitive materials. *Nat Commun* 2019;10. <https://doi.org/10.1038/s41467-019-10875-7>.
- [727] Zhao H, De Geuser F, Kwiatkowski da Silva A, Szczepaniak A, Gault B, Ponge D, et al. Segregation assisted grain boundary precipitation in a model Al-Zn-Mg-Cu alloy. *Acta Mater* 2018;156:318–29. <https://doi.org/10.1016/j.actamat.2018.07.003>.
- [728] Zhao H, Huber L, Lu W, Peter NJ, An D, De Geuser F, et al. Interplay of chemistry and faceting at grain boundaries in a model Al alloy. *Phys Rev Lett* 2020;124. <https://doi.org/10.1103/PhysRevLett.124.106102>.
- [729] Garner A, Euesden R, Yao A, Aboura Y, Zhao H, Donoghue J, et al. Multiscale analysis of grain boundary microstructure in high strength 7xxx Al alloys. *Acta Mater* 2020. <https://doi.org/10.1016/j.actamat.2020.10.021>.
- [730] Spurgeon SR, Ophus C, Jones L, Petford-Long A, Kalinin SV, Olszta MJ, et al. Towards data-driven next-generation transmission electron microscopy. *Nat Mater* 2020;1–6. <https://doi.org/10.1038/s41563-020-00833-z>.
- [731] Basak CB, Meduri A, Hari Babu N. Influence of Ni in high Fe containing recyclable Al-Si cast alloys. *Mater Des* 2019;182:108017. <https://doi.org/10.1016/j.matdes.2019.108017>.
- [732] Kim YS, Park IJ, An BS, Park JG, Yang CW, Lee YH, et al. Improvement of corrosion penetration resistance for aluminum heat exchanger by alloying zirconium. *Mater Chem Phys* 2020;241:122275. <https://doi.org/10.1016/j.matchemphys.2019.122275>.
- [733] Pogatscher S, Antrekowitsch H, Leitner H, Sologubenko AS, Uggowitzer PJ. Influence of the thermal route on the peak-aged microstructures in an Al-Mg-Si aluminum alloy. *Scr Mater* 2013;68:158–61. <https://doi.org/10.1016/j.scriptamat.2012.10.006>.
- [734] Pogatscher S, Kozeschnik E, Antrekowitsch H, Werinos M, Gerstl SSA, Löffler JF, et al. Process-controlled suppression of natural aging in an Al-Mg-Si alloy. *Scr Mater* 2014;89:53–6. <https://doi.org/10.1016/j.scriptamat.2014.06.025>.
- [735] Pogatscher S, Antrekowitsch H, Uggowitzer PJ. Interdependent effect of chemical composition and thermal history on artificial aging of AA6061. *Acta Mater* 2012;60:5545–54. <https://doi.org/10.1016/j.actamat.2012.06.061>.
- [736] Marceau RKW, Sha G, Ferragut R, Dupasquier A, Ringer SP. Solute clustering in Al-Cu-Mg alloys during the early stages of elevated temperature ageing. *Acta Mater* 2010;58:4923–39. <https://doi.org/10.1016/j.actamat.2010.05.020>.
- [737] Sha G, Cerezo A. Early-stage precipitation in Al-Zn-Mg-Cu alloy (7050). *Acta Mater* 2004;52:4503–16. <https://doi.org/10.1016/j.actamat.2004.06.025>.
- [738] Zandbergen MW, Cerezo A, Smith GDW. Study of precipitation in Al-Mg-Si Alloys by atom probe tomography II. Influence of Cu additions. *Acta Mater* 2015;101:149–58. <https://doi.org/10.1016/j.actamat.2015.08.018>.
- [739] Lefebvre W, Danoix F, Hallem H, Forbord B, Bostel A, Marthinsen K. Precipitation kinetic of Al₃(Sc, Zr) dispersoids in aluminium. *J Alloys Compd* 2009;470: 107–10. <https://doi.org/10.1016/j.jallcom.2008.02.043>.
- [740] Porod G. General Theory Int Geophys 1967;10:3–16. [https://doi.org/10.1016/S0074-6142\(08\)60078-9](https://doi.org/10.1016/S0074-6142(08)60078-9).
- [741] Guinier A, Fournet G. Small-angle scattering of X-rays. Wiley; 1955.
- [742] Pedersen JS. Small-angle scattering from precipitates: Analysis by use of a polydisperse hard-sphere model. *Phys Rev B* 1993;47:657–65. <https://doi.org/10.1103/PhysRevB.47.657>.
- [743] Pedersen JS. Analysis of small-angle scattering data from colloids and polymer solutions: Modeling and least-squares fitting. *Adv Colloid Interface Sci* 1997;70: 171–210. [https://doi.org/10.1016/S0001-8686\(97\)00312-6](https://doi.org/10.1016/S0001-8686(97)00312-6).

- [744] Abis S, Boeuf A, Caciuffo R, Fiorini P, Magnani M, Melone S, et al. Investigation of Mg₂Si precipitation in an Al-Mg-Si alloy by small angle neutron scattering. *J Nucl Mater* 1985;135:181–9. [https://doi.org/10.1016/0022-3115\(85\)90076-5](https://doi.org/10.1016/0022-3115(85)90076-5).
- [745] Donnadieu P, Carsughi F, Redjaiimia A, Diot C, Lapasset G. Nanoscale hardening precipitation in AlMgSi alloys: a transmission electron microscopy and small-angle neutron scattering study. *J Appl Crystallogr* 1998;31:212–22. <https://doi.org/10.1107/S002188989701011X>.
- [746] Chang CST, De Geuser F, Banhart J. In situ characterization of β'' precipitation in an Al-Mg-Si alloy by anisotropic small-angle neutron scattering on a single crystal. *J Appl Crystallogr* 2015;48:455–63. <https://doi.org/10.1107/S1600576715002770>.
- [747] Guinier A. Structure of age-hardened aluminium-copper alloys [2]. *Nature* 1938;142:569–70. <https://doi.org/10.1038/142569b0>.
- [748] Tsao CS, Huang EW, Wen MH, Kuo TY, Jeng SL, Jeng US, et al. Phase transformation and precipitation of an Al-Cu alloy during non-isothermal heating studied by in situ small-angle and wide-angle scattering. *J Alloys Compd* 2013;579:138–46. <https://doi.org/10.1016/j.jallcom.2013.04.201>.
- [749] Deschamps A, Bréchet Y, Livet F. Influence of copper addition on precipitation kinetics and hardening in Al-Zn-Mg alloy. *Mater Sci Technol* 1999;15:993–1000. <https://doi.org/10.1179/026708399101506832>.
- [750] Kenesel P, Horváth G, Bernstorff S, Ungár T, Lendvai J. Early stages of nucleation and growth of Guinier-Preston zones in Al-Zn-Mg and Al-Zn-Mg-Cu alloys. *Int J Mater Res* 2006;97:315–20.
- [751] Kabisch O, Drubek G, Löfller H, Brümmer O, Gerlach K. Precipitation and dissolution processes in age-hardenable Al Alloys — A comparison of positron annihilation and X-ray small-angle scattering investigations. II. AlZn(4.5 at%)-Mg(x) (x = 0, 0.2, 1, and 2.5 at%). *Phys Status Solidi* 1980;59:731–42. doi:10.1002/pssa.2210590240.
- [752] Deschamps A, Livet F, Bréchet Y. Influence of predeformation on ageing in an Al-Zn-Mg alloy-I. Microstructure evolution and mechanical properties. *Acta Mater* 1998;47:281–92. [https://doi.org/10.1016/S1359-6454\(98\)00293-6](https://doi.org/10.1016/S1359-6454(98)00293-6).
- [753] Schloth P, Wagner JN, Fife JL, Menzel A, Drezet JM, Van Swygenhoven H. Early precipitation during cooling of an Al-Zn-Mg-Cu alloy revealed by in situ small angle X-ray scattering. *Appl Phys Lett* 2014;105:101908. <https://doi.org/10.1063/1.4894768>.
- [754] Zhang Y, Pelliccia D, Milkereit B, Kirby N, Starink MJ, Rometsch PA. Analysis of age hardening precipitates of Al-Zn-Mg-Cu alloys in a wide range of quenching rates using small angle X-ray scattering. *Mater Des* 2018;142:259–67. <https://doi.org/10.1016/j.matedes.2018.01.037>.
- [755] Marlaud T, Deschamps A, Bley F, Lefebvre W, Baroux B. Evolution of precipitate microstructures during the retrogression and re-ageing heat treatment of an Al-Zn-Mg-Cu alloy. *Acta Mater* 2010;58:4814–26. <https://doi.org/10.1016/j.actamat.2010.05.017>.
- [756] Deschamps A, De Geuser F, Horita Z, Lee S, Renou G. Precipitation kinetics in a severely plastically deformed 7075 aluminium alloy. *Acta Mater* 2014;66:105–17. <https://doi.org/10.1016/j.actamat.2013.11.071>.
- [757] Nicolas M, Deschamps A. Precipitate microstructures and resulting properties of Al-Zn-Mg metal inert gas-weld heat-affected zones. *Metall Mater Trans A Phys Metall Mater Sci* A 2004;35. <https://doi.org/10.1007/s11661-004-0252-z>.
- [758] Deschamps A, Ringeval S, Texier G, Delfaut-Durut L. Quantitative characterization of the microstructure of an electron-beam welded medium strength Al-Zn-Mg alloy. *Mater Sci Eng A* 2009;517:361–8. <https://doi.org/10.1016/j.msea.2009.03.088>.
- [759] Puydt Q, Flouriot S, Ringeval S, De Geuser F, Parry G, Deschamps A. Relationship between microstructure, strength, and fracture in an Al-Zn-Mg electron beam weld: Part I: microstructure characterization. *Metall Mater Trans A Phys Metall Mater Sci* 2014;45:6129–40. <https://doi.org/10.1007/s11661-014-2566-9>.
- [760] Dumont M, Steuwer A, Deschamps A, Peil M, Withers PJ. Microstructure mapping in friction stir welds of 7449 aluminium alloy using SAXS. *Acta Mater* 2006;54:4793–801. <https://doi.org/10.1016/j.actamat.2006.06.015>.
- [761] Fribourg G, Deschamps A, Bréchet Y, Mylonas G, Labbeas G, Heckenberger U, et al. Microstructure modifications induced by a laser surface treatment in an AA7449 aluminium alloy. *Mater Sci Eng A* 2011;528:2736–47. <https://doi.org/10.1016/j.msea.2010.12.018>.
- [762] Dorin T, Deschamps A, De Geuser F, Sigli C. Quantification and modelling of the microstructure/strength relationship by tailoring the morphological parameters of the T1 phase in an Al-Cu-Li alloy. *Acta Mater* 2014;75:134–46. <https://doi.org/10.1016/j.actamat.2014.04.046>.
- [763] De Geuser F, Bley F, Deschamps A. A new method for evaluating the size of plate-like precipitates by small-angle scattering. *J Appl Crystallogr* 2012;45:1208–18. <https://doi.org/10.1107/S0021889812039891>.
- [764] Steuwer A, Dumont M, Altenkirch J, Birocsa S, Deschamps A, Prangnell PB, et al. A combined approach to microstructure mapping of an Al-Li AA2199 friction stir weld. *Acta Mater* 2011;59:3002–11. <https://doi.org/10.1016/j.actamat.2011.01.040>.
- [765] Avettand-Fenoël MN, De Geuser F, Deschamps A. Effect of the ageing on precipitation spatial distribution in stationary shoulder friction stir welded AA2050 alloys. *Mater Charact* 2019;154:193–9. <https://doi.org/10.1016/j.matchar.2019.06.006>.
- [766] De Geuser F, Malard B, Deschamps A. Microstructure mapping of a friction stir welded AA2050 Al-Li-Cu in the T8 state. *Philos Mag* 2014;94:1451–62. <https://doi.org/10.1080/14786435.2014.887862>.
- [767] Jochum T, Günther J-U, Bohling C. Material analysis in fast industrial processes by LIBS. *PhotonicsViews* 2019;16:56–9. <https://doi.org/10.1002/phvs.20190004>.
- [768] Auer M, Oßwald K, Volz R, Woidasky J. Artificial intelligence-based process for metal identification. resource efficient scrap sorting. *Ind Life Cycle Manag* 2019;135–44. <https://doi.org/10.5771/9783957103451-135>.
- [769] Campanella B, Grifoni E, Legnaioli S, Lorenzetti G, Pagnotta S, Sorrentino F, et al. Classification of wrought aluminum alloys by ANN evaluation of LIBS spectra from aluminum scrap samples. *Spectrochim Acta - Part B At Spectrosc* 2017;134:52–7. <https://doi.org/10.1016/j.sab.2017.06.003>.
- [770] Masood Chaudry U, Hamad K, Abuhamd T. Machine learning-aided design of aluminum alloys with high performance. *Mater Today Commun* 2020. <https://doi.org/10.1016/j.mtcomm.2020.101897>.
- [771] Vahid A, Rana S, Gupta S, Vellanki P, Venkatesh S, Dorin T. New Bayesian-Optimization-Based Design of High-Strength 7xxx-Series Alloys from Recycled Aluminum. *JOM* 2018. <https://doi.org/10.1007/s11837-018-2984-z>.
- [772] Cao X, Zhang Y, Chen H. Predicting mechanical properties and corrosion resistance of heat-treated 7N01 aluminum alloy by machine learning methods. *IOP Conf. Ser. Mater. Sci. Eng.*, vol. 774, 2020. doi:10.1088/1757-899X/774/1/012030.
- [773] Ampazis N, Alexopoulos ND. Prediction of aircraft aluminum alloys tensile mechanical properties degradation using Support Vector Machines. *Lect. Notes Comput. Sci. (including Subser. Lect. Notes Artif. Intell. Lect. Notes Bioinformatics)*, vol. 6040 LNAI, 2010, p. 9–18. doi:10.1007/978-3-642-12842-4-5.
- [774] Tamura R, Watanabe M, Mamiya H, Washio K, Yano M, Danno K, et al. Materials informatics approach to understand aluminum alloys. *Sci Technol Adv Mater* 2020. <https://doi.org/10.1080/14686996.2020.1791676>.
- [775] Li J, Zhang Y, Cao X, Zeng Q, Zhuang Y, Qian X, et al. Accelerated discovery of high-strength aluminum alloys by machine learning. *Commun Mater* 2020;1:1–10. <https://doi.org/10.1038/s43246-020-00074-2>.
- [776] Galvão TLP, Novell-Leruth G, Kuznetsova A, Tedim J, Gomes JRB. Elucidating structure-property relationships in aluminum alloy corrosion inhibitors by machine learning. *J Phys Chem C* 2020;124:5624–35. <https://doi.org/10.1021/acs.jpcc.9b09538>.
- [777] Devi MA, Prakash CPS, Chinnannavar RP, Joshi VP, Palada RS, Dixit R. An informatic approach to predict the mechanical properties of aluminum alloys using machine learning techniques. *Proc - Int Conf Smart Electron Commun ICOSEC 2020* 2020;536–41. <https://doi.org/10.1109/ICOSEC49089.2020.9215277>.
- [778] Wang J, Yousefzadi Nobakht A, Blanks JD, Shin D, Lee S, Shyam A, et al. Machine learning for thermal transport analysis of aluminum alloys with precipitate morphology. *Adv Theory Simulations* 2019;2. doi:10.1002/adts.201800196.
- [779] Fernández M, Rezaei S, Rezaei Mianroodi J, Fritzen F, Reese S. Application of artificial neural networks for the prediction of interface mechanics: a study on grain boundary constitutive behavior. *Adv Model Simul Eng Sci* 2020;7:1–27. <https://doi.org/10.1186/s40323-019-0138-7>.
- [780] Balos S, Rajnovic D, Šidjanin L, Janjatovic P, Dramicanin M, Howard D. Cast alloys for reciprocating engine heads-performance evaluation. *Proc - Int Conf Mach Learn Data Eng iCMLDE 2018*, 2019;121–7. <https://doi.org/10.1109/iCMLDE.2018.00030>.
- [781] Narla LM, Rao SV. Identification of metals and alloys using color CCD images of laser-induced breakdown emissions coupled with machine learning. *Appl Phys B Lasers Opt* 2020;126.. <https://doi.org/10.1007/s00340-020-07469-6>.
- [782] Mishra A. Machine learning approach for defects identification in dissimilar friction stir welded aluminium alloys AA 7075-AA 1100 joints. *J Aircr Spacecr Technol* 2020;4:88–95. <https://doi.org/10.3844/jastp.2020.88.95>.

- [783] Zhi L, Zhu Y, Wang H, Xu Z, Man Z. A recurrent neural network for modeling crack growth of aluminium alloy. *Neural Comput Appl* 2016;27:197–203. <https://doi.org/10.1007/s00521-014-1712-z>.
- [784] Chheda AM, Nazro L, Sen FG, Hegadekatte V. Prediction of forming limit diagrams using machine learning. *IOP Conf. Ser. Mater. Sci. Eng.*, vol. 651, 2019. doi: 10.1088/1757-899X/651/1/012107.
- [785] DeCost BL, Jain H, Rollett AD, Holm EA. Computer vision and machine learning for autonomous characterization of AM powder feedstocks. *JOM* 2017;69:456–65. <https://doi.org/10.1007/s11837-016-2226-1>.
- [786] Kolokas N, Vafeiadis T, Ioannidis D, Tzovaras D. Anomaly detection in aluminium production with unsupervised machine learning classifiers. *IEEE Int Symp Innov Intel Syst Appl INISTA 2019 - Proc* 2019. <https://doi.org/10.1109/INISTA.2019.8778419>.
- [787] Kevorkian V, Sustar T, Lesjak I, Degiampietro M, Langus J. Optical emission spectrometry (oes) data-driven inspection of inclusions in wrought aluminium alloys. *Miner Met Mater Sci* 2019;967–72. https://doi.org/10.1007/978-3-030-05864-7_118.
- [788] Muhammad W, Brahme AP, Ibragimova O, Kang J, Inal K. A machine learning framework to predict local strain distribution and the evolution of plastic anisotropy & fracture in additively manufactured alloys. *Int J Plast* 2021;136:1–38. <https://doi.org/10.1016/j.ijplas.2020.102867>.
- [789] Shen H, Yang WD, Liang H, Yao GC. Research advance in harmful effects and removal of impurity Fe from Al and Al alloys. *Adv Mater Res* 2011;295–297:751–9. <https://doi.org/10.4028/www.scientific.net/AMR.295-297.751>.
- [790] Hess JB. PHYSICAL METALLURGY OF RECYCLING WROUGHT ALUMINUM ALLOYS. *Metall Trans A, Phys Metall Mater Sci* 1983;14 A:323–7. doi: 10.1007/bf02644210.
- [791] Dewan MA, Rhamdhani MA, Mitchell JB, Davidson CJ, Brooks GA, Easton M, et al. Control and removal of impurities from Al melts: A review. *Mater Sci Forum* 2011;693:149–60. <https://doi.org/10.4028/www.scientific.net/MSF.693.149>.
- [792] Saravanakumar P, Bhoopashram J, Kavin Prasath M, Jaycharan M. Role of salt fluxes in aluminium refining: a review. *Int J Latest Eng Manag Res* 2017;2:45–51.
- [793] Rabah MA. Preparation of aluminium-magnesium alloys and some valuable salts from used beverage cans. *Waste Manag* 2003;23:173–82. [https://doi.org/10.1016/S0956-053X\(02\)00152-6](https://doi.org/10.1016/S0956-053X(02)00152-6).
- [794] Soares Tenório JA, Espinosa DCR. Recycling of Aluminum. In: Totten GE, MacKenzie DS, editors. *Encycl. Alum. Its Alloy.*, vol. 2, New York: Marcel Dekker, Inc.; 2019, p. 115–54. doi: 10.1201/9781351045636-140000433.
- [795] Andersen SJ, Marioara CD, Friis J, Wenner S, Holmestad R. Precipitates in aluminium alloys. *Adv Phys X* 2018;3:790–814. <https://doi.org/10.1080/23746149.2018.1479984>.
- [796] Ma P, Zhan L, Liu C, Wang Q, Li H, Liu D, et al. Pre-strain-dependent natural ageing and its effect on subsequent artificial ageing of an Al-Cu-Li alloy. *J Alloys Compd* 2019;790:8–19. <https://doi.org/10.1016/j.jallcom.2019.03.072>.
- [797] Gayle FW, Goodway M. Precipitation hardening in the first aerospace aluminum alloy: The Wright Flyer crankcase. *Science (80-)* 1994;266:1015–7. <https://doi.org/10.1126/science.266.5187.1015>.
- [798] Zandbergen HW, Andersen SJ, Jansen J. Structure determination of Mg₅Si₆-particles in Al by dynamic electron diffraction studies. *Science (80-)* 1997;277:1221–5. <https://doi.org/10.1126/science.277.5330.1221>.
- [799] Marioara CD, Lefebvre W, Andersen SJ, Friis J. Atomic structure of hardening precipitates in an Al-Mg-Zn-Cu alloy determined by HAADF-STEM and first-principles calculations: Relation to η -MgZn₂. *J Mater Sci* 2013;48:3638–51. <https://doi.org/10.1007/s10853-013-7158-3>.
- [800] Liu C, Malladi SK, Xu Q, Chen J, Tichelaar FD, Zhuge X, et al. In-situ STEM imaging of growth and phase change of individual CuAl\ltimesX\gtimes precipitates in Al alloy. *Sci Rep* 2017;7. <https://doi.org/10.1038/s41598-017-02081-9>.
- [801] Dwyer C, Weyland M, Chang LY, Muddle BC. Combined electron beam imaging and ab initio modeling of T1 precipitates in Al-Li-Cu alloys. *Appl Phys Lett* 2011;98. <https://doi.org/10.1063/1.3590171>.
- [802] Ravi C, Wolverton C. First-principles study of crystal structure and stability of Al-Mg-Si-(Cu) precipitates. *Acta Mater* 2004;52:4213–27. <https://doi.org/10.1016/j.actamat.2004.05.037>.
- [803] Vissers R, van Huis MA, Jansen J, Zandbergen HW, Marioara CD, Andersen SJ. The crystal structure of the β' phase in Al-Mg-Si alloys. *Acta Mater* 2007;55:3815–23. <https://doi.org/10.1016/j.actamat.2007.02.032>.
- [804] Andersen SJ, Marioara CD, Vissers R, Frøseth A, Zandbergen HW. The structural relation between precipitates in Al-Mg-Si alloys, the Al-matrix and diamond silicon, with emphasis on the trigonal phase U1-MgAl₂Si₂. *Mater Sci Eng A* 2007;444:157–69. <https://doi.org/10.1016/j.msea.2006.08.084>.
- [805] Andersen SJ, Marioara CD, Frøseth A, Vissers R, Zandbergen HW. Crystal structure of the orthorhombic U2-Al4Mg₄Si₄ precipitate in the Al-Mg-Si alloy system and its relation to the β' and β'' phases. *Mater Sci Eng A* 2005;390:127–38. <https://doi.org/10.1016/j.msea.2004.09.019>.
- [806] Matsuda K, Sakaguchi Y, Miyata Y, Uetani Y, Sato T, Kamio A, et al. Precipitation sequence of various kinds of metastable phases in Al-1.0mass% Mg₂Si-0.4mass% Si alloy. *J Mater Sci* 2000;35:179–89. <https://doi.org/10.1023/A:1004769305736>.
- [807] Dumolt SD, Laughlin DE, Williams JC. Formation of a modified β' phase in aluminum alloy 6061. *Scr Metall* 1984;18:1347–50. [https://doi.org/10.1016/0036-9748\(84\)90362-4](https://doi.org/10.1016/0036-9748(84)90362-4).
- [808] Chakrabarti DJ, Laughlin DE. Phase relations and precipitation in Al-Mg-Si alloys with Cu additions. *Prog Mater Sci* 2004;49:389–410. [https://doi.org/10.1016/S0079-6425\(03\)00031-8](https://doi.org/10.1016/S0079-6425(03)00031-8).
- [809] Ding L, Jia Z, Nie JF, Weng Y, Cao L, Chen H, et al. The structural and compositional evolution of precipitates in Al-Mg-Si-Cu alloy. *Acta Mater* 2018;145:437–50. <https://doi.org/10.1016/j.actamat.2017.12.036>.
- [810] Wolverton C. Crystal structure and stability of complex precipitate phases in Al-Cu-Mg-(Si) and Al-Zn-Mg alloys. *Acta Mater* 2001;49:3129–42. [https://doi.org/10.1016/S1359-6454\(01\)00229-4](https://doi.org/10.1016/S1359-6454(01)00229-4).
- [811] Chen K, Liu C, Yang J, Ma P, Zhan L, Huang M, et al. Stabilizing Al-Mg-Si-Cu alloy by precipitation nano-phase control. *Mater Sci Eng A* 2020;769:138513. <https://doi.org/10.1016/j.msea.2019.138513>.
- [812] Liu C, Ma Z, Ma P, Zhan L, Huang M. Multiple precipitation reactions and formation of θ' -phase in a pre-deformed Al-Cu alloy. *Mater Sci Eng A* 2018;733:28–38. <https://doi.org/10.1016/j.msea.2018.07.039>.
- [813] Gerold V. On the structures of Guinier-Preston zones in Al-Cu alloys introductory paper. *Scr Metall* 1988;22:927–32. [https://doi.org/10.1016/S0036-9748\(88\)80077-2](https://doi.org/10.1016/S0036-9748(88)80077-2).
- [814] Ma P, Liu C, Ma Z, Zhan L, Huang M. Formation of a new intermediate phase and its evolution toward θ' during aging of pre-deformed Al-Cu alloys. *J Mater Sci Technol* 2019;35:885–90. <https://doi.org/10.1016/j.jmst.2018.11.022>.
- [815] Silcock JM, Heal TJ. The θ' structure in aluminium-copper alloys. *Acta Crystallogr* 1956;9. <https://doi.org/10.1107/s0365110x56001820>.
- [816] Bourgeois L, Dwyer C, Weyland M, Nie JF, Muddle BC. Structure and energetics of the coherent interface between the θ' precipitate phase and aluminium in Al-Cu. *Acta Mater* 2011;59:7043–50. <https://doi.org/10.1016/j.actamat.2011.07.059>.
- [817] Meetsma A, De Boer JL, Van Smaalen S. Refinement of the crystal structure of tetragonal Al₂Cu. *J Solid State Chem* 1989;83:370–2. [https://doi.org/10.1016/0022-4596\(89\)90188-6](https://doi.org/10.1016/0022-4596(89)90188-6).
- [818] Pang X, Yang W, Yang J, Pang M, Zhan Y. Atomic structure, stability and electronic properties of S(Al₂CuMg)/Al interface: A first-principles study. *Intermetallics* 2018;93:329–37. <https://doi.org/10.1016/j.intermet.2017.10.014>.
- [819] Auld JH, Vietz JT, Polmear IJ. T-phase precipitation induced by the addition of silver to an aluminium-copper-magnesium alloy [4]. *Nature* 1966;209:703–4. <https://doi.org/10.1038/209703a0>.
- [820] Kang SJ, Kim TH, Yang CW, Lee JI, Park ES, Noh TW, et al. Atomic structure and growth mechanism of T1 precipitate in Al-Cu-Li-Mg-Ag alloy. *Scr Mater* 2015;109:68–71. <https://doi.org/10.1016/j.scriptamat.2015.07.020>.
- [821] Kovarik L, Court SA, Fraser HL, Mills MJ. GPB zones and composite GPB/GPBI zones in Al-Cu-Mg alloys. *Acta Mater* 2008;56:4804–15. <https://doi.org/10.1016/j.actamat.2008.05.042>.
- [822] Bendo A, Matsuda K, Lee S, Nishimura K, Nunomura N, Toda H, et al. Atomic scale HAADF-STEM study of η' and η phases in peak-aged Al-Zn-Mg alloys. *J Mater Sci* 2018;53:4598–611. <https://doi.org/10.1007/s10853-017-1873-0>.

- [823] Cao F, Zheng J, Jiang Y, Chen B, Wang Y, Hu T. Experimental and DFT characterization of η' nano-phase and its interfaces in Al–Zn–Mg–Cu alloys. *Acta Mater* 2019;164:207–19. <https://doi.org/10.1016/j.actamat.2018.10.045>.
- [824] Liu CH, Lai YX, Chen JH, Tao GH, Liu LM, Ma PP, et al. Natural-aging-induced reversal of the precipitation pathways in an Al–Mg–Si alloy. *Scr Mater* 2016;115:150–4. <https://doi.org/10.1016/j.scriptamat.2015.12.027>.
- [825] Yin MJ, Chen JH, Liu CH. Effect of interrupted ageing on mechanical property and microstructure of AA2024 alloy. *Zhongguo Youse Jinshu Xuebao/Chinese J Nonferrous Met* 2015;25:3271–81. <https://doi.org/10.19476/j.yxsb.1004.0609.2015.12.003>.
- [826] Liu Y, Han X, Wang S, Wei B, Li W. Subtle atomistic processes of S-phase formation in Al–Cu–Mg alloys. *J Alloys Compd* 2020;838:155677. <https://doi.org/10.1016/j.jallcom.2020.155677>.
- [827] Chung TF, Yang YL, Shiojiri M, Hsiao CN, Li WC, Tsao CS, et al. An atomic scale structural investigation of nanometre-sized η precipitates in the 7050 aluminium alloy. *Acta Mater* 2019;174:351–68. <https://doi.org/10.1016/j.actamat.2019.05.041>.
- [828] Ma P, Liu C, Chen Q, Wang Q, Zhan L, Li J. Natural-ageing-enhanced precipitation near grain boundaries in high-strength aluminum alloy. *J Mater Sci Technol* 2020;46:107–13. <https://doi.org/10.1016/j.jmst.2019.11.035>.
- [829] Chung TF, Kawasaki M, Wang P, Nishio K, Shiojiri M, Li WC, et al. Atomic-resolution energy dispersive X-ray spectroscopy mapping of η precipitates in an Al–Mg–Zn–Cu alloy. *Mater Charact* 2020;166:110448. <https://doi.org/10.1016/j.matchar.2020.110448>.
- [830] Akhtar N, Ahmed R, Arfan M, Ali MN. Mechanical performance and fracture behavior of recycled AA6061-T6 alloy melted from aluminium chips. *Int J Manuf Mater Mech Eng* 2017;7:1–17. <https://doi.org/10.4018/IJMMME.20170101>.
- [831] Saito T, Wenner S, Osmundsen E, Marioara CD, Andersen SJ, Røyset J, et al. The effect of Zn on precipitation in Al–Mg–Si alloys. *Philos Mag* 2014;94:2410–25. <https://doi.org/10.1080/14786435.2014.913819>.
- [832] Liu C, Ma P, Zhan L, Huang M, Li J. Solute Sn-induced formation of composite β'/β'' precipitates in Al–Mg–Si alloy. *Scr Mater* 2018;155:68–72. <https://doi.org/10.1016/j.scriptamat.2018.06.028>.
- [833] Weng Y, Ding L, Zhang Z, Jia Z, Wen B, Liu Y, et al. Effect of Ag addition on the precipitation evolution and interfacial segregation for Al–Mg–Si alloy. *Acta Mater* 2019;180:301–16. <https://doi.org/10.1016/j.actamat.2019.09.015>.
- [834] Qian F, Zhao D, Mørtsell EA, Jin S, Wang J, Marioara CD, et al. Enhanced nucleation and precipitation hardening in Al–Mg–Si(–Cu) alloys with minor Cd additions. *Mater Sci Eng A* 2020;792:139698. <https://doi.org/10.1016/j.msea.2020.139698>.
- [835] Matsuda K, Taniguchi S, Kido K, Uetani Y, Ikeno S. Effects of Cu and transition metals on the precipitation behaviors of metastable phases at 523 K in Al–Mg–Si alloys. *Mater Trans* 2002;43:2789–95. <https://doi.org/10.2320/matertrans.43.2789>.
- [836] Wenner S, Marioara CD, Andersen SJ, Holmestad R. How calcium prevents precipitation hardening in Al–Mg–Si alloys. *Mater Sci Eng A* 2013;575:241–7. <https://doi.org/10.1016/j.msea.2013.03.067>.
- [837] Biswas A, Siegel DJ, Wolverton C, Seidman DN. Precipitates in Al–Cu alloys revisited: Atom-probe tomographic experiments and first-principles calculations of compositional evolution and interfacial segregation. *Acta Mater* 2011;59:6187–204. <https://doi.org/10.1016/j.actamat.2011.06.036>.
- [838] Dai S, Bian Z, Wu W, Tao J, Cai L, Wang M, et al. The role of Sn element on the deformation mechanism and precipitation behavior of the Al–Cu–Mg alloy. *Mater Sci Eng A* 2020;792:139838. <https://doi.org/10.1016/j.msea.2020.139838>.
- [839] Feng L, Sun YM, Zhao XL, Wang RM, Zhang K, Yang JY. Existing form and harmful effects of sodium in Al–4.5%Cu alloy. *Trans Nonferrous Met Soc China (English Ed)* 2015;25:3553–9. [https://doi.org/10.1016/S1003-6326\(15\)63998-X](https://doi.org/10.1016/S1003-6326(15)63998-X).
- [840] Xu R, Lin B, Li H yu, Xiao H qiang, Zhao Y liang, Zhang W wen. Microstructure evolution and mechanical properties of Al–6.5Cu–0.6Mn–0.5Fe alloys with different Si additions. *Trans Nonferrous Met Soc China (English Ed)* 2019;29:1583–91. Doi: 10.1016/S1003-6326(19)65065-X.
- [841] Zheng Y, Liu Y, Wilson N, Liu S, Zhao X, Chen H, et al. Solute segregation induced sandwich structure in Al–Cu(–Au) alloys. *Acta Mater* 2020;184:17–29. <https://doi.org/10.1016/j.actamat.2019.11.011>.
- [842] Liu L, Chen JH, Wang SB, Liu CH, Yang SS, Wu CL. The effect of Si on precipitation in Al–Cu–Mg alloy with a high Cu/Mg ratio. *Mater Sci Eng A* 2014;606:187–95. <https://doi.org/10.1016/j.msea.2014.03.079>.
- [843] Feidlander IN, Tkachenko EA, Parkhomenko NA, Matveets EN. The effect of microalloying on the structure and properties of Al–Zn–Mg–Cu alloys. *Met Sci Heat Treat* 1986;28:285–90. <https://doi.org/10.1007/BF00707659>.
- [844] Cui S, Jung I-HH. Thermodynamic analysis of the recycling of aircraft AL alloys. In: Zhang et. al. L, editor. Miner. Met. Mater. Ser., Springer, Cham; 2017, p. 259–66. Doi: 10.1007/978-3-319-52192-3_25.
- [845] Sato T, Ogura T. Nanocluster Formation Behavior in Al–Zn–Mg Alloys with Microalloying Elements and Improved Mechanical Properties. In: Weiland H. Cassada W.A. RAD, editor. ICAIA13 Pittsburgh, Pittsburgh: Springer, Cham.; 2012, p. 1051–6. Doi: 10.1007/978-3-319-48761-8_157.
- [846] Hirosawa S, Nakamura F, Sato T. First-principles calculation of interaction energies between solutes and/or vacancies for predicting atomistic behaviors of microalloying elements in aluminum alloys. *Mater Sci Forum* 2007;561–565:283–6. <https://doi.org/10.4028/www.scientific.net/msf.561-565.283>.
- [847] Zhu Q, Cao L, Wu X, Zou Y, Couper MJ. Effect of Ag on age-hardening response of Al–Zn–Mg–Cu alloys. *Mater Sci Eng A* 2019;754:265–8. <https://doi.org/10.1016/j.msea.2019.03.090>.
- [848] Wu X, Zhang H, Ma Z, Tao T, Gui J, Song W, et al. Interactions between Fe-rich intermetallics and Mg–Si phase in Al–7Si–xMg alloys. *J Alloys Compd* 2019;786:205–14. <https://doi.org/10.1016/j.jallcom.2019.01.352>.
- [849] Yang H, Watson D, Wang Y, Ji S. Effect of nickel on the microstructure and mechanical property of die-cast Al–Mg–Si–Mn alloy. *J Mater Sci* 2014;49:8412–22. <https://doi.org/10.1007/s10853-014-8551-2>.
- [850] Stadler F, Antrekowitsch H, Fragner W, Kaufmann H, Pinatet ER, Uggowitzer PJ. The effect of main alloying elements on the physical properties of Al–Si foundry alloys. *Mater Sci Eng A* 2013;560:481–91. <https://doi.org/10.1016/j.msea.2012.09.093>.
- [851] Meng L, Zheng XL. Overview of the effects of impurities and rare earth elements in Al–Li alloys. *Mater Sci Eng A* 1997;237:109–18. [https://doi.org/10.1016/S0921-5093\(97\)00096-8](https://doi.org/10.1016/S0921-5093(97)00096-8).
- [852] Sato T, Hirosawa S, Hirose K, Maeguchi T. Roles of microalloying elements on the cluster formation in the initial stage of phase decomposition of Al-based alloys. *Metall Mater Trans A Phys Metall Mater Sci* 2003;34:2745–55. <https://doi.org/10.1007/s11661-003-0176-z>.
- [853] Wenner S, Marioara CD, Andersen SJ, Ervik M, Holmestad R. A hybrid aluminium alloy and its zoo of interacting nano-precipitates. *Mater Charact* 2015;106:226–31. <https://doi.org/10.1016/j.matchar.2015.06.002>.
- [854] Wenner S, Friis J, Marioara CD, Holmestad R. Precipitation in a mixed Al–Cu–Mg/Al–Zn–Mg alloy system. *J Alloys Compd* 2016;684:195–200. <https://doi.org/10.1016/j.jallcom.2016.05.132>.
- [855] Buchanan K, Colas K, Ribis J, Lopez A, Garnier J. Analysis of the metastable precipitates in peak-hardness aged Al–Mg–Si(–Cu) alloys with differing Si contents. *Acta Mater* 2017;132:209–21. <https://doi.org/10.1016/j.actamat.2017.04.037>.
- [856] Gazizov M, Marioara CD, Friis J, Wenner S, Holmestad R, Kaibyshev R. Unique hybrid precipitate structures forming in an Al–Cu–Mg–Si alloy. *J Alloys Compd* 2020;826:153977. <https://doi.org/10.1016/j.jallcom.2020.153977>.
- [857] Weng Y, Jia Z, Ding L, Du K, Duan H, Liu Q, et al. Special segregation of Cu on the habit plane of lath-like β' and QP2 precipitates in Al–Mg–Si–Cu alloys. *Scr Mater* 2018;151:33–7. <https://doi.org/10.1016/j.scriptamat.2018.03.032>.
- [858] Bobel A, Kim K, Wolverton C, Walker M, Olson GB. Equilibrium composition variation of Q-phase precipitates in aluminum alloys. *Acta Mater* 2017;138:150–60. <https://doi.org/10.1016/j.actamat.2017.07.048>.
- [859] Guo MX, Li GJ, Zhang YD, Shi G, Zhang JS, Zhuang LZ, et al. Influence of Zn on the distribution and composition of heterogeneous solute-rich features in peak aged Al–Mg–Si–Cu alloys. *Scr Mater* 2019;159:5–8. <https://doi.org/10.1016/j.scriptamat.2018.09.004>.
- [860] Saito T, Ehlers FJH, Lefebvre W, Hernandez-Maldonado D, Bjørge R, Marioara CD, et al. HAADF-STEM and DFT investigations of the Zn-containing β'' phase in Al–Mg–Si alloys. *Acta Mater* 2014;78:245–53. <https://doi.org/10.1016/j.actamat.2014.06.055>.
- [861] Guo MX, Zhang YD, Li GJ, Jin SB, Sha G, Zhang JS, et al. Solute clustering in Al–Mg–Si–Cu(–Zn) alloys during aging. *J Alloys Compd* 2019;774:347–63. <https://doi.org/10.1016/j.jallcom.2018.09.309>.

- [862] Guo MX, Sha G, Cao LY, Liu WQ, Zhang JS, Zhuang LZ. Enhanced bake-hardening response of an Al-Mg-Si-Cu alloy with Zn addition. *Mater Chem Phys* 2015;162:15–9. <https://doi.org/10.1016/j.matchemphys.2015.07.033>.
- [863] Marlaud T, Deschamps A, Bley F, Lefebvre W, Baroux B. Influence of alloy composition and heat treatment on precipitate composition in Al-Zn-Mg-Cu alloys. *Acta Mater* 2010;58:248–60. <https://doi.org/10.1016/j.actamat.2009.09.003>.
- [864] Gao T, Bian Y, Hu K, Zhao K, Zhang W, Liu X. Structural and morphological evolution of Fe-rich phases in Al-xMg-6Si-4Fe alloys. *Results Mater* 2019;3:100036. <https://doi.org/10.1016/j.rimma.2019.100036>.
- [865] Fan C, Long SY, De Yang H, Wang XJ, Zhang JC. Influence of Ce and Mn addition on α -Fe morphology in recycled Al-Si alloy ingots. *Int J Miner Metall Mater* 2013;20:890–5. <https://doi.org/10.1007/s12613-013-0811-7>.
- [866] Wan B, Chen W, Liu L, Cao X, Zhou L, Fu Z. Effect of trace yttrium addition on the microstructure and tensile properties of recycled Al-7Si-0.3Mg-1.0Fe casting alloys. *Mater Sci Eng A* 2016;666:165–75. <https://doi.org/10.1016/j.msea.2016.04.036>.
- [867] Zhang Z, Li G, Chen XG. Effect of nickel and vanadium on iron bearing intermetallic phases in AA 5657 simulated DC castings. *Mater Sci Technol (United Kingdom)* 2014;30:951–61. <https://doi.org/10.1179/1743284713Y.0000000376>.
- [868] Shi ZM, Gao K, Shi YT, Wang Y. Microstructure and mechanical properties of rare-earth-modified Al-1Fe binary alloys. *Mater Sci Eng A* 2015;632:62–71. <https://doi.org/10.1016/j.msea.2015.02.068>.
- [869] Robles Hernandez FC, Herrera Ramírez JM, Mackay R, Robles Hernandez FC, Herrera Ramírez JM, Mackay R. Al-Si Alloys, Minor, Major, and Impurity Elements. Al-Si Alloy., Springer, Cham; 2017, p. 1–15. Doi: 10.1007/978-3-319-58380-8_1.
- [870] Tzeng YC, Wu CT, Bor HY, Horng JL, Tsai ML, Lee SL. Effects of scandium addition on iron-bearing phases and tensile properties of Al-7Si-0.6Mg alloys. *Mater Sci Eng A* 2014;593:103–10. <https://doi.org/10.1016/j.msea.2013.11.039>.
- [871] Basak CB, Babu NH. Influence of Cu on modifying the beta phase and enhancing the mechanical properties of recycled Al-Si-Fe cast alloys. *Sci Rep* 2017;7:1–10. <https://doi.org/10.1038/s41598-017-05937-2>.
- [872] Zhang Wen, Zhao Y liang, Zhang D tong, Luo Z qiang, Yang C, Li Y yuan. Effect of Si addition and applied pressure on microstructure and tensile properties of as-cast Al-5.0Cu-0.6Mn-1.2Fe alloys. *Trans Nonferrous Met Soc China (English Ed)* 2018;28:1061–72. Doi: 10.1016/S1003-6326(18)64765-X.
- [873] Timpel M, Wandler N, Grothausmann R, Banhart J. Distribution of Fe-rich phases in eutectic grains of Sr-modified Al-10wt.% Si–0.1wt.% Fe casting alloy. *J Alloys Compd* 2013;558:18–25. <https://doi.org/10.1016/j.jallcom.2012.12.009>.
- [874] Sabau AS, Mirmiran S, Glaspie C, Li S, Apelian D, Shyam A, et al. Hot-tearing assessment of multicomponent nongrain-refined Al-Cu alloys for permanent mold castings based on load measurements in a constrained mold. *Metall Mater Trans B Process Metall Mater Process Sci* 2018;49:1267–87. <https://doi.org/10.1007/s11663-018-1204-0>.
- [875] Rakhamonov J, Timelli G, Bonollo F, Arnberg L. Influence of grain refiner addition on the precipitation of fe-rich phases in secondary alsi7cu3mg alloys. *Int J Met* 2017;11:294–304. <https://doi.org/10.1007/s40962-016-0076-9>.
- [876] Du Q, Li YJ. Effect modeling of Cr and Zn on microstructure evolution during homogenization heat treatment of AA3xxx alloys. *Trans Nonferrous Met Soc China (English Ed)* 2014;24:2145–9. [https://doi.org/10.1016/S1003-6326\(14\)63325-2](https://doi.org/10.1016/S1003-6326(14)63325-2).
- [877] Petit T, Besson J, Ritter C, Colas K, Helfen L, Morgeneyer TF. Effect of hardening on toughness captured by stress-based damage nucleation in 6061 aluminum alloy. *Acta Mater* 2019;180:349–65. <https://doi.org/10.1016/j.actamat.2019.08.055>.
- [878] Andersen SJ, Zandbergen HW, Jansen J, Træholt C, Tundal U, Reiso O. The crystal structure of the β'' phase in Al-Mg-Si Alloys. *Acta Mater* 1998;46:3283–98. [https://doi.org/10.1016/S1359-6454\(97\)00493-X](https://doi.org/10.1016/S1359-6454(97)00493-X).
- [879] Shen Y, Morgeneyer TF, Garnier J, Allais L, Helfen L, Crépin J. Three-dimensional quantitative in situ study of crack initiation and propagation in AA6061 aluminum alloy sheets via synchrotron laminography and finite-element simulations. *Acta Mater* 2013;61:2571–82. <https://doi.org/10.1016/j.actamat.2013.01.035>.
- [880] Agarwal H, Gokhale AM, Graham S, Horstemeyer MF. Void growth in 6061-aluminum alloy under triaxial stress state. *Mater Sci Eng A* 2003;341:35–42. [https://doi.org/10.1016/S0921-5093\(02\)00073-4](https://doi.org/10.1016/S0921-5093(02)00073-4).
- [881] Lassance D, Fabrègue D, Delannay F, Pardoen T. Micromechanics of room and high temperature fracture in 6xxx Al alloys. *Prog Mater Sci* 2007;52:62–129. <https://doi.org/10.1016/j.pmatsci.2006.06.001>.
- [882] Xie Q, Lian J, Sidor JJ, Sun F, Yan X, Chen C, et al. Crystallographic orientation and spatially resolved damage in a dispersion-hardened Al alloy. *Acta Mater* 2020;193:138–50. <https://doi.org/10.1016/j.actamat.2020.03.049>.
- [883] Hannard F, Pardoen T, Maire E, Le Bourlot C, Mokso R, Simar A. Characterization and micromechanical modelling of microstructural heterogeneity effects on ductile fracture of 6xxx aluminium alloys. *Acta Mater* 2016;103:558–72. <https://doi.org/10.1016/j.actamat.2015.10.008>.
- [884] Hannard F, Castin S, Maire E, Mokso R, Pardoen T, Simar A. Ductilization of aluminium alloy 6056 by friction stir processing. *Acta Mater* 2017;130:121–36. <https://doi.org/10.1016/j.actamat.2017.01.047>.
- [885] Babot L, Maire E, Fougeres R. Damage initiation in model metallic materials: X-ray tomography and modelling. *Acta Mater* 2004;52:2475–87. <https://doi.org/10.1016/j.actamat.2004.02.001>.
- [886] Sweet L, Zhu SM, Gao SX, Taylor JA, Easton MA. The effect of iron content on the iron-containing intermetallic phases in a cast 6060 aluminum alloy. *Metall Mater Trans A Phys Metall Mater Sci* 2011;42:1737–49. <https://doi.org/10.1007/s11661-010-0595-6>.
- [887] Kuijpers NCW, Tirel J, Hanlon DN, Van der Zwaag S. Quantification of the evolution of the 3D intermetallic structure in a 6005A aluminium alloy during a homogenisation treatment. *Mater Charact* 2002;48:379–92. [https://doi.org/10.1016/S1044-5803\(02\)00289-9](https://doi.org/10.1016/S1044-5803(02)00289-9).
- [888] Blind JA, Martin JW. The effect of dispersoids on the ductile fracture toughness of AlMgSi alloys. *Mater Sci Eng* 1983;57:49–54. [https://doi.org/10.1016/0025-5416\(83\)90026-5](https://doi.org/10.1016/0025-5416(83)90026-5).
- [889] Harrison PM, Henry M, Wendland J. High speed processing applications of high average power diode pumped solid state lasers. *Proc Third Int WLT-Conference Lasers Manuf* 2005;10:1–5. <https://doi.org/10.1051/jp4>.
- [890] Samuel FH, Samuel AM, Doty HW, Valtierra S. Decomposition of Fe-intermetallics in Sr-modified cast 6XXX type aluminum alloys for automotive skin. *Metall Mater Trans A Phys Metall Mater Sci* 2001;32:2061–75. <https://doi.org/10.1007/s11661-001-0018-9>.
- [891] Morgeneyer TF, Starink MJ, Wang SC, Sinclair I. Quench sensitivity of toughness in an Al alloy: Direct observation and analysis of failure initiation at the precipitate-free zone. *Acta Mater* 2008;56:2872–84. <https://doi.org/10.1016/j.actamat.2008.02.021>.
- [892] De Haas M, De Hosson JTM. On the effects of thermomechanical processing on failure mode in precipitation-hardened aluminium alloys. *J Mater Sci* 2002;37:5065–73. <https://doi.org/10.1023/A:1021095801205>.
- [893] Vasudévan AK, Doherty RD. Grain boundary ductile fracture in precipitation hardened aluminum alloys. *Acta Metall* 1987;35:1193–219. [https://doi.org/10.1016/0001-6160\(87\)90001-0](https://doi.org/10.1016/0001-6160(87)90001-0).
- [894] Christiansen E, Marioara CD, Marthinsen K, Hopperstad OS, Holmestad R. Lattice rotations in precipitate free zones in an Al-Mg-Si alloy. *Mater Charact* 2018;144:522–31. <https://doi.org/10.1016/j.matchar.2018.08.002>.
- [895] Hu Y, Wang G, Lue S, Wang J, Wang L, Rong Y. Effects of segregation, quenching rate, and external stress on precipitation behaviors of Al-Cu-Cd alloys. *Mater Des* 2019;184:108189. <https://doi.org/10.1016/j.matdes.2019.108189>.
- [896] Lin L, Liu Z, Bai S, Zhou Y, Liu W, Lv Q. Effects of Ge and Ag additions on quench sensitivity and mechanical properties of an Al-Zn-Mg-Cu alloy. *Mater Sci Eng A* 2017;682:640–7. <https://doi.org/10.1016/j.msea.2016.11.092>.
- [897] Deng YL, Wan L, Zhang YY, Zhang XM. Influence of Mg content on quench sensitivity of Al-Zn-Mg-Cu aluminum alloys. *J Alloys Compd* 2011;509:4636–42. <https://doi.org/10.1016/j.jallcom.2011.01.147>.
- [898] Chiu YC, Du KT, Bor HY, Liu GH, Lee SL. The effects of Cu, Zn and Zr on the solution temperature and quenching sensitivity of Al-Zn-Mg-Cu alloys. *Mater Chem Phys* 2020;247:122853. <https://doi.org/10.1016/j.matchemphys.2020.122853>.
- [899] Lim ST, Yun SJ, Nam SW. Improved quench sensitivity in modified aluminum alloy 7175 for thick forging applications. *Mater Sci Eng A* 2004;371:82–90. [https://doi.org/10.1016/S0921-5093\(03\)00653-1](https://doi.org/10.1016/S0921-5093(03)00653-1).

- [900] Li C, Chen D. Investigation on the quench sensitivity of 7085 aluminum alloy with different contents of main alloying elements. *Metals (Basel)* 2019;9:965. <https://doi.org/10.3390/met9090965>.
- [901] Zheng K, Dong Y, Zheng JH, Foster A, Lin J, Dong H, et al. The effect of hot form quench (HFQ®) conditions on precipitation and mechanical properties of aluminium alloys. *Mater Sci Eng A* 2019;761. <https://doi.org/10.1016/j.msea.2019.06.027>.
- [902] Zheng K, Dong Y, Zheng D, Lin J, Dean TA. An experimental investigation on the deformation and post-formed strength of heat-treatable aluminium alloys using different elevated temperature forming processes. *J Mater Process Technol* 2019;268:87–96. <https://doi.org/10.1016/j.jmatprot.2018.11.042>.
- [903] Polmear I, StJohn D, Nie J-F, Qian M. Physical metallurgy of aluminium alloys. *Light Alloy* 2017;31–107. <https://doi.org/10.1016/b978-0-08-099431-4.00002-6>.
- [904] Zhang Y. Quench Sensitivity of 7xxx Series Aluminium Alloys. PhD Thesis, Dep Mater Eng Monash Univ Clayton, Victoria Aust 2014;198 pp.
- [905] Nie B, Liu P, Zhou T. Effect of compositions on the quenching sensitivity of 7050 and 7085 alloys. *Mater Sci Eng A* 2016;667:106–14. <https://doi.org/10.1016/j.msea.2016.04.095>.
- [906] Zhang Y, Milkereit B, Kessler O, Schick C, Rometsch PA. Development of continuous cooling precipitation diagrams for aluminium alloys AA7150 and AA7020. *J Alloys Compd* 2014;584:581–9. <https://doi.org/10.1016/j.jallcom.2013.09.014>.
- [907] Chakrabarti DJ, Liu RRS, Venema GB. New generation high strength high damage tolerance 7085 thick alloy product with low quench sensitivity. 9th Int Conf Alum Alloy 2004;28:6–11.
- [908] Livak RJ, Papazian JM. Effects of copper on precipitation and quench sensitivity of AlZnMg alloys. *Scr Metall* 1984;18:483–8. [https://doi.org/10.1016/0036-9748\(84\)90426-5](https://doi.org/10.1016/0036-9748(84)90426-5).
- [909] Milkereit B, Wandlerka N, Schick C, Kessler O. Continuous cooling precipitation diagrams of Al-Mg-Si alloys. *Mater Sci Eng A* 2012;550:87–96. <https://doi.org/10.1016/j.msea.2012.04.033>.
- [910] Zhang Y, Yi Y, Huang S, Dong F, Wang H. Investigation of the quenching sensitivity of forged 2A14 aluminum alloy by time-temperature-tensile properties diagrams. *J Alloys Compd* 2017;728:1239–47. <https://doi.org/10.1016/j.jallcom.2017.09.041>.
- [911] Wang H, Yi Y, Huang S. Investigation of quench sensitivity of high strength 2219 aluminum alloy by TTP and TTT diagrams. *J Alloys Compd* 2017;690:446–52. <https://doi.org/10.1016/j.jallcom.2016.08.160>.
- [912] Lin L, Liu Z, Bai S, Ying P, Wang X. Effects of germanium on quench sensitivity in Al-Zn-Mg-Zr alloy. *Mater Des* 2015;86:679–85. <https://doi.org/10.1016/j.matdes.2015.07.169>.
- [913] Dursun T, Soutis C. Recent developments in advanced aircraft aluminium alloys. *Mater Des* 2014;56:862–71. <https://doi.org/10.1016/j.matdes.2013.12.002>.
- [914] Dong J, Cui JZ, Yu FX, Zhao ZH, Zhuo YB. A new way to cast high-alloyed Al-Zn-Mg-Cu-Zr for super-high strength and toughness. *J Mater Process Technol* 2006;171:399–404. <https://doi.org/10.1016/j.jmatprot.2005.07.010>.
- [915] Doroshenko NM, Ovsyannikov BV, Zamyatkin VM, Popov VI. Effect of admixtures of iron and silicon on the structure and cracking of near-edge volumes in rolling of large flat ingots from alloy 7075. *Met Sci Heat Treat* 2005;47:30–5. <https://doi.org/10.1007/s11041-005-0027-1>.
- [916] Zhang XM, Yu CJ, Liu SD, Liu XX, Zhang P, Wang YY. Influence of Fe and Si impurities on the quench sensitivity of Al-Zn-Mg-Cu alloy. *Cailiao Gongcheng/Journal Mater Eng* 2013;3:41–7. <https://doi.org/10.3969/j.issn.1001-4381.2013.10.007>.
- [917] Dons AL, Lohne O. QUENCH SENSITIVITY OF AlMgSi-ALLOYS CONTAINING Mn OR Cr. *Mater Res Soc Symp Proc* 1984;21:723–8.
- [918] Lodgaard L, Ryum N. Precipitation of dispersoids containing Mn and/or Cr in Al-Mg-Si alloys. *Mater Sci Eng A* 2000;283:144–52. [https://doi.org/10.1016/s0921-5093\(00\)00734-6](https://doi.org/10.1016/s0921-5093(00)00734-6).
- [919] Sheppard T. Press quenching of aluminium alloys. *Mater Sci Technol (United Kingdom)* 1988;4:635–43. <https://doi.org/10.1179/mst.1988.4.7.635>.
- [920] Saito T, Marioara CD, Røysæt J, Holmestad R. Influence of low cu addition on quench sensitivity in Al-Mg-Si alloys. *Adv Mater Res* 2014;922:616–21. <https://doi.org/10.4028/www.scientific.net/AMR.922.616>.
- [921] Kassner ME, Geantil P, Li X. A study of the quench sensitivity of 6061-T6 and 6069-T6 aluminum alloys. *J Metall* 2011;2011:1–5. <https://doi.org/10.1155/2011/747198>.
- [922] Tzeng YC, Wu CT, Lee SL. The effect of trace Sc on the quench sensitivity of AL-7Si-0.6 Mg alloys. *Mater Lett* 2015;161:340–2. <https://doi.org/10.1016/j.matlet.2015.08.108>.
- [923] Tiryakioglu M, Shuey RT. Quench sensitivity of 2219-T87 aluminum alloy plate. *Mater Sci Eng A* 2010;527:5033–7. <https://doi.org/10.1016/j.msea.2010.04.060>.
- [924] Meng Y, Cui J, Zhao Z, Zuo Y. Effect of vanadium on the microstructures and mechanical properties of an Al-Mg-Si-Cu-Cr-Ti alloy of 6XXX series. *J Alloys Compd* 2013;573:102–11. <https://doi.org/10.1016/j.jallcom.2013.03.239>.
- [925] Chan KS, Jones P, Wang Q. Fatigue crack growth and fracture paths in sand cast B319 and A356 aluminum alloys. *Mater Sci Eng A* 2003;341:18–34. [https://doi.org/10.1016/S0921-5093\(02\)00196-X](https://doi.org/10.1016/S0921-5093(02)00196-X).
- [926] Huter P, Winter G, Schwab M, Renhart P, Oberfrank S, Grün F, et al. Comparison of microstructural crack paths between hypo-eutectic Al-Si-Cu and Al-Si-Mg cast alloys in high plasticity regimes under rotating bending. *Mater Sci Eng A* 2014;618:578–85. <https://doi.org/10.1016/j.msea.2014.08.062>.
- [927] Huter P, Renhart P, Oberfrank S, Schwab M, Grün F, Stauder B. High- ad low-cycle fatigue influence of silicon, copper, strontium and iron on hypo-eutectic Al-Si-Cu and Al-Si-Mg cast alloys used in cylinder heads. *Int J Fatigue* 2016;82:588–601. <https://doi.org/10.1016/j.ijfatigue.2015.09.015>.
- [928] Kobayashi T. Strength and fracture of aluminum alloys. *Mater Sci Eng A* 2000;286:333–41. [https://doi.org/10.1016/S0921-5093\(00\)00935-7](https://doi.org/10.1016/S0921-5093(00)00935-7).
- [929] Wang QG, Apelian D, Lados DA. Fatigue behavior of A356/357 aluminum cast alloys. Part II - Effect of microstructural constituents. *J Light Met* 2001;1:85–97. [https://doi.org/10.1016/S1471-5317\(00\)00009-2](https://doi.org/10.1016/S1471-5317(00)00009-2).
- [930] Horng JH, Jiang DS, Lui TS, Chen LH. The fracture behaviour of A356 alloys with different iron contents under resonant vibration. *Int J Cast Met Res* 2000;13:215–22. <https://doi.org/10.1080/13640461.2000.11819404>.
- [931] Gall K, Yang N, Horstemeyer M, McDowell DL, Fan J. Influence of modified intermetallics and Si particles on fatigue crack paths in a cast A356 Al alloy. *Fatigue Fract Eng Mater Struct* 2000;23:159–72. <https://doi.org/10.1046/j.1460-2695.2000.00239.x>.
- [932] Yi JZ, Gao YX, Lee PD, Lindley TC. Effect of Fe-content on fatigue crack initiation and propagation in a cast aluminum-silicon alloy (A356-T6). *Mater Sci Eng A* 2004;386:396–407. <https://doi.org/10.1016/j.msea.2004.07.044>.
- [933] Ceschinini L, Boromei I, Morri A, Seiffedine S, Svensson IL. Microstructure, tensile and fatigue properties of the Al-10%Si-2%Cu alloy with different Fe and Mn content cast under controlled conditions. *J Mater Process Technol* 2009;209:5669–79. <https://doi.org/10.1016/j.jmatprot.2009.05.030>.
- [934] Alkahtani S. Mechanical performance of heat treated 319 alloys as a function of alloying and aging parameters. *Mater Des* 2012;41:358–69. <https://doi.org/10.1016/j.matdes.2012.04.034>.
- [935] Zhang Q, Zhu Y, Gao X, Wu Y, Hutchinson C. Training high-strength aluminum alloys to withstand fatigue. *Nat Commun* 2020;11:1–8. <https://doi.org/10.1038/s41467-020-19071-7>.
- [936] Esquivel J, Gupta RK. Review—corrosion-resistant metastable Al alloys: an overview of corrosion mechanisms. *J Electrochem Soc* 2020;167:081504. <https://doi.org/10.1149/1945-7111/ab8a97>.
- [937] E. A. Birbilis N, M.C. J, J. S, Zhou X, E. G. High strength Al-alloys: microstructure, corrosion and principles of protection. In: Ahmad Z, editor. Recent Trends Process. Degrad. Alum. Alloy., InTech; 2011, p. 223–62. Doi: 10.5772/18766.
- [938] Jaramillo G, Scheel A, Wu Q. The effect of impurities on striped phases. *Proc R Soc Edinburgh Sect A Math* 2019;149:131–68. <https://doi.org/10.1017/S0308210518000197>.
- [939] Kucharíková L, Liptáková T, Tillová E, Kajánek D, Schmidová E. Role of chemical composition in corrosion of aluminum alloys. *Metals (Basel)* 2018;8:1–13. <https://doi.org/10.3390/met8080581>.
- [940] Chino Y, Mabuchi M, Otsuka S, Shimojima K, Hosokawa H, Yamada Y, et al. Corrosion and mechanical properties of recycled 5083 aluminum alloy by solid state recycling. *Mater Trans* 2003;44:1284–9. <https://doi.org/10.2320/matertrans.44.1284>.
- [941] Mansurov YN, Kadyrova DS, Rakhamonov J. Dependence of corrosion resistance for aluminum alloys with composition increased impurity content. *Metallurgist* 2019;62:1181–6. <https://doi.org/10.1007/s11015-019-00771-5>.

- [942] Bell S, Davis B, Javaid A, Essadiqi E. Final Report on Effect of Impurities in Aluminum 2006:18. Doi: 10.13140/RG.2.2.34366.28482.
- [943] Zhu Y, Sun K, Garves J, Bland LG, Locke J, Allison J, et al. Micro- and nano-scale intermetallic phases in AA2070-T8 and their corrosion behavior. *Electrochim Acta* 2019;319:634–48. <https://doi.org/10.1016/j.electacta.2019.05.028>.
- [944] Zhu Y, Sun K, Frankel GS. Intermetallic phases in aluminum alloys and their roles in localized corrosion. *J Electrochem Soc* 2018;165:C807–20. <https://doi.org/10.1149/2.093181jes>.
- [945] Lutz A, Malet L, Dill J, de Almeida LH, Lapeire L, Verbeken K, et al. Effect of Zn on the grain boundary precipitates and resulting alkaline etching of recycled Al-Mg-Si-Cu alloys. *J Alloys Compd* 2019;794:435–42. <https://doi.org/10.1016/j.jallcom.2019.04.259>.
- [946] Guo MX, Du JQ, Zheng CH, Zhang JS, Zhuang LZ. Influence of Zn contents on precipitation and corrosion of Al-Mg-Si-Cu-Zn alloys for automotive applications. *J Alloys Compd* 2019;778:256–70. <https://doi.org/10.1016/j.jallcom.2018.11.146>.
- [947] Zheng YY, Luo BH, He C, Ren ZW, Yin Y. Effects of Ag addition on the precipitation hardening behaviours and corrosion properties of Al-Mg-Si alloy. *Int J Electrochem Sci* 2019;14:173–85. <https://doi.org/10.20964/2019.01.30>.
- [948] Zeng Y, Jiang B, Li RH, Liu YH. Influences of alloying elements on the microstructure and properties of Mg-Li alloys. *Zhuzao/Foundry* 2012;61:275–9.
- [949] Iwao S, Asano M. Effect of additional Cu and Mg in Al-Mn-Si alloy on intergranular corrosion susceptibility after heating at 200°C. *Keikinzoku/Journal Japan Inst Light Met* 2009;59:108–13. <https://doi.org/10.2464/jilm.59.108>.
- [950] Zhang X, Lv Y, Hashimoto T, Nilsson JO, Zhou X. Intergranular corrosion of AA6082 Al-Mg-Si alloy extrusion: The influence of trace Cu and grain boundary misorientation. *J Alloys Compd* 2021;853:157228. <https://doi.org/10.1016/j.jallcom.2020.157228>.
- [951] Sharma A, Shin YS, Jung J-P. Influence of various additional elements in Al based filler alloys for automotive and brazing industry. *J Weld Join* 2015;33:1–8. <https://doi.org/10.5781/jwj.2015.33.5.1>.
- [952] Zheng Y, Luo B, Bai Z, Wang J, Yin Y. Study of the precipitation hardening behaviour and intergranular corrosion of Al-Mg-Si alloys with differing Si contents. *Metals (Basel)* 2017;7. Doi: 10.3390/met7100387.
- [953] Oya Y, Kojima Y, Hara N. Influence of silicon on intergranular corrosion for aluminum alloys. *Nippon Kinzoku Gakkaishi/Journal Japan Inst Met* 2014;78:52–9. <https://doi.org/10.2320/jinstmet.J2013058>.
- [954] Sukiman NL, Zhou X, Birbilis N, Hughes AE, Mol JMC, Garcia SJ, et al. Aluminium Alloys - New Trends in Fabrication and Applications 2012. <https://doi.org/10.5772/3354>.
- [955] Keung YW, Nordlien JH, Ono S, Nisancioglu K. Electrochemical activation of aluminum by trace element lead. *J Electrochem Soc* 2003;150:B547. <https://doi.org/10.1149/1.1615996>.
- [956] Premendra P, Terryn H, Mol JMC, De Wit JHW, Katgerman L. A comparative electrochemical study of commercial and model aluminium alloy (AA5050). *Mater Corros* 2009;60:399–406. <https://doi.org/10.1002/maco.200805145>.
- [957] Gundersen JT, Aytaç A, Ono S, Nordlien JH, Nisancioglu K. Effect of trace elements on electrochemical properties and corrosion of aluminium alloy AA3102. *Corros Sci* 2004;46:265–83. [https://doi.org/10.1016/S0010-938X\(03\)00159-8](https://doi.org/10.1016/S0010-938X(03)00159-8).
- [958] Anawati Diplas S, Nisancioglu K. Effect of copper on anodic activity of aluminum-lead model alloy in chloride solution. *J Electrochem Soc* 2011;158. <https://doi.org/10.1149/1.3562946>.
- [959] Das SK. Designing aluminum alloys for a recycling friendly world. *Mater Sci Forum* 2006;519–521:1239–44. <https://doi.org/10.4028/www.scientific.net/msf.519-521.1239>.
- [960] Berlanga C, Bakedano A, De Ciriza AP, Rivero PJ, Mendez S, Rodriguez R, et al. Evaluation of the corrosion resistance of a new AlSi10MnMg(Fe) secondary alloy. *Mater Today Proc*, vol. 10, Elsevier Ltd; 2019, p. 312–8. Doi: 10.1016/j.mtpr.2018.10.411.
- [961] Lu GH, Zhang Y, Deng S, Wang T, Kohyama M, Yamamoto R, et al. Origin of intergranular embrittlement of Al alloys induced by Na and Ca segregation: Grain boundary weakening. *Phys Rev B - Condens Matter Mater Phys* 2006;73. <https://doi.org/10.1103/PhysRevB.73.224115>.
- [962] Bhuiyan MS, Tada Y, Toda H, Hang S, Uesugi K, Takeuchi A, et al. Influences of hydrogen on deformation and fracture behaviors of high Zn 7XXX aluminum alloys. *Int J Fract* 2016;200:13–29. <https://doi.org/10.1007/s10704-016-0092-z>.
- [963] Chen YS, Lu H, Liang J, Rosenthal A, Liu H, Sneddon G, et al. Observation of hydrogen trapping at dislocations, grain boundaries, and precipitates. *Science (80-)* 2020;367:171–5. <https://doi.org/10.1126/science.aaz0122>.
- [964] Yan F, Mouton I, Stephenson LT, Breen AJ, Chang Y, Ponge D, et al. Atomic-scale investigation of hydrogen distribution in a TiMo alloy. *Scr Mater* 2019;162:321–5.
- [965] Breen AJ, Stephenson LT, Sun B, Li Y, Kasian O, Raabe D, et al. Solute hydrogen and deuterium observed at the near atomic scale in high-strength steel. *Acta Mater* 2020;188:108–20. <https://doi.org/10.1016/j.actamat.2020.02.004>.
- [966] Breen AJ, Mouton I, Lu W, Wang S, Szczepaniak A, Kontis P, et al. Atomic scale analysis of grain boundary deuteride growth front in Zircaloy-4. *Scr Mater* 2018;156:42–6. <https://doi.org/10.1016/j.scriptamat.2018.06.044>.
- [967] Tsuru T, Yamaguchi M, Ebihara K, Itakura M, Shiihara Y, Matsuda K, et al. First-principles study of hydrogen segregation at the MgZn2 precipitate in Al-Mg-Zn alloys. *Comput Mater Sci* 2018;148:301–6. <https://doi.org/10.1016/j.commatsci.2018.03.009>.
- [968] Chao P, Karneky RA. Hydrogen isotope trapping in Al-Cu binary alloys. *Mater Sci Eng A* 2016;658:422–8. <https://doi.org/10.1016/j.msea.2016.02.003>.
- [969] Toda H, Oogo H, Horikawa K, Uesugi K, Takeuchi A, Suzuki Y, et al. The true origin of ductile fracture in aluminum alloys. *Metall Mater Trans A Phys Metall Mater Sci* 2014;45:765–76. <https://doi.org/10.1007/s11661-013-2013-3>.
- [970] Polmear I, St John D, Nie J-FJF, Qian MM. Light Alloys: Metallurgy of the Light Metals: Fifth Ed. 2017.
- [971] Apelian D. Aluminum cast alloys: enabling tools for improved performance. *Worldw Report*, Wheel NADCA 2009:1–68.
- [972] Kaufman JG, Rooy EL. *Aluminum Alloy Castings: Properties, Processes, and Applications*. ASM Int.; 2004, ISBN 978-0-87170-803-8.
- [973] Kaufmann H, Uggowitzer PJ. Metallurgy and processing of high integrity light metal pressure castings. Berlin: Schiele & Schön; 2007.
- [974] Ji S, Watson D, Fan Z, White M. Development of a super ductile diecast Al-Mg-Si alloy. *Mater Sci Eng A* 2012;556:824–33. <https://doi.org/10.1016/j.msea.2012.07.074>.
- [975] Casarotto F, Franke R, High-pressure die-cast (HPDC) aluminium alloys for automotive applications. *Adv Mater Automot Eng* 2012;109–49. <https://doi.org/10.1533/9780857095466.109>.
- [976] MatWeb - Aluminum A206.0-T7 Casting Alloy n.d.
- [977] Major J, Hartlieb M. Advances in aluminum foundry alloys for permanent and semi-permanent mold casting. *Int J Met* 2009;3:43–53. <https://doi.org/10.1007/BF03355452>.
- [978] Fragner W, Baumgartner K, Suppan H, Hummel M, Bösch D, Höppel HW, et al. Using scrap in recycling alloys for structural applications in the automotive industry. *Light Met* 2014;9781118889(2014):349–53. <https://doi.org/10.1002/978111888438.ch59>.
- [979] Fragner W. Aluminium recycled cast alloy for safety-critical components. *AMAG AluReport* 2020:37–9. <https://de.calameo.com/read/0034240184e0cee018185>.
- [980] Pucher P, Antrekowitsch H, Böttcher H, Kaufmann H, Uggowitzer PJ. Influence of compositional variations on microstructural evolution, mechanical properties and fluidity of secondary foundry alloy AlSi9Cu3. *Int J Cast Met Res* 2010;23:375–83. <https://doi.org/10.1179/136404610X12682097603803>.
- [981] Pucher P, Antrekowitsch H, Böttcher H, Kaufmann H, Uggowitzer PJ. Einfluss der Legierungszusammensetzung auf die mechanischen Eigenschaften der Sekundärlegierung A226 (AlSi9Cu3) im wärmebehandelten T6-Zustand. *Gießereipraxis* 2009;11:354–8.
- [982] Computherm PanAluminium n.d. <https://computherm.com/docs/pandat-database-manual/database-manual/panaluminum>.
- [983] Hwang JY, Doty HW, Kaufman MJ. The effects of Mn additions on the microstructure and mechanical properties of Al-Si-Cu casting alloys. *Mater Sci Eng A* 2008;488:496–504. <https://doi.org/10.1016/j.msea.2007.12.026>.
- [984] Jin L, Liu K, Chen XG. Evolution of Fe-rich intermetallics in Al-Si-Cu 319 cast alloy with various Fe, Mo, and Mn contents. *Metall Mater Trans B Process Metall Mater Process Sci* 2019;50:1896–907. <https://doi.org/10.1007/s11663-019-01584-2>.
- [985] Mahta M, Emamy M, Daman A, Keyvani A, Campbell J. Precipitation of Fe rich intermetallics in Cr- and Co-modified A413 alloy. *Int J Cast Met Res* 2005;18:73–9. <https://doi.org/10.1179/136404605225022928>.

- [986] Yang H, Ji S, Fan Z. Effect of heat treatment and Fe content on the microstructure and mechanical properties of die-cast Al-Si-Cu alloys. *Mater Des* 2015;85: 823–32. <https://doi.org/10.1016/j.matdes.2015.07.074>.
- [987] Modaresi R, Løvik AN, Müller DB. Component- and alloy-specific modeling for evaluating aluminum recycling strategies for vehicles. *JOM* 2014;66:2262–71. <https://doi.org/10.1007/s11837-014-0900-8>.
- [988] Bösch D, Pogatscher S, Hummel M, Fragner W, Uggowitzer PJ, Göken M, et al. Secondary Al-Si-Mg high-pressure die casting alloys with enhanced ductility. *Metall Mater Trans A Phys Metall Mater Sci* 2015;46:1035–45. <https://doi.org/10.1007/s11661-014-2700-8>.
- [989] Kim HY, Han SW, Lee HM. The influence of Mn and Cr on the tensile properties of A356–0.20Fe alloy. *Mater Lett* 2006;60:1880–3. <https://doi.org/10.1016/j.mlet.2005.12.042>.
- [990] Lin B, Li H, Xu R, Xiao H, Zhang W, Li S. Effects of vanadium on modification of iron-rich intermetallics and mechanical properties in A356 cast alloys with 1.5 wt.% Fe. *J Mater Eng Perform* 2019;28:475–84. <https://doi.org/10.1007/s11665-018-3798-4>.
- [991] Shankar S, Apelian D. Die soldering: Effect of process parameters and alloy characteristics on soldering in the pressure die casting process. *Int J Cast Met Res* 2002;15:103–16. <https://doi.org/10.1080/13640461.2002.11819469>.
- [992] Han QY. Mechanism of die soldering during aluminum die casting. *China Foundry* 2015;12:136–43.
- [993] Nazari KA, Shabestari SG. Effect of micro alloying elements on the interfacial reactions between molten aluminum alloy and tool steel. *J Alloys Compd* 2009; 478:523–30. <https://doi.org/10.1016/j.jallcom.2008.11.127>.
- [994] Mbuya TO, Odera BO, Ng'ang'a SP. Influence of iron on castability and properties of aluminium silicon alloys: Literature review. *Int J Cast Met Res* 2003;16: 451–65. <https://doi.org/10.1080/13640461.2003.11819622>.
- [995] Shabestari SG. The effect of iron and manganese on the formation of intermetallic compounds in aluminum-silicon alloys. *Mater Sci Eng A* 2004;383:289–98. <https://doi.org/10.1016/j.msea.2004.06.022>.
- [996] Darvishi A, Maleki A, Mazar Atabaki M, Zargami M. The mutual effect of iron and manganese on microstructure and mechanical properties of aluminium–silicon alloy. *Metal Metall* 2010;16:11–24. <https://doi.org/10.30544/383>.
- [997] Ferraro S, Timelli G. Influence of sludge particles on the tensile properties of die-cast secondary aluminum alloys. *Metall Mater Trans B Process Metall Mater Process Sci* 2015;46:1022–34. <https://doi.org/10.1007/s11663-014-0260-3>.
- [998] Dietrich BG, Becker H, Smolka M, Keßler A, Leineweber A, Wolf G. Intermetallic sludge formation in fe containing secondary Al-Si alloys influenced by Cr and Mn as preparative tool for metal melt filtration. *Adv Eng Mater* 2017;19:1–7. <https://doi.org/10.1002/adem.201700161>.
- [999] Jorstad JL. UNDERSTANDING SLUDGE. *Trans. - SDCE Int. Die Cast. Expo. Congr. (Society Die Cast. Engine, vol. 30, 1987, p. 30–6.*
- [1000] Zhu X, Blake P, Dou K, Ji S. Strengthening die-cast Al-Mg and Al-Mg-Mn alloys with Fe as a beneficial element. *Mater Sci Eng A* 2018;732:240–50. <https://doi.org/10.1016/j.msea.2018.07.005>.
- [1001] Total Materia: The worlds Most Comprehensive Materials Database: Key to Metals AG 2016 2016. www.totalmateria.com.
- [1002] Ji S, Wang Y, Watson D, Fan Z. Microstructural evolution and solidification behavior of Al-Mg-Si alloy in high-pressure die casting. *Metall Mater Trans A Phys Metall Mater Sci* 2013;44:3185–97. <https://doi.org/10.1007/s11661-013-1663-5>.
- [1003] Tredna G. Solutions for ductile die casting. *Alum Int Today* 2006;18:22–6.
- [1004] Prach O, Trudonoshy O, Randelzhofer P, Körner Durst K. Effect of Zr, Cr and Sc on the Al–Mg–Si–Mn high-pressure die casting alloys. *Mater Sci Eng A* 2019; 759:603–12. <https://doi.org/10.1016/j.msea.2019.05.038>.
- [1005] Stempel L, Mitas B, Kremer T, Otterbach S, Uggowitzer PJ, Pogatscher S. Age-hardening of high pressure die casting AlMg alloys with Zn and combined Zn and Cu additions. *Mater Des* 2019;181. <https://doi.org/10.1016/j.matdes.2019.107927>.
- [1006] Stempel L, Tunès MA, Oberhauser P, Uggowitzer PJ, Pogatscher S. Age-hardening response of AlMgZn alloys with Cu and Ag additions. *Acta Mater* 2020;195: 541–54. <https://doi.org/10.1016/j.actamat.2020.05.066>.
- [1007] Liu K, Cao X, Chen XG. Effect of Mn, Si, and cooling rate on the formation of iron-rich intermetallics in 206 Al-Cu cast alloys. *Metall Mater Trans B Process Metall Mater Process Sci* 2012;43:1231–40. <https://doi.org/10.1007/s11663-012-9694-7>.
- [1008] Liu K, Cao X, Chen XG. Tensile properties of Al-Cu 206 cast alloys with various iron contents. *Metall Mater Trans A Phys Metall Mater Sci*, vol. 45, 2014, p. 2498–507. Doi: 10.1007/s11661-014-2207-3.
- [1009] Suchy J, Pantalejev L, Palousek D, Koutny D, Kaiser J. Processing of AlSi9Cu3 alloy by selective laser melting. *Powder Metall* 2020;63:197–211. <https://doi.org/10.1080/00325899.2020.1792675>.
- [1010] Grant PS. Spray forming. *Prog Mater Sci* 1995;39:497–545. [https://doi.org/10.1016/0079-6425\(95\)00004-6](https://doi.org/10.1016/0079-6425(95)00004-6).
- [1011] Kaufmann H, Galowsky U, Uggowitzer PJ. Cleaning process for contaminated light metals especially separating heavy metal from light metal alloy. Patent AT412348B 2005. <https://patents.google.com/patent/AT412348B/en?oq=AT412348B>.
- [1012] Annadurai D, Lu PY, Tang NK, Chen JK. Iron reduction in 356 secondary aluminum alloy by Mn and Cr addition for sediment separation. *Int J Met* 2020. <https://doi.org/10.1007/s40962-020-00433-2>.
- [1013] Shabestari SG, Gruzleski JE. Gravity segregation of complex intermetallic compounds in liquid aluminum-silicon alloys. *Metall Mater Trans A* 1995;26: 999–1006. <https://doi.org/10.1007/BF02649097>.
- [1014] Zhao L, Guo Z, Wang Z, Wang M. Communication removal of low-content impurities from Al by super-gravity. *Metall Mater Trans B Process Metall Mater Process Sci* 2010;41:505–8. <https://doi.org/10.1007/s11663-010-9376-2>.
- [1015] De Moraes HL, De Oliveira JR, Espinosa DCR, Tenório JAS. Removal of iron from molten recycled aluminum through intermediate phase filtration. *Mater Trans* 2006;47:1731–6. <https://doi.org/10.2320/matertrans.47.1731>.
- [1016] Kim JH, Yoon EP. Elimination of Fe element in A380 aluminum alloy scrap by electromagnetic force. *J Mater Sci Lett* 2000;19:253–5. <https://doi.org/10.1023/A:1006727212353>.
- [1017] Polmeat I. *Wrought aluminium alloys, in Light Alloys (Fourth Edition)*. Oxford: Butterworth-Heinemann; 2005. p. 97–204.
- [1018] Ostermann F. Anwendungstechnologie Aluminium. Springer Berlin Heidelberg; 2014. Doi: 10.1007/978-3-662-43807-7.
- [1019] Ashkenazi D. How aluminum changed the world: A metallurgical revolution through technological and cultural perspectives. *Technol Forecast Soc Change* 2019;143:101–13. <https://doi.org/10.1016/j.techfore.2019.03.011>.
- [1020] Timelli G, Bonollo F. Influence of tin and bismuth on machinability of lead free 6000 series aluminium alloys. *Mater Sci Technol* 2011;27:291–9. <https://doi.org/10.1179/026708309X12595712305799>.
- [1021] Gaustad G, Olivetti E, Kirchain R. Design for Recycling *J Ind Ecol* 2010;14:286–308. <https://doi.org/10.1111/j.1530-9290.2010.00229.x>.
- [1022] Nguyen RT, Imholte DD, Rios OR, Weiss D, Sims Z, Stromme E, et al. Anticipating impacts of introducing aluminum-cerium alloys into the United States automotive market. *Resour Conserv Recycl* 2019;144:340–9. <https://doi.org/10.1016/j.resconrec.2019.02.009>.
- [1023] Granta Design Limited. CES EduPack software. Granta Des Ltd 2009.
- [1024] Manes A, Serpellini F, Pagani M, Saponara M, Giglio M. Perforation and penetration of aluminium target plates by armour piercing bullets. *Int J Impact Eng* 2014;69:39–54. <https://doi.org/10.1016/j.ijimpeng.2014.02.010>.
- [1025] Jena PK, Savio SG, Kumar KS, Madhu V, Mandal RK, Singh AK. An experimental study on the deformation behavior of aluminium armour plates impacted by two different non-deformable projectiles. *Procedia Eng* 2017;173:222–9. <https://doi.org/10.1016/j.proeng.2016.12.001>.
- [1026] Manes A, Pagani M, Saponara M, Mombelli D, Mapelli C, Giglio M. Metallographic characterisation of Al6061-T6 aluminium plates subjected to ballistic impact. *Mater Sci Eng A* 2014;608:207–20. <https://doi.org/10.1016/j.msea.2014.04.064>.
- [1027] Kammer C. Fundamentals and Materials. Alum. Handb., Aluminium Verlag; 2011.
- [1028] Kammer C. Weiterverarbeitung und Anwendung. Alum. Taschenb. 3, Beuth Verlag; 2014.
- [1029] Heinz A, Haszler A, Keidel C, Moldenhauer S, Benedictus R, Miller WS. Recent development in aluminium alloys for aerospace applications. *Mater Sci Eng A* 2000;280:102–7. [https://doi.org/10.1016/S0921-5093\(99\)00674-7](https://doi.org/10.1016/S0921-5093(99)00674-7).
- [1030] Narasayya CVA, Rambabu P, Mohan MK, Prasad NE. Tensile deformation and fracture behaviour of an aerospace aluminium alloy AA2219 in different ageing conditions. *Procedia Mater Sci* 2014;6:322–30. <https://doi.org/10.1016/j.mspro.2014.07.041>.

- [1031] Williams JC, Starke EA. Progress in structural materials for aerospace systems. *Acta Mater* 2003;51:5775–99. <https://doi.org/10.1016/j.actamat.2003.08.023>.
- [1032] Eckelman MJ, Ciacci L, Kavlak G, Nuss P, Reck BK, Graedel TE. Life cycle carbon benefits of aerospace alloy recycling. *J Clean Prod* 2014;80:38–45. <https://doi.org/10.1016/j.jclepro.2014.05.039>.
- [1033] Carle D, Blount G. The suitability of aluminium as an alternative material for car bodies. *Mater Des* 1999. [https://doi.org/10.1016/s0261-3069\(99\)00003-5](https://doi.org/10.1016/s0261-3069(99)00003-5).
- [1034] Hirsch J. Aluminium in innovative light-weight car design. *Mater Trans* 2011;52:818–24. <https://doi.org/10.2320/matertrans.L-MZ201132>.
- [1035] van Schaik A, Reuter MA. The use of fuzzy rule models to link automotive design to recycling rate calculation. *Miner Eng* 2007;20:875–90. <https://doi.org/10.1016/j.mineng.2007.03.016>.
- [1036] Soo VK, Compston P, Doolan M. Interaction between new car design and recycling impact on life cycle assessment. *Procedia CIRP* 2015;29:426–31. <https://doi.org/10.1016/j.procir.2015.02.055>.
- [1037] Soo VK, Compston P, Doolan M. Is the Australian automotive recycling industry heading towards a global circular economy? - A case study on vehicle doors. *Procedia CIRP* 2016;48:10–5. <https://doi.org/10.1016/j.procir.2016.03.099>.
- [1038] Zajac S, Hutchinson B, Johansson A, Gullman LO. Microstructure control and extrudability of Al–Mg–Si alloys microalloyed with manganese. *Mater Sci Technol* (United Kingdom) 1994;10:323–33. <https://doi.org/10.1179/mst.1994.10.4.323>.
- [1039] Santora E, Berneder J, Simetsberger F, Doberer M. Mechanical properties evolution for 8xxx foil stock materials by alloy optimization—literature review and experimental research. *Miner Met Mater Ser*, Springer International Publishing 2019;365–72. https://doi.org/10.1007/978-3-030-05864-7_46.
- [1040] Fang CM, Que ZP, Dinsdale A, Fan Z. Si solution in 0-Al13Fe4 from first-principles. *Intermetallics* 2020;126:106939. <https://doi.org/10.1016/j.intermet.2020.106939>.
- [1041] Feng S, Liotti E, Lui A, Wilson MD, Conolley T, Mathiesen RH, et al. In-situ X-ray radiography of primary Fe-rich intermetallic compound formation. *Acta Mater* 2020;196:759–69. <https://doi.org/10.1016/j.actamat.2020.06.045>.
- [1042] Feng S, Liotti E, Lui A, Kumar S, Mahadevogowda A, O'Reilly KAQ, et al. An in-situ method to estimate the tip temperature and phase selection of secondary Fe-rich intermetallics using synchrotron X-ray radiography. *Scr Mater* 2018;149:44–8. <https://doi.org/10.1016/j.scriptamat.2018.02.001>.
- [1043] Wang Y, Jones H. Effect of growth velocity on the growth temperature of the Al-Al_xFe eutectic in Al-2.85Fe-0.12V alloy. *Metall Mater Trans A Phys Metall Mater Sci* 2001;32:1251–3. <https://doi.org/10.1007/s11661-001-0135-5>.
- [1044] Kumar S, Grant PS, O'Reilly KAQ. Evolution of Fe bearing intermetallics during DC casting and homogenization of an Al-Mg-Si Al alloy. *Metall Mater Trans A Phys Metall Mater Sci* 2016;47:3000–14. <https://doi.org/10.1007/s11661-016-3451-5>.
- [1045] Sha G, O'Reilly KAQ, Cantor B. Characterization of fe-rich intermetallic phases in a 6xxx series al alloy. *Mater. Sci. Forum*, vol. 519–521, Trans Tech Publications, Ltd.; 2006, p. 1721–6. doi: 10.4028/www.scientific.net/msf.519-521.1721.
- [1046] Lui A, Grant PS, Stone IC, O'Reilly KAQ. The role of grain refiner in the nucleation of AlFeSi intermetallic phases during solidification of a 6xxx aluminum alloy. *Metall Mater Trans A Phys Metall Mater Sci* 2019;50:5242–52. <https://doi.org/10.1007/s11661-019-05447-y>.
- [1047] Kumar S, O'Reilly KAQ. Influence of Al grain structure on Fe bearing intermetallics during DC casting of an Al-Mg-Si alloy. *Mater Charact* 2016;120:311–22. <https://doi.org/10.1016/j.matchar.2016.09.017>.
- [1048] Allen CM, O'Reilly KAQ, Cantor B, Evans PV. Intermetallic phase selection in 1XXX Al alloys. *Prog Mater Sci* 1998;43:89–170. [https://doi.org/10.1016/S0079-6425\(98\)00003-6](https://doi.org/10.1016/S0079-6425(98)00003-6).
- [1049] Khalifa W, Samuel FH, Gruzleski JE, Doty HW, Valtierra S. Nucleation of Fe-intermetallic phases in the Al-Si-Fe alloys. *Metall Mater Trans A Phys Metall Mater Sci* 2005;36:1017–32. <https://doi.org/10.1007/s11661-005-0295-9>.
- [1050] Sha G, O'Reilly K, Cantor B, Worth J, Hamerton R. Growth related metastable phase selection in a 6xxx series wrought Al alloy. *Mater Sci Eng A* 2001;304–306:612–6. [https://doi.org/10.1016/S0921-5093\(00\)1545-8](https://doi.org/10.1016/S0921-5093(00)1545-8).
- [1051] Medrano S, Zhao H, De Geuser F, Gault B, Stephenson LT, Deschamps A, et al. Cluster hardening in Al-3Mg triggered by small Cu additions. *Acta Mater* 2018;161:12–20. <https://doi.org/10.1016/j.actamat.2018.08.050>.
- [1052] Engler O, Marioara CD, Hentschel T, Brinkmann HJ. Influence of copper additions on materials properties and corrosion behaviour of Al-Mg alloy sheet. *J Alloys Compd* 2017;710:650–62. <https://doi.org/10.1016/j.jallcom.2017.03.298>.
- [1053] Knight SP, Pohl K, Holroyd NJH, Birbilis N, Rometsch PA, Muddle BC, et al. Some effects of alloy composition on stress corrosion cracking in Al-Zn-Mg-Cu alloys. *Corros Sci* 2015;98:50–62. <https://doi.org/10.1016/j.corsci.2015.05.016>.
- [1054] Polmear IJ, StJohn D, Nie J-F, Qian M. 4 - Wrought Aluminium Alloys. Light Alloy (Fifth Ed 2017;21:1–26. <https://doi.org/10.1016/b978-075066371-7-50007-4>.
- [1055] Liang YH, Shi ZM, Li GW, Zhang RY, Zhao G. Effects of Er addition on the crystallization characteristic and microstructure of Al-2wt%Fe cast alloy. *J Alloys Compd* 2019;781:235–44. <https://doi.org/10.1016/j.jallcom.2018.12.063>.
- [1056] Khalifa W, Samuel FH, Gruzleski JE. Iron intermetallic phases in the Al corner of the Al-Si-Fe system. *Metall Mater Trans A Phys Metall Mater Sci* 2003;34:807–25. <https://doi.org/10.1007/s11661-003-1009-9>.
- [1057] Dorin T, Stanford N, Birbilis N, Gupta RK. Influence of cooling rate on the microstructure and corrosion behavior of Al-Fe alloys. *Corros Sci* 2015;100:396–403. <https://doi.org/10.1016/j.corsci.2015.08.017>.
- [1058] Kim DH, Cantor B. Structure and decomposition behaviour of rapidly solidified Al-Fe alloys. *J Mater Sci* 1994;29:2884–92. <https://doi.org/10.1007/BF01117597>.
- [1059] Chu MG, Granger DA. Solidification and microstructure analysis of rapidly solidified melt-spun Al-Fe alloys. *Metall Trans A* 1990;21:205–12. <https://doi.org/10.1007/BF02656437>.
- [1060] Cotton JD, Kaufman MJ. Microstructural evolution in rapidly solidified Al-Fe alloys: An alternative explanation. *Metall Trans A* 1991;22:927–34. <https://doi.org/10.1007/BF02659002>.
- [1061] Nayak SS, Murty BS, Pabi SK. Structure of nanocomposites of Al-Fe alloys prepared by mechanical alloying and rapid solidification processing. *Bull Mater Sci* 2008;31:449–54. <https://doi.org/10.1007/s12034-008-0070-9>.
- [1062] Nayak SS, Wollgarten M, Banhart J, Pabi SK, Murty BS. Nanocomposites and an extremely hard nanocrystalline intermetallic of Al-Fe alloys prepared by mechanical alloying. *Mater Sci Eng A* 2010;527:2370–8. <https://doi.org/10.1016/j.msea.2009.12.044>.
- [1063] Sasaki TT, Mukai T, Hono K. A high-strength bulk nanocrystalline Al-Fe alloy processed by mechanical alloying and spark plasma sintering. *Scr Mater* 2007;57:189–92. <https://doi.org/10.1016/j.scriptamat.2007.04.010>.
- [1064] Cubero-Sesin JM, Horita Z. Mechanical properties and microstructures of Al-Fe alloys processed by high-pressure torsion. *Metall Mater Trans A Phys Metall Mater Sci* 2012;43:5182–92. <https://doi.org/10.1007/s11661-012-1341-z>.
- [1065] Senkov ON, Froes FH, Stolyarov VV, Valiev RZ, Liu J. Microstructure and microhardness of an Al-Fe alloy subjected to severe plastic deformation and aging. *Nanostructured Mater* 1998;10:691–8. [https://doi.org/10.1016/S0965-9773\(98\)00107-X](https://doi.org/10.1016/S0965-9773(98)00107-X).
- [1066] Duparc OH, Alfred Wilms and the beginnings of Duralumin. *Zeitschrift Fuer Met Res Adv Tech* 2005;96:398–405. <https://doi.org/10.1051/metal:2004157>.
- [1067] Papazian JM. A calorimetric study of precipitation in aluminum alloy 2219. *Mater Trans A* 1981;12:269–80. <https://doi.org/10.1007/BF02655200>.
- [1068] Starink MJ, Wang SC. The thermodynamics of and strengthening due to co-clusters: General theory and application to the case of Al-Cu-Mg alloys. *Acta Mater* 2009;57:2376–89. <https://doi.org/10.1016/j.actamat.2009.01.021>.
- [1069] Styles MJ, Marcea RKW, Bastow TJ, Brand HEA, Gibson MA, Hutchinson CR. The competition between metastable and equilibrium S (Al₂CuMg) phase during the decomposition of AlCuMg alloys. *Acta Mater* 2015;98:64–80. <https://doi.org/10.1016/j.actamat.2015.07.011>.
- [1070] Wang SC, Starink MJ. Precipitates and intermetallic phases in precipitation hardening Al-Cu-Mg-(Li) based alloys. *Int Mater Rev* 2005;50:193–215. <https://doi.org/10.1179/174328005X14357>.
- [1071] Decreus B, Deschamps A, De Geuser F, Donnadieu P, Sigli C, Weyland M. The influence of Cu/Li ratio on precipitation in Al-Cu-Li-x alloys. *Acta Mater* 2013;61:2207–18. <https://doi.org/10.1016/j.actamat.2012.12.041>.

- [1072] Deschamps A, Garcia M, Chevy J, Davo B, De Geuser F. Influence of Mg and Li content on the microstructure evolution of Al[sbnd]Cu[sbnd]Li alloys during long-term ageing. *Acta Mater* 2017;122:32–46. <https://doi.org/10.1016/j.actamat.2016.09.036>.
- [1073] Zabett A, Plumtree A. MICROSTRUCTURAL EFFECTS ON THE SMALL FATIGUE CRACK BEHAVIOUR OF AN ALUMINUM ALLOY PLATE. *Fatigue Fract Eng Mater Struct* 1995;18:801–9. <https://doi.org/10.1111/j.1460-2695.1995.tb00905.x>.
- [1074] Buljac A, Hild F, Helfen L, Morgeneyer TF. On deformation and damage micromechanisms in strong work hardening 2198 T3 aluminium alloy. *Acta Mater* 2018;149:29–45. <https://doi.org/10.1016/j.actamat.2018.01.026>.
- [1075] Cisko AR, Jordon JB, Avery DZ, McClelland ZB, Liu T, Rushing TW, et al. Characterization of fatigue behavior of Al-Li alloy 2099. *Mater Charact* 2019;151:496–505. <https://doi.org/10.1016/j.matchar.2019.03.026>.
- [1076] Meng L, Zheng XL, Tu JP, Liu MS. Effects of deleterious impurities and cerium modification on intrinsic and extrinsic toughening levels of Al-Li based alloys. *Mater Sci Technol* 1998;14:585–91. <https://doi.org/10.1179/mst.1998.14.6.585>.
- [1077] Bron F, Besson J, Pineau A. Ductile rupture in thin sheets of two grades of 2024 aluminum alloy. *Mater Sci Eng A* 2004;380:356–64. <https://doi.org/10.1016/j.msea.2004.04.008>.
- [1078] Bron F, Besson J. Simulation of the ductile tearing for two grades of 2024 aluminum alloy thin sheets. *Eng Fract Mech* 2006;73:1531–52. <https://doi.org/10.1016/j.engfracmech.2006.01.024>.
- [1079] Raghavan V. Al-Cu-Fe (Aluminum-Copper-Iron). *J Phase Equilibria Diffus* 2005;26:59–64. <https://doi.org/10.1007/s11669-005-0061-0>.
- [1080] Gayle FW, Shapiro AJ, Biancaniello FS, Boettinger WJ. The Al-Cu-Fe phase diagram: 0 to 25 At. pct Fe and 50. *Metall Trans A* 1992;23:2409–17. <https://doi.org/10.1007/BF02658044>.
- [1081] Zhao Y, Du W, Koe B, Conolley T, Irvine S, Allan PK, et al. 3D characterisation of the Fe-rich intermetallic phases in recycled Al alloys by synchrotron X-ray microtomography and skeletonisation. *Scr Mater* 2018;146:321–6. <https://doi.org/10.1016/j.scriptamat.2017.12.010>.
- [1082] Sha G, Marceau RKW, Gao X, Muddle BC, Ringer SP. Nanostructure of aluminium alloy 2024: Segregation, clustering and precipitation processes. *Acta Mater* 2011;59:1659–70. <https://doi.org/10.1016/j.actamat.2010.11.033>.
- [1083] Grajna MN, Gancarczyk K, Nowotnicki A, Dychtoni K, Boczkal G. Microstructure and properties of as-cast and heat-treated 2017a aluminium alloy obtained from scrap recycling. *Materials (Basel)* 2021;14:1–25. <https://doi.org/10.3390/ma14010089>.
- [1084] Zhang WW, Lin B, Luo Z, Zhao YL, Li YY. Formation of Fe-rich intermetallic compounds and their effect on the tensile properties of squeeze-cast Al-Cu alloys. *J Mater Res* 2015;30:2474–84. <https://doi.org/10.1557/jmr.2015.215>.
- [1085] Shyam A, Roy S, Shin D, Poplawsky JD, Allard LF, Yamamoto Y, et al. Elevated temperature microstructural stability in cast AlCuMnZr alloys through solute segregation. *Mater Sci Eng A* 2019;765:138279. <https://doi.org/10.1016/j.msea.2019.138279>.
- [1086] Garay-Reyes CG, González-Rodelas L, Cuadros-Lugo E, Martínez-Franco E, Aguilar-Santillan J, Estrada-Guel I, et al. Evaluation of hardness and precipitation in Zn-modified Al2024alloy after plastic deformation and heat treatments. *J Alloys Compd* 2017;705:1–8. <https://doi.org/10.1016/j.jallcom.2017.02.111>.
- [1087] Gumbmann E, Lefebvre W, De Geuser F, Sigli C, Deschamps A. The effect of minor solute additions on the precipitation path of an Al-Cu-Li alloy. *Acta Mater* 2016;115:104–14. <https://doi.org/10.1016/j.actamat.2016.05.050>.
- [1088] Gumbmann E, De Geuser F, Sigli C, Deschamps A. Influence of Mg, Ag and Zn minor solute additions on the precipitation kinetics and strengthening of an Al-Cu-Li alloy. *Acta Mater* 2017;133:172–85. <https://doi.org/10.1016/j.actamat.2017.05.029>.
- [1089] Zhang Y, Weyland M, Milkereit B, Reich M, Rometsch PA. Precipitation of a new platelet phase during the quenching of an Al-Zn-Mg-Cu alloy. *Sci Rep* 2016;6:23109. <https://doi.org/10.1038/srep23109>.
- [1090] Donnadieu P, Shao Y, De Geuser F, Botton GA, Lazar S, Cheynet M, et al. Atomic structure of T-1 precipitates in Al-Li-Cu alloys revisited with HAADF-STEM imaging and small-angle X-ray scattering. *ACTA Mater* 2011;59:462–72. <https://doi.org/10.1016/j.actamat.2010.09.044>.
- [1091] Mondol S, Alam T, Banerjee R, Kumar S, Chattopadhyay K. Development of a high temperature high strength Al alloy by addition of small amounts of Sc and Mg to 2219 alloy. *Mater Sci Eng a-Structural Mater Prop Microstruct Process* 2017;687:221–31. <https://doi.org/10.1016/j.msea.2017.01.037>.
- [1092] Mondol S, Kumar S, Chattopadhyay K. Effect of thermo-mechanical treatment on microstructure and tensile properties of 2219ScMg alloy. *Mater Sci Eng a-Structural Mater Prop Microstruct Process* 2019;759:583–93. <https://doi.org/10.1016/j.msea.2019.05.084>.
- [1093] Lin B, Xu R, Li H, Shi Y, Xiao H, Zhang W. Developing high performance squeeze cast Al-Cu alloys with high Fe and Cu contents. *Int J Cast Met Res* 2019;32:106–13. <https://doi.org/10.1080/13640461.2018.1558559>.
- [1094] Zhang L, Li X, Li R, Jiang R, Zhang R. Effects of high-intensity ultrasound on the microstructures and mechanical properties of ultra-large 2219 Al alloy ingot. *Mater Sci Eng a-Structural Mater Prop Microstruct Process* 2019;763:138154. <https://doi.org/10.1016/j.msea.2019.138154>.
- [1095] Kusoglu IM, Gökce B, Barcikowski S, Goekce B, Barcikowski S. Research trends in laser powder bed fusion of Al alloys within the last decade. *Addit Manuf* 2020;36:101489. <https://doi.org/10.1016/j.addma.2020.101489>.
- [1096] Zhang H, Zhu H, Qi T, Hu Z, Zeng X. Selective laser melting of high strength Al-Cu-Mg alloys: Processing, microstructure and mechanical properties. *Mater Sci Eng a-Structural Mater Prop Microstruct Process* 2016;656:47–54. <https://doi.org/10.1016/j.msea.2015.12.101>.
- [1097] Qi Y, Zhang H, Zhu J, Nie X, Hu Z, Zhu H, et al. Mechanical behavior and microstructure evolution of Al-Cu-Mg alloy produced by laser powder bed fusion: Effect of heat treatment. *Mater Charact* 2020;165:110364. <https://doi.org/10.1016/j.matchar.2020.110364>.
- [1098] Mair P, Kaserer L, Braun J, Weinberger N, Letofsky-Papst I, Leichtfriod G. Microstructure and mechanical properties of a TiB 2-modified Al-Cu alloy processed by laser powder-bed fusion. *Mater Sci Eng a-Structural Mater Prop Microstruct Process* 2021;799:140209. <https://doi.org/10.1016/j.msea.2020.140209>.
- [1099] He H, Yi Y, Huang S, Zhang Y. Effects of deformation temperature on second-phase particles and mechanical properties of 2219 Al-Cu alloy. *Mater Sci Eng a-Structural Mater Prop Microstruct Process* 2018;712:414–23. <https://doi.org/10.1016/j.msea.2017.11.124>.
- [1100] Pasebani S, Charit I, Mishra RS. Effect of tool rotation rate on constituent particles in a friction stir processed 2024Al alloy. *Mater Lett* 2015;160:64–7. <https://doi.org/10.1016/j.matlet.2015.07.074>.
- [1101] Gesing A, Wolanski R. Recycling light metals from end-of-life vehicles. *JOM* 2001;53:21–3. <https://doi.org/10.1007/s11837-001-0188-3>.
- [1102] Das SK, Green JAS, Kaufman JG. Application of the recycling indices to the identification of recycle friendly aluminum alloys. *Phinix Glob Responsab Resour Manag* 2007;1–21.
- [1103] Cui J, Roven HJ. Recycling of automotive aluminum. *Trans Nonferrous Met Soc China (English Ed)* 2010;20:2057–63. [https://doi.org/10.1016/S1003-6326\(09\)60417-9](https://doi.org/10.1016/S1003-6326(09)60417-9).
- [1104] Werheit P, Fricke-Begemann C, Gesing M, Noll R. Fast single piece identification with a 3D scanning LIBS for aluminium cast and wrought alloys recycling. *J Anal At Spectrom* 2011;26:2166–74. <https://doi.org/10.1039/c1ja10096c>.
- [1105] Engler O, Kuhnke K, Hasenclever J. Development of intermetallic particles during solidification and homogenization of two AA 5xxx series Al-Mg alloys with different Mg contents. *J Alloys Compd* 2017;728:669–81. <https://doi.org/10.1016/j.jallcom.2017.09.060>.
- [1106] Kang J, Wilkinson DS, Malakhov DV, Halim H, Jain M, Embury JD, et al. Effect of processing route on the spatial distributions of constituent particles and their role in the fracture process in AA5754 alloy sheet materials. *Mater Sci Eng A* 2007;456:85–92. <https://doi.org/10.1016/j.msea.2006.12.052>.
- [1107] Bale CW, Chartrand P, Degterov SA, Eriksson G, Hack K, Ben Mahfoud R, et al. FactSage thermochemical software and databases. *Calphad* 2002;26:189–228. [https://doi.org/10.1016/S0364-5916\(02\)00035-4](https://doi.org/10.1016/S0364-5916(02)00035-4).
- [1108] FItite - the FACT Light Metal Alloy Database n.d. www.factsage.com/facthelp/FSNew_Databases.htm.
- [1109] Alil A, Popović M, Radetić T, Zrilić M, Romhanji E. Influence of annealing temperature on the baking response and corrosion properties of an Al-4.6 wt% Mg alloy with 0.54 wt% Cu. *J Alloys Compd* 2015;625:76–84. <https://doi.org/10.1016/j.jallcom.2014.11.063>.
- [1110] Carroll MC, Gouma PI, Daehn GS, Mills MJ. Effects of minor Cu additions on a Zn-modified Al-5083 alloy. *Mater Sci Eng A* 2001;319–321:425–8. [https://doi.org/10.1016/S0921-5093\(00\)02021-9](https://doi.org/10.1016/S0921-5093(00)02021-9).
- [1111] Sukiman NL, Gupta RK, Buchheit RG, Birbilis N. Influence of microalloying additions on Al-Mg alloy. Part 1: Corrosion and electrochemical response. *Corros Eng Sci Technol* 2014;49:254–62. <https://doi.org/10.1179/1743278213Y.0000000128>.
- [1112] Sukiman NL, Gupta RK, Zhang R, Buchheit RG, Birbilis N. Influence of microalloying additions on Al-Mg alloy. Part 2: Phase analysis and sensitization behaviour. *Corros Eng Sci Technol* 2014;49:263–8. <https://doi.org/10.1179/1743278213Y.0000000129>.

- [1113] Li X, Xia W, Yan H, Chen J, Li X. Improving strength and corrosion resistance of high Mg alloyed Al–Mg–Mn alloys through Ce addition. *Corros Eng Sci Technol* 2020;55:381–91. <https://doi.org/10.1080/1478422X.2020.1735716>.
- [1114] Gruber B, Grabner F, Falkinger G, Schökel A, Spieckermann F, Uggowitzer PJ, et al. Room temperature recovery of cryogenically deformed aluminium alloys. *Mater Des* 2020;193:108819. <https://doi.org/10.1016/j.matdes.2020.108819>.
- [1115] Aboulfadl H, Deges J, Choi P, Raabe D. Dynamic strain aging studied at the atomic scale. *Acta Mater* 2015;86:34–42. <https://doi.org/10.1016/j.actamat.2014.12.028>.
- [1116] Campbell J. An overview of the effects of bimetallic compounds on the structure and properties of cast alloys. *Metall Mater Trans B Process Metall Mater Process Sci* 2006;37: 857–63. <https://doi.org/10.1007/BF02735006>.
- [1117] Das S, Heyen M, Ho J, Son C. Effect of processing parameters on the formability of recycle friendly AA5754 alloy. *MATEC Web Conf* 2020;326:03005. <https://doi.org/10.1051/matecconf/202032603005>.
- [1118] Que Z, Wang Y, Fan Z. Formation of the Fe-containing intermetallic compounds during solidification of Al–5Mg–2Si–0.7Mn–1.1Fe alloy. *Metall Mater Trans A Phys Metall Mater Sci* 2018;49:2173–81. <https://doi.org/10.1007/s11661-018-4591-6>.
- [1119] Liu Y, Huang G, Sun Y, Zhang L, Huang Z, Wang J, et al. Effect of Mn and Fe on the formation of Fe- and Mn-rich intermetallics in al–5Mg–Mn alloys solidified under near-rapid cooling. *Materials (Basel)* 2016;9:88. <https://doi.org/10.3390/ma9020088>.
- [1120] Liu Y, Luo L, Han C, Ou L, Wang J, Liu C. Effect of Fe, Si and cooling rate on the formation of Fe- and Mn-rich intermetallics in Al–5Mg–0.8Mn alloy. *J Mater Sci Technol* 2016;32:305–12. <https://doi.org/10.1016/j.jmst.2015.10.010>.
- [1121] Liu Y, Sun Y, Zhang L, Zhao Y, Wang J, Liu C. Microstructure and Mechanical Properties of Al–5Mg–0.8Mn Alloys with Various Contents of Fe and Si Cast under Near-Rapid Cooling. *Metals (Basel)* 2017;7:428. Doi: 10.3390/met7100428.
- [1122] Peterson RD. Recycling of automotive wrought alloys. *Light Met*. 2015, John Wiley & Sons, Inc.; 2015, p. 1023–8. Doi: 10.1002/9781119093435.ch172.
- [1123] Que Z, Wang Y, Mendis CL. Heterogeneous nucleation of α -Al on naturally formed MgAl₂O₄ particles during solidification of Al–Mg–Si–Fe–Mn alloys. *Materialia* 2020;14:100900. <https://doi.org/10.1016/j.mtla.2020.100900>.
- [1124] Que Z, Mendis CL. Heterogeneous nucleation and phase transformation of Fe-rich intermetallic compounds in Al–Mg–Si alloys. *J Alloys Compd* 2020;836: 155515. <https://doi.org/10.1016/j.jallcom.2020.155515>.
- [1125] Que Z, Wang Y, Fan Z. Heterogeneous nucleation of eutectic structure in Al–Mg–Si alloys. *Metall Mater Trans A Phys Metall Mater Sci* 2020;51:2697–702. <https://doi.org/10.1007/s11661-020-05735-y>.
- [1126] Que ZP, Zhou YP, Wang Y, Fan Z. Effect of MgO on phase selection in Al–Mg–Si–Fe–Mn alloys. *Trans Indian Inst Met* 2015;68:1167–72. <https://doi.org/10.1007/s12666-015-0664-z>.
- [1127] Que ZP, Wang Y, Zhou YP, Liu L, Fan Z. Effect of Al–5Ti–1B grain refiner addition on the formation of intermetallic compounds in Al–Mg–Si–Mn–Fe alloys. *Mater. Sci. Forum*, vol. 828–829, Trans Tech Publications, Ltd.; 2015, p. 53–7. Doi: 10.4028/www.scientific.net/MSF.828-829.53.
- [1128] Liu C, Jiao X, Nishat H, Akhtar S, Wiesner S, Guo Z, et al. Characteristics of Fe-rich intermetallic compounds and their influence on the cracking behavior of a newly developed high-pressure die cast Al–4Mg–2Fe alloy. *J Alloys Compd* 2021;854:157121. <https://doi.org/10.1016/j.jallcom.2020.157121>.
- [1129] Algendy AY, Liu K, Chen X-G. Formation of intermetallic phases during solidification in Al–Mg–Mn 5xxx alloys with various Mg levels. *MATEC Web Conf* 2020;326:02002. <https://doi.org/10.1051/matecconf/202032602002>.
- [1130] Que Z, Zhou Y, Wang Y, Mendis CL, Fan Z. Effects of Mg addition on the Al₆(Fe, Mn) intermetallic compounds and the grain refinement of α -Al in Al–Fe–Mn alloys. *Mater Charact* 2020. <https://doi.org/10.1016/j.matchar.2020.110758>.
- [1131] Li YJ, Arnborg L. Solidification structures and phase selection of iron-bearing eutectic particles in a DC-cast AA5182 alloy. *Acta Mater* 2004;52:2673–81. <https://doi.org/10.1016/j.actamat.2004.02.015>.
- [1132] Li YJ, Arnborg L. A eutectoid phase transformation for the primary intermetallic particle from Al_m(Fe, Mn) to Al₃(Fe, Mn) in AA5182 alloy. *Acta Mater* 2004; 52:2945–52. <https://doi.org/10.1016/j.actamat.2004.02.041>.
- [1133] Engler O, Kuhnke K, Westphal K, Hasenclever J. Impact of chromium on the microchemistry evolution during solidification and homogenization of the Al–Mg alloy AA 5002. *J Alloys Compd* 2018;744:561–73. <https://doi.org/10.1016/j.jallcom.2018.02.125>.
- [1134] Banhart J, Lay MDH, Chang CST, Hill AJ. Kinetics of natural aging in Al–Mg–Si alloys studied by positron annihilation lifetime spectroscopy. *Phys Rev B - Condens Matter Mater Phys* 2011;83. <https://doi.org/10.1103/PhysRevB.83.014101>.
- [1135] Marioara CD, Andersen SJ, Jansen J, Zandbergen HW. The influence of temperature and storage time at RT on nucleation of the β'' phase in a 6082 Al–Mg–Si alloy. *Acta Mater* 2003;51:789–96. [https://doi.org/10.1016/S1359-6454\(02\)00470-6](https://doi.org/10.1016/S1359-6454(02)00470-6).
- [1136] Lu H, Zhang J, Tian N, Song X, Ma M, Lu G. Recycle-friendly aluminum alloy sheets for automotive applications based on hemming. *Automot Innov* 2018;1: 70–5. <https://doi.org/10.1007/s42154-018-0012-1>.
- [1137] Kuijpers NCW, Kool WH, Koenis PTG, Nilsen KE, Todd I, Van der Zwaag S. Assessment of different techniques for quantification of α -Al(FeMn)Si and β -AlFeSi intermetallics in AA 6xxx alloys. *Mater Charact* 2002;49:409–20. [https://doi.org/10.1016/S1044-5803\(03\)00036-6](https://doi.org/10.1016/S1044-5803(03)00036-6).
- [1138] Kuijpers NCW, Vermolen FJ, Vuik K, Van Der Zwaag S. A model of the β -AlFeSi to α -Al(FeMn)Si transformation in Al–Mg–Si alloys. *Mater Trans* 2003;44: 1448–56. <https://doi.org/10.2320/matertrans.44.1448>.
- [1139] Kuijpers NCW, Vermolen FJ, Vuik C, Koenis PTG, Nilsen KE, van der Zwaag S. The dependence of the β -AlFeSi to α -Al(FeMn)Si transformation kinetics in Al–Mg–Si alloys on the alloying elements. *Mater Sci Eng A* 2005;394:9–19. <https://doi.org/10.1016/j.msea.2004.09.073>.
- [1140] Wang Y, Deng Y, Zhang J, Zhao J, Zhang Y. Eliminating microstructural defects and improving the mechanical and fatigue properties of an Al–Mg–Si alloy extrusion by optimising homogenisation. *Mater Sci Eng A* 2019;764. Doi: 10.1016/j.msea.2019.138188.
- [1141] Wang Y, Deng Y, Dai Q, Jiang K, Chen J, Guo X. Microstructures and strengthening mechanisms of high Fe containing Al–Mg–Si–Mn–Fe alloys with Mg, Si and Mn modified. *Mater Sci Eng A* 2021;803:140477. <https://doi.org/10.1016/j.msea.2020.140477>.
- [1142] Bjurenstedt A, Seifeddine S, Jarfors AEW. The effects of fe-particles on the tensile properties of Al–Si–Cu alloys. *Metals (Basel)* 2016;6.. <https://doi.org/10.3390/met6120314>.
- [1143] Cao X, Campbell J. Morphology of β -Al₅FeSi phase in Al–Si cast alloys. *Mater Trans* 2006;47:1303–12. <https://doi.org/10.2320/matertrans.47.1303>.
- [1144] Ashtari P, Tezuka H, Sato T. Influence of Sr and Mn additions on intermetallic compound morphologies in Al–Si–Cu–Fe cast alloys. *Mater Trans* 2003;44: 2611–6. <https://doi.org/10.2320/matertrans.44.2611>.
- [1145] Sha G, O'Reilly KAQ, Cantor B, Titchmarsh JM, Hamerton RG. Quasi-peritectic solidification reactions in 6xxx series wrought Al alloys. *Acta Mater* 2003;51: 1883–97. [https://doi.org/10.1016/S1359-6454\(02\)00595-5](https://doi.org/10.1016/S1359-6454(02)00595-5).
- [1146] Al-Helal K, Patel JB, Fan Z. Fe-rich intermetallic formation and mechanical properties of recycled AA6111 alloy strips produced by melt conditioning twin roll casting. *JOM* 2020;72:3753–9. <https://doi.org/10.1007/s11837-020-04324-z>.
- [1147] Wang D, Zhang H, Nagamui H, Li X, Cui J. Microstructural refinement and α -dispersoid evolution in direct-chill cast Al–Mg–Si–Fe alloy. *Adv Eng Mater* 2020; 22. Doi: 10.1002/adem.202000517.
- [1148] Nagamui H, Suzuki S, Okane T, Umeda T. Effect of iron content on hot tearing of high-strength Al–Mg–Si alloy. *Mater Trans* 2006;47:2821–7. <https://doi.org/10.2320/matertrans.47.2821>.
- [1149] Sweet L, Easton MA, Taylor JA, Grandfield JF, Davidson CJ, Lu L, et al. Hot tear susceptibility of Al–Mg–Si–Fe alloys with varying iron contents. *Mater Trans A Phys Metall Mater Sci*, vol. 44, 2013, p. 5396–407. Doi: 10.1007/s11661-012-1562-1.
- [1150] Sree SM, Barekar NS, Lazaro-Nebreda J, Patel JB, Fan Z. In-situ microstructural control of A6082 alloy to modify second phase particles by melt conditioned direct chill (MC-DC) casting process – A novel approach. *J Mater Process Technol* 2021;295:117170. <https://doi.org/10.1016/j.jmatprotec.2021.117170>.
- [1151] Kairy SK, Rometsch PA, Diaz K, Nie JF, Davies CHJ, Birbilis N. Exploring the electrochemistry of 6xxx series aluminium alloys as a function of Si to Mg ratio, Cu content, ageing conditions and microstructure. *Electrochim Acta* 2016;190:92–103. <https://doi.org/10.1016/j.electacta.2015.12.098>.
- [1152] Svenningsen G, Larsen MH, Walmsley JC, Nordlien JH, Nisancioglu K. Effect of artificial aging on intergranular corrosion of extruded AlMgSi alloy with small Cu content. *Corros Sci* 2006;48:1528–43. <https://doi.org/10.1016/j.corsci.2005.05.045>.
- [1153] Apple Inc. Recycled Aluminum Alloys From Manufacturing Scrap With Cosmetic Appeal, 2020.

- [1154] Zhu H, Zhang X, Couper MJ, Dahle AK. Effect of initial microstructure on surface appearance of anodized aluminum extrusions. *Metall Mater Trans A Phys Metall Mater Sci* 2009;40:3264–75. <https://doi.org/10.1007/s11661-009-9976-0>.
- [1155] Grubbs CA. Anodizing of aluminum. *Met Finish* 2007;105:397–412. [https://doi.org/10.1016/S0026-0576\(07\)80359-X](https://doi.org/10.1016/S0026-0576(07)80359-X).
- [1156] Ibrahim MF, Garza-Elizondo GH, Samuel AM, Samuel FH. Optimizing the heat treatment of high-strength 7075-type wrought alloys: A metallographic study. *Int J Met* 2016;10:264–75. <https://doi.org/10.1007/s40962-016-0038-2>.
- [1157] Kaufman JG. Applications for aluminum alloys and tempers. *Introd to Alum Alloy tempers*, ASM International 2000:242. <https://doi.org/10.1361/iaat2000p087>.
- [1158] Das SK. *Recycling aluminum aerospace alloys*. *Adv Mater Process* 2008;166:34–5.
- [1159] Lu H, Hou Z, Ma M, Lu G. Effect of Fe-content on the mechanical properties of recycled Al alloys during hot compression. *Metals (Basel)* 2017;7:262. <https://doi.org/10.3390/met7070262>.
- [1162] Knott JF. Fracture resistance in aluminium. In: Lumley R, editor. *Fundam. Alum. Metall. Prod. Process. Appl.*, Woodhead Publishing Limited; 2010, p. 538–73. Doi: 10.1533/9780857090256.2.538.
- [1163] Singh SS, Guo E, Xie H, Chawla N. Mechanical properties of intermetallic inclusions in Al 7075 alloys by micropillar compression. *Intermetallics* 2015;62: 69–75. <https://doi.org/10.1016/j.intermet.2015.03.008>.
- [1164] Chemin A, Marques D, Bisanha L, Moreto A de J, Boe Filho WW, Ruchert COF. Influence of Al7Cu2Fe intermetallic particles on the localized corrosion of high strength aluminum alloys. *Mater Des* 2014;53:118–23. Doi: 10.1016/j.matdes.2013.07.003.
- [1165] Fan X, Jiang D, Meng Q, Zhong L. The microstructural evolution of an Al-Zn-Mg-Cu alloy during homogenization. *Mater Lett* 2006;60:1475–9. <https://doi.org/10.1016/j.matlet.2005.11.049>.
- [1166] Huang S, Zhang X, He K, Zhou W, Zheng X. Microstructural evolution in DC cast aluminum alloy Al-6.3Zn-2.3Mg-2.2Cu-0.1Zr ingot during homogenization and subsequent cooling. *AIP Conf Proc* 2017;1794:020031. <https://doi.org/10.1063/1.4971913>.
- [1167] ZOU X liang, YAN H, CHEN X hui. Evolution of second phases and mechanical properties of 7075 Al alloy processed by solution heat treatment. *Trans Nonferrous Met Soc China* (English Ed) 2017;27:2146–55. Doi: 10.1016/S1003-6326(17)60240-1.
- [1168] Gupta VK, Agnew SR. Fatigue crack surface crystallography near crack initiating particle clusters in precipitation hardened legacy and modern Al-Zn-Mg-Cu alloys. *Int J Fatigue* 2011;33:1159–74. <https://doi.org/10.1016/j.ijfatigue.2011.01.018>.
- [1169] Wang L, Yu H, Lee YS, Kim MS, Kim HW. Effect of microstructure on hot tensile deformation behavior of 7075 alloy sheet fabricated by twin roll casting. *Mater Sci Eng A* 2016;652:221–30. <https://doi.org/10.1016/j.msea.2015.11.079>.
- [1170] I) Sakaguchi N. Hot Tearing in DC Casting Ingot of 7XXX Aluminum Alloys. *Light Met*. 2016, Hoboken, NJ, USA: John Wiley & Sons, Inc.; 2016, p. 651–6. Doi: 10.1002/978111927480.ch109.
- [1171] Martin JH, Yahata BD, Hundley JM, Mayer JA, Schaeder TA, Pollock TM. 3D printing of high-strength aluminium alloys. *Nature* 2017;549:365–9. <https://doi.org/10.1038/nature23894>.
- [1172] Opprecht M, Garandet JP, Roux G, Flameni C, Soulier M. A solution to the hot cracking problem for aluminium alloys manufactured by laser beam melting. *Acta Mater* 2020;197:40–53. <https://doi.org/10.1016/j.actamat.2020.07.015>.
- [1173] Zhou SY, Su Y, Wang H, Enz J, Ebel T, Yan M. Selective laser melting additive manufacturing of 7xxx series Al-Zn-Mg-Cu alloy: Cracking elimination by co-incorporation of Si and TiB₂. *Addit Manuf* 2020;36:101458. <https://doi.org/10.1016/j.addma.2020.101458>.
- [1174] Grosselle F, Timelli G, Bonollo F. Doe applied to microstructural and mechanical properties of Al-Si-Cu-Mg casting alloys for automotive applications. *Mater Sci Eng A* 2010;527:3536–45. <https://doi.org/10.1016/j.msea.2010.02.029>.
- [1175] Duchaussay A. Déformation intense d' alliages d' aluminium à durcissement structural : mécanismes de précipitation et comportement mécanique. Normandie Université, 2020.
- [1176] Duchaussay A, Sauvage X, Edalati K, Horita Z, Renou G, Deschamps A, et al. Structure and mechanical behavior of ultrafine-grained aluminum-iron alloy stabilized by nanoscaled intermetallic particles. *Acta Mater* 2019;167:89–102. <https://doi.org/10.1016/j.actamat.2019.01.027>.
- [1177] 81 Reza A, Zhou J, Duszczuk J. Microstructural Evolution During the Homogenization of Al-Zn-Mg Aluminum Alloys. In: Ahmad Z, editor. *Recent Trends Process. Degrad. Alum. Alloy.* 2. Edition, InTech; 2011, p. 477–516. Doi: 10.5772/34695.
- [1178] Chen S, Li J, Hu G yun, Chen K, Huang L. Effect of Zn/Mg ratios on SCC, electrochemical corrosion properties and microstructure of Al-Zn-Mg alloy. *J Alloys Compd* 2018;757:259–64. Doi: 10.1016/j.jallcom.2018.05.063.
- [1179] Clinch MR, Harris SJ, Hepples W, Holroyd NJH, Lawday MJ, Noble B. Influence of zinc to magnesium ratio and total solute content on the strength and toughness of 7xxx series alloys. *Mater Sci Forum* 2006;519–521:339–44. <https://doi.org/10.4028/www.scientific.net/msf.519-521.339>.
- [1180] Liao Y guo, Han X qi, Zeng M xia, Jin M. Influence of Cu on microstructure and tensile properties of 7XXX series aluminum alloy. *Mater Des* 2015;66:581–6. Doi: 10.1016/j.matdes.2014.05.003.
- [1181] Wang S-S, Huang I-W, Yang L, Jiang J-T, Chen J-F, Dai S-L, et al. Effect of Cu content and aging conditions on pitting corrosion damage of 7xxx series aluminum alloys. *J Electrochem Soc* 2015;162:C150–60. <https://doi.org/10.1149/2.0301504jes>.
- [1182] Sheppard T. Extrusion of aluminium alloys. vol. 53. Boston, MA: Springer US; 1999. Doi: 10.1007/978-1-4757-3001-2.
- [1183] Wang G, Zhao Z, Guo Q, Cui J. Effect of homogenizing treatment on microstructure and conductivity of 7075 aluminum alloy prepared by low frequency electromagnetic casting. *China Foundry* 2014;11:39–45.
- [1184] Wang L, Xu D, Rometsch PA, Gao SX, Zhang Y, He Z, et al. Effect of homogenisation parameters on dissolution and precipitation in aluminium alloy AA7150. *Mater Sci Forum* 2011;693:276–81. <https://doi.org/10.4028/www.scientific.net/MSF.693.276>.
- [1185] El-Shenawy M, Omar AA, Masoud MI. Effect of Cu and Mg contents on similar and dissimilar welding of 7XXX series aluminum alloys. *AEJ - Alexandria Eng J* 2005;44:715–29.
- [1186] Guo Z, Zhao G, Chen XG. Effects of two-step homogenization on precipitation behavior of Al3Zr dispersoids and recrystallization resistance in 7150 aluminum alloy. *Mater Charact* 2015;102:122–30. <https://doi.org/10.1016/j.matchar.2015.02.016>.
- [1187] Sanders RE, Farnsworth DM. Trends in aluminum materials usage for electronics. *JOM* 2011;63:12–5. <https://doi.org/10.1007/s11837-011-0165-4>.
- [1188] Ford S, Despeisse M. Additive manufacturing and sustainability: an exploratory study of the advantages and challenges. *J Clean Prod* 2016;137:1573–87. <https://doi.org/10.1016/j.jclepro.2016.04.150>.
- [1189] Niaki MK, Torabi SA, Nonino F. Why manufacturers adopt additive manufacturing technologies: The role of sustainability. *J Clean Prod* 2019;222:381–92. <https://doi.org/10.1016/j.jclepro.2019.03.019>.
- [1190] Aboulkhair NT, Simonelli M, Parry L, Ashcroft I, Tuck C, Hague R. 3D printing of aluminium alloys: additive manufacturing of aluminium alloys using selective laser melting. *Prog Mater Sci* 2019;106:100578. <https://doi.org/10.1016/j.pmatsci.2019.100578>.
- [1191] Ngo TD, Kashani A, Imbalzano G, Nguyen KTQ, Hui D. Additive manufacturing (3D printing): A review of materials, methods, applications and challenges. *Compos Part B Eng* 2018;143:172–96. <https://doi.org/10.1016/j.compositesb.2018.02.012>.
- [1192] Wimpenny DI, Pandey PM, Jyothish Kumar L. Advances in 3D Printing & additive manufacturing technologies. 2016. Doi: 10.1007/978-981-10-0812-2.
- [1193] Faludi J, Baumers M, Maskery I, Hague R. Environmental impacts of selective laser melting: do printer, powder, or power dominate? *J Ind Ecol* 2017;21: S144–56. <https://doi.org/10.1111/jiec.12528>.
- [1194] Aversa A, Marchese G, Saboori A, Bassini E, Manfredi D, Biamino S, et al. New aluminum alloys specifically designed for laser powder bed fusion: A review. *Materials (Basel)* 2019;12. Doi: 10.3390/ma12071007.
- [1195] Priarone PC, Lunetto V, Atzeni E, Salmi A. Laser powder bed fusion (L-PBF) additive manufacturing: On the correlation between design choices and process sustainability. *Procedia CIRP*, vol. 78, Elsevier B.V.; 2018, p. 85–90. Doi: 10.1016/j.procir.2018.09.058.
- [1196] Vock S, Klöden B, Kirchner A, Weißgärtner B, Kieback B. Powders for powder bed fusion: a review. *Prog Addit Manuf* 2019;4:383–97. <https://doi.org/10.1007/s40964-019-00078-6>.
- [1197] Lutter-Günther M, Gebbe C, Kampf T, Seidel C, Reinhart G. Powder recycling in laser beam melting: strategies, consumption modeling and influence on resource efficiency. *Prod Eng* 2018;12:377–89. <https://doi.org/10.1007/s11740-018-0790-7>.

- [1198] Santecchia E, Spigarelli S, Cabibbo M. Material reuse in laser powder bed fusion: Side effects of the laser—metal powder interaction. *Metals* (Basel) 2020;10:1–21. <https://doi.org/10.3390/met10030341>.
- [1199] Yin J, Wang D, Yang L, Wei H, Dong P, Ke L, et al. Correlation between forming quality and spatter dynamics in laser powder bed fusion. *Addit Manuf* 2020;31:100958. <https://doi.org/10.1016/j.addma.2019.100958>.
- [1200] Young ZA, Guo Q, Parab ND, Zhao C, Qu M, Escano LI, et al. Types of spatter and their features and formation mechanisms in laser powder bed fusion additive manufacturing process. *Addit Manuf* 2020;36:101438. <https://doi.org/10.1016/j.addma.2020.101438>.
- [1201] Simonelli M, Tuck C, Aboulkhair NT, Maskery I, Ashcroft I, Wildman RD, et al. A study on the laser spatter and the oxidation reactions during selective laser melting of 316L stainless steel, Al-Si10-Mg, and Ti-6Al-4V. *Metall Mater Trans A Phys Metall Mater Sci* 2015;46:3842–51. <https://doi.org/10.1007/s11661-015-2882-8>.
- [1202] Sutton AT, Kriewall CS, Leu MC, Newkirk JW, Brown B. Characterization of laser spatter and condensate generated during the selective laser melting of 304L stainless steel powder. *Addit Manuf* 2020;31:100904. <https://doi.org/10.1016/j.addma.2019.100904>.
- [1203] Bajaj P, Wright J, Todd I, Jägle EA. Predictive process parameter selection for selective laser melting manufacturing: applications to high thermal conductivity alloys. *Addit Manuf* 2019;27:246–58. <https://doi.org/10.1016/j.addma.2018.12.003>.
- [1204] Khairallah SA, Anderson AT, Rubenckier AM, King WE. Laser powder-bed fusion additive manufacturing: Physics of complex melt flow and formation mechanisms of pores, spatter, and denudation zones. *Addit Manuf Handb Prod Dev Def Ind* 2017;54:613–28. <https://doi.org/10.1201/9781315119106>.
- [1205] Dowling L, Kennedy J, O'Shaughnessy S, Trimble D. A review of critical repeatability and reproducibility issues in powder bed fusion. *Mater Des* 2020;186:108346. <https://doi.org/10.1016/j.matdes.2019.108346>.
- [1206] Wei LC, Ehrlich LE, Powell-Palm MJ, Montgomery C, Beuth J, Malen JA. Thermal conductivity of metal powders for powder bed additive manufacturing. *Addit Manuf* 2018;21:201–8. <https://doi.org/10.1016/j.addma.2018.02.002>.
- [1207] Swift DL. The thermal conductivity of spherical metal powders including the effect of an oxide coating. *Int J Heat Mass Transf* 1966;9:1061–74. [https://doi.org/10.1016/0017-9310\(66\)90028-7](https://doi.org/10.1016/0017-9310(66)90028-7).
- [1208] Tradowsky U, White J, Ward RM, Read N, Reimers W, Attallah MM. Selective laser melting of AlSi10Mg: Influence of post-processing on the microstructural and tensile properties development. *Mater Des* 2016;105:212–22. <https://doi.org/10.1016/j.matdes.2016.05.066>.
- [1209] Del Re F, Contaldi V, Astarita A, Palumbo S, Squillace A, Corrado P, et al. Statistical approach for assessing the effect of powder reuse on the final quality of AlSi10Mg parts produced by laser powder bed fusion additive manufacturing. *Int J Adv Manuf Technol* 2018;97:2231–40. <https://doi.org/10.1007/s00170-018-2090-y>.
- [1210] Asgari H, Baxter C, Hosseinkhani K, Mohammadi M. On microstructure and mechanical properties of additively manufactured AlSi10Mg_200C using recycled powder. *Mater Sci Eng A* 2017;707:148–58. <https://doi.org/10.1016/j.msea.2017.09.041>.
- [1211] Hadadzadeh A, Baxter C, Amirkhiz BS, Mohammadi M. Strengthening mechanisms in direct metal laser sintered AlSi10Mg: Comparison between virgin and recycled powders. *Addit Manuf* 2018;23:108–20. <https://doi.org/10.1016/j.addma.2018.07.014>.
- [1212] Maamoun AH, Elbestawi M, Dosbaeva GK, Veldhuis SC. Thermal post-processing of AlSi10Mg parts produced by Selective Laser Melting using recycled powder. *Addit Manuf* 2018;21:234–47. <https://doi.org/10.1016/j.addma.2018.03.014>.
- [1213] Bambach MD, Bambach M, Sviridov A, Weiss S. New process chains involving additive manufacturing and metal forming - A chance for saving energy? *Procedia Eng.*, vol. 207, Elsevier B.V.; 2017, p. 1176–81. Doi: 10.1016/j.proeng.2017.10.1049.
- [1214] Yamasaki S, Okuhira T, Mitsuhashi M, Nakashima H, Kusui J, Adachi M. Effect of Fe addition on heat-resistant aluminum alloys produced by selective laser melting. *Metals* (Basel) 2019;9:468. <https://doi.org/10.3390/met9040468>.
- [1215] Gable BM, Shiflet GJ, Starke EA. The effect of Si additions on Ω precipitation in Al-Cu-Mg-(Ag) alloys. *Scr Mater* 2004;50:149–53. <https://doi.org/10.1016/j.scriptamat.2003.09.004>.
- [1216] Jägle EA, Sheng Z, Wu L, Lu L, Risse J, Weisheit A, et al. Precipitation reactions in age-hardenable alloys during laser additive manufacturing. *Jom* 2016;68:943–9. <https://doi.org/10.1007/s11837-015-1764-2>.
- [1217] Froes FH, Kim YW, Krishnamurthy S. Rapid solidification of lightweight metal alloys. *Mater Sci Eng A* 1989;117:19–32. [https://doi.org/10.1016/0921-5093\(89\)90082-8](https://doi.org/10.1016/0921-5093(89)90082-8).
- [1218] Grosselle F, Timelli G, Bonollo F, Tiziani A, Della Corte E. Correlation between microstructure and mechanical properties of Al-Si cast alloys. *Metall Ital* 2009;101:25–32.
- [1219] Sun S, Zheng L, Liu Y, Liu J, Zhang H. Characterization of Al-Fe-V-Si heat-resistant aluminum alloy components fabricated by selective laser melting. *J Mater Res* 2015;30:1661–9. <https://doi.org/10.1557/jmr.2015.110>.
- [1220] Kaufmann H, Fragner W, Suppan H, Spierings AB, Uggowitzer P, Schubert A, et al. Starting Material, use thereof, and additive manufacturing process using said starting materials, US 2020/0149136 A1, 2020.
- [1221] Moorehead C. All rights reserved Index Censorsh 1997;26:203–8. <https://doi.org/10.1177/030642209702600329>.
- [1222] Sun SB, Zheng LJ, Liu JH, Zhang H. Microstructure, cracking behavior and control of Al-Fe-V-Si alloy produced by selective laser melting. *Rare Met* 2017;1–10. <https://doi.org/10.1007/s12598-016-0846-9>.
- [1223] European Aluminium. The aluminium automotive manual - Applications – Car body – Hang-on parts. Https://WwwEuropean-AluminiumEu/Media/1547/3_aam_hang-on-PartsPdf.
- [1224] Das SK, Green JAS, Kaufman JG. Application of the recycling indices to the indefatigation of recycle frendly aluminium alloys. 2007.
- [1225] Müller Robin M. Entwicklung einer duktilitätsoptimierten Aluminium-Druckgusslegierung für Karosserieanwendungen. PhD thesis. University of Erlangen-Nürnberg; 2019.
- [1226] Read N, Wang W, Essa K, Attallah MM. Selective laser melting of AlSi10Mg alloy: Process optimisation and mechanical properties development. *Mater Des* 2015;65:417–24. <https://doi.org/10.1016/j.matdes.2014.09.044>.
- [1227] Louvis E, Fox P, Sutcliffe CJ. Selective laser melting of aluminium components. *J Mater Process Technol* 2011;211:275–84. <https://doi.org/10.1016/j.jmatprotec.2010.09.019>.
- [1228] Pogatscher S, Stemper L, Uggowitzer PJ, Fragner W. Crossover-Legierungen: Aushärtung und Verformungspotenzial. In: Chimani CM, Uggowitzer PJ, Österreicher JA, editors. 11. Ranshofener Leichtmetalltage, 2020, p. 7–12.
- [1229] Naronikar AH, Jamadagni HNA, Simha A, Saikiran B. Optimizing the heat treatment parameters of Al-6061 required for better formability. *Mater Today Proc* 2018;5:24240–7. <https://doi.org/10.1016/j.mtpr.2018.10.219>.
- [1230] Zhong H, Rometsch PA, Wu X, Cao L, Estrin Y. Influence of pre-ageing on the stretch formability of Al-Mg-Si automotive sheet alloys. *Mater Sci Eng A* 2017;697:79–85. <https://doi.org/10.1016/j.msea.2017.05.009>.
- [1231] Zhong H, Rometsch PA, Cao L, Estrin Y. The influence of Mg/Si ratio and Cu content on the stretch formability of 6xxx aluminium alloys. *Mater Sci Eng A* 2016;651:688–97. <https://doi.org/10.1016/j.msea.2015.11.016>.
- [1232] Hino M, Koga S, Oie S, Yanagawa M. Properties of Al-Mg based alloys for automobile body panel. *Kobelco Technol Rev* 1991;1–5.
- [1233] Ratchev P, Verlinden B, De Smet P, Van Houtte P. Precipitation hardening of an Al-4.2 wt% Mg-0.6 wt% Cu alloy. *Acta Mater* 1998;46:3523–33. [https://doi.org/10.1016/S1359-6454\(98\)00033-0](https://doi.org/10.1016/S1359-6454(98)00033-0).
- [1234] Meng C, Zhang D, Cui H, Zhuang L, Zhang J. Mechanical properties, intergranular corrosion behavior and microstructure of Zn modified Al-Mg alloys. *J Alloys Compd* 2014;617:925–32. <https://doi.org/10.1016/j.jallcom.2014.08.099>.
- [1235] Katsushi M, Yasuhiro A, Hidemasa T, Hikaru I, Masataka M, Hideki A. Effects of Zn addition and aging condition on serrated flow in Al-Mg alloys. *Mater Sci Forum* 2014;794–796:483–8. <https://doi.org/10.4028/www.scientific.net/MSF.794-796.483>.
- [1236] Yun J, Kang S, Lee S, Bae D. Development of heat-treatable Al-5Mg alloy sheets with the addition of Zn. *Mater Sci Eng A* 2019;744:21–7. <https://doi.org/10.1016/j.msea.2018.11.145>.
- [1237] Matsumoto K, Aruga Y, Tsuneishi H, Iwai H, Mizuno M, Araki H. Effects of precipitation state on serrated flow in Al-Mg-(Zn) alloys. *Mater Trans* 2016;57:1101–8. <https://doi.org/10.2320/matertrans.L-M2016814>.

- [1238] Meng CY, Zhang D, Liu PP, Zhuang LZ, Zhang JS. Microstructure characterization in a sensitized Al–Mg–Mn–Zn alloy. *Rare Met* 2018;37:129–35. <https://doi.org/10.1007/s12598-015-0665-4>.
- [1239] Stember L, Tunes MA, Dumitraschkewitz P, Mendez-Martin F, Tosone R, Marchand D, et al. Giant hardening response in AlMgZn(Cu) alloys. *Acta Mater* 2021;206. <https://doi.org/10.1016/j.actamat.2020.116617>.
- [1240] Geng Y, Zhang D, Zhang J, Zhuang L. On the suppression of Lüders elongation in high-strength Cu/Zn modified 5xxx series aluminum alloy. *J Alloys Compd* 2020;834:155138.
- [1241] Cao C, Zhang D, Zhuang L, Zhang J. Improved age-hardening response and altered precipitation behavior of Al-5.2Mg-0.45Cu-2.0Zn (wt%) alloy with pre-aging treatment. *J Alloys Compd* 2017;691:40–3. <https://doi.org/10.1016/j.jallcom.2016.08.206>.
- [1242] Cao C, Zhang D, He Z, Zhuang L, Zhang J. Enhanced and accelerated age hardening response of Al-5.2Mg-0.45Cu (wt%) alloy with Zn addition. *Mater Sci Eng A* 2016;666:34–42. <https://doi.org/10.1016/j.msea.2016.04.022>.
- [1243] Hou S, Liu P, Zhang D, Zhang J, Zhuang L. Precipitation hardening behavior and microstructure evolution of Al-5.1 Mg-0.15Cu alloy with 3.0Zn (wt%) addition. *J Mater Sci* 2018;53:3846–61. <https://doi.org/10.1007/s10853-017-1811-1>.
- [1244] Hou S, Zhang D, Ding Q, Zhang J, Zhuang L. Solute clustering and precipitation of Al-5.1Mg-0.15Cu-xZn alloy. *Mater Sci Eng A* 2019;759:465–78. <https://doi.org/10.1016/j.msea.2019.05.066>.
- [1245] Cao C, Zhang D, Wang X, Ma Q, Zhuang L, Zhang J. Effects of Cu addition on the precipitation hardening response and intergranular corrosion of Al-5.2Mg-2.0Zn (wt.%) alloy. *Mater Charact* 2016;122:177–82. <https://doi.org/10.1016/j.matchar.2016.11.004>.
- [1246] Zhu S, Li Z, Yan L, Li X, Huang S, Yan H, et al. Effects of Zn addition on the age hardening behavior and precipitation evolution of an Al-Mg-Si-Cu alloy. *Mater Charact* 2018;145:258–67. <https://doi.org/10.1016/j.matchar.2018.08.051>.
- [1247] Zhu S, Li Z, Yan L, Li X, Huang S, Yan H, et al. Effect of Zn addition on two-step aging behaviour of Al–Mg–Si–Cu alloy. *Mater Sci Technol (United Kingdom)* 2019;35:1291–300. <https://doi.org/10.1080/02670836.2019.1621724>.
- [1248] Glöckel F, Uggowitzer PJ, Felfer P, Pogatscher S, Höppel HW. Influence of Zn and Sn on the precipitation behavior of new Al-Mg-Si alloys. *Materials (Basel)* 2019;12. Doi: 10.3390/ma12162547.
- [1249] Ding XP, Cui H, Zhang JX, Li HX, Guo MX, Lin Z, et al. The effect of Zn on the age hardening response in an Al-Mg-Si alloy. *Mater Des* 2015;65:1229–35. <https://doi.org/10.1016/j.matdes.2014.09.086>.
- [1250] Haga T, Ikawa M, Watari HS. High speed twin roll casting of recycled Al-3Si-0.6 Mg strip. *J Achiev Mater Manuf Eng* 2007;21:7–12.
- [1251] Haga T, Imamura S, Fuse H, Watari H, Nishida S. Roll casting and die casting of si-added al-mg alloy. *Mater. Sci. Forum*, vol. 1007 MSF, 2020, p. 12–7. Doi: 10.4028/www.scientific.net/MSF.1007.12.
- [1252] Otani Y, Sasaki S. Effects of the addition of silicon to 7075 aluminum alloy on microstructure, mechanical properties, and selective laser melting processability. *Mater Sci Eng A* 2020;777. Doi: 10.1016/j.msea.2020.139079.
- [1253] Mangos J, Birbilis N. Computational alloy design and discovery using machine learning. *ArXiv:210514806* 2021.
- [1254] Zhang R, Li J, Li Q, Qi Y, Zeng Z, Qiu Y, et al. Analysing the degree of sensitisation in 5xxx series aluminium alloys using artificial neural networks: A tool for alloy design. *Corros Sci* 2019;150:268–78. <https://doi.org/10.1016/j.corsci.2019.02.003>.
- [1257] Davis JR. Aluminum and aluminum alloys. Alloying: understanding the basics. ASM International; 2001. p. 351–416. ISBN: 978-0-87170-744-4.
- [1258] Belov NA, Aksenen AA, Eskin DG. Phase diagrams of iron-containing aluminum alloys. Iron in aluminum alloys. Taylor & Francis; 2002. p. 1–90. ISBN: 0-415-27352-8.